

General Disclaimer

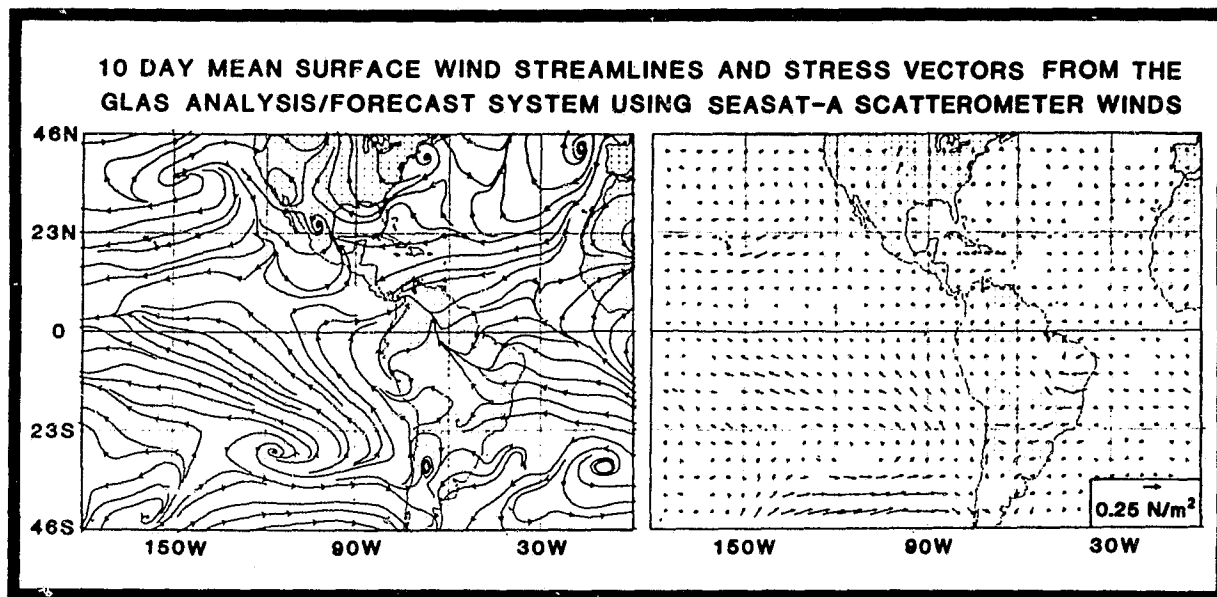
One or more of the Following Statements may affect this Document

- This document has been reproduced from the best copy furnished by the organizational source. It is being released in the interest of making available as much information as possible.
- This document may contain data, which exceeds the sheet parameters. It was furnished in this condition by the organizational source and is the best copy available.
- This document may contain tone-on-tone or color graphs, charts and/or pictures, which have been reproduced in black and white.
- This document is paginated as submitted by the original source.
- Portions of this document are not fully legible due to the historical nature of some of the material. However, it is the best reproduction available from the original submission.



Technical Memorandum 86053

RESEARCH REVIEW-1983



GLOBAL MODELING AND SIMULATION BRANCH
LABORATORY FOR ATMOSPHERIC SCIENCES

JANUARY 1984

National Aeronautics and
Space Administration

Wallops Space Flight Center
Wallops, Maryland 20771



TM 86053

RESEARCH REVIEW - 1983

GLOBAL MODELING AND SIMULATION BRANCH
LABORATORY FOR ATMOSPHERIC SCIENCES

JANUARY 1984

NASA GODDARD SPACE FLIGHT CENTER
GREENBELT, MARYLAND 20771

TABLE OF CONTENTS

I. INTRODUCTION

II. GLOBAL WEATHER/OBSERVING SYSTEMS

A. Analysis and Forecast Studies

Simulation Studies of Proposed Observing Systems and Their Impact on Numerical Weather Prediction . . R. Atlas, E. Kalnay, J. Susskind, W. Baker, and M. Halem 1 ✓

Evaluation of the GLAS Model Precipitation Forecasts for North America during SOP-1 . . R. Atlas and J. Firestone 2 ✓

Observing System Simulation Experiments Related to Space-Borne LIDAR Wind Profiling. Part 1: Forecast Impacts of Highly Idealized Observing Systems . . M. Halem and R. Dlouhy 5 ✓

Observing System Simulation Experiments Related to Space-Borne LIDAR Wind Profiling. Part 2: Sensitivity to Atmospheric and Instrumental Influences . . M. Halem and R. Dlouhy 6 ✓

FGGE Data Impact Studies in the Southern Hemisphere . . E. Kalnay, R. Atlas, W. Baker and M. Halem 7 ✓

SASS Wind Forecast Impact Studies Using the GLAS and NEPRF Systems: Preliminary Conclusions . . E. Kalnay, R. Atlas, W. Baker, D. Duffy, M. Halem and H. M. Helfand 14 ✓

B. Satellite Observing Systems

Regional Correlation Between TOMS Total Ozone from NIMBUS-7 Satellite and Geopotential Height from the GLAS Analysis . . M.-J. Munteanu, P. Piraino, and E. Kalnay 23 ✓

Comparison of AMSU Temperature Soundings with those Produced by HIRS and AMTS D. Reuter and J. Susskind 28 ✓

Water Vapor Profile Retrieval Simulation Studies for the HIRS/MSU and AMTS/MSU Sounders . . D. Reuter and J. Susskind 33 ✓

Results of the Joint NASA/NOAA AMTS/HIRS2 Sounding Simulation Test . . J. Susskind and D. Reuter 41 ✓

Improved HIRS2/MSU Soundings using Tropopause Information . . J. Susskind, M.-J. Munteanu, and P. Piraino 45 ✓

Comparison of GLAS Retrieved Cloud Fields with Model Generated Rainfall Fields J. Susskind and E. Kalnay 49 ✓

High Resolution GLAS Retrievals on the McIDAS . . . J. Susskind, R. Atlas, and A. Pursch	53 ✓
A New Algorithm for Tuning of Computed Radiances for HIRS2/MSU . . . J. Susskind, P. Piraino, and D. Reuter	60 ✓
The Prediction of Tropopause Height from Clusters of Brightness Temperatures and its Application in the Stratified Regression Temperature Retrievals using Microwave and Infrared Satellite Measurements . . M.-J. Munteanu, P. Piraino, and O. Jacobowicz	65 ✓
Applications of Cluster Analysis to Satellite Soundings . . M.-J. Munteanu, O. Jacobowicz, E. Kalnay and P. Piraino	68 ✓
 C. Analysis and Model Development	
Effect of High Latitude Filtering on NWP Skill . . E. Kalnay, L. L. Takacs, and R. Hoffman	79 ✓
The Effect of Compact Implicit Differencing in a Baroclinic Primitive Equations Model . . J. Augenbaum, S. Cohn and D. Marchesin	87 ✓
A Lagrangian Method for a Two Layer Shallow Water Model . . J. Augenbaum	90 ✓
Multivariate Optimum Interpolation of Surface Pressure and Winds Over Oceans S. Bloom	95 ✓
Design of a Linear Projector for use with the Normal Modes of the GLAS 4th Order GCM . . S. Bloom	101 ✓
Computational Aspects of the Nonlinear Normal Mode Initialization of the GLAS 4th Order GCM . . I. M. Navon, S. Bloom, and L. L. Takacs	106 ✓
A User-Friendly Operating System for the GLAS 4th Order Forecast-Analysis System . . J. Pfaendtner	113 ✓
Empirically Derived Second Order Schemes for the Advection Equation with Minimum Dissipation and Dispersion Errors . . L. L. Takacs	119 ✓
On the Effect of Using the Shapiro Filter to Smooth Winds on a Sphere . . L. L. Takacs, and R. C. Balgovind	131 ✓
 D. Atmospheric Dynamics and Diagnostic Studies	
Lagged Average Forecasting, Some Operational Considerations . . R. Hoffman and E. Kalnay	141 ✓
Weather Predictability Beyond a Week: An Introductory Review . . E. Kalnay and R. Livezey	149 ○

Application of Augmented-Lagrangian Methods in Meteorology: Comparison of Different Conjugate-Gradient Codes for Large Scale Minimization . . . I. M. Navon	150 ✓
Predictability Experiments Using a Low Order Empirically Corrected Dynamical Model . . S. Schubert	157 ✓
Investigation of the Equatorial Orographic-Dynamic Mechanism Applying the Bounded Derivative Method . . F. H. M. Semazzi	164 ✓

III. CLIMATE/OCEAN-AIR INTERACTIONS

A. Data Analysis

Postprocessing of the UCLA Climate Model . . J. Abeles, E. Pittarelli, D. Randall, and M. Suarez	171 ✓
The Growth, Propagation and Decay of Global Scale Rossby Waves during FGGE R. S. Lindzen, D. M. Straus, and B. Katz	175 ✓
Interannual Variability of Indian Monsoon Rainfall . . D. Paolino and J. Shukla	180 ✓
The Simulation of Transient Statistics of the Southern Hemispheric Circulation by the GLAS Seasonal Cycle Model: Preliminary Results . . D. M. Straus and J. Shukla	185 ✓
Localized Blocking Accounted for by Slow Variations of the Zonal Driving K. Mo	190 ✓
Teleconnection Patterns in the Southern Hemisphere . . K. Mo and G. H. White	193 ✓
Ocean Fluxes Simulated by the GLAS GCM . . Y. Sud and J. Shukla	196 ✓
On the Role of the Transient Eddies in Maintaining the Seasonal Mean Circulation . . G. H. White and B. J. Hoskins	205 ✓
Two Contrasting Northern Hemisphere Winters: 1980-1981 and 1981-1982 . . G. H. White	209 ✓

B. Climate Modeling

Prospects for Improvement of Zonal Mean Temperatures in the UCLA General Circulation Model . . T. Corsetti, M. Suarez, and D. Randall	215 ✓
Forced Stationary Solutions in a Barotropic Channel: Multiple Equilibria and Theory of Nonlinear Resonance . . S. Rambaldi, K. Mo, and J. Shukla . . .	219 ✓
Stratocumulus Simulations with a General Circulation Model . . D. Randall, J. Abeles, and M. Suarez	222 ✓

Climate Sensitivity with a Seasonal Cycle Energy Balance Model . . M. Suarez	227 ✓
Design for an Efficient Dynamic Climate Model with Realistic Geography . . M. Suarez and J. Abeles	231 ✓
Design of Coupled Ocean-Atmosphere Experiments . . M. Suarez and P. Schopf	233 ✓
Long-Term Dynamical Stability and Transition in a Spectral Model . . R. L. Wobus	239 ✓
Diagnosis of the GLAS Climate Model's Stationary Planetary Waves Using a Linearized Steady State Model . . C. Youngblut	243 ✓
Horizontal Energy Propagation in a Baroclinic Atmosphere with Meridional and Zonal Structure . . C. Youngblut	245 ✓
A One-Column Model with Detailed Physical Parameterizations . . T. Corsetti, and D. Randall	247 ✓

C. Processes and Parameterization

Development and Preliminary Tests of a New Long-Wave Radiation Parameteriza- tion . . Harshvardhan, T. Corsetti, D. Randall, and M. Suarez	251 ✓
Simulations of the Stratocumulus-Topped Boundary Layer with a Third-Order Closure Model . . C.-H. Moeng and D. Randall	254 ✓
Problems with the Process Partitioning Theory of Stratocumulus Entrainment D. Randall	257 ✓
Can Cloud-Top Entrainment Promote Cloud Growth? . . D. Randall	261 ✓
On the Joint Bimodality of Temperature and Moisture near Stratocumulus Cloud Tops . . D. Randall	266 ✓
An Ensemble Formulation of PBL Fluxes in a GCM . . Y. Sud and W. E. Smith	270 ✓
A Note on the Temporal Behavior of Bucket Hydrologies . . M. Suarez	275 ✓
Time Dependent Land and Vegetation Canopy Temperatures Y. Sud	285 ✓
A New Parameterization of 15 Micron Radiative Transfer for a GCM . . R. L. Wobus, J. Susskind, and Man-Li Wu	292 ✓

D. Sensitivity Experiments

GCM Sensitivity to 1982-83 Equatorial Pacific SST Anomalies M. J. Fennessy, L. Marx, and J. Shukla	301 ✓
Impact of Prescribed Diabatic Heating on Short Range Weather Forecasts L. Marx and J. Shukla	312 ✓

The Sensitivity of a General Circulation Model to Saharan Dust Heating . . . 323 ✓
D. Randall, T. Carlson, and Y. Mintz

Influence of Surface Roughness of a Desert . . Y. Sud and W. E. Smith 329 ✓

Role of Soil Moisture in Maintaining Droughts . . Y. Sud and W. E. Smith . . . 335 ✓

E. Software Development

An Asynchronous mlink for use with the UCLA Climate Model . . J. Abeles . . . 343 0

IV. SUMMER LECTURE SERIES

A Dynamical Basis for the Parameterization of Organized Deep Convection
in Large-Scale Numerical Models . . M. W. Moncrieff 347 ✓

Some Properties of Transient Phenomena in the Extra-Tropical Region and
their Importance in the Seasonal Mean Flow . . B. J. Hoskins 349 ✓

Low Frequency Variability and Tropical-Extra tropical Interactions . .
D. L. Hartmann 350 ✓

V. RECENT PUBLICATIONS 353 0

VI. GMSB STAFF 359 0

VII. AUTHOR INDEX 363 0

I. INTRODUCTION

I. INTRODUCTION

The Global Modeling and Simulation Branch (GMSB) of the Laboratory for Atmospheric Sciences (GLAS) is engaged in general circulation modeling studies related to global atmospheric and oceanographic research. The research activities are organized into two disciplines: Global Weather/Observing Systems and Climate/Ocean-Air Interactions.

The Global Weather activities are grouped in four areas: 1) Analysis and Forecast Studies, 2) Satellite Observing Systems, 3) Analysis and Model Development, 4) Atmospheric Dynamics and Diagnostic Studies.

The GLAS Analysis/Forecast/Retrieval System was applied to both FGGE and post FGGE periods. The resulting analyses have already been used in a large number of theoretical studies of atmospheric dynamics, forecast impact studies and development of new or improved algorithms for the utilization of satellite data. The results obtained with the GLAS temperature retrieval system are particularly noteworthy: not only are the atmospheric temperature soundings quite accurate, but as a by-product, remarkably accurate determinations of land and sea surface temperatures, cloud cover, height and temperatures, and snow and ice extent have been obtained from operational TIROS-N sounders.

Climate research has concentrated on the simulation of global cloudiness, and on the sensitivity of the climate to sea surface temperature and ground wetness anomalies. Simulations with a new climate model have produced remarkably realistic cloud distributions, reproducing the observed distributions of cloud type, amount, and height. A variety of off-line studies have been conducted to interpret these results, and to provide a basis for further improvements in the simulated cloud climatology. An extended numerical simulation has demonstrated the global model's ability to simulate the response of the atmosphere to observed sea surface temperature anomalies in the equatorial Pacific. These results suggest that the observed El Nino-Southern Oscillation fluctuations of the climate may be predictable. They pave the way for coupled ocean-atmosphere modeling experiments. Finally, sensitivity studies have shown that the regional circulations associated with droughts and deserts may be partly explained by the distinctive low ground wetness and smooth surface of the deserts themselves.

Ocean studies have focused on the analysis of long-term global sea surface temperature data, for use in the study of the response of the atmosphere to sea surface temperature anomalies.

This research review contains a synopsis of extended abstracts in the Global Weather/Observing System studies, and Climate/Ocean-Air Interaction studies conducted at the Modeling and Simulation Branch for 1983 (Sections II and III). Section IV contains abstracts of the Summer Lecture Series, jointly sponsored by GMSB and the University of Maryland. Section V lists the recent publications by the GMSB and visiting scientists.

II. GLOBAL WEATHER/OBSERVING SYSTEMS

A. ANALYSIS AND FORECAST STUDIES

I. INTRODUCTION

SIMULATION STUDIES OF PROPOSED OBSERVING SYSTEMS AND THEIR IMPACT ON
NUMERICAL WEATHER PREDICTION

R. Atlas, E. Kalnay, J. Susskind, W. E. Baker, and M. Halem

A series of realistic simulation studies is being conducted as a cooperative effort between the European Centre for Medium Range Weather Forecasts (ECMWF), the National Meteorological Center (NMC), and the Goddard Laboratory for Atmospheric Sciences (GLAS) to provide a quantitative assessment of the potential impact of proposed observing systems on large scale numerical weather prediction. A special objective of this project is to avoid the unrealistic character of earlier simulation studies.

The simulation system consists of four essential elements: 1) A long atmospheric model integration to provide a complete record of the simulated "true" state of the atmosphere. This "nature" run is used to fabricate observations and to evaluate forecasts. In order to avoid the "identical twin" character of previous studies, the high resolution ($1.875^\circ \times 1.875^\circ \times 15$ levels) ECMWF model was used to generate the nature run, while the $4^\circ \times 5^\circ \times 9$ levels GLAS model is being used for assimilation and forecasting. 2) Conventional, and remotely sensed observations are being generated from the nature run by NMC and GLAS, taking care to simulate realistically observational errors. In particular, we will generate temperature retrievals by first simulating the radiances that would be observed from the nature's temperature profiles, taking into account effects such as clouds, and then invert the radiance observations using the GLAS retrieval algorithms. 3) Two analysis/forecast cycles will be performed, a control experiment which includes only currently available observations, and an enhanced experiment which in addition includes simulated data corresponding to a proposed future observing system. 4) Forecasts from the two analyses will be performed and compared with the nature run in order to provide an assessment of the proposed satellite observing system.

This study is being conducted in two phases. In the first phase, we are repeating with the simulation system real data impact studies of the type already performed with the FGGE observing system by Halem et al. (1982). This will provide a calibration of the simulation system, and an estimate of its realism. If the results of the first part are satisfactory, we will then test the impact of future observing instruments. The control experiment will then be the present observing system (conventional data, TIROS-N temperature retrievals and cloud tracked winds). The advanced systems will include both satellite temperature sounders (AMTS and AMSU), and lidar wind profilers (WINDSAT).

D2

N84 22051

EVALUATION OF GLAS MODEL PRECIPITATION FORECASTS FOR NORTH AMERICA DURING SOP-1

R. Atlas and J. Firestone

A study has been made of the accuracy of the GLAS fourth order forecast model's precipitation forecasts over North America during the first Special Observing Period (SOP-1) of FGGE and of the impact of the FGGE special observing systems on these forecasts. Fourteen 120 h predictions were generated using the coarse 4° latitude by 5° longitude version of the GLAS model from both the FGGE and NOSAT assimilation cycles, previously described by Halem et al. (1982). These forecasts were then verified against a detailed set of precipitation observations obtained from the Techniques Development Laboratory of the National Weather Service.

Separate verifications were performed for precipitation accumulations > .01 in., > .1 in., and > 1 in. occurring in 6, 12 and 24 time periods. In addition, three different methods of verification were applied. In the first method, model precipitation forecasts are verified against the greatest precipitation amount observed within a 4° latitude by 5° longitude gridbox centered on each gridpoint. For the prediction at a gridpoint to be verified only one observation within the gridbox is required. In the second method, a weighted mean of the closest observations to the gridpoint is used, provided that at least two observations on opposite sides of a gridpoint are available. For the third method, the model precipitation forecasts were interpolated to the observation locations.

The first two methods attempt to minimize the small scale variability of precipitation processes by assuming that the model predictions are representative of either the average precipitation in the vicinity of a gridpoint or the maximum precipitation for a gridbox. The third method does not and hence is the most difficult to verify.

For reasons of brevity the verification statistics presented here will be limited to 24 h accumulations from the NOSAT forecasts using only the second method of verification (i.e. weighted mean of observations to the model grid points).

Figs. 1 and 2 present the model's accuracy in forecasting precipitation > .01 in., and > .1 in. in a 24 h period. Plotted in the lower portion of each figure are the total number of points at which precipitation in the given category was forecast (PF), the total number of points at which precipitation in the given category was observed (PO), and the total number of points at which precipitation in the given category was forecast correctly (FC).

The ratio PF/PO is the bias and represents the degree to which the model overforecasts or underforecasts the extent of precipitation. This is indicated by the distance between the PF and PO curves on the graph. FC/PO is called the prefigurence and measures the areal extent of precipitation that is correctly forecast in each category; FC/PF is the post agreement and measures the percentage of precipitation forecasts which verify. These latter measures are represented by the distance between the FC and PO curves and FC and PF curves, respectively. The bias, prefigurence, and post agreement are combined into a single ratio,

known as the threat score (T_h) which is plotted in the upper portion of the figures. The threat score is defined as follows:

$$T_h = F_c / (P_F + P_O - F_C)$$

Values of threat score range from zero to one with higher values denoting increasing accuracy. In addition to the threat score for the model, the threat score for a random selection of forecast points is also plotted. Since this may be considered as a "no skill" prediction, differences between these threat scores would be representative of the model's skill in forecasting precipitation.

From the figures, it can be seen that for the first two time periods, the model predicts precipitation in the appropriate category at almost all of the points at which precipitation of that category is observed (as measured by the prefigurence) and that a gradual decrease in the prefigurence occurs thereafter. However the model greatly overforecasts the areal extent of precipitation, yielding low values of the post agreement at all time periods. The number of points at which precipitation is forecast increases from 24-48 h and does not change very substantially in the later time periods.

The model threat scores are highest during the first time period but decrease dramatically due to the increase bias of the forecasts. For the 0.01 in. category, the model threat scores decrease slowly from 48-96 h but increase during the last period. For the .1 in. category, the model threat scores decrease slowly from 48-120 h. Most of the variability in threat scores is associated with changes in bias.

The model possesses moderate skill in predicting precipitation $\geq .01$ in. in the first time period, as measured by the difference between model and random threat scores. But the amount of improvement is reduced by about 50% by 48 h and remains at this level throughout the remainder of the forecast. For the .1 in. category, moderate skill relative to a random forecast is evident at 24 and 48 h afterwhich a progressively smaller amount of skill remains.

Verification of the 1 in. category with this method is not presented because the averaging process did not result in any observations of precipitation > 1 in. at model gridpoints. Preliminary verification using the other methods however, did show a very small amount of skill ($< .1$ improvement in threat score over a random forecast) through the first four time periods. Substantial differences between the methods were evident in the .01 and .1 in. categories. Method 1 consistently gave the highest threat scores. Method 3 gave the lowest threat scores for precipitation $\geq .01$ in. but was comparable to method 2 for precipitation $\geq .1$ in.

Preliminary evaluation of forecasts from the FGGE data assimilation cycle showed that on the average, the FGGE satellite data sets had a negligible impact on model precipitation forecasts over North America.

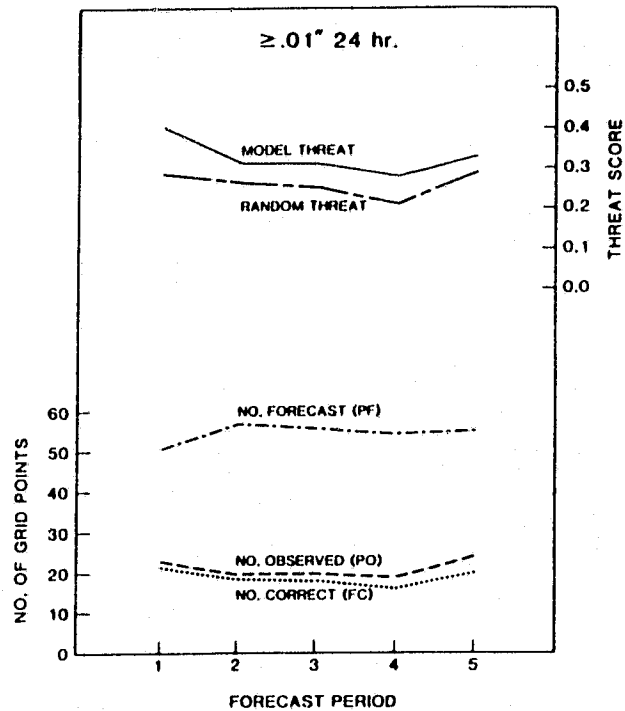


Fig. 1. Average verification results for 14 forecasts of precipitation of at least .01 in. in a 24 h period.

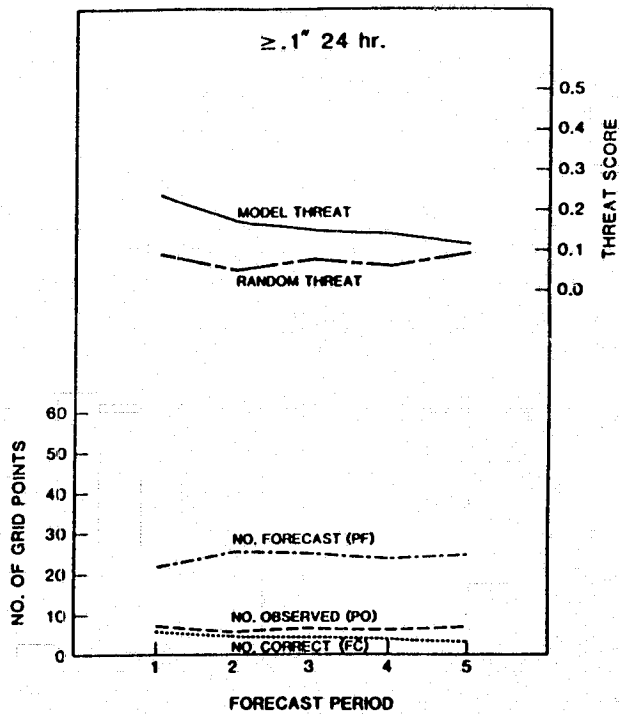


Fig. 2. Same as Fig. 1 for .1 in.

OBSERVING SYSTEM SIMULATION EXPERIMENTS RELATED TO SPACE-BORNE LIDAR WIND
PROFILING. PART 1: FORECAST IMPACTS OF HIGHLY IDEALIZED OBSERVING SYSTEMS

M. Halem and R. Dlouhy

Simulation experiments comparing the relative importance of an idealized LIDAR wind profiling system with idealized temperature and pressure sounding systems on 12 h forecasts are studied for three "nature" fields representing the true evolving atmospheric states. The three fields are obtained respectively from: (i) a long integration of the GLAS 4th Order Model (4° lat x 5° lon x 9 levels), (ii) a continuous sequence of NMC operational analysis and, (iii) a long integration of the ECMWF high resolution (1.875° lat x 1.875° long x 15 layers) operational forecast model. These fields are interpolated to the grid of the GLAS model and used for simulating the observed global analysed fields of winds, temperature, moisture and surface pressure. The same interpolated fields are also used for verification of forecast impact. The effects of clouds, aerosol concentrations, and instrument accuracies on the simulated observation will be discussed in Part 2.

The experiments compare the inferred 12 h forecast fields assuming perfect, complete, instantaneous global wind fields with similar forecasts inferred from completely perfect temperature, moisture, surface pressure, and surface wind fields.

Results show that the LIDAR wind fields infer most meteorological fields in the extratropics significantly more accurately than fields inferred from other meteorological observing systems. The results obtained are consistent for all three "nature" fields. The 12 h forecast errors in the extratropics from wind data alone are almost as accurate as that obtained from the complete specification of all initial conditions. In the tropics, only the LIDAR wind system showed the capability to infer 12 h forecast winds. In addition to statistical evaluations, diagnostic difference maps are presented and analyzed. The studies also demonstrate that while identical twin experiments provide optimistic performance estimates, the conclusions are borne out, even for real data experiments.

24
N84 22053

OBSERVING SYSTEM SIMULATION EXPERIMENTS RELATED TO SPACE-BORNE LIDAR WIND
PROFILING. PART 2: SENSITIVITY TO ATMOSPHERIC AND INSTRUMENTAL INFLUENCES

R. Dlouhy and M. Halem

Three major potential sources of errors that influence the performance of the proposed LIDAR wind profiling systems are accounted for in the following simulation studies.

First, the coherent CO₂ laser system proposed by NOAA/ERL for the WINDSAT requires distributions of 10 μ size aerosol concentrations throughout the atmosphere to determine the doppler shifted backscatter signal. It is generally agreed that while there are probably sufficient aerosol concentrations in the boundary layers and in the stratosphere, there may be insufficient concentrations at high latitudes and in the mid-tropospheres over oceans. Experiments are being performed assuming inadequate signal return for complete global wind determinations in these regions.

Second, atmospheric influences such as clouds and precipitation affect the LIDAR system's ability to obtain complete vertical wind profiles. In this study, we report on experiments in which the complete wind profiles are only available in model generated cloud-free regions down to model cloud tops.

Third, constraints on the available power required for the expected operational lifetime duration of a LIDAR system govern the number of pulses which can be used to sample a 300 km square area. The number of pulses gives radial velocities per model grid and is directly related to the expected errors of mean wind speed. We are conducting two experiments in which we assign random error levels of 3 m/s and 6 m/s, corresponding to 2 pulses or 10 pulses per grid area. These errors are randomly added to the LIDAR wind profiles used in the experiments described earlier. Observation error estimates of temperature and moisture sounding systems will also be added to the idealized systems for comparison with LIDAR wind systems.

FGGE DATA IMPACT STUDIES IN THE SOUTHERN HEMISPHERE

E. Kalnay, R. Atlas, W. Baker and M. Halem

1. INTRODUCTION

The FGGE Special Observing System produced a larger improvement in forecast skill in the Southern Hemisphere than in the Northern Hemisphere (Halem *et al.*, 1983, Bengtsson *et al.*, 1982, Guymer and LeMarshall, 1981). This is not surprising given the vast coverage gaps that the conventional network of upper air observations has in the mostly oceanic Southern Hemisphere, even during FGGE. In the Northern Hemisphere, on the other hand, the conventional upper air network falls below the 500 km density suggested by GARP only in the Pacific and Atlantic Oceans and in the tropics (see, for example, Fig. 6 of Halem *et al.*, 1982).

Of the three major components of the FGGE Special Observing System (SOS), TIROS-N satellite temperature soundings, geostationary satellite cloud-track winds, and drifting buoys, only the drifting buoys no longer exist. The purpose of this paper is to quantify the impact of the FGGE SOS on the GLAS analyses and forecasts in the Southern Hemisphere, and to evaluate the relative importance of its components, and in particular, the impact of the loss of surface buoys.

2. GLAS ANALYSIS/FORECAST SYSTEM USED IN THE EXPERIMENTS

The Analysis/Forecast System used in the experiments reported here is very similar to that of Halem *et al.* (1982). Several modifications were made in the analysis scheme, the most important being the interpolation of the analysis minus 6 h forecast deviations rather than of the analyzed fields themselves. The analysis scheme with the present modifications is described in detail in Baker (1983).

The forecast model is the 4° lat, but 5° lon, with 9 vertical levels GLAS Fourth Order Model (Kalnay-Rivas *et al.*, 1976), also used in Halem *et al.* (1982). During the analysis cycle, a Matsuno time scheme is used to eliminate high frequency gravity waves, in a procedure analogous to dynamic initialization with physical processes included.

It should be noted that the new GLAS Analysis/Forecast system, based on a three-dimensional, multivariate optimal interpolation analysis scheme, and a 2° x 2.5° x 15 level fourth order model will be implemented in the near future.

3. DESCRIPTION OF THE EXPERIMENTS

Two series of analyses were performed for both the first and second FGGE Special Observing Periods, SOP-1, from 5 January to 5 March and SOP-2, from 1

May to 30 June 1979. In one, denoted as in Hålem *et al.*, 1982, the "FGGE" analysis, all Level II-b conventional and special data collected and reformatted in Sweden, were utilized. The second analysis, denoted "NOSAT", made use of only surface data (without drifting buoys), and conventional upper air data (rawinsondes, pilot balloons, and aircraft data).

Fourteen 5 day forecasts were obtained using initial conditions from each analysis. The initial conditions are separated by four days in order to ensure independence in the results.

Two other series of experiments have been partially completed: In the first one, denoted "FGGE minus buoys" the same data base as "FGGE" was utilized except that the buoys were not included. In the second, "NOSAT plus buoys," all the buoy data were added to the "NOSAT" observations. The purpose of these dual experiments is to determine not only the impact of the information provided to the analysis by the buoys but whether the buoys are redundant with other observing systems components still in operation from FGGE. At the time of this writing, we have only partially completed the last two experiments for the SOP-1.

4. FORECAST IMPACT RESULTS

In this paper, we limit ourselves to the discussion of the forecast impact of the FGGE system upon a region between 28°S and 56°S, 50°W-80°W which includes essentially the southern cone of South America. Although forecast skill is verified against the NMC analysis, which used only VTPR but no TIROS-N data in the Southern Hemisphere, enough conventional data exists over this region to avoid biased verifications.

Figures 1a and 1b shows the 24 h and 72 h forecast skill scores over South America for 14 cases made from the FGGE and NOSAT analyses during SOP-1. Similar comparisons for SOP-2 are presented in Figures 1c and 1d. The improvement in forecast skill resulting from the use of the FGGE SOS is striking, both in sea level pressure and 500 mb height fields. These results show a positive impact which is statistically significant within 99% confidence limits.

Figures 1e and 1f present the forecast impact of adding the buoys to the very sparse NOSAT observing system, for a more limited set of 6 forecasts. Here we observe positive impacts at 500 mb which are significant at a 95% confidence level, but less significant at sea level pressure. The mean improvement, however, is smaller than the improvement gained from the SOS. The addition of the buoys seems to have improved the NOSAT forecasts, especially at 3 days. Figures 1g and 1h estimate the loss of forecast skill due to withdrawal of the buoys from the complete FGGE system, for a set of 7 forecasts. No apparent impact, positive or negative, can be inferred from the withdrawal of the data either at one or three days. This indicates that, at least for the present analysis/forecast system, the positive impact due to buoys' surface observations, becomes redundant when satellite temperature profiles and winds are also utilized.

Table 1 compares the average forecast skill obtained from FGGE and NOSAT forecasts during SOP-1 and SOP-2. They indicate that in both summer and winter

the improvement due to the FGGE SOS is such that the three day forecast from the FGGE analyses exhibits skill comparable or better to that of the one day NOSAT forecast. Furthermore, it is important to note that the standard deviation of the FGGE forecasts' skill during the southern summer is also 30%-40% smaller than the standard deviation of the NOSAT forecast, indicating that the FGGE forecasts are consistently better and their skill much less variable. This consistency is less evident in the winter forecasts.

5. COMPARISON OF 72 H FORECASTS FROM 25 JAN 1979

As an example of the effect of FGGE data on Southern Hemisphere forecasting we present the 72 h forecasts from 0000 GMT 25 January 1979. This case illustrates the impact of the FGGE special observing systems as well as the relative importance of buoy data. Figs. 2a and 2b shows the 72 h control and FGGE sea level pressure prognoses, while Figs. 2c and 2d show the corresponding forecasts from the control plus buoy data and FGGE minus buoy data assimilation respectively. The verifying NMC analysis at 0000 GMT 28 January is given in Fig. 2e.

Comparison of Figs. 2a and 2b shows that when all FGGE data are included there is a large improvement in the prediction of the high pressure system penetrating into the south of Chile and Argentina, as well as of the low east of the Andes. Similar improvements can be observed over Australia, although the FGGE forecast depicts too strong a trough. On the other hand, the NOSAT forecast is better in showing cyclonic circulation at about 45°S, 120°W.

Removal of buoy data from the FGGE system has very little effect (Fig. 2d), whereas the addition of the buoys improves the forecast over South America.

6. SYSTEMATIC DIFFERENCES BETWEEN THE FGGE AND NOSAT ANALYSES

We have seen that the instantaneous differences between the FGGE and NOSAT analyses lead to significantly different forecasts. When we study time averages, however, it becomes apparent that the differences between NOSAT and FGGE analyses are much smaller than the changes in the atmosphere itself. For example, Figs. 3a and 3b show the FGGE and NOSAT 200 mb relative vorticity averaged for the first 30 days of SOP-1 (5 Jan to 2 Feb 1979). Some systematic differences between the two analyses do exist. For example, the NOSAT analysis has underestimated the intensity of the belt of travelling cyclones in the roaring forties and fifties. Otherwise, the stationary waves are in good general agreement, although in the NOSAT analysis the January stationary waves over South America (Kalnay and Paegle, 1983) are underestimated, and a spurious cyclonic center appears near southwestern Africa. For comparison, the FGGE averaged 200 mb relative vorticity for the last 30 days of SOP-1 (3 Feb to 5 March 1979) is shown in Fig. 3c. Much larger changes in the position of stationary features are observed, and, for example, the stationary waves over South America, present in both the FGGE and NOSAT analyses in January, have disappeared in February.

The similarity between the average FGGE and NOSAT analyses extends also to quadratic quantities such as variances and covariances (not shown). This indicates that the analysis/forecast system has succeeded in bringing information from data rich into data sparse regions. Since the model has a reasonable climatology, the short range forecasts are able to give a good estimate of the state of the atmosphere even over the vast oceanic regions in the Southern Hemisphere, which would otherwise be "terra incognita."

This observation has an important implication: It is now possible to go back 20 or more years, and produce a continuous analysis of the global atmosphere using the surface and upper air observations available at that time, even if they were very sparse. This can be done with reasonable confidence that although individual synoptic features will be poorly represented in regions without data, the main monthly, seasonal and interannual variations will still be captured.

7. ACKNOWLEDGEMENTS

We are very grateful to the M/A-COM Sigma Data Staff that collaborated in carrying out this work, particularly D. Edlmann, J. Molini, R. Rosenberg, H. Carus, M. Almeida, M. Iredell, J. Jonker, and J. Woollen. The manuscript was prepared by L. Thompson, and the figures drafted by L. Rumburg.

REFERENCES

- Baker, W. E., 1983: Objective analysis and assimilation of observational data from FGGE. Mon. Wea. Rev., 111, 328-342.
- Bengtsson, L., M. Kanamitsu, P. Kallberg and S. Uppala, 1982: FGGE research activities at ECMWF. Bull. Am. Met. Soc., 63, 277-303.
- Guymer, L. B., and J. F. Le Marshall, 1981: Impact of FGGE buoy data on southern hemisphere analyses. Bull. Am. Met. Soc., 62, 38-47.
- Halem, M., E. Kalnay, W. E. Baker, and R. Atlas, 1982: An assessment of the FGGE satellite observing system during SOP-1. Bull. Am. Met. Soc., 63, 407-426.
- Kalnay-Rivas, E., A. Bayliss and J. Storch, 1977: The 4th order GISS model of the global atmosphere. Contrib. to Atmos. Phys., 50, 299-311.
- Kalnay, E., and J. Paegle, 1983: Large amplitude stationary waves in the southern hemisphere: Observations on Theory (Elsewhere in these proceedings).

Table 1: Ensemble forecast skill and standard deviation (in parentheses) for fourteen forecasts during SOP-1 and SOP-2.

ANALYSIS DESCRIPTION	S L P			500 mb		
	24h	48h	72h	24h	48h	72h
FGGE (SOP-1)	55.5 (5.6)	61.4 (7.9)	62.8 (10.2)	46.2 (4.9)	48.2 (6.8)	48.0 (6.6)
NOSAT (SOP-1)	63.4 (9.7)	69.6 (11.0)	74.0 (15.2)	56.6 (7.8)	59.6 (10.7)	58.6 (10.3)
FGGE (SOP-2)	59.9 (10.4)	66.1 (9.5)	69.6 (16.9)	37.9 (7.3)	47.2 (9.2)	47.8 (8.9)
NOSAT (SOP-2)	67.1 (8.8)	75.0 (14.7)	74.9 (16.6)	43.3 (8.2)	53.7 (7.2)	55.7 (8.0)

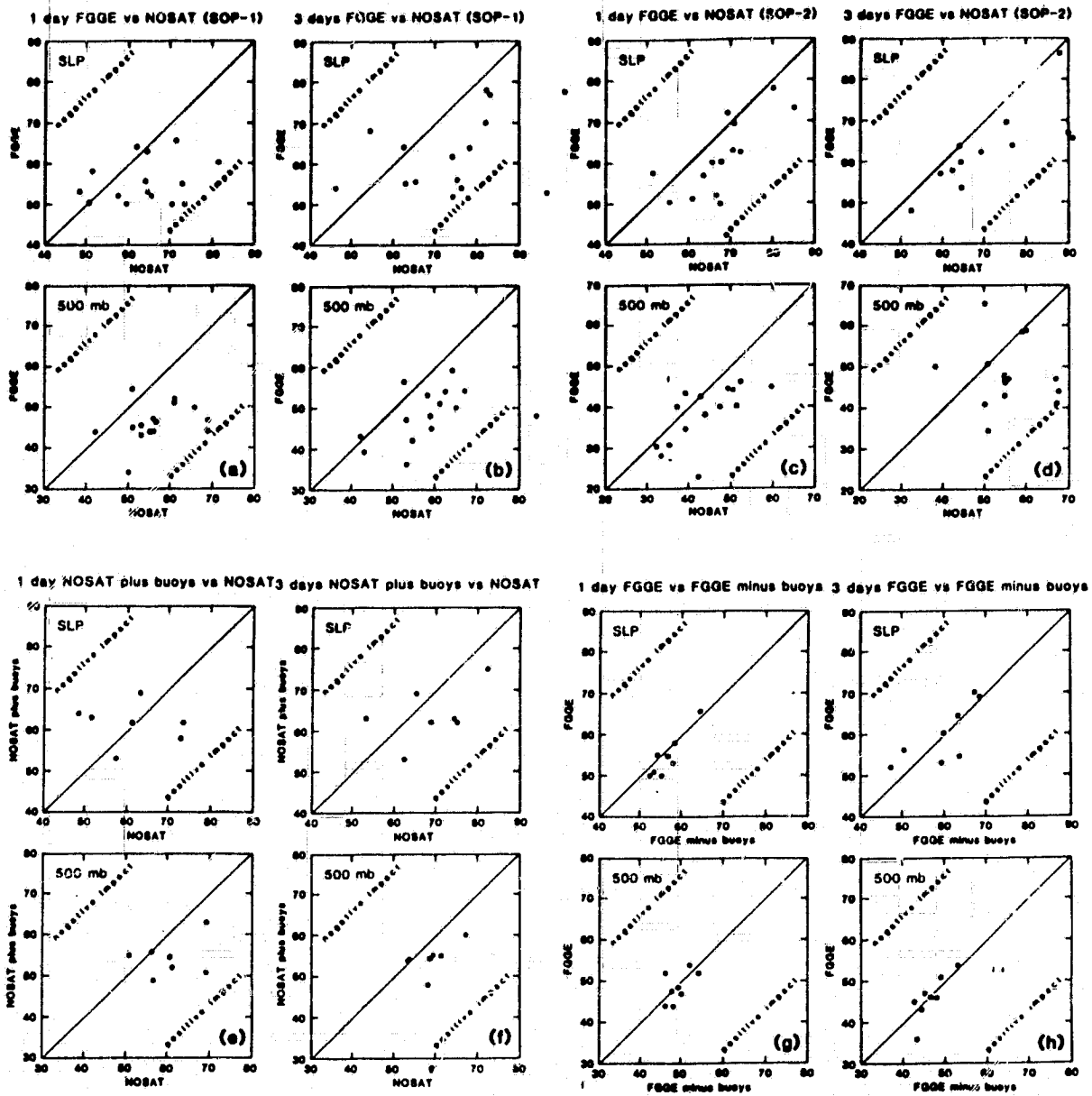


Fig. 1: Comparison of 1 and 3 day forecast S1 skill scores over the region 28°S to 60°S, 80°W to 50°N, verified against NMC's analysis. The average skill scores are represented by an asterisk.

- a - b: From the FGGE and NOSAT analyses for SOP-1.
- c - d: From the FGGE and NOSAT analyses for SOP-2.
- e - f: From the NOSAT plus buoys and NOSAT analyses, SOP-1.
- g - h: From the FGGE and FGGE minus buoys analyses, SOP-1.

ORIGINAL PAGE IS
OF POOR QUALITY

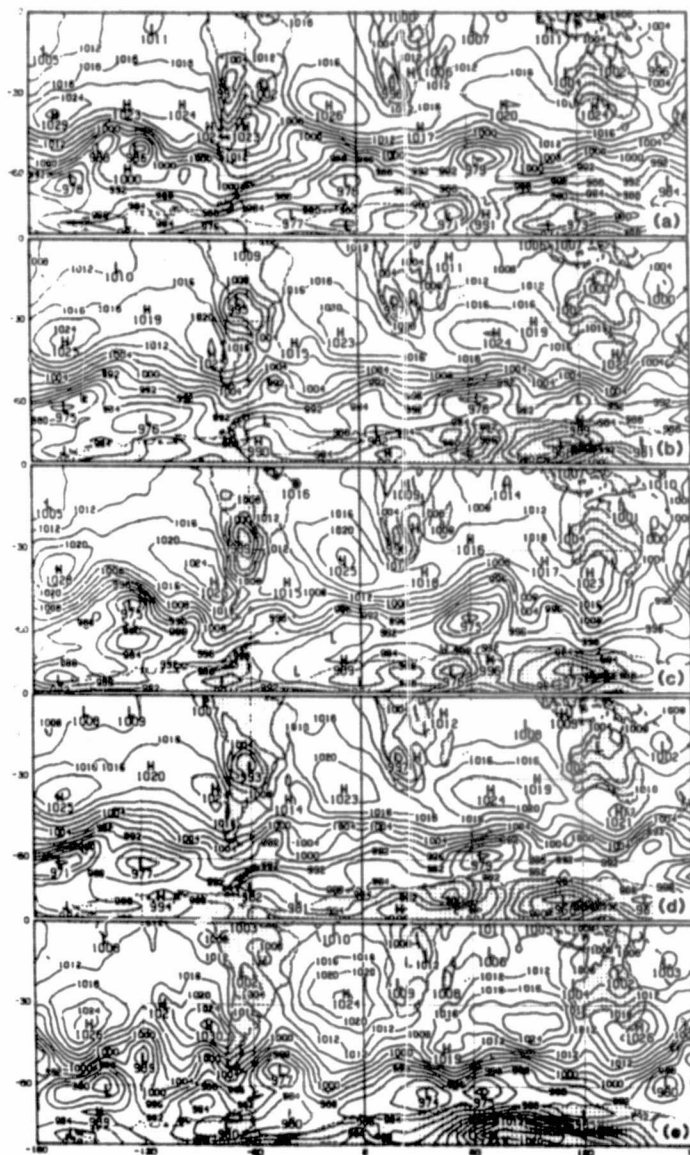


Fig 2:
Southern Hemisphere
sea level pressure
fields for 0000 GMT 28
January 1979:

- a) The 3-day control forecast.
- b) The FGGE forecast.
- c) The control plus buoy forecast.
- d) The FGGE minus buoy forecast.
- e) The verifying analysis.

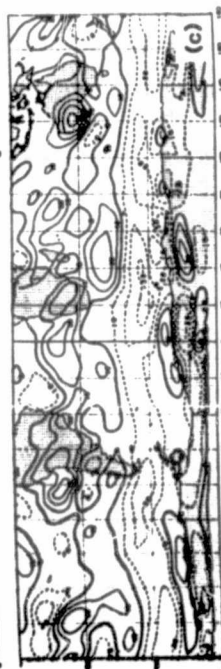
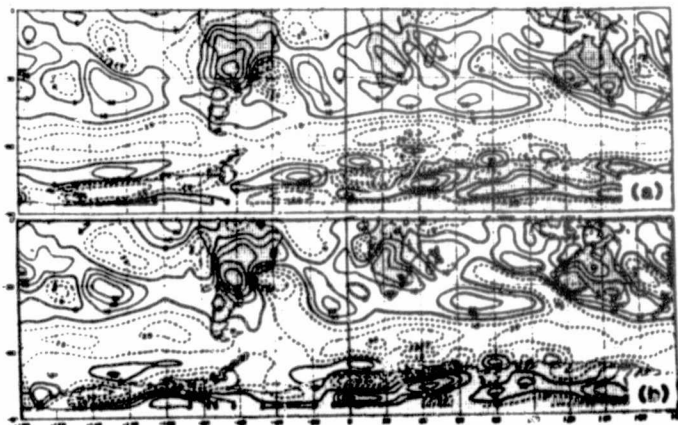


Fig. 3:
30 day average relative
vorticity at 200
mb.

- a) From the 5 Jan -
2 Feb, 1979 FGGE
analysis.
- b) From the 5 Jan -
2 Feb, 1979 NOSAT
analysis.
- c) From the 3 Feb -
5 March, 1979 FGGE
analysis.

26
N84 22055

SASS WIND FORECAST IMPACT STUDIES USING THE GLAS AND NEPRF SYSTEMS:
PRELIMINARY CONCLUSIONS

E. Kalnay, R. Atlas, W. Baker, D. Duffy, M. Halem and M. Helfand

1. INTRODUCTION

1) For this project we developed a version of the GLAS Analysis/Forecast System that includes an objective dealiasing scheme as an integral part of the analysis cycle (Baker et al., 1984). With this system we objectively dealiased the $(100 \text{ km})^2$ binned SASS wind data generated by S. Peteherych of AER, Canada, corresponding to the period 0000 GMT 7 September 1978 to 1200 GMT 13 September 1978. The dealiased wind fields have been requested and received by JPL, NMC and the British Meteorological Office. For further dealiasing we are only limited by the availability of the data, since the conversion of our system to the Cyber 205, which allows for rapid processing, is almost completed.

2) The first 3.5 days of objectively dealiased fields were subjectively enhanced on the McIDAS system. Approximately 20% of the wind directions were modified, and of these, about 70% were changed by less than 90° .

3) We performed two SASS forecast impact studies, using the dealiased fields, with the GLAS and the NEPRF (Navy Environmental Prediction Research Facility) analysis/forecast systems. The characteristics of the systems used are given in Table 1.

Table 1. Characteristics of the GLAS and NEPRF analysis/forecast systems used in the SASS forecast impact studies.

	<u>GLAS</u>	<u>NEPRF</u>
Analysis scheme (upper levels)	SCM (Baker, 1983)	Variational (Barker, 1981)
Surface analysis	SCM, with linear balance correction to SLP	Same as GLAS
Analysis resolution	4° x 5° x 12 mandatory level	2.5° x 2.5° x 12 mandatory level
Initialization	Dynamical (Matsuno time step)	Nonlinear balance equation
Levels affected by SASS winds	945 mb	~ 925 mb and 700 mb
Forecast model	GLAS Fourth Order Model (Kalnay-Rivas <u>et al.</u> , 1977)	NOGAPS model (UCLA, Arakawa, 1977)
Model resolution	4° x 5° x 9 levels	2.4° x 3° x 6 levels
PBL parameterization	Bulk formulation	Randall (1976) parameterization
Other physics	Full GCM parameterization	Full GCM parameterization

2. GLAS EXPERIMENTS

4) Four main experiments were conducted with the GLAS system: "SASS" and "NOSASS" analysis cycles which used all available data except that only the SASS analysis made use of the SASS winds and "SASS-VTPR" and "NOSASS-VTPR" analyses, which differed from the first two in that the temperature soundings from the VTPR remote sensor were not utilized. 3-day forecasts were then performed for each of the analyses with initial conditions corresponding to 0000 GMT 9, 1200 GMT 10, 0000 GMT 12 and 1200 GMT 13 September 1978.

5) The main results of the GLAS forecast experiments are the following (Baker et al., 1984).

- a) In the absence of VTPR sounding, SASS winds had a small positive impact on the Southern Hemisphere forecast skill. The analysis and the forecast impact in the Northern Hemisphere were negligible (Table 2).
- b) In the presence of VTPR soundings, the SASS forecast impact was negligible even in the Southern Hemisphere.
- c) The positive impact of VTPR data in the Southern Hemisphere was much larger than that of SASS data.

It should be noted that a 2-day assimilation and forecast experiment by NMC (without the use of VTPR data) had similar results to ours (Yu and McPherson, 1981).

Table 2. Subjective evaluation of SASS impact on sea level pressure and 500 mb height with the GLAS system.

SASS prognostic charts	North America and Europe		South America and Australia	
	With VTPR	Without VTPR	With VTPR	Without VTPR
Significantly better	0	0	2	5
Slightly better	0	0	0	12
Same	95	96	88	72
Slightly worse	0	0	6	3
Significantly worse	1	0	0	4

3. NEPRF EXPERIMENTS

6) Two analysis cycles, "SASS" and "NOSASS" were run with the NEPRF analysis/forecast system from 00Z 7 to 00Z 13 September 1978, and 3-day forecasts were performed from the same initial conditions corresponding as the GLAS experiment (Duffy et al., 1984). Both analyses used VTPR soundings and all available conventional data, but only the "SASS" analysis utilized the SASS winds. Two significant differences between the GLAS and the NEPRF systems are, a) ship winds were not used in the NEPRF analysis cycle, and b) the NEPRF analysis utilized a nonlinear balancing scheme for initialization.

7) The SASS forecast impact in the NEPRF system was similar to that of the GLAS experiments including VTPR: it was statistically negligible, even in the Southern Hemisphere (Table 3). SASS winds produced analysis differences in the Northern Hemisphere which were larger in the NEPRF system than in the GLAS system possibly because of the differences noted in the previous paragraph. Specific cases of positive and negative impact in both hemispheres tended to cancel on the average.

Table 3. Subjective evaluation of SASS impact of NOGAPS sea level pressure and 500 mb height forecast.

SASS prognostic charts	Northern America and Europe	South America and Australia
Significantly better	1	0
Slightly better	3	3
Same	91	91
Slightly worse	1	2
Significantly worse	0	0

4. DISCUSSION

8) The lack of SASS forecast impact in the presence of VTPR soundings is similar to the data redundancy effect observed with the drifting buoys during FGGE (Kalnay et al., 1983): Drifting buoys were found to have a significant positive impact when added to the conventional (surface and rawinsonde) observing system in the Southern Hemisphere. However, when the buoys were deleted from the complete FGGE observing system the loss of forecasting skill was negligible.

9) Simulation studies (Cane et al., 1981, Halem, 1984) suggest that

significant positive forecast impact may be expected from single level wind data. Our real data studies with the GLAS and NEPRF systems, as well as the NMC study show minimal impact from SASS winds. The discrepancy between these results may be due to, a) Deficiencies in the simulation studies; b) The difficulty of objective dealiasing; and c) Deficiencies in the analysis/forecast system.

10) Deficiencies in the simulation studies: The simulation studies made two important idealizations: a) They used the same model to generate a "nature run" and to forecast. Such "identical twin" experiments imply that the forecast model is perfect, so that no loss of predictability comes from model deficiencies. b) They assumed that SASS data provided perfect winds at the lowest model level (about 945 mb), a strong assumption given the difficulties in inferring PBL winds from surface stress and in dealiasing the SASS winds. In addition, the simulation study assumed that Seasat would give global coverage twice daily as with soundings from NIMBUS-6, whereas SEASAT provided coverage once every 36 hours.

11) Dealiasing of SASS winds: Objective dealiasing, which is the only practical method of dealiasing given the vast amounts of SASS data, minimizes the useful wind direction information. The SASS wind direction is chosen among the 2-4 aliases as the one closest to the first guess (a 6 hour forecast). Therefore, the choice is correct if the forecast is generally accurate, and a wrong alias may be chosen otherwise. As a result, the only truly independent information provided by SASS is wind speed.

12) Deficiencies in the analysis/forecast system. Both the GLAS and the NEPRF experiments were performed with less than optimal systems. For example, the GLAS system had coarse horizontal resolution ($4^\circ \times 5^\circ$), a simplistic bulk formulation of the PBL, and a univariate successive correction method (SCM) analysis scheme, (although the sea level pressure analysis over the ocean was modified through a linear balance equation given the change in wind analysis between the first guess and the forecast). The NEPRF forecast model has higher horizontal resolution ($2.4^\circ \times 3^\circ$), but less vertical resolution (6 levels). No surface winds are used in the analysis (except for SASS winds). The PBL formulation uses an extrapolated surface wind, rather than a prognostic one, and considerable smoothing of small scale features is introduced by the global balancing. A further source of errors in both systems, especially for fast short waves, was the use of a 6 hour forecast with a window of ± 3 hour, which can introduce significant wind direction errors.

13) We are currently developing a system which corrects these deficiencies: a) a $2^\circ \times 2.5^\circ$, 15 level GLAS Fourth Order Model, with an advanced Monin-Obukhov, Mellor-Yamada parameterization scheme to better define the PBL structure (Helfand and Labraga, 1984, Kalnay et al., 1983); b) a new optimal interpolation analysis on the same resolution with a novel multivariate surface analysis and the capability of time-continuous assimilation of SASS data; c) a new simulation study in cooperation with ECMWF and NMC, in which ECMWF will provide a "nature" run realistically different from our forecast model, from which NMC will generate synthetic "conventional observations" and GLAS "advanced instrument observations."

14) We believe that even in the event that Seasat-A data shows negligible forecast impact (because of the instrumental and modeling difficulties pointed out before), it will still be extremely useful for atmospheric and oceanic

studies. The GLAS system can provide not only an objectively dealiased SASS data set but also global surface wind analyses and diagnostic fields such as surface stress and surface fluxes of heat and momentum that are derived when the model is forced by the data. Preliminary analysis indicate large, spatially coherent day-to-day differences between the SASS and NOSASS analyses in the tropics and in other data sparse regions which will greatly influence the estimates of ocean surface fluxes. These diagnosed fields are possibly the most accurate that can be computed with current technology.

15) Forthcoming scatterometer instruments with six antennas providing only 2 directional wind aliases, will essentially allow objective removal of the ambiguity without errors in the vast majority of the cases. Experiments studying the sensitivity of the forecasts to surface wind analysis (Atlas, 1984) indicate that occasional large impacts may be expected from large surface wind/modifications, especially when surface processes play an important role in cyclone development.

16) For these reasons we believe that future scatterometer winds still have a potentially useful role in numerical weather prediction, which should be explored with advanced simulation studies.

REFERENCES

- Arakawa, A., and V. R. Lamb, 1977: Computational design of the basic dynamical processes of the UCLA general circulation model. Methods in Computational Physics, Vol. 17, Academic Press, Inc., New York.
- Atlas, R., W. E. Baker, E. Kalnay, M. Halem, and P. Woiceshyn, 1984: Impact of scatterometer wind data on global weather forecasting. To appear in Frontiers of Remote Sensing of the Oceans and Troposphere from Air and Space Platforms.
- Baker, W. E., R. Atlas, E. Kalnay, M. Halem, P. M. Woiceshyn, S. Peteherych, and D. Edelmann, 1984: Large-scale analysis and forecast experiments with wind data from the Seasat-A scatterometer. Submitted to J. Geophys. Res.
- Baker, W. E., 1983: Objective analysis and assimilation of observational data from FGGE. Mon. Wea. Rev., 111, 328-342.
- Barker, E. H., 1981: Analysis and initialization procedure for the Navy Operational Global Atmospheric Prediction System. Technical Report NEPRF.
- Cane, M. A., V. J. Cardone, M. Halem, and I. Halberstam, 1981: On the sensitivity of numerical weather prediction to remotely sensed marine surface wind data: A simulation study. J. Geophys. Res., 86, 8093-8106.
- Duffy, D., R. Atlas, T. Rosmond, E. Barker, and R. Rosenberg, 1983: The impact on Seasat scatterometer data on the Navy's operational weather prediction model. To be submitted to J.G.R.
- Halem, M., 1984: Simulation studies with future observing systems. To be submitted to Bull. Amer. Meteor. Soc.

- Helfand, H. M., and J. C. Labraga, 1983: A level 2.4 second-order closure model for the prediction of turbulence. Research Activities in Atmospheric and Oceanic Modelling, Report 5, GARP Numerical Experimentation Programme, pp. 5.13-5.15.
- Kalnay, E., R. Balgovind, D. E. Edelman, J. Pfaendtner, L. L. Takacs, and W. Chao, 1983: Documentation of the GLAS Fourth Order Model. NASA Technical Memorandum (in press).
- Kalnay-Rivas, E., A. Bayliss, and J. Storch, 1977: The 4th order GISS model of the global atmosphere. Beitr. Phys. Atmos., 50, 299-311.
- Kalnay, E., R. Atlas, W. Baker, and M. Halem, 1983: FGGE forecast impact studies in the Southern Hemisphere. First International Conference on Southern Hemisphere Meteorology, Sao Jose dos Campos, Brazil, Amer. Meteor. Soc., 180-183.
- Randall, D. A., 1976: The interaction of the planetary boundary layer with large-scale circulations. Ph.D. thesis, Department of Atmospheric Sciences, UCLA.
- Yu, T. W., and R. D. McPherson, 1981: Global data assimilation experiments with scatterometer winds from Seasat-A. Preprints Fifth Conference on Numerical Weather Prediction, Monterey, CA, Amer. Meteor. Soc., Boston, pp.9-13.

B. SATELLITE OBSERVING SYSTEMS

REGIONAL CORRELATION BETWEEN TOMS TOTAL OZONE FROM NIMBUS-7 SATELLITE
AND GEOPOTENTIAL HEIGHT FROM THE GLAS ANALYSIS

M.-J. Munteanu, P. Piraino and E. Kalnay

The great bulk of ozone originates in the upper stratosphere and is transferred to the lower stratosphere, where it is protected from photochemical destruction and becomes a quasi conservative property of the air. It has long been observed (see Craig, 1965 for a review of early studies) that there is a strong negative correlation between total ozone content and the tropopause height. This presumably is because the lower stratosphere, rich in ozone, constitutes a larger than normal proportion of the total atmospheric column in deep tropospheric troughs, where the tropopause is low and warm, and vice versa, ridges with high tropopause have a thin stratospheric layer.

In order to study the relation between ozone and the atmospheric circulation on a global scale, we have computed the global correlation between TOMS total ozone measurements from NIMBUS-7 satellite and collocated geopotential heights analysis at all mandatory pressure levels between 1000-50 mb. The heights are obtained from the 4° x 5° GLAS analysis that uses both conventional (rawinsonde) and the operational TIROS-N satellite soundings (Halem et al., 1982), but no ozone data. Zonal averages, presented in Fig. 1, have been subtracted to eliminate the correlation due merely to latitudinal dependence, and emphasize the correlation associated with synoptic features.

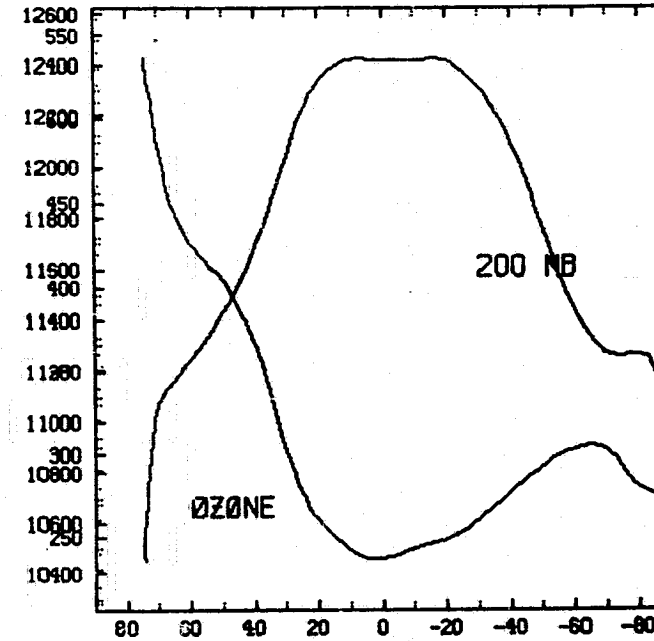
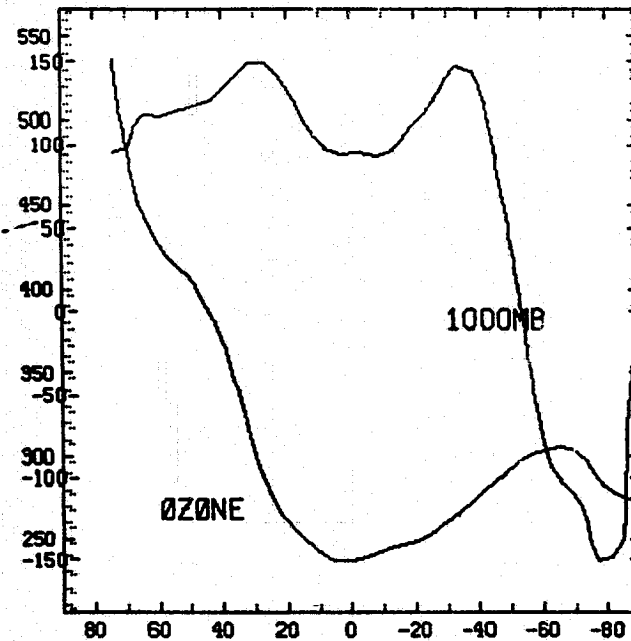
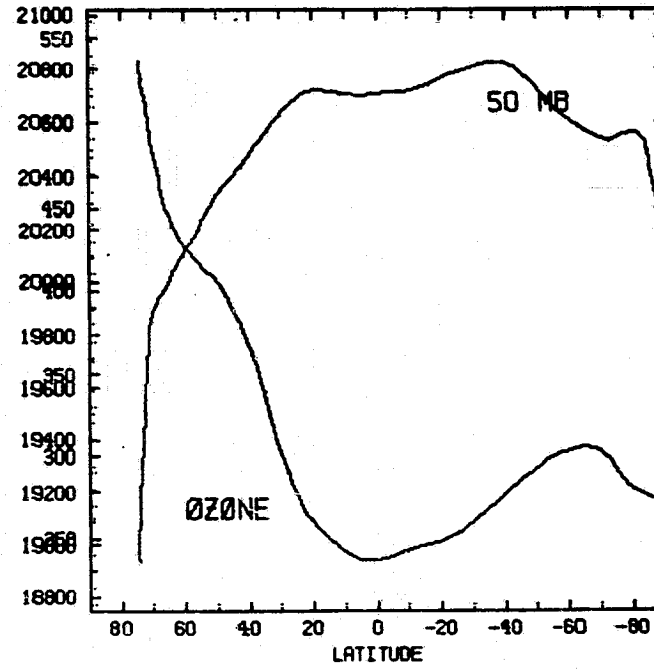
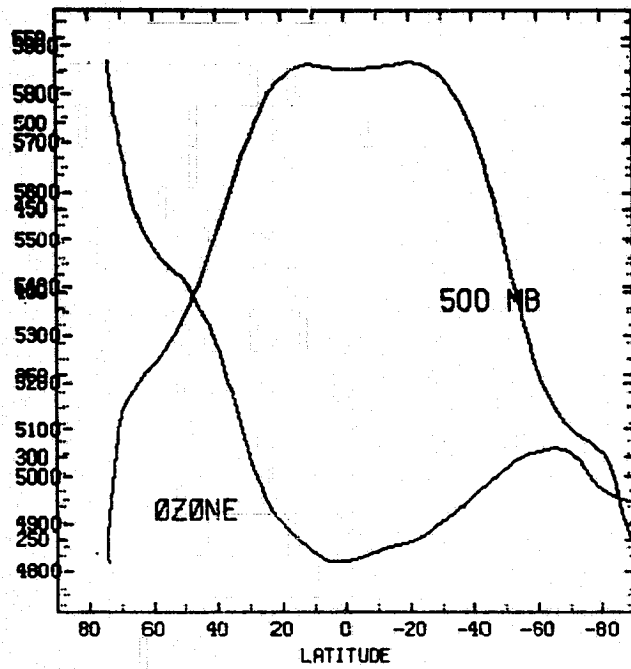
We present tables with correlation coefficients for the four synoptic times covering the Pacific Ocean, Asia, Europe and the Atlantic Ocean, and United States regions. These coverages are approximate since NIMBUS-7 does not observe exactly the same region each day.

The results indicate a strong vertical dependence of the correlation between ozone and heights, as expected, with maximum negative values around 200 mb and smaller positive values near the surface. However, the correlation is also highly variable in time (Fig. 2) and with latitude (Fig. 3).

We plan to compute correlations on a finer grid, for a longer period, and other months. The results so far indicate that total ozone data has significant potential of providing useful additional information for tropospheric and stratospheric analysis, especially in data-sparse regions and cloudy regions. Fig. 4 presents examples of contemporary ozone and upper tropospheric maps, and the corresponding observed correlations in the 20-50 latitude bands.

PRECEDING PAGE BLANK NOT FILMED

LATITUDINAL MEANS OF GEOP HEIGHTS AND OZONE



ORIGINAL PAGE IS
OF POOR QUALITY

Figure 1

ORIGINAL PAGE IS
OF POOR QUALITY

TIME CORRELATION of 200mb
GEOPOTENTIAL HEIGHT with TOTAL OZONE

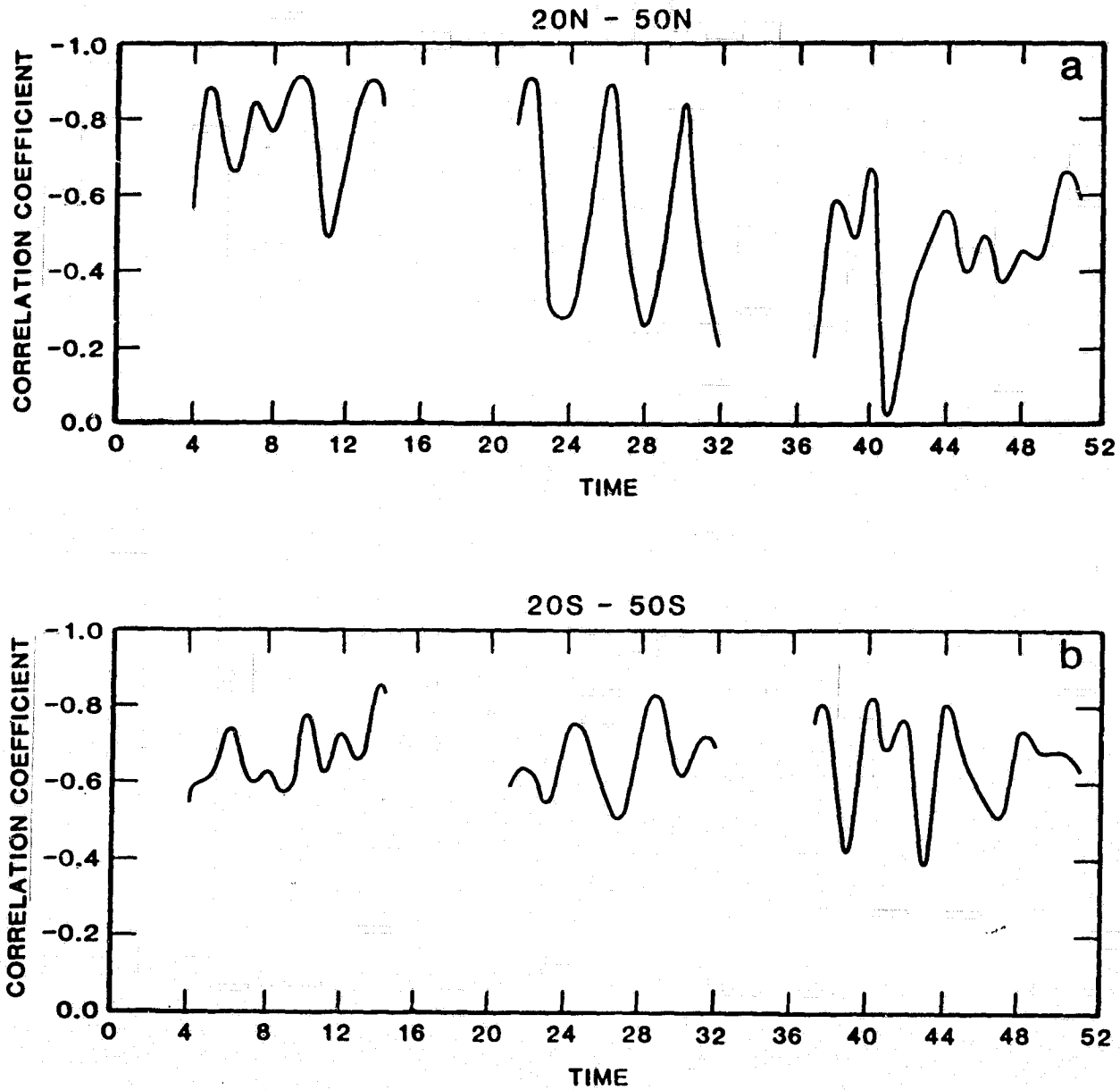
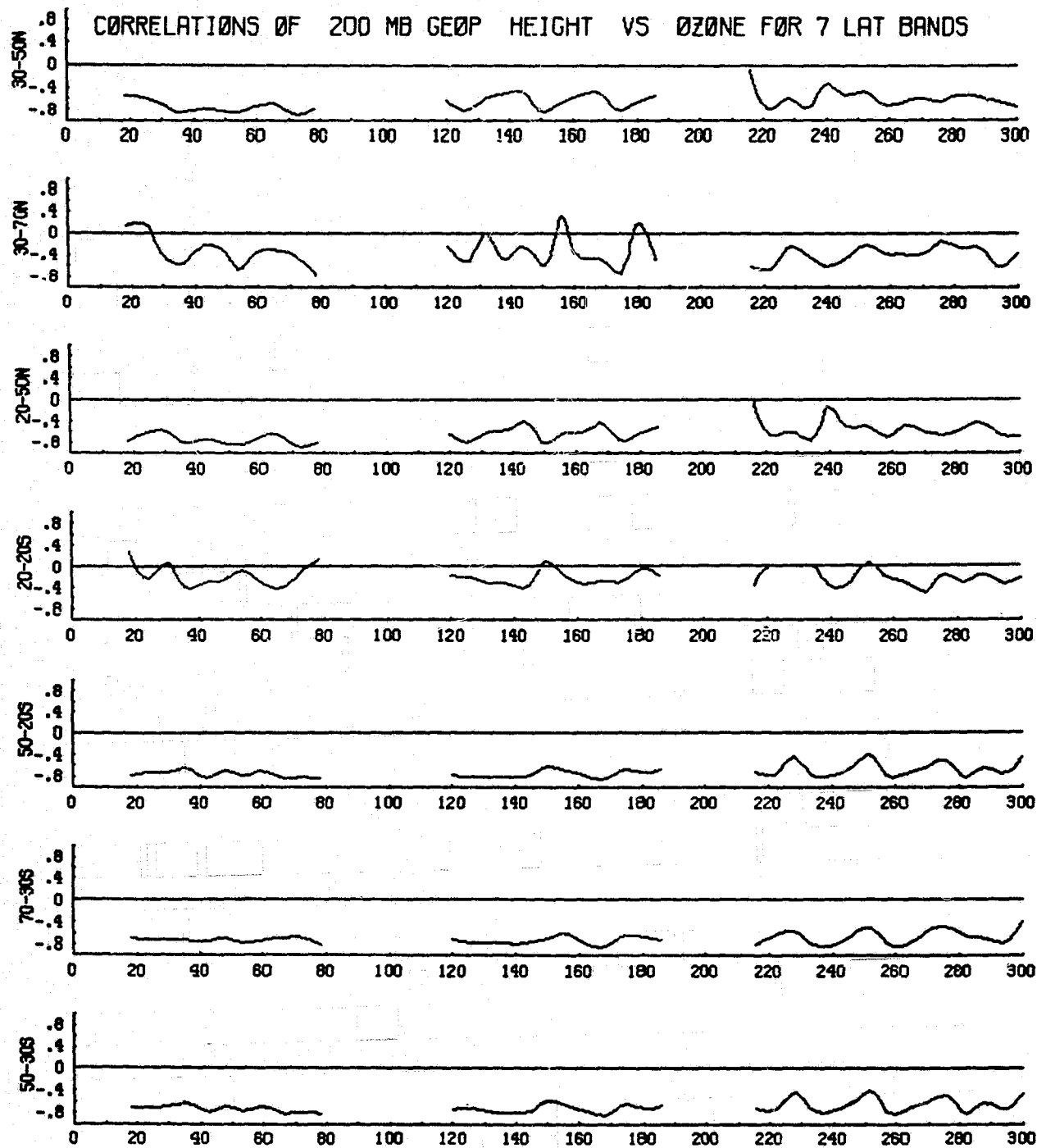
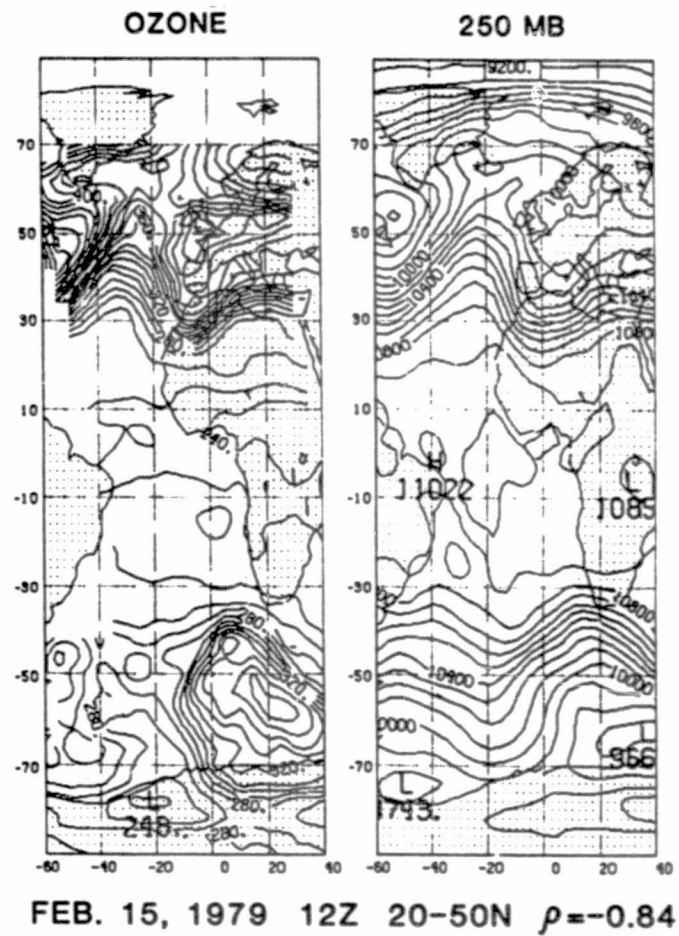
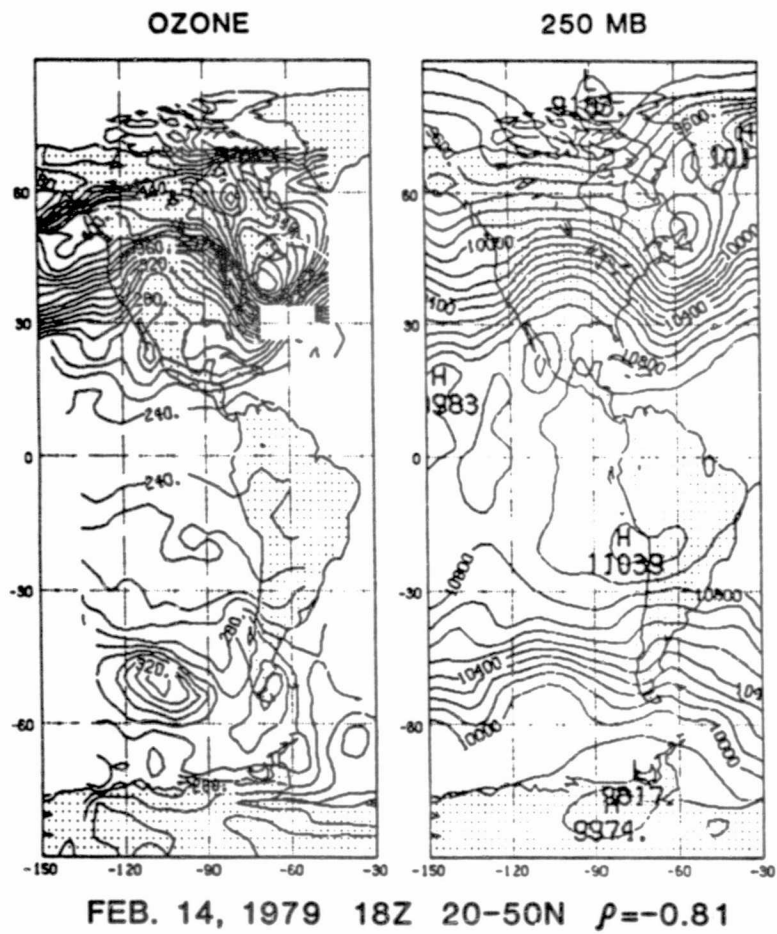


Figure 2



ORIGINAL PAGE IS
OF POOR QUALITY

Figure 3



ORIGINAL PAGE IS
OF POOR QUALITY

Figure 4

Do
N84 22057

COMPARISON OF AMSU TEMPERATURE SOUNDINGS WITH THOSE PRODUCED BY HIRS AND AMTS

D. Reuter and J. Susskind

1. INTRODUCTION

The new generation of satellite borne radiometers to be launched in the late 1980's or early 1990's are currently planned to have as their main temperature sounding unit the AMSU (Advanced Microwave Sounding Unit). This device consists of two units, one of which contains 11 high spectral and spatial resolution channels which are to be used to produce vertical atmospheric temperature soundings. Other channels are to be used to determine atmospheric liquid water and water vapor amounts, as rain detectors, and for surface emissivity determination. This report, however, shall deal only with the accuracy of temperature retrievals. Toward this end studies have been carried out in which atmospheric temperature profiles were retrieved from simulated radiances for the AMSU channels. As a comparison, atmospheric temperature profiles were retrieved from simulated radiances for the currently operational HIRS infrared sounder as well as the proposed advanced infrared sounder AMTS. All simulations were based on a set of 400 mid-latitude radiosondes.

2. SIMULATION AND RETRIEVAL PROCEDURE

In order to use the GLAS physically based retrieval scheme an algorithm for the rapid calculation of atmospheric transmittances as a function of atmospheric temperatures, constituent concentrations, and satellite viewing angle must be available. The process for determining this algorithm has been described elsewhere (Susskind et al., 1983) for the HIRS instrument and will not be discussed here.

In the first step of the simulation and retrieval procedure "exact" atmospheric transmittances are calculated for a number of standard profiles based on experimentally determined spectral line profile parameters for the species which absorb radiation in the bandwidth of the channel. A simple model for transmittance is then fit to these "exact" transmittances. This simple model is used to generate radiances for each instrument for each of the 400 radiosonde profiles. Reasonable instrumental noise is added to these synthetic radiances. For all three instruments effects of reasonable surface temperature were taken into account and for the AMSU the effects of the significant variation of the surface emissivity from unity were accounted for. The small effects of atmospheric water vapor on the AMSU channels were ignored. For the HIRS and AMTS instruments both clear and cloud contaminated radiances were simulated; the latter, using two cloud layers with unit emissivity randomly placed between 300 and 700 mb (Reuter et al., 1982). The microwave sounding channels were assumed to be unaffected by the presence of clouds.

Surface and atmospheric temperature retrievals were performed using the GLAS physically based retrieval system which has been described elsewhere (Susskind et al., 1984). For the AMSU sounder a slight modification was made

to use the known surface temperature to determine the surface emissivity. The RMS error of the retrieved microwave emissivity error was found to be about 0.3%.

3. RESULTS

The results of this comparison study are shown in Figs. 1-3. In Fig. 1 RMS temperature errors are plotted as a function of pressure for the 200 ocean mid-latitude radiosondes under clear conditions. Fig. 2 plots the same function for the 200 land mid-latitude profiles. From these two figures it is apparent that the AMSU retrievals were significantly degraded from the infrared retrievals below about 400 mb. This is not surprising since the sensitivity functions in the troposphere are much sharper for the infrared channels than for the AMSU channels. Above 400 mb the HIRS retrievals are much inferior to either the AMSU or AMTS retrievals, however it must be pointed out that the HIRS instrument by itself was not designed for upper tropospheric and stratospheric sounding and that inclusion of MSU channels, which are on the same satellite as the HIRS instrument, would certainly improve the results. In fact the HIRS retrievals given here are worse than the HIRS/MSU retrievals produced operationally at GLAS.

Fig. 3 compares all three instruments for the entire set of 400 radiances simulated under cloudy conditions. As expected, both the HIRS and AMTS results degrade somewhat, while by definition, the AMSU results remain unchanged. However, the infrared sounders are still superior to the AMSU in the lower and middle troposphere. This points out the fact that, as long as cloud effects can be reasonably well taken into account, the sharper sensitivity functions of the tropospheric infrared sounding channels outweigh the advantage of the insensitivity of the microwave channels to clouds. In this connection it should be pointed out that no a priori information about the cloud distribution was used in infrared retrievals and that a cloud filtering technique similar to that used in the operational HIRS retrievals was used to account for the effects of clouds.

As a final note it should be mentioned that retrievals were also performed using the simulated radiances and a statistical regression technique. The results of the regression analysis were similar to those presented here, except that in all cases the RMS errors increased somewhat. This was especially true for the infrared sounders under cloudy conditions.

4. SUMMARY

It is apparent from the results presented here that at least a subset of the HIRS channels, or preferably the AMTS channels, must be retained if the next generation of sounders is to match, let alone improve upon the tropospheric sounding accuracy of the current sounders. The most important channels are in the 4.3 μm region to monitor the mid-lower troposphere, and in the 11 and 3.7 μm region to determine surface temperature.

REFERENCES

- Susskind, J., J. Rosenfield, and D. Reuter, 1983: An accurate radiative transfer model for use in the direct physical inversion of HIRS2 and MSU temperature sounding data. J. Geophys. Res. 88 No. C13, 8550-8568.
- Reuter, D., J. Susskind, and A. Dalcher, 1982: Simulation studies of the HIRS2/MSU and AMTS/MSU satellite sounding units: Cloudy conditions. Research Review 1982, NASA Technical Memorandum 84983.
- Susskind, J., J. Rosenfield, D. Reuter, and M. T. Chahine, 1984: Remote sensing of weather and climate parameters from HIRS2/MSU on TIROS-N. Accepted for publication in J. Geophys. Res.

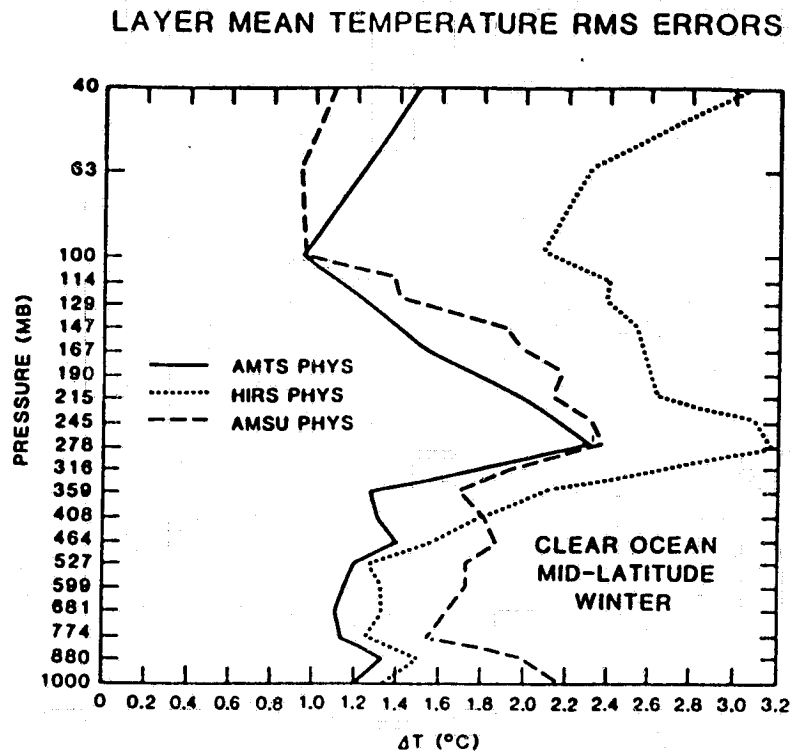


Fig. 1. Comparison of temperature retrieval accuracy for the three sounders AMTS, HIRS, and AMSU. 200 winter ocean mid-latitude (30 N - 60 N) profiles under clear conditions.

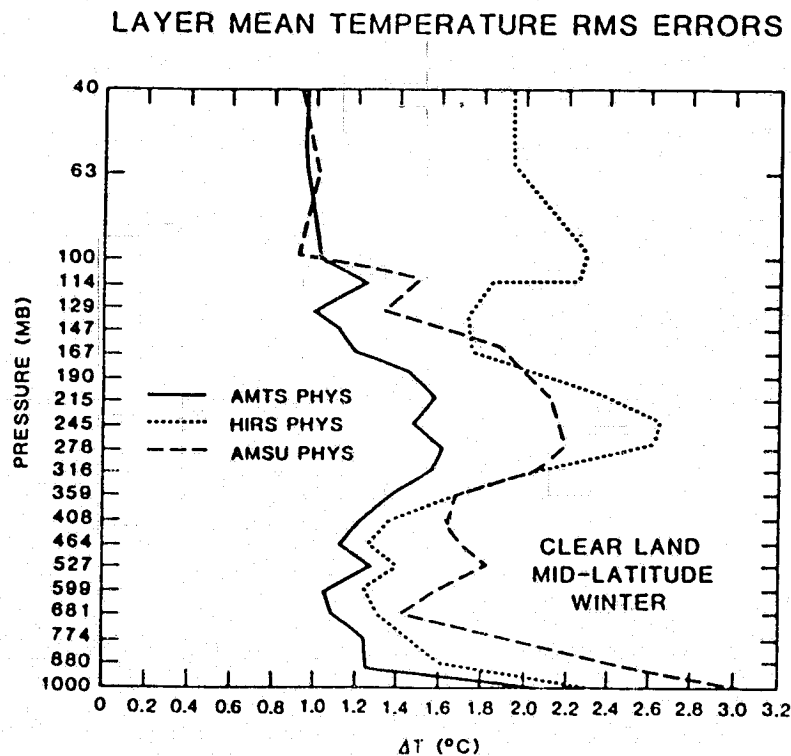


Fig. 2. Same as Fig. 1 but for 200 winter land mid-latitude profiles.

ORIGINAL PAGE IS
OF POOR QUALITY

LAYER MEAN TEMPERATURE RMS ERRORS

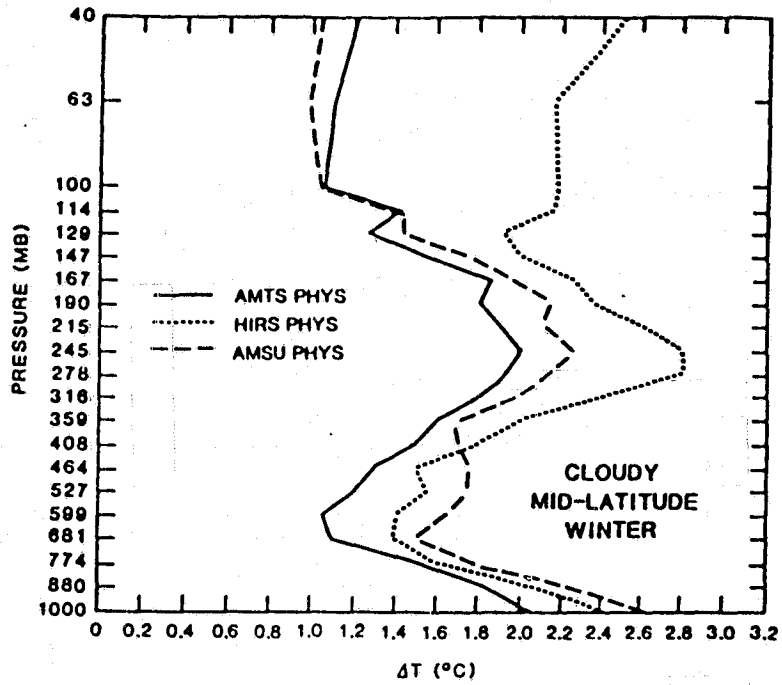


Fig. 3. RMS temperature errors for retrievals performed using simulated cloud contaminated radiances. 400 mid-latitude profiles.

WATER VAPOR PROFILE RETRIEVAL SIMULATION STUDIES FOR THE
HIRS/MSU AND AMTS/MSU SOUNDERS

D. Reuter and J. Susskind

1. Introduction

A combined physical statistical method for the retrieval of atmospheric water vapor column densities has been developed at the Goddard Laboratory for Atmospheric Sciences. In this method differences between observed and calculated clear column brightness temperatures are used in a regression formalism to obtain estimates of integrated column densities in given atmospheric layers. The physics of the radiative transfer problem is contained in the calculated clear column brightness temperatures and in accounting for the effects of clouds on the observed radiances. The regression matrix is equivalent to a set of empirical sensitivity factors.

The GLAS physically based retrieval scheme is currently capable of producing accurate atmospheric and surface temperature retrievals and accurate measures of cloud fields from radiances measured by the HIRS/MSU sounding unit (Susskind et al., 1982a). In this scheme the water vapor field used in the computation of the atmospheric transmittance functions for the temperature sounding channels is obtained from a 6 hour forecast and is not modified in the retrieval process. Improved estimates of water vapor fields may result in improved estimates of the other meteorological parameters obtained from the system. In addition, water vapor is, in itself, a variable of meteorological interest. Both the operational HIRS and the proposed AMTS infrared sounders have a number of channels which are quite sensitive to the amount of water vapor in the satellite field of view. In order to determine the extent of useful water vapor information contained in these channels we have carried out studies in which simultaneous temperature humidity retrievals were performed, based on radiances which were simulated under clear and cloudy conditions. In this study, we used all three humidity sounding channels and the 11 μm window channel 8 for the HIRS, while for the AMTS the seven humidity sounding channels (13-19) were used.

Clear radiances were simulated using an atmospheric transmittance model developed at the Goddard Laboratory for Atmospheric Sciences (Susskind et al., 1983) and temperature and water vapor profiles obtained from a selected set of radiosondes from January and June of 1979. The ground temperatures were specified so as to be meteorologically reasonable. The cloudy radiances were simulated using the same method except that in addition, two layers of broken opaque clouds between 900 and 300 mb were allowed to contaminate the radiances. Details of the clear and cloud radiance simulations may be found in Susskind et al., 1982a, b, and Reuter et al., 1982.

2. Retrieval Process

For a particular atmospheric water vapor and temperature profile (including surface temperature) an estimate of the upwelling thermal radiation which would be observed in a certain channel of a satellite borne sensor may be calculated given an algorithm for the computation of channel averaged atmospheric transmittances as a function of atmospheric conditions and satellite viewing angle.

Differences between the actual observed radiances and the calculated radiances are then due to differences between the actual temperatures and water vapor amounts and the proscribed temperatures and water vapor amounts, errors in the transmittance algorithm, and the estimated effects of clouds if they are present. The currently operational GLAS retrieval scheme uses a combination of microwave and infrared observations and an initial guess to obtain first estimates of the reconstructed clear column brightness temperatures (i.e. the brightness temperatures which would be observed in the absence of clouds (Smith 1968; Chahine 1974)). These estimates of the clear column brightness temperatures are then used to adjust the atmospheric and surface temperatures which are used to obtain new estimates of the reconstructed clear column brightness temperature in an iterative fashion, until the calculated clear column brightness temperatures agree with the reconstructed clear column brightness temperature to within a specified amount. These retrievals use theoretical relationships between changes in atmospheric and surface temperature and changes in channel brightness temperatures.

Because of the limited vertical resolution of the water vapor channels a simpler technique was used in the water vapor retrievals based on statistical relationships between changes in humidity profiles and changes in brightness temperatures. In this procedure, the retrieved atmospheric temperature profile and ground temperature are used along with a first guess water vapor profile, to compute estimated clear column brightness temperatures for those channels most sensitive to water vapor. As in the case of the temperature sounding channels, the differences between the computed and observed brightness temperatures (or reconstructed brightness temperatures in the case of cloud contamination) are a function of numerous parameters. However, since the temperature profiles used in the calculation of the computed clear column brightness temperatures are the retrieved atmospheric temperature profiles, the differences between observed and computed brightness temperatures are attributed to errors in the proscribed first guess water vapor profile. Because these differences are roughly linear with small errors in water vapor profile estimates, a regression relationship may be found which relates known differences between the true water vapor profiles and the first guess profiles to the differences between the observed and computed clear column brightness temperatures. Note that the satellite observations and the computations of the clear column brightness temperatures are carried out at a zenith angle θ . To first order this has the effect of multiplying the water vapor column densities by a factor of $\sec \theta$. Thus the actual water vapor column density differences are scaled by $\sec \theta$ in finding the regression relationship. The entire simulation and retrieval process may be summarized as follows:

- 1) Radiosonde temperature profiles and water vapor profiles $q(\text{TRUE})$ along with meteorologically consistent ground temperatures are used to simulate either clear or cloud contaminated brightness temperatures which would be observed by a satellite viewing at angle θ . These brightness temperatures are contaminated with realistic instrument noise.
- 2) These simulated brightness temperatures are used as input to the GLAS physically based temperature retrieval scheme and retrieved atmospheric and surface temperatures are produced using a climatological relative humidity first guess. In the cloud simulation estimates of the reconstructed clear column brightness temperatures are produced.

- 3) The retrieved temperatures and a first guess water vapor profile $q(\text{FG})$ are used to estimate clear column brightness temperatures $T_B(\text{CALC})$ for those channels which are to be used in the water vapor retrieval scheme.
- 4) Regression expressions are found which relate the difference between the true and first guess water vapor profiles, (Δq) , to the difference between the observed (or reconstructed) clear column brightness temperatures, $\Delta\theta$. Two different regression relationships were tried. In the first method Δq was regressed only against $\Delta\theta$;

$$\Delta q_I = A \Delta\theta + B \quad (1)$$

where, for pressure layer I and satellite zenith angle θ , $\Delta q_I = (q(\text{true})_I - q(\text{FG})_I) \sec\theta$, $q(\text{--})_I$ is the integrated water vapor column density in pressure layer I , and $\Delta\theta = \theta(\text{clear}) - \theta(\text{calc})$.

In the second method an attempt was made to take into account the fact that the height of the water vapor sensitivity function is a function of the total amount of water vapor in the column. Specifically, as the water vapor column density increases, the sensitivity function tends to peak higher in the atmosphere and vice-versa. In this case the regression relationship becomes

$$\Delta q_I = (A' + C(W_I - \bar{W}_I)) \Delta\theta + B' \quad (2)$$

where W_I is the total integrated first guess water vapor column density from the bottom of pressure layer I to the top of the atmosphere, and \bar{W}_I is the same quantity for a fixed climatological water vapor column density profile.

- 5) The regression relationships generated using equation (1) (Method I) or equation (2) (Method II) are used to obtain retrieved water vapor column densities from an independent set of simulated radiances. The simulated radiances, of course, use the true atmospheric temperature and water vapor profiles and true surface temperature as in step 1 above. The calculated clear column radiances for the channels to be used in the water vapor retrievals use retrieved temperatures and a first guess water vapor profile as in step 3 above.

Note that steps 4 and 5 above the $\theta(\text{clear})$ are observed clear column brightness temperatures for the case of the clear simulations and are the reconstructed clear column brightness temperatures in the cloud simulations. For the results shown below, half of the cases are used to generate the regression matrix, while the other half are used as an independent set to verify the results. The first guess water vapor profiles used in these simulation studies were climatological relative humidity profiles. Thus the first guess column density profiles, $(q(\text{FG}))$, take into account some of the correlation between temperature and specific humidity.

3. Results

The results of this study are given in Figures 1 through 5. Figure 1 gives the RMS errors of the retrieved temperatures obtained from the AMTS and HIRS infrared sounders as a function of pressure for the set of winter radiosondes under clear conditions. As may be seen from this figure the AMTS instrument gives superior results throughout the entire atmosphere. Similar results hold for the summer data set and for the cloudy simulations. Figures 2 through 5 show results of the water vapor retrievals for the summer radiosondes. Figure 2 compares the accuracy of the water vapor retrievals obtained from the AMTS sounder using Methods I and II for the clear simulations. The quantity plotted here is the fractional RMS error of the integrated column density from pressure p to the top of the atmosphere (1 mb). This fractional error is defined as the RMS difference between the true water vapor profile and the retrieved water vapor profile divided by the mean water vapor column density of the true profiles. As may be seen from this figure, Method II improves the results below 300 mb where most of the water vapor is. Also shown in this figure is the fractional RMS error in the first guess water vapor profile. A comparison of the retrieval errors with the first guess errors indicates that the retrieved profiles are about twice as accurate as the first guess.

Figure 3 indicates the absolute column density error in g/cm^2 from pressure p to the top of the atmosphere for the retrievals using Method II and for the first guess. From this figure it may be seen that the retrieval error in the total precipitable water vapor is about $.55 \text{ g/cm}^2$. The first guess error is seen to be about 1.3 g/cm^2 .

Figure 4 compares the results obtained from the HIRS sounder with those obtained from the AMTS sounder. The units are the same as in Figure 2. Note that the AMTS retrieval results are 10-20% better than the HIRS results through much of the atmosphere. Also note that first guess water vapor profile is somewhat better for the AMTS than for the HIRS below 300 mb because of the better temperature retrievals from the AMTS. Above 300 mb, however, where the AMTS temperature retrievals are decidedly superior to the HIRS retrievals the HIRS water vapor first guess profiles are better than those for AMTS. This is indicative of the not surprising fact that the assumption of a climatological relative humidity profile is not especially applicable above 300 mb. The relationship between the first guess and retrieved water vapor is not simple since in those regions where the AMTS first guess humidity profile is best relative to the HIRS (600-400 mb), the AMTS and HIRS retrievals are essentially equivalent.

Finally, Figure 5 gives the results for the cloudy simulations. These results are essentially the same as for the clear simulations with the AMTS still being superior to the HIRS. In fact the results are somewhat better than in the clear case, possibly because about 10% of the temperature retrievals are rejected for various reasons and these rejected retrievals are not included in the statistics.

The features illustrated in Figures 2 through 5 are similar in the winter cases also. However, since the radiosondes only extend from 30S to 60N there tends to be less water in the sample in the winter than in the summer. Thus while the relative errors as shown in Figures 2, 4 and 5 increase, the absolute errors as shown in Figure 3 stay about the same.

Based on the results of this study it appears that there is usable water vapor information contained in the HIRS water vapor channels and additional improvements with AMTS. We are presently in the process of refining this technique in the hope that we may implement water vapor retrievals as part of the real HIRS/MSU data analysis scheme.

REFERENCES

- Chahine, M. T., 1974: Remote soundings of cloudy atmosphere. I. The single cloud layer. J. Atmos. Sci., 31, 233-243.
- Smith, W. L., 1968: An improved method for calculating tropospheric temperatures and moisture from satellite radiometer measurements. Mon. Wea. Rev., 96, 387-396.
- Susskind, J., J. Rosenfield, D. Reuter, and M. T. Chahine, 1982a: The GLAS Physical Inversion Method for Analysis of HIRS2/MSU sounding Data. NASA Tech. Memo. 84936.
- Susskind, J., D. Reuter, and A. Dalcher 1982b: Simulation comparison study of the AMTS and HIRS2 sounders, and Reuter, D., J. Susskind, and A. Dalcher, 1982: Simulation studies of the HIRS2/MSU and AMTS/MSU satellite sounding units: Cloudy conditions. NASA Tech. Memo. 84983, pp. 59-76.
- Susskind, J., J. Rosenfield, D. Reuter, 1983: An accurate radiative transfer model for use in the direct physical inversion of HIRS2 and MSU temperature sounding data. J. Geophys. Res., 88, No. C13, 8550-8568.

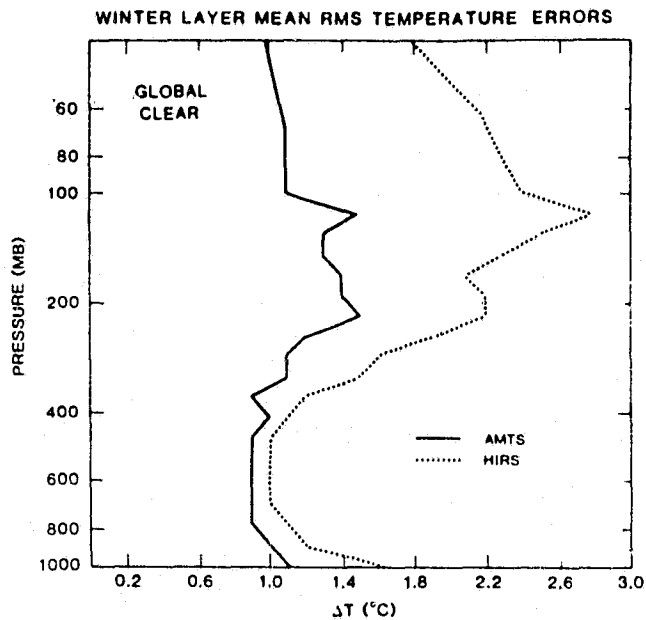


Figure 1. Comparison of temperature retrieval accuracy for the HIRS and AMTS for 800 winter radiosondes under clear conditions.

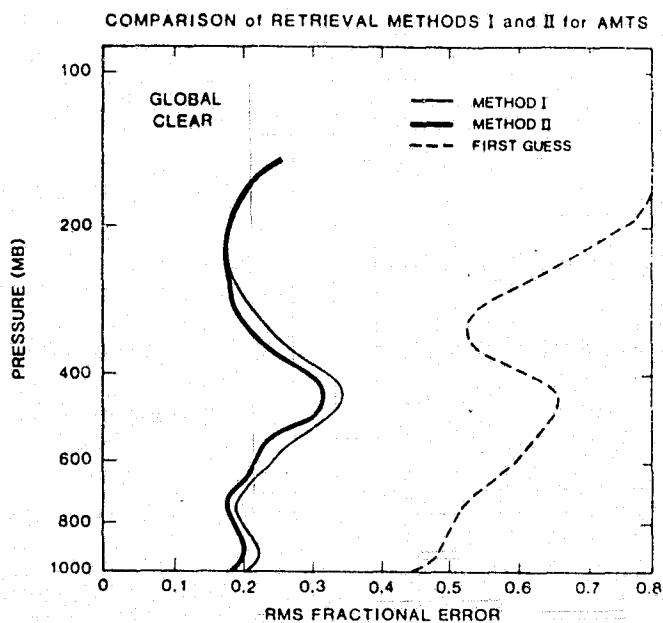
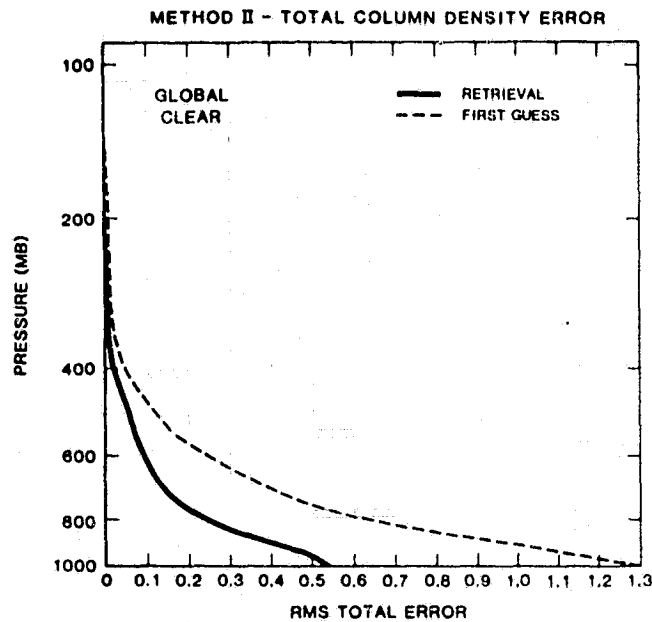


Figure 2. Relative errors for the retrieved integrated column density of water vapor from pressure P to 1 mb for Method I and Method II using AMTS data under clear conditions. The first guess errors are also given.



ORIGINAL PAGE IS
OF POOR QUALITY

Figure 3. RMS total vapor column density error (in G/cm^2) for Method II described in the text. The total column density error for the first guess is plotted also. Clear conditions.

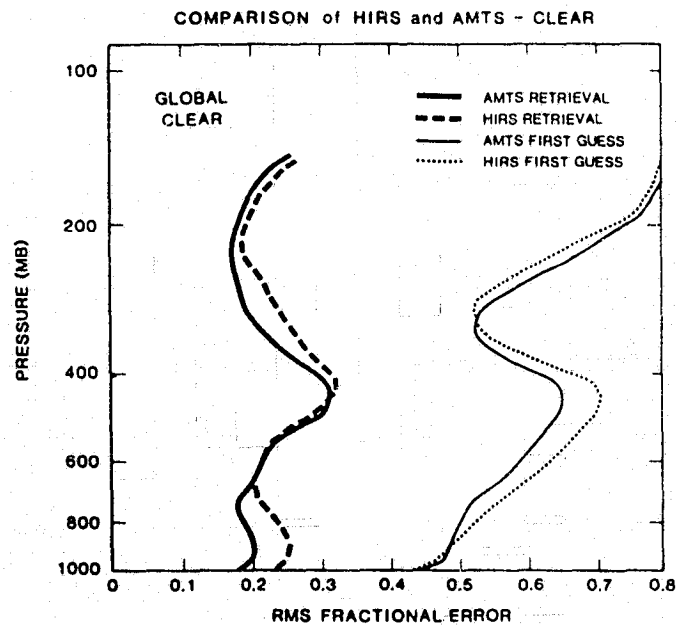


Figure 4. Comparison of relative retrieval errors for the HIRS and AMTS instruments under clear conditions. First guess errors are also given.

ORIGINAL PAGE IS
OF POOR QUALITY

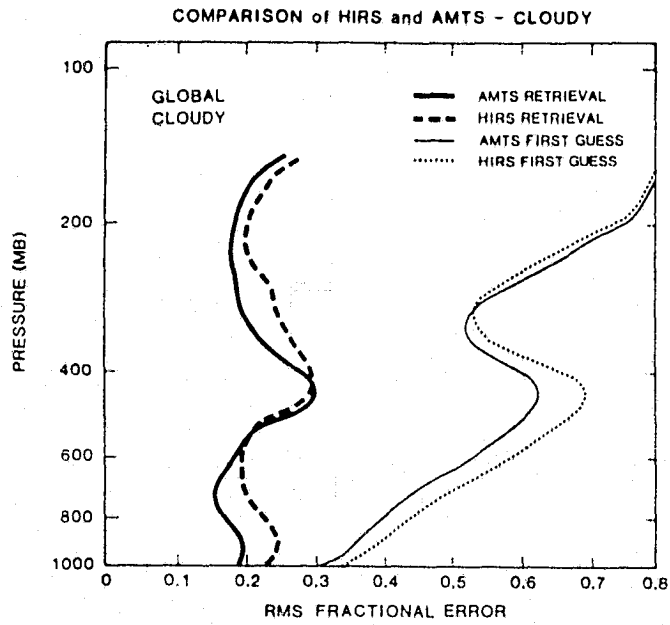


Figure 5. Same as Figure 4 but under simulated cloudy conditions.

RESULTS OF THE JOINT NASA/NOAA AMTS/HIRS2 SOUNDING SIMULATION TEST

J. Susskind and D. Reuter

The joint NASA/NOAA AMTS/HIRS2 sounding simulation test, designed to compare the relative accuracies of atmospheric temperature profiles retrieved from HIRS2, the current operational infra-red temperature sounder, and AMTS, a proposed advanced high-spectral resolution infra-red sounder has been completed. The test compared retrievals generated by GLAS, using their physical retrieval algorithm, and NESDIS, using their operational statistical regression algorithm, for both instruments under clear and cloudy conditions. In the cloudy portion of the test, MSU data, corresponding to the microwave component of the current operational sounding system, was used in conjunction with both instruments to aid in cloud filtering.

The details of the test and the methods used by GLAS to analyze the clear and cloudy data are given in Susskind et al. (1983) and Reuter et al. (1983). The methods are quite similar to those used by GLAS in analysis of HIRS2/MSU TIROS N data (Susskind et al., 1982). The results of the clear test, containing 400 simulated global soundings based on radiosonde reports from the SOP-1 (winter) and SOP-2 (summer) period of FGGE, are shown in Fig. 1. RMS errors of layer mean atmospheric temperatures are shown for 18 tropospheric layers and 4 stratospheric layers whose midpoints are indicated in the chart. In addition, RMS errors of surface skin temperature are plotted at 1000 mb.

The primary reason for doing retrievals for both instruments using both techniques was to determine the degree to which the relative improvement of one instrument over another was method dependent. In addition, the test can be used to compare two methods, though the true test of method, at least for HIRS2, is with real data. It is apparent from Fig. 1 that AMTS retrievals above 300 mb tend to be about 1°C more accurate than HIRS retrievals, relatively independent of method, the physical retrievals being about .3° better than the statistical retrievals for AMTS, but showing less improvement for the HIRS. From 300-600 mb, the average improvement of AMTS over HIRS is about .3°C, again roughly independent of method, with physical retrievals about .2°C better for each instrument. Beneath 600 mb, the improvement of AMTS over HIRS is about 50% larger using the physical retrieval scheme (.3°C) compared to the statistical scheme (.2°C) and the difference in accuracy for retrieval type is bigger than for instrument type. A similar result holds for the surface skin (ground) temperatures.

The results from the cloudy portion of the test, containing 40 land mid-latitude winter cases, are shown in Fig. 2. The same general trends hold for the cloudy case except that the improvement of AMTS over HIRS, especially in the lower troposphere, and of the physical retrieval method over statistical method, are considerably enhanced in the cloudy cases. It should be noted that in the cloudy portion of the test, with cloud fraction ranging from 65% to 95%, GLAS performed retrievals in all 40 test cases, while NESDIS performed retrievals in only 36 cases out of 40, considering 4 cases to be too cloudy to do retrievals. The results of the test are summarized in Table 1 showing RMS temperature errors for 18 tropospheric layers, 4 stratospheric layers, and surface skin temperature.

The results of the test are consistent with our findings with real HIRS2/MSU data (Suskind et al., 1982) which indicate that the GLAS retrievals are more accurate than the operational NESDIS retrievals, especially with increasing cloud cover. As a result of this test, NASA Headquarters has decided to fund the development of an AMTS instrument initially for a shuttle experiment, then possibly for use on a satellite. In addition, NOAA has decided that physically based retrievals are indeed superior to statistically based retrievals and are beginning to develop a physically based system for operational use.

TABLE 1
NASA/NOAA COMPARISON TEST

Clear-Column Case (400 Cases)

Sounder-Retrieval	$\Delta T^{\circ}\text{C}$ Troposphere	$\Delta T^{\circ}\text{C}$ Stratosphere	$\Delta T^{\circ}\text{C}$ SST
AMTS - Physical Relaxation	1.39	1.58	0.28
AMTS - Statistical Regression	1.62	1.69	1.05
HIRS - Physical Relaxation	2.00	2.49	0.72
HIRS - Statistical Regression	2.14	2.46	1.01

Cloudy Case (40 Cases)

Sounder-Retrieval	$\Delta T^{\circ}\text{C}$ Troposphere	$\Delta T^{\circ}\text{C}$ Stratosphere	$\Delta T^{\circ}\text{C}$ SST
AMTS - Physical Relaxation	1.72	1.82	0.73
AMTS - Statistical Regression*	1.97	1.95	1.82
HIRS - Physical Relaxation	2.36	3.03	1.06
HIRS - Statistical Regression*	2.80	3.24	1.76

*36 Cases

REFERENCES

- Reuter, D., J. Susskind, and A. Dalcher, 1982: Simulation studies of the HIRS/MSU and AMTS/MSU satellite sounding units: cloudy conditions. NASA Tech. Memo. 84983, pp. 58-73.
- Susskind, J., J. Rosenfield, D. Reuter, and M. T. Chahine, 1982: The GLAS physical inversion method for analysis of HIRS2/MSU sounder data. NASA Tech. Memo. 84936.
- Susskind, J., D. Reuter, and A. Dalcher, 1983: Simulation comparison study of the AMTS and HIRS2 sounders. NASA Tech. Memo. 84983, pp. 59-67.

Fig. 1

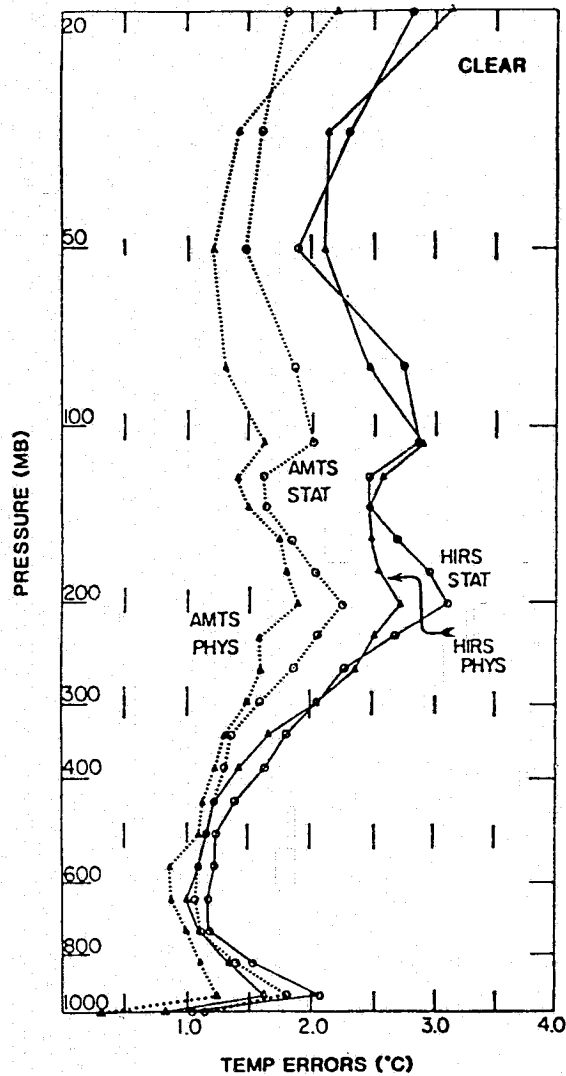


Fig. 1. Vertical distribution of rms retrieval error for 400 clear soundings averaged over all latitudes and both seasons. Values are plotted at the mean log p for each layer.

Fig. 2

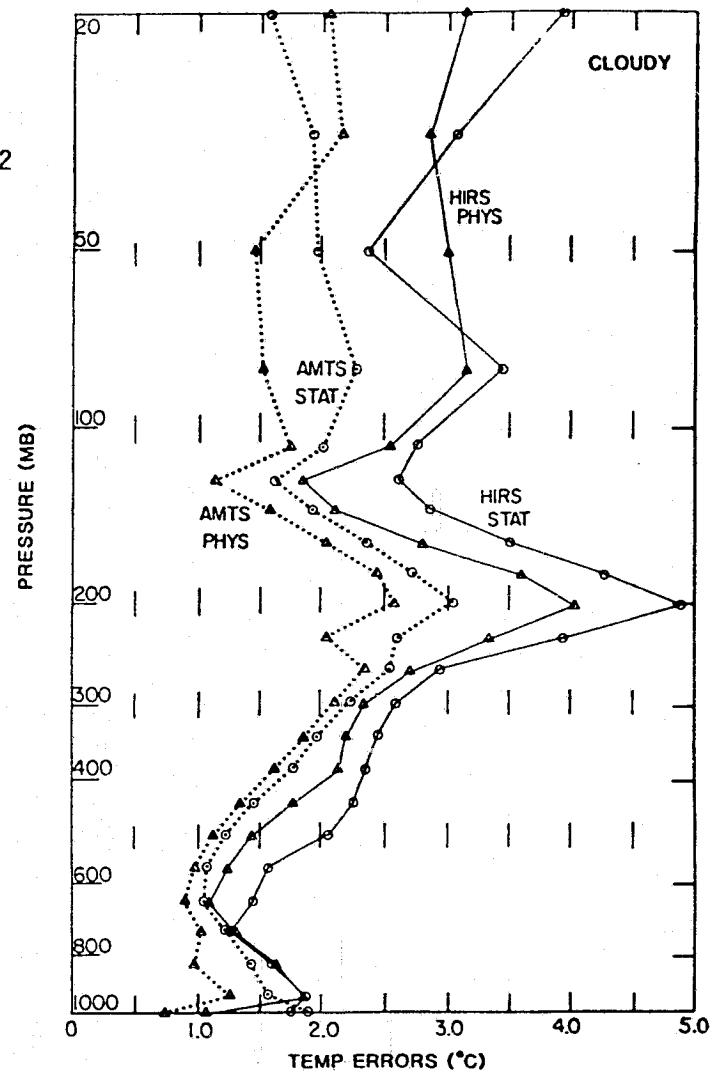


Fig. 2. Vertical distribution of rms retrieval error averaged over forty mid-latitude cloud scenes for HIRS PHYS and 36 cloud scenes for HIRS STAT. Values are plotted at the mean log p for each layer.

ORIGINAL PAGE IS
OF POOR QUALITY

IMPROVED HIRS2/MSU SOUNDINGS USING TROPOPAUSE INFORMATION

J. Susskind, M.-J. Munteanu, and P. Piraino

One of the factors limiting the accuracy of atmospheric temperature soundings from passive sounders is the relatively low vertical resolution of the observations, which are sensitive primarily to changes in temperature averaged over relatively thick atmospheric layers. If atmospheric lapse rates are constant over a thick layer, there is nothing to resolve, and therefore soundings in this part of the atmosphere should be good. In regions containing quite a bit of structure, such as the vicinity of the tropopause, which is characterized by a sharp change in lapse rate, poor soundings can result unless other information is present. Additional information such as a forecast temperature profile, or statistical relationships between satellite observations and temperature profiles, are in fact currently used in physically and statistically based schemes respectively. Nevertheless, the utility of this information depends on its applicability to the synoptic situation under observation. Therefore, tropopause information obtained from an additional source, such as TOMS observations, which give the total ozone burden of the atmosphere, a parameter highly correlated with tropopause height, (Munteanu, 1982) should be useful in improving sounding accuracy.

The first question is how such information should be used. We will work in the context of the GLAS physical retrieval scheme (Susskind et al., 1982). In this scheme, all temperature profiles are expressed as an expansion about a global mean, using empirical orthogonal functions derived from a large sample of radiosondes

$$T(P) = T_G(P) + \sum_i a_i f_i(P) \quad (1)$$

with the coefficients a_i uniquely determining the solution.

Estimates of layer mean temperatures, \bar{T}_j , for all layers between the mandatory levels, are used to determine a_i

$$A = [F'F + \sigma H]^{-1} F' [\bar{T} - \bar{T}_G] \quad (2)$$

where A is the vector a_i , \bar{F}_{ij} is the mean value of $f_i(P)$ in layer j , \bar{T} and \bar{T}_G are the mean of the estimated temperature $T(P)$ and the mean of $T_G(P)$ in layer j , H is a diagonal matrix with H_{ij} being the inverse of the fractional variance of temperature profile explained by $f_i(P)$, and σ is a constant. The estimates of layer mean temperatures come from both radiance and first guess information. Ten layers are used to determine 6 coefficients in an iterative scheme which updates \bar{T} and A .

If, in addition, one knows the tropopause pressure, P_T , and tropopause temperature, $T(P_T)$, one can add another row to the matrices representing \bar{F} , \bar{T} , and \bar{T}_G , where in this case, the bar refers to values of F or T at P_T , rather

than the average value of the quantities over layer j , and again solve for A using equation (2). Because the solution is overdetermined, one will not return the exact estimate of $T(P_T)$ in the solution but treat it as another piece of data.

Table I demonstrates the improvement in retrieval accuracy for a sample of collocated soundings with land radiosondes in SOP-1 of FGGE using a 6 hr forecast first guess. Column 1 gives the RMS accuracy of the forecast guess for the (384) samples in which a retrieval was performed. Column 2 gives the RMS errors of the GLAS retrievals performed in the usual manner, and column 3 gives the RMS errors of the retrievals which used, in addition, perfect knowledge of tropopause pressure and temperature obtained from the radiosonde reports, incorporated into equation (2) in each iteration as described above. Clear improvements are found in the 200-300 mb layer in the vicinity of the tropopause, as expected, when perfect tropopause information is included in the analysis. Also shown in columns 5-7 are analogous results from retrievals starting with a climatology guess. Here, the retrievals are much better than the guess, but poor, especially in the 300-400 mb region, compared to the retrievals generated with a forecast guess. Use radiosonde tropopause information significantly improved their accuracy to be comparable to those using tropopause information with a forecast guess, except near the ground. Potential improvement may still result with less than perfect tropopause information provided that the RMS error of the tropopause temperatures included in the sounding are sufficiently accurate. In fact, according to the scheme used, the temperature does not have to agree with the actual tropopause temperature, only with the temperature at the pressure taken to be the tropopause temperature. Nevertheless, if a single temperature is known reasonably well, its greatest beneficial effect would be at the tropopause, where potential errors are largest.

Reasonable errors of tropopause pressure and tropopause temperature can be obtained from estimates of the layer mean temperatures between the mandatory levels according to

$$\hat{P}_T = B\bar{T} + C \quad (3)$$

where \bar{T} is the vector of layer mean temperatures between mandatory levels starting with 700-500 mb, and ending with 70-50 mb, and

$$\hat{T}(\hat{P}_T) = D\bar{T} + E\bar{T}(P_T) + G \quad (4)$$

where $\bar{T}(\hat{P}_T)$ is the mandatory level slab surrounding (\hat{P}_T) , and B , C , D , E , and G are matrices and vectors to be determined. The coefficients in equation (3) and (4) were determined using a global set of radiosonde layer mean temperatures and tropopauses. The relationships were tested on an independent global sample, again using radiosonde information, for which the RMS error of \hat{P}_T was 21 mb and $\hat{T}(\hat{P}_T)$ was 1.8° .

The ability to estimate tropopause information from layer mean temperatures suggests incorporating the layer mean temperatures estimated from the sounding itself to give estimates of tropopause pressure and temperature. While information completely independent of sounding and first guess data is preferable, new information is in fact added to the system by the statistical relationships between tropopause temperature and pressure and layer mean temperature profiles. This should not be confused with use of statistical relationships between temperature profiles and satellite observations, which form the basis of a statistical retrieval system but is in no way used in the physical retrieval scheme.

Columns 4 and 8 in table 1 show the results of retrievals in which estimates of layer mean temperatures in every iteration, \bar{T}^N , are used to compute \hat{P}_T^N and $\hat{T}(P_T^N)$ using equation (3) and (4), and to get $T(P)^{N+1}$ according to equations (1) and (2) incorporating the estimated tropopause information. In the case of the 6 hour forecast guess, in which the initial guess and retrieved temperature profiles were already very good, little change is found in the solution. In the case of the climatology guess, however, significant improvement in the accuracy of the solution in the mid-upper troposphere is obtained by the new procedure. This procedure appears to have the desirable property of improving a poor retrieval while not harming a good one. Further testing will be done before it is implemented as part of the "operational" GLAS retrieval scheme.

REFERENCES

- Munteanu, M. J., 1982: Study of tropopause height estimate from TOMS total ozone data from NIMBUS-7 and from the microwave regression temperature retrieval of simulated brightness temperatures. NASA Tech. Memo. 84983., pp. 46-54.
- Susskind, J., J. Rosenfield, D. Reuter, M. T. Chahine, 1982: The GLAS physical inversion method for analysis of HIRS/MSU sounder data. NASA Tech. Memo. 84936.

TABLE 1
LAYER MEAN RMS ERRORS °C

LAYER (MB)	FORECAST GUESS	FORECAST RETRIEVAL	WITH RADIOSONDE TROPOPAUSE	WITH ESTIMATED TROPOPAUSE	CLIMATOLOGY GUESS	CLIMATOLOGY RETRIEVAL	WITH RADIOSONDE TROPOPAUSE	WITH ESTIMATED TROPOPAUSE
50-70	2.9	2.1	2.0	2.0	5.7	2.5	2.1	2.3
70-100	2.4	2.1	2.2	2.2	4.8	2.3	2.1	2.4
100-200	2.1	1.9	1.8	2.0	4.4	2.3	1.8	2.2
200-300	2.3	2.0	1.4	1.9	3.8	2.2	1.2	2.5
300-400	2.2	2.0	1.9	2.1	3.6	2.9	1.8	2.2
400-500	2.4	2.1	1.8	2.2	5.0	2.2	2.1	2.3
500-700	2.4	2.0	1.8	2.0	5.9	2.5	2.0	2.1
700-850	2.7	2.1	2.2	2.1	6.9	2.3	2.5	2.5
850-1000	3.5	2.3	2.5	2.3	7.4	3.0	3.1	3.0
TOTAL	2.58	2.07	1.98	2.09	5.42	2.48	1.88	2.40

COMPARISON OF GLAS RETRIEVED CLOUD FIELDS WITH MODEL GENERATED RAINFALL FIELDS

J. Susskind and E. Kalnay

Monthly mean fractional cloud cover, cloud top pressure, and cloud top temperature are important climatological products of the GLAS retrieval system (Susskind et al., 1982). While verification of cloud parameters is difficult, it is of interest to compare the results for consistency with related fields obtained by other approaches. Here, we compare the GLAS retrieved cloud fields for January and February 1979, from SOP 1 of FGGE, with rainfall rates produced in the GLAS forecast/analysis system for the same months.

Figs. 9a and 9c of Susskind et al. (1982) show the monthly average of fractional cloudiness and average cloud top temperature (day and night) corresponding to January 1979. Major features such as the ITCZ, the South Pacific Convergence Zone, the storm tracks in the North Atlantic and North Pacific oceans, dry land regions such as the Australian and Saharan deserts, and dry oceanic regions west of Peru, Northern and Southern Africa, which are dominated by subtropical anticyclones, are readily apparent in the mean cloudiness map. The cloud top temperature map allows for clear identification of deep convective regimes in the tropics, and shallow stratiform clouds west of the continents in the Southern Hemisphere.

Another quantity of interest is the breakdown of cloudiness into day (3 AM) night (3 PM) shown for January and February 1979 in Figs. 1 and 2. Note, for example, the significant increase in the amount of stratus clouds west of the Southern Hemisphere continents at night. It is also remarkable that the intense convective regions of South America, Africa and Indonesia show more intense cloudiness at 3 AM than at 3 PM. In general, the features of Figs. 1 and 2 are quite consistent with maps of outgoing long wave and short wave radiation inferred from AVHRR data (Gruber and Varnadore, 1983).

Figs. 1c and 2c present the total precipitation field derived diagnostically from the GLAS Analysis/Forecast system for January and February 1979. The contour intervals are 1, 2, 4, 8, 16 and 32 mm/day, with the 4 mm/day contour enhanced. As with the cloudiness maps, this field is generally reasonable and consistent with precipitation climatologies and the inter-annual and intra-annual winter variations. The regions of tropical convection over Australia, South America and Africa, the Northern Hemisphere storm tracks, and the subtropical dry regions over oceans mentioned observed in Figs. 1a and 2b are also clearly present in these fields. However, we should point out some particular areas of agreement between the precipitation fields and the cloudiness fields. The very strong band of convective activity east of the coast of South America, which is a result of the presence of a large amplitude stationary wave present during January 1979 and absent during most of February 1979 (Kalnay and Paegle, 1983), is apparent in both January fields and much weaker in the February fields. The very intense South Pacific Convergence Zone (SPCZ) is also much stronger and further to the east in January than in February in both fields. On the other hand, a similar region of oceanic convection southeast of Africa appears to be much stronger in February than in January. A secondary maximum of the SPCZ north of New Zealand is also present in both fields. Of the many regions of coincidence, there is a particularly striking phenomenon: west of

the coast of Peru, at about 20°S, there is a distinct small scale maximum in precipitation which coincides precisely with a maximum in the cloudiness field. We are not aware whether this phenomenon has been previously reported in the meteorological literature.

It is interesting to note that this maximum in cloudiness and precipitation does not appear in the NOAA/NESS fields of albedo and outgoing long-wave radiation (Gruber and Varnadore, 1982), which are normally sensitive to cloud fields. The reasons for this become clear when we look at Figs. 1 and 2, which indicate that these clouds, which are low level with warm tops, are mainly a nocturnal phenomenon. This implies that they do not appreciably affect the albedo (measured during the day) or the outgoing long wave radiation (because they are warm). If this maximum had only been observed in a single derived field, we might have concluded that it was a deficiency of the corresponding system. The fact that it appears in the two independently derived fields is a strong suggestion that it is a real phenomenon, which we plan to study in detail.

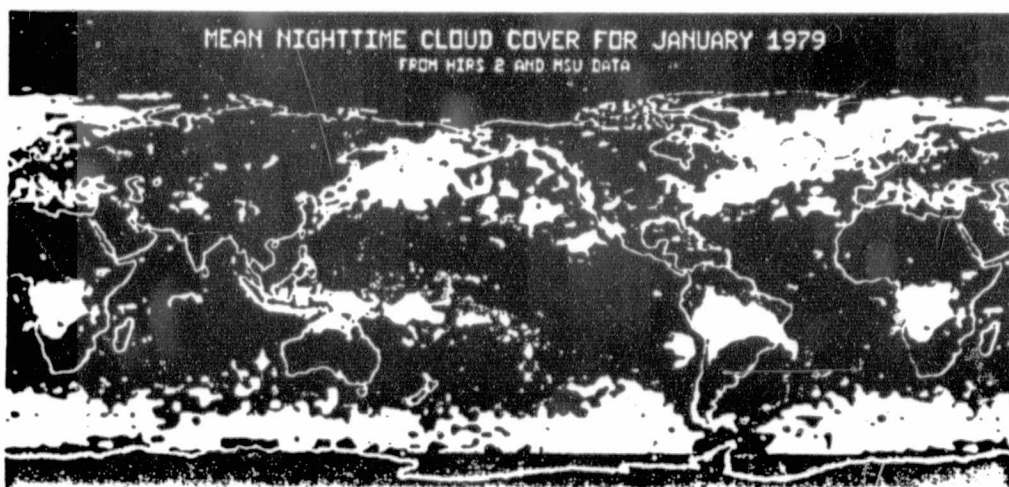
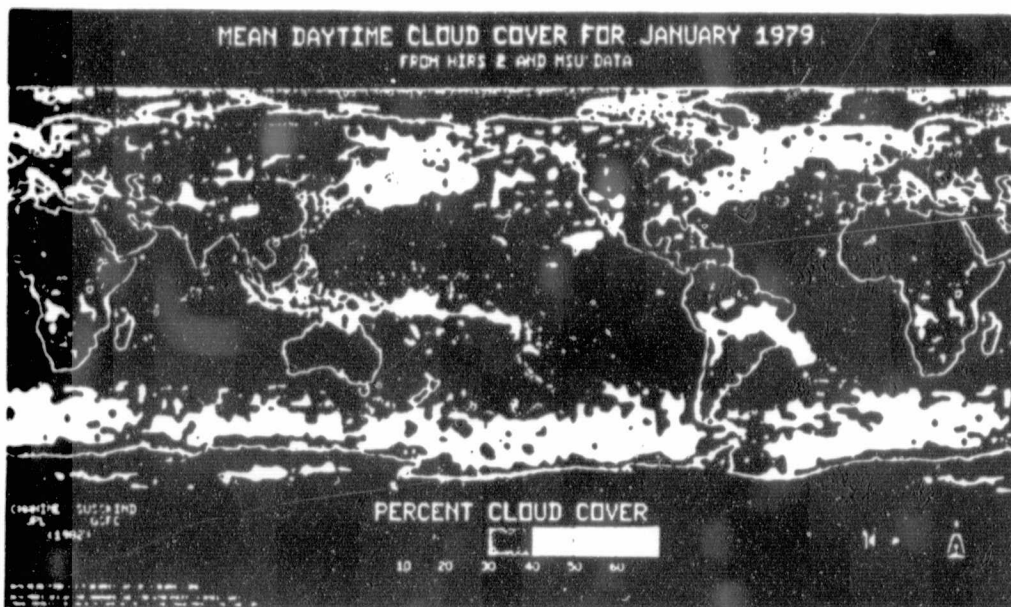
REFERENCES

Gruber, A., and M. Varnadore, 1982: Private communications.

Kalnay, E., and J. Paegle, 1983: Large scale stationary waves in the Southern Hemisphere: observations and theory. Preprint volume First International Conference on Southern Hemisphere, AMS, pp. 89-92.

Susskind, J., J. Rosenfield, D. Reuter, and M. T. Chahine, 1982: The GLAS physical inversion method for analysis of HIRS2/MSU sounding data. NASA Tech. Memo. 84936.

ORIGINAL PAGE IS
OF POOR QUALITY



TOT PREC (MEAN) AFT M/S STATISTICS START 1/ 5/79 TO 2/ 2/79

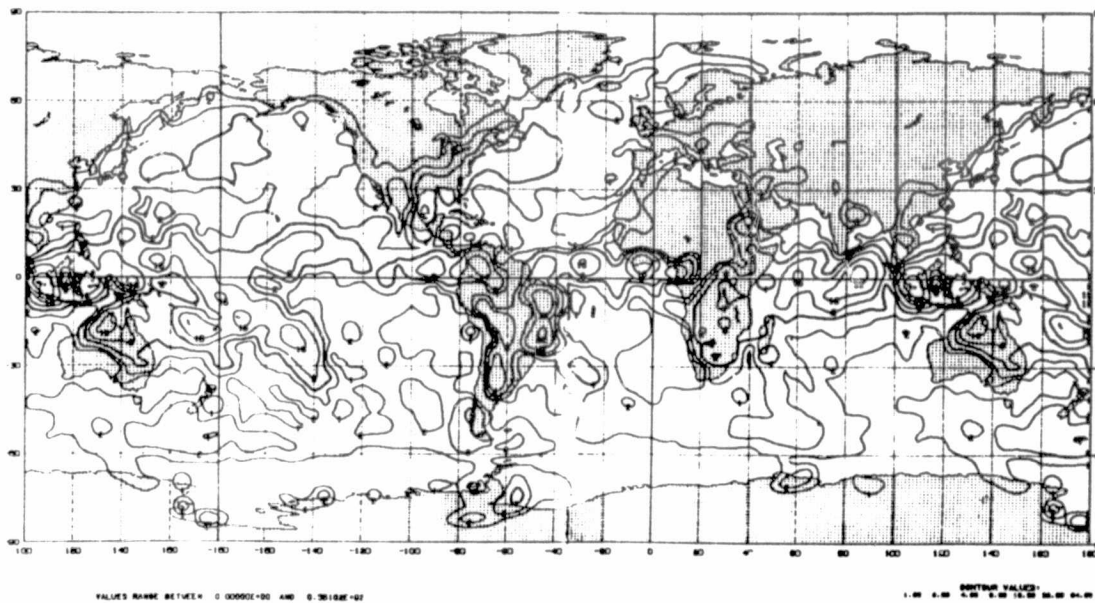
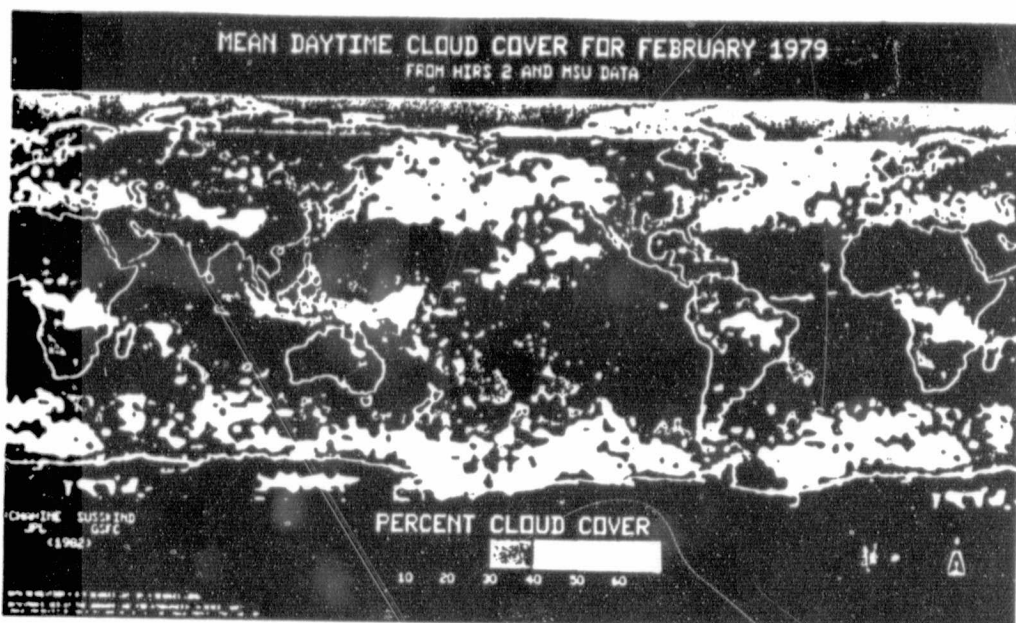


Fig. 1

ORIGINAL PAGE IS
OF POOR QUALITY



TOT PREC (MEAN) AFT MM/DAY STATISTICS START 2/ 3/79 TO 3/ 4/79

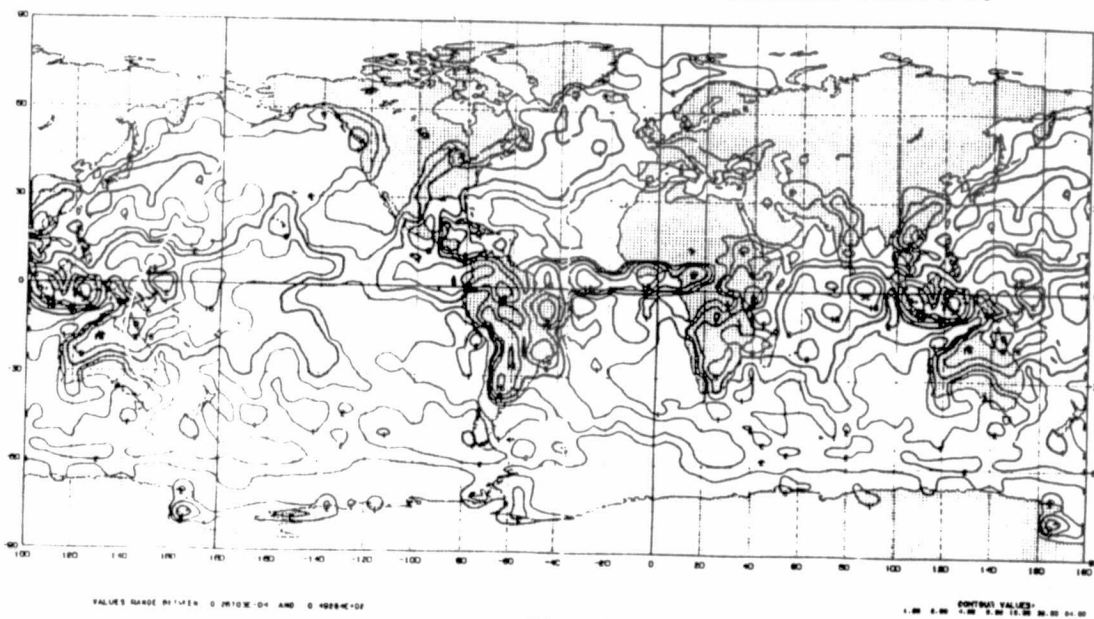


Fig. 2

HIGH RESOLUTION GLAS RETRIEVALS ON THE MCIDAS

J. Susskind, R. Atlas and A. Pursch

The GLAS physical inversion method for analysis of HIRS2/MSU data (Susskind et al., 1982) has been implemented on the McIDAS. The method of analysis is identical to that used in processing global retrievals for six months of 1979, with the exception that the McIDAS retrievals are done on a higher spatial resolution, with one sounding attempted in every 4 x 4 array of HIRS2 spots, corresponding to roughly 80 x 80 km at nadir. This 4 x 4 array is further subdivided in 4 2 x 2 arrays with the sounding being performed utilizing all the spots in the single warmest 2 x 2 quadrant as sensed by the 11 μ m window channel. In contrast, the global scale retrievals were performed on a 250 x 250 km grid, with 1 retrieval performed utilizing all the spots in a single 125 x 125 km quadrant selected as above. As in the global scale retrievals, soundings are objectively edited as a result of non-convergence of the solution or excessive cloudiness.

The McIDAS system can be used in two modes, display and interactive. The display mode can be used to study different synoptic situations, to compare different retrieval systems, and to analyze the performance of the GLAS retrieval system under different conditions to determine if any shortcomings exist which can be corrected. In the interactive mode, a man is used in the loop, performing subjective editing of retrievals for self consistency and consistency with other observations. In addition, key areas for retrievals can be selected and additional information can be supplied which is utilized in the retrieval. The current study was completely non-interactive. The purpose was to determine if accurate retrievals can be performed on the high resolution grid without editing. In addition, we compared different retrievals for a synoptic situation and examined the guess dependence of the high resolution GLAS retrievals.

The case selected for study was the orbit crossing the central United States at 1/21/79 0925Z. Radiosondes at 1200Z are used for comparison. The synoptic situation was marked by a sharp trough centered at about 95°W longitude with a deep pressure low centered at about 35° N, 80° W. Fig. 1a shows the location, and reported values in decameters of the 1000-500 mb thickness given by the radiosonde reports. For comparison, Figs. 1b-1d show the location and values of the thickness derived from the NESS operational soundings, the GLAS global mode soundings, and the GLAS high resolution soundings performed on the McIDAS.

Comparisons of the contoured analyses of the 500-1000 mb thickness fields derived from the satellite retrievals and from the radiosondes are shown in Figs. 2a-2c. All retrievals capture the basic structure of the trough reasonably well. The trough produced by the NESS retrievals in Fig. 2a is somewhat too shallow, however, with errors of 60 meters apparent east, south, and north of the trough. The global scale GLAS retrievals produce a sharper trough in better agreement with the RAOB data to the east and north of the trough. The high resolution GLAS retrieval field is quite similar to that produced at lower resolution but the 540 and 546 decameter contours extend further south, giving better agreement with the RAOB data in this vicinity. It is interesting to note that the center of the trough has been shifted west by about 1° in the

high resolution retrieval field, giving apparently poorer agreement with the radiosonde field than obtained with the GLAS global retrievals. It must be remembered that the retrievals occurred 2 1/2 hours prior to the radiosondes and it is possible that the trough moved slightly to the east in this time. It is particularly encouraging that a smooth reasonable field was produced by the high resolution soundings without the need for any subjective editing. This is counter to the experience obtained during the "special effort" (Atlas et al., 1981) in which regression based soundings, were produced using a 3 x 3 spot resolution.

An important question often asked about physically based retrievals, which start with an initial guess temperature field, is how much of the information in the retrieved field actually came from the guess. Fig. 3a shows the 500-1000 mb 1000 mb thickness field of the 6 h forecast first guess used to produce both the GLAS global mode and high-resolution soundings, superimposed on that of the high resolution retrievals. The first guess field does contain the basic structure of the trough but it is too broad and centered about 4° to the east. These features were corrected by the retrieval.

In order to test the dependence of the solution on the first guess field used, we again performed high resolution retrievals, this time using a totally different first guess field, obtained from the 6 h forecast for 1/18 12Z, shown in Fig. 3b superimposed on the forecast for 1/21 12Z. The incorrect first guess contains a slight ridge, rather than a sharp trough, and differences of up to 300 meters in 500-1000 mb geopotential thickness occurs in many locations. The 500-1000 mb geopotential thickness field retrieved using based on the incorrect first guess is shown in Fig. 3c, superimposed on the field retrieved using the correct first guess. While the center of the trough is not quite as sharp, the general agreement between the fields is excellent, with differences typically of the order of 30 meters. This indicates that most of the horizontal gradient information of relatively thick atmospheric layers is indeed coming from the satellite observations. The first guess information becomes more significant in thinner layers which are not well resolved by the satellite observations.

Aside from atmospheric soundings, the GLAS physical retrieval scheme also produces ground temperatures, surface emissivities, cloud fraction, and cloud top pressure. Retrieved values of these quantities obtained from the high resolution soundings are shown in Figs. 4a-4d. It is encouraging to see relatively noise free fields of ground temperature, given in tenths of degree C minus 200, and surface emissivity, given in percent, produced at high resolution. Fig. 4a shows that the ground-temperatures (2:30 AM local time) are below freezing for most of the area north of 30°N. On the other hand, the warm sea surface temperatures in the Gulf of Mexico clearly stand out. Surface emissivities at 50.3 GHz have the properties that dry land emissivities are about .9 or higher, snow covered land emissivities are less than .9, open water emissivity is .65 or less, and mixed fields of view, such as coasts, have intermediate values. The emissivities shown in Fig. 4b again clearly differentiate the Gulf of Mexico from the mainland and also indicate snow cover in the region northwest of about 38°N, 90°W. The cloud parameters shown in Figs. 4c (percent cloudiness) and 4d (cloud top pressure) indicate clear skies west of 90°W with large amounts of mid-high clouds to the east. The maximum cloudiness, as evidenced by the 11 μ m window observations, is in the vicinity of 37°N, 85°W. The cloud retrieval scheme used in the analysis did not retrieve cloud parameters

at this location as a result of a conceptual bug in the program, resulting from the fact that the brightness temperatures in the window channel was colder than the guess temperature field at any level of the atmosphere, and no solution for cloudiness could be found. This has since been corrected, and total cloudiness is placed at the tropopause under such a condition.

As a result of this and similar studies, we will be switching to the high resolution sounding mode employed on the McIDAS in our global retrievals program run on the CYBER 205 as soon as the program is fully vectorized to further enhance the speed at which soundings are done.

REFERENCES

- Atlas, R., A. Pursch, C. Long, G. Cole, and R. Rosenberg, 1981: Preliminary evaluation of the FGGE special effort for data enhancement. NASA Tech. Memo. 83907., pp. 52-60.
- Susskind, J., J. Rosenfield, D. Reuter, and M. T. Chahine, 1982: The GLAS physical inversion method for analysis of HIRS2/MSU sounder data. NASA Tech. Memo. 84936.

ORIGINAL PAGE IS
OF POOR QUALITY

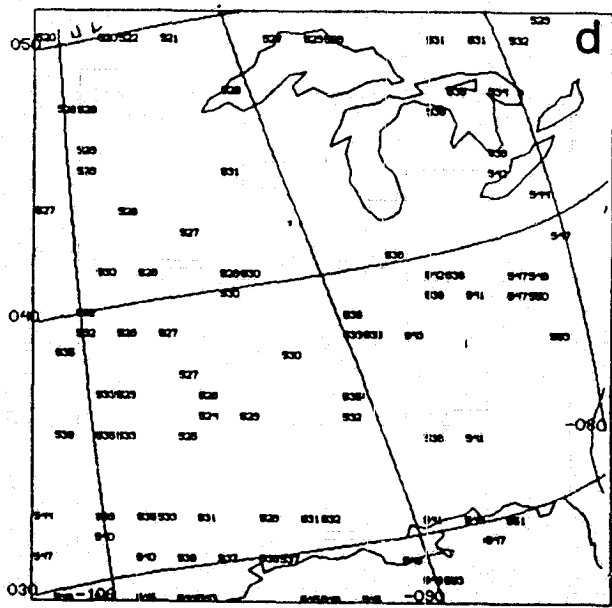
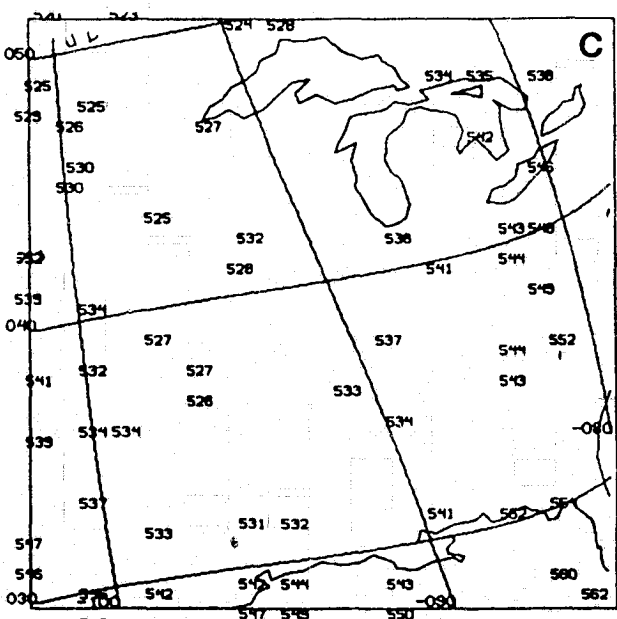
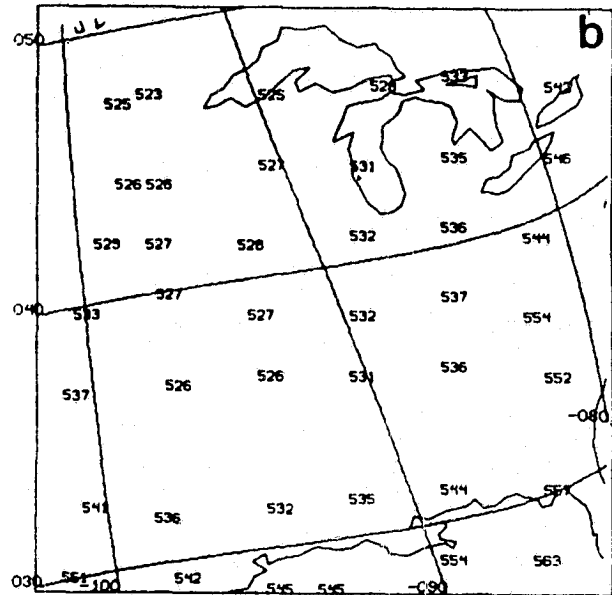
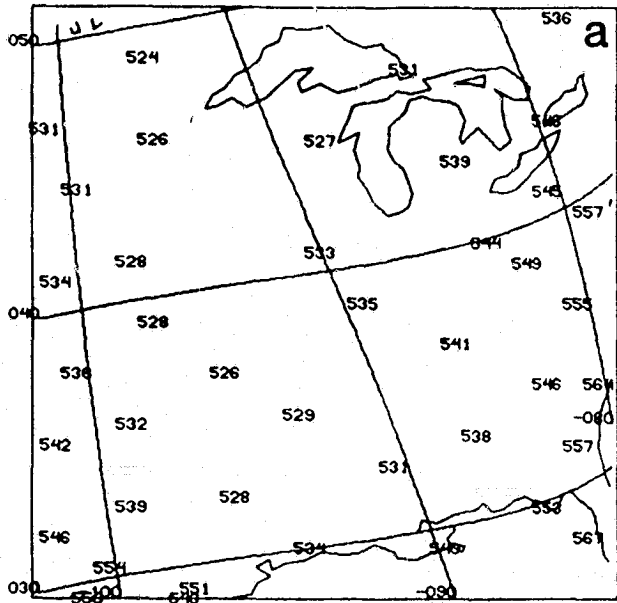


Figure 1. Observed and retrieved 500-1000 mb thickness in decimeters.

ORIGINAL PAGE IS
OF POOR QUALITY

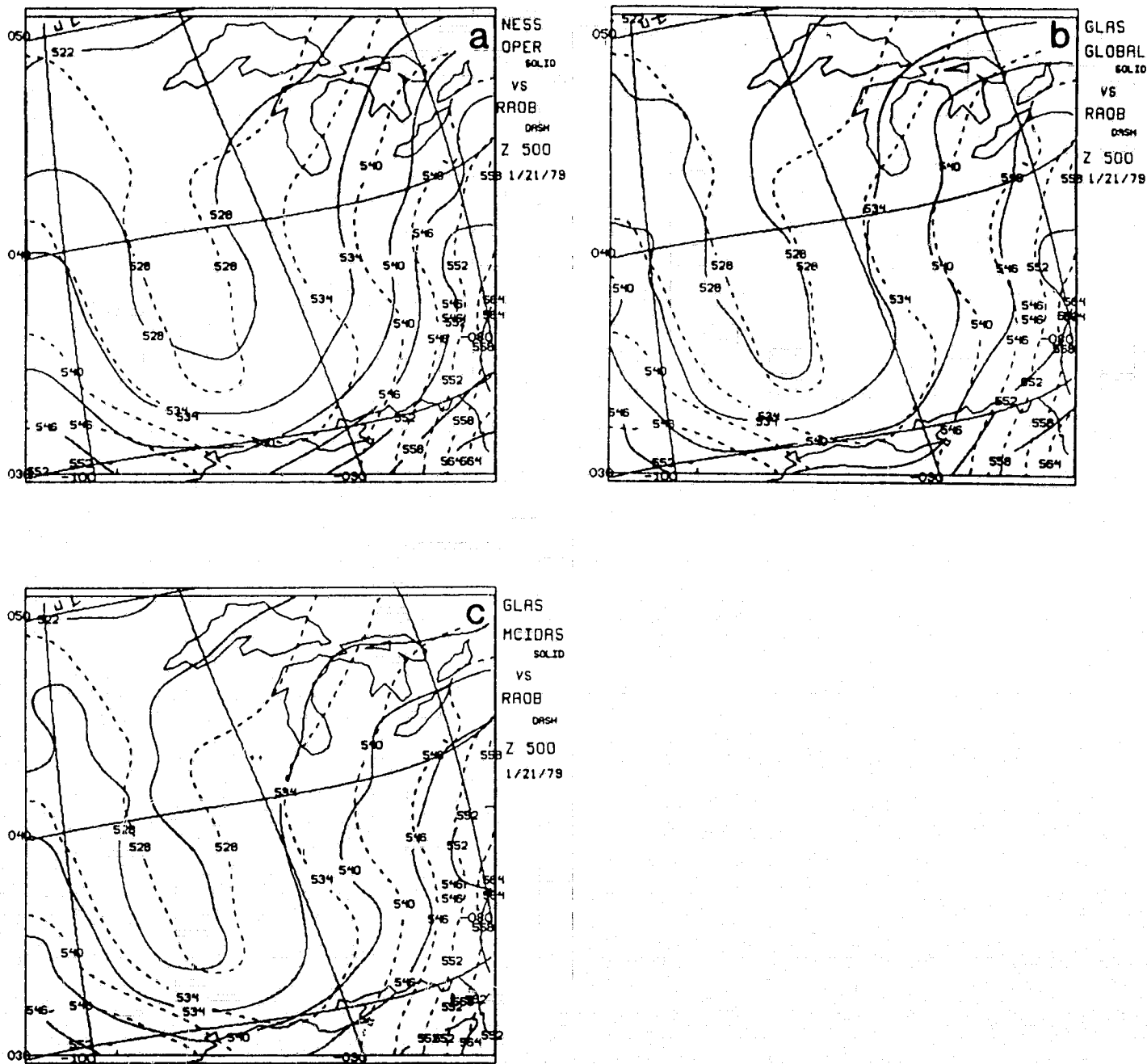


Figure 2. Superposition of analyzed retrieved (solid) and observed (dash) 500-1000 mb thickness fields.

ORIGINAL PAGE IS
OF POOR QUALITY

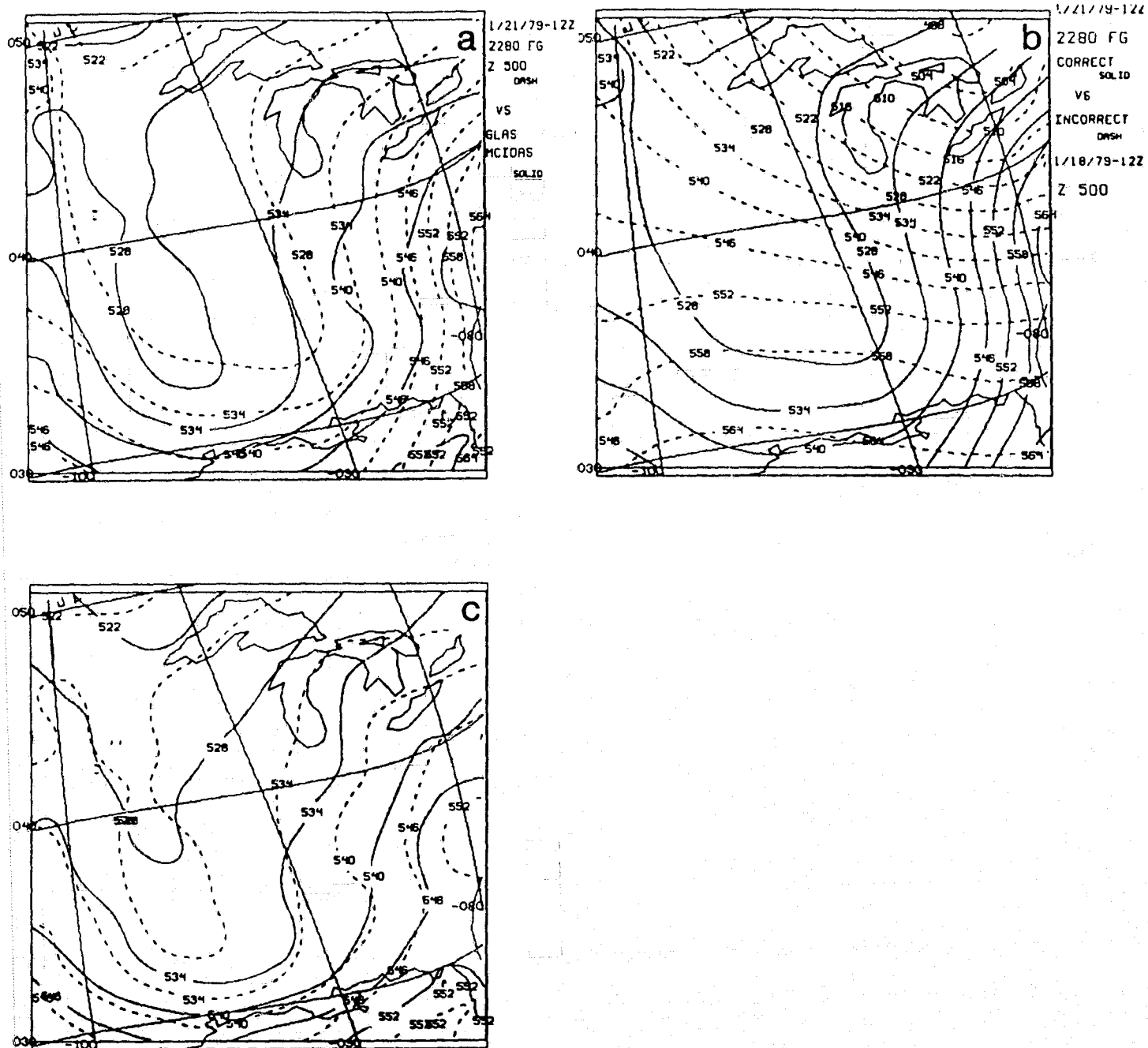
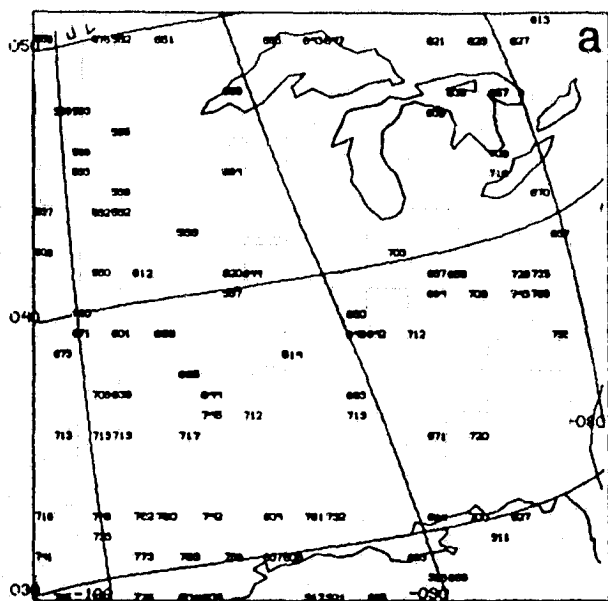
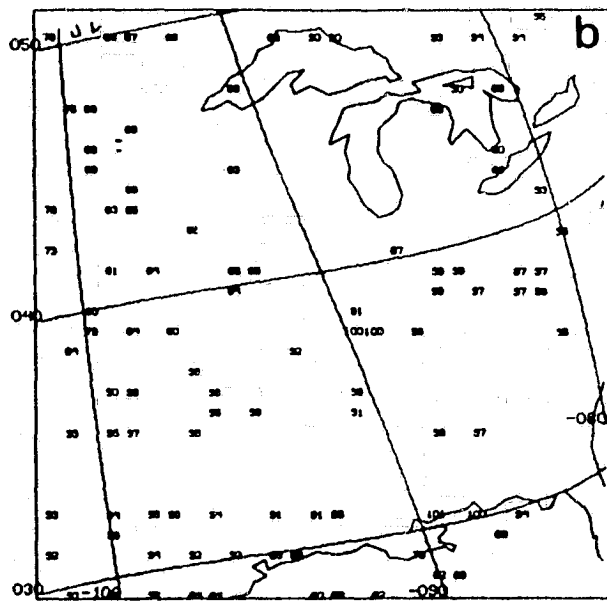


Figure 3. Comparison of 500-1000 mb fields, a) correct first guess (dash) vs. GLAS retrievals from correct guess (solid); b) correct first guess (solid) vs. incorrect first guess (dash); c) retrievals from incorrect guess (solid) vs. retrievals from correct guess (dash).

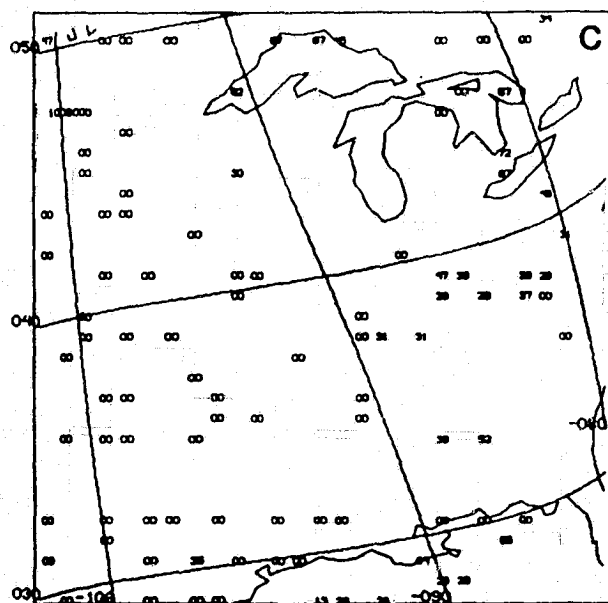
ORIGINAL PAGE IS
OF POOR QUALITY



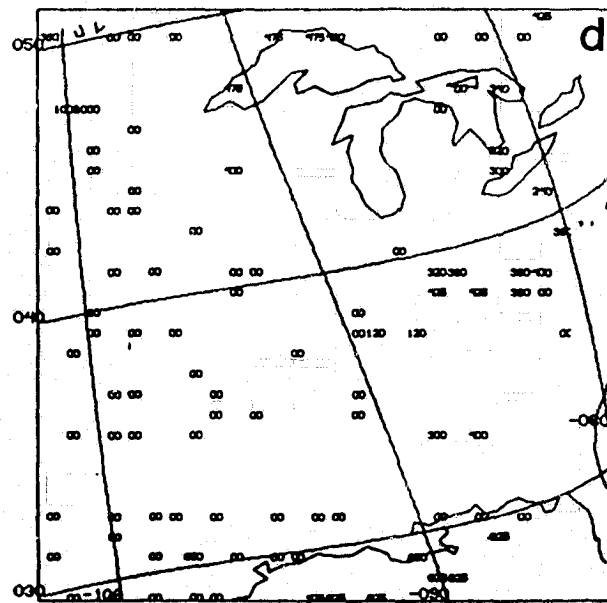
a GLAS
MCIORS
GROUND
TEMP.
1/21/79
09232



b GLAS
MCIORS
EMISS.
1/21/79
09232



c GLAS
MCIORS
CLOUD
FRACTION
1/21/79
09232



d GLAS
MCIORS
CLOUD
HEIGHTS
1/21/79
09232

Figure 4. Locations and values of retrieved ground temperature, surface emissivity, cloud fraction, and cloud top pressure from the GLAS high resolution retrieval.

D14
N84 22063

A NEW ALGORITHM FOR TUNING OF COMPUTED RADIANCES FOR HIRS2/MSU

J. Susskind, P. Piraino, D. Reuter

The GLAS physical inversion method for analysis of HIRS2/MSU satellite data finds atmospheric and surface conditions, which, when substituted in the radiative transfer equations representing the observations in the individual spectral channels, matches these observations to a given expected noise level (Susskind et al., 1982). Before accurate retrievals can be produced, one must first be able to compute accurate channel averaged radiances given the true atmospheric and surface conditions. As shown in Susskind et al. (1982), small biases of the order of 1°C exist in brightness temperatures computed for a number of atmospheric sounding channels using radiosonde reports of atmospheric temperature humidity profile compared to those of collocated HIRS2/MSU observations on TIROS N. These biases have been attributed to errors in the computed atmospheric transmittances functions, $\tau_i(P)$, representing the transmittances in channel i from atmospheric pressure P to the top of the atmosphere. Channel dependent empirical tuning coefficients, ϵ_i , have been found such that the biases in the channel brightness temperatures are removed if the transmittances used to calculate these brightness temperatures are modified according to

$$\tau'_i(P) = \tau_i(P)^{1+\epsilon_i} \quad (1)$$

The procedure not only removes biases, but, when biases are significant ($\approx 1^\circ\text{C}$), also reduces the standard deviation somewhat (Susskind et al., 1982). This indicates that in fact at least some of the observed bias is computational, rather than instrumental.

Possible shortcomings of this method are that some of the bias errors may be due to instrumental calibration problems and that the part that is computational may not be of the form assumed in equation 1. An additional shortcoming of tuning according to equation 1 is the computational time involved and the difficulty in vectorizing the computation. Therefore a new form of tuning was implemented in the calculation which has the potential of distinguishing between calibration and calculation errors and is also computationally faster and more easily vectorizable.

The form of the tuning was derived from considerations based on statistical regression analysis of sounding data, which has the advantage of being relatively independent of atmospheric transmittance calculations, but the disadvantage of not being able to account for various physical factors, aside from atmospheric temperature, affecting radiances. Statistical regression uses the form

$$T(P) - \bar{T}(P) = A[\theta - \bar{\theta}] \quad (2)$$

where $T(P)$ is the atmospheric temperature profile, θ is the vector of observed brightness temperatures, the bar represents the mean over a sample, and A is an empirically determined matrix. If the atmospheric transmittance or instrumental

response were slightly different, and a slightly different set of brightness temperatures, θ' and $\bar{\theta}'$, were observed, one would still obtain basically the same results by the regression relationship

$$T(P) - \bar{T}(P) = B[\theta' - \bar{\theta}'] \quad (3)$$

from which we derive

$$\theta' = [B'B]^{-1} B'A[\theta - \bar{\theta}] + \bar{\theta}' \quad (4)$$

or equivalently

$$\theta' = (C+I)\theta + D. \quad (5)$$

Equation 5 is the form we use for tuning the computed brightness temperatures θ to empirically corrected brightness temperatures θ' which are used to match the observations. Note that equation 5 allows the possibility of a bias due to calibration problems in the vector D, and a calibration gain error in the diagonal of the matrix C. In addition, different calculation errors as a function of atmospheric temperature profile, which is represented by the computer brightness temperatures θ , are accounted for by the off diagonal terms of the matrix C.

Another advantage of the new tuning procedure is the ability to utilize cloudy cases in determining the tuning coefficients. In cloudy cases, the clear column radiances, \tilde{R}_i , are reconstructed according to

$$\tilde{R}_i = R_{i,1} + \eta[R_{i,1} - R_{i,2}] \quad (6)$$

where $R_{i,1}$ and $R_{i,2}$ are radiances for channel i in two fields of view and η is determined as part of the iterative scheme using a combination of infra-red and microwave channels [Suskind et al., 1982].

Oceanic observations, from 50°N to 50°S, under both clear and partially cloudy conditions, were used to determine the coefficients C and D. Radiances were computed for every one hundredth observation using the NMC analysis for temperature-humidity profile and climatology for sea-surface temperature. First those observations considered to be clear, using untuned calculations to determine η , were used to determine C and D according to

$$CD = (\tilde{\theta} - \theta) \theta_1' [\theta_1' \theta_1' + \lambda_1^2]^{-1} \quad (7)$$

where CD is the $N \times N+1$ matrix containing the matrix C($N \times N$) and the vector D,

$(\tilde{\theta}-\theta)$ is the matrix (NxM) of reconstructed minus observed brightness temperatures for the N channels for each of the M cases in the sample, θ_1 is the matrix (N+1 x M), of computed brightness temperatures with an additional row of 1's, and λ_1 is a ridge regression vector taken as 20 for all N channels and .2 for the last value, corresponding to the unit term in θ_1 . Once C and D are determined from (7) using the clear cases, η is determined using tuned computations and a new matrix CD is recomputed as in equation (7), using all cases with $\eta < 2$. This tuning, under clear and cloudy cases, is consistent with the method used in the retrieval scheme to compute cloud corrections and should produce unbiased retrievals under clear and cloudy conditions, provided the sample is general enough.

Table 1 shows the mean and standard deviation of the reconstructed minus computed brightness temperatures for December 1981 NOAA 7 data for the 11 channels used in the tuning. Significant biases exist in a number of channels, which are much larger than those encountered with TIROS N data. The sources of these biases are not yet understood. Nevertheless, it is encouraging to see that the standard deviations are comparable to, if not better than, those obtained with TIROS N data. The largest standard deviations occur in HIRS2 channel 2 and MSU channel 4, which are sensitive to unknown temperatures in the mid-upper stratosphere, and in HIRS2 channels 7 and 13, which are sensitive to the sea-surface temperature which was fixed at climatology. The tuning removes the biases under clear conditions but does not significantly decrease the standard deviations even in cases where large biases existed. The results under cloudy conditions are slightly worse but imply accurate retrievals should be obtainable under cloudy conditions as well. Channels 5, 6 and 7, which degrade more under cloudy conditions, are not used for temperature sounding.

Table 2 shows the accuracy of retrieved temperature profiles for a 4 day period in December 1982 as compared to a global set of radiosondes collocated to + 3 hours, + 110 km. Results are shown for retrievals done using the old tuning procedure and the new procedure. The new procedure produced significant improvements in bias errors in the mid-lower troposphere and also produced a small improvement in standard deviations throughout most of the atmosphere.

REFERENCE

Susskind, J., J. Rosenfield, D. Reuter, and M. T. Chahine, 1982: The GLAS physical inversion method for analysis of HIRS2/MSU sounder data. NASA Tech. Memo. 84936.

Table 1

RECONSTRUCTED - OBSERVED BRIGHTNESS TEMPERATURES DECEMBER 1981 OCEAN

CHANNEL	CLEAR (87 CASES)				CLOUDY (345 CASES)			
	UNTUNED MEAN	UNTUNED STD. DEV.	TUNED MEAN	TUNED STD. DEV.	UNTUNED MEAN	UNTUNED STD. DEV.	TUNED MEAN	TUNED STD. DEV.
2	1.29	1.66	.00	1.66	1.09	1.84	-.00	1.83
4	.32	.43	.00	.43	.36	1.04	.00	1.04
5	.96	.59	.00	.56	1.02	1.49	.00	1.48
6	1.57	.75	.00	.73	1.62	1.83	.00	1.83
63 7	1.97	1.15	.01	1.14	1.92	2.11	.00	2.12
13	-3.91	.97	-.01	.97	-3.88	.94	-.01	.95
14	.57	.63	.00	.63	.59	.89	.00	.89
15	-2.87	.63	-.00	.59	-2.79	1.04	-.00	1.02
M2	-.88	.61	-.00	.59	-.89	.75	-.00	.75
M3	-1.19	.65	-.00	.65	-1.16	.77	-.00	.76
M4	.52	1.08	-.00	1.06	.31	1.27	.00	1.25

ORIGINAL PAGE IS
OF POOR QUALITY

Table 2

RETRIEVAL ERRORS COMPARED TO GLOBAL RADIOSONDES \pm 3 HRS \pm 110 KM

DEC 1 - DEC 4 1983

LAYER (MB)	OLD TUNING			NEW TUNING		
	MEAN	RMS	STD. DEV.	MEAN	RMS	STD. DEV.
850-1000	-1.02	2.33	2.10	.30	2.24	2.22
700-850	-.98	2.11	1.87	.35	1.75	1.71
500-700	-1.44	2.31	1.81	-.69	1.90	1.77
400-500	-1.12	2.11	1.79	-.84	1.91	1.72
300-400	-.66	2.13	2.02	-.53	1.99	1.92
200-300	.18	2.33	2.32	.29	2.33	2.31
100-200	-.12	1.86	1.85	.07	1.93	1.93
70-100	-.30	2.61	2.60	-.40	2.69	2.66
50-70	-.59	2.18	2.10	-.79	2.19	2.04

THE PREDICTION OF TROPOPAUSE HEIGHT FROM CLUSTERS OF BRIGHTNESS TEMPERATURES
AND ITS APPLICATION IN THE STRATIFIED REGRESSION TEMPERATURE RETRIEVALS
USING MICROWAVE AND INFRARED SATELLITE MEASUREMENTS

M.-J. Munteanu, P. Piraino and O. Jakubowicz

The object of this study is to derive a temperature retrieval based on the prediction of tropopause height from clusters of brightness temperatures. We use a total of 1575 radiosondes from N. Phillips and the corresponding simulated brightness temperatures. The 8 simulated channels, namely, 3 MSU and 5 IR of the TIROS-N satellite are used by the GLAS temperature retrieval method. We have clustered the 3 MSU and 5 IR brightness temperatures into 17 cluster groups and generated within each cluster a regression for the prediction of the tropopause height in mb. The overall r.m.s. for the tropopause prediction is excellent, namely, around 16 mb for the summer and 23 mb for the winter. We can correctly identify 98% of the time the correct cluster of brightness temperatures by the method of discriminatory classification if it is approximately a normal distribution or, in general, by the method of the nearest neighbor.

The concepts and formulas of cluster analysis and discriminatory classification are described in a companion project whose main object is the study of cluster analysis of temperature profiles and brightness temperatures. The method used in the prediction of the tropopause within each cluster of brightness temperatures is the following: Construct the regressions using all but one of the data points in the cluster of brightness temperatures and predict the remaining point. After predicting the tropopause height in the first stage, in the second stage we generate temperature retrievals based on a set of regressions from the summer profiles of the sample and separately for the winter profiles. The summer and winter profiles give us stratified regression temperature retrievals for each 30 mb layer of tropopause pressures. A control experiment is performed on the same data set, namely we have divided the summer and winter data into the usual land and ocean and latitude bands. As can be seen in our tables with r.m.s., the performance of the stratified by tropopause regression temperature retrievals for the summer as well as for the winter is excellent, much better than the performance of regression temperature retrievals generated within the usual groups used by most meteorological centers. (See Fig. 1 and Fig. 2).

Another important advantage of the method is in predicting the tropopause height within the clusters of brightness temperatures which could be correctly found in 98% of the cases.

Comparison of RMS Retrieved Temperature Errors Stratified by Tropopause for Different Tropopause Intervals (Summer)

Tropopause Intervals	90-119	120-149	150-179	180-209	210-239	240-269	270-299	300-329	Total RMS
50 mb	1.814	1.973	1.388	1.379	1.882	1.608	1.689	0.780	1.5641
70 mb	1.812	2.027	1.262	1.129	1.416	1.447	1.132	0.170	1.2994
100 mb	1.957	2.068	1.292	1.285	1.483	1.607	1.160	0.146	1.3749
150 mb	2.174	1.913	1.323	1.456	1.469	2.048	1.707	0.940	1.6288
200 mb	1.735	1.517	1.455	1.618	1.462	1.566	1.519	0.814	1.4666
250 mb	1.882	1.737	1.979	1.538	1.539	1.133	1.577	0.715	1.5123
300 mb	1.748	1.640	1.503	2.463	2.786	1.280	1.237	1.000	1.7070
400 mb	1.908	1.940	1.460	1.964	1.951	2.153	1.661	0.784	1.7276
500 mb	1.730	1.607	1.525	1.863	1.961	2.287	1.707	0.865	1.6131
700 mb	1.596	1.716	1.771	2.159	1.953	2.056	1.751	1.578	1.8225
850 mb	2.005	2.024	2.696	2.470	2.643	2.216	3.097	1.532	2.0353
1000 mb	2.155	2.643	1.947	3.148	2.734	2.935	2.519	1.914	2.3993

Fig. 1

Pressure	SUMMER		WINTER	
	Stratified by Tropopause (Total RMS)	Control Experiment	Stratified by Tropopause (Total RMS)	Control Experiment
30 mb			2.02	4.71
50 mb	1.56	1.88	1.81	2.88
70 mb	1.29	1.69	2.33	1.89
100 mb	1.37	1.66	2.20	2.31
150 mb	1.62	1.93	1.97	2.15
200 mb	1.46	2.51	1.69	2.36
250 mb	1.51	2.36	1.82	2.42
300 mb	1.70	2.03	1.90	2.53
400 mb	1.72	1.80	2.22	2.40
500 mb	1.61	1.63	2.27	2.62
700 mb	1.82	1.89	2.10	2.57
850 mb	2.03	2.29	2.57	2.75
1000 mb	2.39	2.29	2.62	2.72

Fig. 2

216
N84 22065

APPLICATIONS OF CLUSTER ANALYSIS TO SATELLITE SOUNDINGS

M.-J. Munteanu, O. Jakubowicz, E. Kalnay and P. Piraino

The purpose of this work is to evaluate the advantages of the use of cluster analysis in the improvement of satellite temperature retrievals. The use of natural clusters, which are associated with atmospheric temperature soundings characteristic of different types of air masses, has the potential for improving stratified regression schemes in comparison with currently used methods which stratify soundings based on latitude, season, and land/ocean.

The method of cluster analysis is performed on the basis of Euclidean distances. It is an iterative algorithm for minimizing the sum of squared distances from the cluster means. The cluster means are constantly recomputed as the clustering is performed. We have used the method of discriminatory analysis to locate the correct cluster. The method of discriminatory analysis is based on two concepts: The generalized square distance is defined as

$$D_j^2(x) = (x - \bar{x}_j) \text{COV}^{-1} (x - \bar{x}_j)$$

\bar{x}_j being the average of the j-th cluster. The posterior probability of membership in each cluster is

$$\text{PR}(j/x) = \exp(-.5 D_j^2(x)) / \sum_k \exp(-.5 D_k^2(x)).$$

We have chosen for our study 1575 radiosondes selected by N. Phillips which contain vertical temperature profiles distributed over ocean and land from 30°S to 60°N, summer and winter. From these temperature profiles we have simulated TIROS-N clear column radiances (5 infrared and 3 microwave channels) and then applied a linear regression matrix to account for angle correction.

The use of the cluster analysis method on the brightness temperatures, and the temperature profiles resulted in an optimum number of 14 clusters for winter soundings and 17 clusters for the summer (Fig. 1, representing 17 clusters for all 1575 soundings).

As a control experiment using the same data set, we divided the temperature profiles into land, ocean, latitude bands, summer and winter. Within each cluster or group of data we have developed regressions to derive temperature retrievals at mandatory levels from simulated brightness temperatures and overall r.m.s. for summer and winter are computed.

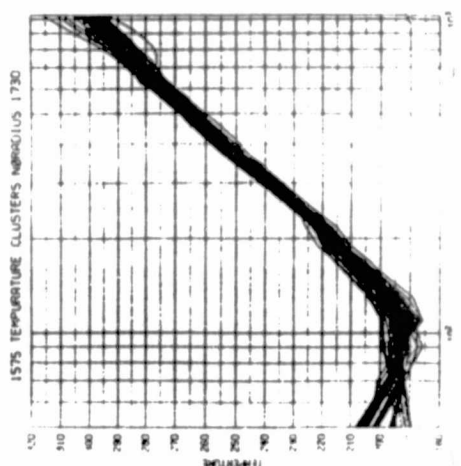
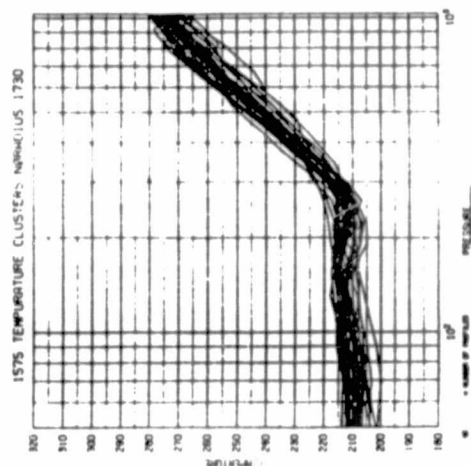
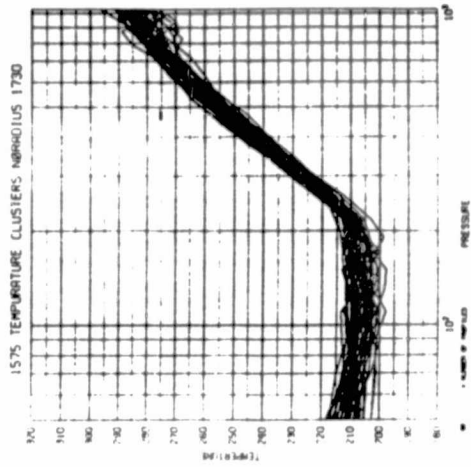
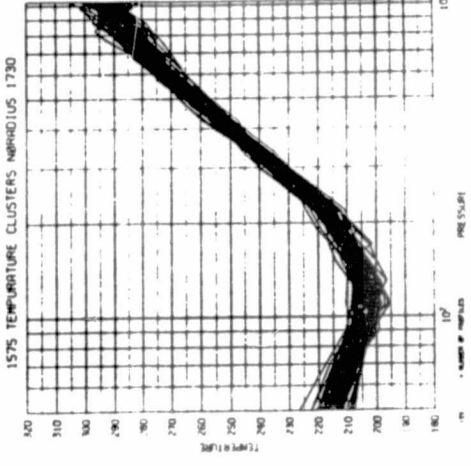
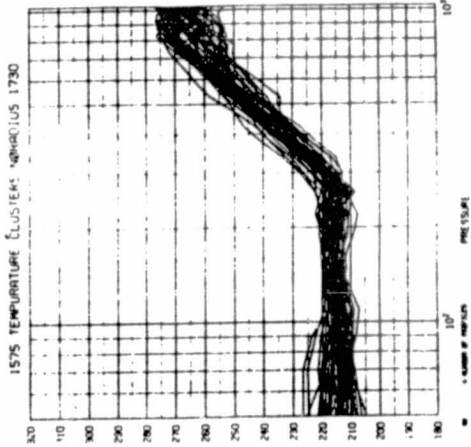
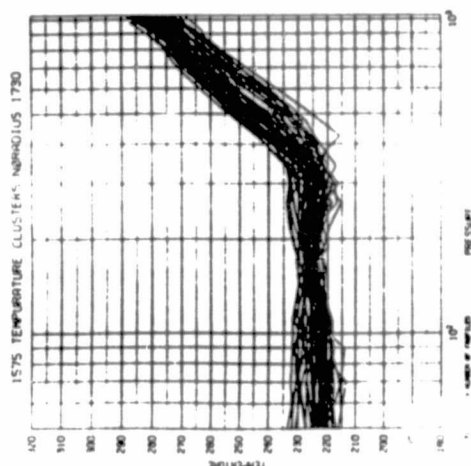
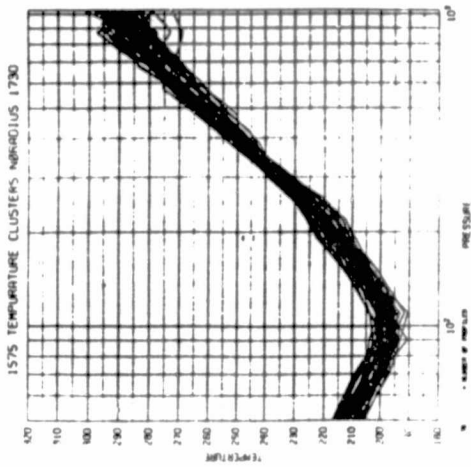
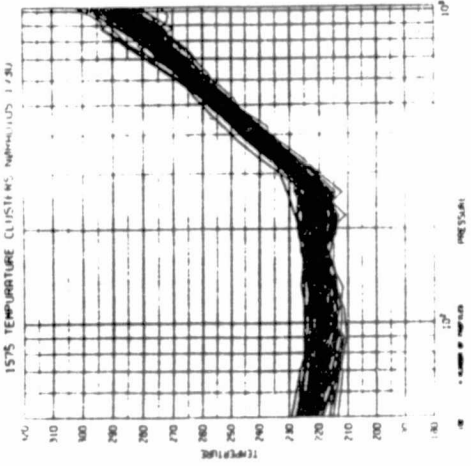
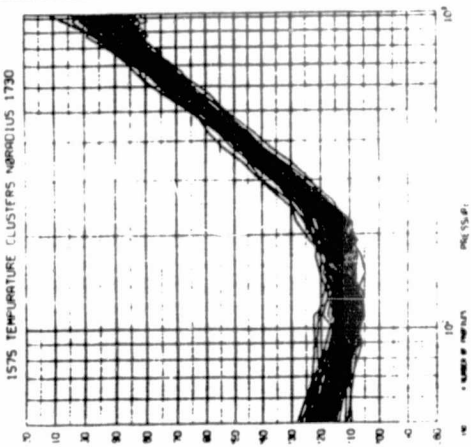
We want to point out a few improvements in the ability to locate the correct cluster of temperatures. Because obtaining the vertical temperature profile from satellite brightness temperature measurements is an ill-posed problem, locating the correct cluster of temperature profiles from satellite measurements is correct 85% of the time at the very best, when we use discriminatory analysis and combine some of the neighboring clusters. Other methods

of locating the correct cluster, such as the nearest neighbor, gave us poorer results than discriminatory analysis, viz., the best case was 76%, since the cluster distribution is multi-normal.

Graphically and computationally we have used the first 3 EOFs of the temperature profiles and of the brightness temperatures because they explain more than 92% of the variance for nonweighted temperature profiles, more than 97% for weighted temperatures and more than 98% for brightness temperatures.

Clustering by the coefficients of the first three EOFs gave us practically the same clusters and is computationally very efficient. Graphically we have plotted the profiles with the clusters of temperatures against the first two principal components (EOFs) of temperatures in Fig. 2. In Fig. 3 we plotted the brightness temperatures corresponding to the clusters of temperatures against the first two principal components of brightness temperatures. In Fig. 2 the separation of clusters is excellent, while in Fig. 3 certain clusters of temperatures are in fairly distinct groups and others are mixed together making the separation rather fuzzy.

With all this fuzziness in the separation of temperature clusters, we can locate the correct cluster in 85% of the cases and in the rest of the cases we know what the possible choices are and make a decision either to combine several clusters or use clusters of brightness temperatures to predict important parameters such as tropopause height (this is the subject of another extended abstract). The use of clusters of brightness temperatures has the great advantage of being able to locate the cluster 98% of the time. As a final and most important result we can say that considerable improvement is observed at all mandatory levels using regression temperature retrievals derived in the clusters of temperatures (weighted and nonweighted) in comparison with the control experiment and with the regression retrievals derived in the clusters of brightness temperatures of 3 MSU and 5 IR channels (see Figs. 4 and 5).



ORIGINAL PAGE IS
OF POOR QUALITY

Figure 1a

ORIGINAL PAGE IS
OF POOR QUALITY

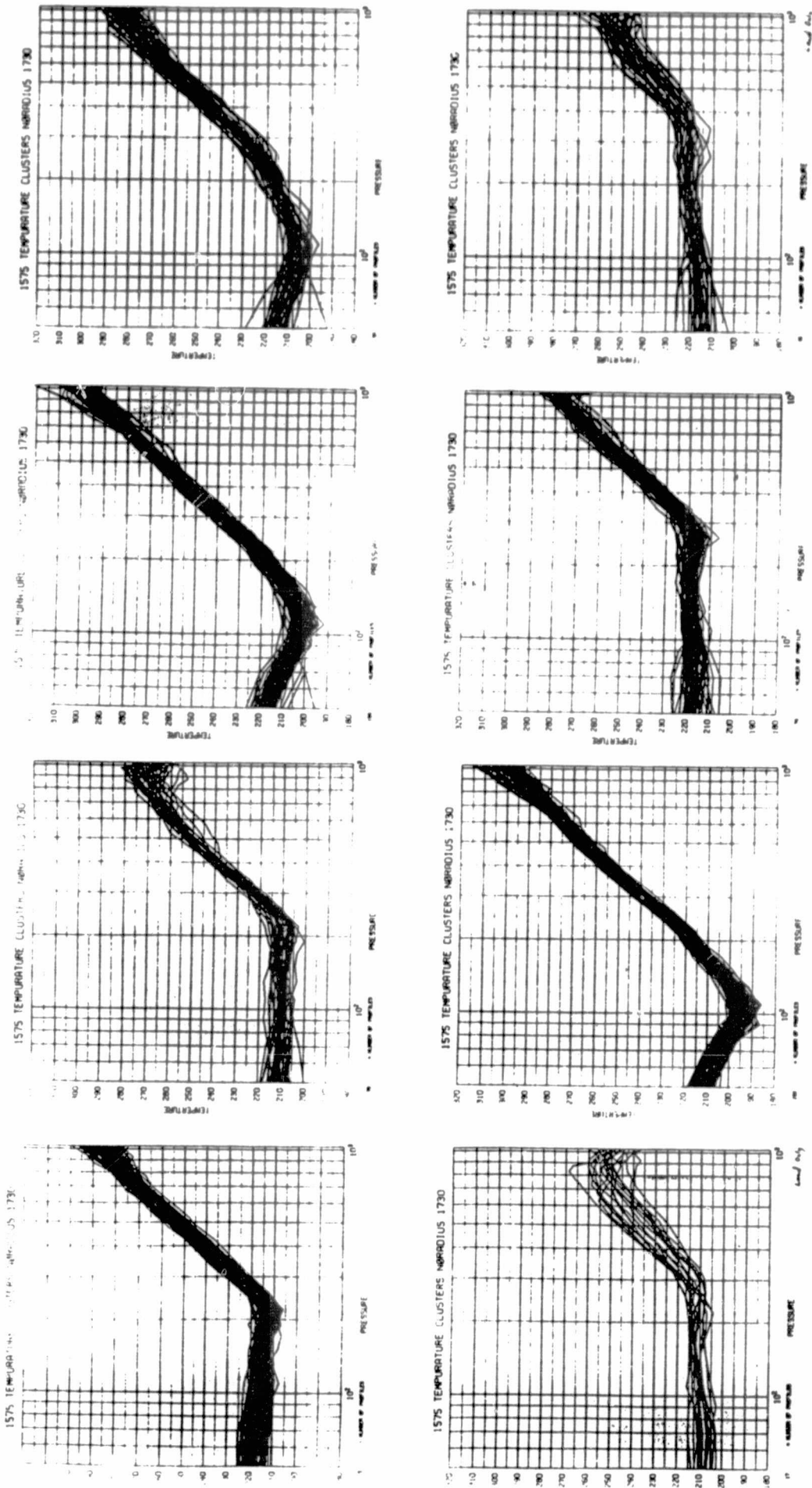
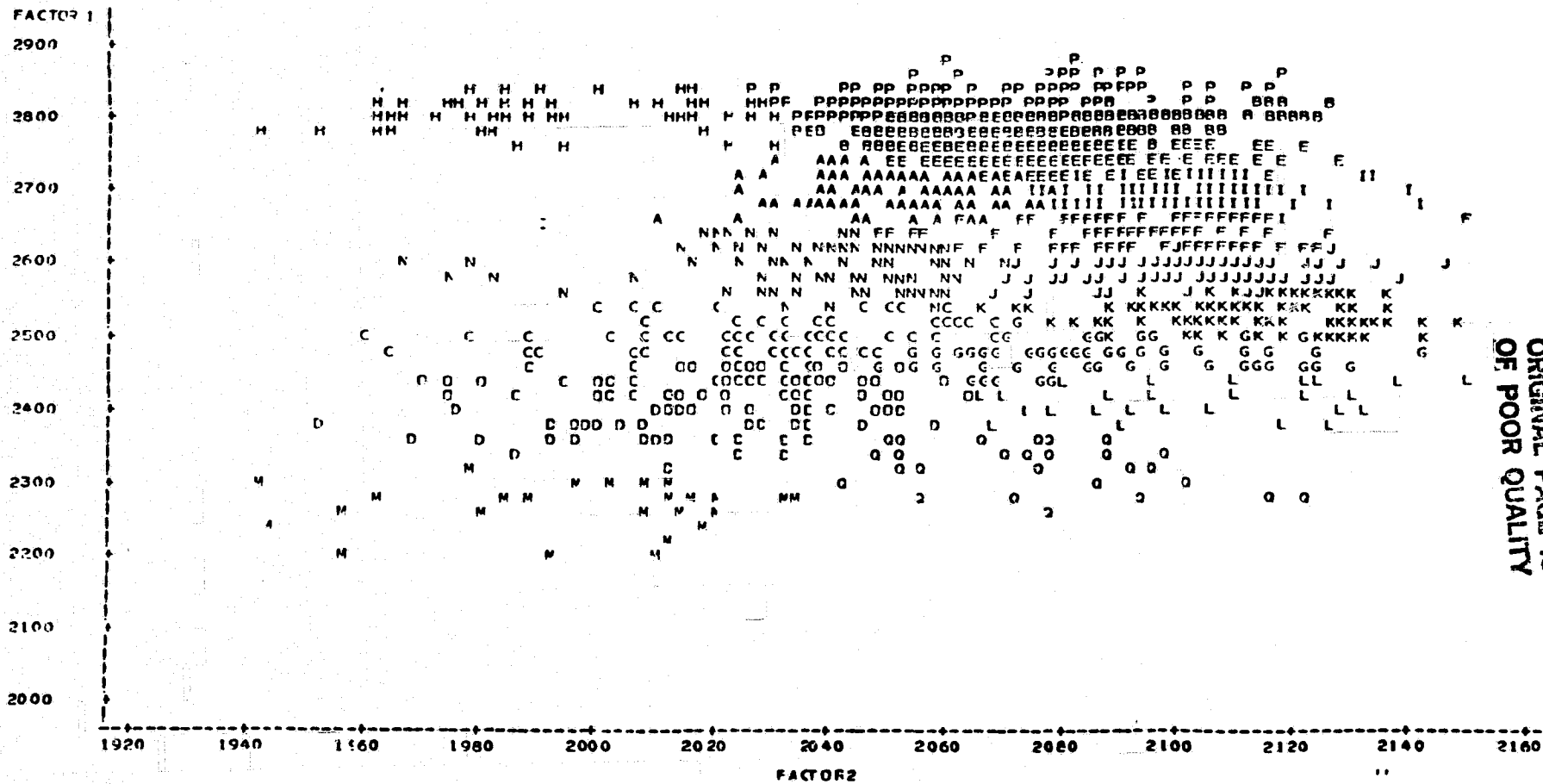


Figure 1b



ORIGINAL PAGE IS
OF POOR QUALITY

NOTE: 664 OBS HIDDEN

PRINCIPAL COMPONENTS PLOT OF CLUSTERS 8:37 THURSDAY, SEPTEMBER 22, 1963 94
17 WINTER AND SUMMER CLUSTERS BY FACTORS R=37 NC=17 NI=5

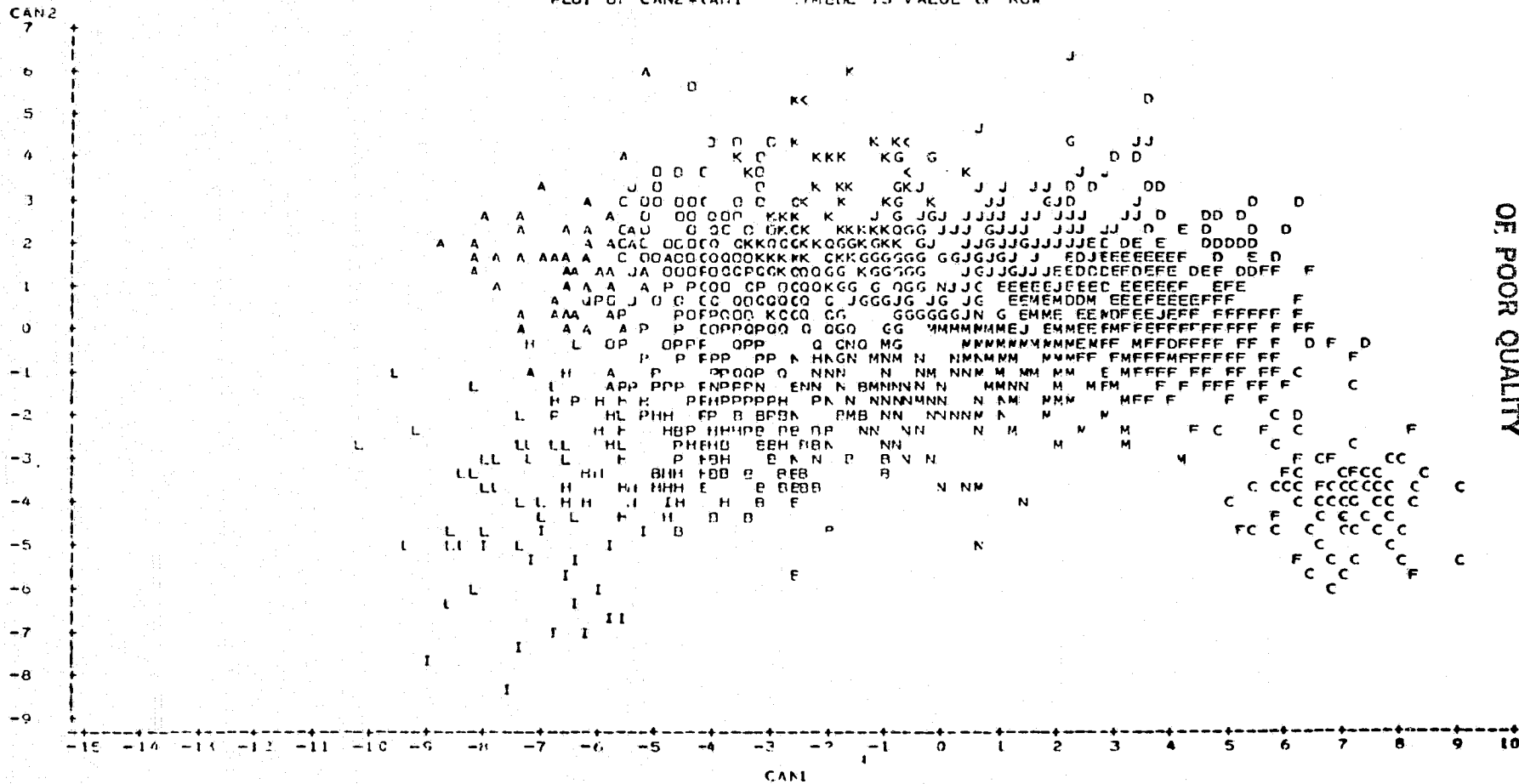
Figure 2

ANG COR NCSER R=27

CANONICAL DISCRIMINANT ANALYSIS OF TEMP CLUSTERS
17 1575 PTS CLUSTERED BY TEMPS VARIABLES MC=17 MI=30

9:41 THURSDAY, NOVEMBER 3, 1983 7

PLOT OF CAN2*(CAN1 SYMBOL IS VALUE OF ROW



ORIGINAL PAGE IS
OF POOR QUALITY

C-2

NOTE: 600 OPS MINLEN

Figure 3

Comparison of RMS Temperature Retrievals (Summer) 5IR & 3 MSU

Pressure	Control Experiment	Clusters of Weighted Temperatures	Clusters of Temperature (Nonweighted)	Clusters of 5 IR & 3 MSU
30 mb	2.00	1.94	1.92	2.02
50 mb	1.88	1.76	1.76	1.90
70 mb	1.69	1.56	1.59	1.70
100 mb	1.66	1.54	1.52	1.63
150 mb	1.93	1.59	1.69	1.94
200 mb	2.51	1.78	1.87	2.40
250 mb	2.36	1.62	1.80	2.20
300 mb	2.03	1.55	1.59	1.98
400 mb	1.80	1.51	1.37	1.77
500 mb	1.63	1.35	1.28	1.57
700 mb	1.84	1.59	1.51	1.84
850 mb	2.29	2.03	1.86	2.04
1000 mb	2.29	2.16	2.16	2.28

Figure 4

Comparison of RMS Temperature Retrievals (Winter)

Pressure	Control Experiment	Clusters of Weighted Temperatures	Clusters of Temperature (Nonweighted)	Clusters of 5 IR & 3 MSU
30 mb	4.71	4.43	4.19	5.00
50 mb	2.88	2.52	2.43	3.01
70 mb	1.89	1.71	1.74	1.92
100 mb	2.31	1.92	1.94	1.92
150 mb	2.15	1.87	1.97	2.17
200 mb	2.36	1.99	2.16	2.51
250 mb	2.43	1.83	1.86	2.34
300 mb	2.53	1.89	1.81	2.36
400 mb	2.40	1.87	1.73	2.33
500 mb	2.62	1.96	1.77	2.33
700 mb	2.57	2.11	1.86	2.44
850 mb	2.75	2.37	2.18	2.57
1000 mb	2.72	2.39	2.30	2.47

Figure 5

C. ANALYSIS AND MODEL DEVELOPMENT

PRECEDING PAGE BLANK NOT FILMED

EFFECT OF HIGH LATITUDE FILTERING ON NWP SKILL

E. Kalnay, L. L. Takacs and R. Hoffman

1. INTRODUCTION

Takacs et al. (1981) showed that the high latitude filtering techniques commonly employed in global grid point models to eliminate the high frequency waves associated with the convergence of meridians, can introduce serious distortions which ultimately affect the solution at all latitudes.

Takacs and Balgovind (1983), denoted T-B hereafter, followed a personal communication of A. Arakawa and showed that the zonal pressure gradient $\partial\phi/\partial\lambda$ filtering as in Arakawa (1972) introduces a spurious source of vorticity due to the non-cancellation of the finite difference analog of $\nabla \times \nabla\phi$. Furthermore, T-B showed that the filtering of winds in the zonal horizontal divergence as in Arakawa (1972) also introduces spurious sources of divergence (and hence of vorticity) due to the non-cancellation of the analogs of $\nabla \times \nabla\psi$ and $\nabla \times \nabla\chi$, where ψ and χ are the stream function and velocity potential. T-B indicated that other techniques in use, such as filtering of mass and wind fields (e.g. Kalnay-Rivas et al., 1977), or of their time derivatives (e.g. Vanderman, 1972, Temperton, 1977) also produce similar distortions.

T-B introduced a new filter, denoted PG for pressure gradient, which does not suffer from these drawbacks. Since no filtering of the winds (unless performed directly on ψ and χ) is free from spurious divergence and vorticity generation, T-B do not filter the wind divergence. To compensate for this, they square the strength of the filter applied on the zonal pressure gradient:

$$\frac{-F}{\phi_k} = \left(\frac{\omega_{\max}}{\omega} \frac{\Delta\lambda}{\Delta\psi} \cos\psi \right)^2 \phi_k \quad (1)$$

where ϕ_k is the amplitude of the geopotential field with zonal wavenumber k , $(\)^F$ denotes the filtered amplitude, $\omega = \sin k\Delta\lambda$ or $4/3 \sin k\Delta\lambda - 1/6 \sin 2k\Delta\lambda$, $\omega_{\max} = 1$ or 1.37 for second order or fourth order differences respectively. This filter results from requiring that the fastest zonally propagating gravity wave have a frequency not larger than the fastest meridionally propagating gravity wave.

Following a personal communication of Arakawa, they ensure irrotationality of the pressure gradient by using the filtered pressure field in both zonal and meridional components of the pressure gradient:

$$\frac{\partial u}{\partial t} = \dots - \frac{1}{a \cos \psi} \frac{\partial}{\partial \lambda} \left(\frac{-F}{\phi_k} \right); \quad \frac{\partial v}{\partial t} = \dots - \frac{1}{a} \frac{\partial}{\partial \psi} \left(\frac{-F}{\phi_k} \right) \quad (2)$$

Elsewhere the unfiltered pressure is used.

T-B performed experiments with a coarse resolution (8.18° lat by 10° lon) shallow water model and a Rossby-Haurwitz wave #4 (Phillips, 1959) and showed that only the PG filter reproduced well the short timestep, no-filter control run. Other methods (filtering the time derivatives, the fields, and the zonal component of the divergence and pressure gradient) were increasingly worse.

These results depend on wavelength as well as model resolution. Experiments with $4^\circ \times 5^\circ$ resolution and zonal wavenumber 4 showed little distortion for about 20 days. Operational models have much higher resolution than the model used in T-B, but, on the other hand, there are significant atmospheric phenomena associated with wavenumbers much higher than 4. The purpose of this paper is to explore whether polar filtering may be seriously affecting the skill of latitude-longitude NWP models such as those of ECMWF, NMC, the Navy's NOGAPS, and GLAS.

2. FILTERING EXPERIMENTS WITH THE GLAS FOURTH ORDER MODEL

The experiments were performed with the GLAS Fourth Order Model (Kalnay-Rivas, et al., 1977) with a resolution of 4° lat, 5° lon and 9 uniform σ -levels. An explicit Matsuno time scheme was used in every case.

2.1. No Filter Runs

Experiments with a short time step ($\Delta t = 1$ min), and no filter are made possible by the availability of the highly vectorized version of the GLAS Fourth Order model developed on the CDC 205 by R. Balgovind, M. Iredell, J. Pfaendtner and L. L. Takacs. It takes 12 min. per simulated day.

2.2. Operational Filter Runs

In the operational model, winds, temperature and sea level pressure are filtered after every time step. The intensity of the filter has been empirically determined in order to run stably with $\Delta t = 10$ min., and minimize the damping (see forthcoming documentation by Kalnay et al., 1983). Filtering is performed between $\pm 58^\circ$ and $\pm 86^\circ$; and the model requires 3.5 min. per simulated day.

2.3. PG Filter Runs

The PG filter of T-B (eq. 1 and 2) was implemented with the following modifications: a) both terms of the pressure gradient term in σ - coordinates were filtered; and b) it was found necessary to apply further damping of the fields at the three latitudes closest to the poles (86° , 82° and 78°) due to excessive build-up of small scale noise. It should be pointed out that this extra filtering was also necessary with realistic topography and initial conditions in the shallow water scheme, $4^\circ \times 5^\circ$ resolution and $\Delta t = 10$ min. On the other hand the PG method did not require extra filtering when applied to a $4^\circ \times 5^\circ$ shallow water model with a potential enstrophy conserving scheme (Arakawa and Lamb, 1981) and fourth order differences developed by K. Takano. This

model, however, required the use of a smaller time step of $\Delta t = 7.5$ min.

3. RESULTS

At the time of this writing (Feb. 1983) we have only limited results available. The initial conditions and verifying analysis come from the GLAS FGGE Analysis/Forecast system (Baker, 1983, Halem *et al.*, 1982).

3.1. Comparisons of 3-day Forecasts with the PG and Operational Filters

Five 3-day forecasts were run, starting with initial conditions of 0Z Jan 9, 13, 17, 21 and 25, 1979. Sea level pressure and 500 mb results were compared in the eastern and western sections of the Northern Hemisphere and in the Southern Hemisphere. Several small scale forecast differences were observed, but it was difficult to determine which forecast was closer to the verifying analysis. The single case of significant forecast differences found is shown in Fig. 1. In this case, the use of the PG filter has clearly improved the forecast of the deep low east of Scandinavia, and avoided the excessive deepening of the secondary low further east, at 110°C , 60°N .

3.2 Comparison of 5-day Forecasts with No Filter

Two 5-day forecasts were made from Jan 9 and 29, 1979. Unfortunately, in this case the models used had also other minor differences ("mild" programming errors which were corrected in the no-filter but not in the operational filter runs).

Fig. 2 presents the northeastern quarter of the sea level pressure maps. Overall, the differences between the two 5-day forecasts are not much larger than may be expected from just predictability theory. The no-filter run, however, seems to be slightly better. Fig. 3 compares the global 500 mb geopotential fields, also with very small differences, which in some regions may favor the operational filter forecast (trough near Japan, short waves over North America).

4. PRELIMINARY CONCLUSIONS

The limited experiments completed so far with the $4^{\circ} \times 5^{\circ}$, 9-level GLAS Fourth Order Model indicate that the high latitude filter currently in operation affects only minimally its forecasting skill. In one case, however, the use of the PG filter has significantly improved the forecast.

5. ACKNOWLEDGEMENTS

We are grateful to R. Balgovind and J. Pfaendtner for their development of

the vectorized GLAS Fourth Order Model, to L. Thompson and J. Wentz for typing the manuscript, and to D. Edelmann and M. Almeida for their generous help. K. Takano provided the 4th order enstrophy conserving scheme for the shallow water model.

REFERENCES

- Arakawa, A., 1972: Design of the UCLA general circulation model. Numerical Simulation of Weather and Climate, Dept. of Meteorology, Univ. of California, Los Angeles, 90024, Tech. Rept. 7, 116 pp.
- Arakawa, A., and V. R. Lamb, 1981: A potential enstrophy and energy conserving scheme for the shallow water equations. Mon. Wea. Rev., 109, 18-36.
- Baker, W. E., 1983: Objective analysis and assimilation of observational data from FGGE. Mon. Wea. Rev., 111, in press.
- Halem, M., E. Kalnay, W. E. Baker and R. Atlas, 1982: An assessment of the FGGE satellite observing system during SOP-1. Bull. Am. Meteorol. Soc., 63, 407-426.
- Kalnay-Rivas, E., A. Bayliss and J. Storch, 1977: The 4th order GISS model of the global atmosphere. Contrib. Atmos. Phys., 50, 306-311.
- Phillips, N. A., 1959: Numerical integration of the primitive equations on the hemisphere. Mon. Wea. Rev., 87, 333-345.
- Takacs, L. L. and R. C. Balgovind, 1983: High latitude filtering in global grid point models. Mon. Wea. Rev., 111, 2005-2015.
- Takacs, L. L., R. C. Balgovind, M. Iredell and E. Kalnay, 1981: On the effect of high latitude filtering in global grid point models. Fifth Conference on Numerical Weather Prediction, American Meteorological Society, 115-121.
- Temperton, C., 1977: Normal modes of a barotropic version of the ECMWF grid-point model. Internal Report 12, Research Dept., European Centre for Medium Range Weather Forecasts. Bracknell, England, 33 pp.
- Vanderman, L. W., 1972: Forecasting with a global, three layer, primitive equation model. Mon. Wea. Rev., 100, 856-868.

ORIGINAL PAGE IS
OF POOR QUALITY

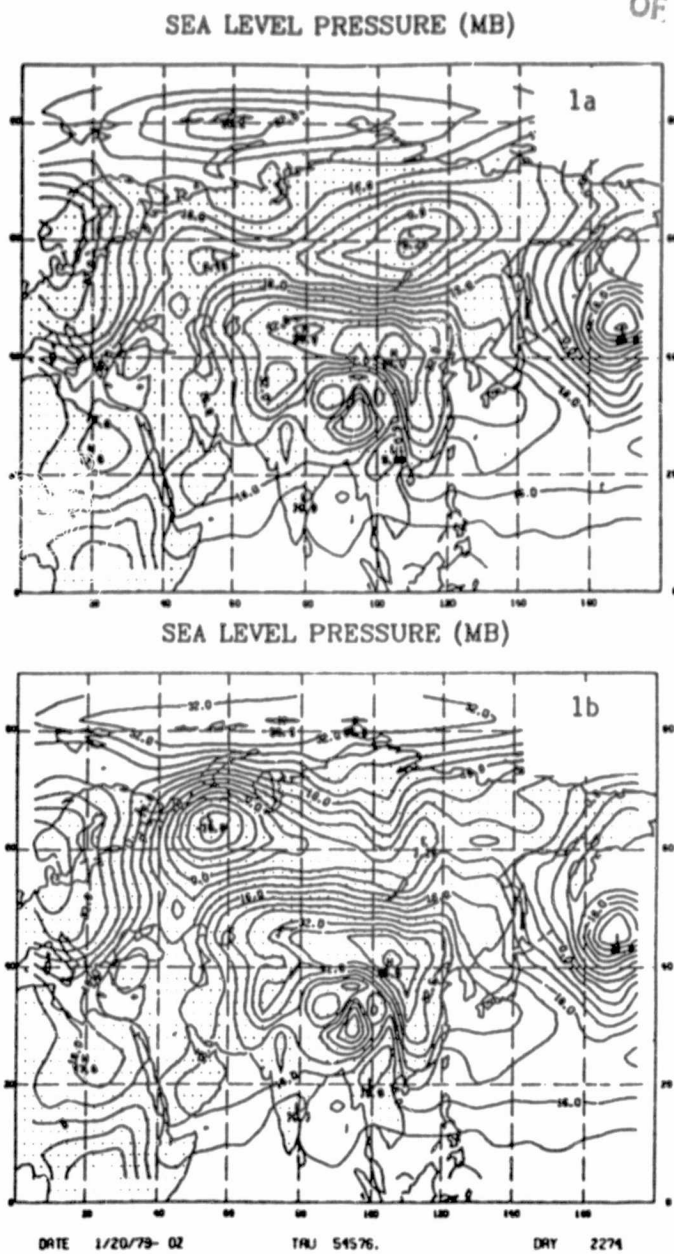
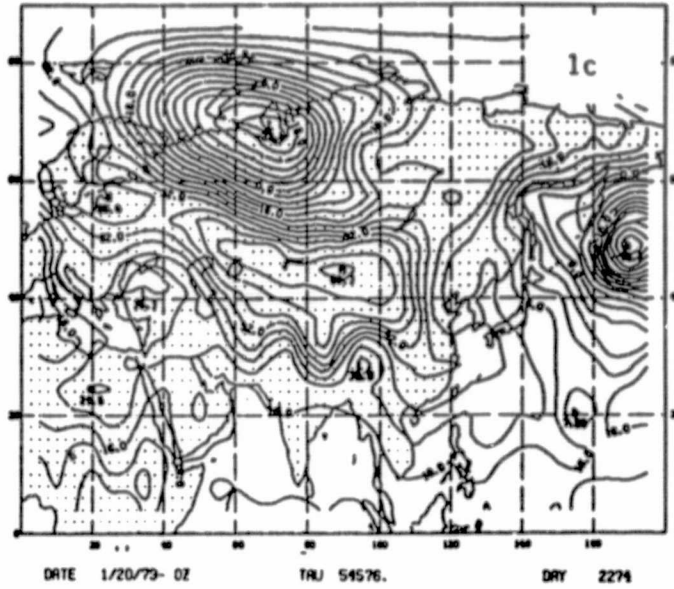


Fig. 1. 3-day forecasts of sea level pressure field from GLAS analysis of OZ Jan. 17, 1979. a) Operational filter; b) PG filter; c) Verifying analysis.

ORIGINAL PAGE IS
OF POOR QUALITY

SEA LEVEL PRESSURE (MB)



SEA LEVEL PRESSURE (MB)

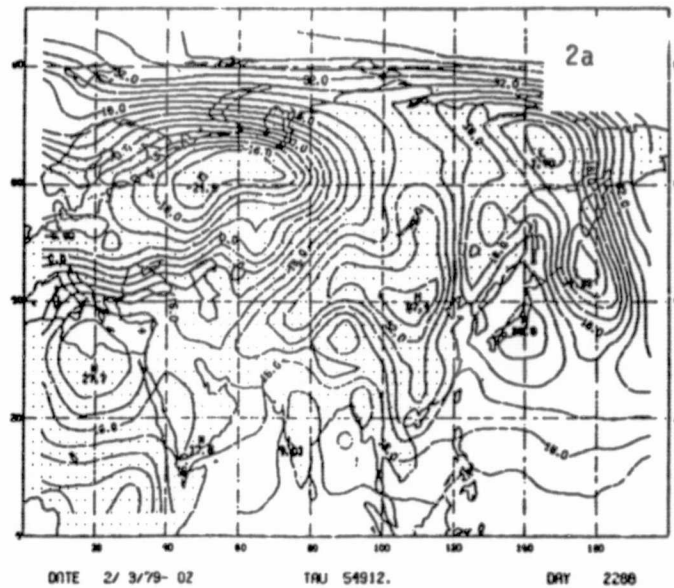
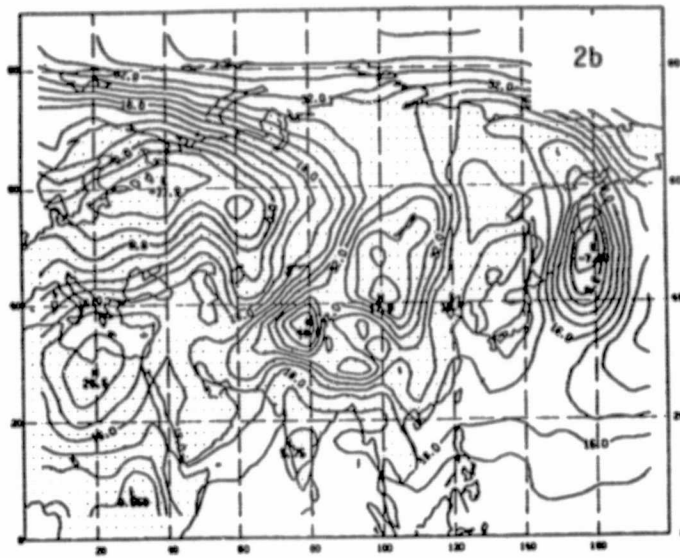


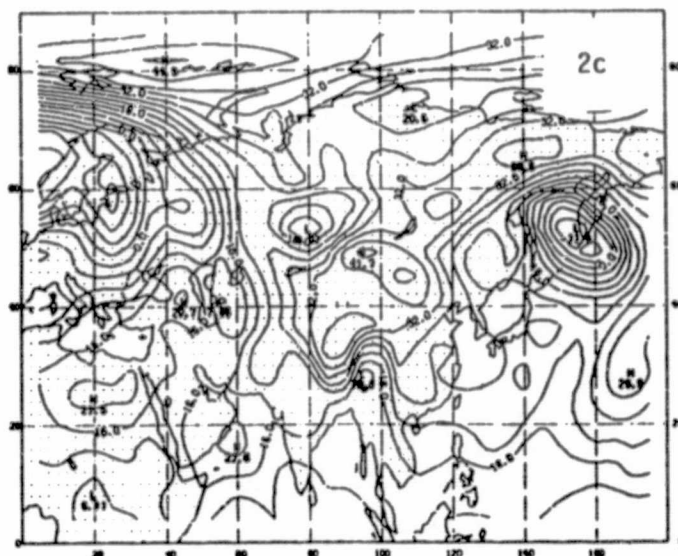
Fig. 2. 5-day forecasts of sea level pressure field from GLAS analysis of OZ Jan 29, 1979. a) Operational filter (model Version 6); b) No filter ($\Delta t = 1$ min), model Version 8; c) Verifying analysis

SEA LEVEL PRESSURE (MB)



DATE 2/ 3/79- 02 TRAJ 54912. DAY 2286

SEA LEVEL PRESSURE (MB)



DATE 2/ 3/79- 02 TRAJ 54912. DAY 2286

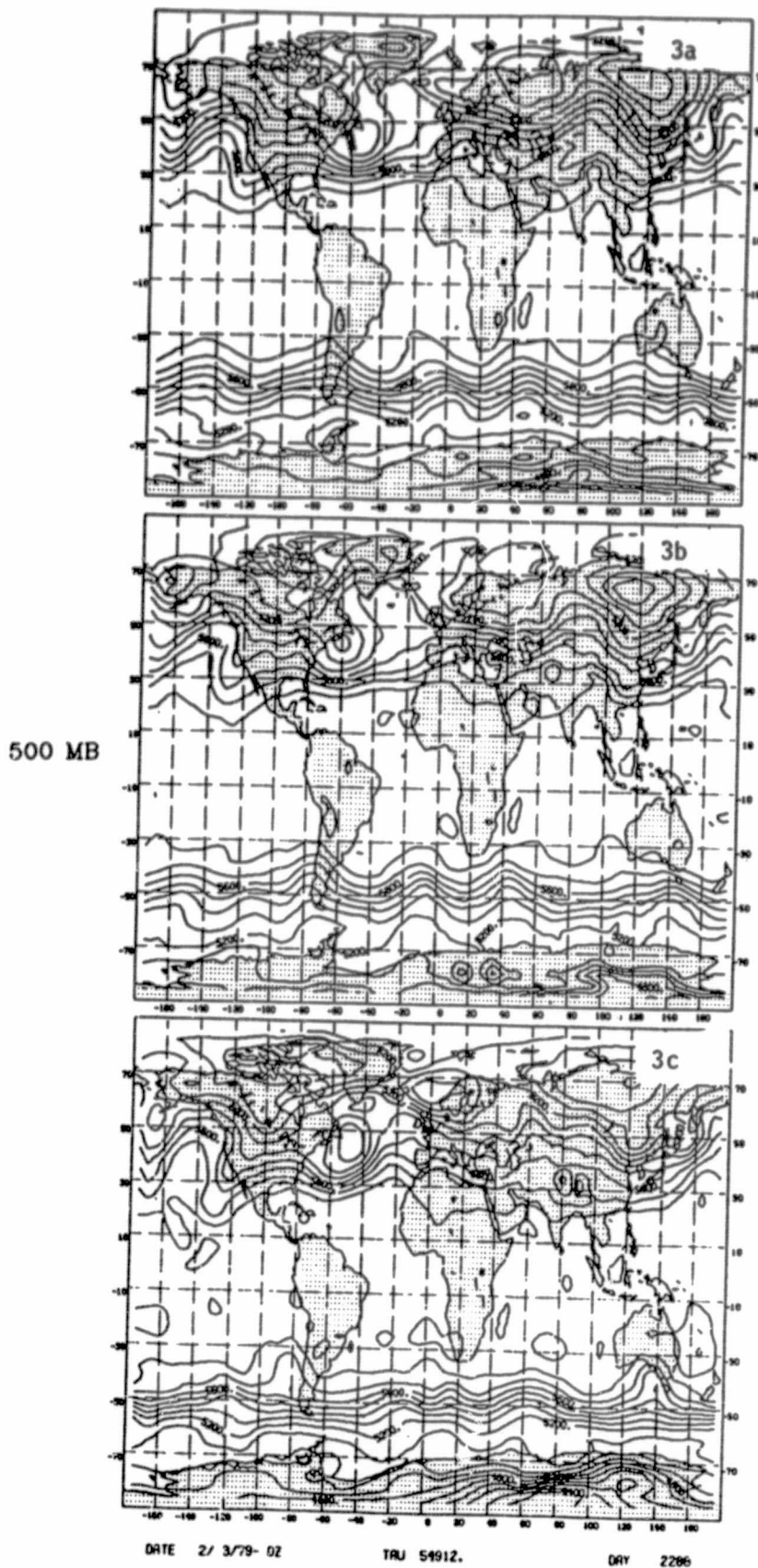


Fig. 3. Same as Fig. 2
but for 500 mb
geopotential
heights.

THE EFFECT OF COMPACT IMPLICIT DIFFERENCING IN A BAROCLINIC
PRIMITIVE EQUATIONS MODEL

J. M. Augenbaum, S. E. Cohn¹ and D. Marchesin²

In an effort to improve forecast accuracy, the horizontal accuracy of grid-point forecast models at a number of numerical weather prediction (NWP) centers has been increased from second order to fourth order. Increased vertical accuracy is more difficult to obtain because the small number of layers used in the models makes it impractical to implement fourth order accurate explicit difference formulas. The current Goddard Laboratory for Atmospheric Sciences (GLAS) model (Kalnay-Rivas and Hoitsma, 1979) uses second-order explicit finite-difference formulas in the vertical and fourth-order explicit finite-difference formulas in the horizontal. Here we describe experiments indicating the increased forecast accuracy gained by use of compact fourth-order finite differences in a simple baroclinic model.

A method for obtaining fourth-order vertical accuracy in grid-point baroclinic models has been described by Kalnay-Rivas (1977) and by Cohn et al. (1982). The method is based on the compact implicit formula

$$\left(\frac{1}{6} f'_{i+1}\right) + \left(\frac{2}{3} f'_i\right) + \left(\frac{1}{6} f'_{i-1}\right) = \frac{1}{2}\Delta s (f_{i+1} - f_{i-1}) + \frac{1}{180}\Delta s^4 f^{(5)}_i \quad (1)$$

for calculating the derivative $f'(s)$ of a function $f=f(s)$ over a grid ($s_i = i\Delta s$, $i = 1, 2, \dots, N$). The formula is applicable for vertical discretization since it involves only three points. Use of this formula leads to constant-coefficient tridiagonal linear systems, which can be solved efficiently by standard methods. This formula would also be advantageous for horizontal discretization since it is six times more accurate than the standard five-point explicit formula

$$f'_1 = \frac{2}{3}\Delta s (f_{i+1} - f_{i-1}) - \frac{1}{12}\Delta s (f_{i+2} - f_{i-2}) + \frac{1}{30}\Delta s^4 f^{(5)}_i \quad (2)$$

We illustrate the effect of the compact implicit formula for vertical and horizontal discretization in a baroclinic model for a height-longitude plane section of the atmosphere. The model equations, described in Cohn et al. (1983), are identical to those of the GLAS model, except that meridional derivatives are neglected. We denote the continuous model equations by

$$F(W) = 0, \quad (3)$$

¹ Courant Institute of Mathematical Sciences, New York University, New York, NY 10012.

² Dept. of Mathematics, Pontifícia Universidade Católica do Rio de Janeiro, Rio de Janeiro-RJ, CEP22453, Brazil.

where W is the solution vector, and the discrete model by

$$F_{\Delta}(W_{\Delta}) = 0. \quad (4)$$

To determine the forecast accuracy of the discrete model, we use the technique described in Marchesin (1984). Suppose W_{Δ}^0 is a prescribed flow of interest; then we modify the discrete model to solve

$$F_{\Delta}(W_{\Delta}) = F_{\Delta}(W_{\Delta}^0). \quad (5)$$

Since the exact solution $W_{\Delta} = W_{\Delta}^0$ of (5) is known, rms forecast errors can be computed.

We show in Table 1 the rms errors in the zonal wind u , the vertical velocity σ , and the potential temperature θ after 12 hours of integration, for three versions of the difference scheme. Scheme F_{Δ}^1 uses second-order explicit differences in the vertical and fourth-order explicit differences (2) in the horizontal, and corresponds roughly to the current GLAS model. Scheme F_{Δ}^2 uses the fourth-order implicit formula (1) in the vertical and the fourth-order explicit formula (2) in the horizontal. Scheme F_{Δ}^3 uses the fourth-order implicit formula (1) in both directions. All experiments used 12 layers, 16 grid points horizontally, and a time step of 30 minutes. A sixteenth-order Shapiro filter (Kalnay-Rivas and Hoitsma, 1979) was applied in the horizontal direction in all cases.

	F_{Δ}^1	F_{Δ}^2	F_{Δ}^3
u	12000×10^{-6}	78×10^{-6}	25×10^{-6}
σ	25000×10^{-6}	210×10^{-6}	67×10^{-6}
θ	4400×10^{-7}	26×10^{-7}	11×10^{-7}

Table 1

The first two columns of the table indicate an increase in forecast accuracy by a factor of 100-150 by use of fourth-order instead of second-order vertical discretization. While increased accuracy can certainly be expected in a full three-dimensional model, such a large factor is unlikely. Our results were obtained using a rather simple prescribed flow W_{Δ}^0 , described in Cohn et al., 1982.

The improvement by a factor of three between the second and third columns in Table 1 is less than the factor of six expected by comparison of the truncation error in equations (1) and (2). This is due to the fact that horizontal truncation error is only one component of the total forecast error in a NWP model.

We plan to implement the fourth-order compact implicit difference formula (1) in a fully three-dimensional primitive equations model.

REFERENCES

- Cohn, S., D. Dee, and D. Marchesin, 1982: Baroclinic models with fourth-order vertical accuracy: preliminary report. Segundo Congresso Brasileiro de Meteorologia, Proceedings, to appear.
- Cohn, S., D. Dee, E. Isaacson, D. Marchesin, and G. Zwas, 1983: A fully implicit scheme for the baroclinic primitive equations: two-dimensional models. Submitted to Mon. Wea. Rev.
- Kalnay-Rivas, E., 1977: Numerical experiments with fourth order conservative finite difference equations. Unpublished manuscript.
- Kalnay-Rivas, E., and D. Hoitsma, 1979: Documentation of the Fourth Order Band Model. NASA Tech. Memo. 80608.
- Marchesin, D., 1984: Using exact solutions to develop an implicit scheme for the baroclinic primitive equations. Mon. Wea. Rev., in press.

219
N84 22068

A LAGRANGIAN METHOD FOR A TWO LAYER SHALLOW WATER MODEL

J. M. Augenbaum

1. INTRODUCTION

All current operational primitive equation models are based on an Eulerian formulation. That is, all physical quantities are stored at grid points frozen in the region of interest. This is due to their ease in programming and higher order of accuracy. However, one of the biggest drawbacks of Eulerian methods is the presence of the nonlinear convective terms $\bar{u} \cdot \nabla \bar{u}$ which leads to inaccurate representations of advection and fronts.

An alternative and conceptually simpler approach is the Lagrangian approach. In this approach the fluid particles themselves are tracked and equations are derived based on local spatial interaction. In this formulation the nonlinear convective terms do not appear. The main drawback with the Lagrangian formulation, however, is that the local spatial interactions are time dependent. That is, at each time level, one must know the current neighbors of a given particle to accurately compute the forces acting on the particle. Thus, a grid which is continuously deforming and always linking nearest neighbors is needed. Such a grid, the "Voronoi Mesh" has been around for a long time but has only recently been introduced into hydrodynamics codes [1, 3]. The Voronoi Mesh is defined as follows: Given a set of N fluid marker points, each point represents all the area that is closer to that point than to any other. An efficient construction of the Voronoi Mesh on a sphere has been given in [2]. Thus, a grid system can be constructed by placing points where satellite and other measured data is available.

A numerical scheme for the shallow water equations on the sphere based on the Voronoi Mesh has already been developed [1]. This model has been successfully tested for its ability to handle non-meteorological discontinuous, shock profiles. However, extensive tests with realistic meteorological data remains to be done.

2. MODEL

As a first step towards a full 3D Lagrangian primitive equation code we study a two layer, one dimensional fluid on a periodic domain. In each layer the assumptions of shallow water theory are applied. Following the one layer case [3], we then construct the one dimensional Voronoi Mesh for each layer (see Fig. 1). The equations of motion are:

$$m_k^{(1)} \frac{dU_k^{(1)}}{dt} + g \sum_{j=1}^{NPTS(1)} m_j^{(1)} \frac{\partial Z_j^{(1)}}{\partial X_k^{(1)}} + g \sum_{j=1}^{NPTS(2)} m_j^{(2)} \frac{\partial Z_j^{(2)}}{\partial X_k^{(1)}} = 0 \quad (1a)$$

$$m_k^{(2)} \frac{dU_k^{(2)}}{dt} + g \sum_{j=1}^{NPTS(2)} m_j^{(2)} \frac{\partial Z_j^{(2)}}{\partial X_k^{(2)}} = 0 \quad (1b)$$

$$\frac{dX_k^{(1)}}{dt} = U_k^{(1)}, \quad \frac{dX_k^{(2)}}{dt} = U_k^{(2)} \quad (2a,b)$$

$$Z_j^{(1)} = 1/2 H_j^{(1)} \quad (3a)$$

$$Z_j^{(2)} = 1/2 \sum_j \{ [H_j^{(2)}]^2 - [H_j^{(1)}]^2 \} L_{j'j}^{(2)} / \sum_j (H_j^{(2)} - H_j^{(1)}) L_{j'j}^{(2)} \quad (3b)$$

where

- $X_k^{(\ell)}$ = horizontal position of point in layer ℓ .
- $U_k^{(\ell)}$ = horizontal velocity of point k in layer ℓ .
- $\rho^{(\ell)}$ = density of fluid in layer ℓ .
- $m_k^{(\ell)}$ = mass of cell k in layer ℓ .
- $H_k^{(\ell)}$ = height of cell k in layer ℓ , measured from ground.
- $Z_k^{(\ell)}$ = height of center of mass of cell k in layer ℓ , measured from ground.
- $L_k^{(\ell)}$ = length of base of cell k in layer ℓ .
- L_{jk}^{12} = length of overlap of bases of cells j in layer 1 and k in layer 2.
- g = gravity
- $NPTS(\ell)$ = number of fluid marker points in layer ℓ .
- $\ell = 1$ = bottom layer
- $\ell = 2$ = top layer

3. RESULTS

As a test problem we simulate the onset of a Kelvin-Helmholtz instability. Two cases were tried; one in which the Richardson number is less than the critical value 1/4 (stable regime) and the other where the Richardson number is slightly

greater than $1/4$ (unstable regime). The results of the unstable case are shown in Fig. 2. In both cases the parameters chosen were $\rho^{(1)} = 1$, $\rho^{(2)} = .9$, $U^{(1)} = 0$, $g = 9.8$. In the first case $U^{(2)} = 2$ and in the second case $U^{(2)} = 4$. The computational parameters were $\Delta t = .025$, $TMAX = 30$, $NPTS(1) = NPTS(2) = 50$, $period = 250$. The initial conditions consist of a perturbed height field in the bottom layer $h^{(1)} = 2 + .1 \sin X$, $h^{(2)} = 4$. The results show that when $Ri < 1/4$ the flow remains stable and the perturbation in $h^{(1)}$ propagates as an internal wave. When we increase the shear by increasing $U^{(2)}$ so that $Ri > 1/4$, then a slight instability develops at about $t = 27$ which increases in time. By the time $t = 30$ the Kelvin-Helmholtz instability is well developed to the point of wave breaking. Since this model is one dimensional we cannot expect to see the waves break as that is a 2D phenomena.

6. CONCLUSIONS

We have demonstrated the effectiveness of a simple Lagrangian method for simulating the onset of a Kelvin-Helmholtz instability in a 2 layer fluid. We are planning to develop a Lagrangian method for an N layer primitive equation vertical slice model.

REFERENCES

1. J. Augenbaum: "A New Lagrangian Method for the Shallow Water Equations on a Rotating Sphere", Thesis, New York University (1982).
2. J. Augenbaum and C. Peskin: "On the Construction of the Voronoi Mesh on a Sphere" (1983), submitted to J. Comp. Phys.
3. J. Augenbaum: "A Lagrangian Method for the Shallow Water Equations Based on a Voronoi Mesh-One Dimensional Results" (1984), J. Comp. Phys. In press.
4. J. Augenbaum: "A Lagrangian Method for a Two Layer Shallow Water Model" in preparation.

ORIGINAL PAGE IS
OF POOR QUALITY.

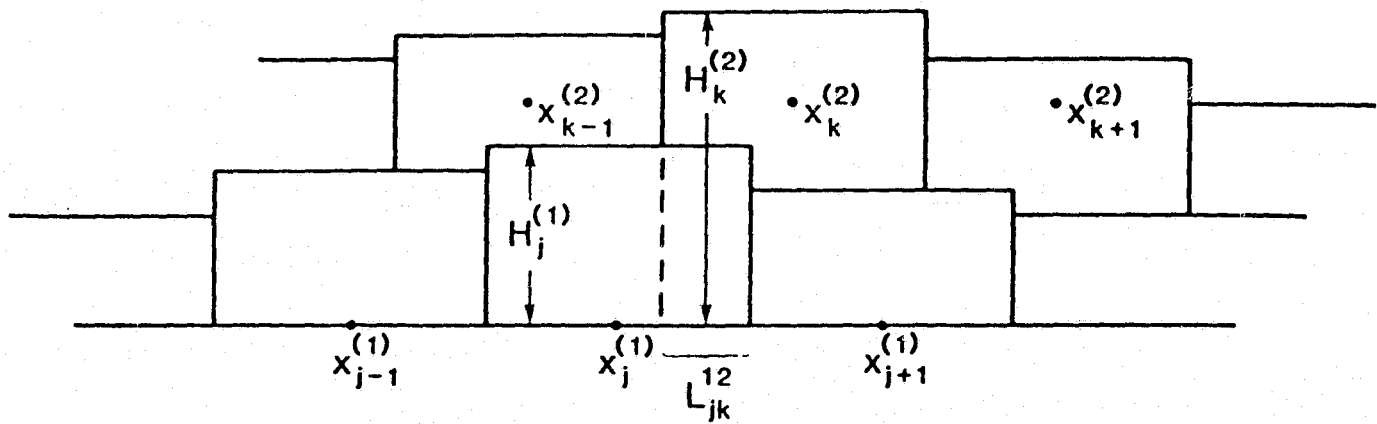


Figure 1. Portion of Voronoi Mesh for two layer fluid.

ORIGINAL PAGE IS
OF POOR QUALITY

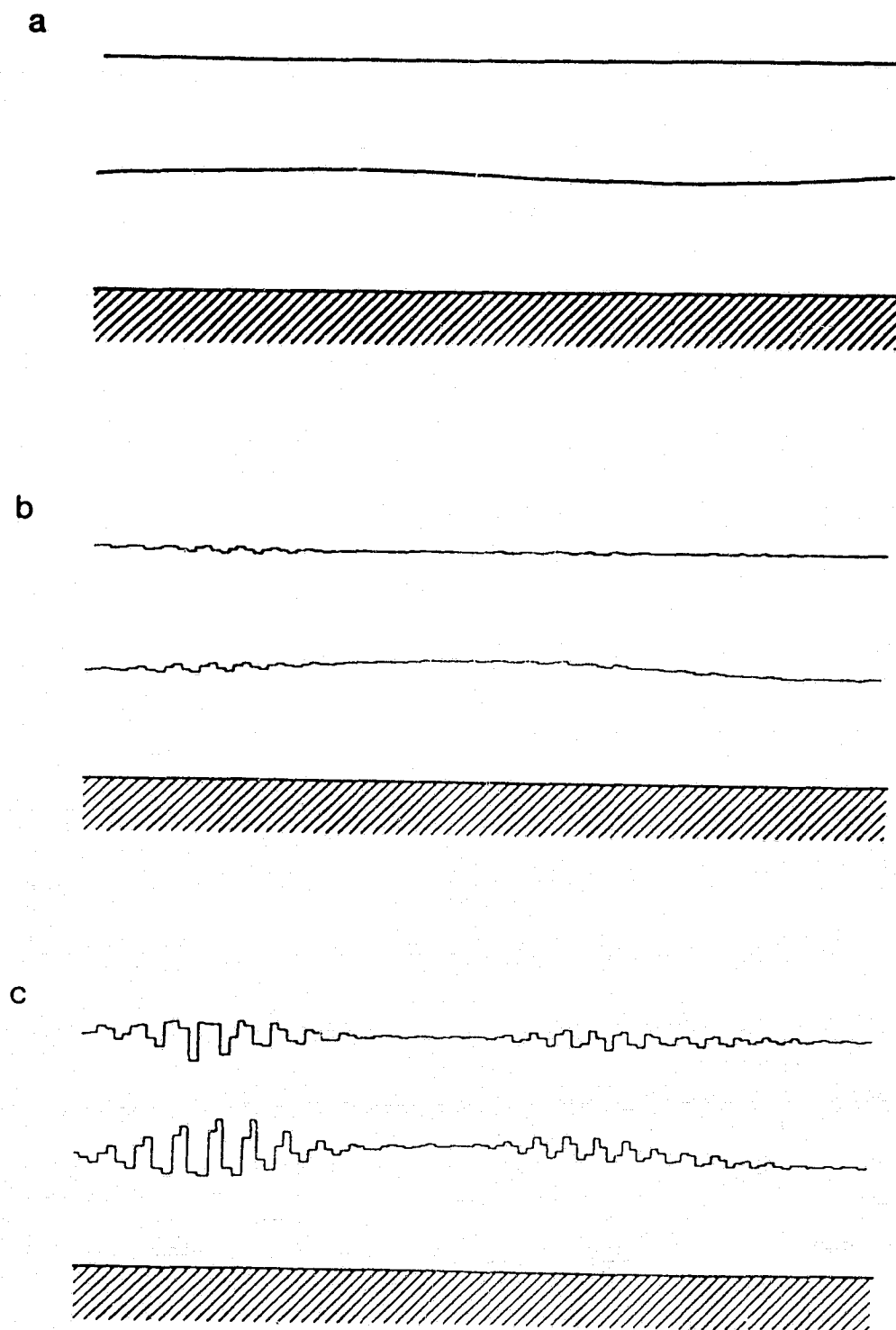


Figure 2. Development of Kelvin-Helmholtz instability in two layer fluid with Richardson number $Ri > 1/4$ at time, a) $t=0$, b), $t=27$, c) $t=30$ sec.

MULTIVARIATE OPTIMUM INTERPOLATION OF SURFACE PRESSURE AND WINDS OVER OCEANS

S. Bloom

The observations of surface pressure are quite sparse over oceanic areas. This note describes an effort to improve the analysis of surface pressure over oceans through the development of a multivariate surface analysis scheme which makes use of surface pressure and wind data. Although the present research has used ship winds, future versions of this analysis scheme could utilize winds from additional sources, such as satellite scatterometer data.

Let the analyzed values of (U_s, V_s, P_s) at a gridpoint 'G' be \tilde{A}_G , their first guess (i.e. 6 hr. forecast using the GLAS GCM) values be \tilde{F}_G , and let the differences between first guess and observational values at observation location 'I' be $(O_I - F_I)$; then a general analysis process would be:

$$\tilde{A}_G = \tilde{F}_G + \sum_{I=1}^{NOBS} W_{I,G} (O_I - F_I). \quad (1)$$

Note that equation (1) describes a multivariate analysis, since observed values of one variable can influence the analysis of a different variable through the coupling of off-diagonal terms in the weight matrices W . The analysis error of

this process can be obtained by subtracting the true fields from all terms in equation (1):

$$\tilde{E}_G^A = \tilde{E}_G^F + \sum_{I=1}^{NOBS} W_{I,G} (E_I^O - E_I^F). \quad (2)$$

Thus the error in this analysis at a particular gridpoint can be seen to be a weighted combination of the errors inherent in the observations and the errors in the first guess due to inaccuracies in the forecast model.

Equation (1) is a multivariate optimum interpolation if the weight matrices are chosen in a manner that minimizes the variance of the analysis error. Let $\langle \rangle$ denote a statistical averaging process; the variance of the analysis error at a gridpoint is then $\langle E_G^A E_G^A \rangle$. The insertion of equation (2) into

the analysis error variance and the minimization of the result with respect to the analysis weights results in a set of equations which relate the weight matrices to observational and first guess error covariances:

$$\langle E_I^F E_G^F \rangle = \sum_{J=1}^{NOBS} W_{J,G} [\langle E_I^F E_J^F \rangle + \langle E_I^O E_J^O \rangle], \quad I=1, NOBS. \quad (3)$$

Correlations between E^F and E^O have been ignored in equation (3). The observa-

tion error statistics can be obtained from a consideration of the characteristics of specific observing systems; for the surface analyses, observations at different locations are assumed to be uncorrelated, and measured values are used for the observation error variances. While there do exist theoretical methods for estimating accurately the forecast error covariances (for example, Kalman filtering, see Ghil et al., 1981), such methods require more computational power than is currently available at GLAS. Thus methods of approximating the forecast error statistics are used to set up and solve equation (3) for the analysis weights.

The term $\langle \tilde{E}_I^F \tilde{E}_J^F \rangle$ denotes a 3 x 3 matrix, a shorthand for the nine forecast error covariances between points I and J: $\langle P_S P_S \rangle_{IJ}$, $\langle P_S U_S \rangle_{IJ}$, $\langle U_S P_S \rangle_{IJ}$. . . $\langle V_S V_S \rangle_{IJ}$. This analysis scheme follows other multivariate OI analyses (Cf. Schlatter et al., 1976) by empirically fitting $\langle P_S P_S \rangle$ with a particular covariance model, and by using some form of wind law (for example, winds geostrophically derived from pressure gradients) to obtain the remaining covariances in terms of spatial derivatives of $\langle P_S P_S \rangle$. The empirical fit is performed as follows: an ensemble of 6 h forecasts of P_S are compared with verifying analyses; variances (σ_I^2) are computed at each point I; a damped cosine correlation model is used to fit the correlations between points I and J having a great circle separation distance S_{IJ} :

$$\langle P_S P_S \rangle_{IJ} = \sigma_I \sigma_J \mu_{IJ}$$

$$\mu_{IJ} = \frac{C_1 \cos(C_2 S_{IJ}) + C_3}{[1 + (C_4 S_{IJ})^2]^{C_5}} \quad (4)$$

Constants C_1 through C_5 are determined by the fitting process.

The surface winds are assumed to be related to the surface pressures via geostrophy modified by surface drag:

$$\frac{1}{\rho} \nabla P_S + f \vec{k} \times \vec{V}_S - \frac{1}{\rho} \frac{\partial \vec{\tau}}{\partial z} = 0 \quad (5)$$

where $\vec{V}_S = (U_S, V_S)$
 $\vec{\tau}(z) =$ stress vector in surface layer
 $\rho =$ density.

If the stress decreases linearly to zero through the depth (H) of the surface layer, and if the surface drag is linearized about a first guess value, then the friction term can be expressed as follows:

$$-\frac{1}{\rho} \frac{\partial \vec{\tau}}{\partial z} \approx \frac{1}{\rho} \frac{\vec{\tau}(0)}{H} \approx \frac{D_R \vec{V}_S}{H} \quad (6)$$

where D_R is a drag coefficient which is functionally dependent on the first guess stability and surface wind speed. It should be noted that the first guess surface winds must be estimated by extrapolating model winds down into the surface layer. The GLAS model's formulation of D_R is used in these analyses.

Combining equations (5) and (6), letting $D_F \equiv \frac{\rho D_R}{H}$, the linearized wind relation in component form is:

$$\begin{aligned} U_S &= -F \frac{\partial P_S}{\partial x} - C \frac{\partial P_S}{\partial y} \\ V_S &= C \frac{\partial P_S}{\partial x} - F \frac{\partial P_S}{\partial y} \end{aligned} \quad (7)$$

where

$$F = \frac{D_F}{D_F^2 + (\rho f)^2} \quad \text{and} \quad \frac{\rho f}{D_F^2 + (\rho f)^2}$$

Equation (7) allows the expression of all the error covariances in terms of $\langle P_S P_S \rangle$ and its derivatives; an example:

$$\langle P_S U_S \rangle_{IJ} = -F_J \frac{\partial}{\partial x} \langle P_S P_S \rangle_{IJ} - C_J \frac{\partial}{\partial y} \langle P_S P_S \rangle_{IJ}$$

In summary, the relations in equation (7) are used with the modeled covariance $\langle P_S P_S \rangle$ in equation (4) to solve for the analysis weights W in

equation (3). Those weights are used in equation (1) to perform an analysis at a gridpoint. This process occurs at each surface gridpoint in the model domain which is completely surrounded by oceanic gridpoints.

This analysis scheme has been tested on a FGGE data set - 3 February 1979, 0Z. Fig. 1 shows the result of the multivariate surface analysis, while Fig. 2 shows a univariate (i.e. only P_S analyzed) analysis for the same time over the same region. Note that the multivariate analysis (over oceans) is designed to be univariate in P_S over land. Fig. 3 is a plot of the differences between the fields in Figs. 1 and 2; note that the maximum values in Fig. 3 are a few mb. The multivariate analysis differs more strongly from the first guess field than it does from the univariate analysis, as can be seen by comparing Figs. 4 and 3. This result is reflected in the global RMS differences; (Mul. - Uni)_{press} = 0.6 mb, (Mul. - F.G.)_{press} = 2.8 mb. Yet to be performed are tests which assess

the impact of multivariate surface analysis on model forecasts.

REFERENCES

Ghil, M., S. Cohn, J. Tavantzis, K. Bube and E. Isaacson, 1981: Applications of Estimation Theory to Numerical Weather Prediction. Dynamic Meteorology: Data Assimilation Methods, Springer-Verlag, 139-224.

Schlatter, T. W., G. W. Branstator, and L. G. Thiel, 1976: Testing a Global Multivariate Statistical Objective Analysis Scheme with Observed Data. Mon. Wea. Rev., 104, 765-783.

MULTIVARIATE SLP ANALYSIS (MB)

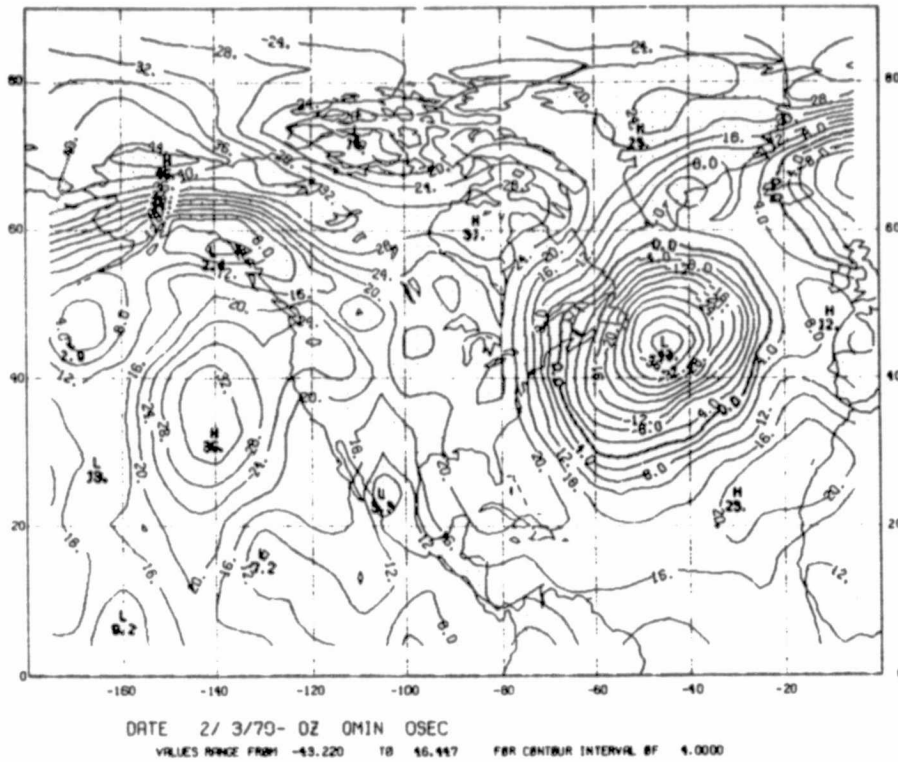


Fig. 1

UNIVARIATE SLP ANALYSIS (MB)

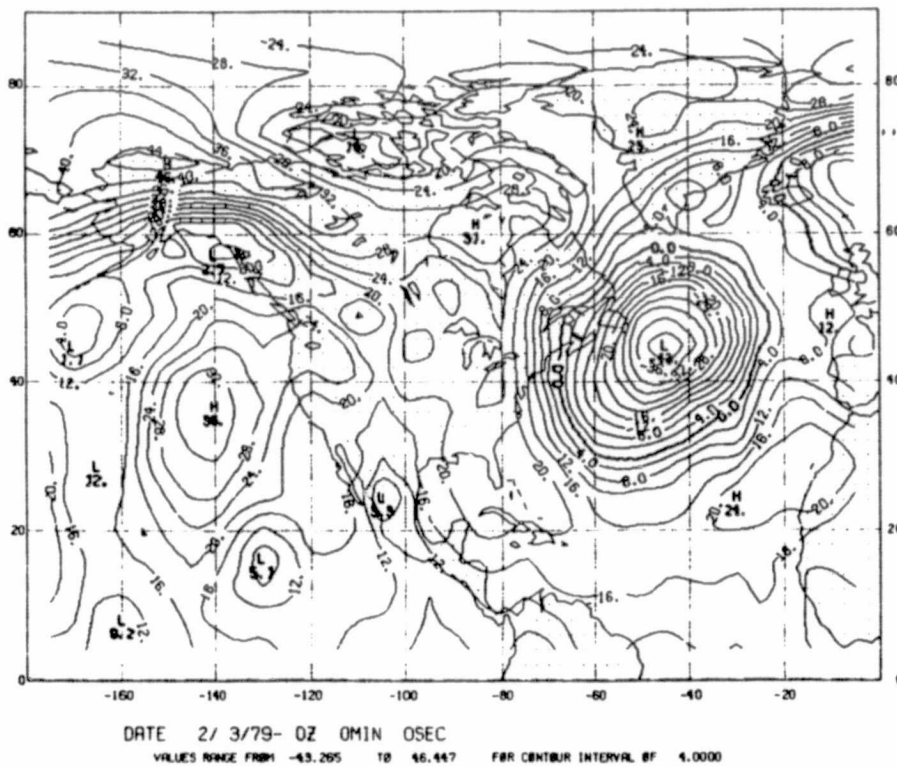


Fig. 2

ORIGINAL PAGE IS
OF POOR QUALITY

MULTIVARIATE - UNIVARIATE

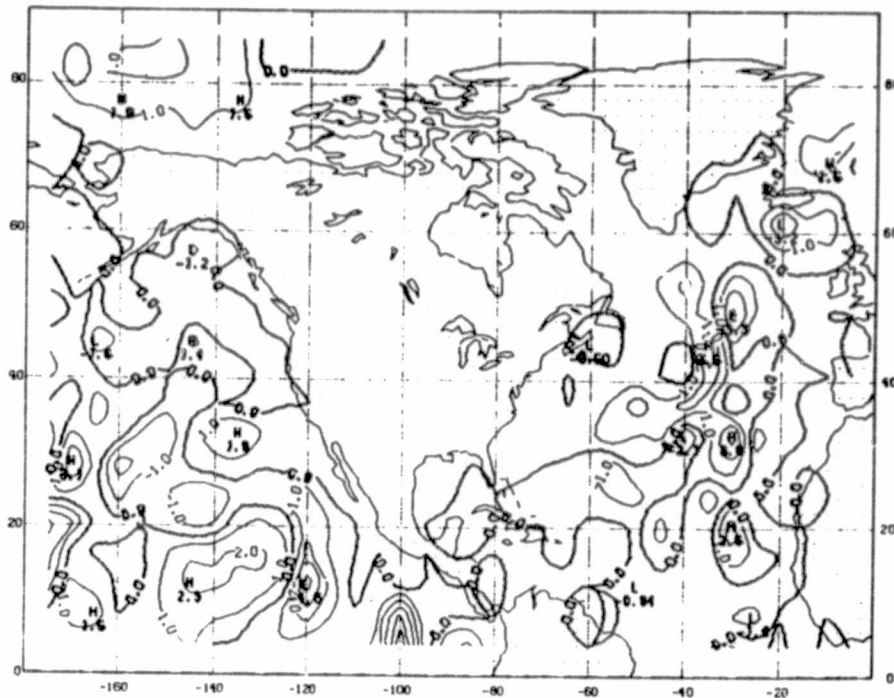


Fig. 3

DATE 2/ 3/79- 0Z 0MIN 0SEC
VALUES RANGE FROM -5.8635 TO 3.5989 FOR CONTOUR INTERVAL OF 1.0000

MULTIVARIATE - 1ST GUESS

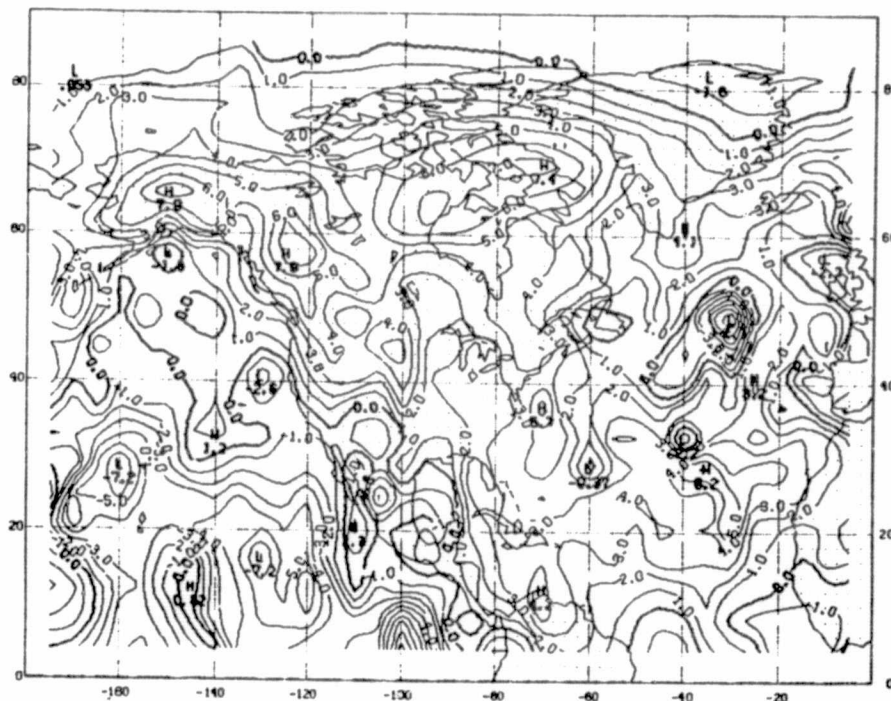


Fig. 4

DATE 2/ 3/79- 0Z 0MIN 0SEC
VALUES RANGE FROM -10.607 TO 7.0016 FOR CONTOUR INTERVAL OF 1.0000

DESIGN OF A LINEAR PROJECTOR FOR USE WITH THE NORMAL MODES OF THE
GLAS 4TH ORDER GCM

S. C. Bloom

1. MODAL STRUCTURE

A central element in any normal mode initialization scheme is the process by which a set of data fields - winds, temperatures or geopotentials, and surface pressures - are expressed ('projected') in terms of the coefficients of a model's normal modes. This process is completely analogous to the Fourier decomposition of a single field (indeed a FFT applied in the zonal direction is a part of the process).

As discussed in Bloom (1983), complete separability in all three spatial dimensions is assumed. Thus, the basis functions for the modal expansion are of the form:

$$F_{\ell km}^P(\sigma, \lambda, J) = V_{\ell}(\sigma) e^{ik\lambda} M_m^P(\ell, k; J) \quad (1)$$

where σ = vertical coordinate ; ℓ = vertical structure index
 λ = longitude ; k = zonal wavenumber
 J = latitude and field index ; m = meridional mode index
 P = index referring to the equatorial symmetry/antisymmetry of the meridional model.

The index J denotes a fixed ordering of the variables (u, v, H) by latitude; for a longer discussion of the meridional structure functions $M_m^P(\ell, k; J)$, see Bloom (1983). An important feature of the normal modes is their coupling of the structures of different fields, thus a coefficient in a normal mode expansion would contain both mass and momentum information.

2. DATA PREPARATION

The normal modes of any model are solutions to a set of equations which represent linear deviations from some mean basic state. A similar approach must be taken with the data fields if they are to be expanded in normal mode functions. While this presents no problems with wind fields (since the mean base state is assumed to have $\bar{U} = \bar{V} = 0$), it does require that care be taken with the projection of mass field data.

A mean temperature $\bar{T}(\sigma)$ and a mean surface pressure \bar{P}_S define the basic state mass fields. Although the GLAS model uses T and Π (equal to $p_S - p_{TOP}$, p_{TOP} a constant) as prognostic variables, the normal mode equations combine them into one linearized mass variable (the specific nature of this variable will be discussed in the next section):

$$g H_* = \phi' + \frac{C_p T}{\bar{p}^\kappa} (p^\kappa)' \quad (2)$$

where

$$\bar{p} = \sigma(\bar{p}_s - p_{TOP}) + p_{TOP}$$

$$(p^\kappa)' = p^\kappa - \bar{p}^\kappa$$

$$\phi' = \text{linearized geopotential}$$

$$\kappa = R/C_p$$

Therefore the data mass fields must be prepared in the following manner: (i) generate $T' = T - \bar{T}$ and $(p^\kappa)'$, (ii) generate ϕ' by integrating a linearized version of the GLAS model's hydrostatic equation using T' and $(p^\kappa)'$, and (iii) use equation (2) to generate H_* .

A final step in the preparation of the data involves symmetrizing and antisymmetrizing (u , V , H_*) with respect to the equator, and shuffling the results so that the three variables are stored in the correct latitudinal order (indexed by J). Denote this final linearized symmetrized and reordered set of data by $D^P(\sigma, \lambda, J)$.

3. LINEARIZATION OF THE MASS VARIABLE - A CAUTIONARY NOTE

The detailed nature of H depends both on the specific design of a model and on the method one chooses to linearize that model. Consider the pressure gradient force term in the horizontal momentum equation in σ -coordinate:

$$\nabla_\phi + RT \nabla \ln p \quad (3)$$

where $\nabla \equiv$ horizontal gradient on σ -surface, and $\phi =$ geopotential. In one version of the ECMWF model (Temperton and Williamson, 1981), $p = \sigma p_s$ and (1) is readily linearized:

$$\nabla \phi' + R\bar{T} \nabla \ln p_s \quad (4)$$

which leads to

$$g H \equiv \phi' + RT \ln p_s \quad (5)$$

The variable $\ln p_s$ occurred throughout the linearized equations of that version of the ECMWF model, so it was a natural variable to linearize.

However, the GLAS GCM employs a modified σ -coordinate, $p = \sigma(p_s - p_{TOP}) + p_{TOP} = \sigma\Pi + p_{TOP}$. In addition, p^κ rather than $\ln p_s$ is the commonly occurring variable; note that (3) can be expressed as

$$\nabla\phi + \frac{\sigma RT}{p} \nabla\Pi \quad (6a)$$

or

$$\nabla\phi + C_p T \nabla \ln p^\kappa \quad (6b)$$

A first attempt to linearize the GLAS model was based on equation 6a; \bar{p}_s (or equivalently, $\bar{\Pi}$) was chosen as the linearization variable, and Π' was the linearized perturbation variable:

$$\nabla\phi' + \frac{RT\sigma}{\bar{p}} \nabla\Pi' \quad (7)$$

which implied the mass variable:

$$g H \equiv \phi' + \frac{RT\sigma}{\bar{p}} \Pi' \quad (8)$$

A better method of linearizing the GLAS model is based on equation 6b, and it leads to the mass variable discussed in the previous section:

$$g H_* \equiv \phi' + \frac{C_p T}{\bar{p}^\kappa} (p^\kappa)'$$

and a pressure gradient term

$$\nabla\phi' + \frac{C_p T}{\bar{p}^\kappa} \nabla(p^\kappa)' \quad (9)$$

One can see that linearization (9) is superior to that of (7) by comparing them with an exact formulation in the following table:

	exact	(7)	(9)
σ level	$R \ln(1 + \sigma \Pi' / \bar{p}_\ell)$	$R \sigma \Pi' / \bar{p}_\ell$	$C_p(p^k)' / p^k$
9	-196.8	-142.4	-178.8
1	-158.9	-122.0	-146.9

where $\Pi' = -503$ mb, $\bar{p}_s = 1013$ mb; representative of data over very high (Himalayan) topography.

4. PROJECTION PROCESS

The process by which the model coefficients $C_{\ell km}^P$ which correspond to a particular set of linearized data $D^P(\sigma, \lambda, J)$ are found is called a forward projection onto the model's normal modes:

$$C_{\ell km}^P = \sum_{\sigma} \sum_{\lambda} \sum_J V_{\sigma}^{-1}(\ell) e^{-ik\lambda} R_J(\ell) M_J^P(\ell, k, m) D^P(\sigma, \lambda, J) [\cos \phi_J]^{1/2} \quad (10)$$

where

$R_J(\ell)$ = scale factors (see Bloom, 1983)

$M_J^P(\ell, k, m)$ = transpose (or inverse if $k = 1$) of $M_m^P(\ell, k, J)$

$V_{\sigma}^{-1}(\ell)$ = inverse of $V_{\ell}(\sigma)$ (see equation 1)

To recover the linearized data fields from the mode coefficients, one performs a backward projection from the model's normal modes:

$$D^P(\sigma, \lambda, J) = \sum_{\ell} \sum_k \sum_m R_J^{-1}(\ell) C_{\ell km}^P F_{\ell km}^P(\sigma, \lambda, J) / [\cos \phi_J]^{1/2} \quad (11)$$

Note that the sums over λ and k in (10) and (11) are performed by using FFT's. Finally, the recovery of the full T and P_s fields requires: (1) a combination of linearized hydrostatic, thermodynamic and continuity equations to compute $(P^k)'$ from H^* ; (2) a nonlinear solver to extract P_s' from $(P^k)'$; and (3) an

inversion of the linearized hydrostatic relation to extract T' from $(P^*)'$ and H^* .

The projection process was tested in a number of ways. Projected and reconstructed fields are identical if all $C_{\ell km}^P$ are used in the reconstruction. A more interesting experiment is the recomposition of fields using a subset of $C_{\ell km}^P$ - this is linear initialization. By setting $C_{\ell km}^P = 0$ for $\ell = 1$ and a particular range of m , all external gravity wave modes are eliminated from the reconstituted fields. This proved to be a useful diagnostic; when (7) linearization was used, a -109 mb adjustment to P_s over the Himalayas occurred, with (9) linearization a +21 mb adjustment was obtained in the same region. The latter figure is in rough agreement with results presented in Temperton and Williamson (1981).

Currently work is underway to recast the projector code into vector form for running on the Cyber 205. With fairly minor additions, the vectorized projector can be used in conjunction with the GLAS model to perform nonlinear normal mode initialization.

REFERENCES

- Bloom, S. C., 1983: Normal Modes of the GLAS 4th Order Model. Research Review - 1982, NASA Tech. Memo. 84983, 99-103.
- Temperton, C. and D. L. Williamson, 1981: Normal Mode Initialization for a Multilevel Grid-Point Model. Part I: Linear Aspects. Mon. Wea. Rev., 109, 729743.

D
22
N84 22071

COMPUTATIONAL ASPECTS OF THE NONLINEAR NORMAL MODE INITIALIZATION OF
THE GLAS 4TH ORDER GCM

I. M. Navon, S. Bloom and L. Takacs

1. INTRODUCTION

Using the normal modes of the GLAS 4th Order Model, a Machenhauer nonlinear normal mode initialization (NLNMI) was carried out for the external vertical mode using the GLAS 4th Order shallow water equations model for an equivalent depth corresponding to that associated with the external vertical mode.

A simple procedure was devised which was directed at identifying computational modes by following the rate of increase of BAL_m , the partial (with respect to the zonal wavenumber m) sum of squares of the time change of the normal mode coefficients (for fixed vertical mode index) varying over the latitude index ℓ of symmetric or antisymmetric gravity waves.

A working algorithm is presented which speeds up the convergence of the iterative Machenhauer NLNMI. A 24 h integration using the NLNMI state was carried out using both Matsuno and leap-frog time-integration schemes; these runs were then compared to a 24 h integration starting from a non-initialized state. The maximal impact of the nonlinear normal mode initialization was found to occur 6-10 hours after the initial time.

2. A MODIFIED NLNMI INCLUDING "COMPUTATIONAL-MODES" FILTERING

Our algorithm for NLNMI consisted of:

- a) A linear normal mode initialization
- b) A first nonlinear normal mode initialization where suspected computational modes were identified by the rate of increase of BAL_m

$$BAL_m = \sum_{m'} \sum_{\ell \in G}^m \frac{\partial c}{\partial t} \frac{\partial c}{\partial t} * = \sum_{m'} \sum_{\ell \in G}^m [\delta t c(k, m', \ell, 0)] [\delta t c(k, m', \ell, 0)] * \\ c = c(k, m, \ell, 0)$$

between subsequent latitude indices ℓ of the symmetric or antisymmetric gravity waves for fixed vertical mode k ($k=1$, exterior vertical mode). The gravity modes with latitudinal indices ℓ ($14 \leq \ell \leq 44$) which had a relative increase in BAL_m over a prescribed threshold were identified as "computational modes" and the coefficients of these modes were filtered out by zeroing (linear initialization) instead of using these "computational" coefficients in a full NLNMI.

c) Subsequently a full Machenhauer nonlinear iteration including all indices ℓ was carried out.

The rationale behind this procedure is that the balance, which is the sum of squares of the time change of the coefficients, is affected by the nonlinear terms introduced by the change in the coefficients over the short forecast. The difference $[c(k,\ell,m,\Delta t)]_{\mu} - [c(k,\ell,m,0)]_{\mu}$ should be greater for the latitude indices ℓ where computational modes occur - as they are out of balance with the eigenfrequencies (ν') employed in the Machenhauer iterative nonlinear correction. In Figs. 1 and 2 we present the evolution of BAL_m for $m = 5$ and $m = 1$ for $\ell = 14$ to 44 for the first Machenhauer iteration and the identification of the suspected "computational modes." Other methods for identifying computational modes can be found in F. Baer and P. J. Sheu (1982) and by B. B. Katz (1982).

The present method identifies only those computational modes which affect the convergence of the NLNMI and it filters them out via a linear normal mode initialization.

3. INSENSITIVITY OF THE NLNMI TO EXCLUSION OF THE UPPER THIRD OF THE ZONAL WAVE NUMBERS M (26-37) FROM THE NONLINEAR BALANCE

Following a suggestion of Dr. E. Kalnay (private discussion) we modified the nonlinear normal mode initialization procedure so that the high zonal wavenumbers from $m = 26$ to $m = 37$ were only linearly normal mode initialized. We then compared the behavior of the modified process with that of the full NLNMI. The effect on the balance (BAL_m) (see Fig. 4) as well as on the subsequent integration was negligible. This result can be explained by the fact that there are fewer physical modes in the high-wave number range (see also Baer and Sheu, 1983).

4. IMPACT OF THE NLNMI ON SHORT-RANGE FORECASTS (24 H)

A 24 h forecast starting from a nonlinearly initialized state was made using the GLAS 4th Order shallow water equations model using either a leap-frog or a Matsuno time-differencing scheme. The results of those forecasts were compared to the results with 24 h integrations starting from a non-initialized state.

In Fig. 5 we plot the time variation of the height field at a grid point for a non-initialized integration and an integration initialized with two nonlinear Machenhauer iterations; both integrations used a Matsuno time-differencing scheme. Fig. 6 differs from Fig. 5 in that a leap-frog time scheme was used.

5. TIME OF MAJOR IMPACT ON SHORT-RANGE FORECASTS

By following the hourly evolution of the height field for a short-range forecast (24 h) with both nonlinear normal mode initialization and a run with no initialization, we observe a major impact for periods of 6-10 hours (see

Figs. 7-10) for both time-differencing schemes. In the case of a leap-frog time-differencing scheme the impact is still visible after 24 h, whereas for a Matsuno time integration scheme the impact of the NLNMI nearly vanished after 24 hours of integration.

6. CONCLUSIONS

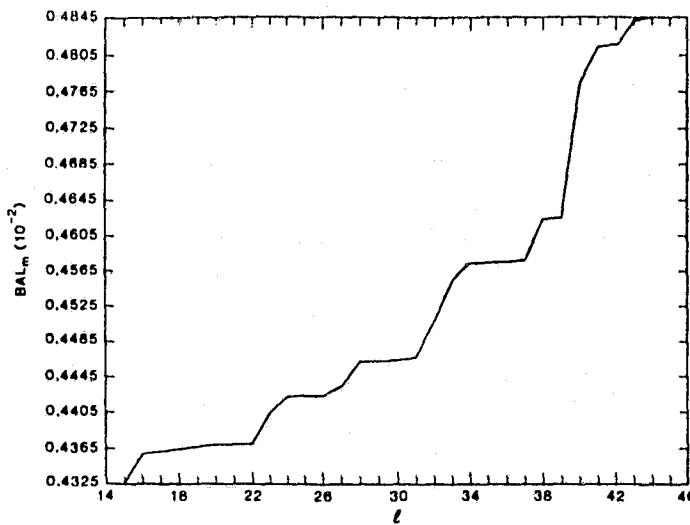
A nonlinear normal mode initialization was successfully applied to the exterior vertical mode of the GLAS 4th Order Model. A new algorithm was developed permitting the identification and subsequent filtering out of 'suspect' computational modes which affect the convergence of the Machenhauer iterative procedure.

By looking at the latitudinal eigenstructures of u , v and ϕ we certified that our procedure identifies computational gravity modes. It is however not exhaustive, as it identifies only the computational modes which affect most significantly the convergence of the Machenhauer iteration. The Machenhauer NLNMI was found to be insensitive to the deletion of high zonal wavenumbers (#26-#37) from the nonlinear balancing process. These zonal waves are only linearly initialized, which results in increased computational efficiency.

24h integrations using both non-dissipative (leap-frog) and dissipative (Matsuno) explicit time-integration schemes were carried out with both non-linearly initialized and non-initialized data sets. The time of maximum impact of the nonlinear normal mode initialization was located between 6-10 hours. We also found that for the Matsuno scheme the results after 24h are nearly identical for both the non-initialized and the NLNMI states, while for the leap-frog scheme the impact of the nonlinear initialization was still evident after 24h.

REFERENCES

- Baer, F. and P. J. Sheu, 1982: Optimal spatial representations for numerical weather prediction models based on normal mode analysis. AFGL Report No. AFGL-TR-82-0028, 86 pp.
- Baer, F. and F. G. Sheu, 1983: Computational modes in numerical weather prediction. Sixth Conference on Numerical Weather Prediction. AMS, June 6-9, 1983, Omaha, Nebraska, pp. 279-384.
- Bloom, S., 1982: Normal modes of the GLAS 4th Order Model. NASA Tech. Memo. 84983, 99-103.
- Katz, B. B., 1982: Classification of normal modes of the primitive equations of atmospheric motion. MSc Thesis, Dept. of Meteorology, University of Maryland, College Park, MD, 115 pp.



ORIGINAL PAGE IS
OF POOR QUALITY

Fig. 1. Evolution of BAL_m for fixed vertical mode $k = 1$ and given zonal wave number $m = 5$, for latitude indices $l = 14$ to $l = 44$ for symmetric gravity modes.

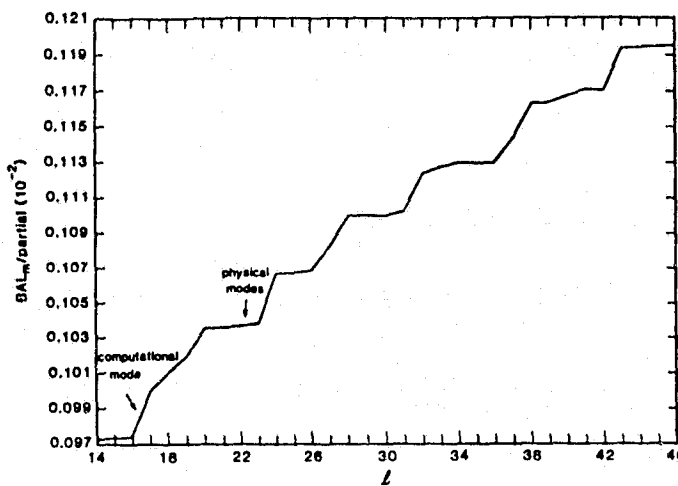


Fig. 2. Evolution of BAL_m for fixed vertical model $k = 1$ and given zonal wave number $m = 1$, for latitude indices $l = 14$ to $l = 46$ for symmetric gravity modes.

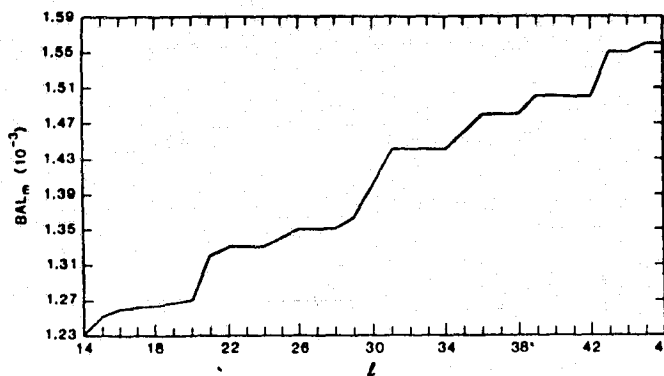
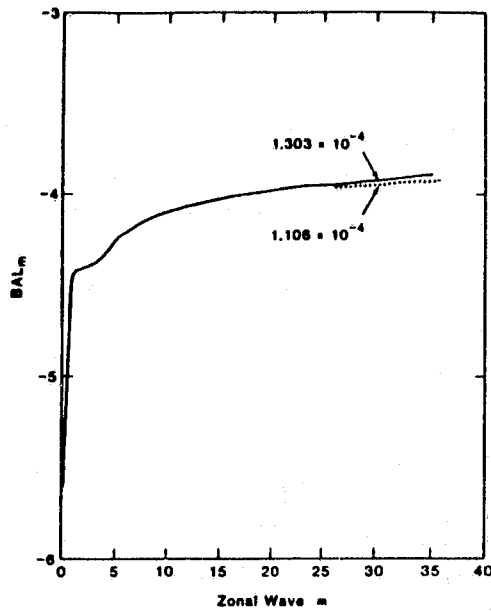


Fig. 3. Evolution of BAL_m for fixed vertical model $k = 1$ and given zonal wave number $m = 1$, for latitude indices $l = 14$ to $l = 46$, for antisymmetric gravity modes.



ORIGINAL PAGE IS
OF POOR QUALITY

Fig. 4. Evolution of BAL_m as a function of the zonal wave numbers with full nonlinear Machenhauer iteration for all zonal wave numbers (solid line) and with linear normal model initialization for zonal wave numbers 26-37.

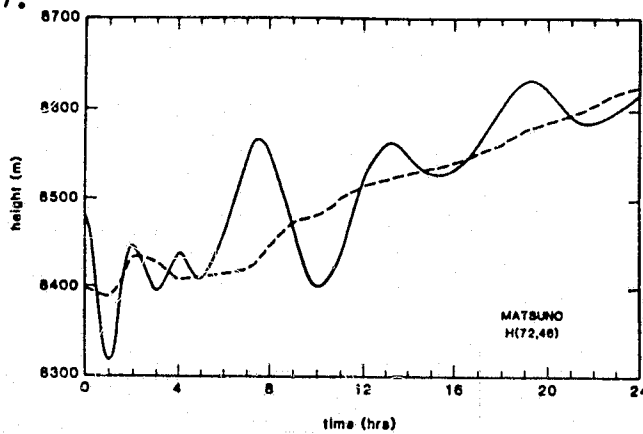


Fig. 5. Time variation of the height field for 24 h at grid point (72, 46) after 2 nonlinear Machenhauer iterations (dotted line) and without initialization (solid line) using Matsuno time differencing scheme.

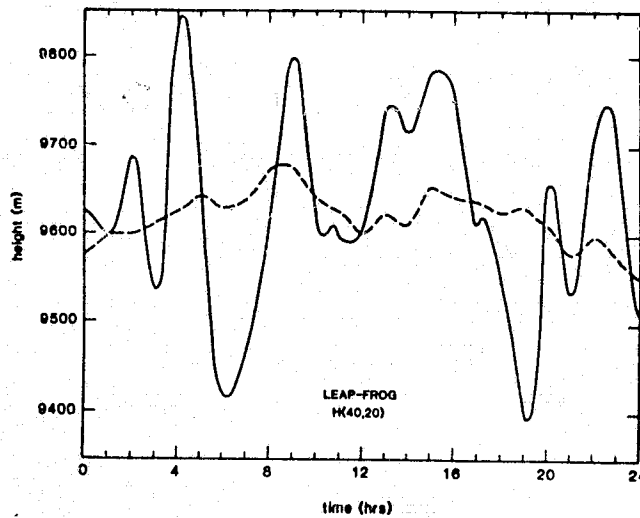


Fig. 6. Time variation of the height field for 24 h at grid point (40, 20) after 2 nonlinear Machenhauer iterations (dotted) and with no initialization (solid line) using a leap-frog time differencing scheme.

TIME = 0.25 DAYS

H

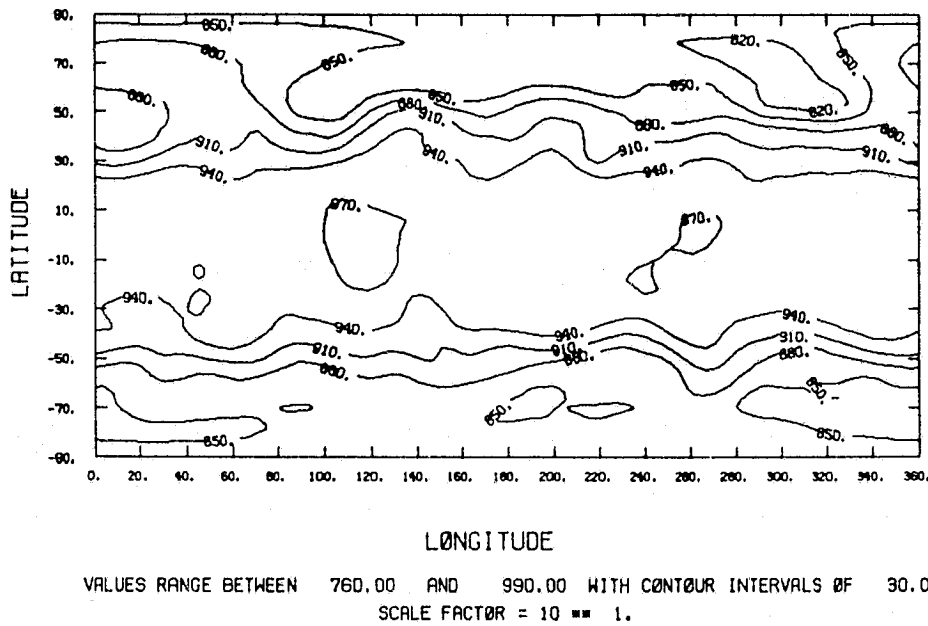


Fig. 7. The height field after 6 hours (0.25 days) starting from nonlinear normal model initialized conditions (values between 7600 m to 9900 m with 300 m contour intervals) (and intergration) with leap-frog scheme.

TIME = 0.25 DAYS

H

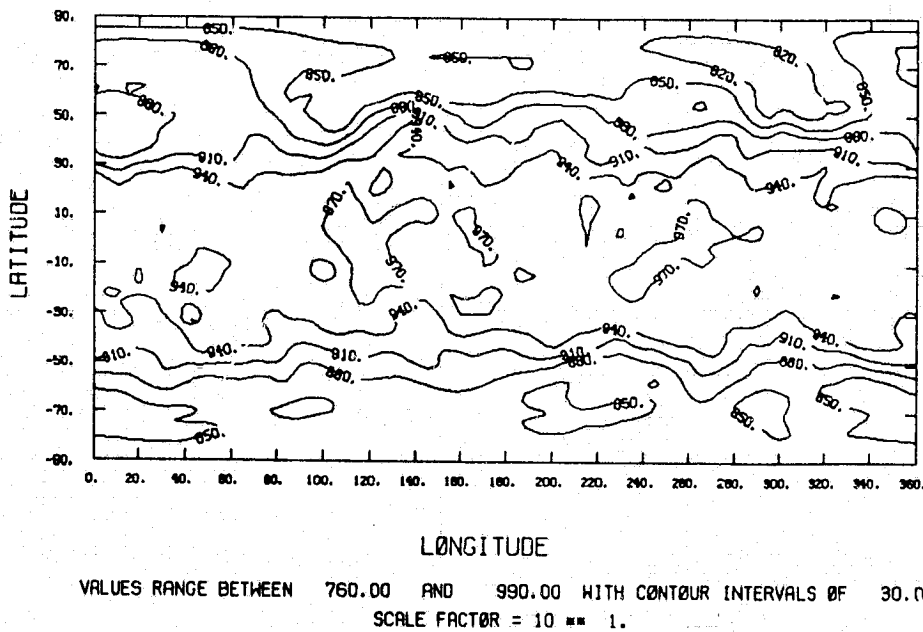


Fig. 8. The height field after 6 hours starting from non initialized conditions and integrated with leap-frog scheme.

ORIGINAL PAGE IS
OF POOR QUALITY

TIME = 0.33 DAYS

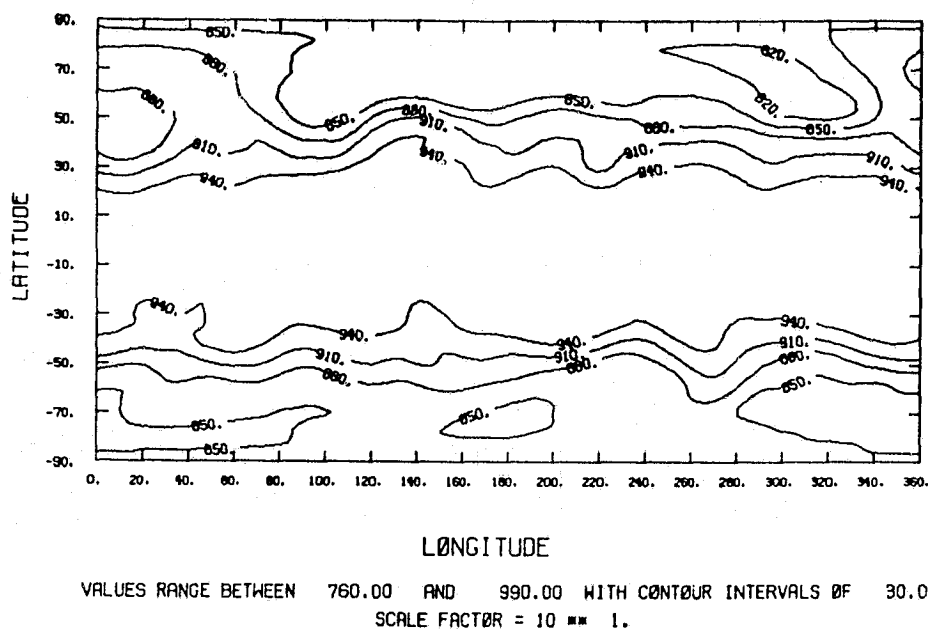


Fig. 9. The height field after 8 hours of integration using the Matsuno time scheme starting from nonlinearly normal model initialized conditions.

TIME = 0.33 DAYS H

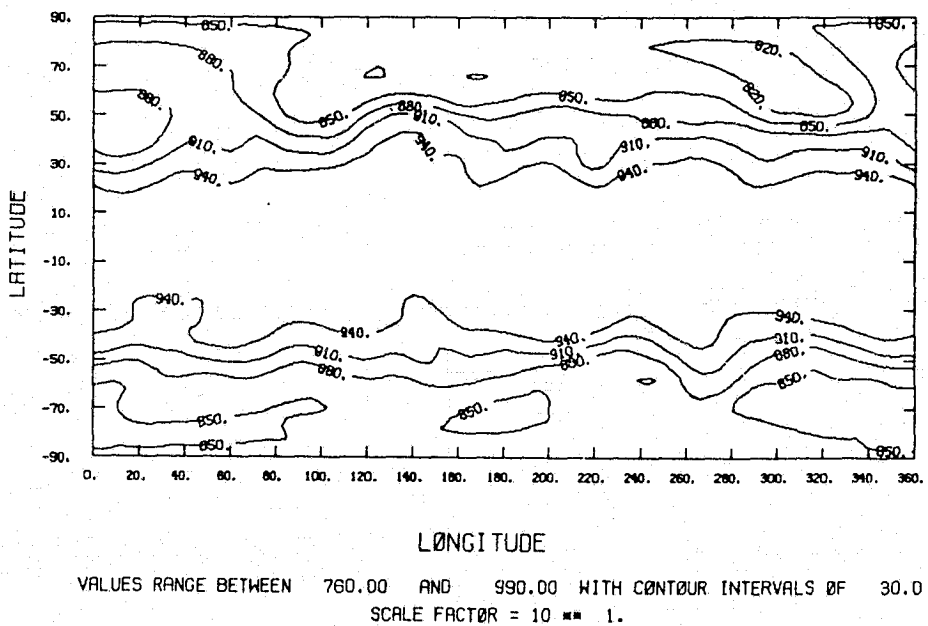


Fig. 10. The height field after 8 hours of integration using the Matsuno time scheme starting from non initialized conditions.

A USER FRIENDLY OPERATING SYSTEM FOR THE GLAS 4TH ORDER FORECAST-ANALYSIS SYSTEM

J. Pfaendtner

1. INTRODUCTION

With the acquisition of the CYBER 205 computer in the summer of 1982, the volume (and complexity) of numerical experimentation which could be done in a given time by the Global Modeling and Simulation Branch increased by an order of magnitude. Experiments, which until then had taken weeks, could be done in a matter of days. It soon became apparent that a major revision would be needed in the way experiments were set-up, controlled during execution and examined when finished. An operating system ideally suited to our needs would have a number of characteristics:

- o The software defining the entire system would be maintained in a form which guarantees the reproducibility and quality of the experimental results consistent with high scientific standards.
- o The individual system components (forecast models, objective analysis programs, post-processing programs, job control procedures, etc.) would be easy to modify, so that the alterations needed to define the experiments could be done in a straightforward manner.
- o The possibility of stopping and restarting experiments would have to be part of the system. The production of archival history tapes containing the experimental results should occur in a clean, almost automatic fashion independent of the way in which the experimental computations are scheduled.
- o Preliminary results from each experiment should be made available as soon as possible. The large investment in computational resources needed by these experiments requires that quality checks of the results be made periodically as the experiments progress.

The next section describes the GLAS 4th Order Forecast-Analysis System in terms of its operating system requirements. Section 3 contains a description of the operating system structure and components.

2. THE GLAS FORECAST-ANALYSIS SYSTEM

For research purposes, the Modeling and Simulation Branch has developed a complete forecast-analysis cycle similar to those used at large forecast centers. Although the GLAS system does not have to contend with the severe constraints imposed by having to produce actual forecasts in real time, it must provide for a degree of flexibility for research purposes which is usually not encountered at an operational forecast center. Fig. 1 shows the main components of the forecast-analysis cycle in schematic fashion. Some parts of the cycle, most importantly the GLAS retrievals program, have not yet been fully incorporated into the operating system. However, the operating system is designed to support

the complete cycle as shown in Fig. 1 and to monitor the generation of short, medium and extended range forecasts made with the GLAS 4th order GCM.

The GLAS physical inversion retrievals program (Suskind et al., 1983) computes vertical profiles of temperature and humidity as well as a number of surface parameters from satellite soundings of brightness temperatures (radiances) in selected spectral channels. The retrievals are derived by modeling physical processes directly rather than by the use of statistical (regression) methods. In addition to operating within the forecast analysis cycle, the retrievals program must also function in a stand-alone mode for testing and high-volume diagnostic experiments.

There are two essentially different versions of the GLAS objective analysis program which can be used in the cycle. First, the SCM (successive correction method) analysis program (Baker, 1983), is fully operational and uses distance and data quality weighted corrections to analyze the model prognostic variables (temperature, wind, humidity) individually on pressure surfaces. The program requires a first guess (the six hour model forecast) and a set of meteorological observations (the size and composition of which can vary from case to case). The second program, the OI (optimal interpolation) analysis, differs from the SCM in that the algorithm uses multivariate statistical methods to derive estimates of the meteorological fields at a particular grid point from a number of nearby observations. The OI analysis is currently being tested and compared to the SCM. Other analysis schemes, (modifications of the SCM or OI), incorporating new, simulated or proposed observing systems must also function within the cycle operating system for research purposes.

The GLAS 4th order forecast model (Kalnay et al., 1983) is in a constant process of improvement, as are all other components of the cycle. The operating system must not only support the frozen fully tested model versions, but in addition be available for testing and model development.

In addition to the three main components of the cycle, a large number of auxiliary programs are needed to both prepare data for input (reformatting, data staging, quality checks) and to analyze and archive the experimental results (data staging, graphics, diagnostic studies). Although some of these programs do not belong to the cycle proper, they all interface with it and provisions must accordingly be made in the operating system.

Software management for the cycle components (forecast model, objective analysis programs, retrievals programs and post-processing programs) is afforded the highest priority. The programs for each of the individual components are kept on CMS library machines where they are maintained by analysts and programmers responsible for their quality. An update facility, described in the model documentation (Kalnay et al., 1983), is used which allows a number of programmers to independently modify an existing program base. The various versions which have been placed in production are defined on the library machines by a set of masters and a collection of permanent updates (changes to the masters). In this way a clear distinction can be made between program versions which are frozen and in production and versions which are being developed and tested. The changes required to define a test version from one of the production versions are kept in local update files residing on the user machine of the person making the changes. These local updates do not interfere with either the production code or test versions being developed by other users.

3. THE OPERATING SYSTEM FOR THE GLAS FORECAST-ANALYSIS CYCLE

The forecast-analysis cycle depicted in Fig. 1 runs on the facilities at the NASA High Speed Computing Facility. Details which are pertinent to an understanding of the operating system for the cycle are shown in Fig. 2. In most cases experiments are performed on the CYBER 205 because of its superior speed. But, for testing purposes and as emergency back-up in case the CYBER is unavailable for a prolonged period, all aspects of the cycle can also be run on either of the two Amdahl computers. No attempt will be made here to describe the back-up operating procedures.

The operating system software exists as a collection of CMS execs, CYBER procedures, general purpose libraries, utility FORTRAN programs and MVS procedures. The production versions of the model, analysis programs, etc. are kept in pool files on the 819 disks where they are readily accessible from the CYBER. The code management procedures for the operating system software have been designed so that a return to a previous operating system is possible.

Before a forecast-analysis experiment can be started, the input data must be prepared in a form acceptable to the operating system. The programs to do the data preparation are an integral part of the operating system.

- o If GLAS retrievals are to be done, the raw radiance data from satellite observations are staged to a set of buffer data sets on the MASSTOR device.
- o If GLAS objective analysis is to be done, conventional meteorological observations (radiosondes, ship and aircraft reports, surface reports, etc.) are also staged to buffer data sets on MASSTOR.
- o For comparison purposes during a simulated real-time cycle or an extended forecast, the analysis from another GLAS assimilation experiment or analysis from another forecast center (NMC or ECMWF) are also staged to MASSTOR.
- o A set of initial conditions for the forecast-analysis cycle has to be prepared and placed either on MASSTOR or the 3350 disks. The initial conditions can come from an analysis done elsewhere or from a previously run GLAS experiment.
- o Namelist files have to be prepared and placed on the 3350 disks. These files specify a multitude of switch settings and parameters which are read by the cycle programs and define the run time options and parameterizations which are to be used for the experiment.

After the above mentioned set-up steps have been completed for the experiment, the work can be submitted to the CYBER for execution. The experiments usually require more time on the CYBER than could reasonably be submitted in one computer run. Hence, the operating system has been designed to permit the experiment to be easily segmented. The operating system CMS exec GCMSET is used to submit work to the CYBER. This exec will prompt the user for all information it needs to ensure that the submitted job deck has a high probability of running. Among other things, GCMSET does the following:

- o It checks all account information on the jobs it will submit.

- o It checks to see that all program versions requested are available to the operating system.
- o It checks the data environment to see that the input data required by the job is available to the operating system.
- o It checks to see that all needed namelist files exist, and allows the user to view and edit them if desired.
- o It allows the user to specify the generation of plots and statistics during cycle execution on the CYBER so that preliminary results can be viewed as they are generated.
- o It does job scheduling, ensuring that the jobs will enter and leave the CYBER at specified times, using priorities assigned by the production staff.
- o It allows submission of test jobs which can by-pass the generation of archive history tapes. Hence, GCMSET is used for program development as well as for production runs.
- o It creates the MVS job deck for the "merge job" which runs after the experiment segment has finished on the CYBER. This MVS job, which is submitted to the Amdahl V7B from the CYBER, merges the segment of archive history which is sent to MASSTOR from the CYBER into the history tape sequence for the experiment. The merge job also updates the operating systems catalog of experiment history tapes and prepares the data set environment on MASSTOR and the 3350 disks for the next computational segment for the experiment.

When an experiment is finished, the operating system will have ensured that a complete set of archive history tapes has been generated. These tapes contain copies of the source code used in the cycle for the experiment as well as a time series of experimental results. The operating system contains post-processing programs and execs which can extract useful diagnostic products from the archive tapes such as contour plots, time averages and statistics.

The GLAS forecast-analysis cycle has been controlled by the operating system described here since December of 1982. During its first year of operation the system has been expanded to encompass an increasing number of functions. The experience to date has been favorable and plans are continuing for the integration of more software and procedures into the operating system.

REFERENCES

- Baker, W. E., 1983: Objective Analysis and Assimilation of Observational Data from FGGE. Mon. Wea. Rev., 111, 328.
- Kalnay, E., R. Balgovind, D. Edelmann, J. Pfaendtner, L. Takacs, and W. Chao, 1983: Documentation of the GLAS Fourth Order General Circulation Model. NASA Tech. Memo. (to appear).
- Susskind, J., J. Rosenfield, D. Reuter, and M. T. Chahine, 1982: The GLAS Physical Inversion Method for Analysis of HIRS/MSU Sounding Data. NASA Tech. Memo. 84936.

ORIGINAL PAGE IS
OF POOR QUALITY.

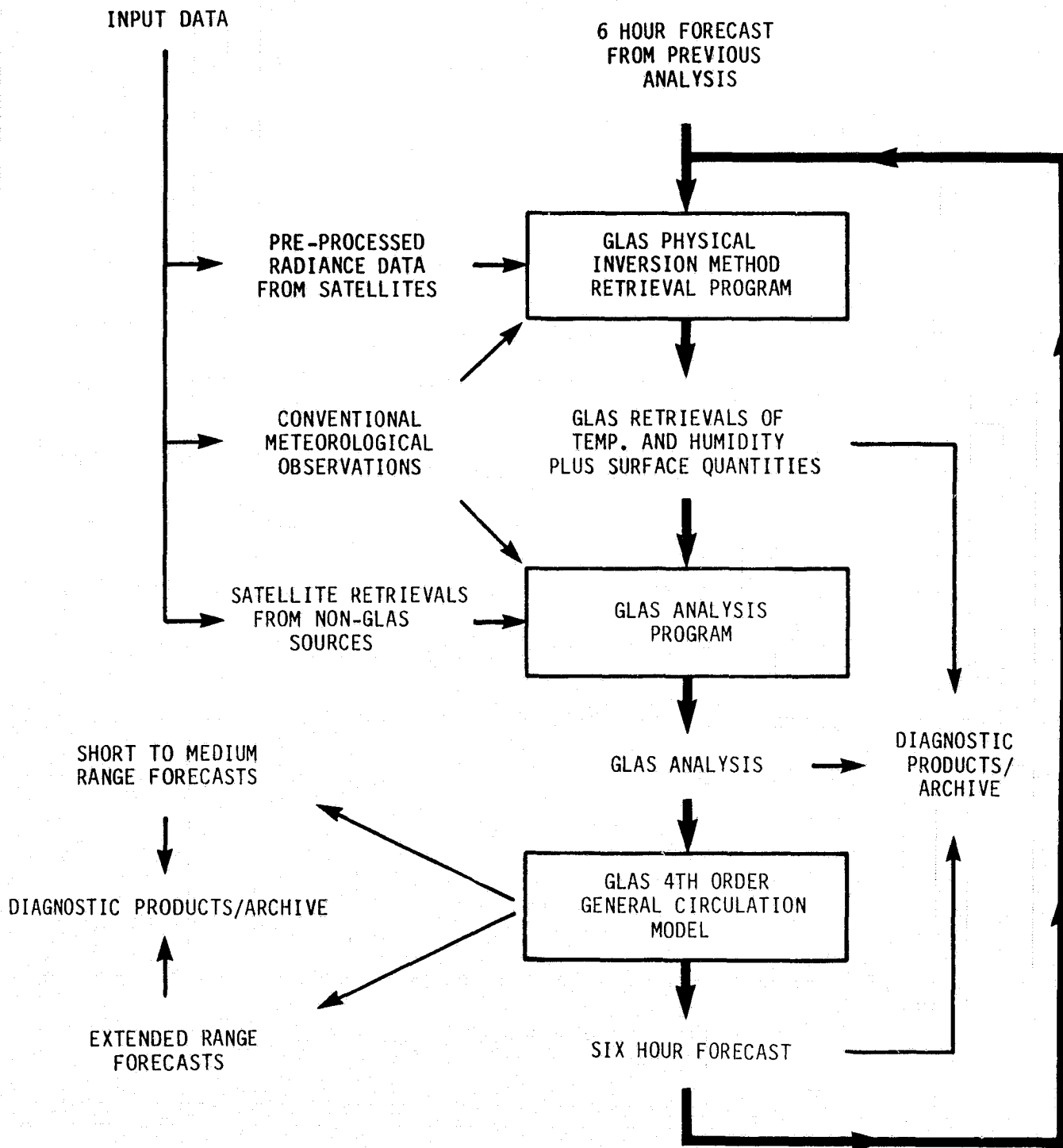


Fig. 1. Schematic view of the GLAS forecast-analysis cycle.

ORIGINAL PAGE IS
OF POOR QUALITY

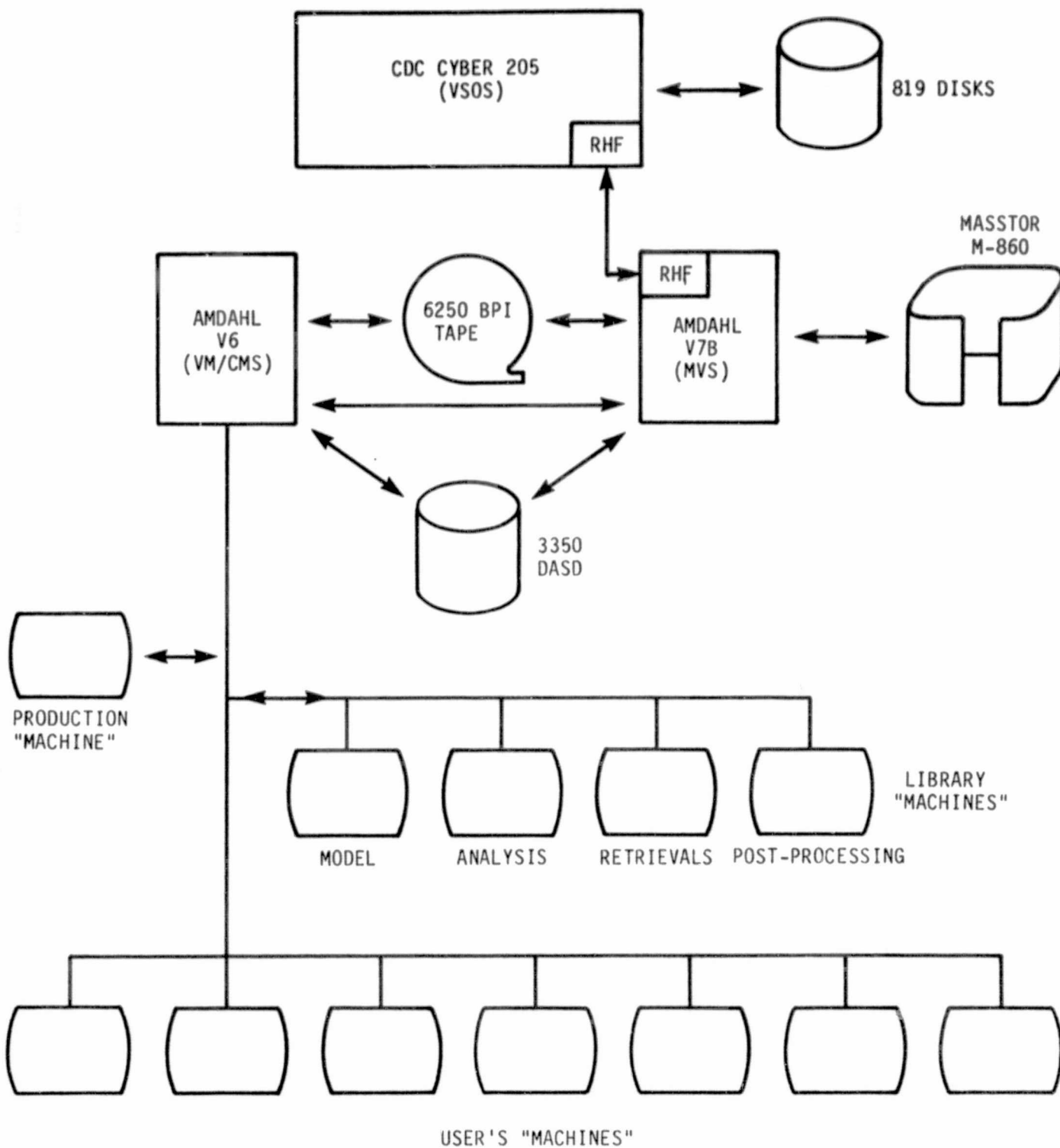


Fig. 2. Schematic view of computer facility components used by forecast-analysis cycle operating system.

EMPIRICALLY DERIVED SECOND ORDER SCHEMES FOR THE ADVECTION EQUATION WITH
MINIMUM DISSIPATION AND DISPERSION ERRORS

L. L. Takacs

ABSTRACT

Two second-order advection schemes of the Lax-Wendroff type are empirically derived which have accuracy and phase characteristics similar to that of a third-order scheme. The new schemes are compared with other currently used methods, and are shown to have superior behavior in simulating the advection of localized disturbances. The schemes are derived for constant flow and generalized to two-dimensional non-uniform flow.

1. INTRODUCTION

One of the most common ways of measuring the relative merit of a given numerical scheme for advection is to consider the scheme's dissipation and dispersion properties. Following the work of Crowley (1968), Molenkamp (1968), and Anderson and Fattahi (1974) on the comparison of numerical schemes for the advection equation, it has been shown that high-order schemes tend to shift their dissipation and dispersion errors toward the high wavenumbers of a given solution. In choosing a scheme of a given order, however, an objective criteria must be devised which will determine the scheme which minimizes some measure of error. In this paper a scheme has been derived which gives an optimal balance between the two errors, i.e. a scheme which dissipates most strongly those waves whose phase speed is most poorly represented. For this derivation, we will restrict ourselves to second-order schemes of the Lax-Wendroff type.

2. GENERALIZED SCHEME

For simplicity, the formulation of the scheme will be based on the one-dimensional advection equation given by

$$\frac{\partial q}{\partial t} + c \frac{\partial q}{\partial x} = 0 \quad (1)$$

Here q represents any arbitrary quantity being advected, while c is the constant velocity of the flow field in the x -direction.

In general we can write a finite-difference version of (1) as

$$q_j^{n+1} = \sum_j a_j q_{j+j}^n, \quad j = 0, \pm 1, \pm 2, \dots \quad (2)$$

Here the subscripts j and $j+j'$ denote the location in space, while the superscripts n and $n+1$ denote the time index. The weighted coefficients a_j are presently arbitrary.

For a given order of accuracy, certain restrictions are placed on the coefficients. By using a Taylor series substitution, it can be shown that first-order accuracy requires:

$$\begin{aligned}\sum_j a_j &= 1 \\ \sum_j j a_j &= -\mu\end{aligned}\quad (3)$$

where μ is the Courant-Friedrichs-Lewy (CFL) stability parameter given by

$$\mu = \frac{c \Delta t}{\Delta x} \quad (4)$$

Second-order accuracy requires in addition to (3) the requirement

$$\sum_j j^2 a_j = \mu^2 \quad (5)$$

In general, for m th-order accuracy there are $m+1$ requirements beginning with (3) and ending with

$$\sum_j j^m a_j = (-\mu)^m \quad (6)$$

When these requirements are satisfied, the scheme will be m th-order accurate both in time and in space.

3. FORMULATION OF THE SECOND-ORDER SCHEME

We will only be considering two-step second-order schemes. Using three grid-points centered about q_j^n , second-order accuracy uniquely defines the second-order Lax-Wendroff scheme described by Leith (1965). By including one more grid-point, third-order accuracy may be achieved thus reducing the order of magnitude of the phase error. However, rather than satisfying third-order accuracy analytically, the extra grid-point will act as a free parameter in a second-order regime to minimize specific measurements of dissipation and dispersion error. The following, then, is a summary of the steps taken in the formulation of the second-order scheme.

1. Use one more point than the minimum needed for the desired accuracy. In this case, four points were used ($j' = 1, 0, -1, -2$) for a second-order scheme.
2. Let the coefficient of the extra point be a free parameter.
3. Using the free parameter, obtain a family of stable schemes.

4. From this family of stable schemes, find the scheme which minimizes some measure of error.

The form of the second-order scheme under consideration is given by

$$q_j^{n+1} = a_1 q_{j+1}^n + a_0 q_j^n + a_{-1} q_{j-1}^n + a_{-2} q_{j-2}^n \quad (7)$$

where the coefficients a_j are found by requiring second-order accuracy and have the form

$$\begin{aligned} a_1 &= \mu(\mu-1)/2 - a_{-2} & a_0 &= 1 - \mu^2 + 3a_{-2} \\ a_{-1} &= \mu(\mu+1)/2 - 3a_{-2} & a_{-2} &= \alpha\mu(\mu-1) \end{aligned} \quad (8)$$

The form of the free parameter a_{-2} was chosen so that for $\mu = 0$ or 1 , the scheme is exact. In order to obtain a family of stable schemes, restrictions were placed on the first non-zero derivation of the amplification factor associated with the scheme, producing bounds on the free parameter α given by

$$0 \leq \alpha \leq 1/2 \quad (9)$$

It should be again noted that when $\alpha = 0$, the scheme reduces to the second-order Lax-Wendroff scheme.

4. ONE-DIMENSIONAL RESULTS

In order to obtain the optimum value for α , experiments similar to those of Crowley (1968), Molenkamp (1968), and others were performed in which a cone-shaped disturbance with a base-width of 10 grid-points was advected over a distance of 70 grid-points. Three measurements of error were taken representing the total error, the dissipation error, and the dispersion error, shown in Fig. 1.

From Fig. 1 we see that a minimization of the total error occurs within the possible range of α , with the optimal α lying near 0.25. As μ approaches 0 or 1, the error tends toward zero as expected. The dissipation error, however, is affected more strongly by the advective speed rather than the free parameter α . Also, the dissipation error is an order of magnitude less than the total RMS error. Thus we see that the extra grid-point added to the second-order scheme has very little effect on reducing dissipation error. Finally, we see that the error associated with dispersion is most responsible for the observed total error. The order of magnitude of the dispersion error is the same as that for the total error, and is minimized by the same optimal α .

From these three error measurements we see that for values of μ larger than 0.5, the optimum value of α is near 0.3 while for small μ values, the optimum value of α lies near 0.2. Choosing $\alpha = 0.25$ yields the one-dimensional

scheme derived by Fromm (1968) in which a forward and backward timestep of the second-order Lax-Wendroff scheme was linearly combined to 'zero-out' the phase lag in each step. This scheme is given by

$$q_j^{n+1} = q_j^n - \frac{\mu}{4} (q_{j+1}^n + 3q_j^n - 5q_{j-1}^n + q_{j-2}^n) + \frac{\mu^2}{4} (q_{j+1}^n - q_j^n - q_{j-1}^n + q_{j-2}^n). \quad (10)$$

This scheme will be referred to as Scheme A25 in future reference.

For the case where the effective Courant number is small (such as that due to advection in general circulation models), choosing $\alpha = 0.2$ is more appropriate. The scheme is given by

$$q_j^{n+1} = q_j^n - \frac{\mu}{10} (3q_{j+1}^n + 6q_j^n - 11q_{j-1}^n + 2q_{j-2}^n) + \frac{\mu^2}{10} (3q_{j+1}^n - 4q_j^n - q_{j-1}^n + 2q_{j-2}^n). \quad (11)$$

This scheme will be referred to as Scheme A20 in future reference.

Finally, for comparative purposes, the second-order Lax-Wendroff scheme derived with $\alpha = 0$ is given by

$$q_j^{n+1} = q_j^n - \frac{\mu}{2} (q_{j+1}^n - q_{j-1}^n) + \frac{\mu^2}{2} (q_{j+1}^n - 2q_j^n + q_{j-1}^n). \quad (12)$$

This scheme will be referred to as Scheme A0 in future reference.

Figs. 2-5 show the results for advecting two initial profiles through two translations of the 70 grid-point domain. In each figure a comparison is shown for the three schemes previously discussed in addition to the first-order forward-upstream scheme given by

$$q_j^{n+1} = q_j^n - \mu (q_j^n - q_{j-1}^n), \quad (13)$$

the centered fourth-order with leapfrog scheme,

$$q_j^{n+1} = q_j^n - 2\mu \left[\frac{4}{3} \left(\frac{q_{j+1}^n - q_{j-1}^n}{2} \right) - \frac{1}{3} \left(\frac{q_{j+2}^n - q_{j-2}^n}{4} \right) \right], \quad (14)$$

and the third-order accurate scheme in time and space derived from equation

$$(8) \quad q_j^{n+1} = q_j^n - \frac{\mu}{6} (2q_{j+1}^n + 3q_j^n - 6q_{j-1}^n + q_{j-2}^n) + \frac{\mu^2}{2} (q_{j+1}^n - 2q_j^n + q_{j-1}^n) - \frac{\mu^3}{6} (q_{j+1}^n - 3q_j^n - 3q_{j-1}^n + q_{j-2}^n). \quad (15)$$

Figs. 2 and 3 show the results for advecting the cone with $\mu = 0.2$ and $\mu = 0.7$, while Figs. 4 and 5 show the same for the step initial profile. In each plot the total error, dissipation error, and dispersion error are also presented

scaled by the total number of iterations.

In all figures we see the drastic decrease in dissipation error obtained by going from the first-order scheme (a) to the second-order scheme (b). The dispersion error, however, generally increases due to the poor phase properties of the non-dissipated wave components. By including the extra grid-point, as in schemes (c) and (d), the dispersion error is seen to decrease significantly. Both of these schemes are very similar to the third-order accurate scheme (f). Finally, the fourth-order with leapfrog scheme (e), although having no dissipation error, shows significant dispersion error.

5. TWO-DIMENSIONAL RESULTS

Two-dimensional versions of Schemes A20 and A25, based on two passes of one-dimensional flux formulations of the schemes, are also available. As a two-dimensional test, the cone-shaped disturbance having a base diameter of 10 grid-points was advected by solid-body rotation.

Fig. 6 shows the initial condition for this experiment and the scheme solution after one and two complete revolutions using Schemes A0 and A20. Again we see the improved phase characteristics of Scheme A20. Also, because of the dispersive nature of Scheme A0, the solution continues to deteriorate upon the second rotation while that of Scheme A20 remains almost unchanged.

6. SUMMARY

By using four grid-points for a second-order finite-difference formulation of the advection equation, schemes with optimal dissipation and dispersion properties are empirically devised. Numerical experiments indicate that the new schemes compare favorably with other currently used methods.

REFERENCES

- Anderson, D. and B. Fattahi, 1974: A comparison of numerical solutions of the advection equation. J. Atmos. Sci., 31, 1500-1506.
- Crowley, W. P., 1968: Numerical advection experiments. Mon. Wea. Rev., 96, 1-11.
- Fromm, J. E., 1968: A method for reducing dispersion in convective difference schemes. J. Comp. Phys., 3, 176-189.
- Leith, C. E., 1965: Numerical simulations of the earth's atmosphere. Methods of Computational Physics, 4, Academic, New York and London, 1-28.
- Molenkamp, C. R., 1968: Accuracy of finite difference methods applied to the advection equation. J. Appl. Meteor., 7, 160-167.

FIGURE CAPTIONS

Fig. 1. Total RMS error, dissipation error, and dispersion error as a function of scheme and CFL parameter after advecting initial condition one complete translation of the 70 grid-point domain.

Fig. 2. Numerical solutions for a) upstream scheme, b) Scheme A0, c) Scheme A20, d) Scheme A25, e) fourth-order with leapfrog, and f) third-order scheme, after two complete translations using $\mu = 0.2$.

Fig. 3. As in Fig. 2 but for $\mu = 0.7$.

Fig. 4. As in Fig. 2.

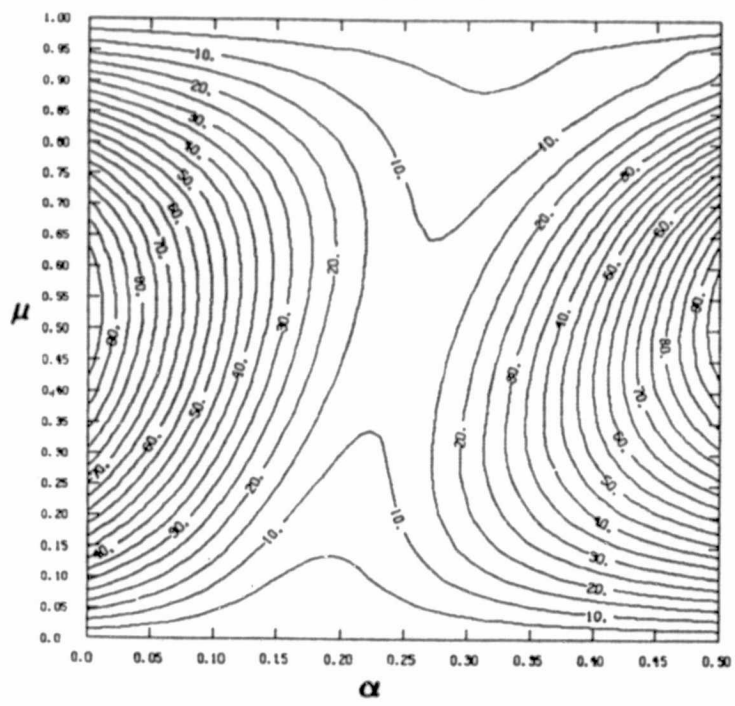
Fig. 5. As in Fig. 2 but for $\mu = 0.7$.

Fig. 6. Initial condition and numerical solutions for Schemes A0 and A20 after one and two complete rotations.

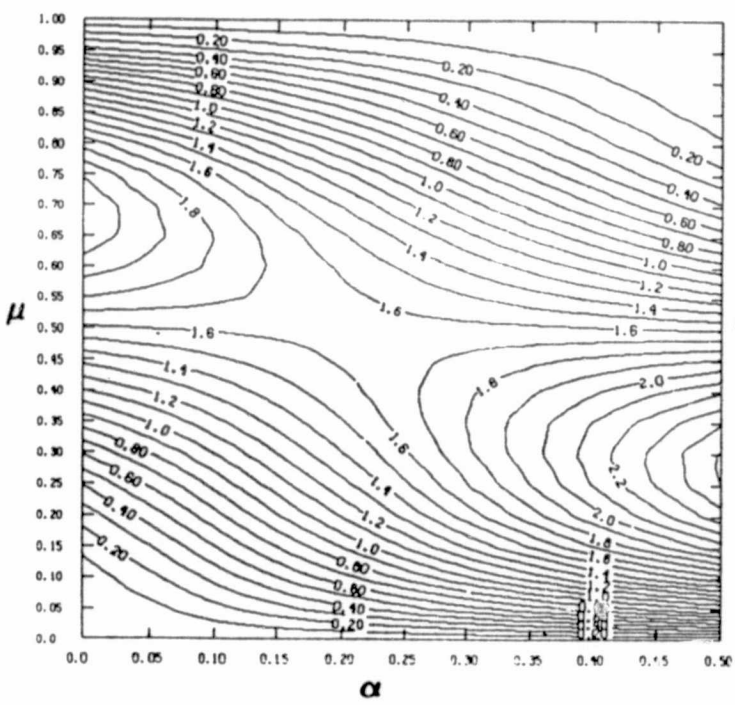
Fig. 1

ORIGINAL PAGE IS
OF POOR QUALITY

TOTAL ERROR



DISSIPATION ERROR



DISPERSION ERROR

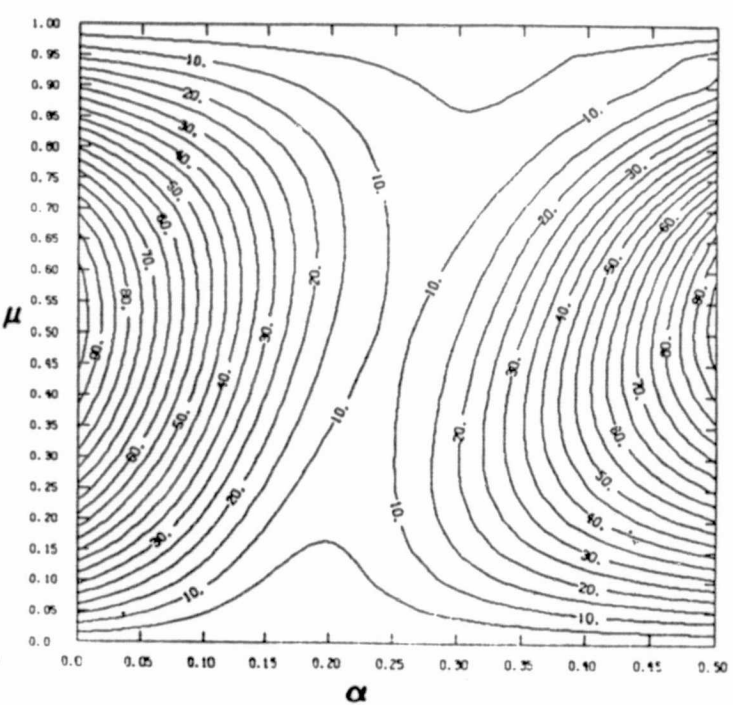


Fig. 2

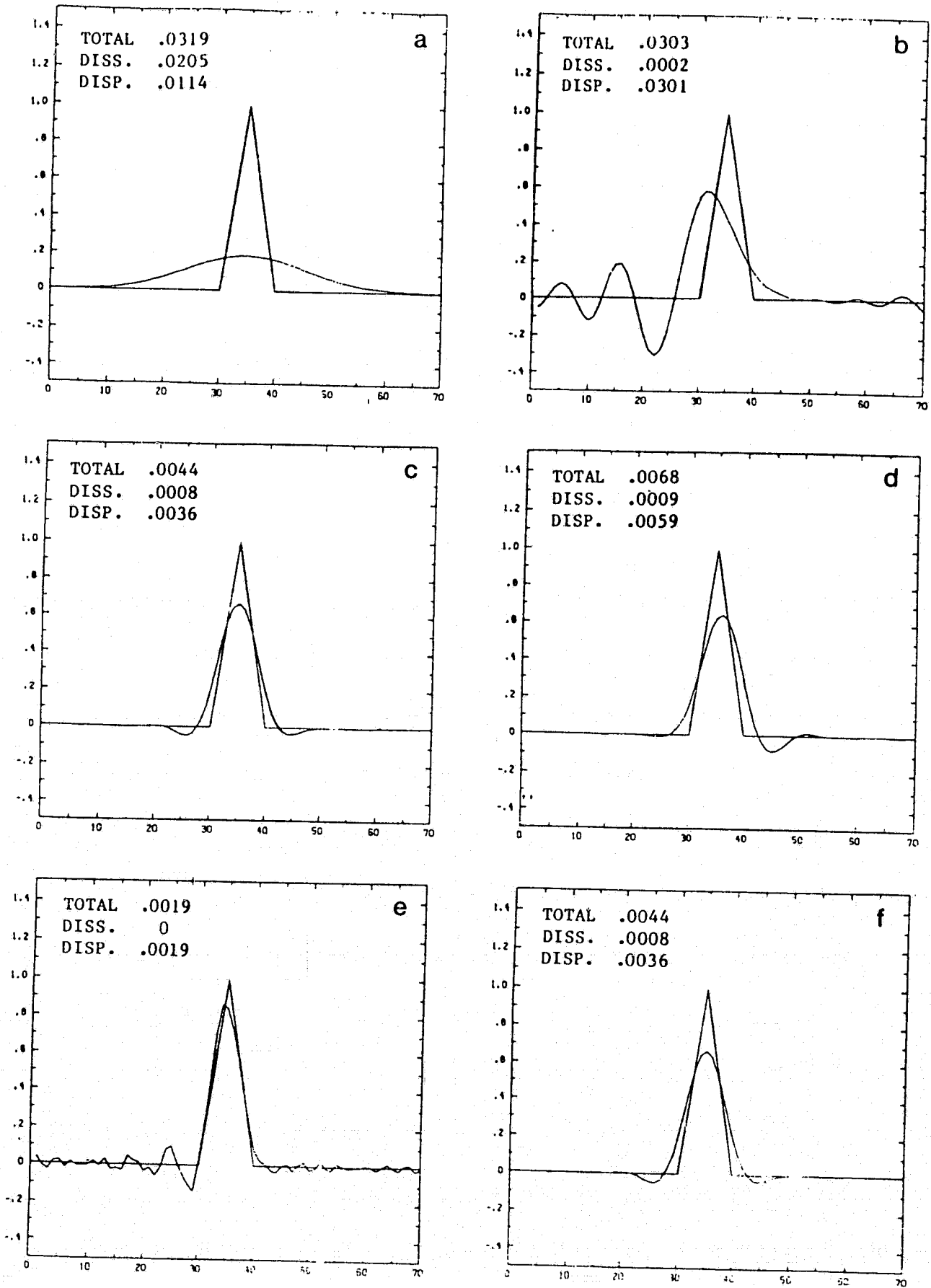
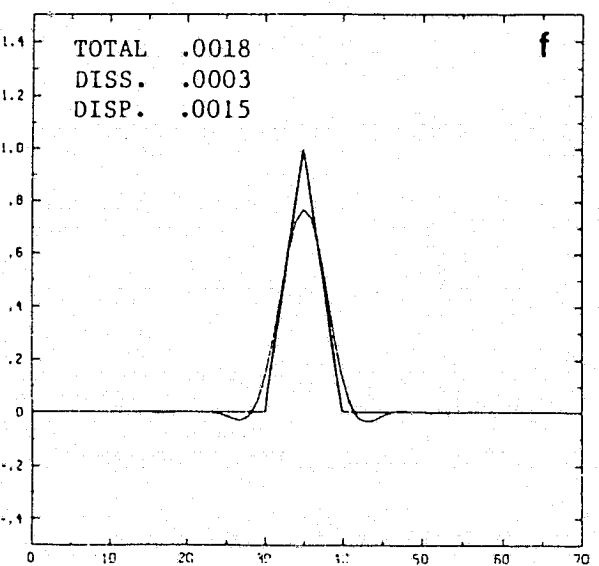
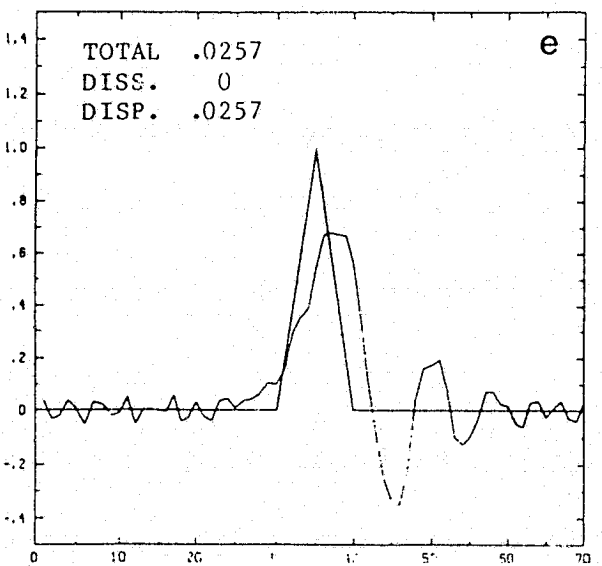
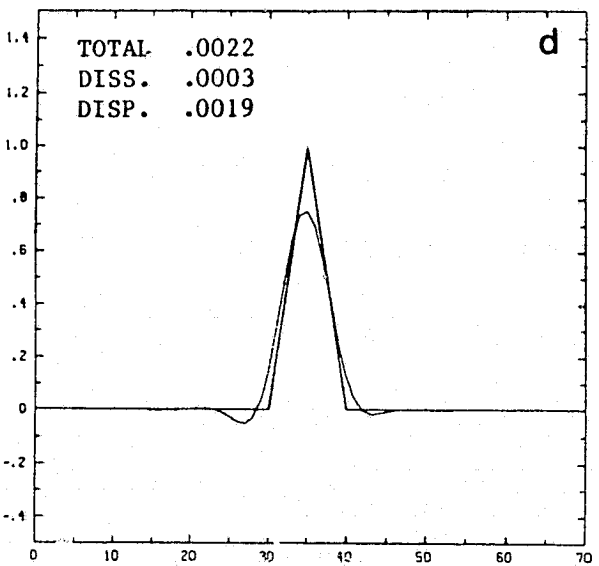
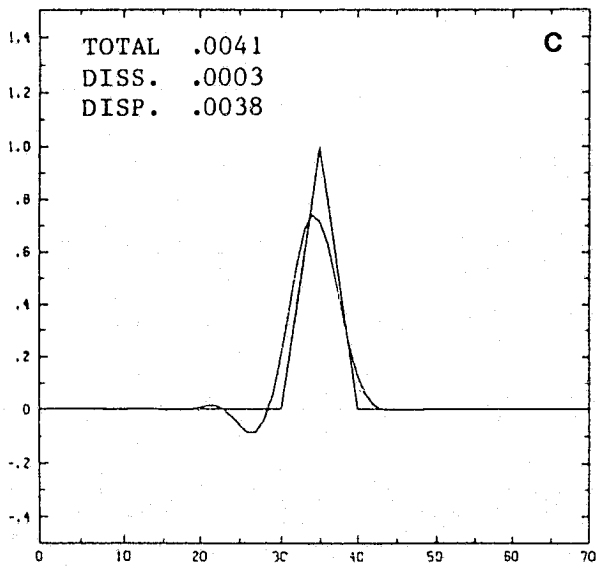
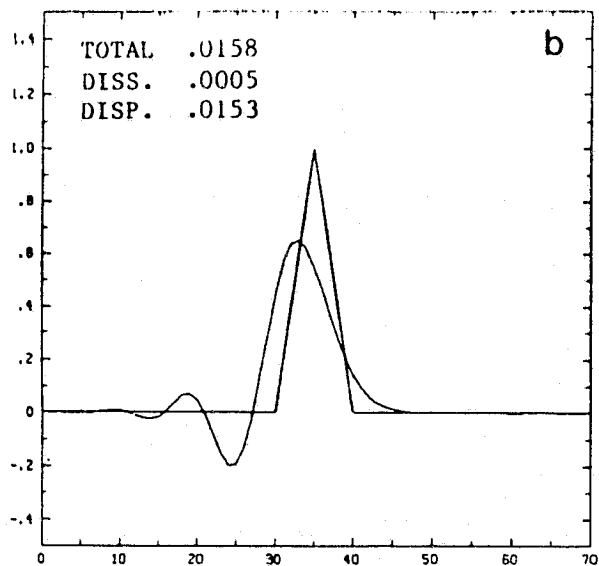
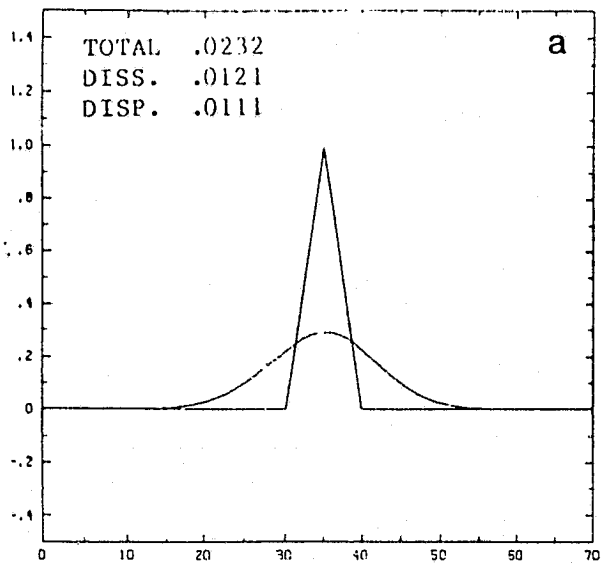
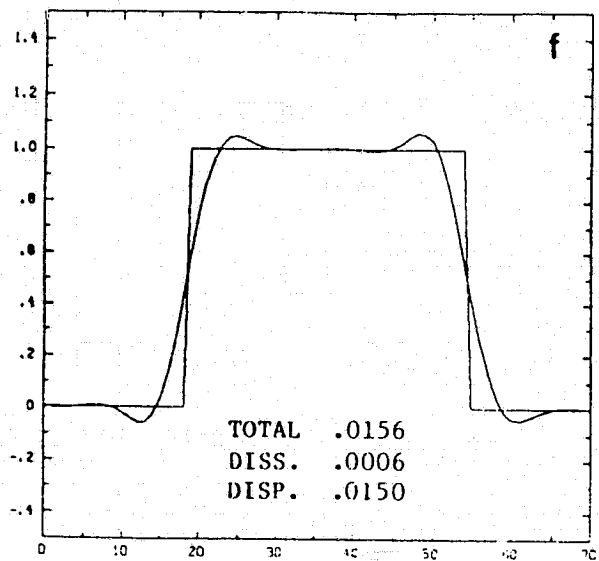
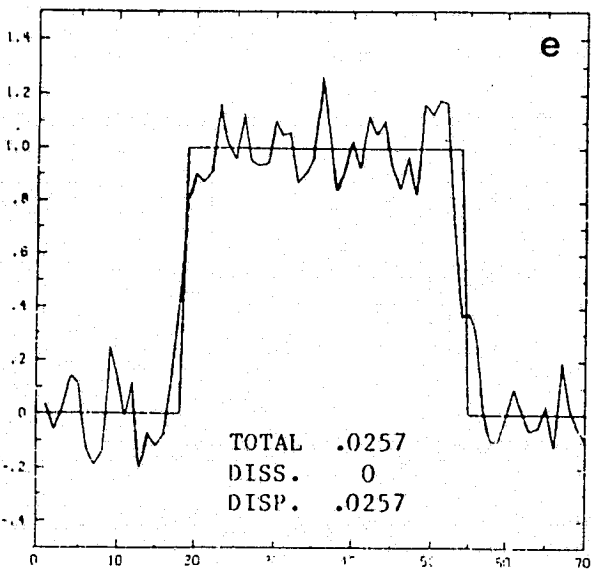
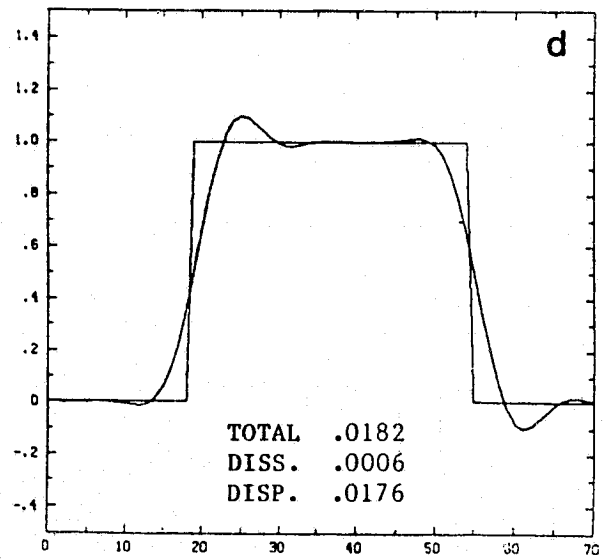
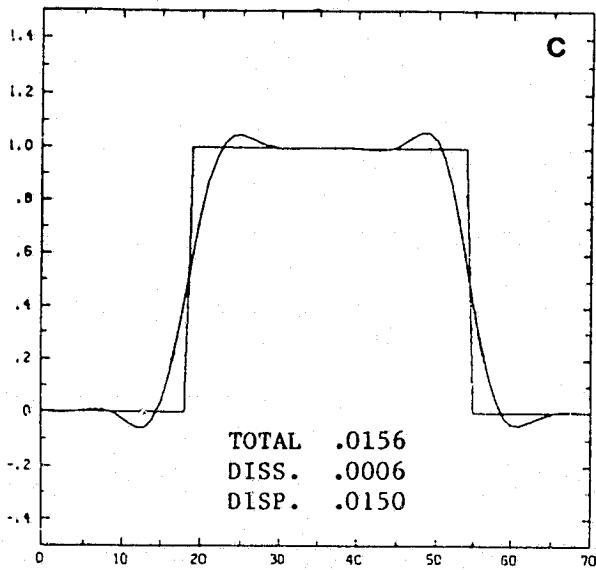
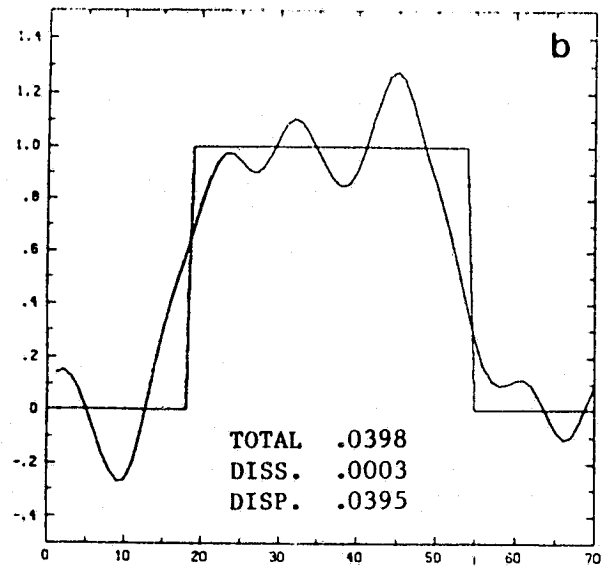
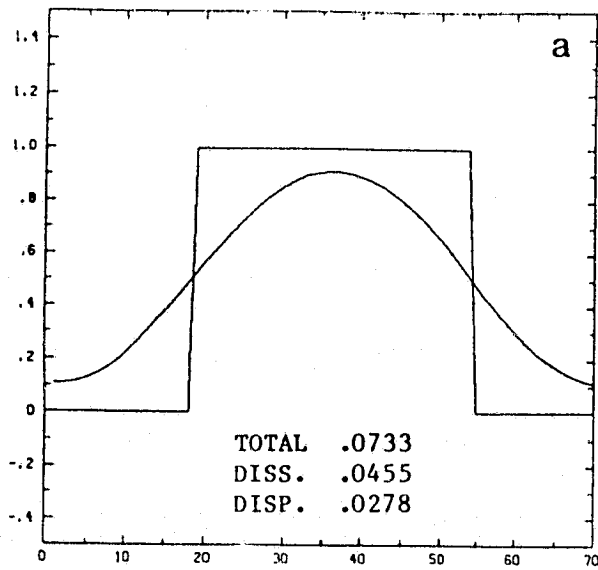
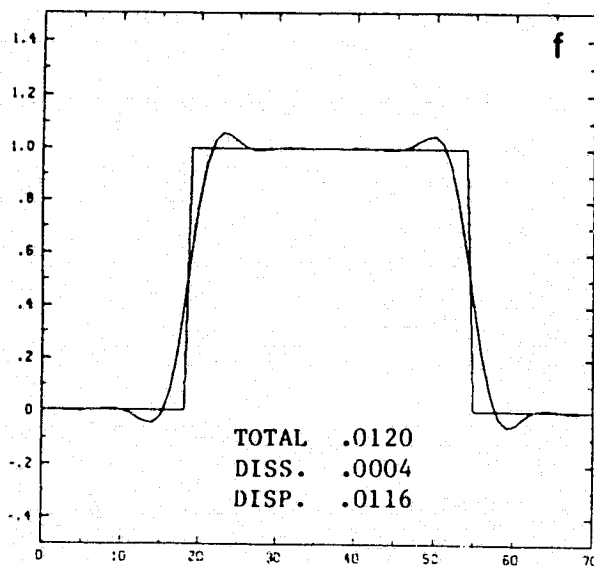
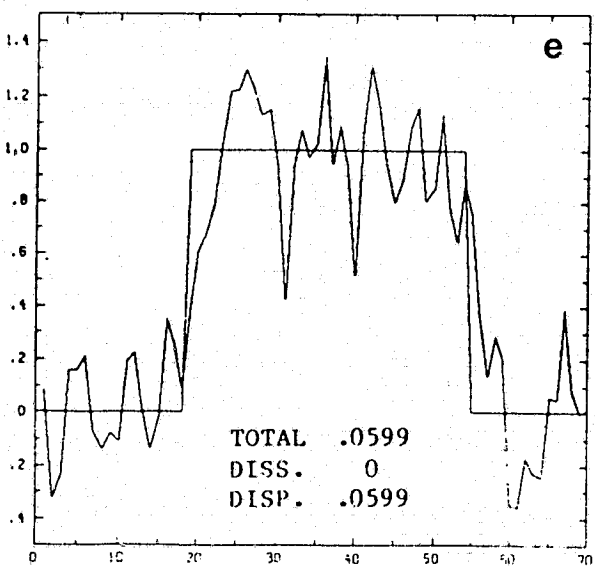
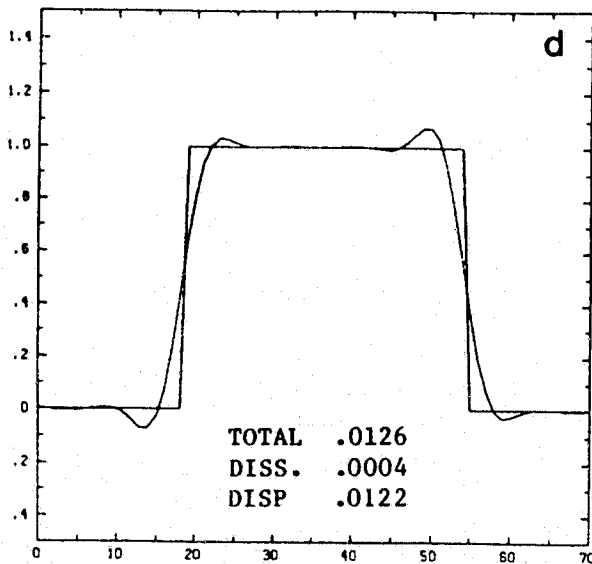
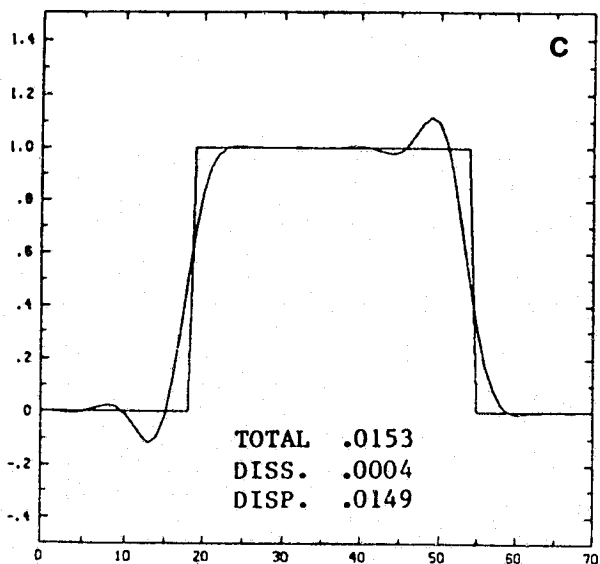
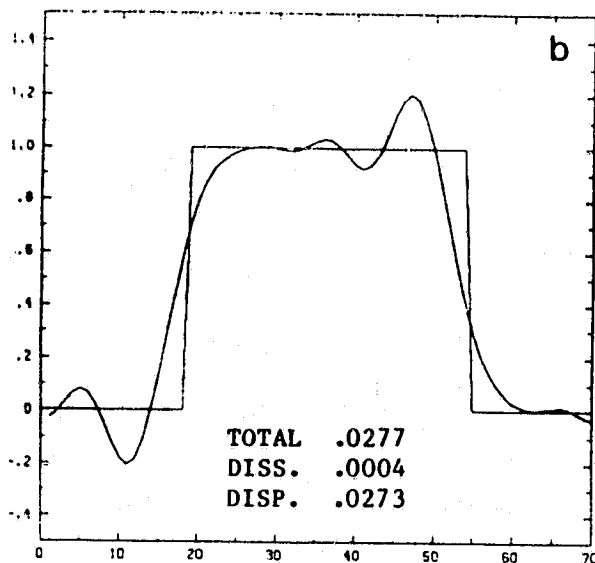
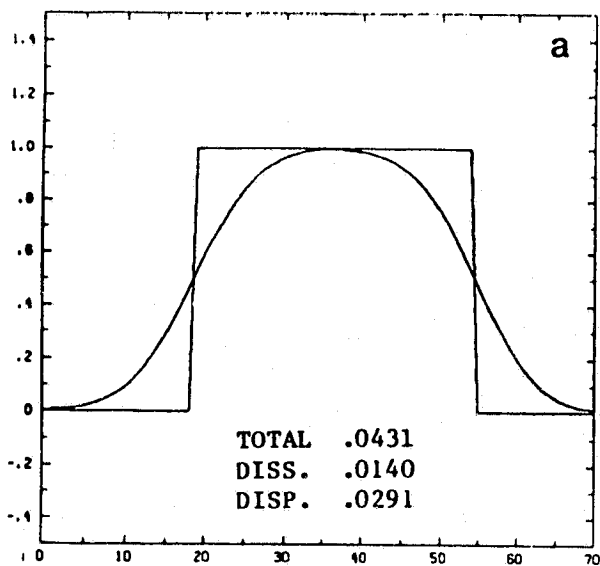


Fig. 3

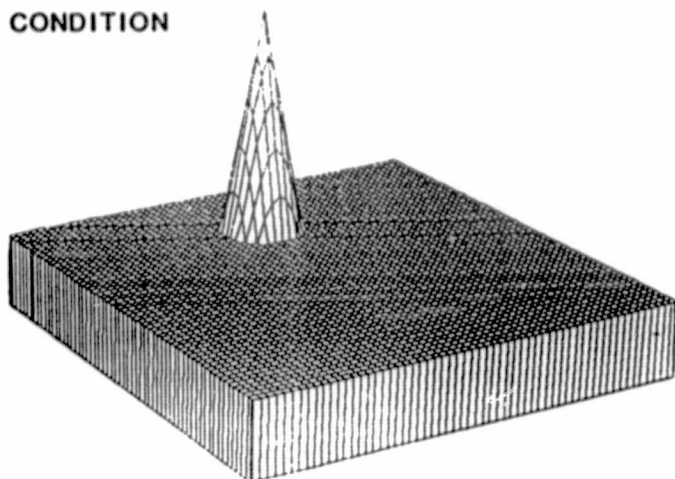




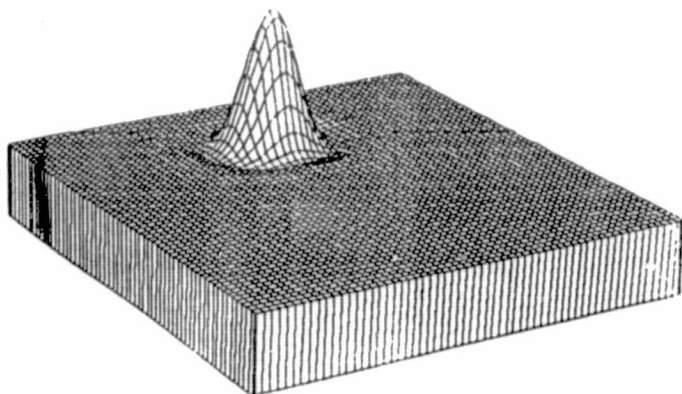


ORIGINAL PAGE IS
OF POOR QUALITY

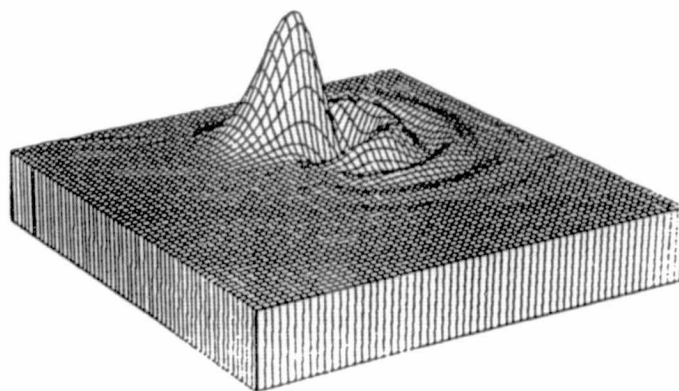
INITIAL
CONDITION



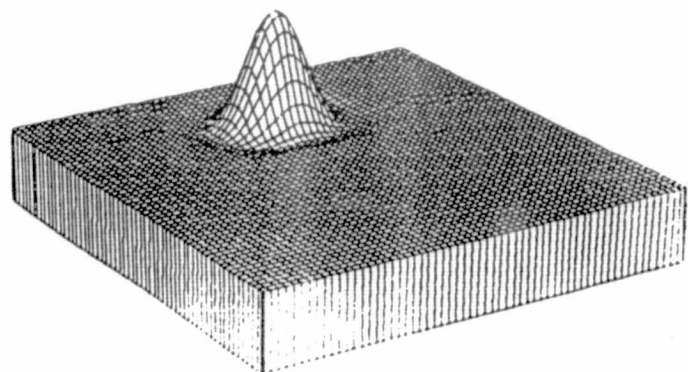
SCHEME A 20
1 REVOLUTION



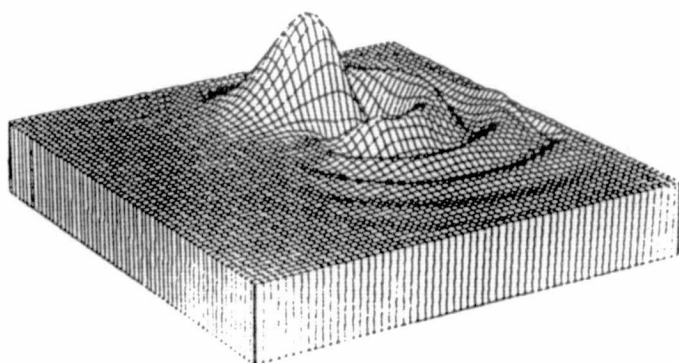
SCHEME A 0
1 REVOLUTION



SCHEME A 20
2 REVOLUTIONS



SCHEME A 0
2 REVOLUTIONS



ON THE EFFECT OF USING THE SHAPIRO FILTER TO SMOOTH WINDS ON A SPHERE

L. L. Takacs and R. C. Balgovind

ABSTRACT

Spatial differencing schemes which are not enstrophy conserving nor implicitly damping require global filtering of short waves to eliminate the build-up of energy in the shortest wavelengths due to aliasing. Takacs and Balgovind (1983) have shown that filtering on a sphere with a latitude dependent damping function will cause spurious vorticity and divergence source terms to occur if care is not taken to ensure the irrotationality of the gradients of the streamfunction and velocity potential. Using a shallow water model with fourth-order energy-conserving spatial differencing, it is found that using a 16th-order Shapiro (1979) filter on the winds and heights to control nonlinear instability also creates spurious source terms when the winds are filtered in the meridional direction.

1. INTRODUCTION

The process of filtering in global grid point models is fairly common in meteorological studies. High latitude filtering or smoothing is generally done in order to avoid the use of a prohibitively short time step required due to the convergence of the meridians near the poles. Global filtering, on the other hand, is applied in order to maintain nonlinear computational stability, as well as to eliminate short wave computational noise. Global filtering, as performed by Yee and Shapiro (1981), was applied by using an 8th-order Shapiro (1979) filter on the vorticity fields in a non-divergent global barotropic model, while Kalnay-Rivas *et al.* (1977) used a 16th-order Shapiro filter on the sea level pressure and potential temperature in their fourth-order general circulation model.

Takacs and Balgovind (1983) (here-after referred to as TB) have shown that when using latitude dependent filter functions it is crucial to maintain in finite-difference form the conservation of vorticity under the pressure gradient force and the irrotationality of the gradients of the streamfunction and velocity potential.

In this paper it will be shown that by using the latitude independent Shapiro filter on the winds in the meridional direction, the scalar quantities defined by the streamfunction and velocity potential become effectively filtered with a latitude dependent damping function. This effective filtering of the streamfunction and velocity potential results in spurious sources of vorticity and divergence to be generated near the poles and ultimately affects the solution at all latitudes.

2. THE SHAPIRO FILTER

As applied in Kalnay-Rivas *et al.* (1977), the form of the two-dimensional 16th-order Shapiro filter is simply two passes of the one-dimensional filter applied in succession. To obtain the high order of the filter, eight passes of the 3-point second-order operator are used as given by

$$\bar{q}_{i,j} = [1 - (F_{\phi}^2)^8][1 - (F_{\lambda}^2)^8]q_{i,j} \quad (1)$$

where

$$F_{\lambda}^2(q_{i,j}) = 1/4 (q_{i+1,j} - 2q_{i,j} + q_{i-1,j}), \quad (2)$$

$$F_{\phi}^2(q_{i,j}) = 1/4 (q_{i,j+1} - 2q_{i,j} + q_{i,j-1}). \quad (3)$$

Here, q is any quantity being filtered while λ and ϕ are the longitudinal and latitudinal components on the sphere.

We see that the coefficients used in the difference equations (2) and (3) are latitude-independent and symmetric about the center point. Because of this, the filter only affects the amplitude of a given wave component while its phase remains unchanged. Because the response is independent of latitude, the problem associated with latitude dependent filters is apparently eliminated. The response for one pass of the one-dimensional 16th-order Shapiro filter is shown in Fig. 1. Because the filter is highly scale selective, waves longer than 4Δ are virtually unchanged.

To understand the effect of using the Shapiro filter on the winds, let us consider the simplified case of the application of the second-order 3-point Shapiro filter on the u field first in the zonal direction and then in the meridional direction. In the zonal direction we have

$$\bar{u}_{i,j}^{\lambda} = u_{i,j} - 1/4 (u_{i+1,j} - 2u_{i,j} + u_{i-1,j}). \quad (4)$$

Since the u wind may be written as

$$u = \frac{1}{a \cos \phi} \left[\frac{\partial \chi}{\partial \lambda} - \cos \phi \frac{\partial \psi}{\partial \phi} \right] \quad (5)$$

where ψ and χ are the streamfunction and velocity potential, we can then relate the filtered zonal wind to a filtered form of the streamfunction and velocity potential by

ORIGINAL PAGE IS
OF POOR QUALITY

$$\bar{u}_{i,j}^{\lambda} = \frac{1}{a \cos \phi_j} \left[\frac{\partial}{\partial \lambda} \tilde{\chi}_{i,j}^{\lambda} - \cos \phi_j \frac{\partial}{\partial \phi} \tilde{\psi}_{i,j}^{\lambda} \right], \quad (6a)$$

where

$$\tilde{\chi}_{i,j}^{\lambda} = \chi_{i,j} - 1/4 (\chi_{i+1,j} - 2\chi_{i,j} + \chi_{i-1,j}) \quad (6b)$$

$$\tilde{\psi}_{i,j}^{\lambda} = \psi_{i,j} - 1/4 (\psi_{i+1,j} - 2\psi_{i,j} + \psi_{i-1,j}). \quad (6c)$$

We can see that the form of the filter used on the u field in (4) is directly transferred to the streamfunction and velocity potential in (6b) and (6c). A similar equation may be obtained for the v field. This consistent transformation between the filtered winds in the zonal direction and the streamfunction and velocity potential is necessary in order to preserve the irrotational properties discussed by TB.

If we now consider the application of the filter in the meridional direction, we have

$$\bar{u}_{i,j}^{\phi} = u_{i,j} - 1/4 (u_{i,j+1} - 2u_{i,j} + u_{i,j-1}). \quad (7)$$

Relating this to the streamfunction and velocity potential we have

$$\bar{u}_{i,j}^{\lambda} = \frac{1}{a \cos \phi_j} \left[\frac{\partial}{\partial \lambda} \tilde{\chi}_{i,j}^{\phi} - \cos \phi_j \frac{\partial}{\partial \phi} \tilde{\psi}_{i,j}^{\phi} \right], \quad (8a)$$

where

$$\tilde{\chi}_{i,j}^{\phi} = \chi_{i,j} - 1/4 \left(\frac{\cos \phi_j}{\cos \phi_{j+1}} \chi_{i,j+1} - 2\chi_{i,j} + \frac{\cos \phi_j}{\cos \phi_{j-1}} \chi_{i,j-1} \right) \quad (8b)$$

$$\tilde{\psi}_{i,j}^{\lambda} = \psi_{i,j} - 1/4 (\psi_{i,j+1} - 2\psi_{i,j} + \psi_{i,j-1}). \quad (8c)$$

It can be seen that although there is a consistent transformation between the u field and the streamfunction, the velocity potential now has weights which are latitude dependent and non-symmetric, thereby giving rise to both amplitude and phase changes. A similar analysis on the v field would show the same behavior on the streamfunction. The vorticity generated by the filtered winds would thus become dependent on the velocity potential, causing spurious source terms to appear.

Figs. 2 and 3 show the amplitude and phase change at various latitudes of the velocity potential derived from using a 16th-order Shapiro filter on the u field in the meridional direction (i.e., the 16th-order equivalent of (8b)). We can see that application of the filter near the equator results in a response very similar to that given in Fig. 1. Although some phase change results, it only occurs for wavelengths which are severely damped. However, as one approaches the pole, not only do phase changes become significant for all wavelengths but also the amplitudes of some waves are actually increased.

By using the meridional Shapiro filter on the winds, the irrotational properties discussed by TB in relation to the streamfunction and velocity potential would no longer be satisfied, thus creating spurious sources of vorticity and divergence. It can be seen that using the Shapiro filter on anything other than scalar fields such as the heights; streamfunction or velocity potential, would cause spurious source terms to develop.

This problem can be avoided by eliminating the meridional filtering of the winds. Fig. 4 shows, using a coarse-grid (36 x 23) shallow water model and a Rossby-Haurwitz wave as an initial condition, the time evolution of the globally integrated eddy kinetic energy. Curve (a) is the time evolution when the filter is applied to the winds and heights in both the zonal and meridional directions, while curve (b) is the time evolution when the filter is applied to the heights in both directions and the winds in the zonal direction only. Curve (c) is the time evolution when no filter is applied. Although curve (b) does not coincide exactly with the non-filtered run, it falls much closer to the true case than curve (a).

3. CONCLUDING REMARKS

We have seen that using the Shapiro filter on the winds in the meridional direction creates spurious vorticity and divergence source terms near the poles to occur which ultimately affect the solution at all latitudes. These spurious source terms are due to the effective latitude dependent filter applied to the streamfunction and velocity potential after use of the Shapiro filter on the winds in the meridional direction. By eliminating the use of the Shapiro filter on the winds in the meridional direction, this problem may be avoided.

REFERENCES

- Kalnay-Rivas, E., A. Bayliss and J. Storch, 1977: The 4th Order GISS Model of the Global Atmosphere. Contrib. Atmos. Phys., 50, 306-311.
- Kalnay-Rivas, E., and D. Hoitsma, 1979: Documentation of the Fourth Order Band Model. NASA Tech. Memo. 80608, Greenbelt, MD 20771.
- Shapiro, R., 1979: Linear Filtering on the Surface of a Sphere. AFGL-TR-79-0263, Environ. Res. Paper No. 683, Air Force Geophysics Laboratory, Hanscom AFB, MA 01731.

Takacs, L. L., and R. C. Balgovind, 1983: High Latitude Filtering in Global Grid Point Models. Mon. Wea. Rev., 111, in press.

Yee, S. Y. K. and R. Shapiro, 1981: The Interaction of Model Dynamics and Numerical Errors in a Nondivergent Global Barotropic Model. Mon. Wea. Rev., 109, 687-700.

ORIGINAL PAGE IS
OF POOR QUALITY

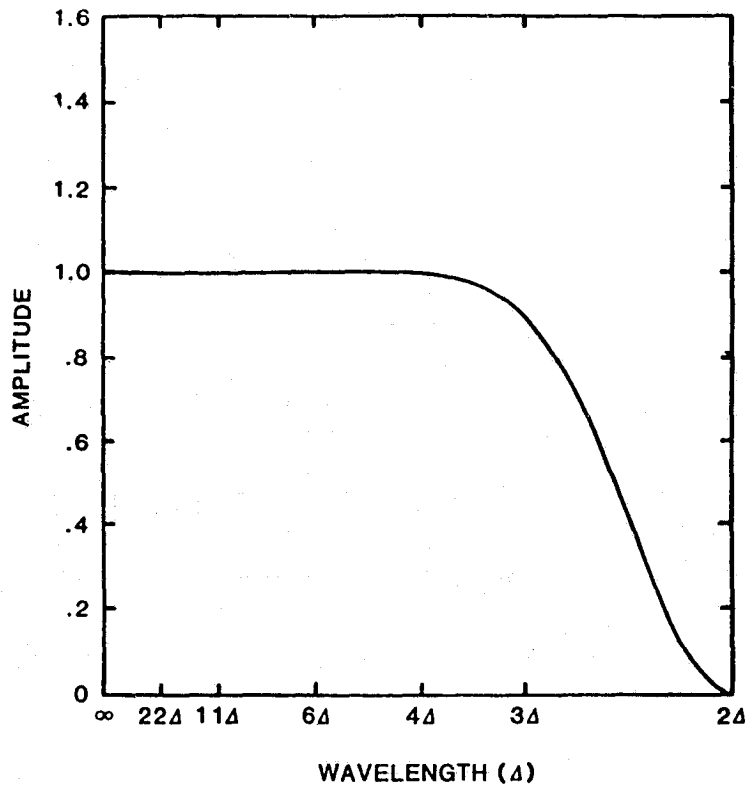


Fig. 1. Wavelength response of the amplitude change from one pass of the 16th-order Shapiro filter.

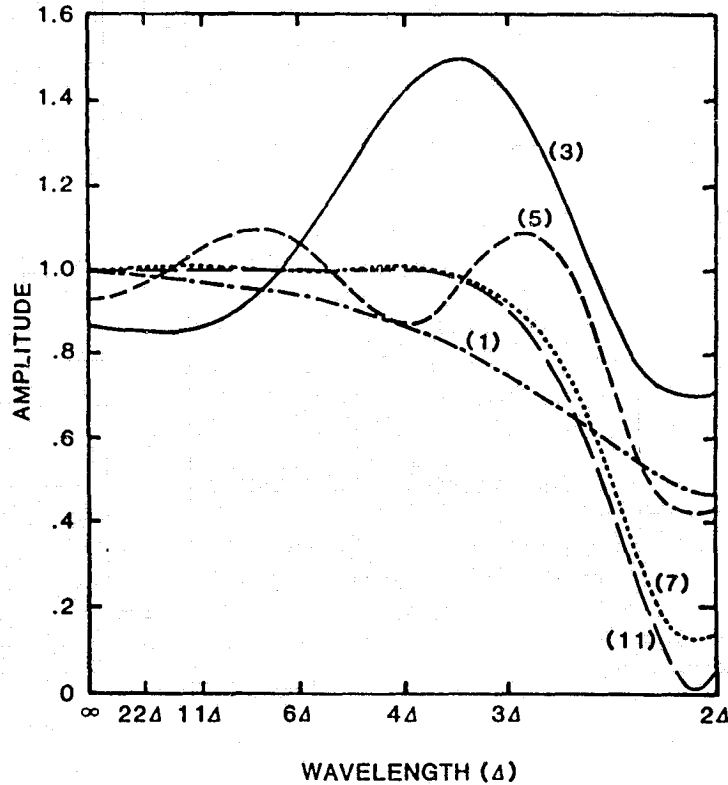


Fig. 2. Wavelength response of the amplitude change from one pass of the transformed 16th-order Shapiro filter applied at 1, 3, 5, 7 and 11 grid points away from pole. Note, 11 grid points away from the pole is the same as 1 grid point from the equator.

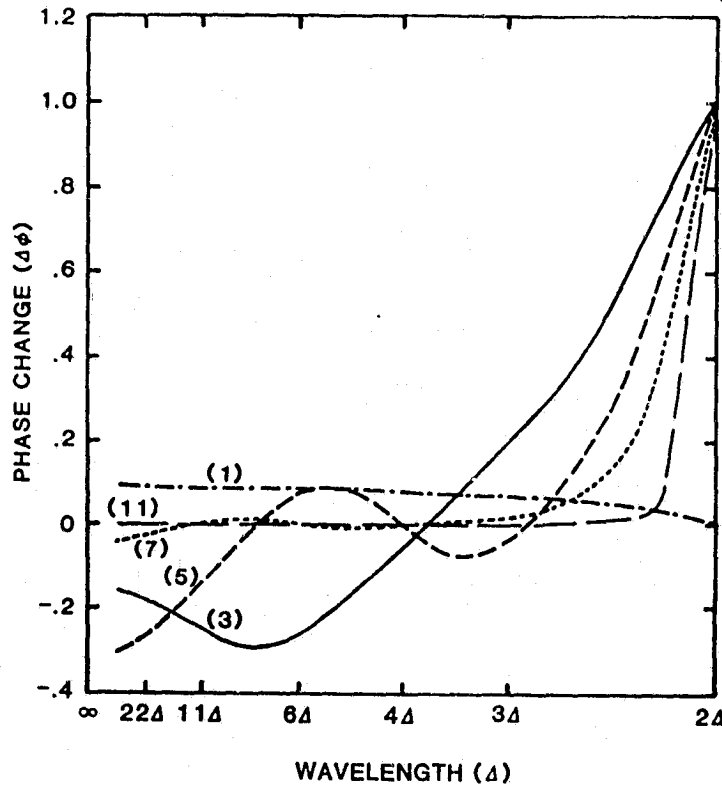


Fig. 3. As in Fig. 2, except for phase change.

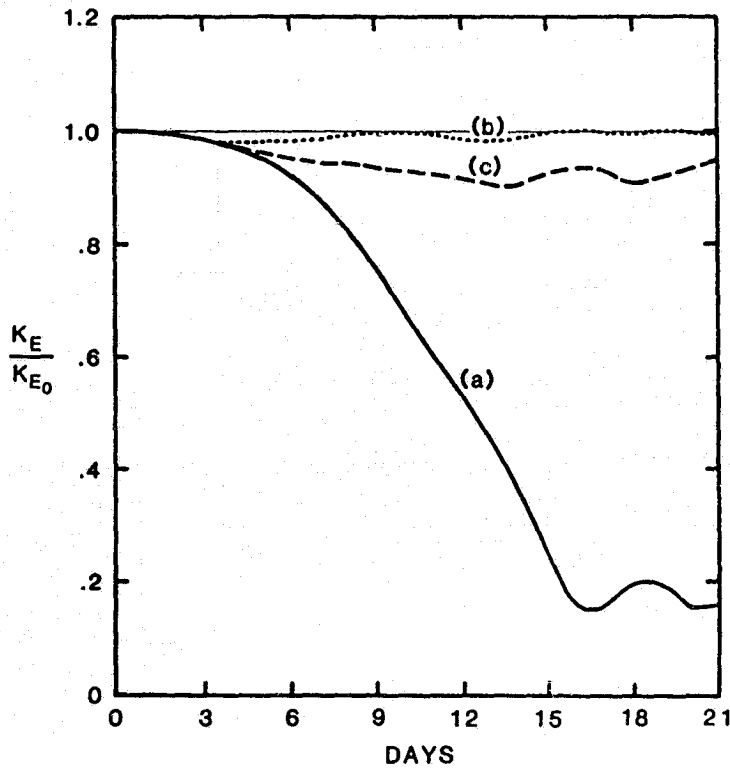


Fig. 4. Globally averaged and normalized eddy kinetic energy for: a) Shapiro filter applied to the winds and height field in both directions, b) Shapiro filter applied to the winds in the zonal direction and to the heights in both directions, c) no filter.

D. ATMOSPHERIC DYNAMICS AND DIAGNOSTIC
STUDIES

PRECEDING PAGE BLANK NOT FILMED

LAGGED AVERAGE FORECASTING, SOME OPERATIONAL CONSIDERATIONS

R. N. Hoffman and E. Kalnay

ABSTRACT

We have previously described the lagged average forecast (LAF) method as an alternative to the Monte Carlo forecast (MCF) method¹. The LAF differs from the MCF in the definition of the ensemble of initial states which are used to generate the ensemble of forecasts. The LAF initial states are the current analysis and the forecasts made from previous analyses verifying the current time. Thus the LAF ensemble is composed of forecasts which are made by a regular operational system of numerical weather prediction and the LAF method is therefore operationally attractive.

The application of our previous ideas and results¹, to an operational model requires the resolution of what might be called the degrees of freedom problem, i.e. how to obtain a homogeneous sample large enough to calculate stable statistics. We suggest that this problem may be solved by carefully modeling the required statistics in terms of a small set of parameters and then estimating only these few parameters from the data. We also note that there may be considerable information in each initial ensemble relating to the predictability of each particular case, and that this information may be incorporated in the model of the statistics.

1. INTRODUCTION

In order to use the information present in past observations and simultaneously to take advantage of the benefits of stochastic dynamic prediction we have formulated and tested an ensemble average forecast method, which we have called the lagged average forecast (LAF) method¹. Each LAF is an average of an ensemble of forecasts whose initial conditions are the current and past analyses. For example, if we label the current time as $t = 0$ h, then forecasts started at $t = 0$ h, -12 h -24 h ... -48 h all integrated to $t = +72$ h would be averaged to yield the 72 h LAF forecast. We will now summarize the main ideas and results of our earlier experiments.

2. RESULTS FROM TESTS WITH A SIMPLE MODEL

In our tests of the LAF method¹, we used a highly simplified atmospheric model. This model is a two layer low order spectral model on a doubly periodic f-plane forced by asymmetric Newtonian heating of the lower layer. These experiments are not identical twin experiments since there is a continuous external source of forecast error. The quasigeostrophic model used for forecasting is imperfect since the observations used for initialization and verification are based on a long primitive equation 'nature' run.

In terms of forecast skill, the LAF was found to be slightly superior to the MCF, ordinary dynamical forecast (ODF) and persistence climatology forecast (PFC) (Fig. 1). Purely statistical means are sufficient to hedge the ODF towards the climate mean. The same regression techniques were also applied to the ensemble forecasts, resulting in the tempered ODF, LAF and MCF (tODF, tLAF and tMCF). The regression analysis naturally generates different weights for the individual forecasts in the LAF ensemble; the more recent the initial conditions, the greater the regression weight. The tLAF was found to be marginally superior to all the other methods. At long range all the tempered forecasts have the same skill since they become climate mean forecasts.

Unfortunately the improvement in forecast skill obtained due to ensemble averaging is quite small. This conclusion is related to the predictability properties of the model, by which we mean the evolution of forecast error. Although the rms forecast error was found to grow roughly linearly with time until it reaches saturation (Fig. 1), we found that the typical evolution of forecast error for an individual case has a relatively short episode of rapid error growth (Fig. 2). Furthermore, the timing of this forecast breakdown varies substantially from case to case. This behavior is reminiscent of the behavior of initially small triangles on the attractor of the 3-component system of Lorenz which was shown to the workshop by Professor Dutton. In the Lorenz³ system this behavior is due to the presence of the homoclinic orbit passing through the origin as described by Lanford⁴. These observations suggest that ensemble average forecasts can attain skill only slightly better than a statistically filtered ODF. This statement is justified by the following argument: For short forecast times, an ensemble forecast is no better than a forecast made from the ensemble average initial conditions, because nonlinear effects are absent. For long forecast times, the ensemble spreads out over the entire attractor; the ensemble forecast is therefore close to the climate mean and its superiority over a climate mean forecast is negligible. The possible advantage of an ensemble forecast is therefore confined to intermediate forecast times, specifically to those periods for each case when the forecast error is of intermediate size. As we have described, these periods are rather short.

Since the skill of the forecast model varies considerably from case to case (Fig. 2) we made a priori predictions of forecast skill for individual cases. Not unexpectedly we found that the spreading of the ensemble is closely correlated with the average forecast error of forecasts in the ensemble. When other factors which account for model imperfections are included in the analysis, good predictions of the time of forecast breakdown are obtained (Fig. 3).

One might not expect an ensemble forecast method with an ensemble size as small as 4 or 8, which are the sizes we have been using, to be so successful at predicting the forecast error, which is after all, a second order statistic. However if we neglect model errors, the forecast error of the discrete model is governed approximately by linear homogeneous ordinary differential equations until the errors become large. During the period when the linearization is valid we may therefore represent the evolution of any initial error in terms of the transition matrix, i.e. the matrix which obeys the linear equations and which is initially the identity matrix. A complete discussion along these lines was given by Lorenz⁵. In general the largest exponent will control the growth of error. Since an arbitrary initial error will almost always have some projection on the eigenvector corresponding to the dominant characteristic exponent we expect that even an ensemble of size 2 may be useful in predicting

forecast skill.

3. REMARKS ON OPERATIONAL APPLICATIONS

A straightforward implementation of the LAF method in an operational setting is not possible: there are far too many parameters to be estimated from a regression analysis of a limited sample. Quite similar problems have been studied by Lorenz⁶ and we refer the reader to his detailed discussion of this problem. A further difficulty here is that the sample must be further subdivided or stratified since it is not homogeneous; for example, predictability varies with season. There are two basic solutions to this problem: obtain a larger sample or reduce the number of independent parameters which must be estimated. The following discussion centers on the problems to be expected with the second approach and offers some possible solutions. We should note that the choice of the tempering weights and the coefficients relating forecast error to ensemble spread described in the previous section are both least squares problems.

Let us first consider, as a simple example, the problem of tempering an ODF. Let \underline{h} be the forecast deviation from climatology of the variable of interest; for example \underline{h} might be a 120 h forecast anomaly of 500 mb geopotential. We consider estimates of \underline{h} given by

$$\hat{h}_m = \sum_i a_{im} h_i \quad (1)$$

where i and m index the components of the representation, which might be grid point values or coefficients of spherical harmonics, normal modes or empirical functions. One interesting possibility especially for the extended range problem is to use the amplitudes of a selected set of teleconnection patterns⁷. The least squares solution, for each m , satisfies

$$\langle \tilde{h}_m h_n \rangle = \sum_i a_{im} \langle h_i h_n \rangle \quad n = 1, \dots,$$

where \tilde{h} is the true value and the angle brackets indicate statistical expectation. The sum over i may be severely restricted; for example only grid points within a distance of 2000 km might be included. We must now choose between modeling the covariances and solving the normal equations at each grid point or modeling the a_{im} in terms of fewer secondary coefficients, and considering the resulting condensed least squares problem. While both of these approaches have merit, we will restrict our discussion to the approach in which the covariances are modeled. This is the approach usually taken in optimum interpolation. In a grid point model the covariances are expected to vary smoothly with respect to position so we may increase the sample used to estimate the covariances by using all the data in a given region, e.g. a 20° x 20° latitude-longitude window, under the assumption that the covariances are independent of position under the window. We would consider the estimate obtained valid at the center of the window and then move the center of window from grid point to grid point. Another approach with the same effect would be to represent each

of these parameters in terms of a small number of spherical harmonics, determining the coefficients of the spherical harmonics to give a best fit to the covariances observed in the sample. For example we might suppose the correlation function between a given location and any other location depends only on distance and has gaussian shape; then all the covariances are determined once the variance and correlation length are specified. Further discussion of modeling of covariances may be found in the optimum interpolation literature (see Lorenc⁸ and references therein).

To further simplify the discussion we will now assume that sums like Equation (1) are truncated to the single term $i = m$: only predictions at a given grid point or of a given mode are to be used in estimating the true value. Now when several forecasts are available, which is the case when tempering a LAF, estimates of covariances between different forecasts are required. As discussed previously¹, it is nearly equivalent to estimate the differences between two forecasts or between a forecast and nature. A great deal of information about the actual initial differences is present in the initial ensemble. The remaining problem is to estimate how fast the differences grow; these growth rates are the traditional objects of predictability studies. Again, there is not a sufficient sample to get stable estimates of these growth rates for each component of the representation at each time during the forecast, and we must use some modeling assumption. Since predictability varies with the scale of motion under consideration^{9,10}, it might be useful to use a spectral representation where each component has an associated scale and calculate statistics for all variables associated with similar scales, i.e. by wave band. It may also be possible to fit the growth rates to simple functions of forecast time; several candidate functions are offered by other authors in this volume. In our previous work¹ we found it was adequate to assume the growth rates are constants until saturation is reached.

In practice the severe truncation assumed above would not be made, but the general problem can be reduced to the simple problem by assuming that the general correlation function is the product of a 'spatial' correlation function depending only on the location of the two grid points and an 'ensemble' correlation function depending only on the two forecasts. This is analogous to the treatment of the 'spatial' correlation function as the product of 'horizontal' and 'vertical' correlation functions which is made in optimum interpolation⁸ and which may be used here.

Predictability varies with season as well as with location and scale and this would have the effect of greatly reducing our sample if we were to stratify our sample by month of the year. A temporal window technique similar to the spatial window technique described above could be used. Alternately the coefficients or covariances could be modeled as simple functions of time of year¹¹. Much of the seasonal effect could be removed by using variables standardized by removing the climate mean and scaling by the climate variances, where these climate statistics vary with time of year. In the case we have been considering, all that is left is to model the seasonality of the growth rate parameters.

Another sampling problem concerns the ensemble of forecasts. Intuitively, forecasts in the LAF ensemble which have no skill at $t = 0$ h, should not be included in later ensembles. Unless the covariances are modeled this would be another cause for sample stratification. However there is considerable infor-

mation in the observed ensemble spread at the initial time. In fact the initial difference between pairs of forecasts is known precisely and good approximations of the differences between the various forecasts and nature may be constructed using the current analysis and estimates of its error. This information combined with the difference growth rates found using the methods described above is sufficient to calculate estimates of all the statistics needed for the tempered LAF method. When the initial differences are estimated to be large the estimated covariances will be small and poor initial forecasts will effectively be deleted from the ensemble.

For the purpose of predicting forecast skill, there is also additional information in the initial ensemble. The difference between two forecasts may be considered to be a finite difference approximation of the product of the transition matrix defined in the previous section and a vector representing the initial difference between these forecasts. The accuracy of such an estimate is expected to increase as the initial difference decreases and to increase as the difference between the current analysis and the average of the initial states decreases. Further, the dimension spanned by the initial difference vectors should give some indication of the probability that the behavior associated with the largest eigenvalue has been captured by the sample.

4. CONCLUDING REMARKS

We feel that the LAF method is a promising technique. While our tests¹, and discussion above indicate that operational implementation of the LAF method should not be too difficult, two uncertainties remain. First, can a large enough sample be obtained for developing the required statistics? Second, is the interval between the initial states of successive operational forecasts small enough for the initial ensemble to be acceptable? With respect to this last question, the interval of 24 h currently available from operational ECMWF forecasts may be too large.

The LAF may be directly applied to forecasts of time averaged quantities, e.g. 500 mb height averaged from 120 h to 240 h. There is some evidence favoring the use of the LAF method for long range forecasting of time averaged quantities, although the sampling problem becomes more acute as the forecast interval increases. Recent identical twin experiments^{10,12} suggest that ensemble average forecasts of time averaged quantities are useful beyond the range of day to day predictability. Also, long range, ensemble forecasts can make good use of observed boundary conditions¹³ filtering the synoptic scales and at very long range the ensemble of forecasts will simulate the climate ensemble associated with the particular boundary conditions¹⁴ known at the initial time.

5. ACKNOWLEDGEMENTS

We thank R. Livezey for sharing his insights on this problem with us. We had useful discussions with B. Legras. Ross N. Hoffman was supported by NASA Contract NAS-54-27297.

REFERENCES

1. R. N. Hoffman and E. Kalnay, Tellus, 35A, 100 (1983).
2. R. N. Hoffman, J. Atmos. Soc., 38, 514 (1981).
3. E. N. Lorenz, J. Atmos. Soc., 20, 130 (1963).
4. O. E. Lanford, Ann. Rev. Fluid Mec., 14, 347 (1982).
5. E. N. Lorenz, Tellus, 17, 321 (1965).
6. E. N. Lorenz, Mon. Wea. Rev., 105, 590 (1977).
7. J. M. Wallace and D. S. Gutzler, Mon. Wea. Rev., 109, 784 (1981).
8. A. C. Lorenc, Mon. Wea. Rev., 109, 701 (1981).
9. E. N. Lorenz, Tellus, 21, 289 (1969).
10. J. Shukla, J. Atmos. Sci., 38, 2547 (1981).
11. K. Hasselmann and T. P. Barnett, J. Atmos. Sci., 38, 2275 (1981).
12. A. N. Seidman, Mon. Wea. Rev., 109, 1367 (1981).
13. J. Shukla, European Centre for Medium Range Weather Forecasts Seminar 1981, Problems and Prospects in Long and Medium Range Weather Forecasting 4 - 18 September, 261 (1981).
14. C. E. Leith, Nature, 276, 352 (1978).

ORIGINAL PAGE IS
OF POOR QUALITY

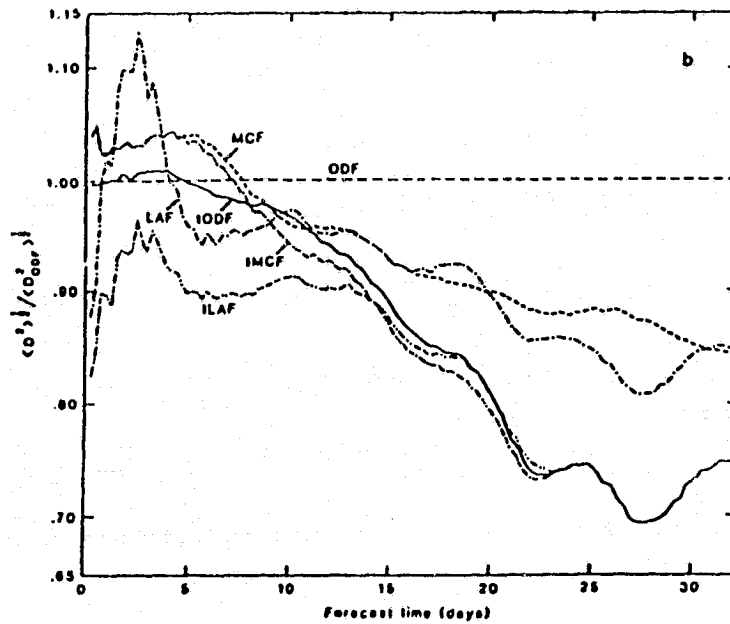
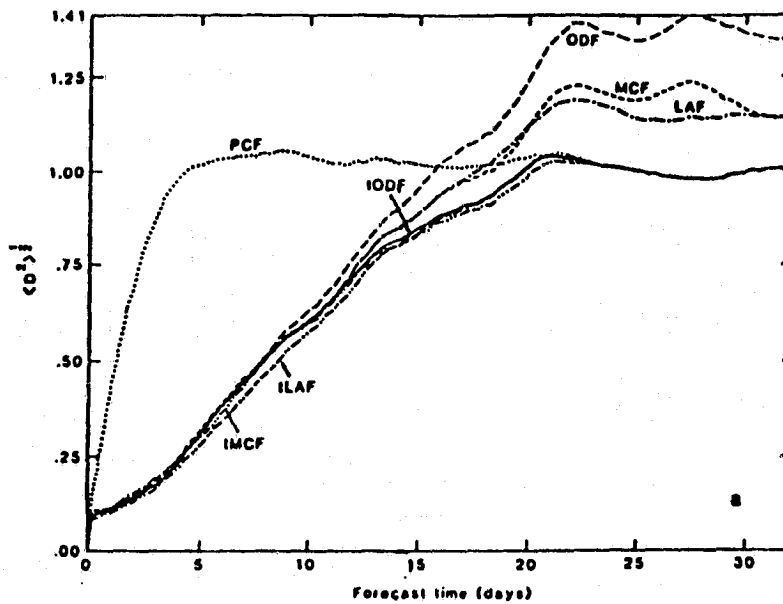


Fig. 1. Comparison of the skills of the different forecast methods. In (a) $\langle D^2 \rangle^{1/2}$ and in (b) $\langle D^2 \rangle^{1/2} / \langle D_{ODF}^2 \rangle^{1/2}$ are plotted as functions of forecast time, t , for the ODF (---), MCF (----), LAF (— · — · —), PCF (·····), tODF (———), tMCF (— · — · — · —), and tLAF (— · — · — · —). D is a skill score which is also the distance in the model phase space from forecast to observation normalized by the expected skill of a climate mean forecast. The angle brackets indicate an average over all cases.

ORIGINAL PAGE IS
OF POOR QUALITY

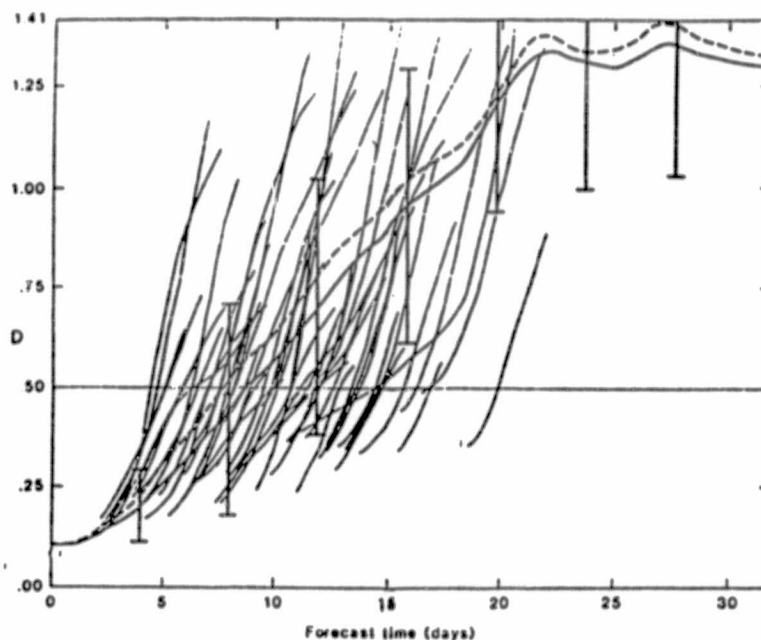


Fig. 2. Time evolution of D for the ODF experiments. Shown are selected portions of the evolution of D for each case (light —). These have been smoothed to eliminate the roughness caused by the white noise observing error. Also shown are $\langle D^2 \rangle^{1/2}$ (— —) and $\langle D \rangle$ (heavy —). Error bars are calculated as $(\langle D^2 \rangle - \langle D \rangle^2)^{1/2}$.

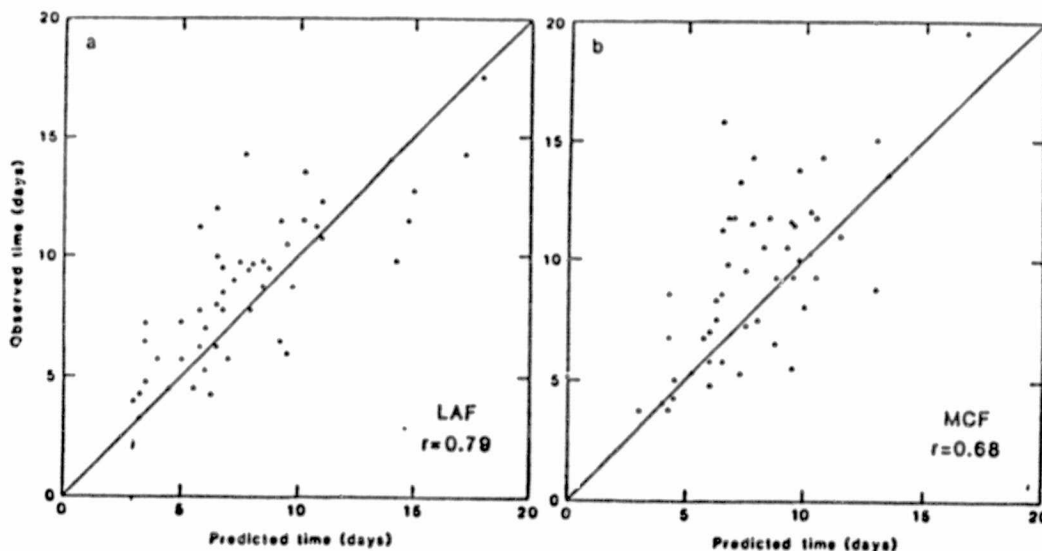


Fig. 3. Scatter plots of predicted versus observed time for the breakdown of forecast skill for the LAF (a) and the MCF (b). The time of forecast breakdown was taken to be the time when the normalized skill score reaches a value of 0.5. See ref. (1) for details.

MIT

WEATHER PREDICTABILITY BEYOND A WEEK: AN INTRODUCTORY REVIEW

E. Kalnay and R. Livezey

In this paper* the problem of weather prediction beyond a few days is introduced with an example of two 20-day forecasts performed using two slightly different real atmospheric analyses as initial conditions. From this example, the main result of classical and recent weather predictability studies becomes apparent: the unstable nature of the atmospheric circulation precludes the possibility of detailed weather forecasts beyond about two weeks. More recent studies in the theory of forecast error growth are also presented.

The rest of the paper is devoted to the problem of the prediction of weather statistics, such as time and space averages, rather than individual weather systems. The following subjects are discussed: relative importance of internal dynamics and slowly varying boundary conditions; climate noise and potential predictability; predictability of long lasting phenomena such as

atmospheric blocking and anomalies associated with El Niño and the Southern Oscillation; teleconnections and their role in extended prediction; the use of statistical methods, simplified dynamical models and detailed general circulation models for extended weather prediction; and, finally, the current status of operational long range weather forecasting.

*To appear in "Turbulence and Predictability in Geophysical Fluid Dynamic and Climate Dynamics" M. Ghil, R. Benzi and G. Parisi, eds. North-Holland Publishing Company, Amsterdam, New York, Oxford.

D
27
N84 22076

APPLICATION OF AUGMENTED-LAGRANGIAN METHODS IN METEOROLOGY: COMPARISON OF
DIFFERENT CONJUGATE-GRADIENT CODES FOR LARGE-SCALE MINIMIZATION

I. M. Navon

ABSTRACT

A Lagrange multiplier method using techniques developed by Bertsekas (1982) was applied to solving the problem of enforcing simultaneous conservation of the nonlinear integral invariants of the shallow water equations on a limited area domain.

This application of nonlinear constrained optimization is of the large dimensional type and the conjugate gradient method was found to be the only computationally viable method for the unconstrained minimization. In this study several conjugate-gradient codes were tested and compared for increasing accuracy requirements. Robustness and computational efficiency were our principal criteria.

1. THE AUGMENTED LAGRANGIAN ALGORITHM

We consider the problem

$$\text{minimize } f(\underline{x}) \quad (1)$$

$$\text{subject to } \underline{x} \in R^m \text{ and } h(\underline{x}) = 0$$

$$h: R^m \rightarrow R^m$$

The augmented Lagrangian function is

$$L(\underline{x}, \underline{\lambda}, c) = f(\underline{x}) + \underline{\lambda}^T h(\underline{x}) + (1/2c) |h(\underline{x})|^2 \quad (2)$$

where c is a penalty parameter and λ a multiplier vector.

The augmented Lagrangian algorithm is an iteration involving a series of unconstrained minimization problems (see Gill, Murray and Wright, 1982; Bertsekas, 1982) of an n -dimensional differentiable function, Lagrange multiplier estimates and penalty term updates - where the primary purpose of the penalty term is to make \underline{X}^* an unconstrained minimum.

2. THE MODEL ALGORITHM

We briefly describe an iteration of the Augmented Lagrangian method. The following are assumed to be available: an initial selection of the constraint functions; an initial-estimate of the Lagrange-multipliers $\underline{\lambda}_0$; a penalty parameter c , a positive integer K serving as upper bound on the number of unconstrained minimizations to be performed and an initial point \underline{x}_0 . Set $k \leftarrow 0$ and perform the following steps:

AL1. (Check termination criteria). If X_k satisfies optimality conditions, the algorithm terminates with X^k as the solution. If $k > K$, the algorithm, terminates with a failure.

AL2. (Minimize the augmented Lagrangian function). With X_k as starting point execute a procedure (using a conjugate-gradient code) to solve the sub-problem:

$$\begin{aligned} \text{Minimize } L(\underline{X}, \lambda_k, c) & \quad (3) \\ \underline{x} \in R^m & \end{aligned}$$

Let X_{k+1} denote the best approximation to the solution of (3).

AL3. (Update the multiplier estimate). If appropriate, modify specification of h . Compute λ_{k+1} , an updated estimate of the Lagrange multipliers.

AL4. (Increase the penalty parameter if necessary). Increase c if the constraint violations at X_{k+1} have not decreased sufficiently from those at X_k .

AL5. (Update the iteration count). Set $k \leftarrow k+1$ and go back to AL1.

3. COMPARISON OF CONJUGATE-GRADIENT (C-G) METHODS

C-G methods form a class of minimization algorithms that generate directions of minimum search without requiring the storage of a matrix. These methods are essential when the Hessian matrix is too large or too dense.

In our case we had 2000 variables, ($\underline{X} = (X_1, X_2, \dots, X_{2000})$).

a) The Fletcher-Reeves (1964) C-G Algorithm

We solve the problem

$$\begin{aligned} \text{Minimize } f(\underline{X}) & \quad \underline{X} = (X_1, \dots, X_m) & \quad (4) \\ \underline{x} \in R^m & \end{aligned}$$

$$\begin{aligned} \text{AL1. Compute } g_0 &= -\nabla f(X_0) \\ \text{Set } d_0 &= -g_0 \end{aligned} \quad (5)$$

then for $k = 1, 2, 3, \dots, m$

$$\text{Set } X_{k+1} = X_k + \alpha_k d_k \quad (6)$$

Where α_k is obtained via a line search procedure $f(X_k + \alpha_k d_k) = \min_{\alpha} f(X_k + \alpha d_k)$.

3. Compute

$$g_{k+1} = \nabla f(X_{k+1}) \quad (7)$$

(4) generate d_{k+1} by:

$$d_{k+1} = -g_{k+1} + \beta_k d_k \quad (8)$$

$$\text{Where } \beta_k = \frac{\nabla f(X_{k+1})^T \nabla f(X_{k+1})}{\nabla f(X_k)^T \nabla f(X_k)} = \frac{g_{k+1}^T g_{k+1} / g_k^T g_k}{\nabla f(X_k)^T \nabla f(X_k)} \quad (9)$$

b) The Polak-Ribiere (1969) Algorithm

The algorithm is totally identical in its steps to the Fletcher-Reeves algorithm except that β_k is calculated as

$$\beta_k = \frac{(g_{k+1} - g_k)^T g_{k+1}}{g_k^T g_k} = \frac{(\nabla f(X_{k+1}) - \nabla f(X_k))^T \nabla f(X_{k+1})}{\nabla f(X_k)^T \nabla f(X_k)} \quad (9^*)$$

For the Fletcher-Reeves and Polak-Ribiere algorithms we used the Numerical Algorithms Group (NAG) subroutine E04DBF with its associated service routines.

c) The Powell Conjugate Gradient Method with Restarts

This method based on the work of Beale (1972) and Powell (1977) allows us to restart after a C-G cycle with a computed direction d_t - rather than starting with the steepest gradient - g_t .

In order to ensure that the successive directions are conjugate, the following recurrence relation is used for a cycle of n directions for $k = 0, 1, \dots, n-1$

$$d_{k+1} = -g_{k+1} + \beta_k d_k + \gamma_k d_t \quad (10)$$

d_t is known as the restart direction and is the last direction of the previous C-G cycle along which a linear search was made. Powell (1977) uses the Beale restarts every n steps or whenever

$$|g_{k+1}^T g_k| \geq 0.2 \|g_{k+1}\|^2 \quad (11)$$

which checks that the direction d_k is "sufficiently downhill."

We also check that

$$-1.2 \|g_k\|^2 \leq d_k^T g_k \leq -.08 \|g_k\|^2 \quad (12)$$

If this requirement is not satisfied, a new cycle commences with d_{k-1} as the restart direction and with d_k re-computed from (8). For the Powell method we used the ZXCGR subroutine of the IMSL library with slight modifications.

d) The Shanno C-G Method Viewed as a Memoryless Quasi-Newton Method

Quasi-Newton Method

Different authors - Shanno (1978), Shanno and Phua (1980), Perry (1976), have found an analogy between the Quasi-Newton method of the form

$$x_{k+1} = x_k + d_k d_k \quad (13)$$

$$d_k = -D_k^{-1} \nabla f(x_k)$$

where D_k is a positive definite matrix approximating the Hessian, and between the C-G method if we compute D_k by updating the identity matrix with a limited number of Quasi-Newton corrections.

Although the direction of search, d_k , is equivalent to the product of a matrix and a vector, the matrix is never stored explicitly. Rather, only the vectors defining the updates are retained. Shanno (1978) used such a "memoryless" Quasi-Newton (Q-N) method combined with Beale restarts and Powell's restart criteria.

For the Shanno method we used the Shanno and Phua routine CONMIN supplied to us by Prof. Shanno which allows one either a BFGS (Broyden-Fletcher-Goldfarb-Shanno) Q-N variable metric algorithm or a Beale restarted C-G algorithm.

4. NUMERICAL RESULTS

A program (METHODS) comparing the 4 C-G algorithms for a meteorological

problem (see Navon and De-Villiers (1983)) with 2000 variables, for increasing accuracy requirements was developed (available now on YFIMN machine at NASA/GLAS) and the different methods were compared for computational efficiency, number of iterations and number of function calls.

Our accuracy criteria was

$$\|g(\underline{X})\|^2 \leq \epsilon_a \quad (14)$$

Accuracy $\epsilon_a = 10^{-3}$

Method	Iter No. of C-G cycles	IFUN No. of Function evaluations	CPU (Sec)
Fletcher-Reeves	2	25	0.11
Polak-Ribiere	2	25	0.10
Powell	2	25	0.09
Shanno	2	25	0.09
Function value at minimum = $.6047 \times 10^{-5}$			
Accuracy $\epsilon_a = 10^{-5}$			
Fletcher-Reeves	4	81	0.17
Polak-Ribiere	5	121	0.21
Powell	3	64	0.14
Shanno	4	81	0.17
Function value at minimum = $.4211 \times 10^{-5}$			
Accuracy $\epsilon_a = 10^{-7}$			
Fletcher-Reeves	11	523	0.44
Polak-Ribiere	Failed	-	-
Powell	8	379	0.34
Shanno	8	324	0.36
Function value at minimum = $.4187 \times 10^{-5}$			

Method	Iter No. of C-G cycles	IFUN No. of Function evaluations	CPU (Sec)
Accuracy $\epsilon_a = 10^{-9}$ (double precision)			
Fletcher-Reeves	Failed		
Polak-Ribiere	Failed		
Powell	16	986	0.65
Shanno	12	625	0.51
Function value at minimum = $.418549 \times 10^{-5}$			
Accuracy $\epsilon_a = 10^{-11}$ (double precision)			
Powell	19	1542	0.96
Shanno	12	676	0.58
Function value at minimum = $.48154561 \times 10^{-5}$			

5. CONCLUSIONS

For this large dimensional problem and for moderate accuracy (10^{-5}) all the 4 C-G algorithms performed well, with the Powell and Shanno C-G algorithms being slightly faster. For higher accuracy requirements both the Fletcher-Reeves and the Polak-Ribiere algorithms fail to converge for the upper limit of C-G cycles (25) and only the Powell and Shanno algorithms continue to perform with an increased advantage for the Shanno algorithm as the accuracy requirements increase to 10^{-9} or 10^{-11} .

These methods were tested on the problem of enforcing conservation of nonlinear integral invariants of the shallow water equations using both a finite difference model (Navon and de-Villiers, 1983) or a finite element model (Navon, 1983). We intend to test the same methods for constrained nonlinear normal mode initialization.

REFERENCES

- Bertsekas, D. K., 1982: Constrained optimization and Lagrange multiplier methods. Academic Press, New York, 412 pp.
- Gill, P. E., W. Murray, and M. H. Wright, 1981: Practical optimization. Academic Press, New York, 401 pp.

- Fletcher, R., C. M. Reeves, 1964: Function minimization by conjugate-gradients. Computer Journal, 7, 149-154.
- Polak, E., G. Ribiere, 1969: Note sur la convergence de Methodes de Directions Conjuguees. Rev. Franc. Informat. Rech. Operationnelle, 16, 35-43.
- Beale, E. M. L., 1972: A derivation of conjugate-gradients. In F. A. Lootsma, ed. Numerical Methods for Nonlinear Optimization. Academic Press, London, pp. 39-43.
- Powell, M. J. D., 1977: Restart procedures for the conjugate-gradient method. Math. Programming, 12, 241-254.
- Shanno, D. F., 1978: Conjugate-gradient methods with inexact searches. Math. Oper. Res., 3, 244-256.
- Shanno, D. F., and K. H. Phua, 1980: Remark on algorithm 500. ACM Trans. on Math. Software, 6, 618-622.
- Perry, A., 1976: A modified conjugate-gradient algorithm. Disc. Paper, 229, Northwestern Univ.
- Navon, I. M., and R. deVilliers, 1983: Combined penalty-multiplier optimization methods to enforce integral invariants conservation. Mon. Wea. Rev., 111, 1228-1243.
- Navon, I. M., 1983: A Numerov-Galerkin technique applied to a finite element shallow water equations model with enforced conservation of integral invariants and selective lumping. J. Comput. Phys., 52, 313-339.

PREDICTABILITY EXPERIMENTS USING A LOW ORDER EMPIRICALLY
CORRECTED DYNAMICAL MODEL

S. Schubert

1. INTRODUCTION

It is generally accepted that day to day weather variations possess a finite range of predictability estimated to be approximately two weeks (e.g. Lorenz, 1965). However, considerable observational evidence points to the existence of a number of low frequency flow regimes which are potentially predictable beyond this limit. These include blocking events and teleconnection patterns such as those described in Wallace and Gutzler (1981). The present study addresses the problem of the predictability of such modes by employing a highly simplified dynamical model projected onto the modes of interest. These modes are computed from an empirical orthogonal function (EOF) analysis of 10-day averaged anomalies (deviations from the mean seasonal cycle) of the 500 mb stream function for the winters of 1967-76. The first three EOF's are associated with an index cycle and some of the teleconnection patterns. The fourth and ninth are related to North Pacific and North Atlantic blocking, respectively. Details of the calculations and mode structures may be found in Schubert (1983) (hereafter S83).

2. THE EOF ANOMALY MODEL

The model is equivalent barotropic and includes crude representations of the effects of friction and orography. A long wave correction term is not included due to the filtering effect of the EOF expansion (see S83). The model is formulated as a prognostic equation for the anomalies where the mean flow acts as an inhomogeneous forcing. In its final form, the model is written as a system of prognostic equations for the EOF coefficients or principal components (PC's) (see S83 for details) as

$$\begin{aligned}
 \dot{\tilde{z}} &= D(\tilde{z})\tilde{z} + (1+\epsilon)G\tilde{z} + \gamma F\tilde{z} \\
 \text{tendency} & \quad \text{nonlinear} & \quad \text{beta} & \quad \text{orography} \\
 & \quad \text{interaction} & & \\
 + \tilde{R}z & - \kappa \tilde{A}z + \tilde{z}^* \\
 \text{mean/anomaly} & \quad \text{friction} & \quad \text{inhomogenous} \\
 \text{interaction} & & \quad \text{forcing}
 \end{aligned} \tag{1}$$

Here $\tilde{z}(t)$ is the vector of principal components and ϵ , γ and κ are constants which are fit to the data to provide the best representation of the observed PC

time tendencies.

In S83 it was found that the mean flow is barotropically unstable and that a major contribution to the variance of the dominant EOF's is very likely due to this instability. For simplicity it was assumed that the climatological winter flow is a constant equal to the overall winter mean. For purposes of extended range predictions the model has been modified to allow for variations in the mean flow. To accomplish this the evolution of the mean seasonal cycle of the stream function from Dec. 2 through March 31 is approximated by cubic polynomials. As a consequence the constant matrix (R) in (1) is replaced by

$$R'(t) = R_0 + tR_1 + t^2R_2 + t^3R_3 \quad (2)$$

Evidence that this variation may be important for predictions beyond a few days is shown in Fig. 1 for the first 12 PC's. Each curve shows the variation in the growth rates during the course of the winter for the simple case when the structure of the perturbation on the mean flow is constrained to be the associated EOF itself. Considerable variations are found, particularly for PC's 2 and 3. For example, at the beginning of the winter the second mode more than doubles its amplitude after 10 days; whereas, at the end of winter this mode would only increase its amplitude by a factor of 1.4 in 10 days.

3. MODEL EXPERIMENTS (SOME PRELIMINARY RESULTS)

The initial forecast experiments have been carried out for the 1967/68 winter using the highest truncation considered in S83. This version of the model incorporates only the first 12 PC's. Since the terms involving the boundary layer parameterizations were fit to the same data, the following experiments should more properly be called hindcasts. However, in view of the very small contribution to the overall variance from these terms (see S83) the experiments are essentially forecasts and will be called such throughout this report.

For each of the 120 days a 10-day forecast was made. In order to determine at what point in the forecasts the prediction is no longer useful, it is compared to persistence. Fig. 2 shows the autocorrelation functions of the first 12 PC's computed for 1967/68. During this year the first two PC's are the most persistent having e-folding times of about 10 days. The other modes are considerably less persistent.

Figs. 3a and 3b show the correlations between the forecast and observed values (dashed line) as a function of forecast period for PC's 1 and 2, respectively. In both cases it seems that the model does slightly better for up to 4 day forecasts after which persistence (the autocorrelations; solid line) would be the better forecast. Figures 4a and 4b show results for the 3rd and 4th PC's, respectively. In contrast to PC's 1 and 2, the model seems to do better than persistence for all forecast periods. Comparisons between the predictions suggest that PC's 1, 2, 4, 10 and 11 are the most predictable (as measured by the decay in the correlations) while the 8th is the least predictable.

4. CONCLUSIONS

Preliminary results of this study suggest that a highly truncated equivalent barotropic model retaining only the first 12 EOF's possesses a degree of predictability greater than that of persistence alone.

While PC's 1 and 2 show some of the strongest correlations between the observed and forecast values, they are actually forecast the poorest when compared to persistence. This is due to the highly persistent nature of these two modes.

These results must, however, be viewed with caution since they are based on a limited sample (120 ten-day forecasts) and further experiments will be run in order to try to verify these results. However, recent evidence which supports these conclusions may be found in a study by Kruse (1983). In a similar spectral model with 68 degrees of freedom, improvement over persistence was found for the medium waves (zonal wavenumbers 4-8) while essentially no improvement was found for the very long waves (zonal wavenumbers 1-3).

REFERENCES

- Kruse, H., 1983: A statistical-dynamical low-order spectral model for tropospheric flows. *Hamburger Geophysikalische Einzelschriften*, Heft 59.
- Lorenz, E. N., 1965: A study of the predictability of a 28-variable atmospheric model. *Tellus*, 17, 321-333.
- Schubert, S. D., 1983: A statistical-dynamical study of the large-scale intraseasonal variability of the northern hemispheric winter circulation. Scientific Report #3, Dept. of Meteorology, Univ. of Wisconsin-Madison, June 1983.
- Wallace, J. M. and D. S. Gutzler, 1981: Teleconnections in the geopotential height field during the northern hemisphere winter. *Mon. Wea. Rev.*, 109, 784-812.

STABILITY PLOTS

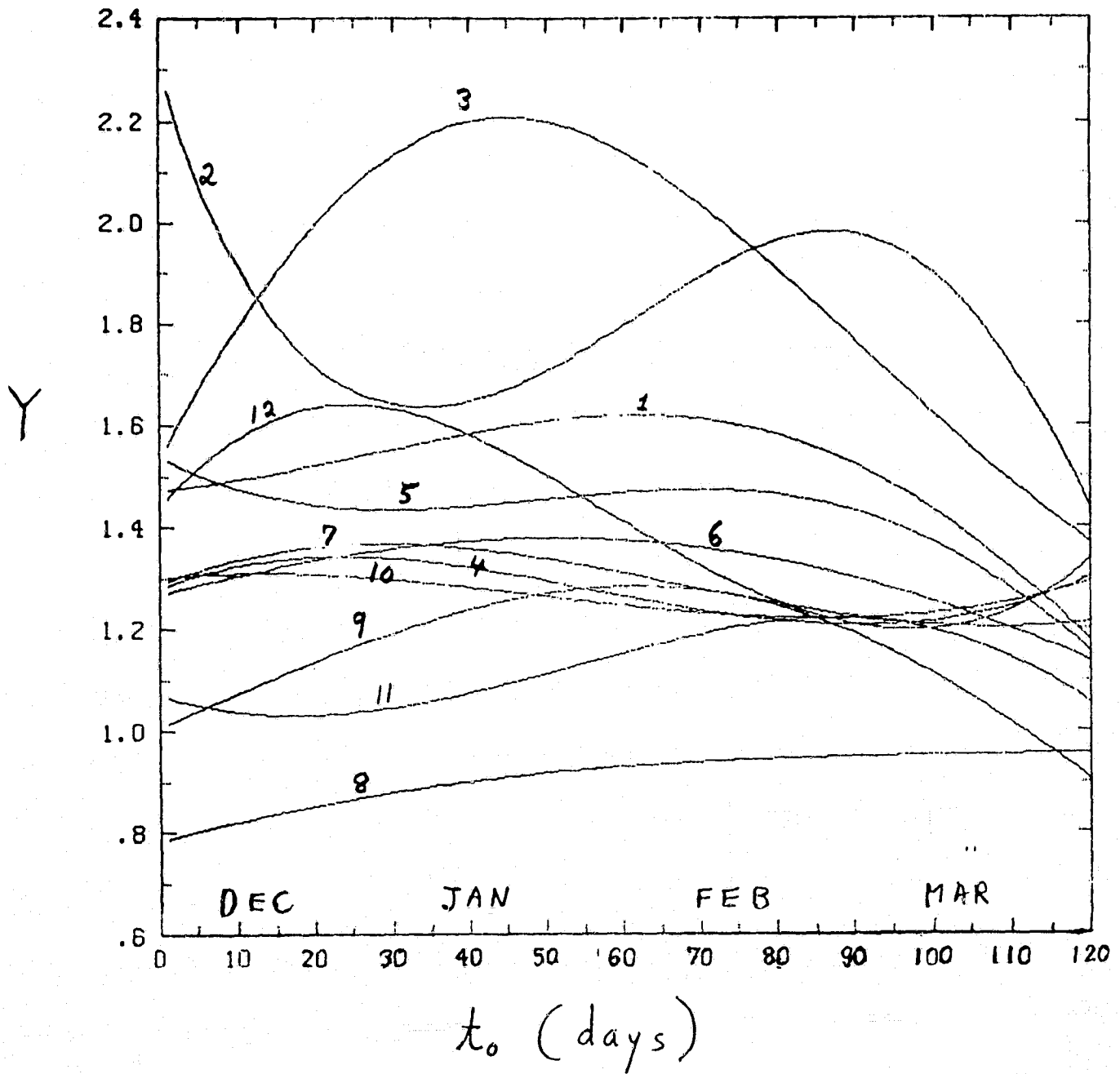


Fig. 1. Variation in the growth rates during the winter season for the first 12 PC's. $Y = z(t_0 + 10)/z(t_0) = \text{EXP} \{a^{-1} \int_{t_0}^{t_0 + 10} r(t) dt\}$. Here (a) and $r(t)$ are the diagonal elements of the t_0 matrices A and R in equation (1). The inhomogeneous forcing and the boundary parameterizations are neglected.

ORIGINAL PAGE IS
OF POOR QUALITY

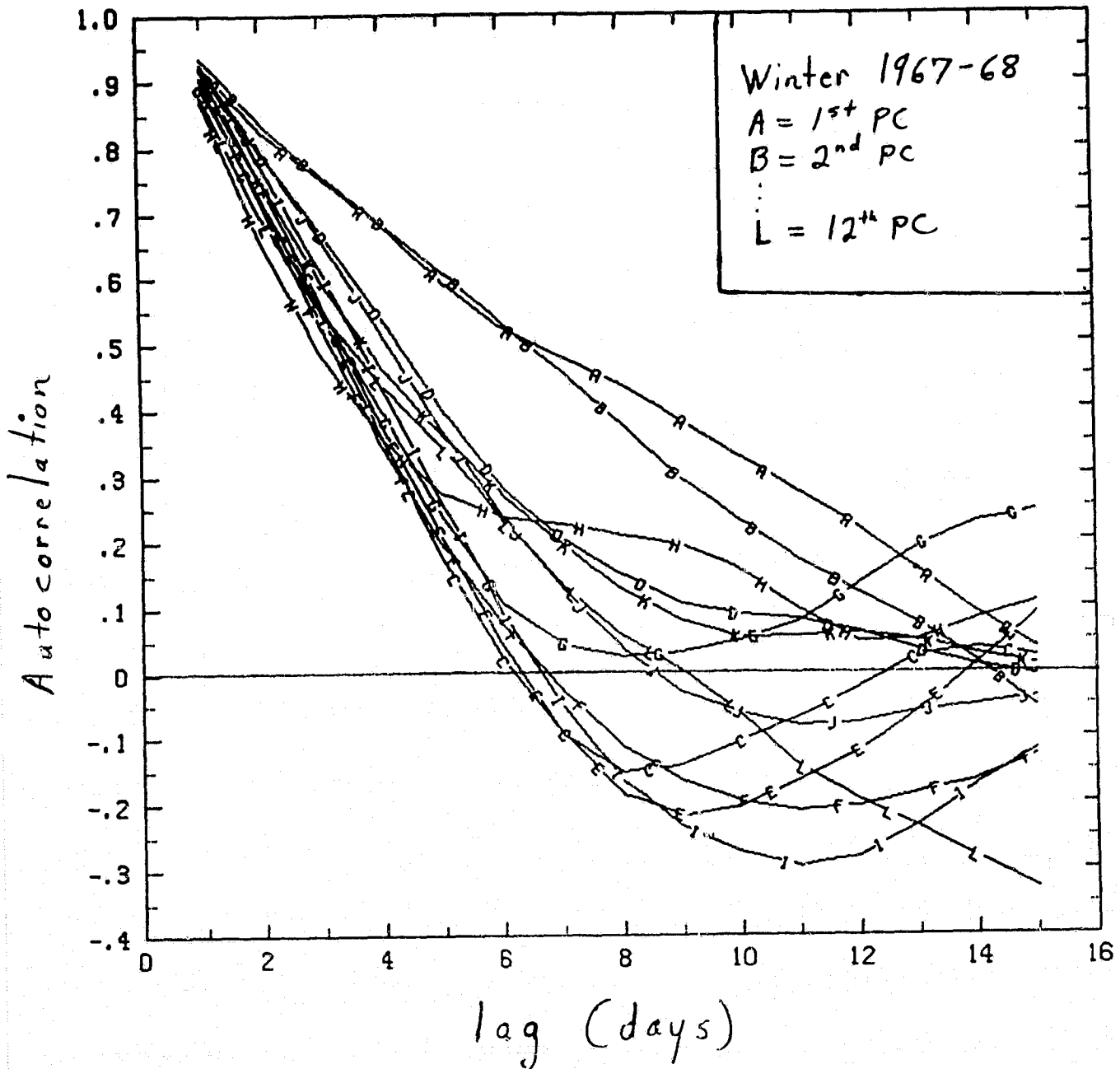


Fig. 2. The autocorrelation functions for the first 12 PC's computed for the 1967/68 winter.

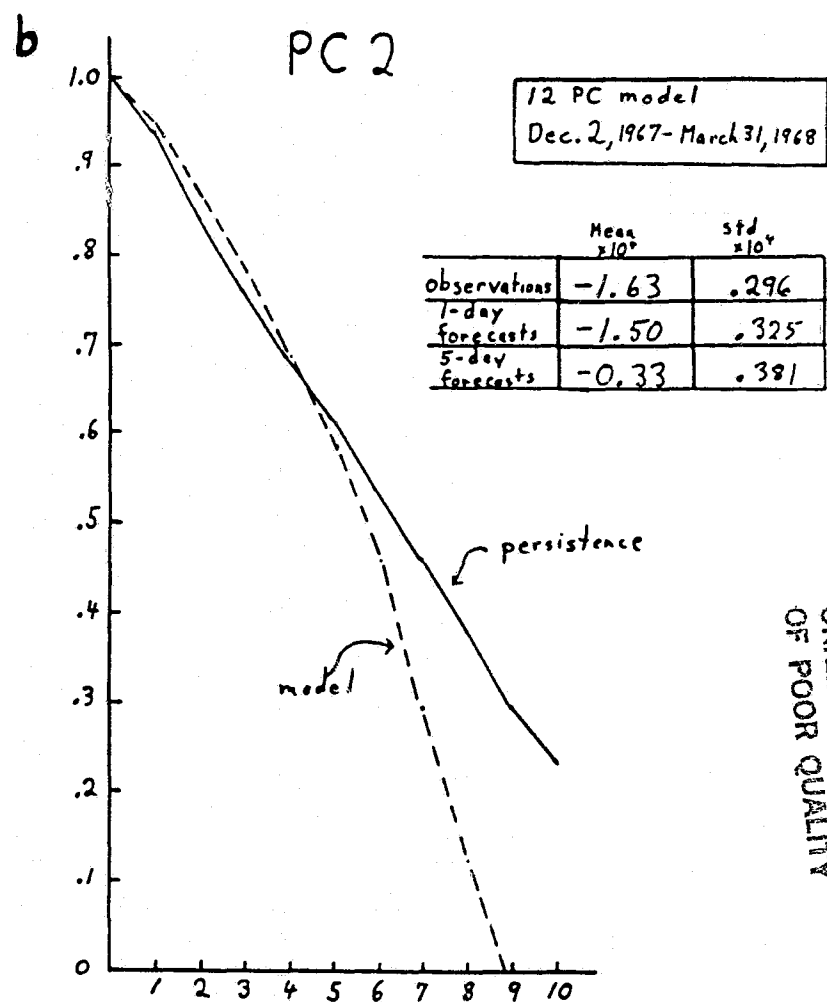
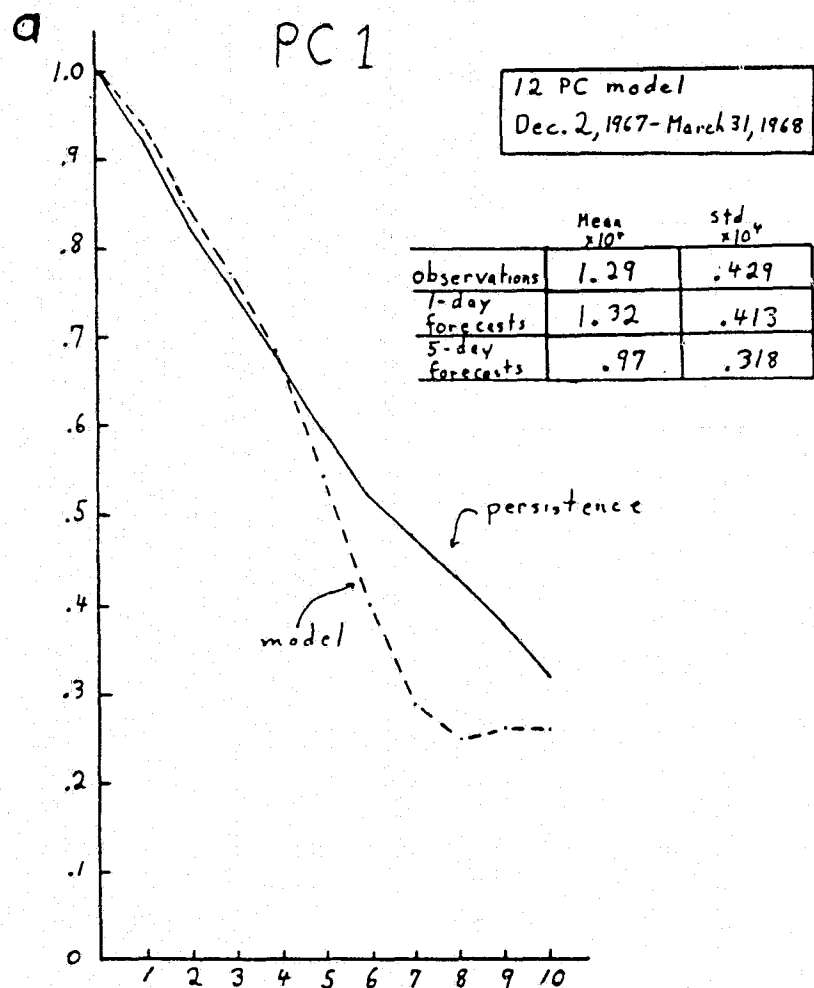
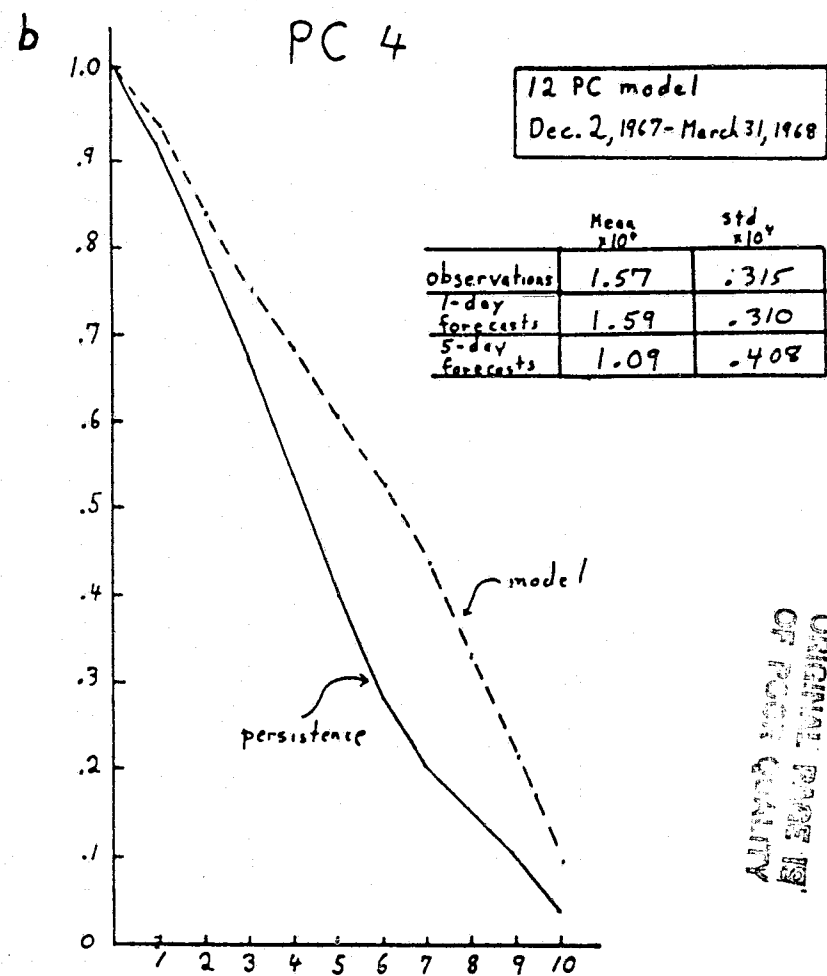
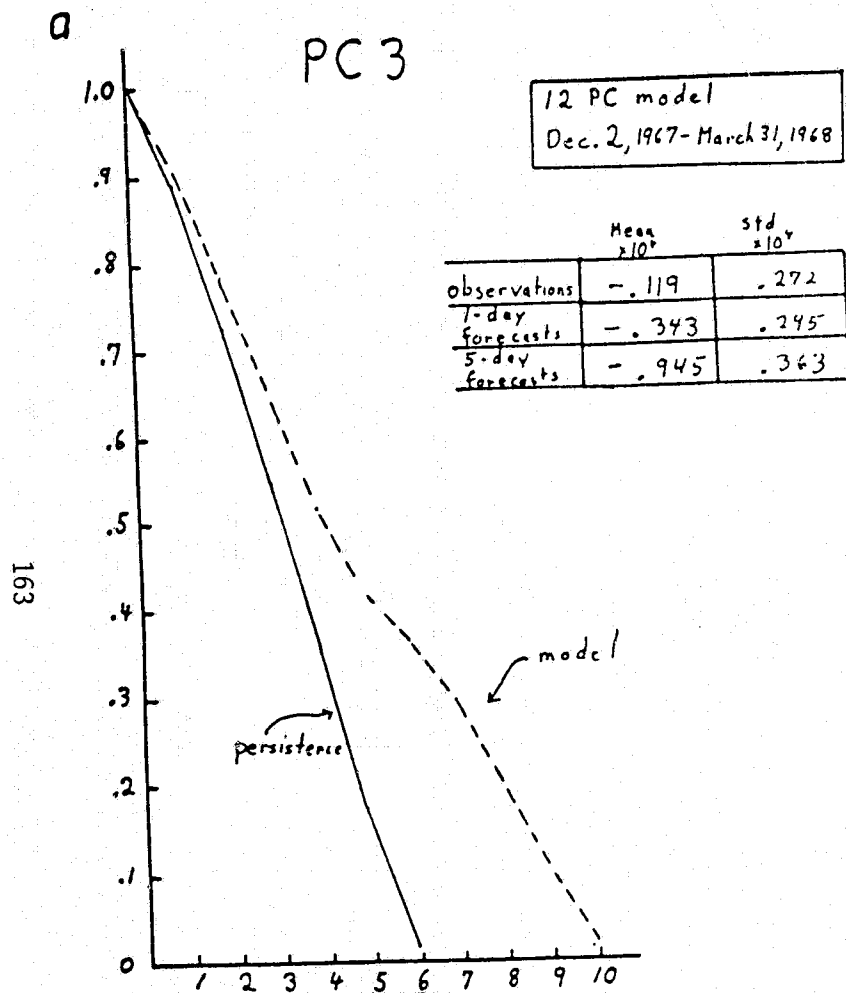


Fig. 3. Correlations between the model forecasts and observations as a function of forecast period (dashed line) compared to persistence (the autocorrelations; solid line). Also given are the means and standard deviations for the observations and 1 and 5 day forecasts for a) the first PC, and b) the second PC.



ORIGINAL PAGE IS
OF POOR QUALITY

Fig. 4. Same as Fig. 3 except for the third and fourth PC.

D₂A
 N84 22078

INVESTIGATION OF THE EQUATORIAL OROGRAPHIC-DYNAMIC MECHANISM APPLYING THE
 BOUNDED DERIVATIVE METHOD

F. H. M. Semazzi

1. INTRODUCTION

On the equatorial beta-plane, where $y=0$ is the equator we use the following system of equations which describe the motion of a barotropic fluid in presence of bottom topography

$$u_t + uu_x + vu_y + \phi_x - \beta yv = 0 \quad (1)$$

$$v_t + uv_x + vv_y + \phi_y + \beta yu = 0 \quad (2)$$

$$\begin{aligned} \phi_t + (u\phi)_x + (v\phi)_y + \phi_0(u_x + v_y) \\ - (u\phi)_x - (v\phi)_y = 0 \end{aligned} \quad (3)$$

The meaning of the symbols is as follows: t is time, (x,y) is cartesian axis directed (eastward, northward), (u,v) is (x,y) component of velocity, $\phi_0 (=10^5 \text{m}^2 \text{s}^{-2})$ is areal mean geopotential height of the free surface, ϕ is deviation from ϕ_0 , ϕ is geopotential height of orography, $\beta = (2\Omega \cos \theta_0)/R$, θ_0 is latitude coordinate origin ($=0$), Ω is angular rotation of the earth ($=7.292 \times 10^{-5} \text{s}^{-1}$), R is mean radius of the earth ($=6.37122 \times 10^6 \text{m}$). For the lateral boundary conditions we assume

$$v = u_y = 0 \quad \text{and} \quad \phi_y = -\beta yu \quad (4)$$

In the zonal direction we assume cyclic conditions. The orography (Fig. a) is a function of x and y and mathematically expressed by

$$\phi = \phi_0 [0.25(1 - \cos k_1 x)(1 - \cos k_2 y)]^7 \quad (5)$$

where $\phi_0 = 2 \times 10^4 \text{m}^2 \text{s}^{-2}$, $k_1 = 2\pi/A$, $k_2 = 2\pi/B$. $A=B(=4 \times 10^6 \text{m})$ corresponding. There are 80 grid points both in the zonal and meridional directions. Centered differencing is adopted in space and time. Time increment is 90s thus satisfying the C.F.L. criterion for linear computational stability. The total time integration is 6 days.

The basic character of the initial state is comprised of an easterly uniform zonal current (\bar{u}) and geopotential height ($\bar{\phi}$) which satisfy steady state

conditions in absence of mountains. Before commencing time integration this balance is further slightly modified through the application of the bounded derivative initialization method after Browning et al. (1980) and Semazzi (1983) to suppress gravitational oscillations.

2. RESULTS AND CONCLUSIONS

A stationary orographic trough (Fig. b) also reported by Semazzi (1980a,b; 1983) is simulated. The geopotential and zonal motion (Fig. c) have maximum deviation from the mean state at the top of the mountain. Regarding meridional speed, outflow occurs on the windward slope and inflow on the leeward slope. Divergence (Fig. c) of order 10^{-6}s^{-1} is found on the windward slope while convergence of the same order of magnitude resides on the leeward slope. This outcome may have interesting implications regarding real climatology occurring over the equatorial regions of continental land masses.

REFERENCES

- Browning, G., A. Kasahara, and H. O. Kreiss, 1980: Initialization of the Primitive Equations by the Bounded Derivation Method. J. Atmos. Sci., 37, 1424-1436.
- Semazzi, F. H. M., 1980a: Numerical Experiments on the Orographic-Dynamic Phenomenon over a Tropical Belt. Arch. Met. Geoph. Biokl. Ser. A., 29, 55-65.
- Semazzi, F. H. M., 1980b: Stationary Barotropic Flow Induced by a Mountain over a Tropical Belt. Mon. Wea. Rev., 108, 922-930.
- Semazzi, F. H. M., 1983: On the Bounded Derivative Initialization Method. Ph.D. Thesis (University of Nairobi).

ORIGINAL PAGE IS
OF POOR QUALITY

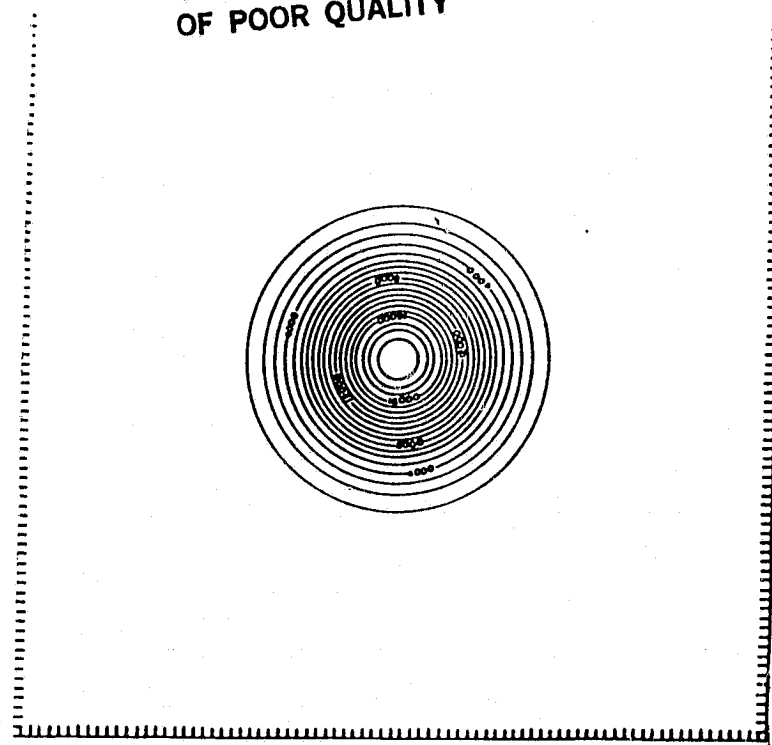


Fig. a. Geopotential ϕ of orography given by (a). Contour values are in units of m^2s^{-2} . Orography maximum = $2 \times 10^4 m^2s^{-2}$.

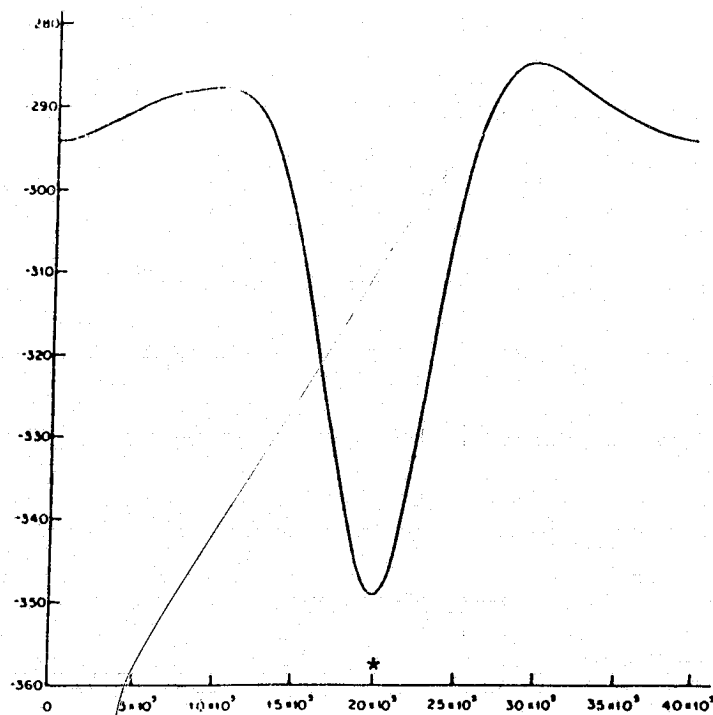


Fig. b. Geopotential deviation ϕ along the equator (i.e. $y=0$) at day 6. Distance is measured in meters and geopotential deviation in units of m^2s^{-2} . The location of the mountain top is represented by (*).

ORIGINAL PAGE IS
OF POOR QUALITY.

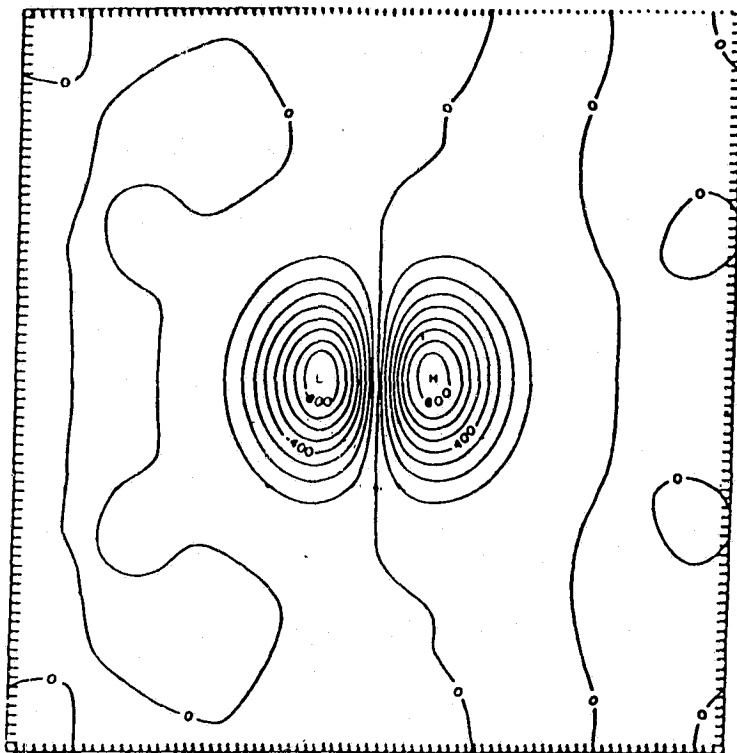


Fig. c. Divergence field at day 6. The units are $10^{-8} s^{-1}$.

III. CLIMATE/OCEAN-AIR INTERACTIONS

A. DATA ANALYSIS

PRECEDING PAGE BLANK NOT FILMED

GE 168 INTENTIONALLY BLANK

POSTPROCESSING FOR THE UCLA CLIMATE MODEL

J. Abeles, E. Pittarelli, D. Randall, and M. Suarez

Several experiments have been run using the UCLA general circulation model. In order to analyze the results, elaborate "postprocessing" software has been developed.

The following postprocessing programs have been written to analyze the results of the model:

- i. vertical interpolation from sigma surfaces to pressure surfaces;
- ii. time average;
- iii. grid point history convert (CDC words to IBM words);
- iv. grid point history sort;
- v. grid point history plotting package;
- vi. model plotting package.

Fig. 1 summarizes the data flow from the model through the postprocessing procedures.

The model history data is interpolated to pressure surfaces, converted from 64-bit Cyber words to 32 bit IBM words, and transferred to tape for further analysis. The interpolation program works on 15-day periods.

The time average program reads the interpolation output tape and produces 15-day time averages. Six months of averages are put on each tape.

The model outputs a very detailed record for selected grid points. This data is sent to a tape in Cyber full words. The conversion program changes the format of the tape from 64 bit Cyber words to 32 bit IBM words, processing a month of data at a time. The grid-point history sorting program inputs the converted grid point history tape and sorts it by time. The end product is a tape with a time history of each field for every point. After the PBP data has been sorted, it can be plotted. The plotting package is flexible, and allows the choice of fields and grid points. An index is printed to assist in finding plots. The one-dimensional fields are plotted as functions of time, and a daily summary is also produced. For the two-dimensional fields, time-height cross sections and daily summaries are produced. The time-height cross sections also show the planetary boundary layer depth. An example is shown in Fig. 2.

The Model Plotting Package produces plots for all fields on the time average and pressure tapes. These plots include world maps, polar projections, zonal means, vectors, streamlines, and latitude-height plots. The plotting program runs in two stages. The first set of programs reads in the data, sorts it and stages the data to disk files. The program can also average any number of 15-day means to obtain seasonal or yearly means. The main program reads this data and produces the plots on an output tape. This tape can be used to produce plots on an electrostatic plotter or on microfiche. By using an interactive setup exec, individual fields or groups of data can be selected for plotting. If all the fields are plotted, more than 400 frames will be produced by the program. Sample output is shown in Fig. 3.

ORIGINAL PAGE IS
OF POOR QUALITY

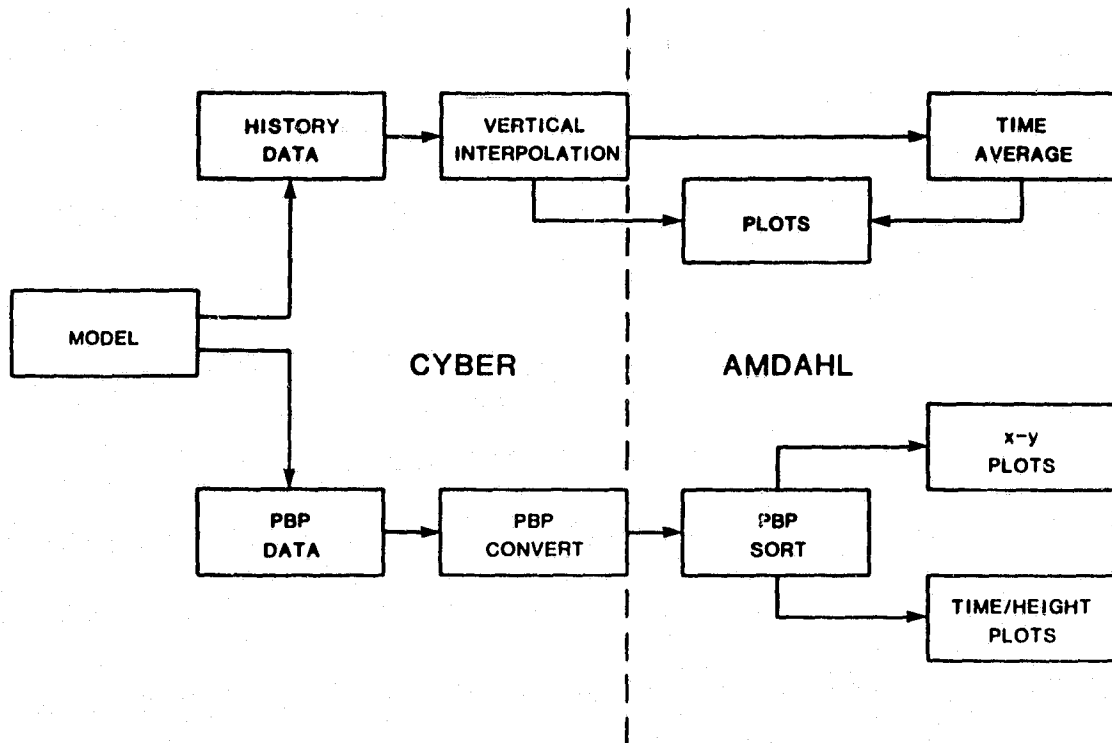
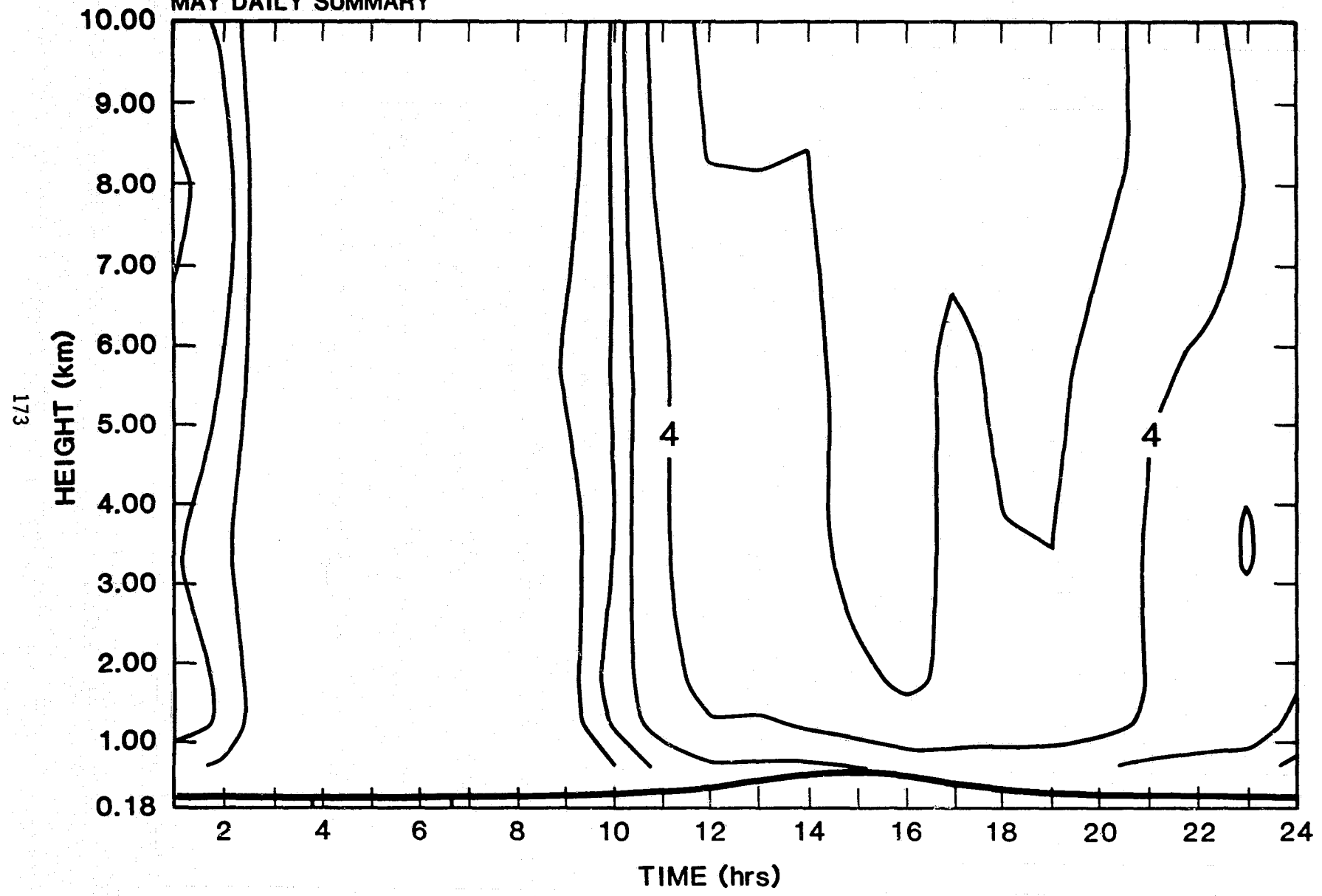


Figure 1

MOIST CONVECTIVE HEATING (K day⁻¹)

MAY DAILY SUMMARY



OKLAHOMA (LATITUDE 34N LONGITUDE 90W)

Figure 2

ORIGINAL PAGE 19
OF POOR QUALITY

GEOPOTENTIAL HEIGHT AT 200 MB

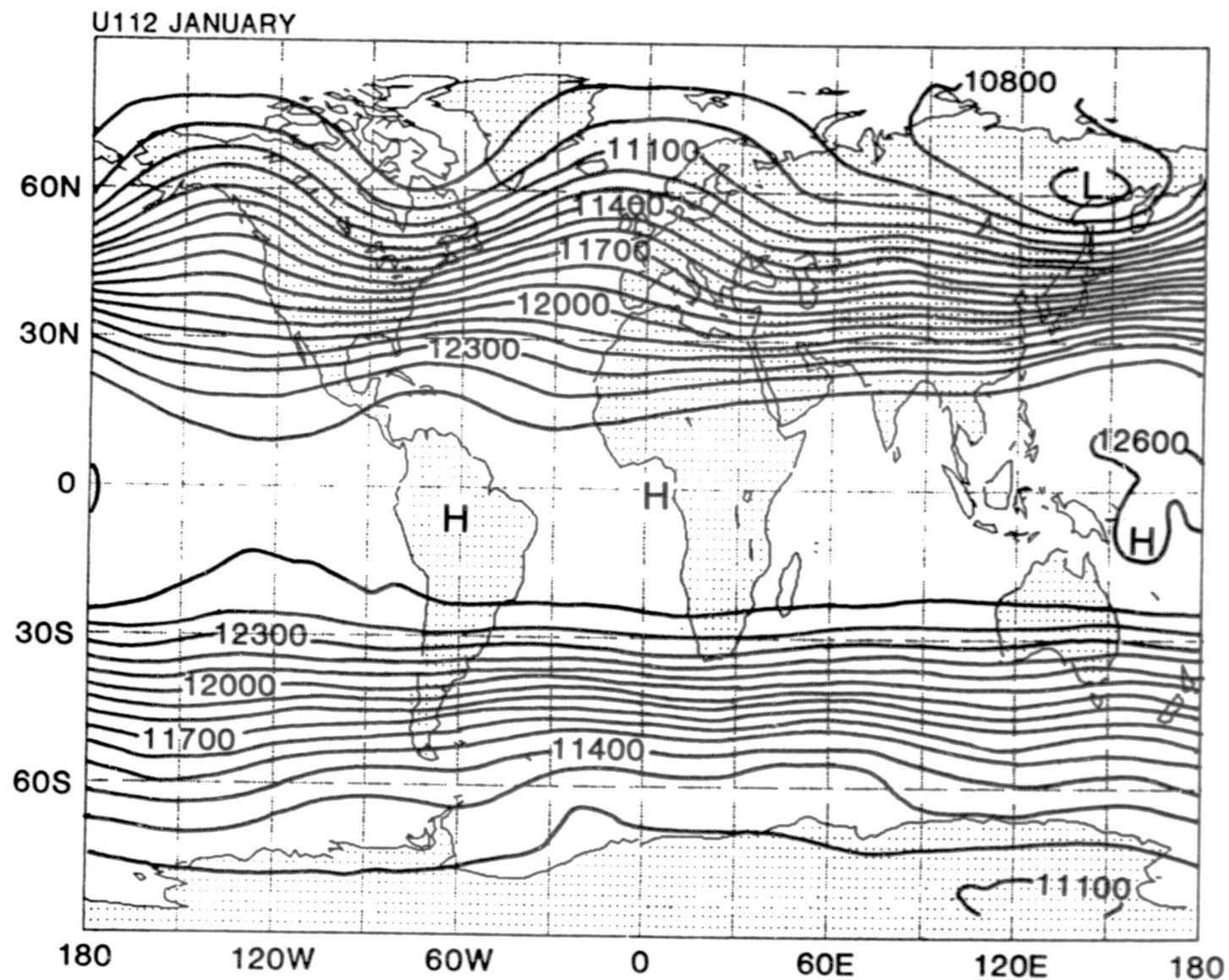


Figure 3

ORIGINAL PAGE IS
OF POOR QUALITY

THE GROWTH, PROPAGATION AND DECAY OF GLOBAL SCALE ROSSBY WAVES DURING FGGE

R. S. Lindzen, D. M. Straus, and B. Katz

In a rotating spherical atmosphere, in the absence of relative mean winds and damping, there will exist free oscillations or normal modes, described by Laplace's tidal equation. These oscillations fall into two categories: gravity waves modified by rotation, and Rossby waves which owe their existence to the variation of the vertical component of the rotation vector with latitude (more precisely to the meridional variation of potential vorticity). The latter, westward propagating waves, were first studied in explicit correction with their potential meteorological significance by Rossby et al. (1939). In the presence of a spatially variable mean wind, these discrete Rossby waves should still exist for the longest scales (lowest wavenumbers), as shown explicitly by Kasahara (1980). The study of such waves--both theoretically and observationally--has been conducted fairly extensively since 1940, and a comprehensive review of this work is given by Madden (1978).

Kasahara (1980) and Ahlquist (1982), in calculating the horizontal normal mode eigenfunctions (Hough modes) in the presence of realistic meridional distributions of zonal wind, found that for the largest scales the wind altered predicted periods but only mildly changed the Hough modes themselves.

The purpose of this paper is to present a portrait of the evolution of these global scale Rossby waves for the FGGE year. Emphasis is placed on the temporal evolution of the amplitude and phase of Hough mode projections, rather than on characteristics of the time spectra of these waves. On the basis of previous work (Madden, 1978; Kasahara, 1980; Salby, 1981a, 1981b; Ahlquist, 1982), we felt it would be adequate to consider the 500 mb level in isolation from the others, and that the Hough functions (which are vector functions of the horizontal wind components and the height field) were good approximations to the "true" eigenfunctions. Thus, the first steps of the analysis consisted of projecting the 500 mb height and wind data (obtained from the ECMWF analyses) onto Hough functions for each synoptic time. The seasonal cycle and time mean were removed separately for each season, and all remaining eastward propagating components removed on a seasonal basis; all remaining westward propagating components were retained.

A sample of the results is given in Fig. 1, which shows the evolution of the amplitude and phase of the (1,4) mode (zonal wavenumber 1, meridional index 3; i.e., second symmetric mode for wavenumber 1) as a function of time for the winter season. The amplitude scale gives the value of the geopotential height at 66°N, the latitude where the (1,4) Hough mode is strongest. (The phase is plotted only when the amplitude is above 20% of its maximum value). This mode exhibits several features which all the modes have in common. The amplitude evolution takes the form of a series of pulses of duration 5-20 days, indicating that the waves have an episodic nature, growing and decaying on time scales not longer than a few wave periods, at most. The phase progresses westward with a phase speed remarkably close to that predicted by Kasahara (1980), given by the dotted line.

This type of analysis was carried out for the following modes for all four seasons: (1,2), (1,3), (1,4), (2,3), (2,4), (2,5), (3,4), (3,5), (3,6). On

the whole, the slope of the phase history lines agrees with the theoretical predictions of Kasahara (1980). However, this agreement does not always hold; in fact, some disagreement is to be expected based on the discrepancies between the variable, latitude-height profile of the zonal wind occurring in nature and the climatological barotropic zonal wind assumed by Kasahara. However, in a given set of modes for the same zonal wavenumber (e.g. (1,2), (1,3) and (1,4)), the phase speed of each mode, variable as it is, is still noticeably different from the phase speed of the neighboring mode.

As the meridional index of the mode increases, the amplitudes become larger, and the time scale for their change generally increases. While episodes of well defined wave propagation generally last for at least one-half of a wave period, they rarely, if ever, endure for more than three wave periods.

It is of some interest to determine whether the behavior of these global waves exhibits a large seasonal dependence. Examination of all nine modes across the four seasons indicates a remarkable statistical homogeneity with respect to the time of year.

The total Rossby wave field consisting of the sum of the westward propagating components of all nine Hough modes can be fairly large. Figure 2 shows the geopotential height of the Rossby wave field at 500 mb for 12Z on 12 January, 1979. The maximum amplitude of 131 m is large enough to cause serious errors in analyzed or forecast fields if these waves are not correctly handled by a model. The high center of 131 meters at 65°N, 85°E can be followed as far back in time as 0Z on 9 January, when it was at 65°N, 125°E with an amplitude of 78 m, and as far forward as 12Z of 19 January, at 65°N, 30°E with amplitude 120 m. The total time span for which the height field remains above 100 m at 65°N, 85°E is about 3-1/2 days. Although this is not long enough to meet the usual criteria for persistent anomalies (Dole and Gordon, 1983), it suggests that Rossby waves can contribute to such anomalies.

The evolution of Rossby waves as portrayed from the ECMWF analyses were compared to equivalent results obtained from data produced by the GLAS analysis scheme (Baker et al., 1981) for the three months of May-July, 1979. The correspondence between the evolution of both amplitude and phase is generally very good, confirming that the picture presented of the evolution of global scale Rossby waves is not an artifact of the analysis scheme. The physical cause for the amplification of these waves remains to be elucidated.

REFERENCES

- Ahlquist, J. E., 1982: Normal-mode global Rossby waves: Theory and observations. J. Atmos. Sci., 39, 193-202.
- Baker, W., D. Edlmann, M. Iredell, D. Han, and S. Jakkempudi, 1981: Objective analysis of observational data from the FGGE Observing Systems. NASA Tech. Memo. 82062.
- Dole, R. M., and N. D. Gordon, 1983: Persistent anomalies of the extratropical Northern Hemisphere wintertime circulation: Geographical distribution and regional persistence characteristics. Mon. Wea. Rev., 111, 1567-1586.

- Kasahara, A., 1980: Effect of zonal flows on the free oscillations of a barotropic atmosphere. J. Atmos. Sci., 37, 917-929.
- Madden, R. A., 1978: Further evidence of traveling planetary waves. J. Atmos. Sci., 35, 1605-1618.
- Rossby, C.-G., et al., 1939: Relations between variations in the intensity of the zonal circulation of the atmosphere and the displacements of the semi-permanent centers of actions. J. Mar. Res., 2, 38-55.
- Salby, M. L., 1981a: Rossby normal modes in nonuniform background configurations. Part I: Simple fields. J. Atmos. Sci., 38, 1803-1826.
- Salby, M. L., 1981b: Rossby normal modes in nonuniform background configurations. Part II: Equinox and solstice conditions. J. Atmos. Sci., 38, 1827-1840.

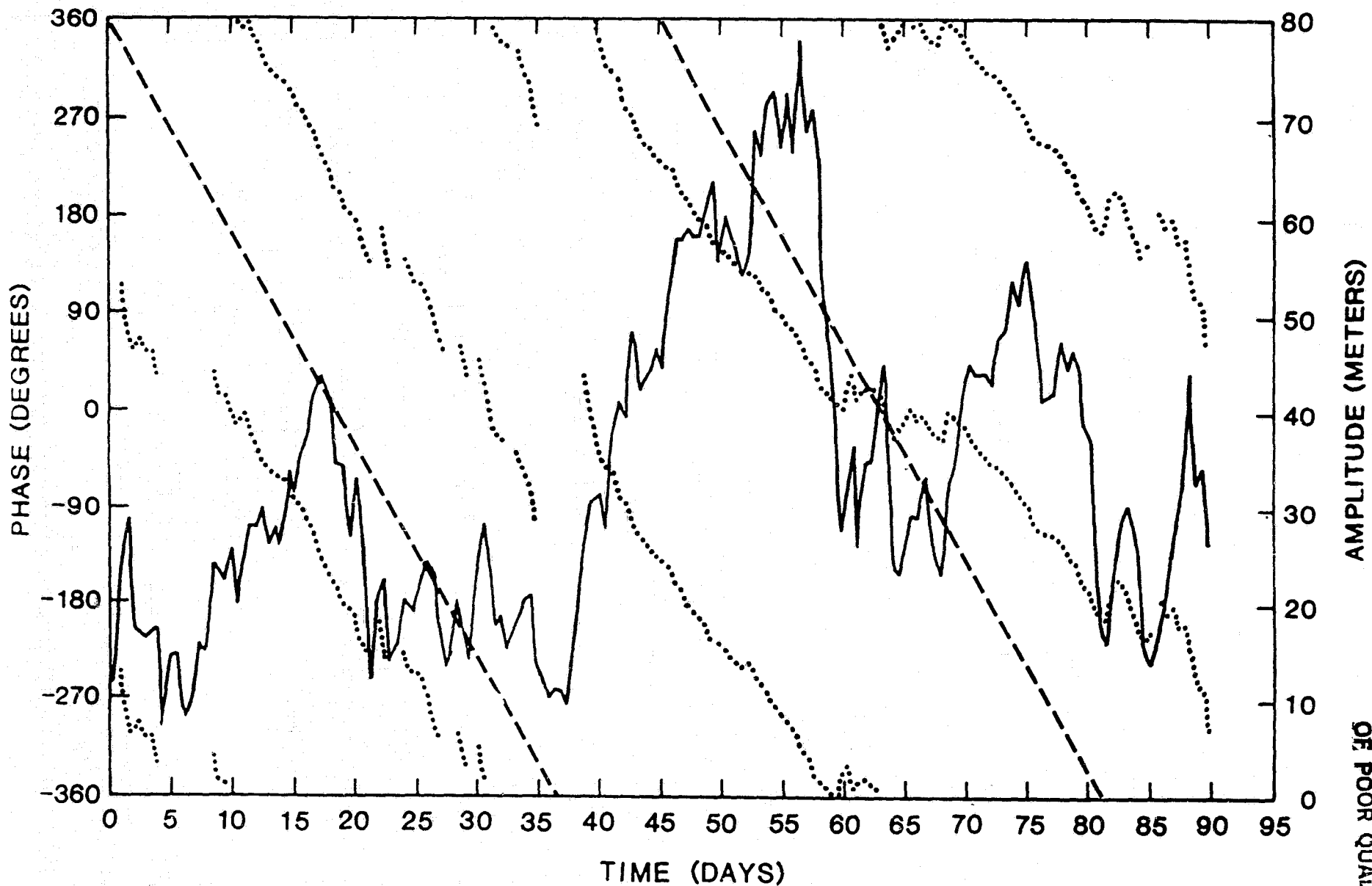
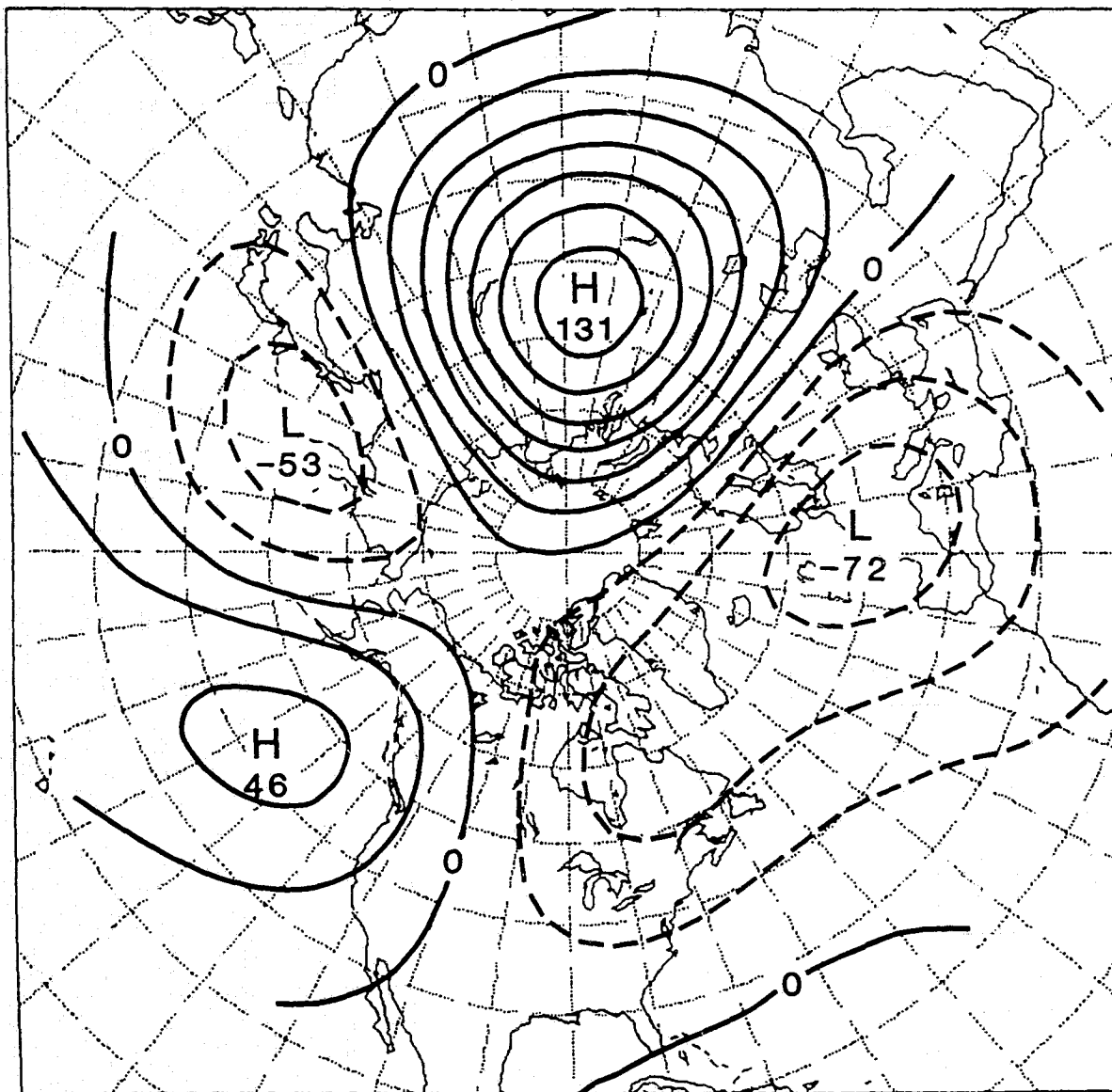


Figure 1. Amplitude and phase of (1,4) Hough mode during winter. The amplitude is given by the solid line, with the corresponding scale on the right, while the phase is given by the dotted line, with the corresponding scale on the left. Two cycles of the phase are plotted. The dashed line corresponds to the phase evolution that would occur were the Hough function to propagate uniformly westward with the period given by Kasahara (1980). The phase is omitted whenever the amplitude falls below 20% of its maximum value.

ORIGINAL PAGE IS
OF POOR QUALITY



ORIGINAL PAGE IS
OF POOR QUALITY

Figure 2. Geopotential height field consisting of the sum of all nine westward propagating Hough modes at 500 mb for 12Z of 12 January, 1979. Contour interval of 20 m.

D32
N84 22081

INTERANNUAL VARIABILITY OF INDIAN MONSOON RAINFALL

D. A. Paolino and J. Shukla

The summer monsoon is a yearly event which provides most of the annual rainfall over India. Drought or excessive rainfall often affects large contiguous areas in any one year. Such large scale anomalies may be predictable by a study of global atmospheric fluctuations or anomalous boundary conditions. We have undertaken a study of the interannual variability of the Indian summer monsoon and its relationships with other atmospheric fluctuations in hopes of gaining some insight into the predictability of the rainfall.

Rainfall data for 31 meteorological subdivisions over India were provided by the India Meteorological Department (IMD). The subdivisional rainfalls are compiled from all raingauge stations reporting for any particular data period. A percentage departure from normal rainfall is calculated by subtracting the mean of all stations reporting in a subdivision from a standard 50 year (1901-1950) normal. Since the stations reporting in any year will not be identical, the percentage departure value will be a better parameter than a total rainfall.

The monthly and seasonal rainfall time series were subjected to an exhaustive check for errors and inconsistencies. Suspicious values were checked with staff of the IMD, and all discrepancies were resolved. The data set we now possess is of a high quality and suitable for an investigation of the interannual variability of the monsoon rainfall. A detailed discussion of the rainfall data and its variability in space and time is published elsewhere (Shukla, 1983). Figure 1 gives the standard deviation of the seasonally (for the summer monsoon, the season is defined as June, July, August and September) averaged percentage departure rainfall for 31 subdivisions, 1901-1981. Minima are present in the northeast and on the west coast. Maximum variability occurs to the northwest.

The areal extent of rainfall anomalies in a particular year is usually larger than one or two subdivisions. Figure 2 shows those subdivisions displaying a correlation coefficient greater than .5 for 81 years of seasonal percentage departure rainfall. Rainfall averaged over all of India can then be considered to be a good indicator of the general performance of the summer monsoon. In order to study the variability of rainfall on a larger spatial scale, the subdivisional rainfalls were averaged into larger regions. The regional average rainfall is computed by weighting all subdivisional rainfalls in the region by the area of that subdivision. Two regions used for forecasting by IMD (Jagannathan, 1968) are Northwest and Peninsula and are shown in Fig. 3. Those two regions correspond to the two areas of multiple correlation in Fig. 2. The remaining subdivisions were averaged in the Northeast and Southern regions, also shown in Fig. 3. Time series for these four regions, and for the whole of India, are shown in Fig. 4. Northeast India displays a smaller variability, as well as somewhat opposite fluctuations when compared to other regions.

Fifty-three years of seasonal mean anomaly sea-level pressure (SLP) fields (20°N-pole) were used to determine if any relationships could be detected between fluctuations in Northern Hemisphere surface pressure and Indian monsoon rainfall. Maps of correlation coefficients were computed between the seasonal SLP anomaly fields at lags from seven seasons before the monsoon to five seasons after the

monsoon. Maps did not generally show any coherent, statistically significant patterns. Results of an empirical orthogonal function (EOF) analysis of these SLP fields were used to check whether the dominant patterns of Northern Hemisphere SLP were related to monsoon anomalies. This analysis, identical to that presented in Trenberth and Paolino (1981), correlated the dominant EOF coefficient time series for each season with the regional monsoon rainfall time series. Results showed only a weak, probably insignificant relationship between rainfall departures and EOF 1 for summer SLP.

The Southern Oscillation, the global see-saw in surface pressure between the South Pacific and Indonesia, was shown by Walker (1924) to be connected with variations of monsoon rainfall over India. Previous studies have shown that the Southern Oscillation tends to follow monsoon rainfall, i.e. correlation tends to be better during and after rather than before the monsoon (Pant and Parthasarathy, 1981). Fig. 5 composites three month running mean sea-level pressure anomalies at Darwin (close to one of the centers of the Southern Oscillation) for months preceding and following extreme years for rainfall averaged over all of India. As previously noted, anomalies are small before the monsoon, but are quite large in months following the summer season. However, there is a large decrease in Darwin pressure for months preceding a heavy monsoon, while a deficient monsoon is preceded by a sharp increase in Darwin pressure. If we construct a time series of the tendency of Darwin SLP between the Northern Hemisphere winter (DJF) and spring (MAM) and compute a correlation coefficient between it and 81 years of rainfall average over all of India, we get a C. C. of -0.46 (Shukla and Paolino, 1983), which is higher than any other previously computed predictor of the monsoon rainfall.

This relationship can also be used to make a qualitative forecast for rainfall over the whole of India by considering the sign of the tendency in extreme monsoon years. In the 81 years of data studied, there were only two instances (1901, 1941) when a negative trend of DJF to MAM Darwin pressure anomaly was followed by a rainfall anomaly of less than one standard deviation below normal; so a prediction of non-occurrence of drought over India can be made with good confidence when Darwin SLP trend is negative. In the case where the pressure tendency at Darwin is rising from DJF to MAM, there were only three cases where rainfall exceeded one standard deviation above normal (1916, 1933, 1961); so positive trend is an indicator of non-occurrence of heavy rains over India.

REFERENCES

- Jagannathan, P., 1968: Seasonal Forecasting in India - A review. India Met. Dept., 79 pp.
- Pant, G. B., and B. Parthasarathy, 1981: Some aspects of an association between the Southern Oscillation and Indian summer monsoon. Arch. Met. Geoph. Biokl. Ser. B, 29, 245-252.
- Shukla, J., 1983: Interannual variability of monsoons. Chap 5.3, Monsoons, John Wiley and Sons, Inc., editors: Jay S. Fein and Pamela L. Stephens.
- Shukla, J., and D. Paolino, 1983: The Southern Oscillation and long-range forecasting of the summer monsoon rainfall over India. Mon. Wea. Rev., 111, 1830-1837.

Trenberth, K., and D. Paolino, 1981: Characteristic patterns of variability of sea level pressure in the Northern Hemisphere. Mon. Wea. Rev., 109, 1169-1189.

Walker, G., 1924: Correlation in seasonal variation of weather IX: A further study of world weather. Mem. India Meteor. Dept., 24, 275-332.

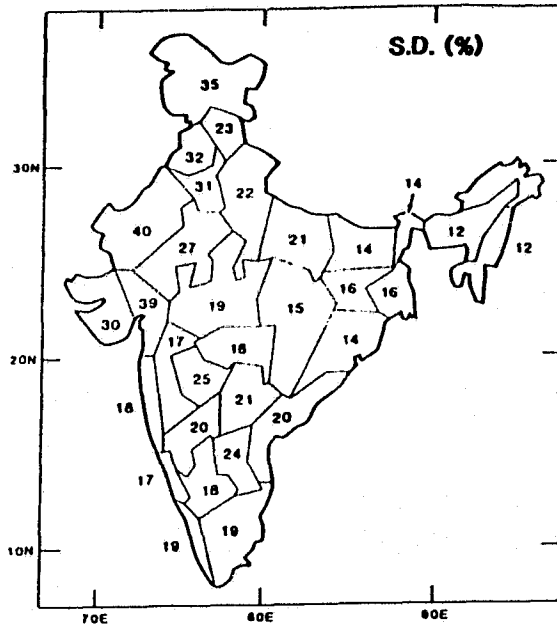


Fig. 1. Standard deviations of seasonal (JJAS) percentage departure from normal rainfall, 1901 - 1981.

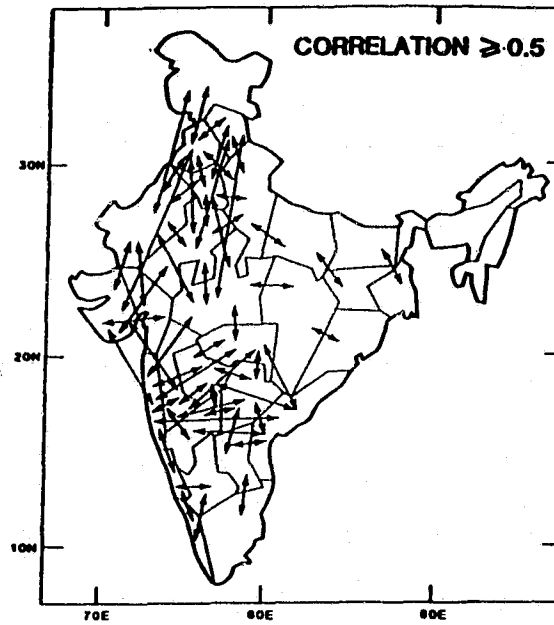


Fig. 2. Subdivisions which have a correlation coefficient of .5 or greater between them are linked by an arrow. Correlations are computed using JJAS subdivisional rainfalls, 1901 - 1981.

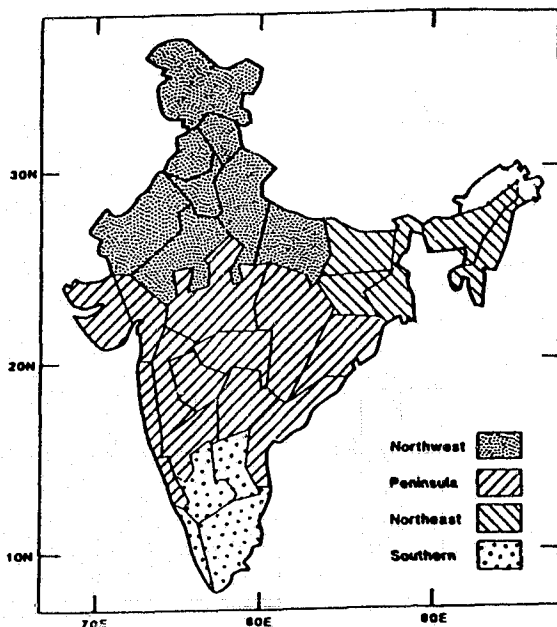


Fig. 3. Subdivisions contained in Northwest, Northeast, Peninsula and Southern regions.

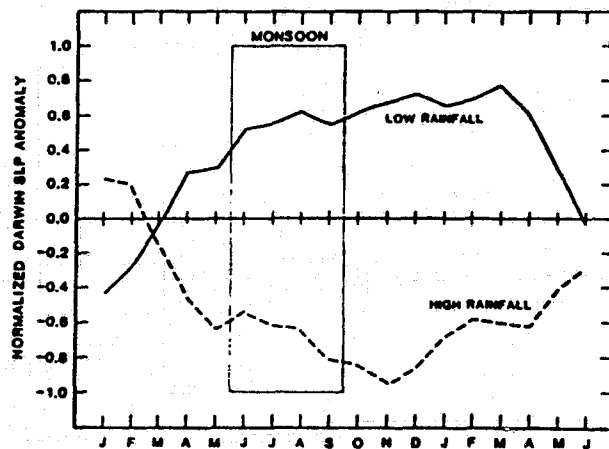


Fig. 5. Composite of normalized Darwin pressure anomaly (three-month running mean) for 12 heavy monsoon years and 14 deficit monsoon years.

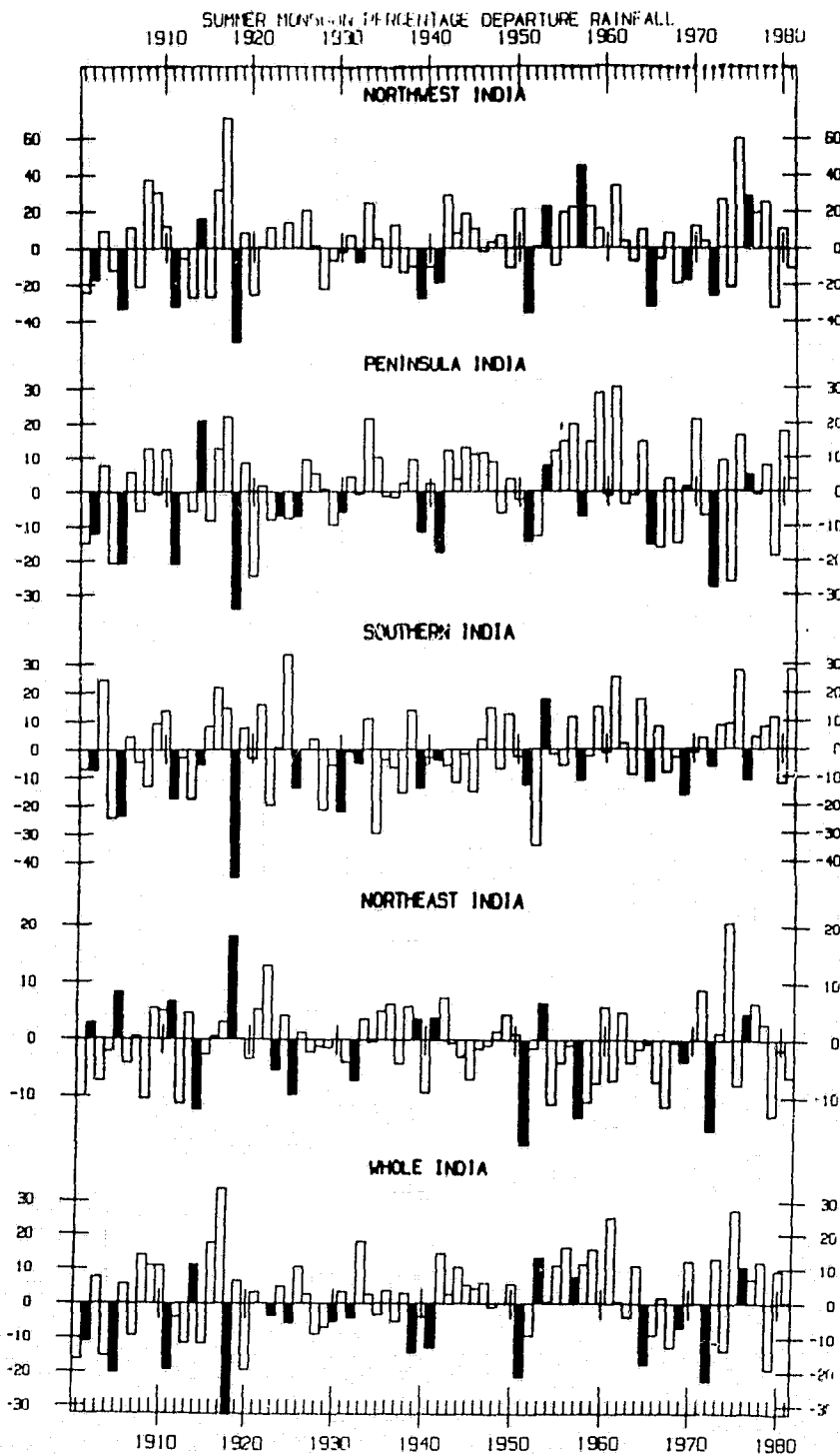


Fig. 4. Time series of regional seasonal (JJAS) percentage departure from normal rainfall, 1901 - 1981. Darkened bars correspond to el nino years.

THE SIMULATION OF TRANSIENT STATISTICS OF THE SOUTHERN HEMISPHERIC CIRCULATION
BY THE GLAS SEASONAL CYCLE MODEL: PRELIMINARY RESULTS

D. M. Straus and J. Shukla

The general circulation of the Southern Hemisphere is quite different from that of the Northern Hemisphere in many important (and intriguing) ways. These include the barotropic nature of the stationary waves and the presence of a strong barotropic component to the mean zonal wind, the lack of a strong seasonal dependence of the transient eddies, and the dominant role played by eddies with periods less than 10 days compared to longer period fluctuations (see Trenberth, 1981, and references therein). Such differences attest to the importance of the altered nature of the orographic and thermal land-sea forcings in the Southern Hemisphere compared to the Northern Hemisphere.

The successful simulation of the Southern Hemisphere circulation thus becomes an important test for general circulation models. We present here some of the important features of the Southern Hemisphere circulation as simulated by the GLAS Seasonal Cycle Model (SCM) and compare them to observed data.

The SCM is an improved version of the GCM discussed by Shukla *et al.* (1981), with the changes consisting of: (i) a new boundary layer parameterization; (ii) a new parameterization of evapotranspiration from land surfaces; (iii) a new parameterization of the interaction between clouds and radiation; (iv) a new scheme to maintain computational stability near the poles; and (v) a new vertical differencing scheme. These changes are detailed by Randall (1982). The simulation to be discussed started from initial conditions of November 15, 1978 and was carried out for 24 months. The sun's declination, sea surface temperature, sea ice, and snow cover extent and soil moisture were prescribed to follow a smooth annual cycle.

In this article we discuss the geographical patterns of local variability and their seasonal shifts in the SCM and compare them to observations. The observational results we use for comparison are taken from Trenberth (1982), who examined the Australian analyses from May 1972 to November 1980. The analysis is confined to 500 mb, as that is the only level for which these observations are reliable (Trenberth, 1981).

The observed band-passed variance of geopotential height in winter and summer is shown in Figures 1a and 1b. In calculating this variance, Trenberth first removed the seasonal cycle from the height data and then applied the spectral filter of Lorenz (1979). The band-pass variance was constructed by summing several contiguous bands, giving a nominal range of periods of 2-8 days (Trenberth, 1982). Thus, Figures 1a and 1b give an indication of the position of the storm tracks. In winter, the observed storm track lies at 50°S, and extends from the mid-Atlantic eastward all the way across the Indian Ocean to the dateline. The maximum variance lies in the Indian Ocean. The only major change from winter to summer is the weakening of the variance; the position of the storm track remains unchanged.

The band-pass variance of geopotential height simulated by the SCM for winter and summer is given in Figures 2a and 2b. Just as the observational maps result from averaging as many winters and summers as are available, the

SCM maps result from averaging the two model winters and summers. The basic model time series had the seasonal cycle removed, and the band-pass filter used consisted of a simple harmonic filter retaining periods of 2.0 to 7.5 days. Since this filter is not identical to that used in processing the observations, the absolute magnitudes of the variances should not be compared too precisely. Both the winter and summer SCM maps look very realistic. Not only are the storm tracks located correctly, but their seasonal shift is very well simulated. The variance in the Indian Ocean decreases in summer, and the relative importance of the variance in the Pacific compared to that in the Indian Ocean increases in summer, as observed.

The observed maps of low pass geopotential height variance (Figures 3a, 3b) were computed by removing the seasonal cycle and then combining several contiguous bands of the Lorenz filter; the nominal periods retained are 8-64 days. The winter map shows strong maxima in three distinct locations: polewards of New Zealand at 60°S, in the central Indian Ocean at 50°S and polewards and east of the tip of South America at 60°S. These regions overlap strongly with areas of a high incidence of persistent anomalies ("blocking" episodes), as discussed by Mo (1983). In summer, these three regions are still present, although the variances are weaker and the positions have shifted slightly.

The SCM simulation of the low pass variance (shown in Figures 4a and 4b) was computed by removing the seasonal cycle from the basic time series of heights, and then applying a simple harmonic filter which retains periods of 8.2-90 days. In winter, the SCM produces maxima in each of the three positions indicated in the winter observations. However, these maxima are barely discernible in Figure 4a because they are embedded in a high latitude band of very high variance extending around the globe. The one maximum in the variance that does stand out (in the eastern Pacific at 70°S) is spurious. The observed maximum poleward of New Zealand stands out somewhat more in the SCM summer results (Figure 4b) than in the SCM winter map, although the observed equatorward shift with season is not simulated. The simulated Indian Ocean maximum weakens far too much in the summer, while the observed summer maximum southeast of South America is totally absent. There are large spurious variances in the eastern Pacific at 60°S and south of Africa at 50°S.

This small set of maps clearly indicates that while the SCM successfully reproduces the geographical distribution of cyclone-type activity, it fails to simulate the correct pattern of low frequency variability. It is interesting to note that this failure is not necessarily due to the failure to simulate persistent anomalies, nor is it due to the lack of low frequency variability. In fact, the SCM produces too much low frequency variability in the Southern Hemisphere. Future work will concentrate on documenting these and other aspects of the space/time variability of the SCM, and comparing the results to more complete and up-to-date sources of Southern Hemisphere data, such as the FGGE-IIb data.

REFERENCES

- Lorenz, E. N., 1979: Forced and free variations of weather and climate. J. Atmos. Sci., 36, 1367-1376.
- Mo, K. C., 1983: Persistent anomalies of the Southern Hemisphere circulation. Proceedings of the First International Conference on Southern Hemisphere Meteorology, A.M.S., pp. 70-72.

Randall, D., 1982: Monthly and seasonal simulations with the GLAS Climate Model. ECMWF Workshop Proceedings.

Shukla, J., D. Straus, D. Randall, Y. Sud, and L. Marx, 1981: Winter and summer simulations with the GLAS Climate Model. NASA Tech. Memo. 83866, 282 pp.

Trenberth, K. E., 1981: Observed Southern Hemisphere eddy statistics at 500 mb: Frequency and spatial dependence. J. Atmos. Sci., 38, 2585-2605.

Trenberth, K. E., 1982: Seasonality in Southern Hemisphere eddy statistics at 500 mb. J. Atmos. Sci., 39, 2507-2520.

ORIGINAL PAGE IS
OF POOR QUALITY

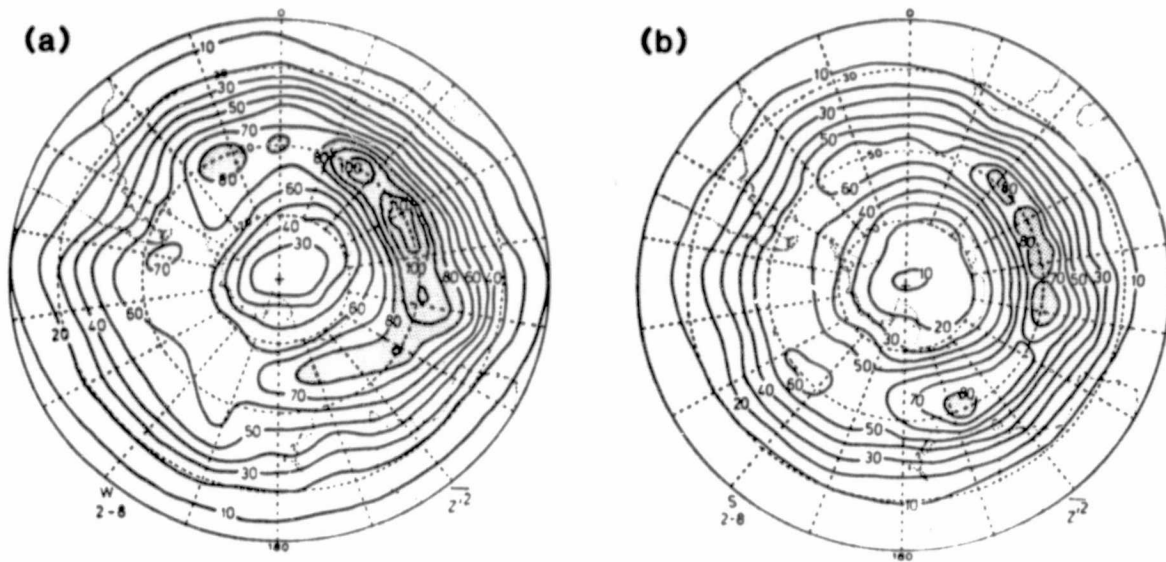


Figure 1. Observed variance of geopotential height in the Southern Hemisphere winter (a), and summer (b), in the 2-8 day range, in units of 100 m^2 . Contour interval is 1000 m^2 . Taken from Trenberth (1982).

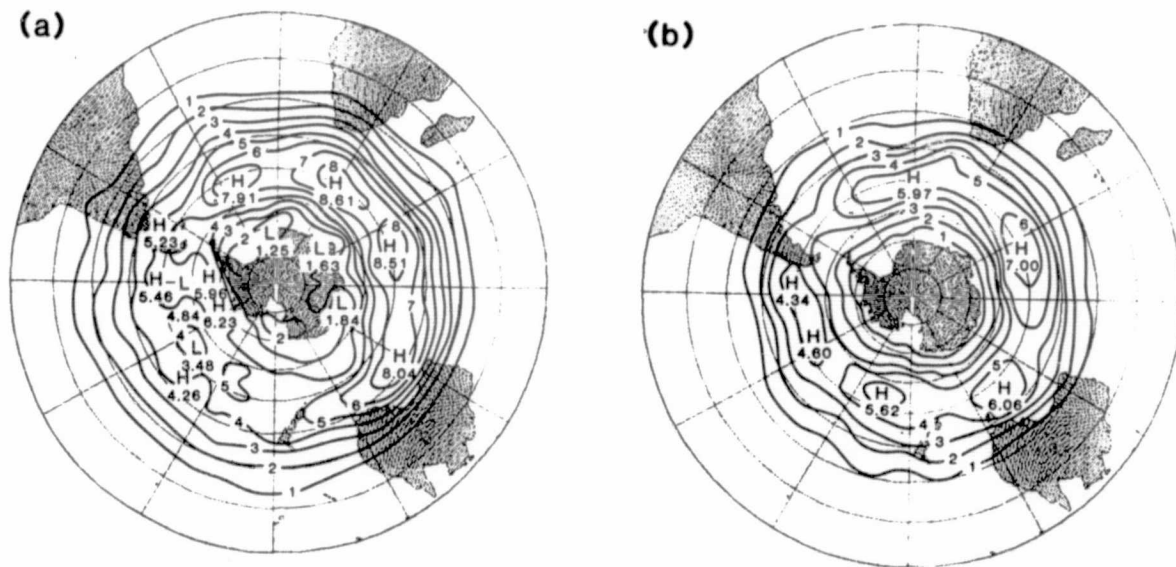


Figure 2. Simulated variance of geopotential height in the Southern Hemisphere winter (a), and summer (b), in the 2-7.5 day range. Contour interval is 1000 m^2 .

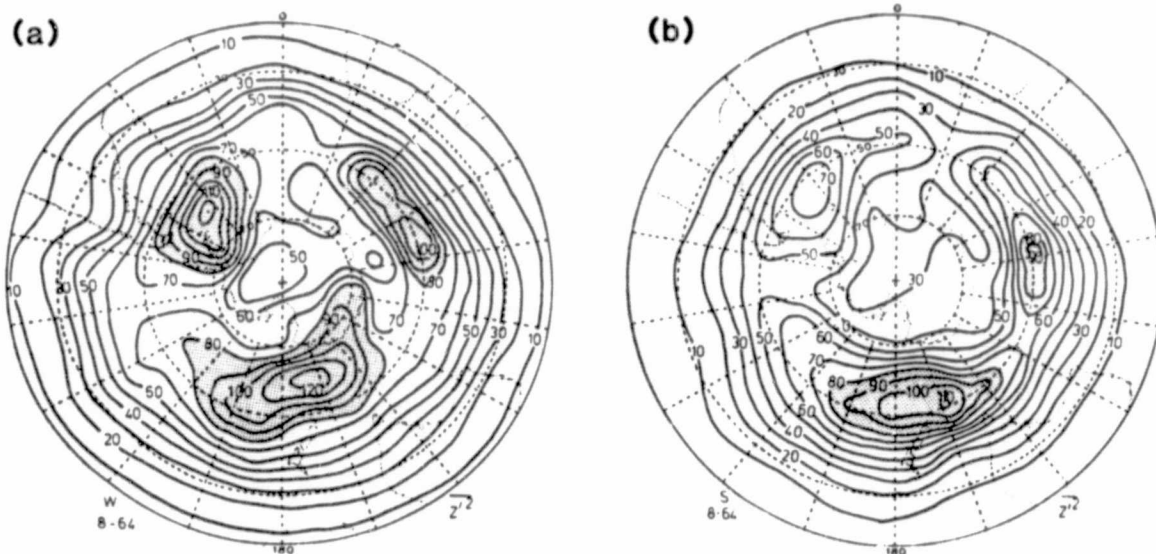


Figure 3. Observed variance of geopotential height in the Southern Hemisphere winter (a), and summer (b), in the 8-64 day range, in units of 100 m^2 . Contour interval is 1000 m^2 . Taken from Trenberth (1982).

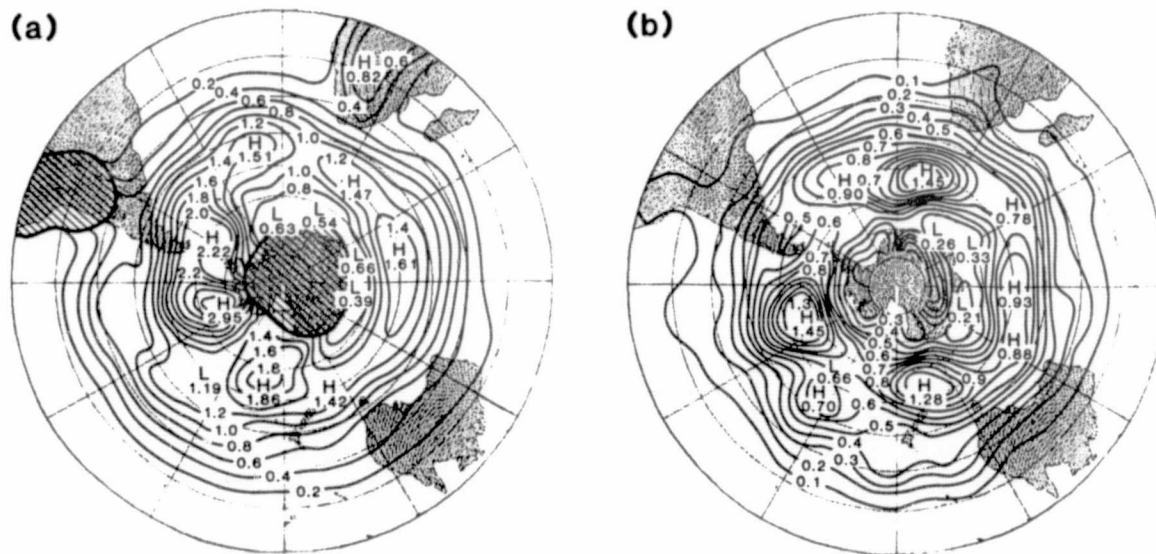


Figure 4. Simulated variance of geopotential height in the Southern Hemisphere winter (a), and summer (b), in the 8-64 day range, in units of 10^4 m^2 . Contour interval for (a) is 2000 m^2 , and for (b) it is 1000 m^2 .

D 34
N84 22083

LOCALIZED BLOCKING ACCOUNTED FOR BY SLOW VARIATIONS OF THE ZONAL DRIVING

K. C. Mo

Charney, Shukla and Mo (1980, hereafter referred as CSM) extended the work of Charney and Devore (1979) to incorporate observed zonal topography in a barotropic nonlinear channel model. The governing potential vorticity equation may be written as

$$\frac{\partial}{\partial t} \nabla^2 \psi + J(\psi, \nabla^2 \psi + \beta y + f h) = - \frac{D_E f}{2H} \nabla^2 (\psi - \psi^*)$$

where ψ is the streamfunction ψ^* is the driving streamfunction, $f = 1 \times 10^{-4}/s$ is the Coriolis parameter, $H = 8$ km is the mean height of the fluid, h is the perturbation height of the topography, $D_E = 320$ m is the Ekman depth. All parameters and notations used here are the same as CSM. ψ and ψ^* can be written as the part corresponding to the top hat profile, and Fourier expansion in $\sin y$

$$\psi = - Uy + \phi \sin y$$

$$\psi^* = - U^* y$$

where U and U^* vanish at its boundaries $y = 0$ and πL ($L = 1.167 \times 10^6$ m).

CSM determined the constant U^* by requiring one of the solution be a normal winter flow predicted by Charney and Eliassen (1949). When this U^* was applied to the model, they found two stable solutions corresponding to wavenumber 2 and 3 resonances. However, that model cannot explain the regional features of blocking.

To account for the regional blocking Charney suggested employing a two scale method to allow small slow variation of the momentum driving U^* and its corresponding U . Since the topography h and perturbation ϕ are dominated by wavenumber 2 or larger, we assume that U^* and U have the constant part and wavenumber 1 part.

$$U^* = U_0^* + U_1^* \cos \alpha(x - \gamma)$$

$$U = U_0 + U_1 \cos \alpha(x - \gamma_0)$$

where $\alpha = L/a \cos \phi_0$, a is the radius of the earth, $\phi_0 = 45^\circ$ is the mean latitude. U_0^* will be fixed at the value determined by CSM (the nondimensional $U_0^* = U_0^*/fL = 0.534$) and γ is 150E, where the perturbation driving is maximum. For given U^* , multiple solutions have been found. The solutions labelled by U_0 , U_1 , and γ_0 , and their linear instability ($e^{\sigma t}$) are listed in Table 1.

The subresonant solutions for $U_0^*/fL = 0.1068$ are plotted in Fig. 1. The super-resonant solutions are always unstable. When U_0^*/fL is small (< 0.1068), one of the equilibria resembles the wavenumber 2 Atlantic blocking with the ridge much stronger than the Pacific ridge. When the U_0^*/fL is strengthened (> 0.1068), the wavenumber 3 Pacific blocking occurs with the ridge in the Pacific stronger

than the one in the Atlantic. In the latter case, the solution is stable. In the case of the Atlantic blocking the solution is weakly unstable with the e-folding time longer than 40 days.

REFERENCES

Charney, J. G. and J. G. Devore 1979: Multiple flow equilibria in the atmosphere and blocking. J. Atmos. Sci., 36, 1205-1216.

Charney, J. G. and A. Eliassen 1949: A numerical method for predicting the perturbations of the midlatitude westerlies. Tellus, 1, 38-54.

Charney, J. G., J. Shukla and K. C. Mo 1981: Comparison of barotropic blocking theory with observation. J. Atmos. Sci., 38, 762-779.

ORIGINAL PAGE IS
OF POOR QUALITY

Table 1

Equilibrium Solutions and Stability Analysis

U_1^* Non-dimensional	n wave number	U_0 m/s	U_1 m/s	γ	σ_0	e-folding time (days)
0.0534	sub #3	13.24	4.22	124W	0.008	14.6
	super #3	13.42	2.81	102W	0.0007±0.0148i	14.3
	sub #2	15.23	2.42	50E	0.0026±0.026i	71.6
	super #2	16.58	4.02	52E	0.0198	5.7
0.1068	sub #3	12.95	4.10	122W	0.0044±0.0021i	26.5
	super #3	13.41	1.52	94W	0.016	7.0
	sub #2	15.46	3.56	63E	0.003±0.0091i	38.0
	super #2	19.21	2.97	45E	0.0204	5.6
0.2067	super #3	12.66	3.39	134W		STABLE
	sub #3	13.41	0.08	2W	0.022	5.0
	super #2	19.16	2.38	40E	0.021	5.6

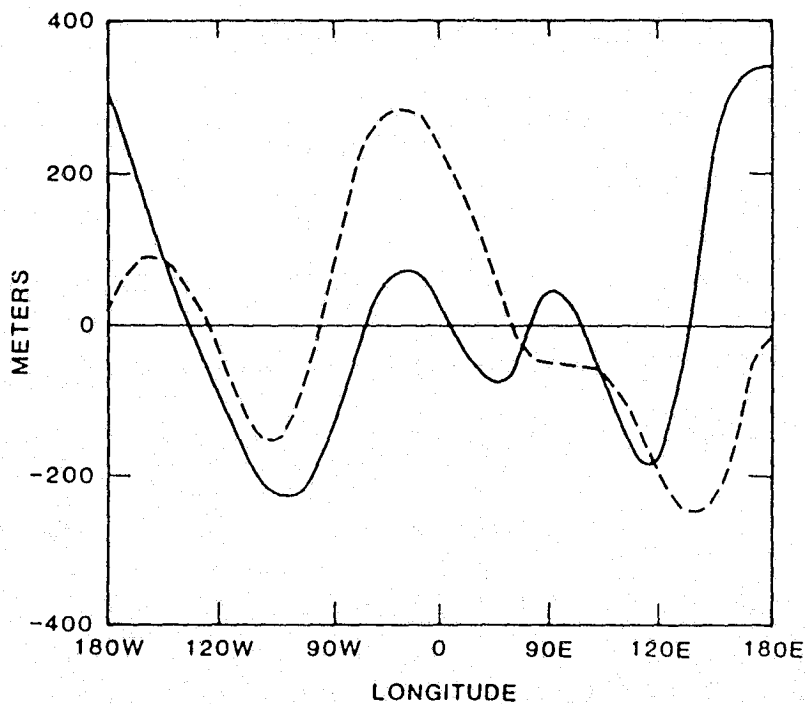


Figure 1. Perturbation height ϕ in meters for subresonant wavenumber 2 (dashed line) and subresonant wavenumber 3 (solid line) solutions for $U_{1D}^* = 0.1068$.

TELECONNECTION PATTERNS IN THE SOUTHERN HEMISPHERE

K. C. Mo and G. H. White

Contemporaneous correlations between geopotential heights on a given pressure surface at widely separated points on Earth, commonly referred to as teleconnections, are calculated from monthly mean sea level pressure and 500 mb geopotential height analyses for the Southern Hemisphere for five-month winter and summer seasons. The monthly means were calculated from operational analyses prepared by the World Meteorological Centre in Melbourne, Australia, for the period from June 1972 to November 1980. The climatological annual cycle for the period was removed before correlations were calculated.

Zonally averaged 500 mb geopotential heights in mid-latitudes are negatively correlated with heights in the subtropics and polar regions. Sea level pressure displays a similar pattern with weaker correlations.

Fig. 1 shows the correlation of anomalies in 500 mb geopotential height with 500 mb anomalies at 18°S, 60°W during summer (November-March). Anomalies over the three continents occur out of phase with anomalies over the subtropical oceans and in a wavenumber 3 pattern over the Southern Ocean near 55°S. The subtropical part of the pattern appears largely associated with the interannual variation of the seasonal cycle and annual mean. A similar pattern with weaker correlations also appears in sea level pressure in summer. Another teleconnection pattern in summertime sea level pressure features a strong negative correlation between Cocos Island and Tahiti and associated mid-latitude features. It strongly resembles a pattern found by van Loon and Madden (1981) in a study of interannual variability associated with the Southern Oscillation.

In winter (May-September) 500 mb geopotential heights over Africa exhibit positive correlations with heights over South America and the central South Pacific near New Zealand and negative correlations with height over the Southern Ocean. A striking wavenumber three pattern is apparent in Fig. 2, which shows the correlation of 500 mb geopotential height anomalies with 500 mb anomalies at 50°S, 95°E during winter. The strong positive correlations between 50°S, 95°E and 58°S, 150°W and 38°S, 15°W contrast with negative correlations over Antarctica and in low latitudes. Time variations in a similar pattern in sea level pressure are in phase with variations in the 500 mb pattern, suggesting an equivalent barotropic structure. This wavenumber three pattern, in independent analyses by the European Centre for Medium Range Weather Forecasts, dominates the Southern Hemisphere circulation in July 1981 (Wallace and Blackmon, 1983). A wavenumber three pattern can also be seen in many blocking cases in the Southern Hemisphere.

The above features are well-reproduced in both halves of the period.

Teleconnection patterns in the Southern Hemisphere appear much larger in spatial scale and less wavetrain-like than teleconnection patterns in the Northern Hemisphere (Wallace and Gutzler, 1981).

REFERENCES

- van Loon, H., and R. A. Madden, 1981: The Southern Oscillation. Part I: Global associations with pressure and temperature in northern winters. Mon. Wea. Rev., 109, 1150-1162.
- Wallace, J. M., and M. L. Blackmon, 1983: Observations of low-frequency atmospheric variability. In Large-Scale Dynamical Processes in the Atmosphere, B. J. Hoskins and R. P. Pearce (eds.), Academic Press, New York.
- Wallace, J. M., and D. S. Gutzler, 1981: Teleconnections in the geopotential height field during the Northern Hemisphere winter. Mon. Wea. Rev., 109, 784-812.

ORIGINAL PAGE IS
OF POOR QUALITY

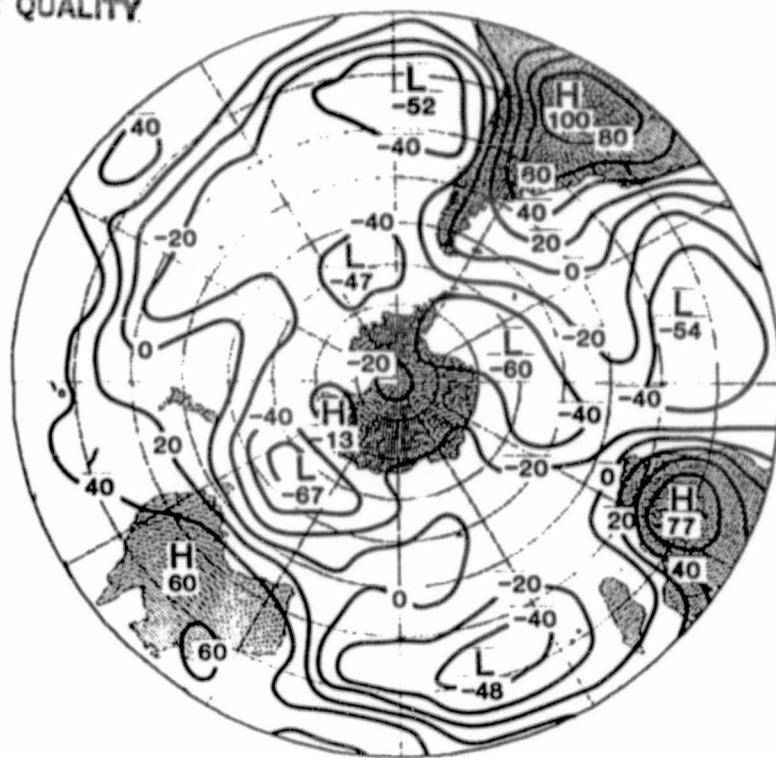


Fig. 1. Correlation coefficients between anomalies in 500 mb geopotential height and 500 mb anomalies at 18°S, 60°W during summer (November-March). Contour labels x 100, interval 0.2. The edge of the map is 10°S. Latitude circles every 10°, longitude lines every 30°.

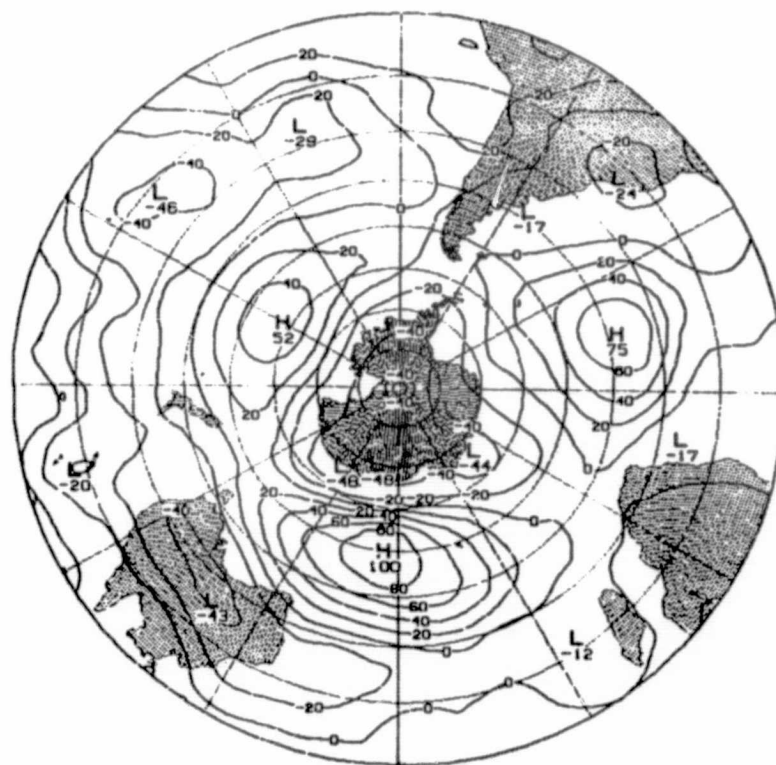


Fig. 2. Correlation coefficients between anomalies in 500 mb geopotential height and 500 mb anomalies at 50°S, 95°E during winter (May-September).

36
N84 22085

OCEAN FLUXES SIMULATED BY THE GLAS GCM

Y. C. Sud and J. Shukla

A two year run with the GLAS climate model with prescribed but seasonally varying boundary conditions provided mean monthly fluxes of sensible heat, latent heat, and radiative energy. These fluxes were analyzed to examine the energy exchange processes between the atmosphere and the ice-free ocean. A mean annual plot of monthly zonal fluxes of sensible heat, latent heat, and net radiation was produced. From these, northward transport of heat flux that would follow if the GCM simulated fluxes were consistent with oceanic circulation were produced. These results are compared with observations.

The GCM simulation was started from November 15, 1978. The initial conditions were based on the NMC analysis of global observations for that day. A two year integration, i.e., until the end of November, 1980, was made. In this long simulation all the boundary conditions at the surface of the earth were externally prescribed as monthly mean values. From these, daily values were linearly interpolated at 00Z everyday. The prescribed fields are comprised of: sea surface temperature, soil moisture, surface albedo, permanent ice (over land and sea) and orography.

There are several reasons for conducting this investigation. Firstly, it is important to know how oceanic surface fluxes vary over the model simulated annual cycle, and whether they are realistic. Secondly, because the oceans play a major role in influencing weather and climate, an analysis of these fluxes can enable us to parameterize feedback effects due to ocean-atmospheric interactions. Lastly, by comparing the model simulations with estimates based on observations (Esbensen and Kushnir, 1981) the strengths and weaknesses of the model can be identified which can help us to improve the model and to interpret the simulation experiments in a better way.

The calculation of surface fluxes of heat and moisture follows Deardorff (1972). The basic equations are:

$$S\uparrow = \rho C_p C_H C_U U_m (\theta_g - \theta_m)$$

$$\lambda E\uparrow = \rho \lambda C_p C_H C_U U_m (q^*g - q_m)$$

where S and λE are sensible and latent energy fluxes, ρ is the density of air, C_p is the specific heat, C_U and C_H are bulk friction and heat transport coefficients, respectively. U_m is the mean wind speed in the mixed layer.

θ_m and q_m are the mean potential temperature and mixing ratio in the mixed layer; θ_g and q^*g are potential temperature and saturation mixing ratio at the atmosphere-ocean interface. The bulk aerodynamic coefficients, C_U and C_H under neutral conditions, are functions of ratio of PBL height to surface roughness height. The former is taken to be 600 m, whereas the latter is equal to 2.0×10^{-4} m, everywhere over the oceans. For non-neutral situations, the correction for stability dependence is introduced. U_m , θ_m , and q_m are calculated at 600 m from U , θ , and q values at the lowest two layers.

The solar radiation calculation is based on Lacis and Hansen (1974) parameterization whereas the longwave radiation is due to Wu (1980). In this simulation the convective clouds are not allowed to interact with radiative transfer processes and the supersaturation clouds are assumed to fill the entire volume of the grid. However, very high supersaturation clouds are thin and often with small areal coverage, therefore, these clouds too are assumed transparent to radiation. The solar radiation is calculated at the beginning of every physical time step whereas the longwave calculation is performed every five hours.

Regardless, the ocean is prescribed as a constant temperature surface of water and therefore radiative transfers at the surface of the ocean have no effect on the atmosphere or the ocean; those are merely pointers to the realism of the GCM simulation. See Randall (1982) for more details about the model and these calculations.

Using diagnostics of the two year simulations, we produced monthly seasonal and annual maps of oceanic surface fluxes of sensible heat, latent heat, and net radiation at the surface. We then calculated the net energy flux into the ocean. Assuming no advection, we were able to calculate the hypothetical SST anomalies that such fluxes would generate. The calculation allowed for the change in SST to affect an assumed mixed layer depth of 70 m. Alternatively, if the SST anomaly was not allowed to form, the excess energy must be advected away. Zonal average of excess energy flux was calculated and used to obtain northward transport of this flux by starting the integration at the South Pole. The basic equations are:

a) Net oceanic flux at a grid point:

$$F_{ij} \downarrow = R_{ij} \downarrow - S_{ij} \uparrow - \lambda E_{ij} \uparrow \quad (1)$$

b) Excess zonally averaged oceanic flux:

$$F_j \downarrow = (1/N_j) \sum_{u=1}^{72} \{ F_{ij} \downarrow - C_p \rho h_{ij} (\Delta T_{ij} + \delta T) \} \quad (2)$$

In a fully coupled ocean-atmosphere system:

$$\int_{j=1}^{46} N_j F_j \downarrow \cos \phi_j \equiv 0 \quad (3)$$

Equations (2) and (3) yield the value of constant δT . The northward flux is obtained from the equation

$$\bar{F}_j \downarrow = F_j \downarrow + \bar{F}_{j-1} (N_{j-1} \cos \phi_{j-1} / N_j \cos \phi_j) \quad (4)$$

where $F_{ij} \downarrow$ is the net heat flux into the ocean at a grid point i, j . It is equal to the sum of net radiation $R_{ij} \downarrow$, sensible heat flux, $S_{ij} \uparrow$, and latent heat flux, $\lambda E_{ij} \uparrow$. The excess flux is advected. It is equal to $F_{ij} \downarrow$ minus (plus) the energy required to heat (cool) the ocean based on climatology of SST change, ΔT_{ij} .

To ensure that the global integral of heat flux in the ocean vanishes, an arbitrary constant, δT , is added. This uniformly distributes the error due to incompatibility of simulated fluxes from the ocean with that of the global energy balance of a constant height mixed layer undergoing a prescribed temperature change. Finally, when (4) is used in a recursive manner (starting at the South Pole), it gives the northward oceanic flux of heat.

Figs. 1, 2 and 3 show zonal average plots of sensible heat, latent heat and net radiative fluxes. Figs. 4 and 5 show the estimates of net downward energy flux into the ocean and the magnitude of northward transport of excess energy flux as estimated from the set of equations. A comparison of these results with the estimates of Esbensen and Kushnir (1981), based on marine observations for ice-free oceans, reveal the following:

1) There are several discrepancies between the observed and the model simulated sensible heat fluxes. During the months of May, June, July and August, the model simulated values are about four times larger than the observed. During the same period of the year, the observed sensible heat flux is negative in the northern mid-latitudes whereas it is generally positive in the model simulations.

Since the ocean temperatures are prescribed from the observations, discrepancies between the observed and the model simulated values could be attributed primarily to the inadequate simulation of the air temperatures and wind velocities in the lower layers of the GCM atmosphere, however, uncertainty in the observed fluxes could also be quite considerable.

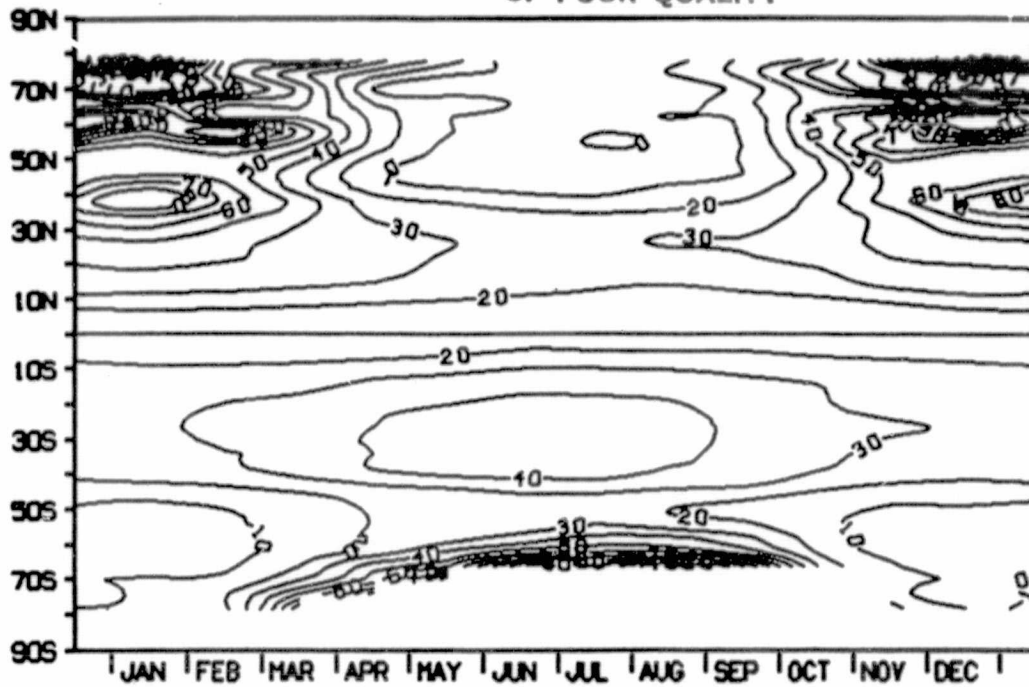
2) The magnitude and the annual variability of the latent heat fluxes is simulated reasonably well. The Northern Hemispheric mid-latitude minima during June, July and August is well simulated. The maxima during May, June and July is near 15°S in the observations but at the equator in the model simulations. The observed maxima near 30°N during December and January is well simulated by the model.

3) The simulated radiative fluxes at the ocean surface have some discrepancies compared to the observations, especially at the higher latitudes. The observed map shows large positive values north of 50°N during May, June, and July which increase with latitude whereas the simulated radiative fluxes decrease with latitude. During December, January, and February, the simulated radiative fluxes northwards of 50°N are not as negative as seen in the observations.

4) The latitudinal distribution of the total energy flux into the ocean surface is very different in the model simulations as compared to the observations. During the months of May, June, July and August, the total energy flux steadily increases with latitude in the Northern Hemisphere and decreases in the Southern Hemisphere with maximum positive values near 70°N and minimum values near 70°S . During the same period of the year, the model simulated total energy fluxes are maximum positive near 50°N and then decrease northward, and minimum negative at 35°S and then increase southward. Similar discrepancies in latitudinal distribution are also found in the other months of the year.

REFERENCES

- Deardorff, J. W., 1972: Parameterization of the planetary boundary layer for use in general circulation models. Mon. Wea. Rev., 100, 93-106.
- Esbensen, S. K., and Y. Kushnir, 1981: The heat budget of the global ocean: An atlas based on estimates from surface marine observations. Report No. 29, Climate Research Institute and Dept. of Atmospheric Science, Oregon State University, Corvallis, OR 97331.
- Lacis, A. A., and J. E. Hansen, 1974: A parameterization for the absorption of solar radiation in the earth's atmosphere. J. Atmos. Sci., 31, 118-133.
- Randall, D. A., 1982: Monthly and seasonal simulations with the GLAS Climate Model. Proceedings of the workshop on Intercomparison of Large-Scale Models used for Extended Range Forecasts of the European Centre for Medium Range Weather Forecasts, Reading, England, pp. 107-166.
- Wu, M. L., 1980: The exchange of infrared radiative energy in the troposphere. J. Geophys. Res., 85, 4084-4090.



VALUES RANGE BETWEEN 0.41 AND 193.17 FOR CONTOUR INTERVALS OF 10.00

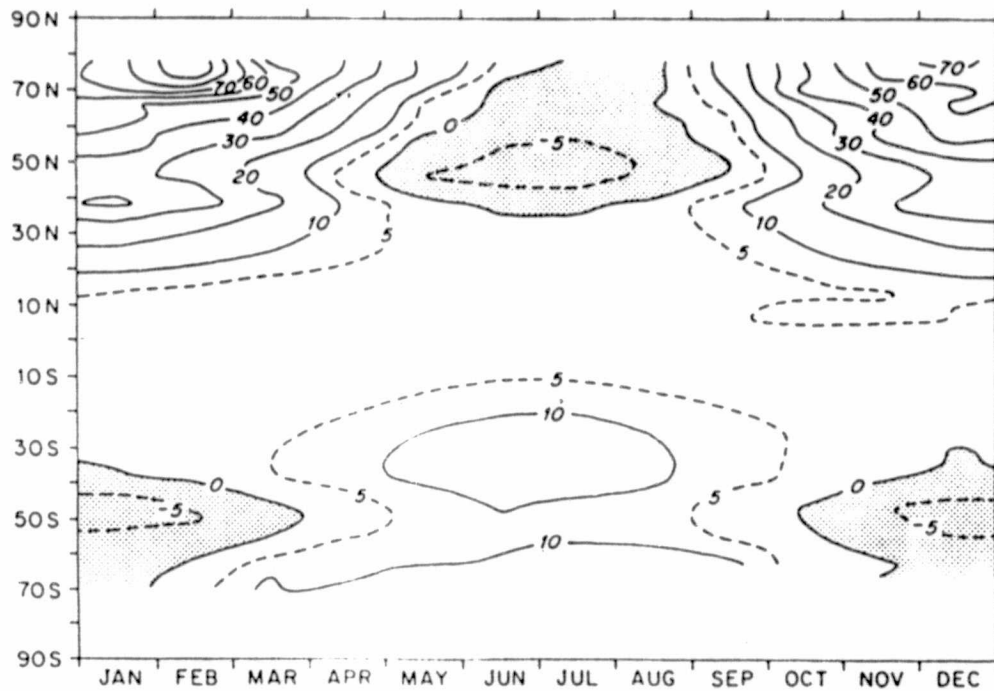
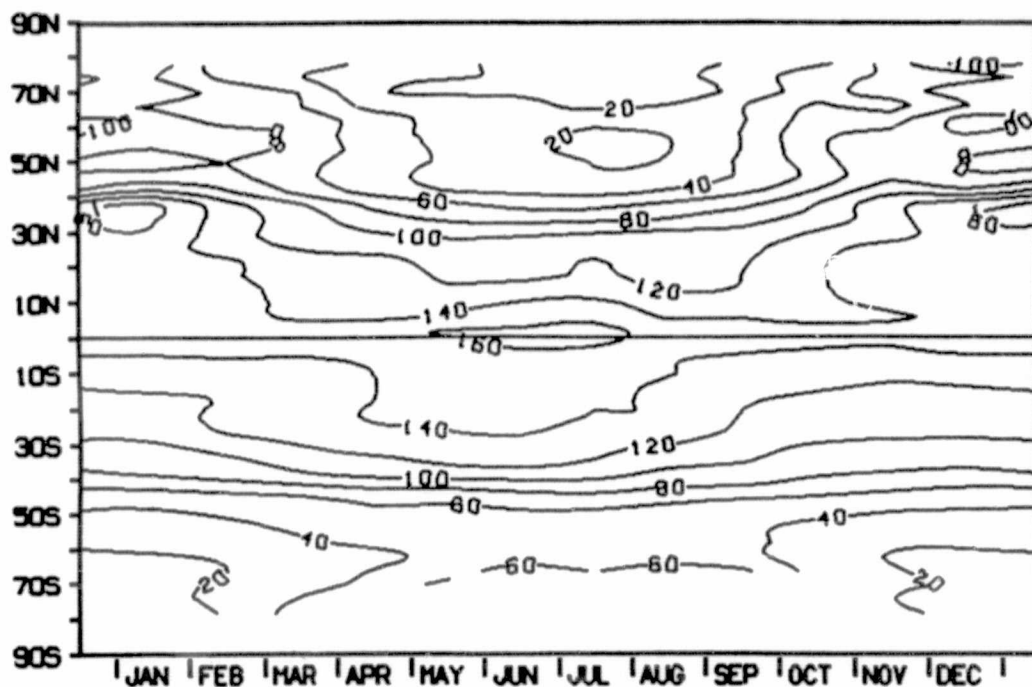


Fig. 1. Zonal mean sensible heat flux in W/m^2 from the surface of ice-free ocean. Top panel: simulated by the model. Bottom panel: observations (Esbensen and Kushnir, 1981).

ORIGINAL PAGE IS
OF POOR QUALITY



VALUES RANGE BETWEEN 10.11 AND 165.01 FOR CONTOUR INTERVALS OF 20.00

Zonal mean latent heat flux (W m^{-2})

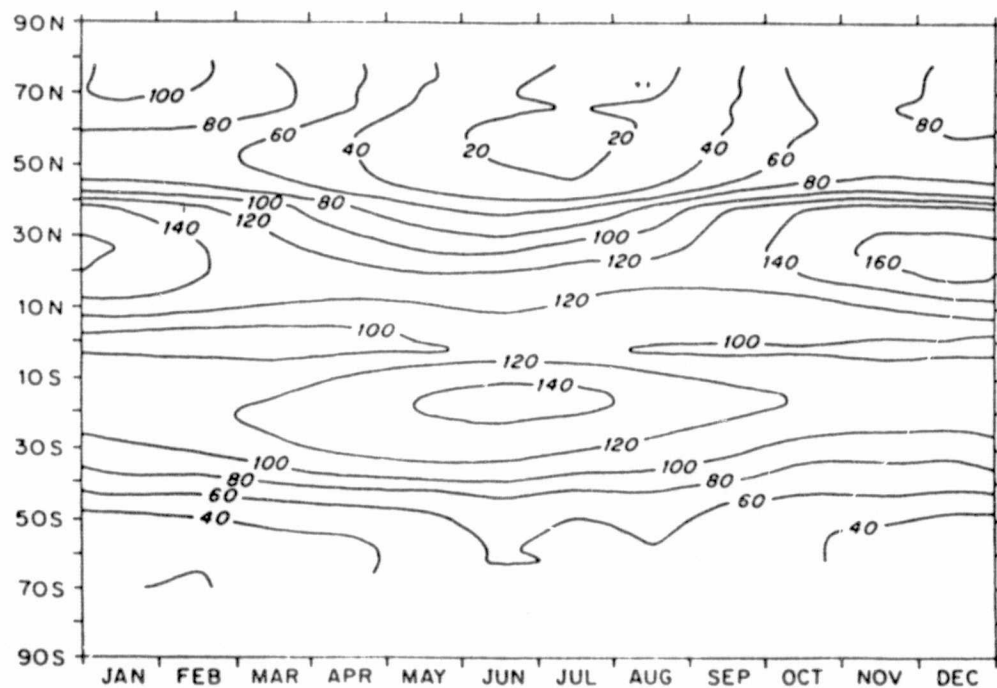
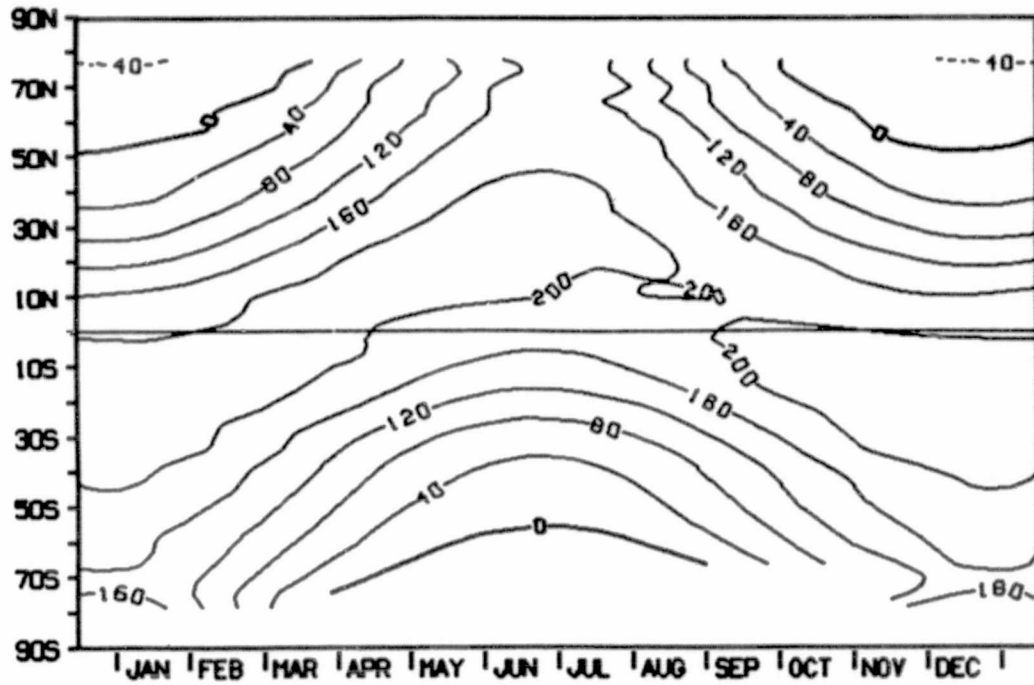


Fig. 2. Zonal mean latent heat flux in W m^{-2} from the surface of ice-free ocean. Top panel: simulated by the model. Bottom panel: observations (Esbensen and Kushnir, 1981).

ORIGINAL PAGE IS
OF POOR QUALITY



VALUES RANGE BETWEEN -44.14 AND 233.65 FOR CONTOUR INTERVALS OF 40.00

(zonal mean net downward radiative flux (W m⁻²))

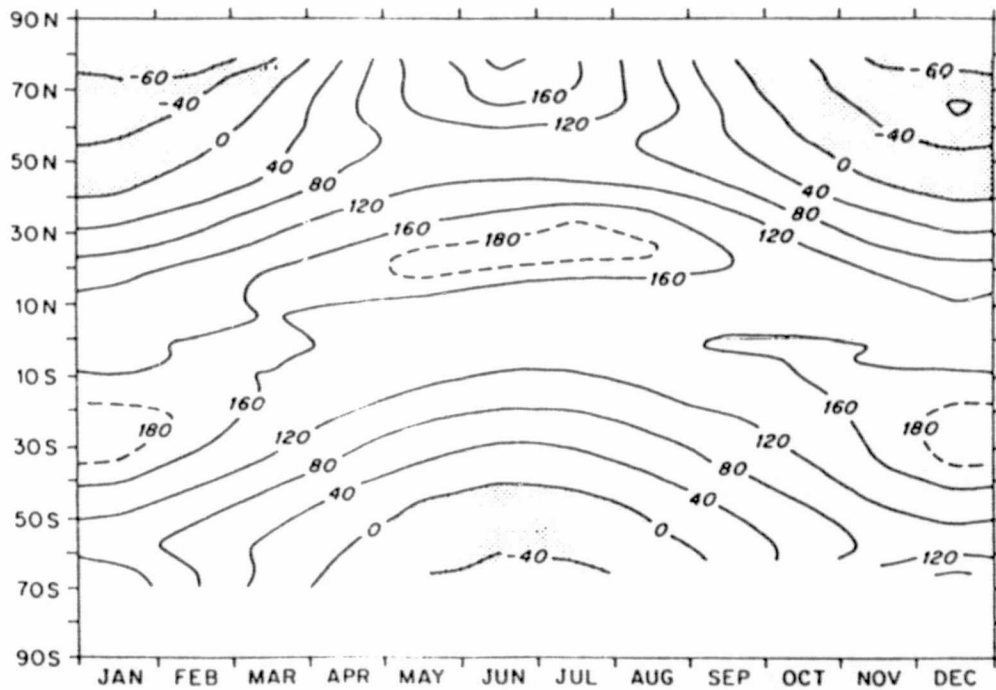
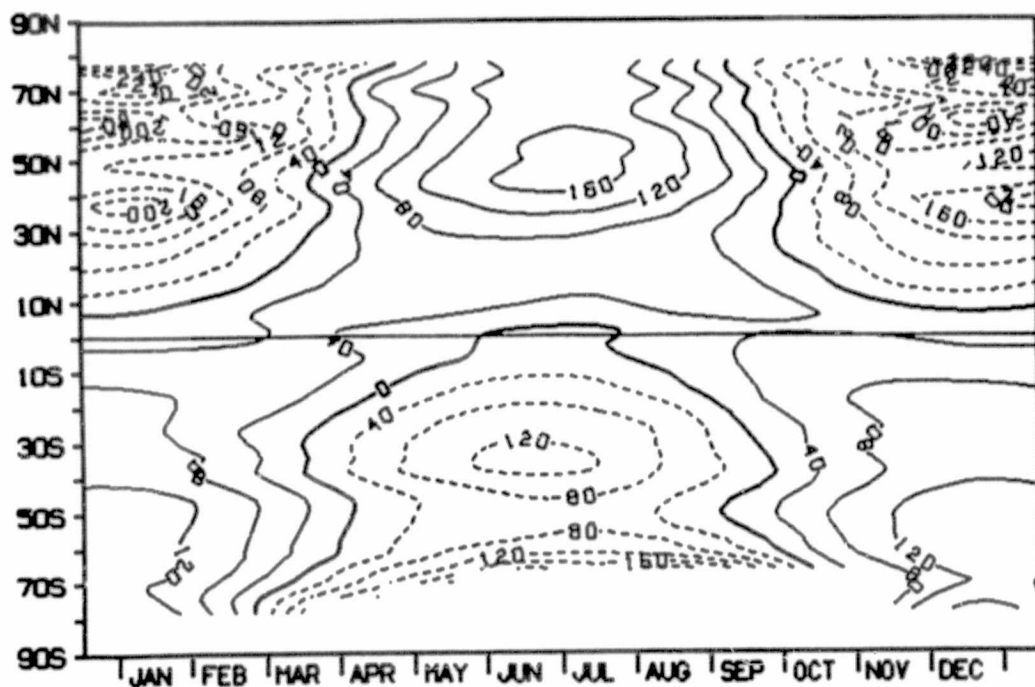


Fig. 3. Zonal mean net radiative flux in W/m^2 into the surface of ice-free ocean. Top panel: simulated by the model. Bottom panel: observations (Esbensen and Kushnir, 1981).

ORIGINAL PAGE IS
OF POOR QUALITY



VALUES RANGE BETWEEN -343.18 AND 173.11 FOR CONTOUR INTERVALS OF 40.00

Zonal mean net downward heat flux ($W m^{-2}$)

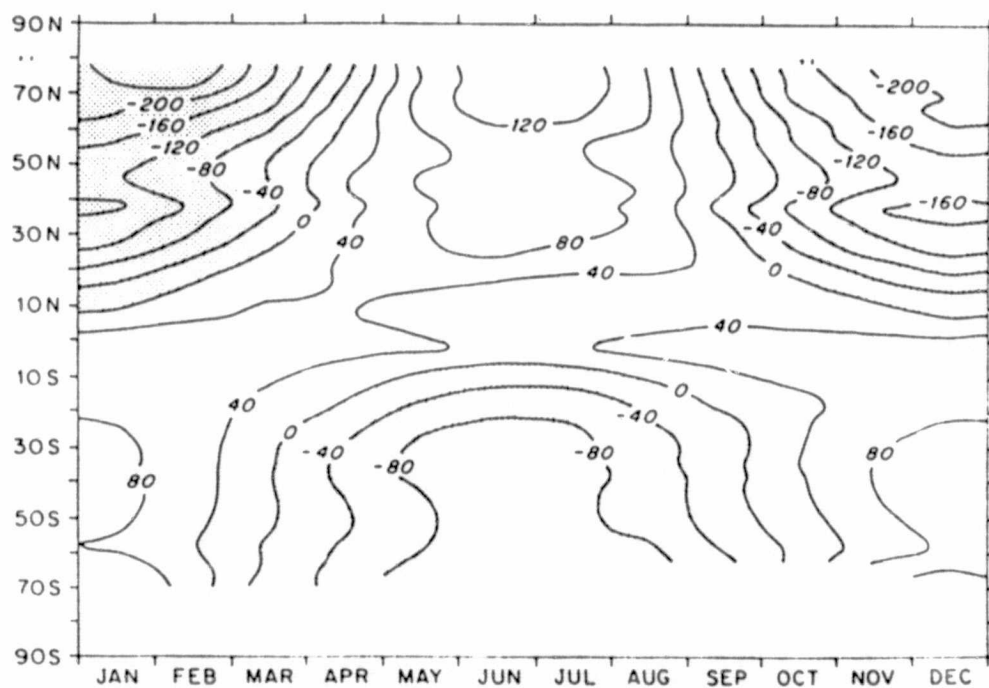
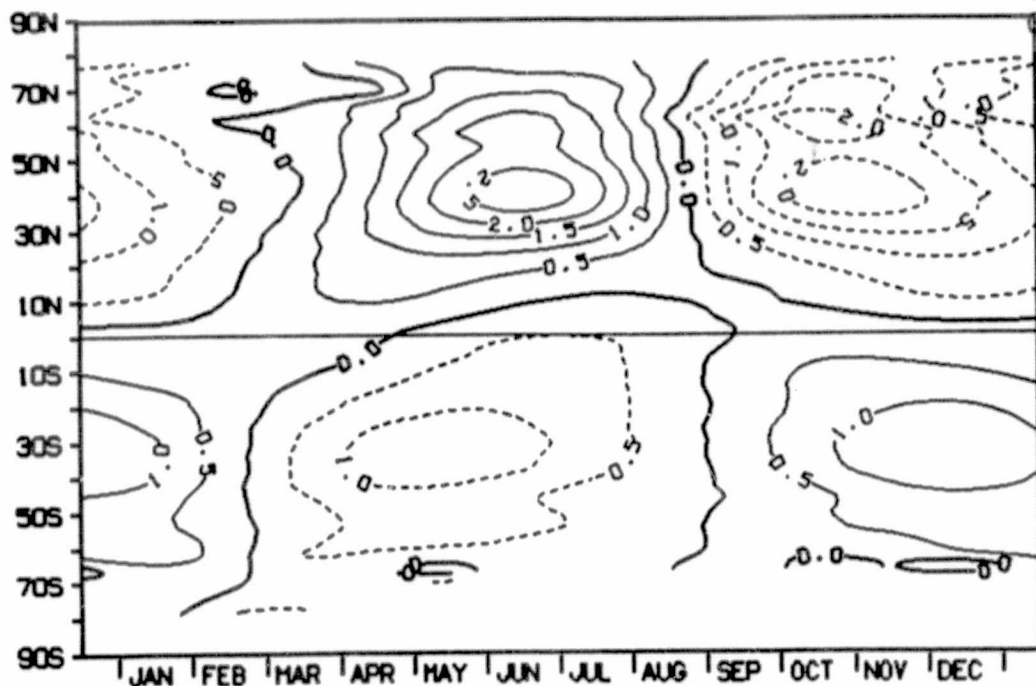


Fig. 4. Zonal mean net downward energy in W/m^2 into the surface of ice-free ocean. Top panel: simulated by the model. Bottom panel: observations (Esbensen and Kushnir, 1981).

ACTUAL SEA SURFACE TEMP CHANGES °C

OCEAN

ORIGINAL PAGE IS
OF POOR QUALITY

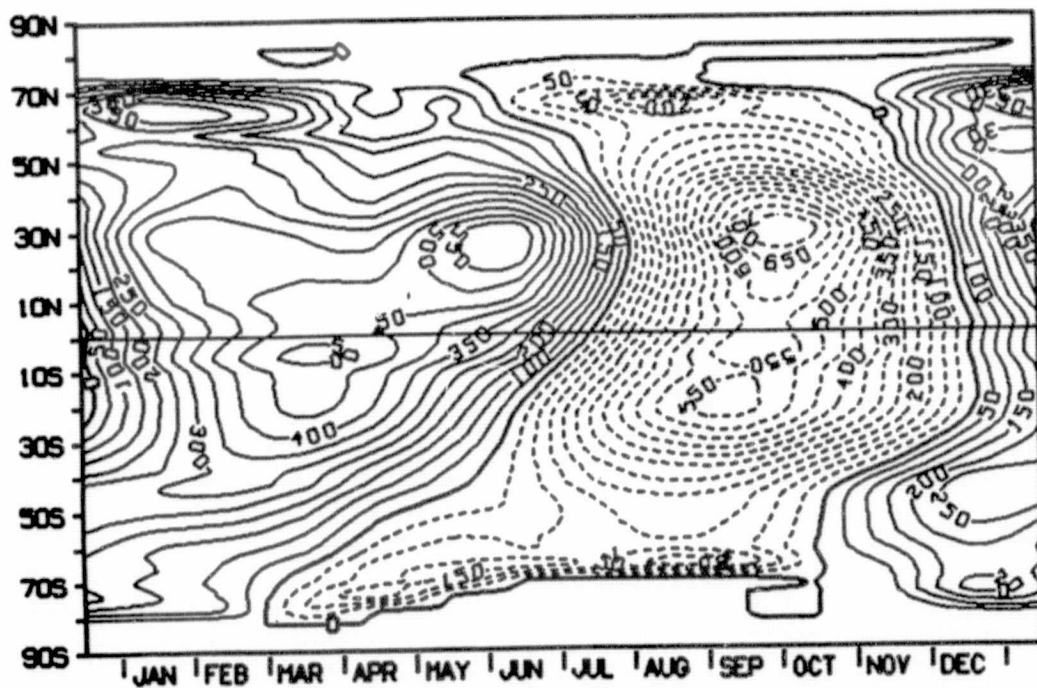


VALUES RANGE BETWEEN -2.28 AND 2.81 FOR CONTOUR INTERVALS OF 0.50

NORTHWARD TRANS NET ENERGY

W/M²

OCEAN



VALUES RANGE BETWEEN -702.45 AND 585.82 FOR CONTOUR INTERVALS OF 50.00

Fig. 5. Zonal mean SST change and northward transport of energy flux in $W m^{-2}$ in the ice-free ocean.

ON THE ROLE OF THE TRANSIENT EDDIES IN MAINTAINING
THE SEASONAL MEAN CIRCULATION

G. H. White and B. J. Hoskins

The role of transient eddies in maintaining the observed local seasonal mean atmospheric circulation was investigated by examining the time-averaged momentum balances and omega equation, using seasonal statistics calculated from daily operational analyses by the European Centre for Medium Range Weather Forecasts. While both the Northern and Southern Hemispheres and several seasons were studied, emphasis was placed upon the Northern Hemisphere during December 1981-February 1982. The results showed that transient eddies played a secondary role in the seasonal mean zonal momentum budget and in the forcing of seasonal mean vertical and ageostrophic motion.

In the time-averaged zonal momentum balance, the advection of zonal momentum by the time-mean flow was found to be primarily balanced by the seasonal mean ageostrophic wind, as Lau (1978) showed. The acceleration of the rotational component of the seasonal-mean zonal flow by the effective transient eddy flux of westerly momentum (Hoskins et al., 1983) is shown in Fig. 1, in which the seasonal mean zonal wind and the vector $\underline{V}_e = (1/f) [(\partial/\partial x) \overline{u'v'} \hat{i} + (\nabla \cdot \underline{E}) \hat{j}]$ at the 250 mb level are plotted for Dec. 1981-Feb. 1982. Here $\underline{E} = (\overline{v'^2} - \overline{u'^2}) \hat{i} - \overline{u'v'} \hat{j}$, $\overline{(\)}$ indicates a time-mean quantity and $(\)' = (\) - \overline{(\)}$ represents the departure from the time-mean, u and v are the zonal and meridional wind and f is the Coriolis parameter. A poleward vector indicates a westerly acceleration of the seasonal mean zonal wind by the effective transient eddy momentum flux, while an equatorward vector implies easterly acceleration. The transient eddy momentum flux is shown in Fig. 1 to accelerate the wind in the jet exit regions. Overall, little correlation was found between the advection of zonal momentum by the time-mean flow and acceleration of the flow by the transient eddy momentum flux.

The forcing of seasonal mean vertical velocity was examined in terms of the Q vector, a solution to the quasigeostrophic omega equation developed by Hoskins and Pedder (1978) and Hoskins et al. (1980) and examined in a time-averaged form by White (1983a). The forcing of vertical velocity by the transient eddies can be written:

$$\underline{\nabla} \cdot [(f^2/2) \partial \underline{V}_e / \partial z] - \underline{\nabla} \cdot [(g/2\overline{\theta}) \underline{\nabla} (\underline{\nabla}_3 \cdot \underline{v}_3' \overline{\theta}')]]$$

where $\overline{\theta}$ is potential temperature, g is the acceleration of gravity, and $\underline{v} = u\hat{i} + v\hat{j} + w\hat{k}$. The first term represents the forcing of vertical motion due to the variation with height of transient eddy momentum (or equivalently, vorticity (Holopainen, 1978)) flux and the second the forcing of vertical motion due to the divergence or convergence of transient eddy heat flux. Figure 2 shows the two terms at 500 mb. Time-filtering has been used to emphasize eddies of time scales associated with baroclinic instability. The two terms are of comparable magnitude. Both show rising motion to the north of the oceanic stormtracks and sinking to the south. The forcing of vertical motion by the seasonal mean flow was found to be substantially larger than the transient eddy forcing and to dominate the pattern of the total forcing of vertical motion.

Since mid-tropospheric Q vectors tend to be proportional in magnitude to and opposite in direction from the upper tropospheric ageostrophic wind (White, 1983a,b), the Q vector can give insight into the relative forcings of the ageostrophic wind by the transient eddies and by the time-mean flow. As can be inferred from Figure 2, such an analysis suggests that transient eddies force an equatorward ageostrophic flow in the upper troposphere over the oceanic storm tracks, and by continuity a poleward flow at low levels. Such a vertical circulation forced by the transient eddies decreases at upper levels the effect of the westerly acceleration due to transient eddy momentum flux convergence and increases it at lower levels, acting to decrease the vertical shear of the zonal flow and increase surface westerlies over the midlatitude oceans. The component of the ageostrophic wind associated with the transient eddies, however, appeared significantly smaller than the total ageostrophic wind.

Such an analysis does not consider the possible role of transient eddies as a catalyst, either dynamically or by latent heat release over the oceanic storm tracks, for the time-mean flow.

REFERENCES

- Holopainen, E. O., 1978: On the dynamic forcing of the long-term mean flow by the large-scale Reynolds' stresses in the atmosphere. J. Atmos. Sci., 35, 1596-1604.
- Hoskins, B. J., and M. A. Pedder, 1980: The diagnosis of middle latitude synoptic development. Quart. J. Roy. Meteor. Soc., 106, 707-720.
- Hoskins, B. J., I. Draghiçi, and H. C. Davies, 1978: A new look at the ω -equation. Quart. J. Roy. Meteor. Soc., 104, 31-38.
- Hoskins, B. J., I. N. James, and G. H. White, 1983: The shape, propagation and mean-flow interaction of large-scale weather systems. J. Atmos. Sci., 40, 1595-1612.
- Lau, N.-C., 1978: On the three-dimensional structure of the observed transient eddy statistics of the Northern Hemisphere wintertime circulation. J. Atmos. Sci., 35, 1900-1923.
- White, G. H., 1983a: Estimates of the seasonal mean vertical velocity fields of the extratropical Northern Hemisphere. Mon. Wea. Rev., 111, 1418-1433.
- White, G. H., 1983b: The Global Circulation of the Atmosphere December 1981-November 1982 Based on ECMWF Analyses. Technical Report, Dept. Meteor., University of Reading, U.K., 209 pp.

1

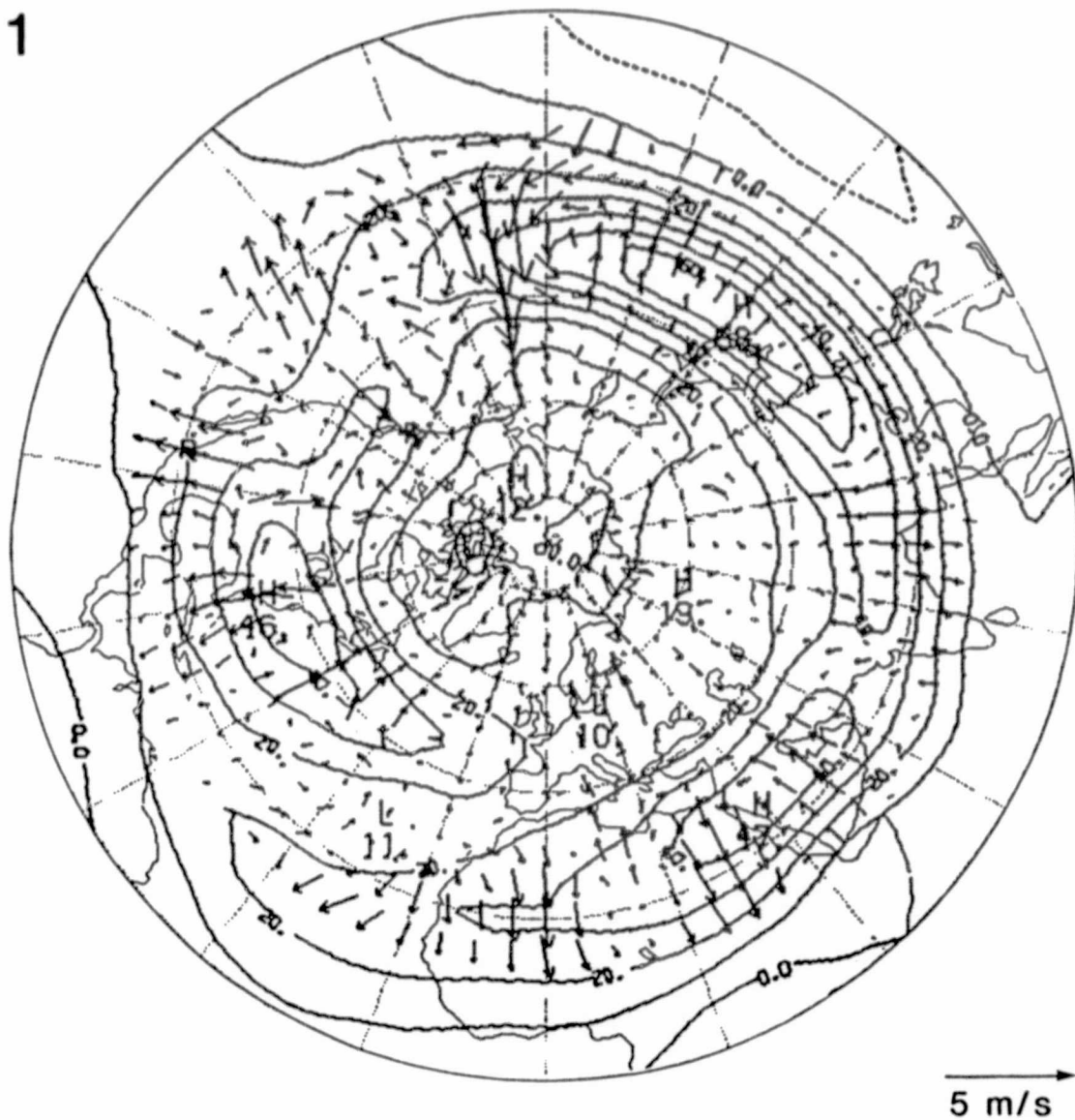
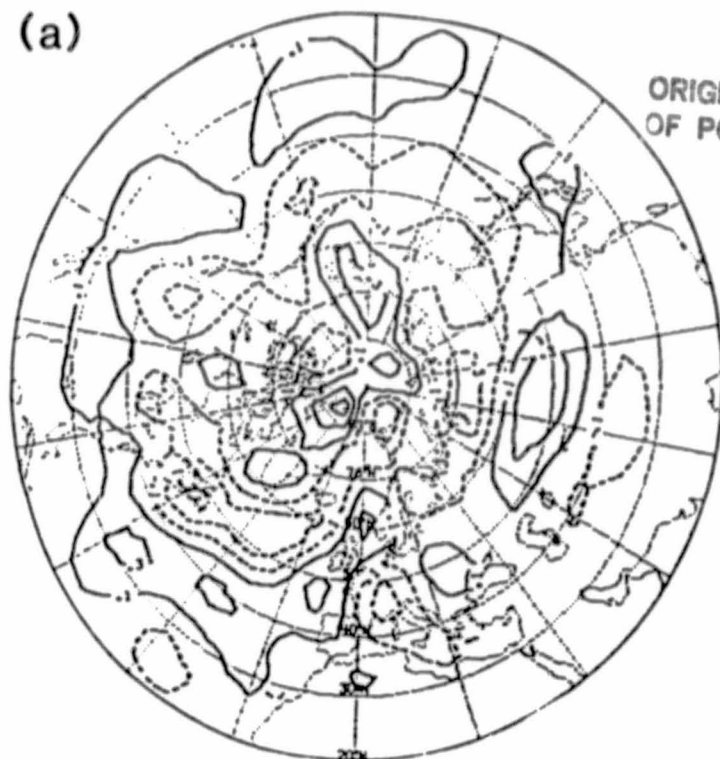


Figure 1. The seasonal mean zonal wind (contour interval 10 m/s) and $\bar{v}_e = 1/f (\partial/\partial x \overline{u'v'} \hat{i} + (\nabla \cdot \mathbf{E}) \hat{j})$ at 250 mb for December 1981-February 1982. The edge of the map is the equator; latitude and longitude markings occur every 20°. A poleward vector indicates a westerly acceleration of the seasonal mean zonal wind by the effective transient eddy momentum flux; an equatorward vector easterly acceleration.

2

(a)

ORIGINAL PAGE IS
OF POOR QUALITY

(b)

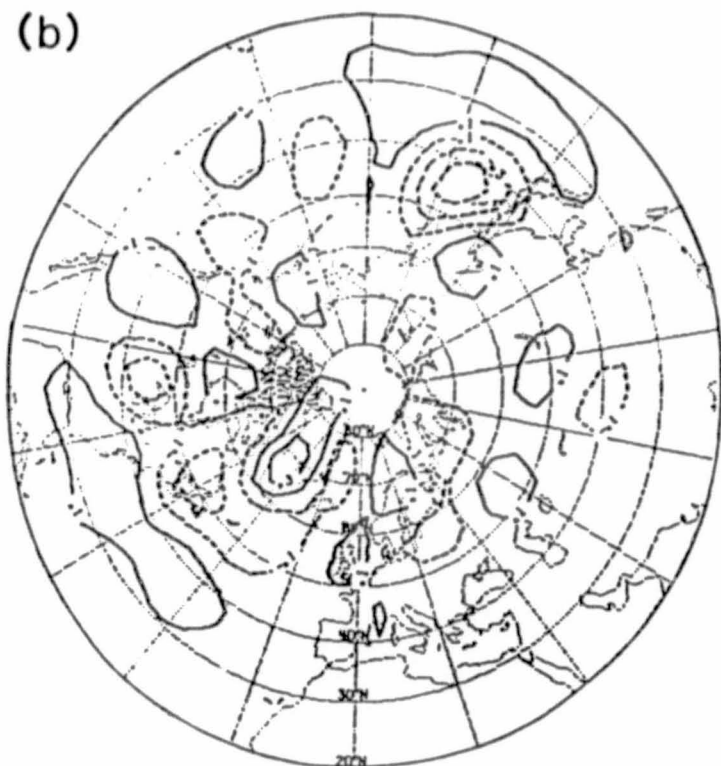


Figure 2. The forcing of seasonal mean vertical motion at 500 mb by: a) the transient eddy momentum flux, and b) the transient eddy heat flux during December 1981-February 1982. Contours $-.5, -.3, -.1, .1, .3 \times 10^{-18} \text{ s}^{-3} \text{ m}^{-1}$. Dashed indicates the forcing of rising motion, solid the forcing of sinking motion. The data has been high-pass filtered to emphasize eddies of baroclinic time scales. The edges of the maps are at 20°N . Latitude circles occur every 10° , longitude lines every 20° .

TWO CONTRASTING NORTHERN HEMISPHERE WINTERS: 1980-81 AND 1981-82

G. H. White

Seasonal statistics calculated from daily operational analyses by the European Centre for Medium Range Weather Forecasts for December 1980-February 1981 (season 1) and December 1981-February 1982 (season 2) were used to contrast the two seasonal mean circulation patterns present in the Northern Hemisphere and to investigate possible causes for the differences.

Fig. 1 shows the isotachs and ageostrophic winds at 250 mb for season 1 (Figure 1a) and season 2 (Figure 1b). The second winter displays a much more zonal flow over western North America and the Atlantic. Local changes between the two seasons of up to 20 m/s in the 250 mb seasonal mean zonal wind were observed. Figure 2 shows the change in 250 mb geopotential height from season 1 to season 2. A similar pattern of weaker magnitude was found at 1000 mb, implying an equivalent barotropic vertical structure. The pattern in Fig. 2 resembles observed teleconnection patterns (Wallace and Gutzler, 1981) and patterns of variability associated with the Southern Oscillation. It is opposite in sign but similar in pattern and comparable in magnitude north of 30°N to the height anomaly (from climatology) for January 1983, when a record negative Southern Oscillation index and large negative anomalies in outgoing infrared radiation (implying strong latent heat release) in the eastern equatorial Pacific were observed (National Meteorological Center (NMC) Climate Analysis Center (CAC), private communication). The change in 150 mb winds from season 1 to season 2 resembled the difference found by Arkin (1982, Figure 5) between opposite phases of the Southern Oscillation. While season 1 occurred in a negative phase of the Southern Oscillation and season 2 in a positive phase, in neither season was a strong Southern Oscillation Index observed (NMC CAC, private communication). Neither were large differences in outgoing IR between season 1 and season 2 observed in the eastern equatorial Pacific.

The relationship of changes in the transient eddies to changes in the time-mean flow was also examined. Differences between the two seasons in the baroclinic instability of the seasonal mean lower troposphere as measured by Charney's (1947) baroclinic height scale (White, 1982) appeared to be associated with changes in the position and intensity of the storm tracks, suggesting that changes in the time-mean flow may be responsible for changes in the transient eddies. Changes in the lower tropospheric transient eddy heat flux from season 1 to season 2 acted to dissipate differences in the lower tropospheric seasonal mean thermal field. Changes in the transient eddies appeared to play a secondary role in the changes in the time-averaged zonal momentum balance, in the seasonal mean ageostrophic wind and in the forcing of seasonal mean vertical motion. Thus transient eddies did not appear to be a major cause of the differences between season 1 and season 2, although the possibility that transient eddies act as a "catalyst" in forcing the seasonal mean flow while seeming unimportant in balance and maintenance equations cannot be excluded.

The vertically averaged seasonal mean zonal wind and E vector, a measure of the anisotropy of the transient eddies (Hoskins *et al.*, 1983) over the Pacific is shown in Figure 3 for season 1 (Figure 3a) and season 2 (Figure 3b). The pattern in season 2, but not season 1, resembles that found by Simmons *et al.*

(1983) in a modeling study of barotropic instability. One possible explanation for the differences between season 1 and season 2 is a weak change in tropical heating associated with the Southern Oscillation, the effect of which in mid-latitudes was amplified by the occurrence of barotropic instability over the Pacific in season 2, but not season 1.

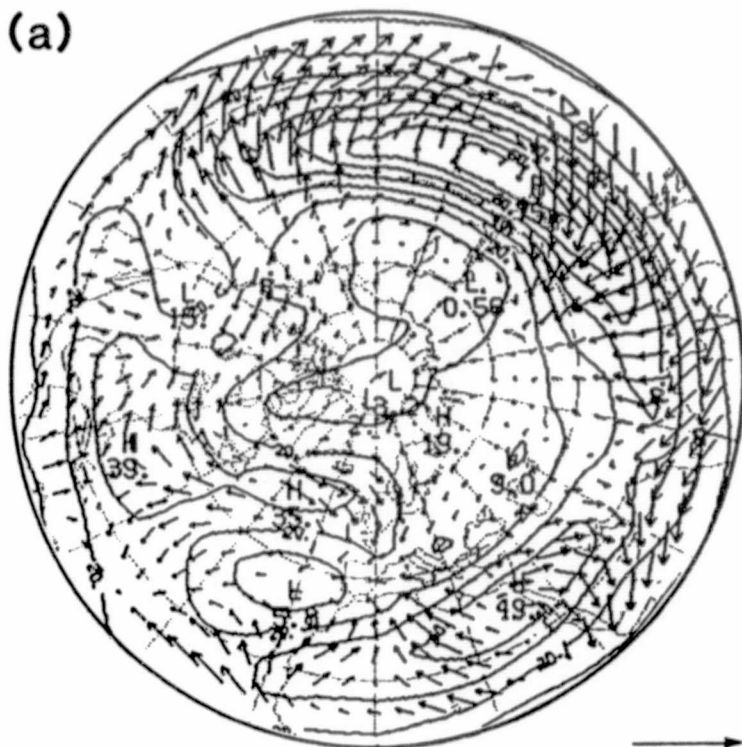
REFERENCES

- Arkin, P. A., 1982: The relationship between interannual variability in the 200 mb tropical wind field and the Southern Oscillation. Mon. Wea. Rev., 110, 1393-1404.
- Charney, J. G., 1947: The dynamics of long waves in a baroclinic westerly current. J. Meteor., 4, 135-162.
- Hoskins, B. J., I. N. James, and G. H. White, 1983: The shape, propagation and mean-flow interactions of large-scale weather systems. J. Atmos. Sci., 40, 1595-1612.
- Simmons, A. J., J. M. Wallace, and G. W. Branstator, 1983: Barotropic wave propagation and instability, and atmospheric teleconnection patterns. J. Atmos. Sci., 40, 1363-1392.
- Wallace, J. M., and D. S. Gutzler, 1981: Teleconnections in the geopotential height field during the Northern Hemisphere winter. Mon. Wea. Rev., 109, 784-812.
- White, G. H., 1982: An observational study of the Northern Hemisphere extratropical summertime general circulation. J. Atmos. Sci., 39, 24-40.

ORIGINAL PAGE IS
OF POOR QUALITY

1

(a)



15 m/s

(b)

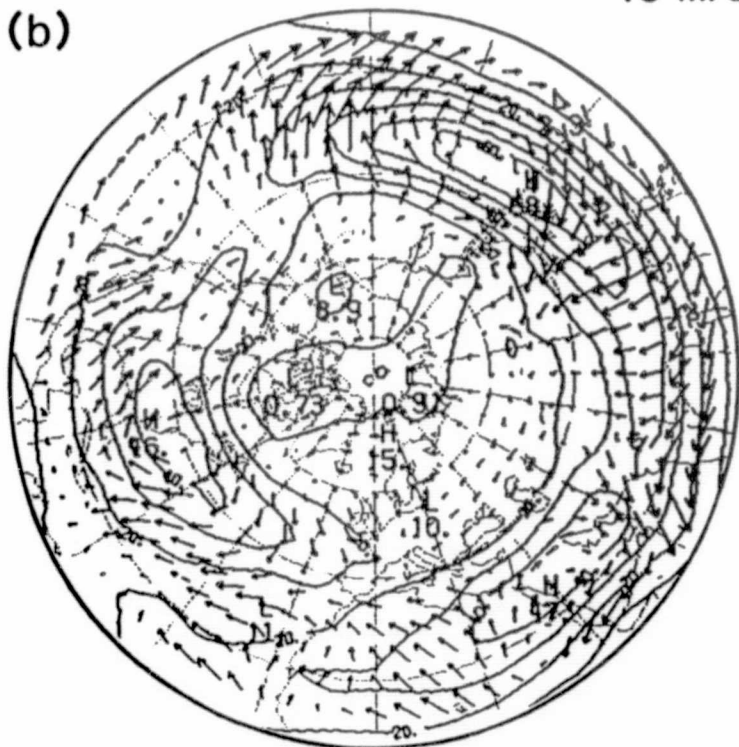


Fig. 1. Seasonal mean isotachs (contour interval 10 m/s) and ageostrophic winds at 250 mb for a) December 1980-February 1981, and b) December 1981-February 1982. The edge of the map is 10°N.

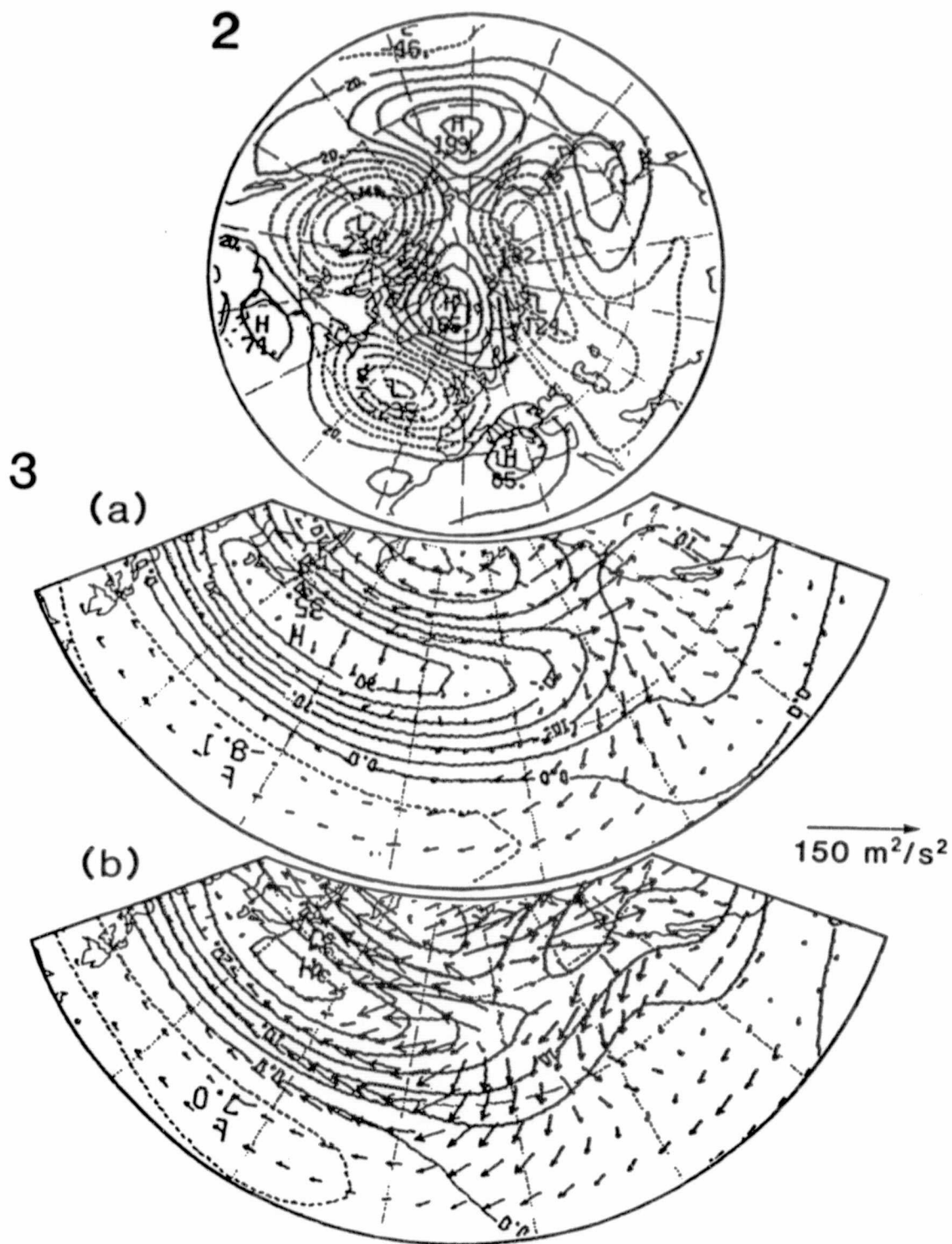


Fig. 2. Change in seasonal mean 250 mb geopotential height from December 1980-February 1981 to December 1981-February 1982. Contours at ... -60 m, -20 m, 20 m, 60 m, ... Edge of the map is 20°N.

Fig. 3. Vertically averaged seasonal mean zonal wind (contour interval is 5 m/s; dashed depicts easterlies) and $\bar{E} [=(\overline{v'^2-u'^2}) \uparrow - \overline{u'v'} \downarrow]$ for a) December 1980-February 1981 and b) December 1981-February 1982. Map is a sector from 120°E to 100°W. Latitude circles every 20°.

B. CLIMATE MODELING

ORIGINAL PAGE IS
OF POOR QUALITY

N84 22088

239

PROSPECTS FOR IMPROVEMENT OF ZONAL MEAN TEMPERATURES
IN THE UCLA GENERAL CIRCULATION MODEL

T. Corsetti, M. J. Suarez and D. A. Randall

Recent versions of the UCLA GCM have used the scheme proposed by Katayama for the calculation of long-wave radiative cooling rates. This scheme is described in Schlesinger (1976). In the near future we plan to start using the scheme of Chou (1983) and Harshvardhan (1984). In preparation for this change we've made a number of off-line calculations to test the new code. The results of these, which we present here, suggest that the new scheme should alleviate the model's "cold pole" problem.

The first figure shows the meridional cross-section of January zonal mean temperature produced by a 15-layer version of the model using Katayama's scheme. For comparison, January 1979 temperatures from the ECMWF analysis are also shown. The model produces a high, relatively warm tropical tropopause, and unrealistically low temperatures at high latitudes. The difference between the two is shown in Figure 2. The largest "errors" in the northern hemisphere are at $\sim 70^\circ\text{N}$ and 15 km, where the simulation is 20° colder than January 1979. Note also the low temperatures near the surface at the winter pole.

As a test preliminary to a long GCM calculation we took the simulated temperatures shown in Figure 1, as well as simulated humidities, and computed infrared cooling rates using both codes. For simplicity, both calculations were done without clouds. Figure 3 shows the difference between the two. Regions where the Katayama scheme cools more than the new code have dashed contours. Thus the initial tendency of using the Harshvardhan code will be to warm these regions and cool regions with solid contours. The general pattern is remarkably similar to the pattern of errors shown in Figure 2. In particular, in high latitude the distribution of the lower troposphere and the warming in the upper stratosphere are of the right sign to correct errors in the simulation.

A more definitive assessment will have to await the full GCM calculation, but we feel these results hold promise of a significant improvement in the model's zonal mean climatology.

REFERENCES

- Harshvardhan, 1984: Longwave radiation parameterization for the UCLA/GLAS GCM. In preparation.
- Chou, M.-D., 1984: Broadband water vapor transmission functions for atmospheric I.R. flux computations. Submitted to J. Atmos. Sci.
- Schlesinger, M. E., 1976: A numerical simulation of the general circulation of atmospheric ozone. Ph.D. Thesis, Dept. Atmos. Sci., University of California, Los Angeles, CA 90024, 376 pp.

PRECEDING PAGE BLANK NOT FILMED

215

PAGE 216 INTENTIONALLY BLANK

ORIGINAL PAGE IS
OF POOR QUALITY

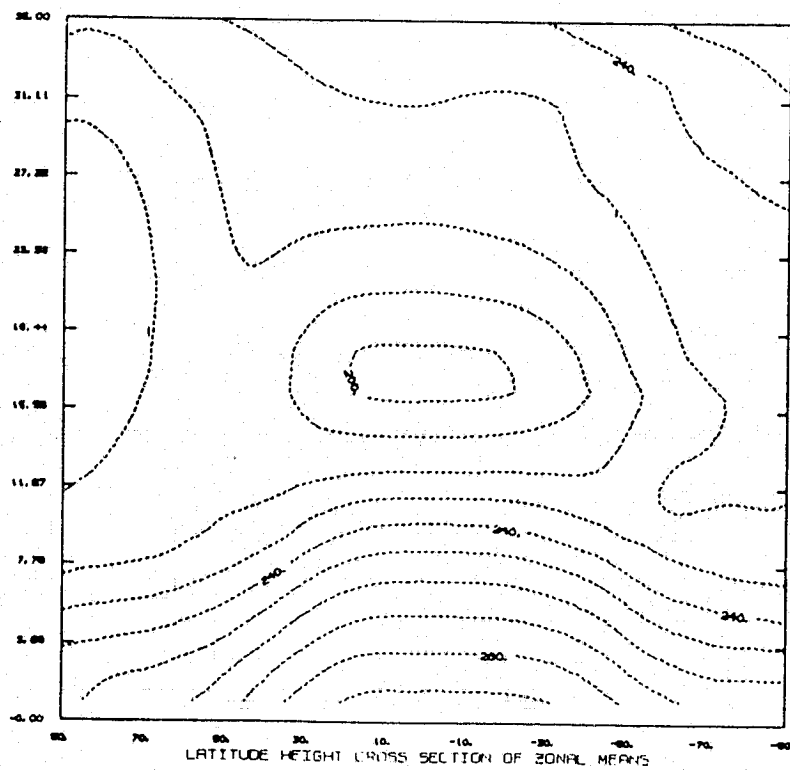
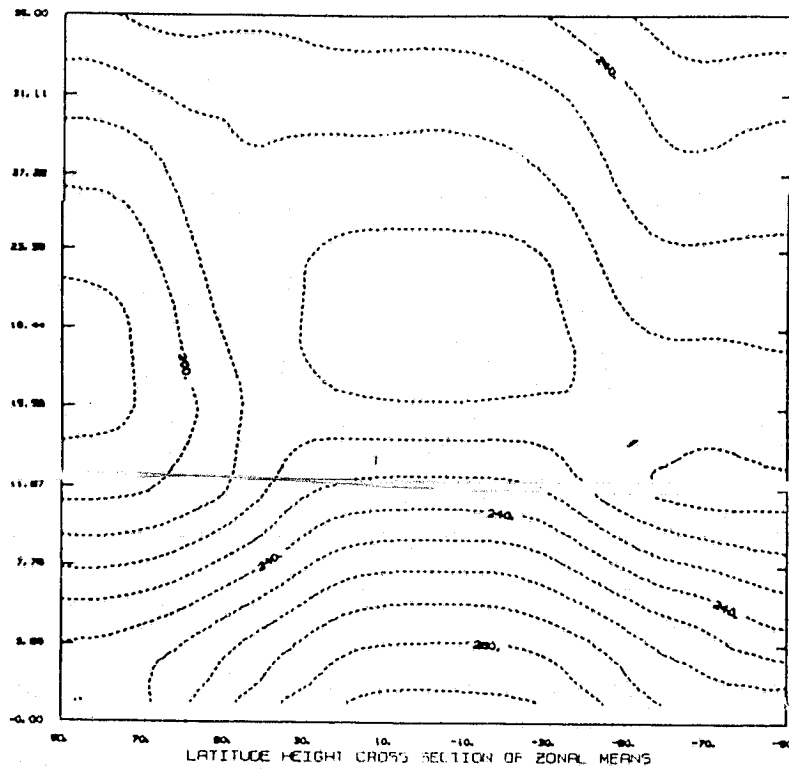


Figure 1. Top panel: January mean temperatures simulated by the UCLA model using Katayama's radiation scheme. Bottom panel: Observed January 1979 temperatures from ECMWF analysis.

ORIGINAL PAGE IS
OF POOR QUALITY

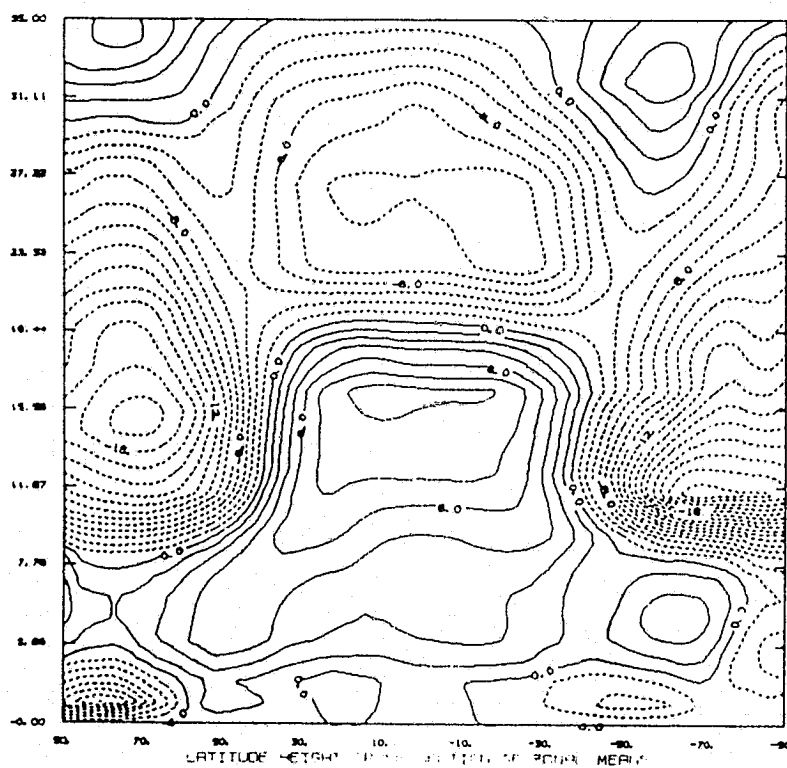


Figure 2. January mean temperature difference (computed-observed).

ORIGINAL PAGE IS
OF POOR QUALITY

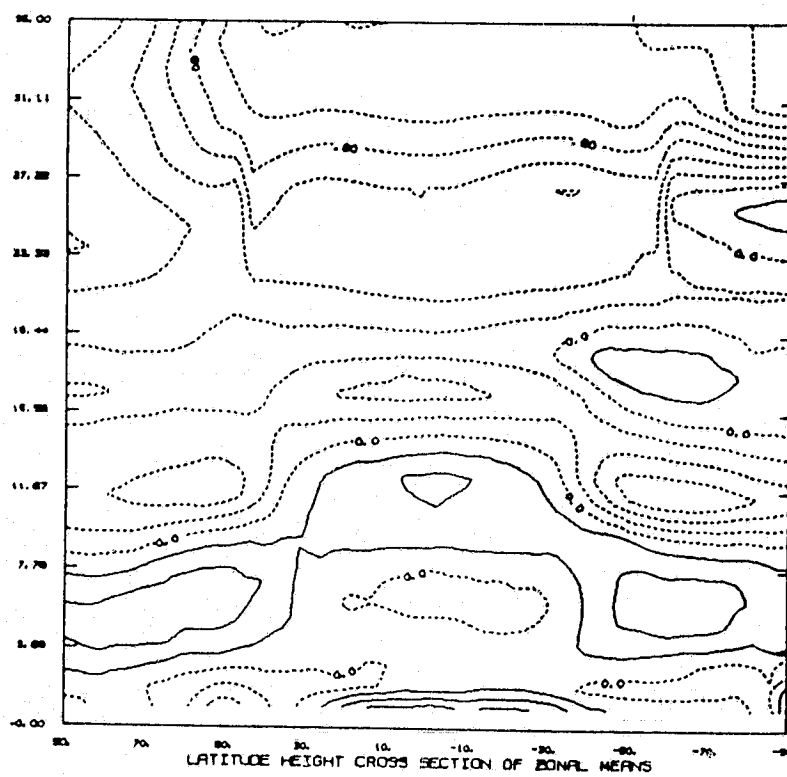


Figure 3. Difference in heating rates produced by the two radiation schemes using the "computed" temperatures shown in Figure 1.

FORCED STATIONARY SOLUTIONS IN A BAROTROPIC CHANNEL:
MULTIPLE EQUILIBRIA AND THEORY OF NONLINEAR RESONANCE

S. Rambaldi, K. C. Mo and J. Shukla

We have studied a barotropic flow over sinusoidal topography in a beta channel in the presence of forcing and dissipation.

Our work can be divided into two main parts: in the first part we have computed numerically the stationary solutions of the model, using Newton's method together with a finite difference approximation, and we have compared our solutions with the solutions of the linear theory; in the second part we have successfully developed a nonlinear theory that reproduce, very closely, our numerical solutions.

In the first part of the work we have shown the following results:

- i) In our model multiple equilibria do exist, i.e. multiple equilibria are not artificially introduced by the mathematical technique of crude truncation previously used, but they are a consequence of the resonance present in our physical system.
- ii) Even if we are dealing with a small topography (we have considered Fourier components of the real topography which have amplitudes of a few hundred meters, small values compared with the depth of the atmosphere) the linear theory fails in the region close to the resonance to give forced waves with amplitude of any relevance.

In the second part of this work we have studied carefully, with an appropriate spectral decomposition, the nonlinear interactions, and we have pointed out how the linear solution must be modified as the system goes close to the resonance.

We have shown how to split the nonlinear interaction term into two parts, one always negligible (for small topography) and another one crucial when the system is close to the resonance.

Based on these considerations, we have developed a nonlinear theory that successfully explains the qualitative and quantitative features of the numerical solutions.

The striking difference from the linear and the nonlinear theory can be seen from the following figures.

In Fig. 1a we show the amplitude of the streamfunction of the forced wave in phase with respect to the wavenumber 3 topography; in Fig. 1b we show the amplitude of the streamfunction of the forced wave out of phase with respect to the same topography as predicted by linear theory.

In Figs. 2a and 2b we show the same quantities as predicted by our nonlinear theory; these values agree nicely with those obtained with the finite difference model.

We have considered a sinusoidal topography with an amplitude of 400 meters. Different curves correspond to different planetary wavenumbers (from one to five). The nonlinear curves cannot be superimposed.

We observe that:

- a) Our theory predicts generally lower amplitude waves, in particular for the out of phase wave.
- b) The position of the resonance is shifted toward lower values of the mean zonal wind, and is strongly bent.
- c) All the resonance regions of the forced waves with different wavenumbers are more close together, in particular also wavenumber one can resonate for small values of the mean zonal wind.
- d) The nonlinear effects are less important for higher planetary wavenumbers.

ORIGINAL PAGE IS
OF POOR QUALITY.

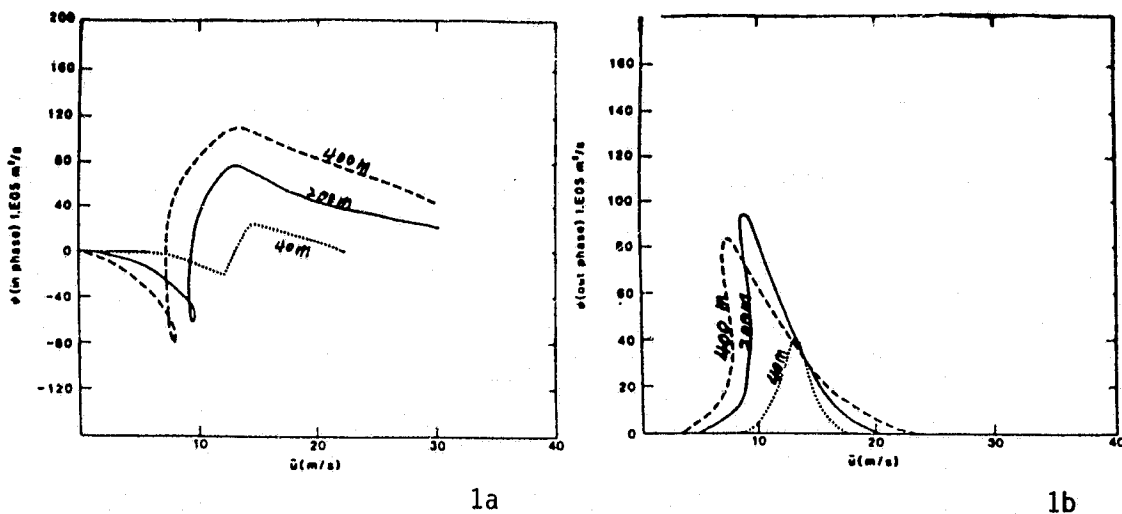


Fig. 1. The streamfunction, (a) in phase (b) out of phase, with the topography in units of $1E05 \text{ m}^2/\text{s}$ for wave 3 with amplitudes of 40 m (dotted line), 200 m (solid line), and 400 m (dashed line).

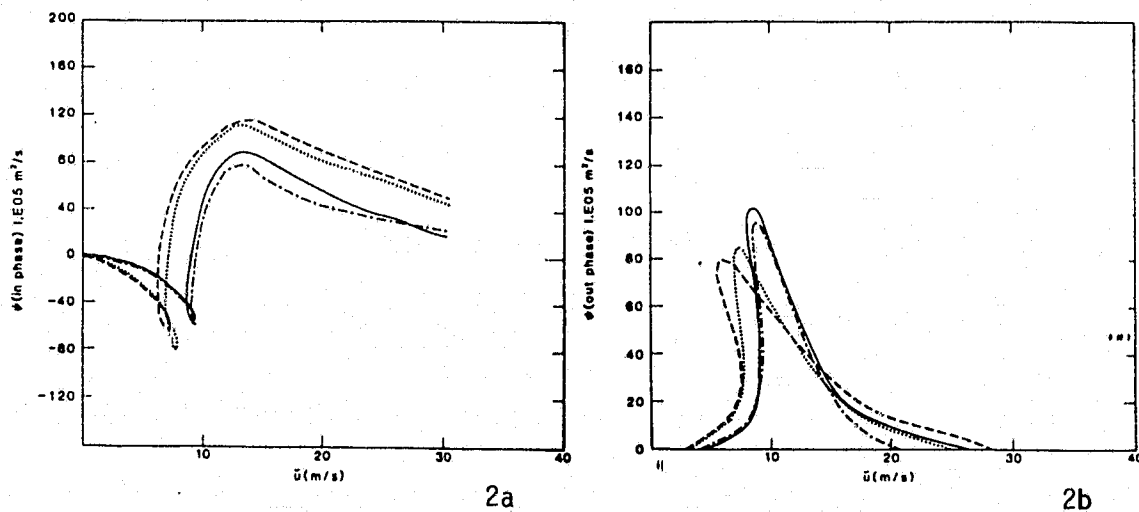


Fig. 2. The streamfunction, (a) in phase (b) out of phase, with the topography in units of $1E05 \text{ m}^2/\text{s}$ for wave 3 with amplitudes of $h=200 \text{ m}$ and 400 m (line), 200 m (solid line), and 400 m (dashed line):

- $h = 200 \text{ m}$ nonlinear theory
- · - · - $h = 200 \text{ m}$ numerical methods
- - - $h = 400 \text{ m}$ nonlinear theory
- · · · · $h = 400 \text{ m}$ numerical methods

D41
N84 22090

STRATOCUMULUS SIMULATIONS WITH A GENERAL CIRCULATION MODEL

D. A. Randall, J. Abeles, and M. Suarez

Stratus and stratocumulus cloud sheets are among the most common cloud types over the world. They are characteristic of the undisturbed subtropical marine boundary layer over the eastern oceans (Lilly, 1968), where cool water and large-scale sinking motion suppress penetrative cumulus convection. They also occur over the Arctic Ocean, particularly in summer (Vowinckel and Orvig, 1970), and behind cold outbreaks over the western oceans in winter. Observational studies have been conducted by Neiburger *et al.* (1961), Brost *et al.* (1981a,b), Caughey *et al.* (1982), and Hanson (1983). Further observations are now being planned under the auspices of FIRE¹.

Results will be presented from the 9-level version of the GCM, which has its top at 50 mb. The GCM uses a modified sigma coordinate, in which the PBL top is a coordinate surface, and the PBL itself is the lowest model layer. The PBL depth is a prognostic variable of the model. The mass sources and sinks for the PBL consist of large-scale convergence or divergence, turbulent entrainment, and the cumulus mass flux. This cumulus mass flux is determined by using the cumulus parameterization of Arakawa and Schubert (1974). The model includes both the diurnal and seasonal cycles. Further description of the GCM is given by Suarez *et al.* (1983) and references therein.

Stratocumulus clouds are assumed to be present in the PBL whenever the temperature and mixing ratio at the PBL top (as determined by a mixed-layer assumption) correspond to supersaturation, provided that the stability criterion of Randall (1980a) is met. The presence of stratocumulus clouds is felt by the GCM in two ways. First, the solar and terrestrial radiation parameterizations of the model recognize the existence of the stratocumulus clouds. Second, the parameterization of turbulent entrainment takes into account the generation of turbulence kinetic energy through buoyancy fluxes associated with cloud-top radiative cooling and phase changes (Randall, 1980b, 1983). As a result of these buoyancy fluxes, presence of a stratocumulus layer in the PBL tends to favor more rapid entrainment and, therefore, a deeper PBL.

When the PBL top is supersaturated but the cloud-top entrainment stability criterion (Randall, 1980a) is not met, the PBL is assumed to exchange mass with the free atmosphere. The amount of mass exchange is that required to remove the supersaturation, or to restore stability, whichever is less. The PBL depth is assumed to remain uncharged during this process. We refer to this as "layer cloud instability" (LCI).

Fig. 1a shows the simulated January distribution of stratocumulus depth. Maxima occur over the Gulf Stream and Kuroshio, in qualitative agreement with observations (Chou and Atlas, 1981; Ninomiya and Akiyama, 1976). Figs. 2a, b, c, and d show the time-evolution of the stratocumulus depth, surface air temperature, meridional surface wind component, and surface buoyancy flux at 130°E longitude, 26°N latitude (in the region of the Kuroshio) for the first 20 days of January.

¹ FIRE is the First ISCCP Regional Experiment. The ISCCP is the International Satellite Cloud Climatology Project.

Three well-defined cold-air outbreaks are evident; all three are accompanied by PBL stratocumulus clouds.

Fig. 1a also shows January maxima of stratocumulus depth off the west coasts of South America and South Africa, in agreement with observations.

The simulated July distribution of stratocumulus depth is shown in Fig. 1b. Maxima are evident off the west coasts of North America, South America, South Africa, and Australia. The positions of these maxima are in good agreement with observations (e.g., Neiburger et al., 1961; Miller and Feddes, 1971), but the clouds occur too infrequently.

Future efforts to improve the parameterization will focus on improving the simulated frequency of stratocumulus occurrence in the marine subtropics, devising a more realistic parameterization of cloud-top entrainment instability and the associated fractional cloudiness, and understanding why the model does not produce a realistic summer maximum of Arctic stratus.

Future applications of the parameterization will include attempts to forecast the formation, evolution, and destruction of observed stratus decks, through numerical weather prediction experiments.

REFERENCES

- Arakawa, A., and W. H. Schubert, 1974: The interaction of a cumulus cloud ensemble with the large-scale environment, Part I. J. Atmos. Sci., 31, 674-701.
- Brost, R. A., D. H. Lenschow, and J. C. Wyngaard, 1982: Marine stratocumulus layers. Part I: Mean conditions. J. Atmos. Sci., 39, 800-817.
- Brost, R. A., J. C. Wyngaard, and D. H. Lenschow, 1982: Marine stratocumulus layers. Part II: Turbulence budgets. J. Atmos. Sci., 39, 818-836.
- Caughey, S. J., B. A. Crease, and W. T. Roach, 1982: A field study of nocturnal stratocumulus: II. Turbulence structure and entrainment. Quart. J. Roy. Met. Soc., 108, 125-144.
- Chou, S.-H., and D. Atlas, 1982: Satellite estimates of ocean-air heat fluxes during cold air outbreaks. Mon. Wea. Rev., 110, 1434-1450.
- Hanson, H. P., 1983: EPOCS 1981 Summary Data Report: Aircraft measurements of radiation, turbulent transport, and profiles in the atmospheric and oceanic boundary layers of the Pacific off California. NOAA Technical Memo. ERL ESG-1, 157 pp.
- Lilly, D. K., 1968: Models of cloud-topped mixed layers under a strong inversion. Quart. J. Roy. Meteor. Soc., 94, 292-309.
- Miller, D. B., and R. G. Feddes, 1971: Global atlas of relative cloud cover 1967-1970. Joint production by U.S. Dept. of Commerce and U.S. Air Force. Washington, DC, September, 1971.

- Neiburger, M., D. S. Johnson, and C.-W. Chien, 1961: Studies of structure of the atmosphere over the eastern Pacific Ocean in summer. I. The inversion over the eastern north Pacific Ocean. University of California Press. Berkeley and Los Angeles.
- Ninomiya, K., and T. Akiyama, 1976: Structure and heat energy budget of mixed layer capped by inversion during the period of polar outbreak over Kuroshio region. J. Met. Soc. Japan, 54, 117-131.
- Randall, D. A., 1980a: Conditional instability of the first kind, upside-down. J. Atmos. Sci., 37, 125-130.
- Randall, D. A., 1980b: Entrainment into a stratocumulus layer with distributed radiative cooling. J. Atmos. Sci., 37, 148-159.
- Randall, D. A., 1984: Buoyant production and consumption of turbulence kinetic energy in cloud-topped mixed layers. Accepted for publication in J. Atmos. Sci.
- Suarez, M. J., A. Arakawa, and D. A. Randall, 1983: The parameterization of the planetary boundary layer in the UCLA general circulation model: Formulation and results. Mon. Wea. Rev. (to appear).
- Vowinckel, E., and S. Orvig, 1970: The Climate of the North Polar Basin in World Survey of Climatology, Vol. 14, Climates of the Polar Regions. S. Orvig (ed.), New York: Elsevier, 370 pp.

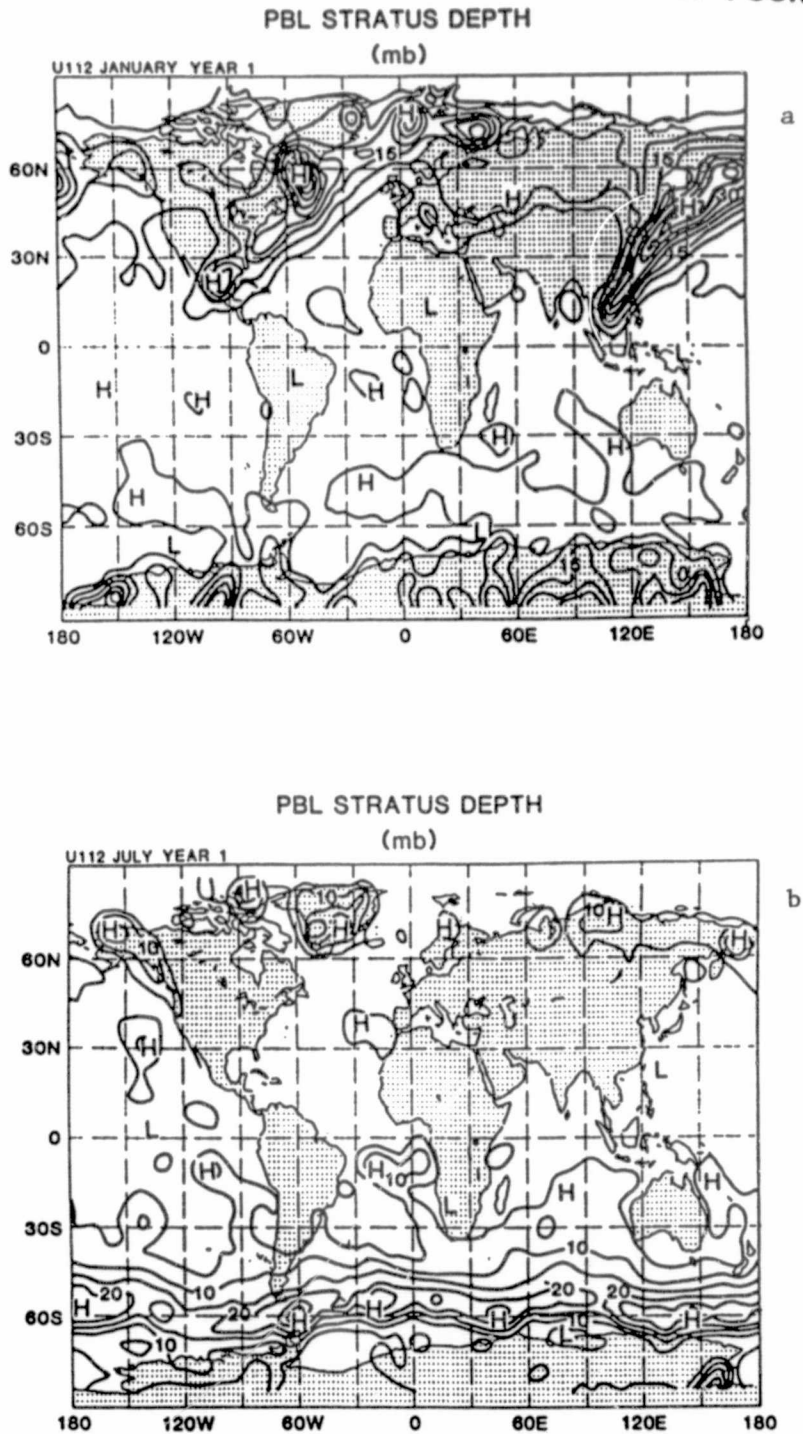


Fig. 1. Simulated monthly mean maps of the simulated PBL stratus depth, in mb, for a) January, and b) July. The contour interval is 5 mb.

ORIGINAL PAGE IS
OF POOR QUALITY

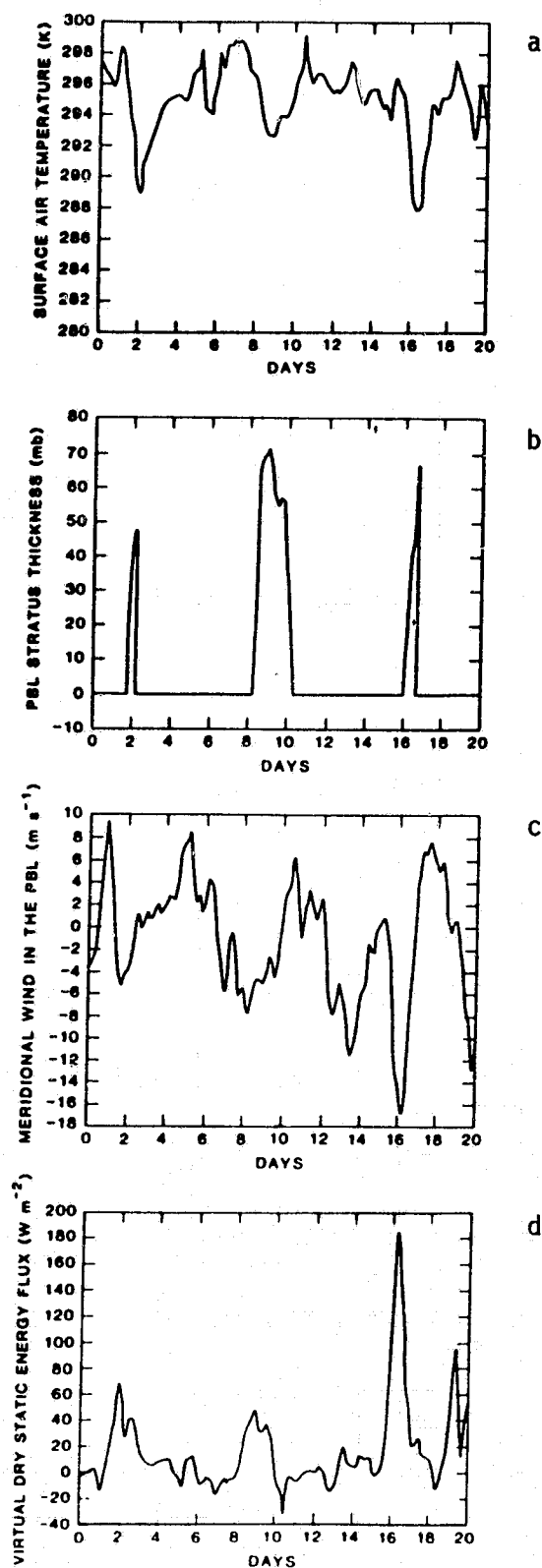


Fig. 2. Simulated time-evolution for the first 20 days of January of a) the surface air temperature, b) the PBL stratus thickness in mb, c) the meridional component of the surface wind in m s^{-1} , and d) the surface virtual dry static energy flux in W m^{-2} . The location is 130°E longitude, 26°N latitude.

CLIMATE SENSITIVITY WITH A SEASONAL CYCLE ENERGY BALANCE MODEL

M. J. Suarez

The work of Held, Linder and Suarez (1981) suggests that the sensitivity of climate may have a local maximum as the ice cap passes through a mid-latitude region where the atmosphere's transport efficiency varies strongly with latitude. This behavior, found in a two-level primitive equations climate model forced with annual mean insolation, was then reproduced in an energy balance model (EBM) by making the diffusion coefficient a function of latitude. To illustrate the effect, we take the simplest of energy balance models:

$$\phi) Q + \frac{1}{a^2 \cos \phi} \frac{\partial}{\partial \phi} \cos \phi D(\phi) \frac{\partial T}{\partial \phi}, \quad (1)$$

where ϕ is the latitude, T the surface temperature, Q the solar constant divided by four and A and B are constants. The co-albedo $A(T)$ is discontinuous at a freezing temperature, T_0 . Taking the diffusion coefficient, $D(\phi)$, as a function of latitude as shown in Figure 1 (the figure also gives observed values obtained from the total annual mean atmospheric heat flux and 1000 mb temperature gradient), gives the equilibrium diagram and sensitivity shown in Figures 2 and 3. Comparable diagrams for $D = \text{constant}$ are also shown. The distinctive peak in sensitivity is clearly separate from small and larger ice-cap instabilities, and dependent on the structure of $D(\phi)$.

In this note we show that the effect may still be present in the seasonally varying case. For this purpose we take the two-level seasonally varying EBM described in Suarez and Held (1970), and use the diffusion coefficient of Held, Linder and Suarez (1981). Figure 4 shows the global mean surface temperature vs. solar constant for this model. Two regions of enhanced sensitivity appear. The one at 2.08 ly/min is associated with the approach of the summertime sea ice limit to the region of varying diffusion coefficient. The second, between 2.07 ly/min and 2.06 ly/min is associated with the sudden appearance of a mid-latitude band of perennial snowcover over land. The snowcover distributions around the year for three cases are shown in Figure 5.

REFERENCES

- Held, I. M., D. I. Linder and M. J. Suarez, 1981: Albedo feedback, the meridional structure of the effective heat diffusivity, and climatic sensitivity: Results from dynamic and diffusive models. J. Atmos. Sci., 38, 1911-1927.
- Suarez, M. J., and I. M. Held, 1979: The sensitivity of an energy balance climate model to variations in the orbital parameters. J. Geophys. Res., 32, 4825-4236.

ORIGINAL PAGE IS
OF POOR QUALITY

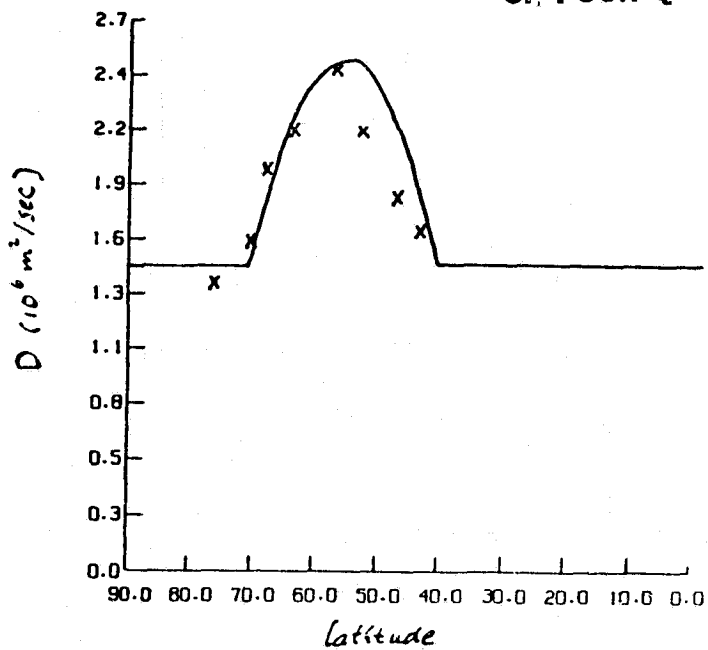
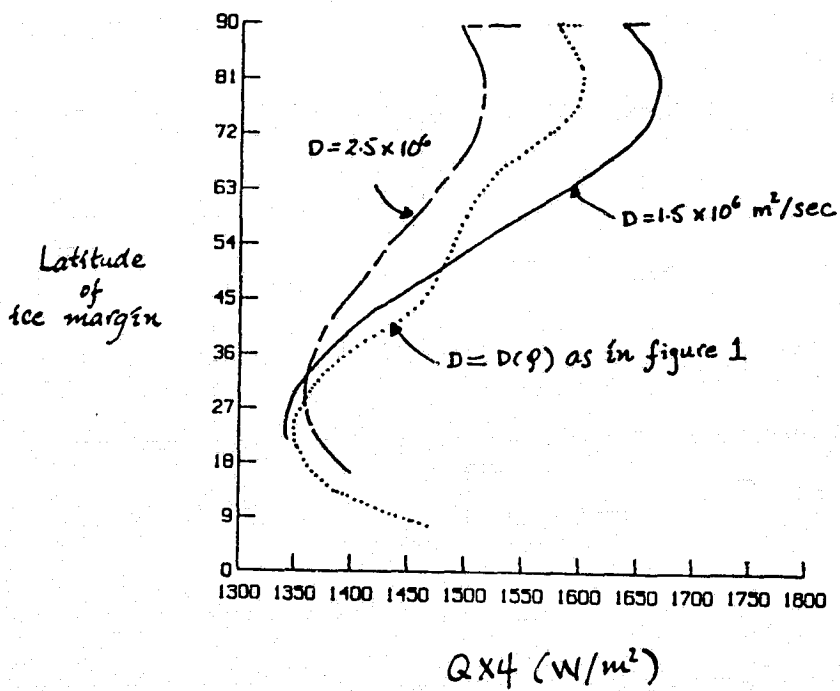


Fig. 1



$Q \times 4$ (W/m²)

Fig. 2

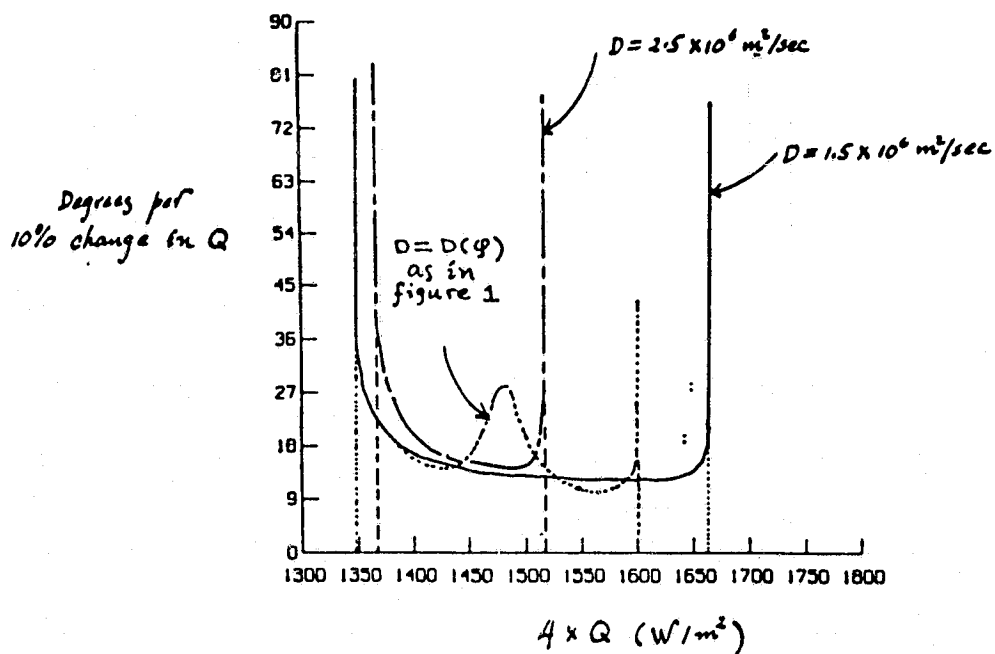


Fig. 3

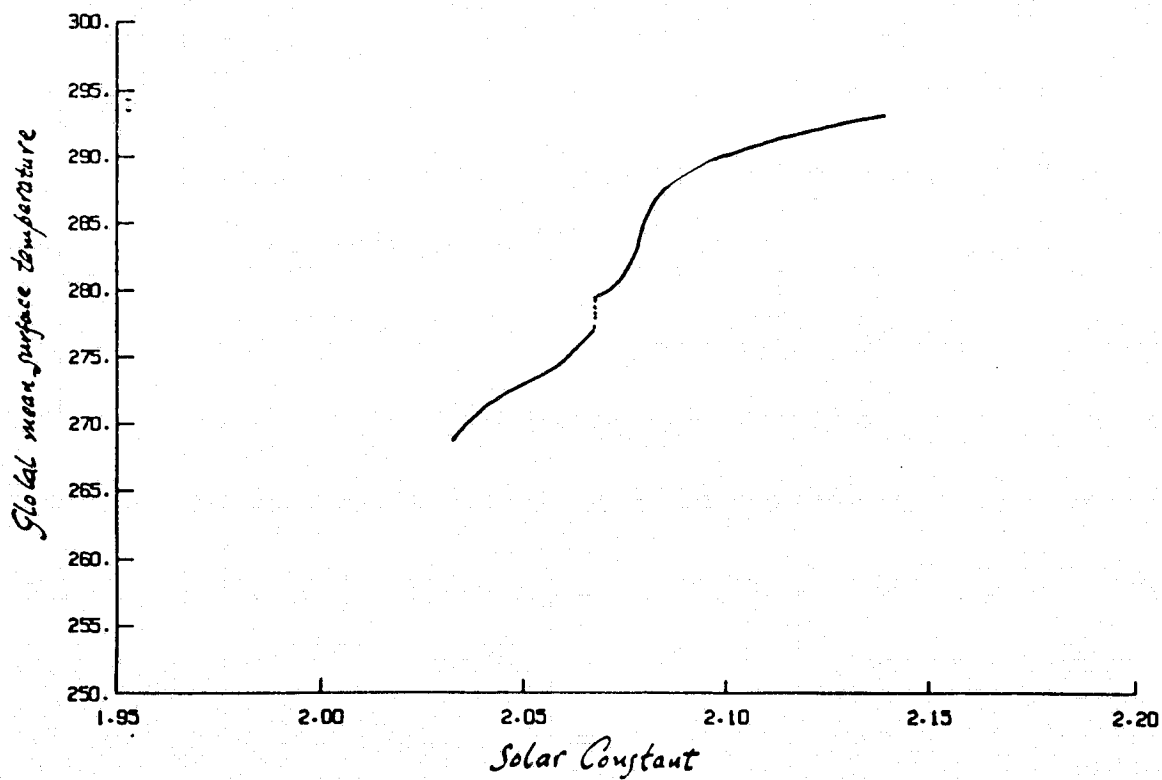


Fig. 4

ORIGINAL PAGE IS
OF POOR QUALITY.

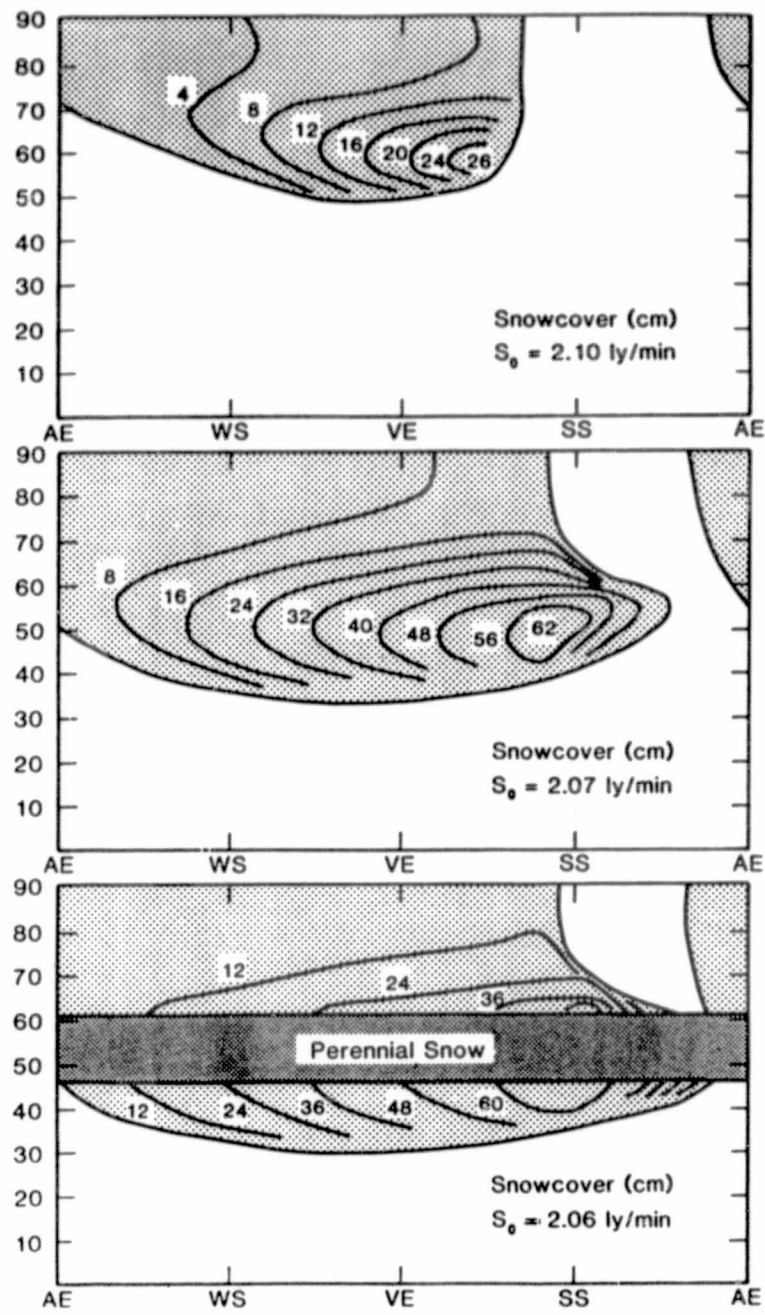


Fig. 5

DESIGN FOR AN EFFICIENT DYNAMIC CLIMATE MODEL WITH REALISTIC GEOGRAPHY

M. J. Suarez and J. Abeles

Studies of long-term climate sensitivity that include realistic atmospheric dynamics are severely restricted by the expense of integrating atmospheric general circulation models. Taking as an example models used at GSFC for this purpose, a nine-level model with a resolution of 4° latitude by 5° longitude uses 3 to 5 minutes of Cyber 205 time to simulate 1 day. Low-resolution spectral models, such as the Community Climate Model at NCAR, simulate a day in less than two minutes. In studies where one is investigating the sensitivity of statistical steady states of the model to variations in some external parameter, it is frequently necessary to bring the model to equilibrium, and collect sufficient statistics to obtain significant estimates of sensitivity for some 10 values of the parameter. If only annual mean forcing is used, integrations of two or three hundred days are adequate. These are feasible, though expensive, using the latest generation of computers, and should be quite easy on the next generation. If, however, one is interested in the very important effects resulting from seasonally varying forcing or of coupling to a slowly varying ocean, each calculation needs to be of the order of tens of years. For such specialized purposes conventional GCM's are not useful.

For these reasons, most studies of the gross sensitivity of long-term climate have used energy balance models (EBMs), in which the effects of atmospheric dynamics are approximated by diffusive transport of heat. Although useful in understanding many aspects of the problem, EBMs are severely limited by this serious approximation.

The alternative is to use dynamic models of much lower horizontal or vertical resolution. The model of Held and Suarez (1977) is an extreme example of this approach. The model uses only two-levels in the vertical and, although it has conventional grid resolution in the meridional direction, horizontal resolution is reduced by keeping only a few degrees of freedom in the zonal wavenumber spectrum. Without zonally asymmetric forcing this model simulates a day in roughly 1/2 second on a CRAY. The model we are building now is a fully finite-differenced, zonally asymmetric version of the Held-Suarez model. Our hope is to get speeds of a few seconds a day roughly 50 times faster than moderate resolution, multi-layer GCM's.

The model two levels are placed at 250 mb and 750 mb, and the surface pressure is fixed. The vertical finite differencing is as in Held and Suarez (1978). It conserves total energy, and global integrals of the potential temperature and its square. The horizontal difference schemes, which are now two-dimensional, differ substantially from Held-Suarez. A staggered (c) grid is used with second order differencing throughout. To try to minimize the amount of diffusion needed to maintain computational stability, the momentum equations use the enstrophy-conserving scheme of Sadourny. A semi-implicit volume is used for gravity waves, thus the time step is limited only by advection.

Diabatic terms are the same as in Held and Suarez, except there is no special treatment of eddies; all grid points are treated as the zonal mean was in that model. The seasonal variation of insolation is also being included.

REFERENCE

Held, I. M., and M. J. Suarez, 1978: A two-level primitive equation atmospheric model designed for climate sensitivity experiments. J. Atmos. Sci., 35, 206-229.

DESIGN OF COUPLED OCEAN-ATMOSPHERE EXPERIMENTS

M. J. Suarez and P. Schopf

During the coming year we plan to make a series of numerical experiments coupling an atmospheric general circulation model to an ocean model in an idealized basin. The objective of the work will be to study the role of ocean-atmosphere interactions in the development of anomalous sea surface temperatures during an El Niño event.

Using a basin model of the equatorial Pacific Ocean, Schopf (1983) has shown that it is possible to produce sea surface temperature anomalies suggestive of some phases of the El Niño by varying the wind stress at the ocean surface. He also found that the response was sensitive to the assumption made for the damping of anomalies through heat exchange with the atmosphere. Proper inclusion of that negative feedback, as well as the modeling of positive feedbacks that may result from dynamic interactions between the two systems, will require comprehensive atmospheric calculations.

Our plan is to couple this tropical basin ocean to a global atmospheric general circulation model. We will first obtain the climatology of the atmospheric GCM from a multi-year run over observed climatological sea surface temperatures. (The results presented below are from the first year of that calculation). Next the ocean will be spun-up using the GCM's climatology as forcing. The results (an ocean consistent with a GCM climatology that is in turn tied to observed sea surface temperatures) will serve as control for the experiments.

We will then attempt to simulate an El Niño event by giving the ocean an artificial wind anomaly in the western Pacific and doing a "coupled" calculation in which the atmosphere "feels" the observed surface temperatures plus the ocean's anomaly, while the ocean is simply forced by the resulting atmosphere.

In preparation for this study, we've been looking at the surface heat flux that the atmospheric model produces over observed sea surface temperature. Since the surface temperature is fixed, the ocean acts as an infinite source or sink of heat to the atmosphere, and the net flux is unconstrained by surface budget requirements. From it we can get some feeling for how well the ocean will be forced by this atmospheric model, and as we will see below, for the strength of the thermodynamic damping of sea-surface temperature anomalies. The atmospheric model is the UCLA GCM. A 9-layer version of it with horizontal resolution of 4° latitude by 5° longitude has been integrated at GLAS for one year of simulated time.

The upper panel of Figure 1 shows the annual mean heat flux into the ocean from that run. For comparison, the lower panel shows an "observed" estimate of the same quantity (Weare et al. 1981). We will restrict our attention to this part of the Pacific, which is roughly the domain we will use for the ocean model.

The results are in good agreement with Weare's estimate, with strong heating over the cold sea surface temperatures at the equator in the eastern Pacific and along the Peruvian coast. Two notable discrepancies are the cooling the

model produces off the Mexican coast and in the western equatorial Pacific. Figure 2 shows the same quantity month by month for the seasonal cycle. The cooling in the subtropics is in January and July, while the warming at the equator and off the South American coast favors the Northern Hemisphere winter months.

It is interesting that at low latitudes most of the temporal and longitudinal structure of the heat flux is due to the evaporation. This is illustrated in Figure 3 which shows the two quantities as functions of longitude and time of year at the equator.

This simple behavior by the model should lead to a good correlation between net heat flux and surface temperature. Figure 4 is a scatter plot of deviation of these two quantities from their monthly zonal means at the equator. The plot suggests increasing sensitivity of the heat flux with increasing temperature. The slope is roughly $25 \text{ w/m}^2 \text{ deg}^{-1}$ for negative temperature deviations and $75 \text{ w/m}^2 \text{ deg}^{-1}$ for positive deviations. If this turns out to be representative of the model's response to imposed anomalies, it implies a very strong negative feedback. For a 50 m deep mixed layer, for example, the two numbers represent time scales of 100 days for negative anomalies and 30 days for positive ones.

References

- Schopf, P. S., 1983: On equatorial waves and El Niño: II. Effects of air-sea thermal coupling. J. Phys. Oceanogr., 13, (in press).
- Weare, B. C., P. T. Strub, and M. D. Samuel, 1981: Annual mean surface heat fluxes in the tropical Pacific Ocean. J. Phys. Oceanogr., 11, 705-720.

ORIGINAL PAGE IS
OF POOR QUALITY

TOTAL ANNUAL MEAN HEAT FLUX

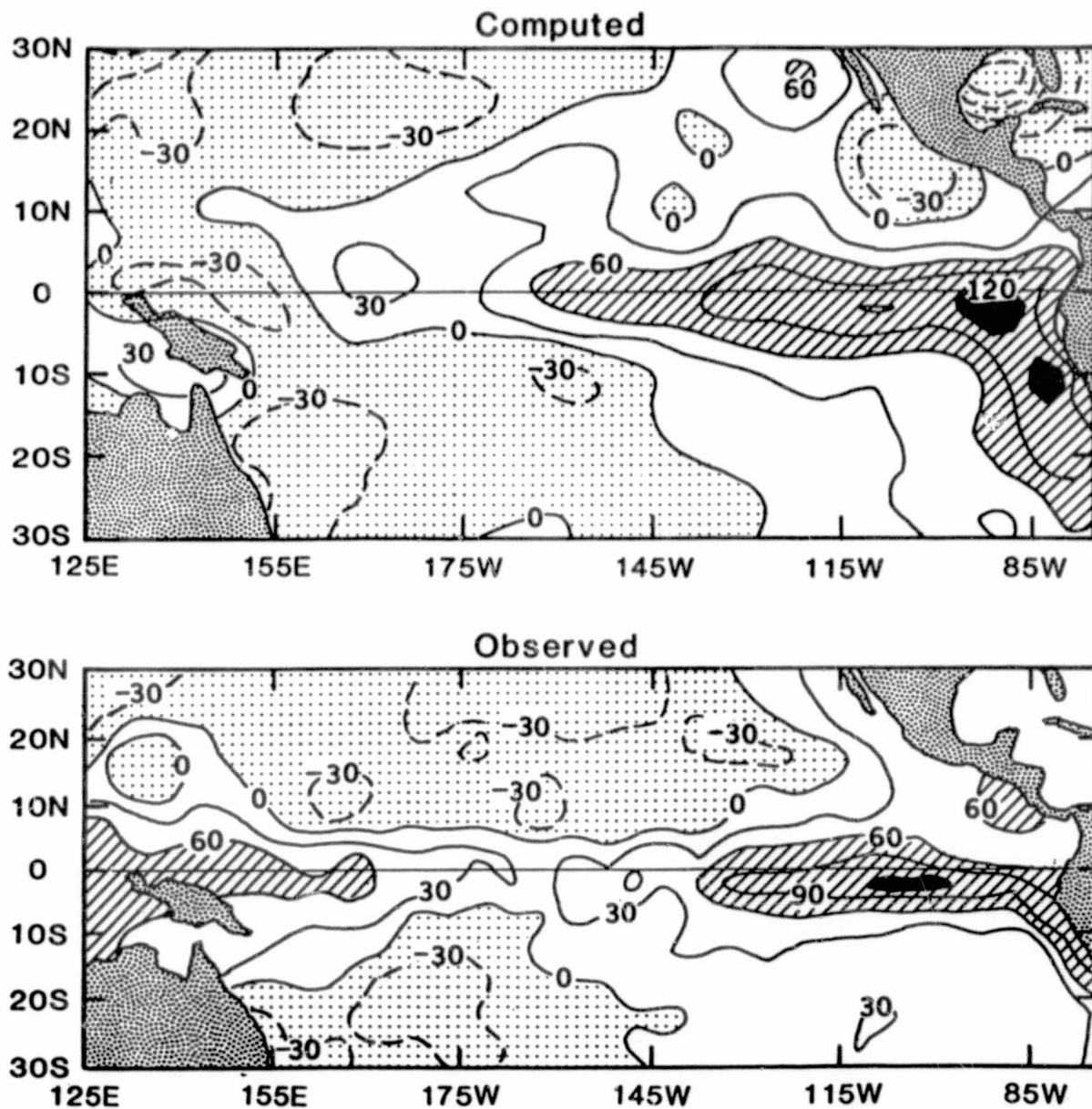
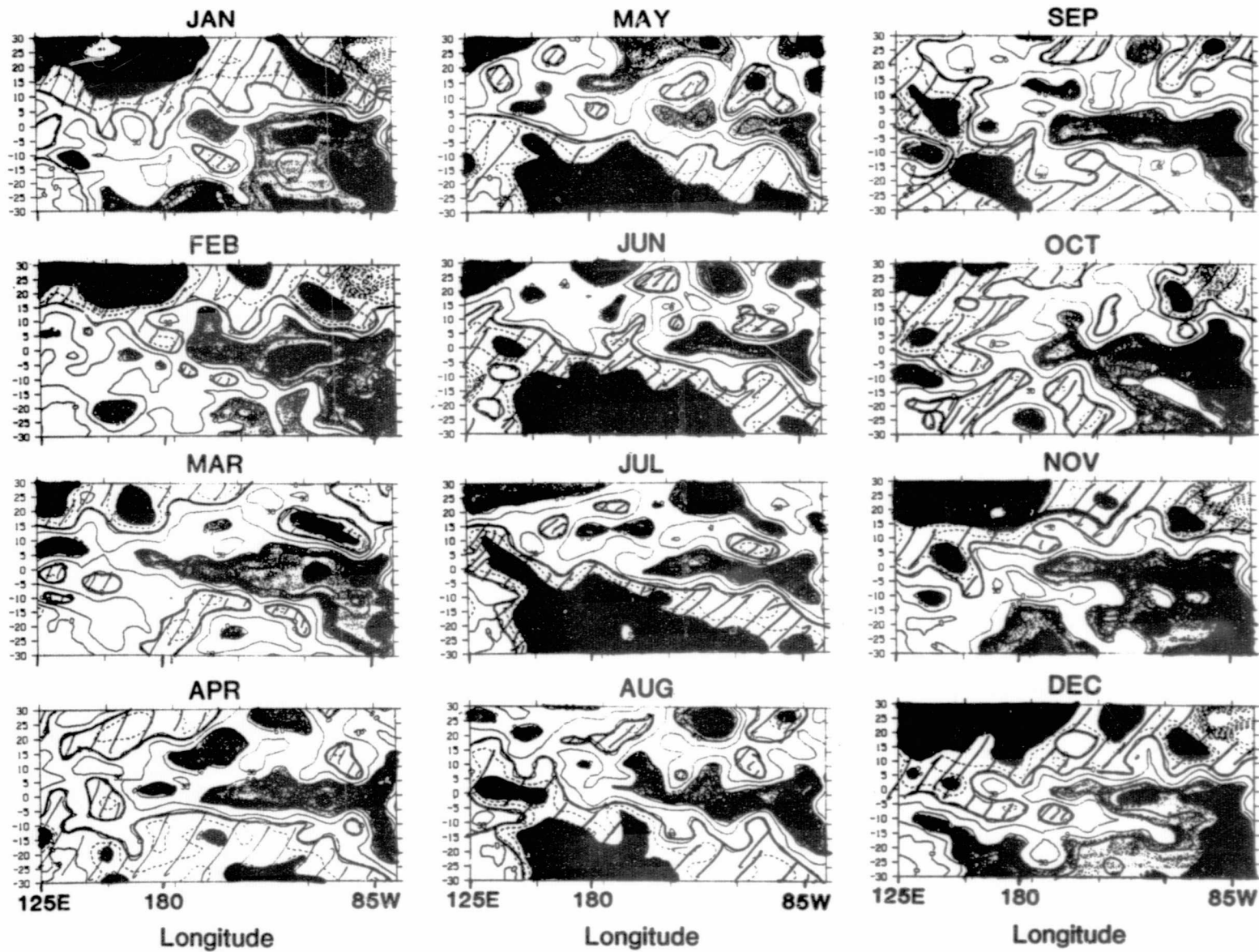


Fig. 1. Annual mean heat flux into the ocean. Observed is Weare's (1981) estimate. Computed is from a one year seasonal cycle simulation of the UCLA atmospheric GCM with prescribed sea surface temperatures.



ORIGINAL PAGE IS
OF POOR QUALITY

Fig. 2. Same as the "computed" in Fig. 1, but for the twelve months. Hatched and black areas are where the heat flux is out of the ocean.

ORIGINAL PAGE IS
OF POOR QUALITY

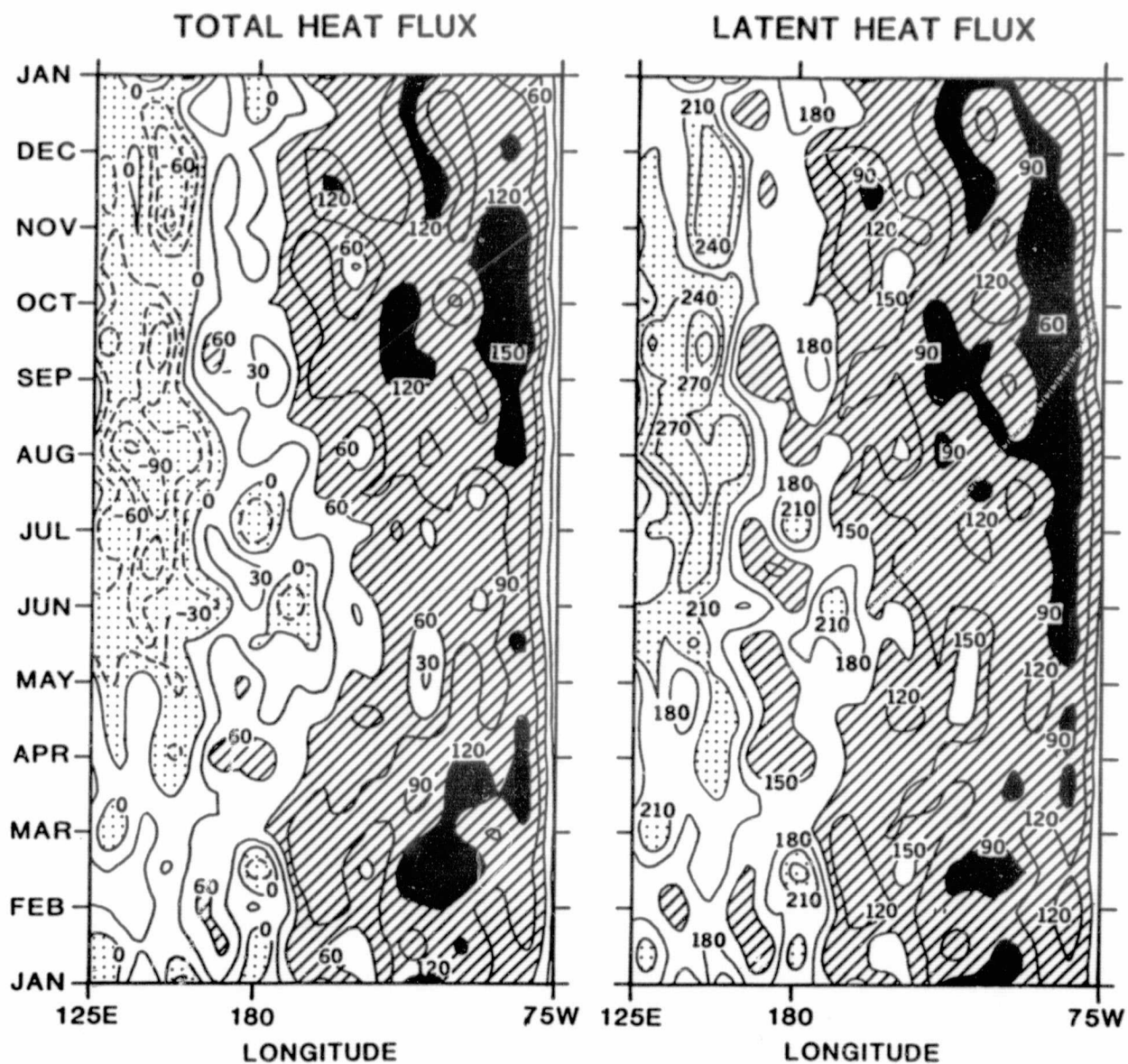


Fig. 3. Longitude-time section of computed heat fluxes at the equator.

ORIGINAL PAGE IS
OF POOR QUALITY

YEAR

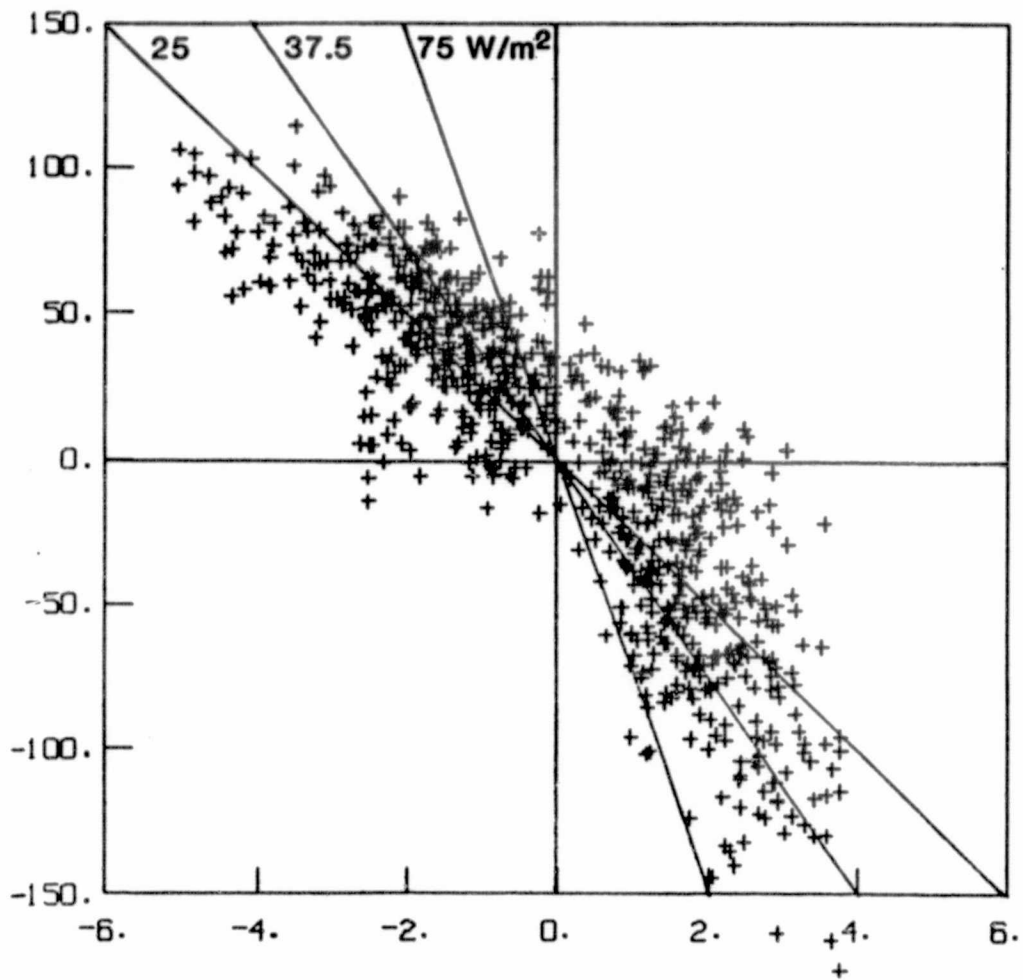


Fig. 4. Scatter of total heat flux vs sea surface temperature, from the GCM calculation. Both quantities are deviations from the zonal mean in the tropical Pacific.

LONG-TERM DYNAMICAL STABILITY AND TRANSITION IN A SPECTRAL MODEL

R. L. Wobus

The relationship between blocking and multiple equilibria is investigated in a two-layer model of the Northern Hemisphere (Wobus, 1981). January heating and boundary conditions are imposed. The truncation varies over global wavenumbers 4-8 (21-73 degrees of freedom) and the coefficients of horizontal diffusion of heat and potential vorticity are varied about realistic values.

The low resolution ($n=4$ to 6) versions of the model exhibit various stationary and limit-cycle regimes. At certain transitions there can exist a second stable or quasi-stable regime, as illustrated in Fig. 1. In this case, the transition from the quasi-stable to the stable state is delayed by more than 180 days and does not closely resemble atmospheric regime transitions.

At higher resolution such transitions become more continuous. The chaotic regime occurs for small but reasonable values of the diffusion coefficients; in long integrations in this regime there are episodes resembling blocking along the west coast of North America, which appear to be associated with an unstable limit cycle of a period near 90 days. One such blocking episode is shown in Fig. 2 and the ensemble mean and standard deviation of nine such episodes (centered in time on the maximum of northerly thermal wind) are shown in Fig. 3. The transitions to and from the blocked state are often associated with episodes of strong baroclinic wave growth and propagation. North American blocking episodes tend to alternate with deep trough formation over eastern Asia; however, only the North American troughs strongly suppress ensemble variance downstream.

These and related results show that while severely truncated models can exhibit multiple quasi-equilibria under realistic domain, forcing, and boundary conditions, somewhat higher resolution is required to allow realistic transitions to be mediated by strong baroclinic wave activity. The implication for extended-range forecasting is that blocking transitions are not likely to be forecast well unless we can forecast, at least statistically, the associated synoptic events.

REFERENCES

- Wobus, R. L., 1981: A numerical model study of long-term planetary wave predictability. Ph.D. Thesis, University of Wisconsin, 194 pp.

ORIGINAL PAGE IS
OF POOR QUALITY

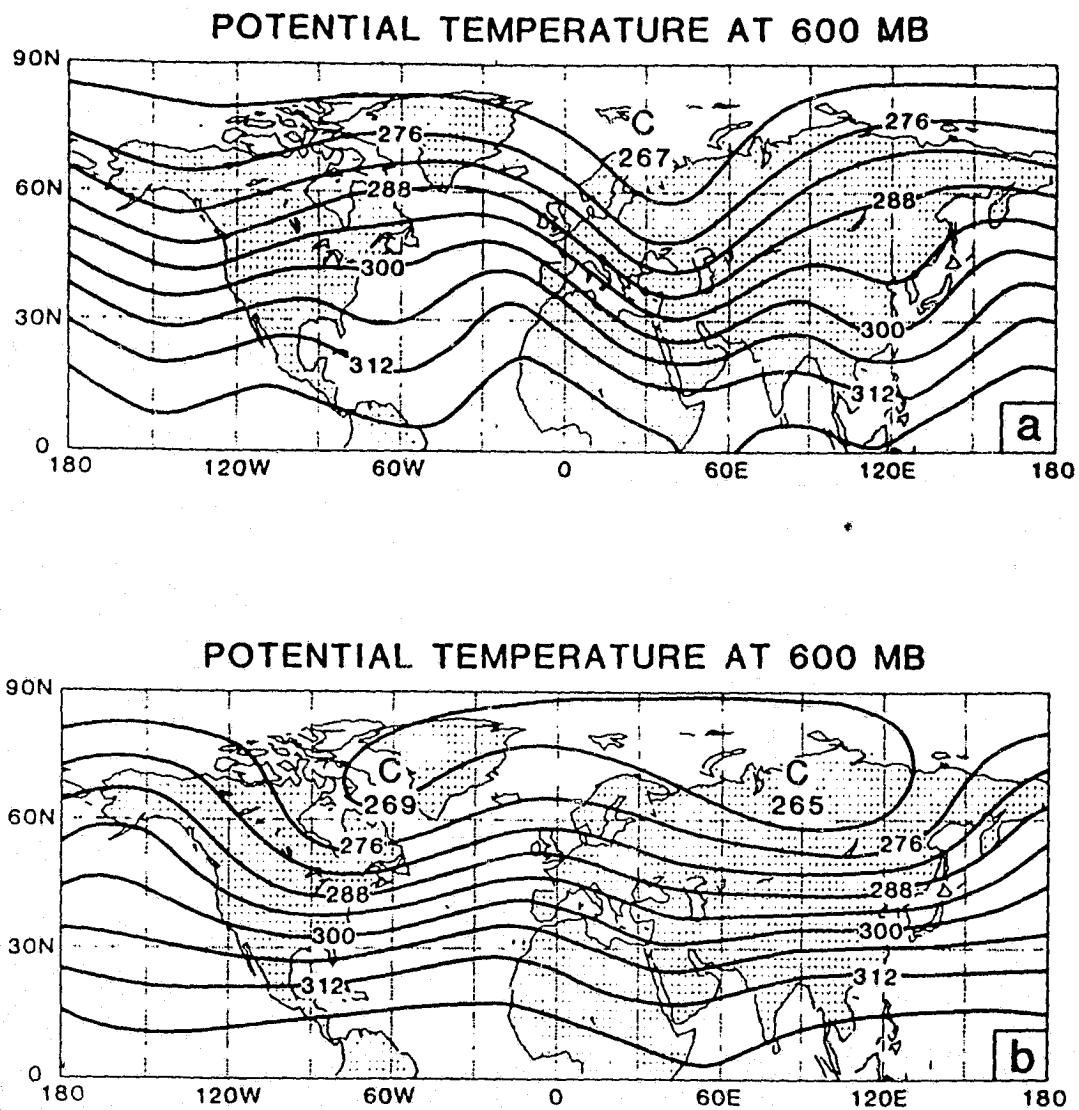


Figure 1. Maps of 600 mb potential temperature for 90-day means of a) the equilibrium, and b) another quasi-stable limit cycle. Wave 6 truncation (43 d.f.), horizontal diffusion coefficients $1.97 \times 10^6 \text{ m}^2 \text{ s}^{-1}$ (upper layer vorticity) and $.75 \times 10^6 \text{ m}^2 \text{ s}^{-1}$ (heat and lower vorticity).

ORIGINAL PAGE IS
OF POOR QUALITY

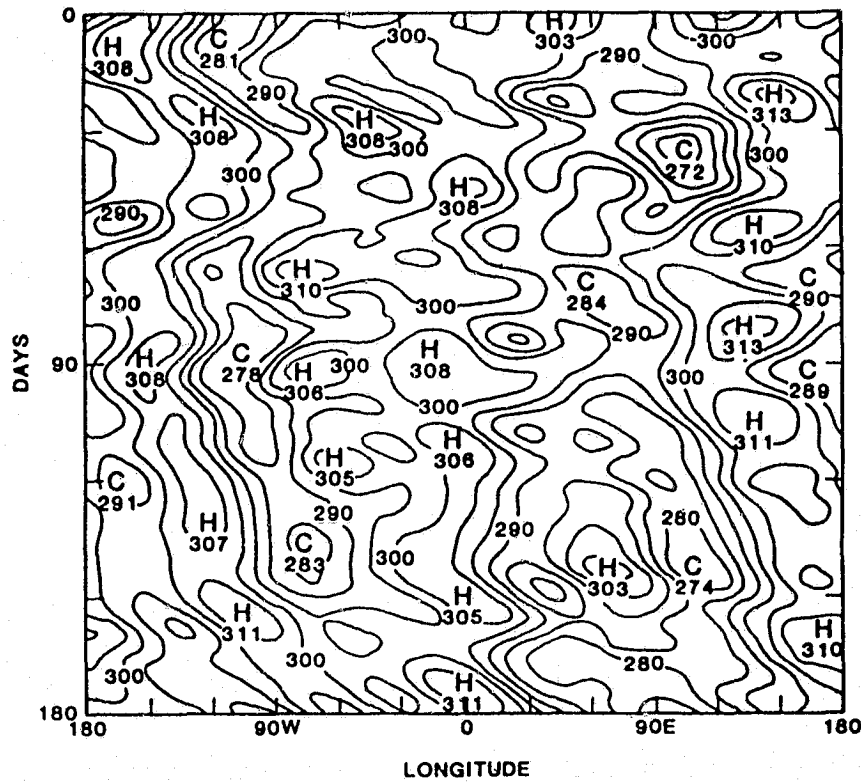


Figure 2. Time-longitude diagram of 600 mb potential temperature at 45°N for one blocking episode. Wave 8 truncation (73 d.f.), horizontal diffusion coefficients $.47 \times 10^6 \text{ m}^2 \text{ s}^{-1}$ (upper layer vorticity) and $.94 \times 10^6 \text{ m}^2 \text{ s}^{-1}$ (heat and lower vorticity).

ORIGINAL PAGE IS
OF POOR QUALITY

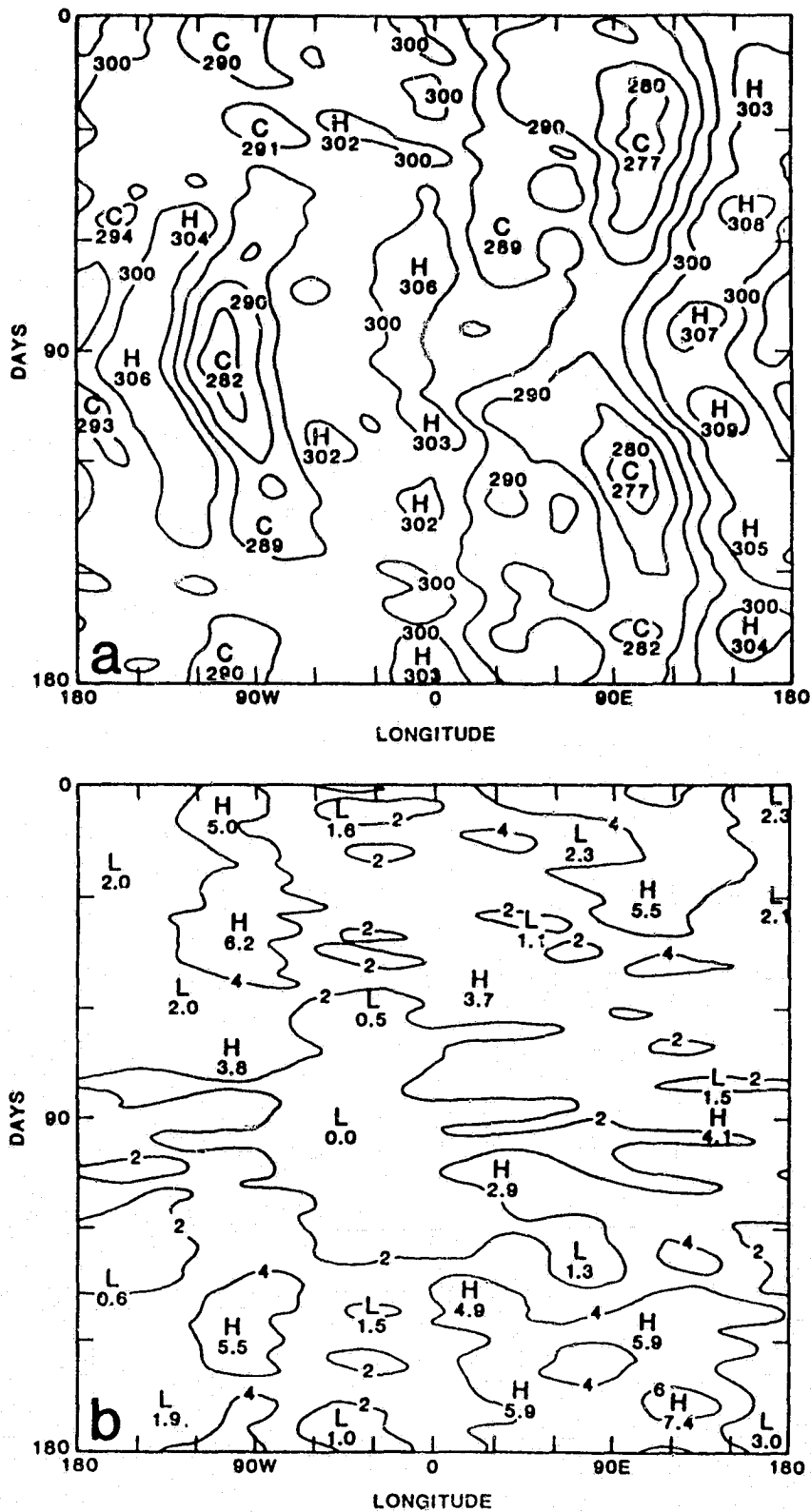


Figure 3. Time-longitude diagrams of 600 mb potential temperature at 45°N for (a) ensemble mean, and (b) ensemble standard deviation for 9 blocking episodes including Figure 2.

D46
N84 22095

DIAGNOSIS OF THE GLAS CLIMATE MODEL'S STATIONARY PLANETARY WAVES USING A LINEARIZED STEADY STATE MODEL

C. Youngblut

1. Background

Orography and geographically fixed heat sources force a zonally asymmetric motion field. Straus and Shukla (1981) reported an extensive space-time spectral analysis of the GLAS climate model (D130) response and comparison with observations. The discrepancy between the GCM's simulated stationary waves (time-averaged response) and those observed was one of the more troublesome aspects of the comparison.

An updated version of the model (D150) showed a remarkable improvement in the simulation of the standing waves (see Straus, 1981). The main differences in the model code were an improved boundary layer flux computation and a more realistic specification of the global boundary conditions. The specific processes responsible for the improved performance of the GCM however are not entirely clear.

2. Stationary Wave Model

To provide a theoretical basis for interpreting GCM climate experiments a linearized, steady-state, primitive equation model has been developed. The model consists of the horizontal equations of motion in their vorticity and divergence form, the thermodynamic equation, the continuity equation, and the hydrostatic equation (Hoskins and Simmons, 1975). The dependent variables are expressed as a truncated series of spherical harmonics

$$\sum_{m,n} A_n^m p_n^m(\mu) e^{im\lambda}.$$

Second-order finite differences are used in the vertical.

In a linearized calculation, the solution for each zonal wavenumber m will be independent and can be calculated separately. The atmospheric state for wavenumber m can be written as a vector $\underline{X} = (\underline{\xi}, \underline{iD}, \underline{T}, \ln p^*)$. At level k , the wavenumber m component of vorticity is

$$\xi = \sum_{a=m}^{m+j} \xi_a^{k,m} p_a^m(\mu) e^{im\lambda}.$$

The vector $\underline{\xi}$ is

$$\underline{\xi} = (\xi_m^{1,m}, \xi_{m+1}^{1,m}, \dots, \xi_{m+j}^{1,m}, \xi_m^{2,m}, \dots, \xi_{m+j}^{NL,m})$$

where NL = number of levels. The other fields and vectors are similarly defined. The linearized equations can be transformed to

$$0 = i \underline{A} \underline{X} + \underline{R} \underline{X} + \underline{F}.$$

The matrix A is determined by integrating numerically various functions of the basic state from pole to pole. R represents linear and bi-harmonic dissipation. F represents orographic and prescribed thermal forcing. The solution X can be computed by routine Gaussian elimination routines. For example, a 5-layer hemispheric model truncated at R26 requires the inversion of a 208 x 208 complex array for each zonal wavenumber.

3. Continuing Work

The model has been tested using simple isolated thermal and orographic forcings. Currently underway are a series of experiments with the basic state and thermal forcing derived from the GLAS GCM climate model history tapes. The steady-state linear model solutions will be compared with the time-average asymmetric GCM fields.

REFERENCES

- Hoskins, B. J. and D. J. Karoly, 1981: The steady linear response of a spherical atmosphere to thermal and orographic forcing. J. Atmos. Sci., 38, 1179-1196.
- Hoskins, B. J. and A. J. Simmons, 1975: A multi-layer spectral model and the semi-implicit method, Quart. J. Roy. Meteor. Soc., 101, 637-655.
- Straus, D. M. and J. Shukla, 1981: Space-time spectral structure of a GLAS general circulation model and a comparison with observations, J. Atmos. Sci., 38, 901-917.
- Straus, D. M. and J. Shukla, 1981: Global and local fluctuations of winter and summer simulations with the GLAS climate model, NASA T. M. 83907, 231-236.

HORIZONTAL ENERGY PROPAGATION IN A BAROCLINIC ATMOSPHERE
WITH MERIDIONAL AND ZONAL STRUCTURE

C. Youngblut

1. Background

The concept that wave energy may be forced in one region of the atmosphere and then propagate to and influence other regions is often used to explain various aspects of atmospheric motion (Branstator, 1983). Horizontal energy propagation from steady sources has recently received great interest due to the isolation of global-scale teleconnection patterns in monthly and seasonally averaged data and their link to El-Nino/Southern Oscillation events. Traditionally, stationary wave models have been linearized about longitudinally invariant basic states which only crudely represent the time-mean flow. These models ignore the interactions of the perturbations with the mean meridional flow and the time-mean asymmetric flow.

Simmons (1982), Webster and Holton (1982), Karoly (1983), Branstator (1983) and Simmons, Wallace and Branstator (1983) have investigated the latter interaction using barotropic models. Two principal findings of these studies are that cross-equatorial propagation is possible through regions of westerly wind in the zonal mean easterlies and that an increased wave response can occur in a zonally varying basic state.

2. Model

As a step towards a more realistic representation of the propagation of wave energy away from steady sources in the time-mean atmospheric flow a baroclinic model has been developed. The model is linear, steady-state, baroclinic (2-level) and based on the primitive equations (Webster (1972), and Opsteegh and van den Dool, 1980). The unique features of the model are

1. The basic state \bar{u} and \bar{T} fields are functions of λ , θ , and p .
2. A mean meridional circulation \bar{v} , \bar{w} , which may be a function of λ , θ , and p may be included.
3. Dissipation may be a function of θ , λ , p (e.g., differ over land and sea).

Because the basic state is a function of longitude, the equations are not separable in λ and the usual semi-spectral solution procedure is not applicable. The model solutions can be found in a straight-forward (brute force) way by discretizing the model equations directly on a λ , θ , p grid. There are six dependent (perturbation) variables: u , v , and geopotential at levels 1 and 2. The thermal forcing is prescribed at the intermediate vertical level. The linearized equations may be written

$$\underline{A} \underline{X} = \underline{F} \quad (*)$$

where \underline{A} is a large, very sparse, real square matrix of side (approx. $6 \times NX \times NY$);

N_X and N_Y are the number of grid points in λ and θ , respectively. F represents the thermal and/or orographic forcing and X is the solution vector. The system (*) is solved using the Harwell Fortran subroutines for sparse linear equations (Duff, 1977).

3. Model Tests and Development

The model has been tested on a $30^\circ \times 7.5^\circ (\lambda, \theta)$ global grid using Real*8 variables on the Amdahl V6. For this grid, A is of order 1704, with 16000 non-zero elements (approx. 1% full). The solution of (*) uses $\sim 3M$ bytes of storage. The Harwell code has been designed so that repeated solutions of (*) with different right-hand sides are very fast, approximately 1 second on the above test case. The solution X is checked by substituting X into the finite-difference form of the equations.

The model's response for a zonally symmetric basic state and isolated tropical forcing agrees well with Webster (1972). Further preliminary tests have extended these results to zonally varying basic states. The mid-latitude response is related to the position of the equatorial source relative to the zonally asymmetric basic state.

Work on increasing the resolution of global version of the model is underway. Besides the global model, which because of the solution technique must be put on a coarse grid, models with restricted domains are being designed. Future work will include a hemispheric and an equatorial strip model. A series of experiments is being designed to examine how energy propagation away from steady sources is influenced by the horizontal structure of the background flow.

REFERENCES

- Branstator, G., 1983: Horizontal energy propagation in a barotropic atmosphere with meridional and zonal structure. J. Atmos. Sci., 40, 1690-1708.
- Duff, I. S., 1977: MA28—a set of Fortran subroutines for sparse unsymmetric linear equations. AERE Report R.8730, HMSO, London.
- Karoly, D. J., 1983: Rossby wave propagation in a barotropic atmosphere. Dyn. Atmos. and Oceans, 7, 111-125.
- Opsteegh, J. D. and H. M. Van Den Dool, 1980: Seasonal differences in the stationary response of a linearized primitive equation model: prospects for long-range weather forecasting? J. Atmos. Sci., 37, 2169-2185.
- Simmons, A. J., 1982: The forcing of stationary wave motion by tropical diabatic heating. Quart. J. Roy. Meteor. Soc., 108, 503-534.
- Simmons, A. J., J. M. Wallace, and G. W. Branstator, 1981: Barotropic wave propagation and instability, and atmospheric teleconnection patterns. J. Atmos. Sci., 40, 1363-192.
- Webster, P. J., 1972: Response of the tropical atmosphere to local steady forcing. Mon. Wea. Rev., 100, 518-541.

omit

A ONE-COLUMN MODEL WITH DETAILED PHYSICAL PARAMETERIZATIONS

T. Corsetti and D. A. Randall

A one-dimensional (1-D) model utilizing physical parameterizations from the UCLA General Circulation Model has been developed. These physical parameterizations incorporate a sophisticated cumulus parameterization (Arakawa and Schubert, 1974; Lord et al., 1982), an elaborate planetary boundary layer parameterization (Randall, 1976; Suarez et al., 1983), and a new long-wave radiation parameterization developed by Harshvardhan, based on the work of Chao, Peng, and Rogers.

Since the model consists of only one grid point, the forcing for the hydrodynamics must be prescribed. A GATE dataset of observations at three-hour intervals running from August 31 to September 18 during the GATE experiment is used (Thompson et al., 1979). Forcing from this dataset includes values of divergence, temperature and moisture tendencies due to horizontal advection, and winds at each of 37 levels in the vertical. The observed quantities are Fourier-interpolated for each time step of a simulation.

The main motive for developing a 1-D version of the UCLA physics is to make it possible to assess the impact of various modifications within the physics routines quickly and inexpensively. Simulations can be run without consuming the huge amount of computational time required for a comparable integration with the global general circulation model.

We are currently conducting several tests of alternative time-differencing schemes, vertical resolutions, and vertical-differencing schemes.

REFERENCES

- Arakawa, A., and W. H. Schubert, 1974: The interaction of a cumulus cloud ensemble with the large-scale environment, Part I. J. Atmos. Sci., 31, 674-701.
- Lord, S. J., W. C. Chao, and A. Arakawa, 1982: Interaction of a cumulus cloud ensemble with the large-scale environment. Part IV. The discrete model. J. Atmos. Sci., 39, 104-113.
- Randall, D. A., 1976: The interaction of the planetary boundary layer with large-scale circulations. Ph.D. Thesis, The University of California, Los Angeles, 247 pp.
- Suarez, M. J., A. Arakawa, and D. A. Randall, 1983: The parameterization of the planetary boundary layer in the UCLA general circulation model: Formulation and results. Mon. Wea. Rev. (to appear).
- Thompson, R. M., S. W. Payne, E. E. Recker, and R. J. Reed, 1979: Structure and properties of synoptic scale wave disturbances in the Intertropical Convergence Zone of the eastern Atlantic. J. Atmos. Sci., 36, 53-72.

C. PROCESSES AND PARAMETERIZATION

PRECEDING PAGE BLANK NOT FILMED

DEVELOPMENT AND PRELIMINARY TESTS
OF A NEW LONG-WAVE RADIATION PARAMETERIZATION

Harshvardhan, T. Corsetti, D. Randall and M. Suarez

The most time-consuming computation in the integration of a general circulation model is the longwave radiation code. This is primarily because the physics involves interactions of each atmospheric level with all layers in the atmosphere, and because radiative properties are spectrally varying such that the total flux is the sum of fluxes over several bands. However, the code can be made computationally efficient if an accurate broad-band model with a minimum of spectral bands is used, and if advantage is taken of the fact that there is no horizontal interaction between neighboring grid points. This latter feature can be used to write very fast code for vector processors such as the Cyber 205.

We have taken full advantage of these two computational techniques. We use an efficient broad-band longwave radiation code based on the work of Chou and Peng (1983) and Chou (1983) for CO₂ and H₂O, and Rodgers (1968) for O₃. There are two bands each in the CO₂ and H₂O absorption regions, one for the band-center and one for the band-wings. One band covers O₃ absorption and the overlapping H₂O continuum. Overlap is also considered in the CO₂ region, and there is H₂O continuum absorption where applicable, following Roberts *et al.* (1976)*. Clouds are considered non-reflecting in the longwave. Therefore partial cover or partial transmission can be allowed for, by considering a cloud fraction at each atmospheric level. A special subroutine has been written to allow for maximum or random overlap of clouds that may be used in the future. All algorithms have been written with vectorization in mind, and, as mentioned above, as far as possible, identical operations are made for all horizontal grid points in a latitude circle. Where possible, operations are carried out covering the vertical grid points as well, yielding long vectors for efficient computations.

The radiation code has been tested off-line for various standard atmospheric profiles (McClatchey *et al.*, 1972) and conditions, as part of an international intercomparison project that is currently in progress. Table 2 shows the changes in fluxes at various levels that result from a doubling of CO₂ from 300 ppm to 600 ppm. These have been compared with narrow and broad band results given in Kiehl and Ramanathan (1983), and found to correspond quite closely.

REFERENCES

- Chou, M. D., 1983: Broadband water vapor transmission functions for atmospheric IR flux computations. Submitted to J. Atmos. Sci.
- Chou, M. D., and L. Peng, 1983: A parameterization of the absorption in the 15 μ m CO₂ spectral region with application to climate sensitivity studies. J. Atmos. Sci., 40, (to appear in September).

* Table 1 gives the spectral bands of the model.

Kiehl, J. T., and V. Ramanathan, 1983: CO₂ radiative parameterization used in climate models: Comparison with narrow band models and with laboratory data. J. Geophys. Res., 88, 5191-5202.

McClatchey, R. A., R. W. Fenn, J. E. A. Selby, F. E. Volz and J. S. Garing, 1972: Optical Properties of the Atmosphere (Third edition). AFCRL-047297. 108pp.

Roberts, R. E., J. E. A. Selby and L. M. Biberman, 1976: Infrared continuum absorption by atmospheric water vapor in the 8-12 μ m window. Applied Optics, 15, 2085-2090.

Rodgers, C. D., 1968: Some extensions and applications of the new random model for molecular band transmission. Quart J. Roy. Meteor. Soc., 94, 99-102.

TABLE 1

Spectral regions in the longwave radiation parameterization

	H ₂ O band	H ₂ O band	CO ₂ band	CO ₂ band	O ₃
Spectral range (cm ⁻¹)	0-340 1380-1900	340-540 800-980 1100-1380 1900-3000	620-720	540-620 720-800	980-1100

TABLE 2

Change in fluxes ($W m^{-2}$) due to doubled CO_2 (300 ppm \rightarrow 600 ppm), for three atmospheric profiles at the surface, near the tropopause, and in the stratosphere. For all profiles, the surface is at 1013 mb, and the stratospheric level is at 26.8 mb. The tropopause level is at 100 mb for the tropical profile, 152.6 mb for the midlatitude summer profile, and 314.9 mb for the subarctic winter profile.

	Tropical	Midlatitude Summer	Subarctic Winter
ΔF_{\uparrow} (surface) CO_2	8.04	7.49	4.36
$CO_2 + H_2O + O_3$	2.98	3.20	3.22
$CO_2 + H_2O + cont. + O_3$	0.31	0.68	3.00
ΔF_{net} (tropopause) CO_2	-7.23	-6.79	-3.68
$CO_2 + H_2O + O_3$	-6.15	-5.96	-3.58
$CO_2 + H_2O + cont. + O_3$	-5.69	-5.65	-3.57
ΔF_{\uparrow} (stratosphere) CO_2	-5.25	-4.43	-2.01
$CO_2 + H_2O + O_3$	-4.17	-3.60	-1.91
$CO_2 + H_2O + cont. + O_3$	-3.71	-3.29	-1.90

49
N84 22098

SIMULATIONS OF THE STRATOCUMULUS-TOPPED BOUNDARY LAYER WITH A
THIRD-ORDER CLOSURE MODEL

C.-H. Moeng and D. A. Randall

In third-order closure models, the closure assumptions are applied in the third-moment equations, using the quasi-normal assumption for the fourth-moment transport terms. However, the quasi-normal assumption is known to lead to violations of realizability; in spectral closures, an eddy damping term, which represents the effect of pressure fluctuations on third moments, is added to prevent the violations. The eddy damping coefficient can be derived theoretically, for example, by using the test-field model to fit the Kolmogorov energy spectra (Herring *et al.*, 1982). However, these studies are made in Fourier space, and the results are difficult to apply to real space.

Deardorff (1978), studying a simple diffusion problem, derived a diffusive eddy damping term in addition to the classical quasi-normal terms, to parameterize the fourth-moment transport term in real space. However, the eddy damping coefficient is undetermined.

We have used a third-order closure model, proposed by Andre *et al.* (1982), in which the time-rate-of-change terms, the relaxation and rapid effects for the pressure-related terms, and the clipping approximation are included along with the quasi-normal closure, to study turbulence in a cloudy layer which is cooled radiatively from above. The results (Fig. 1) show a spurious oscillation which is strongest near the inversion. An analysis of the problem shows that the oscillation arises from the mean-gradient and buoyancy terms of the triple-moment equations; these terms are largest near the cloud top. The oscillation is physical, rather than computational. However, in nature the oscillation is effectively damped, by a mechanism which apparently is not included in our model.

In the stably stratified layer just above the mixed-layer top, turbulence can excite gravity waves, whose energy is radiated away. Because our closure assumption for the pressure terms does not take into account the transport of wave energy, our model generates spurious oscillations.

We have found that we can damp the oscillations by introducing diffusion terms into the triple-moment equations (Deardorff, 1978). With a large enough choice for the diffusion coefficient, the oscillation is effectively eliminated. Unfortunately, however, our results are quite sensitive to the ad hoc eddy coefficient.

We conclude that further research is needed to parameterize the gravity-wave damping of the oscillatory modes.

REFERENCES

- Andre, J. C., G. De Moor, and K. Traore, 1982: Pressure effects on triple correlations in turbulent convective flows. Turbulent Shear Flows 3, 243-252.

Deardorff, J. W., 1978: Closure of second- and third-moment rate equations for diffusion in homogeneous turbulence. Phys. Fluids 21, 525-530.

Herring, J. R., D. Schertzer, M. Lesieur, G. R. Newman, J. P. Chollet, and M. Larcheveque, 1982: A comparative assessment of spectral closure as applied to passive scalar diffusion. J. Fluid Mech., 124, 411-437.

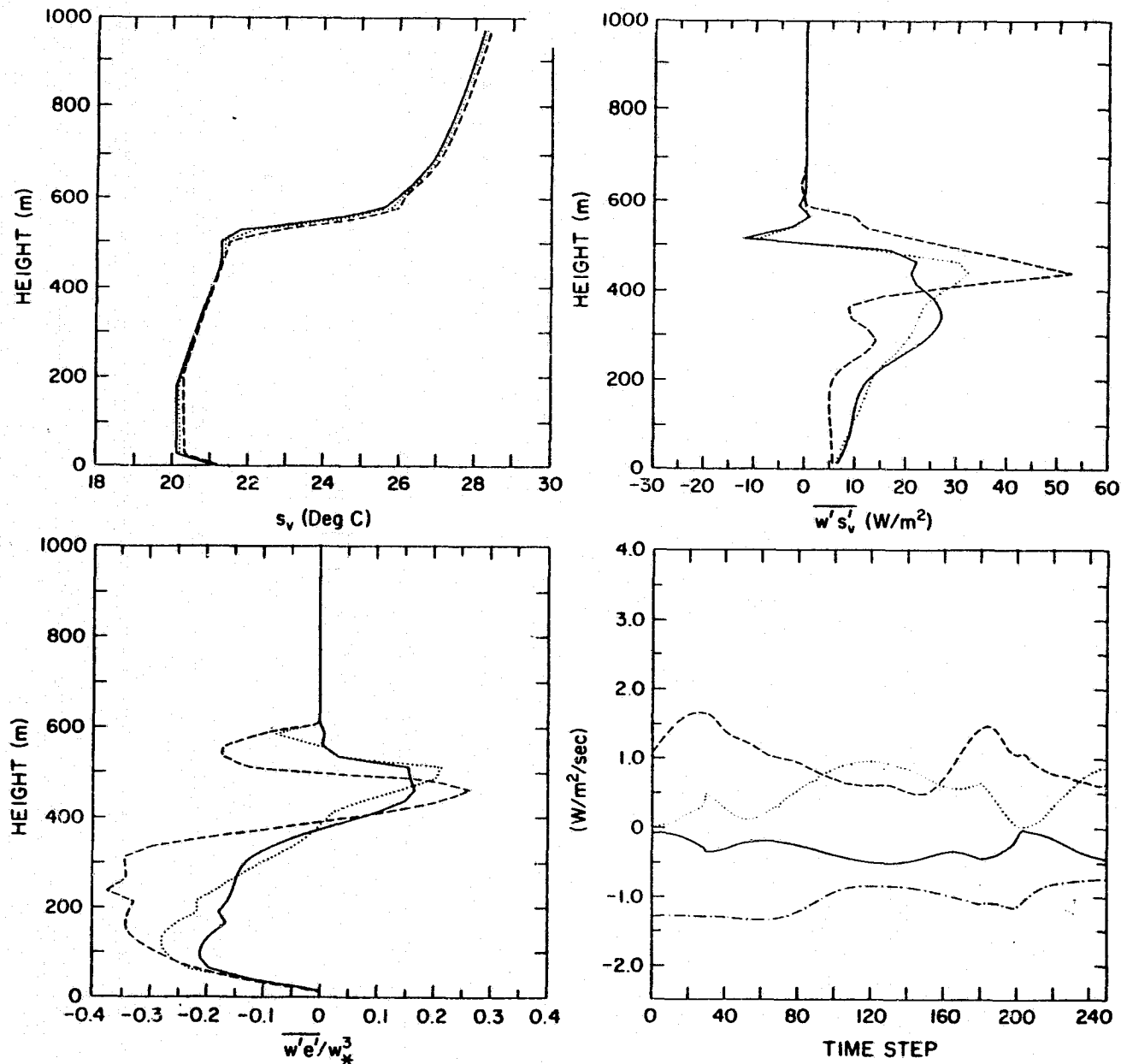


Fig. 1. Vertical profiles of (a) the virtual dry static energy, (b) the buoyancy fluxes, and (c) the transport of turbulent energy at hours 18 (long-dashed line), 19 (short-dashed line), and 20 (solid line); (d) time evolution of the budget terms of the $w'h'$ equation at the level right below the cloud top. The long-dashed line is for the transport term, the short-dashed line is for the buoyancy term, the dash-dotted line is for the mean gradient term, and the solid line is for the pressure term.

ORIGINAL PAGE IS
OF POOR QUALITY

PROBLEMS WITH THE PROCESS PARTITIONING THEORY
OF STRATOCUMULUS ENTRAINMENT

David A. Randall

To parameterize the rate of entrainment into the planetary boundary layer (PBL) it is generally assumed that the dissipation rate is a constant fraction of the gross rate of TKE production. However, in order to proceed, it is necessary to define the gross production rate.

Three different approaches to partitioning have been proposed. Ball (1960), Lilly (1968), and Deardorff et al. (1969, 1974) considered the sign of the net buoyancy flux at each level. If the net flux is positive, it is counted as TKE-producing; otherwise, it is counted as TKE-consuming. This approach can be called "Eulerian partitioning." The second approach can be called "process partitioning." It is assumed that the various processes acting in concert each produce and consume the same energy as if they acted independently (Manins and Turner, 1978). The total rates of TKE production and consumption are obtained by summing the effects of all the forcing processes. The third approach is "Lagrangian partitioning." Each air parcel is considered as either producing or consuming TKE, according to the sign of the product of its density and vertical velocity anomalies.

Stage and Businger (1981a,b) have applied process partitioning to the cloud-topped mixed layer. One of the most important processes influencing entrainment into such a layer is cloud-top radiative cooling. This cooling reduces the positive buoyancy of entrained parcels, and so tends to reduce the buoyant consumption due to entrainment (Brost et al., 1982). On the other hand, the entrainment of warm air reduces the ability of radiative cooling to promote convection by creating negatively buoyant parcels near cloud top. The production and consumption due to entrainment and radiative cooling are thus closely related.

Nevertheless, Stage and Businger assume that the buoyant consumption due to the entrainment of warm air is independent of the cloud-top radiative cooling rate, and that the buoyant production due to cloud-top radiative cooling is independent of the rate of entrainment of warm air. One possibility is that cloud-top radiative cooling acts as a positive contribution to P . This is based on the plausible idea that the cooling helps to drive convection in the mixed layer. A second, equally plausible possibility is that the cooling reduces N by making it easier to entrain warm air from the inversion layer, i.e., it "defends" the turbulence against buoyant consumption. For convenience, we refer to these alternative assumptions as "offensive" and "defensive" cooling, respectively. Offensive cooling promotes production; defensive cooling prevents consumption. In either case, stronger cooling produces stronger entrainment. Both possibilities are consistent with the profile of the net buoyancy flux. However, the two alternatives lead to the very different model results shown in Fig. 1.

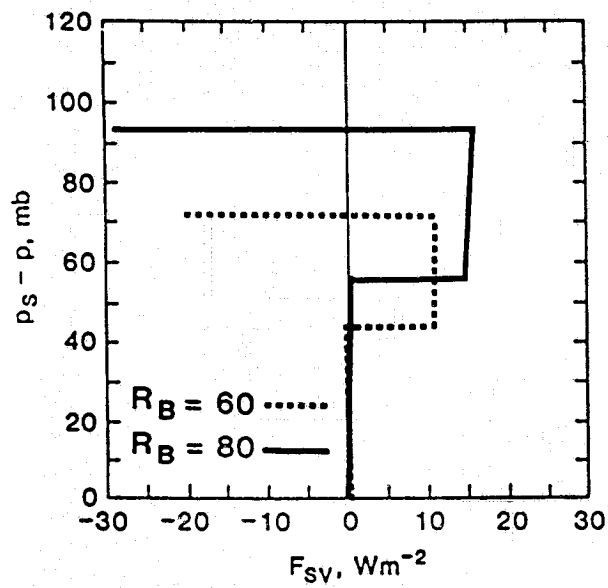
Randall (1980b) and Fravallo et al. (1981) show that a mixed-layer model based on Eulerian partitioning is sensitive to $\delta\rho$. The reason is that the net buoyancy flux is smaller, in the upper part of the cloud layer, than it

would be if the cooling did not extend down to that level; for Eulerian partitioning, this increases N and decreases P . On the other hand, SB show that their model is insensitive to δ_{pr} . They included the effects of δ_{pr} as a negative contribution to P , but they did not allow δ_{pr} to influence N . Fig. 2 shows the δ_{pr} -sensitivity of three models: one based on Eulerian partitioning, the SB model, and a modified version of the SB model in which the δ_{pr} -term is included as a positive contribution to N rather than as a negative contribution to P . For all three cases, $R_B = 70 \text{ W m}^{-2}$. The results show that the first and third models are sensitive to δ_{pr} ; only the SB model is insensitive.

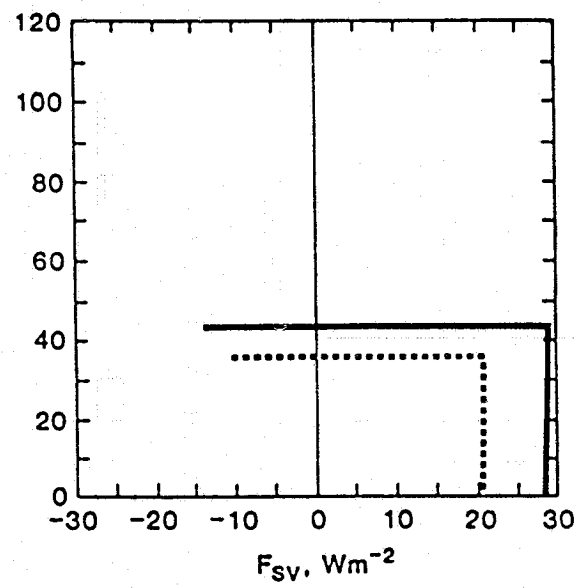
Process partitioning can be formulated in many different ways. The examples given in this paper show that model results are sensitive to the choice of formulation. A quantitative link between process partitioning and Lagrangian partitioning has yet to be established.

REFERENCES

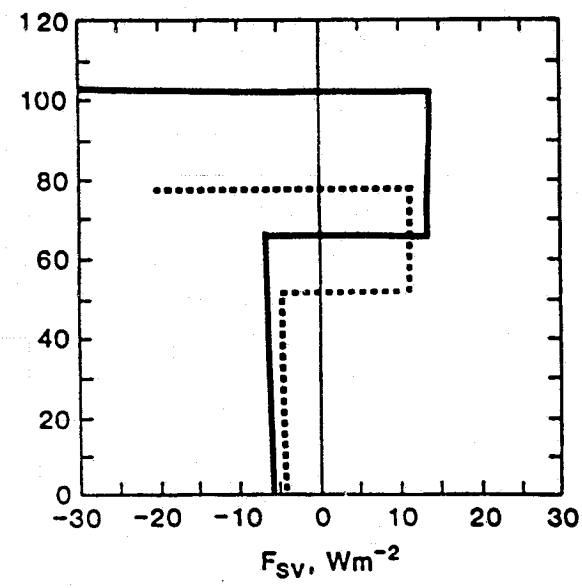
- Ball, F. K., 1960: Control of inversion height by surface heating. Quart. J. Roy. Meteor. Soc., 86, 483-494.
- Brost, R. A., J. C. Wyngaard, and D. H. Lenschow, 1982: Marine stratocumulus layers. Part II: Turbulence budgets. J. Atmos. Sci., 39, 818-836.
- Deardorff, J. W., G. E. Willis, and D. K. Lilly, 1969: Laboratory investigation of non-steady penetrative convection. J. Fluid Mech., 35, 7-31.
- Deardorff, J. W., G. E. Willis, and D. K. Lilly, 1974: Comment on the paper by A. K. Betts 'Non-precipitating cumulus convection and its parameterization.' Quart. J. Roy. Meteor. Soc., 100, 122-134.
- Deardorff, J. W., 1980: Stratocumulus-capped mixed layers derived from a three-dimensional model. Boundary Layer Meteor., 18, 495-527.
- Fravalo, D., Y. Fouquart, and R. Rosset, 1981: The sensitivity of a model of low stratiform clouds to radiation. J. Atmos. Sci., 38, 1049-1062.
- Lilly, D. K., 1968: Models of cloud-topped mixed layers under a strong inversion. Quart. J. Roy. Meteor. Soc., 94, 292-309.
- Manins, P. C., and J. S. Turner, 1978: The relation between flux ratio and energy ratio in convectively mixed layers. Quart. J. Roy. Meteor. Soc., 104, 39-44.
- Stage, S., and J. Businger, 1981a: A model for entrainment into a cloud-topped marine boundary layer. Part I: Model description and application to a cold-air outbreak episode. J. Atmos. Sci., 38, 2213-2229.
- Stage, S., and J. Businger, 1981b: A model for entrainment into a cloud-topped marine boundary layer. Part II: Discussion of model behavior and comparison with other models. J. Atmos. Sci., 38, 2230-2242.



(a)



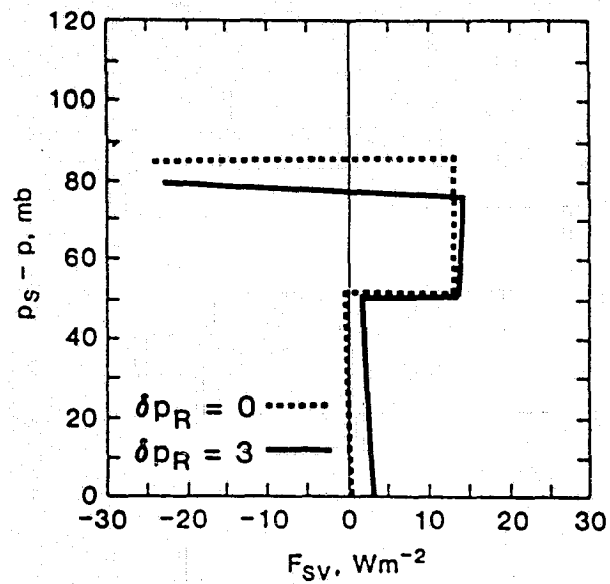
(b)



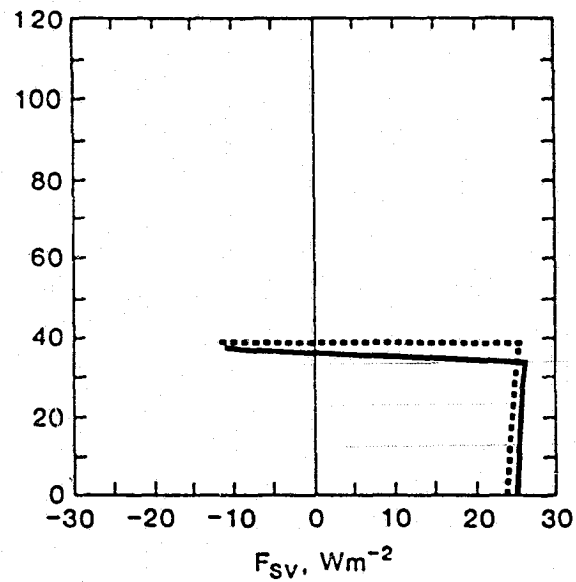
(c)

Figure 1: Buoyancy flux profile for $R_B = 60 \text{ Wm}^{-2}$ and 80 Wm^{-2} , for: a) Eulerian partitioning; b) process partitioning with offensive cooling; c) process partitioning with defensive cooling.

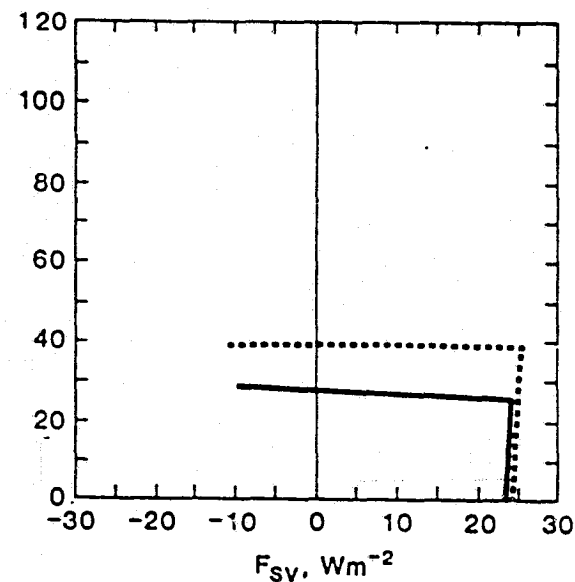
ORIGINAL PAGE IS
OF POOR QUALITY



(a)



(b)



(c)

Figure 2: Buoyancy flux profile for $\delta p_R = 0$ and 3 mb, for: a) Eulerian partitioning; b) process partitioning as implemented by Stage and Businger; c) process partitioning modified so that δp_R increases N rather than decreases P. See text for details.

CAN CLOUD-TOP ENTRAINMENT PROMOTE CLOUD GROWTH?

David A. Randall

Entrainment has traditionally been viewed as inimical to cloud development. Dry environmental air evaporates cloud water, cooling the cloud and reducing its liquid water content. Cloud-top entrainment evaporatively cools a cloud, but it also lifts cloud-top height. There are conditions under which the latter effect actually dominates, resulting in "cloud deepening through entrainment" (CDE; with a little imagination, this can be pronounced as "seed").

For a stratocumulus cloud in the upper portion of a well-mixed layer (Lilly, 1968), the cloud-top liquid water mixing ratio, λ_B , depends on the moist static energy, h_M , the total water mixing ratio, r_M , the mixed layer's pressure depth, δp_M , and the surface pressure, p_S . By the chain rule,

$$L \frac{\partial \lambda_B}{\partial t} = L \left(\frac{\partial \lambda_B}{\partial h_M} \right)_{r_M, \delta p_M} \frac{\partial h_M}{\partial t} + \left(\frac{\partial \lambda_B}{\partial r_M} \right)_{h_M, \delta p_M} L \frac{\partial r_M}{\partial t} + L \left(\frac{\partial \lambda_B}{\partial \delta p_M} \right)_{h_M, r_M} \frac{\partial \delta p_M}{\partial t} + L \left(\frac{\partial \lambda_B}{\partial p_S} \right)_{h_M, r_M} \frac{\partial p_S}{\partial t} \quad (1)$$

For simplicity, we consider only the time rates of change associated with entrainment, i.e.

$$\frac{\partial h_M}{\partial t} = g \frac{E \Delta h}{\delta p_M} \quad (2a)$$

$$\frac{\partial r_M}{\partial t} = g \frac{E \Delta r}{\delta p_M} \quad (2b)$$

$$\frac{\partial \delta p_M}{\partial t} = g E \quad (2c)$$

$$\frac{\partial p_S}{\partial t} = 0 \quad (2d)$$

Here g is the acceleration of gravity; E is the entrainment mass flux; and Δh and Δr are the "jumps" of h and r across cloud top, respectively. Substituting (2) into (1), and collecting terms, we obtain

$$L \frac{\partial \lambda_B}{\partial t} = \frac{g E}{\delta p_M} \left(L \frac{\partial \lambda_B}{\partial h_M} \Delta h + \frac{\partial \lambda_B}{\partial r_M} L \Delta r + L \delta p_M \frac{\partial \lambda_B}{\partial \delta p_M} \right) \quad (3)$$

It is easy to see that $\partial \lambda_B / \partial h_M < 0$, $\partial \lambda_B / \partial r_M > 0$, and $\partial \lambda_B / \partial \delta p_M > 0$. We can show that these three partial derivatives are functions of T_B and p_B , with only a very slight dependence on p_S . Let

$$\Delta \sigma_d \equiv [\Delta h - (1 - \delta \epsilon) L \Delta r] / c_p, \quad (4a)$$

$$\Delta \sigma_m \equiv (\beta \Delta h - \epsilon L \Delta r) / c_p, \quad (4b)$$

where the positive thermodynamic coefficients δ , ϵ , and β are those defined by Randall (1980). As discussed in that paper, $\Delta \sigma_d < 0$ is the criterion for dry static instability at the PBL top; and $\Delta \sigma_m < 0$ is the criterion for cloud-top entrainment instability, which is a type of moist static instability associated with the evaporative cooling of entrained air (Randall, 1980; Deardorff, 1980). Of course, these stability criteria apply only in the unsaturated and saturated cases, respectively. Nevertheless, we can use (4a-b) to formally define both $\Delta \sigma_d$ and $\Delta \sigma_m$ whether or not the PBL top is saturated. By using (4), we can rewrite (3) as

$$\frac{L}{c_p} \frac{\partial \lambda_B}{\partial t} = \frac{gE}{\delta p_M} (\Lambda_0 + \Delta \sigma_d \Lambda_d + \Delta \sigma_m \Lambda_m), \quad (5)$$

where

$$\Lambda_0 \equiv (L/c_p) \delta p_M \partial \lambda_B / \partial \delta p_M, \quad (6a)$$

$$\Lambda_d \equiv (-\epsilon L \frac{\partial \lambda_B}{\partial h_M} - \beta \frac{\partial \lambda_B}{\partial r_M}) / D, \quad (6b)$$

$$\Lambda_m \equiv [(1 - \delta \epsilon) L \frac{\partial \lambda_B}{\partial h_M} + \frac{\partial \lambda_B}{\partial r_M}] / D, \quad (6c)$$

$$D \equiv -\epsilon + \beta (1 - \delta \epsilon). \quad (6d)$$

Inspection of (6a-c) shows that Λ_0 is a temperature, while Λ_d and Λ_m are nondimensional. We can show that $\Lambda_0 > 0$, $\Lambda_d < 0$, and $\Lambda_m > 0$. As p_B decreases, Λ_0 increases significantly, while Λ_d and Λ_m change only slightly.

Let

$$X \equiv \Lambda_0 + \Delta \sigma_d \Lambda_d + \Delta \sigma_m \Lambda_m, \quad (7)$$

so that, according to (5), entrainment will tend to increase or decrease Λ_B according to whether $X > 0$ or $X < 0$. For $\delta p_M = 150$ mb, Fig. 1 shows isolines of X , the relative humidity above cloud-top, $\Delta h/c_p$, and Δr . In constructing this figure, negative values of $\Delta \sigma_d$ were not considered, but both positive and negative values of $\Delta \sigma_m$ were allowed. We have considered the limit of infinitesimal cloud thickness. For given values of $\Delta \sigma_d$ and $\Delta \sigma_m$, only the relative humidity above cloud-top depends on r_M ; X , $\Delta h/c_p$, and Δr are independent of r_M . No contours are plotted for the regions where the relative humidity above cloud-top is greater than 100% or less than zero; these regions are colored in black.

Isopleths of X are straight lines sloping from the lower left to the upper right. CDE occurs where $X > 0$. There is a triangular region within which $\Delta\sigma_m < 0$, while $X > 0$. The size of this region increases as the PBL depth increases. As discussed by Randall (1980), for $\Delta\sigma_m < 0$ the entrainment process "runs away," since entrainment then actually favors buoyant convection near cloud top. Randall argued that this runaway entrainment of dry air tends to destroy the stratocumulus layer. However, the present analysis shows that within the triangular region entrainment actually tends to deepen the cloud sheet, not to destroy it.

CDE also occurs in a portion of the domain for which the cloud-top entrainment instability cannot occur in there, since $\Delta\sigma_m > 0$. There is a third region for which CDE does not occur, but cloud-top entrainment instability does occur, so that a cloud sheet breaks up into fragments, as discussed by Randall (1980). Finally, there is a portion of the domain for which neither CDE nor the cloud-top entrainment instability occur.

CDE is favored by large values of δp_m . The reason is that the drying effects of the entrained air are minimized when it is mixed through a deep layer.

The primary significance of CDE is that it can prevent the cloud-top entrainment instability from destroying a cloud deck. Without suppressing the instability, CDE transforms it from a cloud-destroyer to a cloud-builder.


The analysis presented in this paper does not depend on an entrainment hypothesis. Moreover, it is not restricted to PBL stratocumulus sheets. Stratiform clouds in the free atmosphere can be subject to CDE; we need only reinterpret p_s as the pressure at the base of an elevated turbulent mixed layer. Modest departures from well-mixedness will alter the results quantitatively but not qualitatively. Processes other than entrainment, such as surface evaporation, radiative cooling, and advection will often work with CDE to build a cloud layer; but of course they can also oppose CDE by reducing the relative humidity.

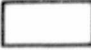



If we make the weak assumption that the deepening of a cloud layer favors an increase in the cloud-top entrainment rate (without specifying any particular functional relationship) we are let to speculate that CDE can cause runaway cloud growth, even in the absence of cloud-top entrainment instability. Through CDE, entrainment leads to a deeper cloud, which leads to stronger entrainment.

REFERENCES

- Deardorff, J. W., 1980: Cloud-top entrainment instability. J. Atmos. Sci., 37, 131-147.
- Lilly, D. K., 1968: Models of cloud-topped mixed layers under a strong inversion. Quart. J. Roy. Meteor. Soc., 94, 292-309.
- Randall, D. A., 1980: Conditional instability of the first kind, upside-down. J. Atmos. Sci., 37, 125-130.

Figure 1: Contour plot of X (K), $\Delta h/c_p$ (K), Δr (g kg^{-1}), and the relative humidity above cloud-top (%), over the $(\Delta\sigma_d, \Delta\sigma_m)$ plane, for $\delta p_M = 50$ mb and $r_M = q_B^*$.

For each plot,  denotes regions where the relative humidity above cloud top is either less than zero or greater than 100%;

 denotes the region in which both CDE and cloud-top entrainment instability occur;  denotes CDE but no cloud-top entrainment instability;  denotes neither CDE nor cloud-top entrainment instability; and  denotes cloud-top entrainment instability without CDE.

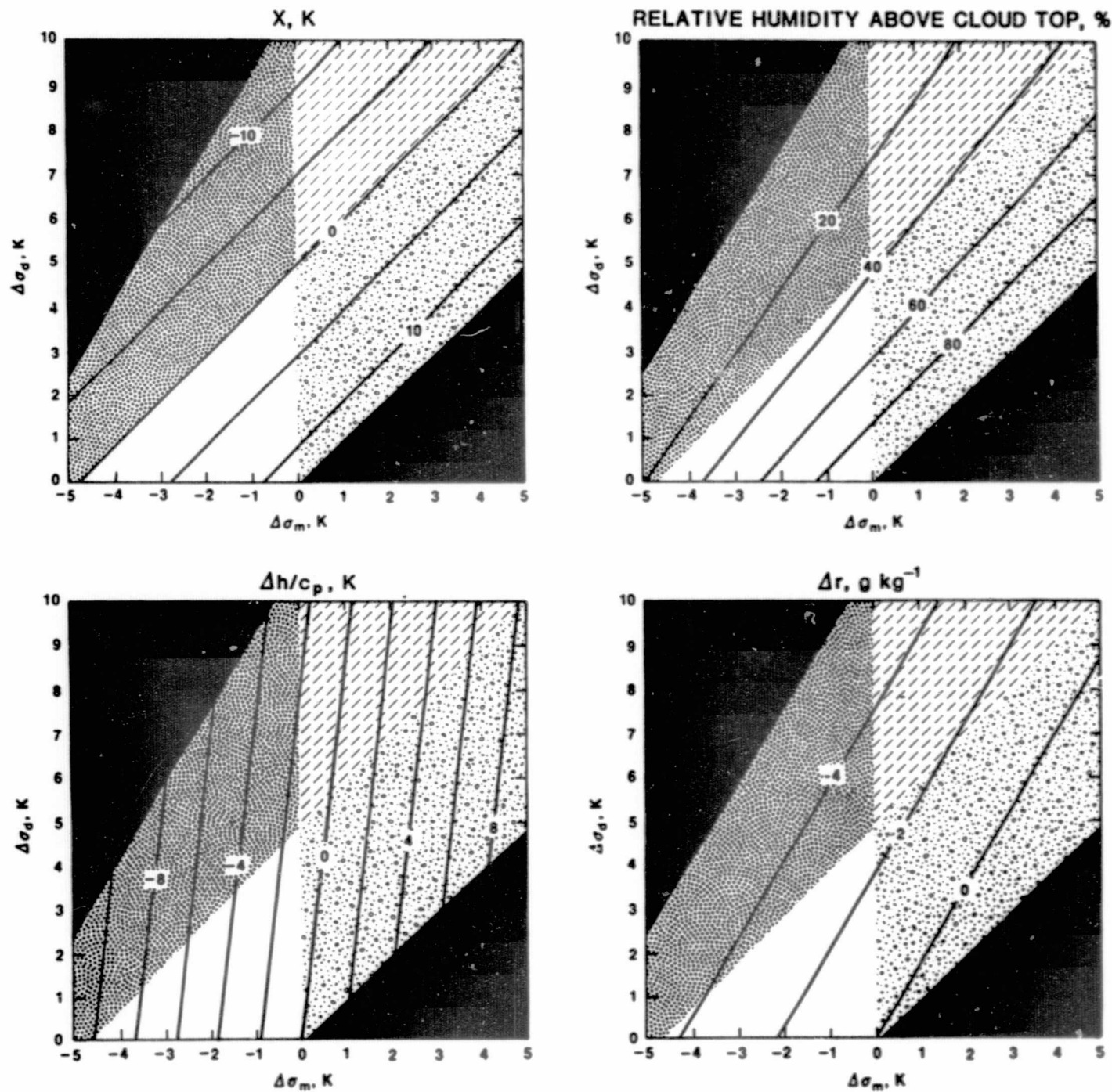


Figure 1

ORIGINAL PAGE IS
OF POOR QUALITY

N84 22101

ON THE JOINT BIMODALITY OF TEMPERATURE AND MOISTURE
NEAR STRATOCUMULUS CLOUD TOPS

D. A. Randall

The upper boundary of a layer of stratocumulus clouds is inevitably somewhat irregular; turrets can be pushed up here and there by convective turbulence, and shearing instabilities can give rise to wave-like features. The bumpiness of cloud top complicates the theoretical description of such important cloud-top processes as radiative cooling and turbulent entrainment, since at a given level the fractional cloudiness is greater than zero but less than one. The clear air near cloud top is typically very warm and dry compared to the cool, moist cloudy air lying nearby at the same height (Fig. 1).

Up to now, only the high-resolution three-dimensional model of Deardorff (1980) has explicitly simulated the effects of partial cloudiness near cloud top; Deardorff remarked that even in his model the vertical resolution (50 m) appeared to be inadequate to accurately represent processes near cloud-top. He advocated the use of a parameterization of sub-grid fractional cloudiness as an aid in the simulation of cloud-top processes (Deardorff and Sommeria, 1977; Mellor, 1977; Bougeault, 1981a,b).

The observed distributions of the thermodynamic variables near stratocumulus top are highly bimodal (Mahrt and Paumier, 1982). This suggests a model based on the assumption of a joint bimodal distribution of parcels, obtained as the weighted sum of two binormal distributions, i.e.

$$p(s,q) = f_1 G(s - s_1, \sigma_{s_1}, q - q_1, \sigma_{q_1}, r_{sq_1}) \\ + (1 - f_1) G(s - s_2, \sigma_{s_2}, q - q_2, \sigma_{q_2}, r_{sq_2}) \quad (1)$$

where G is the joint-normal distribution:

$$G(x, \sigma_x, y, \sigma_y, r_{xy}) \equiv [2\pi\sigma_x\sigma_y(1 - r_{xy}^2)^{1/2}]^{-1} \\ \exp \left[-\frac{1}{2(1 - r_{xy}^2)} \frac{x^2}{\sigma_x^2} - \frac{2r_{xy}xy}{\sigma_x\sigma_y} + \frac{y^2}{\sigma_y^2} \right] \quad (2)$$

and $r_{xy} \equiv \overline{xy}/(\sigma_x\sigma_y)$ is the correlation between x and y within each population. We have assigned weight f_1 to population 1, and weight $(1 - f_1)$ to population 2. Of course,

$$\int_{-\infty}^{\infty} \int_{-\infty}^{\infty} p(s,q) dsdq = 1 \quad (3)$$

Using the properties of the joint-normal distribution G, we can derive the following relations:

$$\bar{s} = f_1 s_1 + (1 - f_1) s_2 \quad , \quad (4)$$

$$\bar{q} = f_1 q_1 + (1 - f_1) q_2 \quad , \quad (5)$$

$$\overline{s'^2} = f_1 [\sigma_{s_1}^2 + (s_1 - \bar{s})^2] + (1 - f_1) [\sigma_{s_2}^2 + (s_2 - \bar{s})^2] \quad , \quad (6)$$

$$\overline{q'^2} = f_1 [\sigma_{q_1}^2 + (q_1 - \bar{q})^2] + (1 - f_1) [\sigma_{q_2}^2 + (q_2 - \bar{q})^2] \quad , \quad (7)$$

$$\overline{s'q'} = f_1 [(s_1 - \bar{s})(q_1 - \bar{q}) + (\overline{s'q'})_1] + (1 - f_1) [(s_2 - \bar{s})(q_2 - \bar{q}) + (\overline{s'q'})_2] \quad , \quad (8)$$

$$\overline{s'^3} = f_1 (s_1 - \bar{s}) [3\sigma_{s_1}^2 + (s_1 - \bar{s})^2] + (1 - f_1) (s_2 - \bar{s}) [3\sigma_{s_2}^2 + (s_2 - \bar{s})^2] \quad , \quad (9)$$

$$\overline{q'^3} = f_1 (q_1 - \bar{q}) [3\sigma_{q_1}^2 + (q_1 - \bar{q})^2] + (1 - f_1) (q_2 - \bar{q}) [3\sigma_{q_2}^2 + (q_2 - \bar{q})^2] \quad , \quad (10)$$

$$\begin{aligned} \overline{s'^2 q'} &= f_1 \{ [\sigma_{s_1}^2 + (s_1 - \bar{s})^2] (q_1 - \bar{q}) + 2(s_1 - \bar{s})(\overline{s'q'})_1 \} \\ &\quad + (1 - f_1) \{ [\sigma_{s_2}^2 + (s_2 - \bar{s})^2] (q_2 - \bar{q}) + 2(s_2 - \bar{s})(\overline{s'q'})_2 \} \quad , \end{aligned} \quad (11)$$

$$\begin{aligned} \overline{s'q'^2} &= f_1 \{ (s_1 - \bar{s}) [\sigma_{q_1}^2 + (q_1 - \bar{q})^2] + 2(q_1 - \bar{q})(\overline{s'q'})_1 \} \\ &\quad + (1 - f_1) \{ (s_2 - \bar{s}) [\sigma_{q_2}^2 + (q_2 - \bar{q})^2] + 2(q_2 - \bar{q})(\overline{s'q'})_2 \} \quad . \end{aligned} \quad (12)$$

In (8), (11), and (12), $(\overline{s'q'})_1$ and $(\overline{s'q'})_2$ are the covariances associated with populations 1 and 2, respectively. The 9 equations (4 - 12) involve the 11 unknowns s_1 , s_2 , q_1 , q_2 , $\sigma_{s_1}^2$, $\sigma_{s_2}^2$, $\sigma_{q_1}^2$, $\sigma_{q_2}^2$, f_1 , $(\overline{s'q'})_1$, and $(\overline{s'q'})_2$.

Two additional equations will be required for solution of the system. These additional equations essentially determine $(\overline{s'q'})_1$ and $(\overline{s'q'})_2$.

We can solve (4-12) analytically for the case $(\overline{s'q'})_1 = (\overline{s'q'})_2 = 0$. Is this sufficient? Such a solution will have $s_1 \neq s_2$ and $q_1 \neq q_2$ whenever $\overline{s'q'} \neq 0$.

Thus we will almost always have two distinct populations. However, the joint distribution of s and q need not necessarily have two maxima. Perhaps the additional generality provided by non-zero values of $(s'q')_1$ and $(s'q')_2$ is not needed. Further study is needed to resolve this issue.

REFERENCES

- Bougeault, Ph., 1981a: Modeling the trade-wind cumulus boundary layer. Part I: Testing the ensemble cloud relations against numerical data. J. Atmos. Sci., 38, 2414-2428.
- Bougeault, Ph., 1981b: Modeling the trade-wind cumulus boundary layer. Part II: A high order one dimensional model. J. Atmos. Sci., 38, 2429-2439.
- Deardorff, J. W., and G. Sommeria, 1977: Subgrid-scale condensation in models of nonprecipitating clouds. J. Atmos. Sci., 34, 344-355.
- Deardorff, J. W., 1980: Stratocumulus-capped mixed layers derived from a three-dimensional model. Boundary-Layer Meteor., 18, 495-527.
- Mahrt, L., and J. Paumier, 1982: Cloud-top entrainment instability observed in AMTEX. J. Atmos. Sci., 38, 622-634.
- Mellor, G. L., 1977: The Gaussian cloud model relations. J. Atmos. Sci., 34, 356-358.

ORIGINAL PAGE IS
OF POOR QUALITY

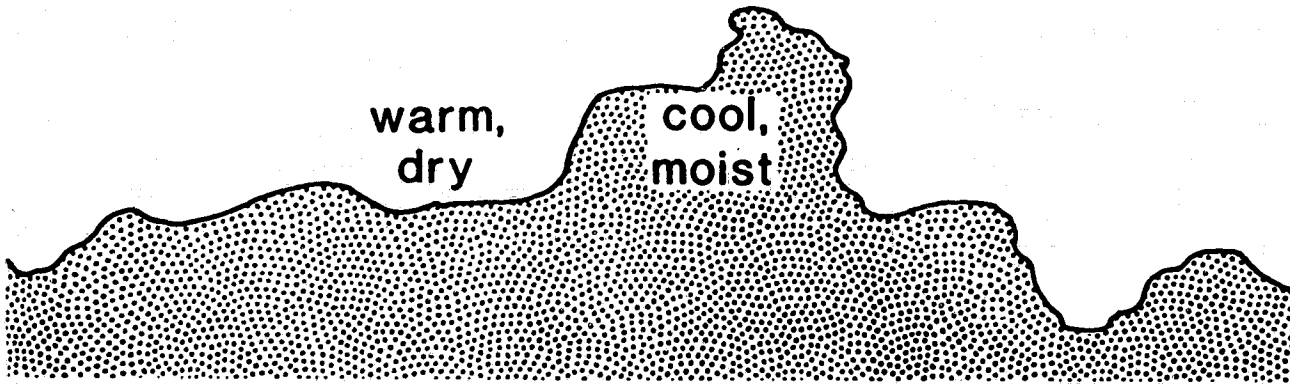


Figure 1

253
N84 22102

AN ENSEMBLE FORMULATION OF PBL FLUXES IN A GCM

Y. C. Sud and W. E. Smith

Some of the major PBL parameterizations used in GCMs have been summarized by Carson (1981). All of them use some form of bulk friction and heat transport coefficients to parameterize PBL fluxes. The validation of these parameterizations is often based on comparison with observations. The observations in turn are made over homogeneous terrains, while the parameterizations try to simulate PBL fluxes on a very coarse grid often encompassing large subgrid scale inhomogeneities, particularly over land. This suggests an ensemble approach which has not been adequately stressed by the GCM modellers thus far. To do this, we identify the bulk Richardson number as the key parameter. It is clear that this approach is necessary for all other physical parameterizations as well, though we attempt it only for the PBL calculations.

Among the PBL related weaknesses of the GLAS climate model are: too much ET over land, and correspondingly, too much precipitation, and occasional burst Δt (Δt being the physical time step) oscillation in the surface fluxes of heat and moisture.

An ensemble averaging calculation was carried out to re-derive the bulk friction and heat transport coefficients for the mean conditions. Wind velocity of 4 and 5 m sec⁻¹ and the temperature variability of 2 K and 0.5 K were used in these calculations for land and ocean, respectively. To account for variability of the atmosphere, the calculated standard deviation of the bulk Richardson number was simply doubled. The derived C_U and C_H curves were fitted using the polynomial.

$$y = A + Bx + C \log_e (x_f - x) + D [\log_e (x_f - x_e)]^2 + E (x + x_D) / [(x + x_D)^2 + y_D^2]$$

The variable y represents C_U or C_H . A , B , C , D and E are constants of the polynomial that are determined by least square fit (see Table 1 for values). The variable x is the bulk Richardson number, and x_f is a scale shifting parameter which must be more than 16 to avoid a logarithm of negative numbers. Figs. 1a and 1b show derived C_U and C_H values vis-a-vis Deardorff (1972) values as functions of bulk Richardson number.

Clearly some arbitrariness in the choice of variability of parameters is evident in the formulation but the primary aim of this exercise was to show the importance and need for invoking this concept.

Other modifications to the model were: a) the relationship between actual and potential ET to accord with Sud and Fennessy (1982); b) maximum permissible instantaneous ET at any time is 1.5 mm/hr; c) moisture distribution in low level cumulus convection to be consistent with no precipitation; d) appearance of supersaturation clouds to be consistent with supersaturation condition at that level; e) invoking a simple function for stomatal diffusion effect in the ET calculation.

With the above modifications, a new simulation was made for 47 days. The integration started from the observed initial state of the global atmosphere on June 15, 1979 as analyzed by NMC. An identical simulation with the original GLAS climate GCM was also made. The new simulation (S_N) was compared with the old simulation (S_O) as well, with observations where possible. The following differences are noteworthy.

The PBL fluxes simulated by S_N are more realistic. The 47 day time series at several selected land points showed no $2-\Delta t$ oscillation in the surface fluxes. This can be easily inferred from area averaged plots over the U.S. in Figs. 2a and 2b.

Land surface evaporation reduced considerably which in turn produced a thermal low over the entire land mass in the Northern Hemisphere. In another simulation, without the introduction of stomatal effect, this influence was nonexistent. We infer that due to large variation in the vegetation cover over land a global dataset of stomatal resistance, and roughness height (z_0) is necessary.

Some simple modifications to the cumulus and large scale cloud parameterizations alleviated the problem of too much low level cloudiness. Simultaneously, improvement was found in the global precipitation heat balance, planetary albedo and geopotential heights at various pressure levels.

Too much precipitation in the Sahara Desert was recognized as a major weakness of the new run. However, in our simulation, studies using smaller roughness heights for land surface in deserts, this condition is effectively corrected. (See "Influence of Roughness Height in Deserts" by Sud and Smith in this Report.)

REFERENCES

- Carson, D. J., 1981: Current parameterization of land surface processes in atmospheric general circulation models. JSC Study Conference on Land-Surface Processes in Atmospheric General Circulation Models, Jan. 5-10, NASA/Goddard Space Flight Center, Greenbelt, MD 20771.
- Deardorff, J. W., 1972: Parameterization of the planetary boundary layer for use in general circulation models. Mon. Wea. Rev., 93, 93-106.
- Sud, Y. C., and M. J. Fennessy, 1982: An observational data based evapotranspiration function for General Circulation models. Atmosphere-Ocean, 20, 301-316.

Table 1

I Constants x_D and y_D

<u>Constants</u>	CU Land	CT Land	CU Ocean	CT Ocean	CU Sea-ice	CT Sea-ice
XD	-2.00	1.25	-2.50	-1.00	-2.50	-1.00
YD	14.00	15.50	13.50	12.50	13.50	12.50

II Constants A, B, C, D, and E

Bulk transfer coefficient	Value of Constants of the Polynomial				
	A	B	C	D	E
CU Land	.45074e-01	.14060e-03	-.24848e-02	.36210e-02	-.89813
CT Land	.66074e-01	.45848e-03	-.16459e-01	.10857e-01	-1.5125
CU Ocean	.66074e-01	.17231e-04	.23036e-02	.83532e-03	-.22346
CT Ocean	.13545e-01	.19767e-04	.12879e-02	.19922e-02	-.27129
CU Sea Ice	.92111e-02	.10559e-04	.28117e-02	.59197e-03	-.21361
CT Sea Ice	.12310e-01	.60590e-05	.31227e-02	.13161e-02	-.26603

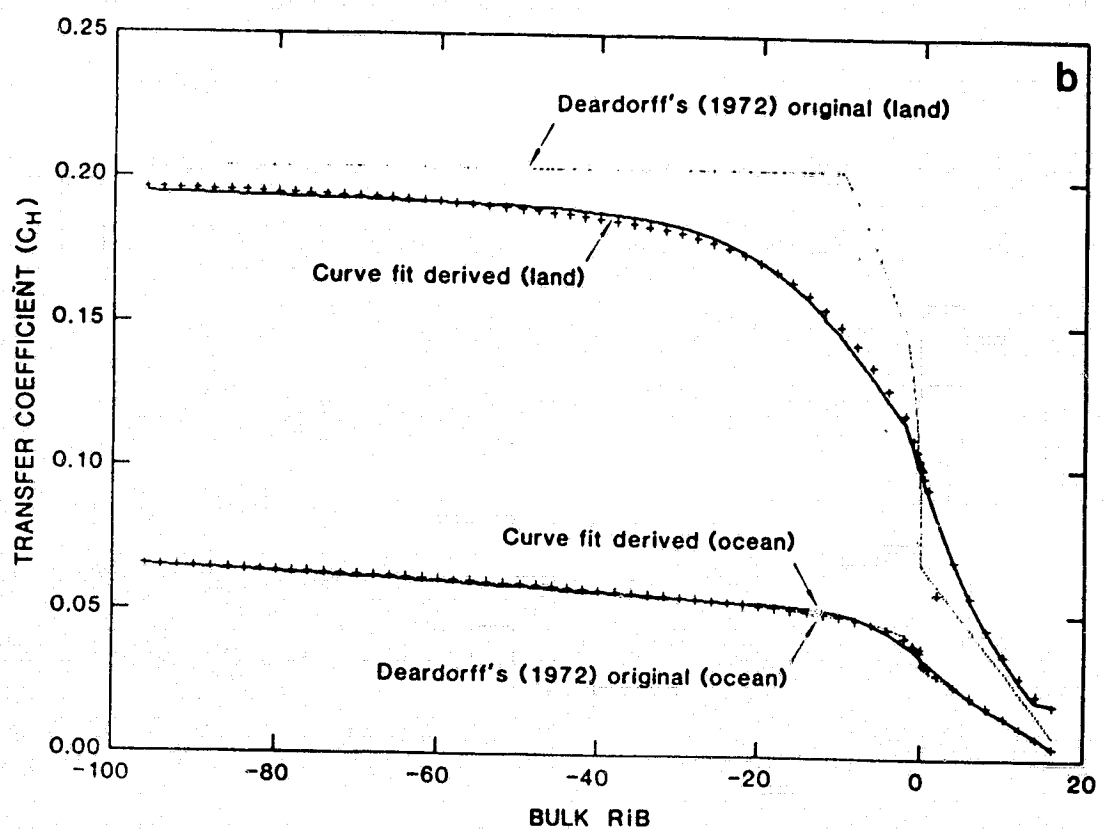
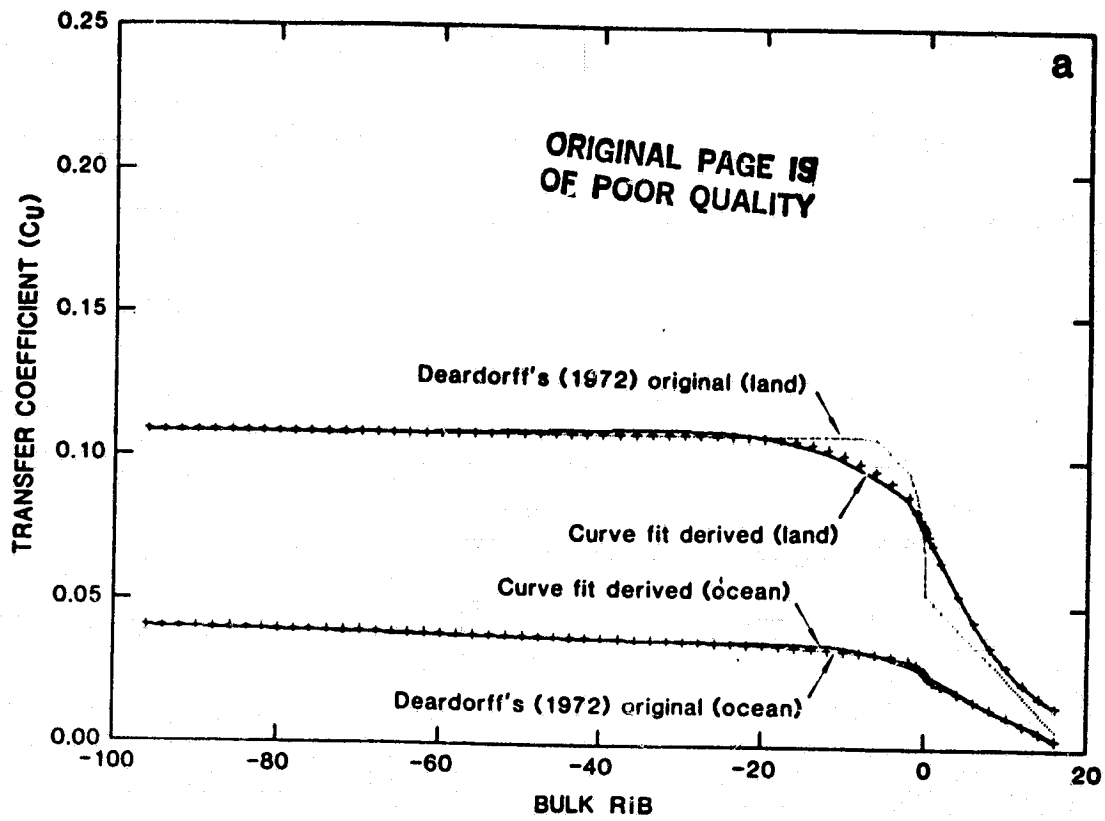


Fig. 1. Ensemble average friction and heat transfer coefficients based on the Deardorff (1972) formulation.

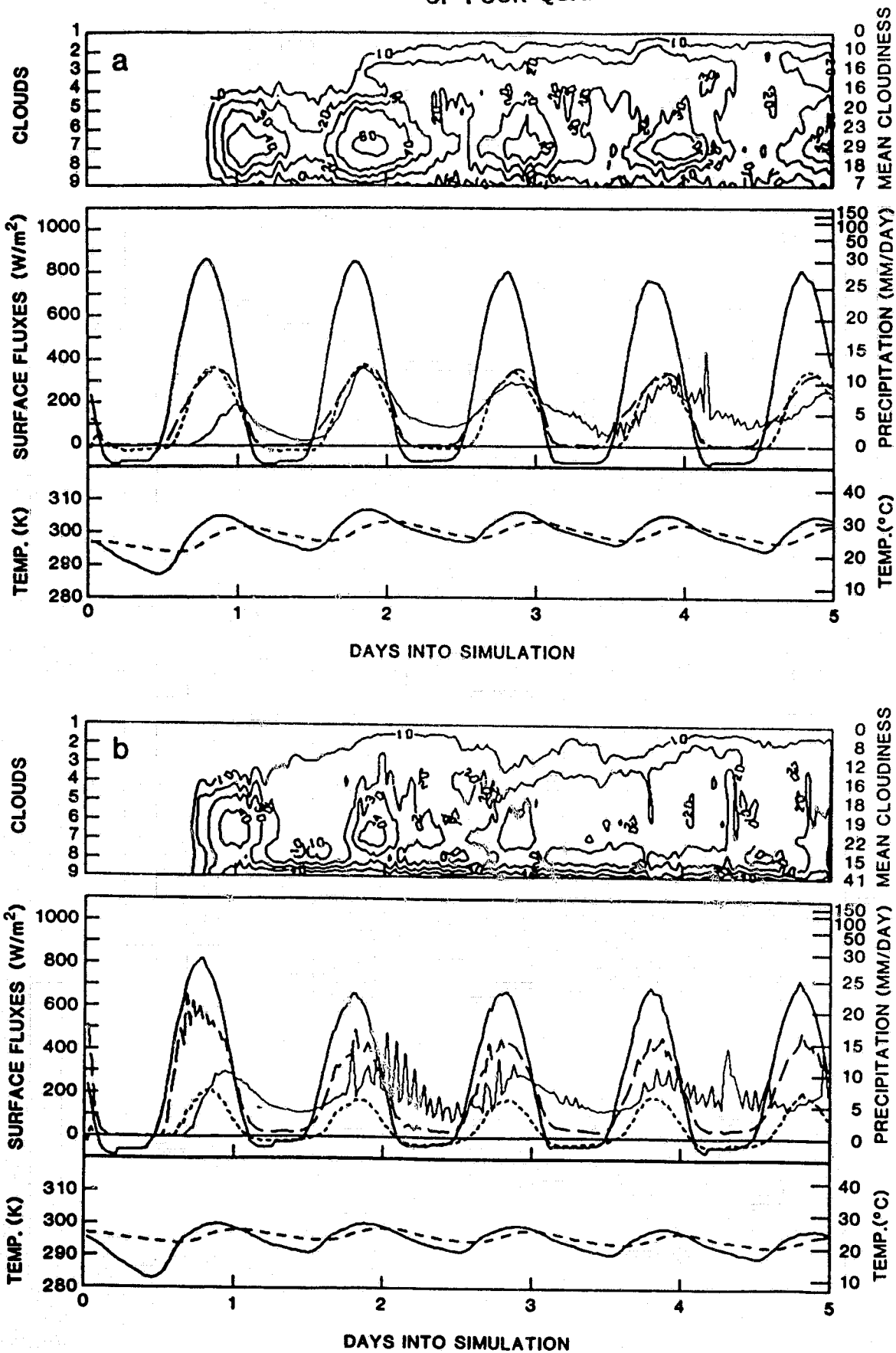


Fig. 2. Time-evolution of 5 day sample of 47 grid point-averaged fields. Top panel: percentage cloudiness. Bottom panel: ground (—) and surface (---) temperatures. Middle panel: net radiation (—), sensible (---), latent (— · —) fluxes and precipitation (—) for (a) new simulations (S_N), and (b) old simulations (S_O).

A NOTE ON THE TEMPORAL BEHAVIOR OF BUCKET HYDROLOGIES

M. J. Suarez

Most GCM studies to date have used a very simple "bucket" hydrology to model evaporation over land surfaces. At each grid point the models keep a budget of ground water as though it accumulated in a bucket some 15 cm deep. Precipitation is added, evaporation removed, and run-off spilled out when the bucket is full. The result of this calculation, the amount of water in the bucket, is used to parameterize the evaporation.

Typically the evaporation, E , is taken as some fraction of the potential evaporation, E_p -that is the evaporation one would expect over a saturated surface at the same temperature,

$$E \equiv \beta E_p \quad (1)$$

The ability of plants to control transpiration is modelled in a crude way by allowing β to depend on the amount of water in the bucket, w . Below we will use the simple relation

$$\beta = \min(1.5 w/wc, 1) \quad (2)$$

where wc is the depth of the bucket.

Much more sophisticated parameterizations of the role of vegetation in the thermodynamics of continental surfaces are now being developed for use in general circulation models. These rely heavily on our understanding of plant physiological processes, and attempt to account for differences between plant communities. One of the many ways in which the formulation of evaporation in these models differs from the bucket model described above is in the inclusion of interception loss--evaporation directly off wet leaf surfaces. The purpose of this note is to compare the temporal behavior of the traditional bucket model with one that mimics the effects of interception loss.

Results are presented in terms of the spectral response of the parameterization to a hypothetical white noise forcing. Although the sample cases considered hardly warrant this detailed numerical analysis, they are included as an example of the sort of idealized tests that might be made with more complex parameterizations.

We take the land surface to have no heat capacity so that the surface energy budget is

$$F = -\sigma T_S^4 + R - S - LE = 0 \quad (3)$$

where T_S is the temperature of the surface, R is the net shortwave plus incident longwave radiation at the ground, S is the sensible heat flux from the surface to the air, and L is the latent heat of condensation. For the sensible heat flux and the evaporation from a saturated surface we use the bulk aerodynamic formulas

$$S = \rho_a C_D C_p (T_S - T_a) \quad (4)$$

ORIGINAL PAGE IS
OF POOR QUALITY

$$E_p = \rho_a C_D (q^*(T_a) - h q^*(T_a)). \quad (5)$$

where T_a is the atmospheric temperature at the surface, and h is the atmospheric relative humidity. $q^*(T)$ is the saturation mixing ratio at temperature T .

For small air-surface temperature differences, (5) may be linearized about T_a

$$E_p \approx \rho_a C_D q^*(T_a) [(1 - h) + \gamma_a (T_s - T_a)], \quad (6)$$

where

$$\gamma_a \equiv \frac{1}{q^*} \frac{dq^*}{dT} \Big|_{T_a}. \quad (7)$$

In the calculations, we use $C_D = 1.1 \times 10^{-3}$ and $h = 0.8$.

Using (6) with the "bucket" model in (3) gives

$$\Delta T \equiv T_s - T_a = (F(T_a, \beta) / \frac{\partial F}{\partial \Delta T}) \Big|_{\Delta T = 0}, \quad (8)$$

with which the evaporation may be obtained from (6) and (1) as a function of R , T_a , and β . Figure 1 shows E as a function of (w/w_c) , using (2) and $R = 540$ w/m^2 , $T_a = 300^\circ K$.

The bucket's water budget for $w/w_c < 1$ is

$$\frac{dw}{dt} = -E + P \quad (9)$$

$$= -\kappa w + P \quad (10)$$

Figure 2 shows κ^{-1} which is inversely proportional to the slope of the evaporation in Figure 1. It varies between 15 and 45 days because of the increase in saturation vapor pressure with increasing temperature.

If P in (10) is taken to be a random process with power spectrum $|\mathcal{P}|^2$, the spectrum of w should be

$$|\mathcal{W}|^2 = \frac{|\mathcal{P}|^2}{\nu^2 + \kappa^2} \quad (11)$$

where ν is the frequency.

Figure 3 shows the results of a 10000 day integration for a case in which no run-off occurs. \mathcal{P} here is white noise with a distribution for which half the days have no precipitation and the other half a random amount between 0 and 8 mm. The forcing is shown in the top panel. The mean precipitation and evaporation, are 2 mm/day. From Figure 1 we see the mean w should be about 8 mm, for which κ^{-1} would be ~ 35 days.

Figure 4 shows the spectra of precipitation (white noise), ground wetness, and evaporation, the solid line in the center panel is a plot of (11) with $\kappa^{-1} = 35$ days.

The spectrum of wetness is very much as expected from the preceding discussion; although at low frequency both ground wetness and evaporation have significantly higher power than expected. For comparison, the calculations were repeated for the first order Markov process,

$$W_i = \alpha W_{i-1} + P, \quad (12)$$

where P is the same as in Figure 3 and $\alpha = .971243$ --corresponding to a κ^{-1} of 35 days, when i indexes days. The results are shown in Figure 5.

Clearly the redness shown in Figures 3 and 4 make even 100 day averages (roughly 3 independent samples) of wetness and evaporation poor estimates of the long-term mean. Further variability introduced by varying atmospheric conditions or by redness in the precipitation should make matters even worse.

The effect of interception loss is crudely represented by putting a small "canopy" bucket above the usual bucket. Evaporation is assumed to proceed at the potential rate as long as there is water in the canopy and at the rate given by (1) and (2) when the canopy is dry. Precipitation falls into the canopy which overflows into the ground bucket. For the calculation shown the canopy is given a capacity of 3mm and all other parameters are as before. The forcing is identical to that shown in Figure 3. Figure 6 shows the ground wetness and evaporation, and Figure 7 the corresponding spectra. The evaporation is now nearly white, reflecting directly the spectrum of the precipitation. In the wetness, high frequency variability is reduced by the buffering effect of the canopy, but as one would expect, the low frequency is hardly altered.

Finally Figure 8 shows the scatter of an effective β from this calculation. Clearly the inclusion of interception loss will be a fundamental change in the parameterization of evapotranspiration.

ORIGINAL PAGE IS
OF POOR QUALITY

EVAPORATION

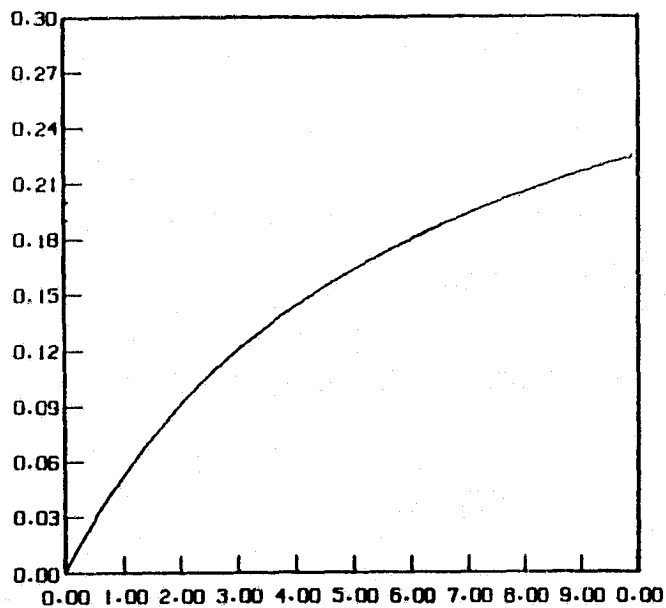


Figure 1

DECAY TIME

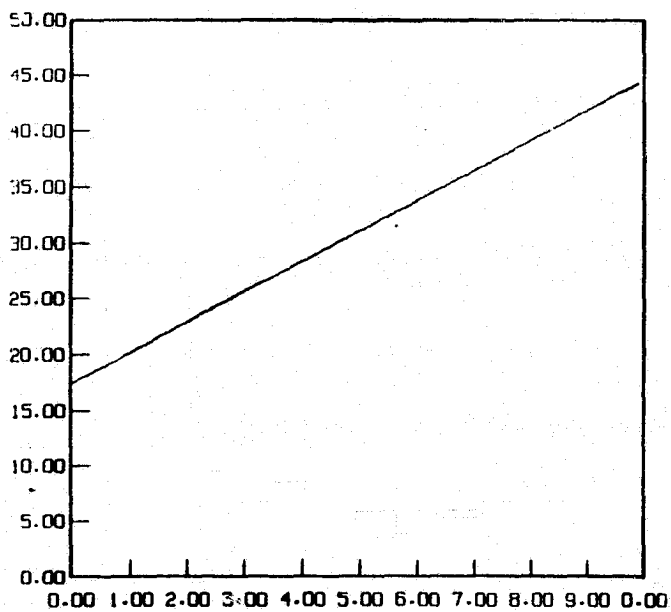
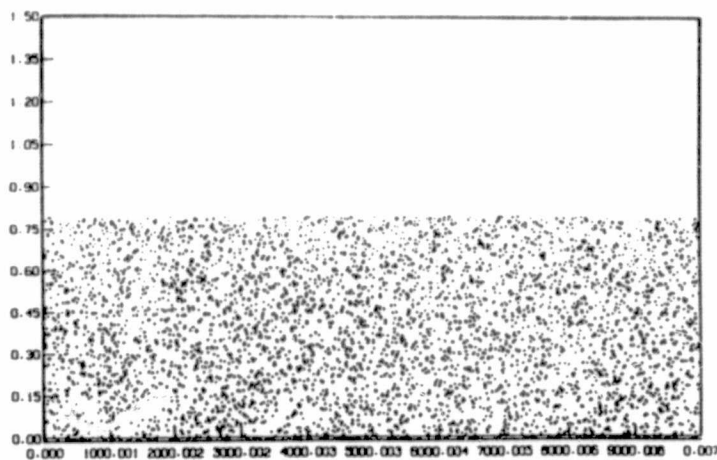


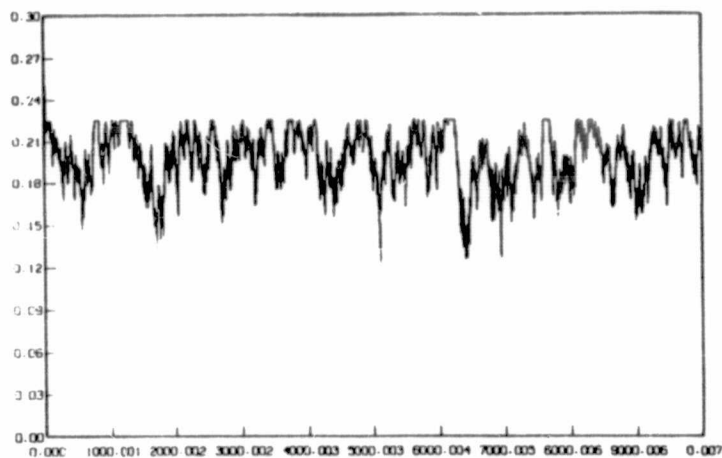
Figure 2

ORIGINAL PAGE IS
OF POOR QUALITY

PRECIPITATION



EVAPORATION



GROUND WETNESS

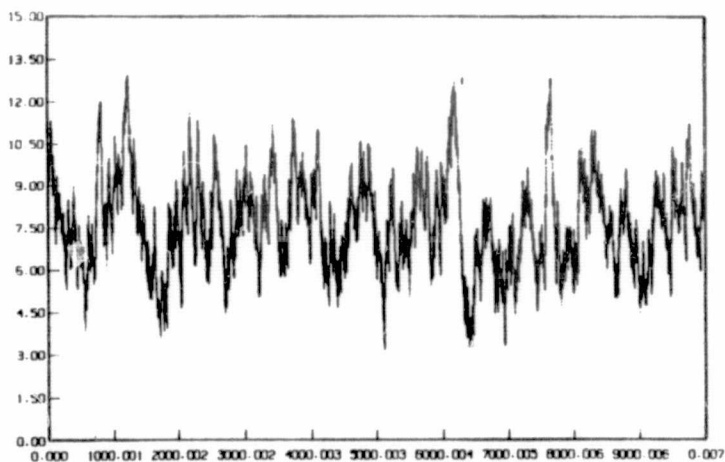
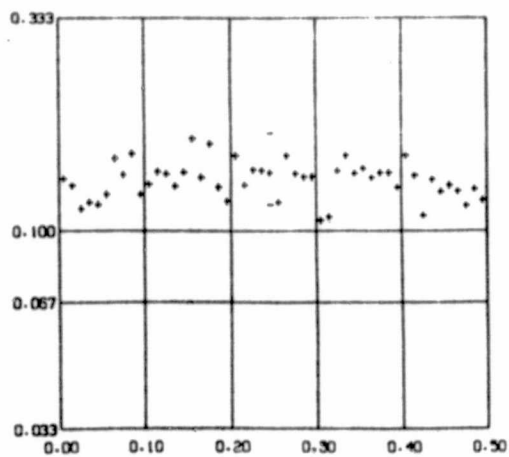


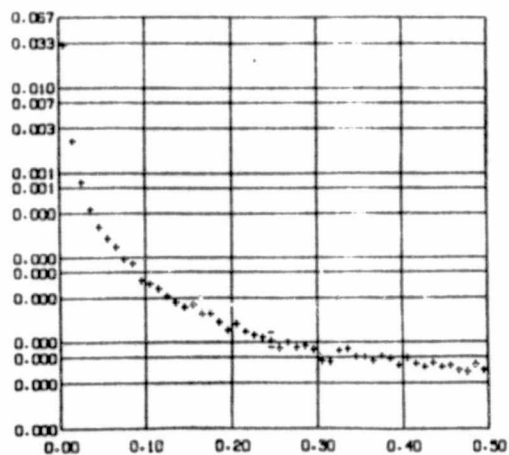
Figure 3

ORIGINAL PAGE IS
OF POOR QUALITY

PRECIPITATION



EVAPORATION



GROUND WETNESS

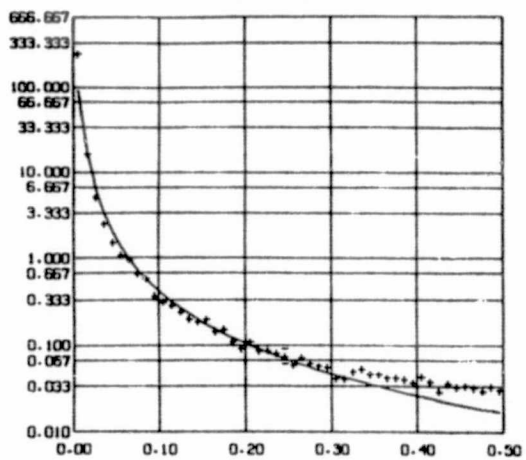


Figure 4

ORIGINAL PAGE IS
OF POOR QUALITY

GROUND WETNESS

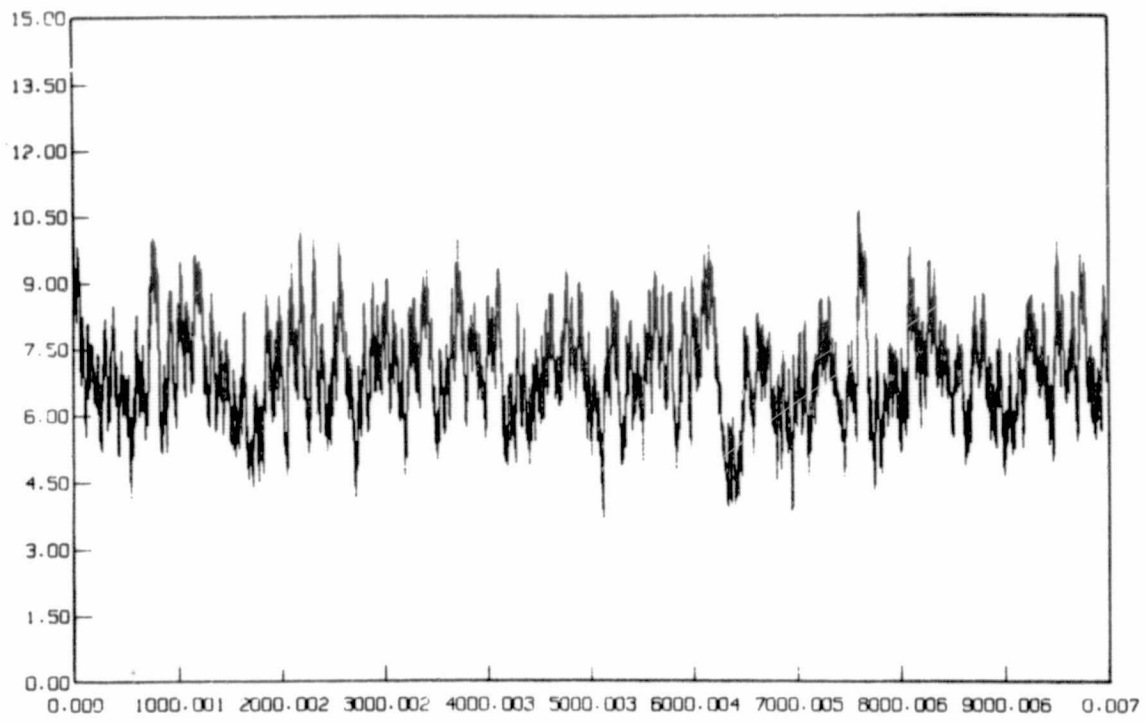
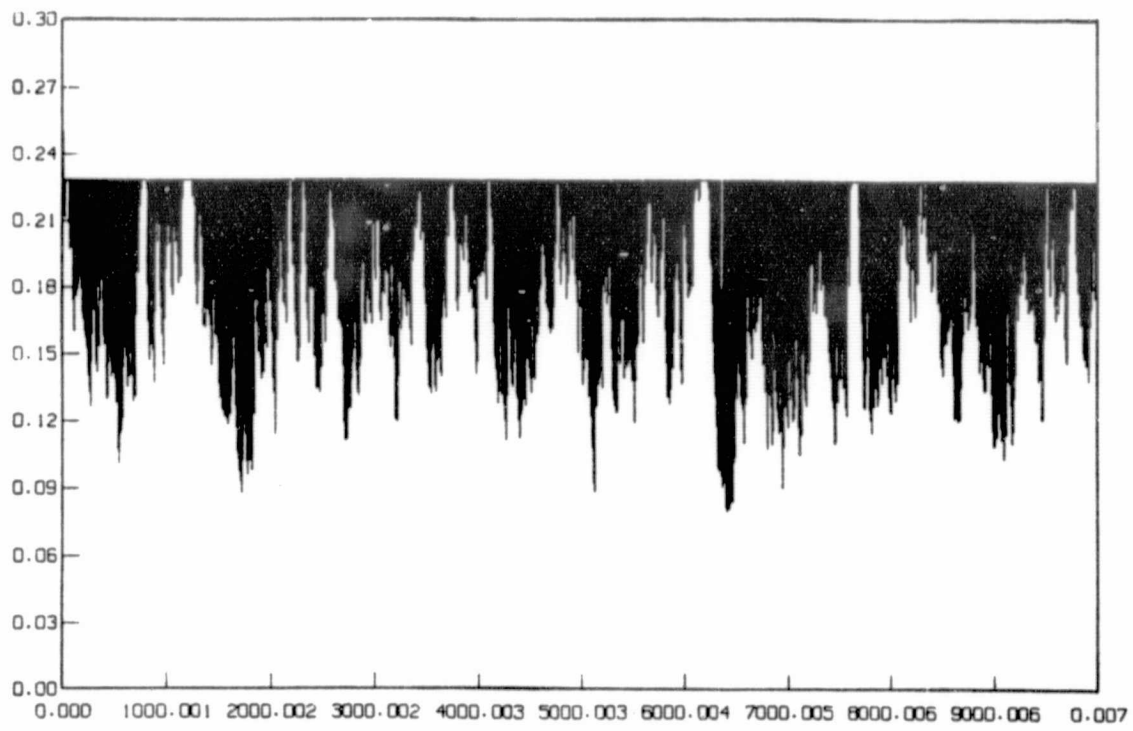


Figure 5

ORIGINAL PAGE IS
OF POOR QUALITY

EVAPORATION



GROUND WETNESS

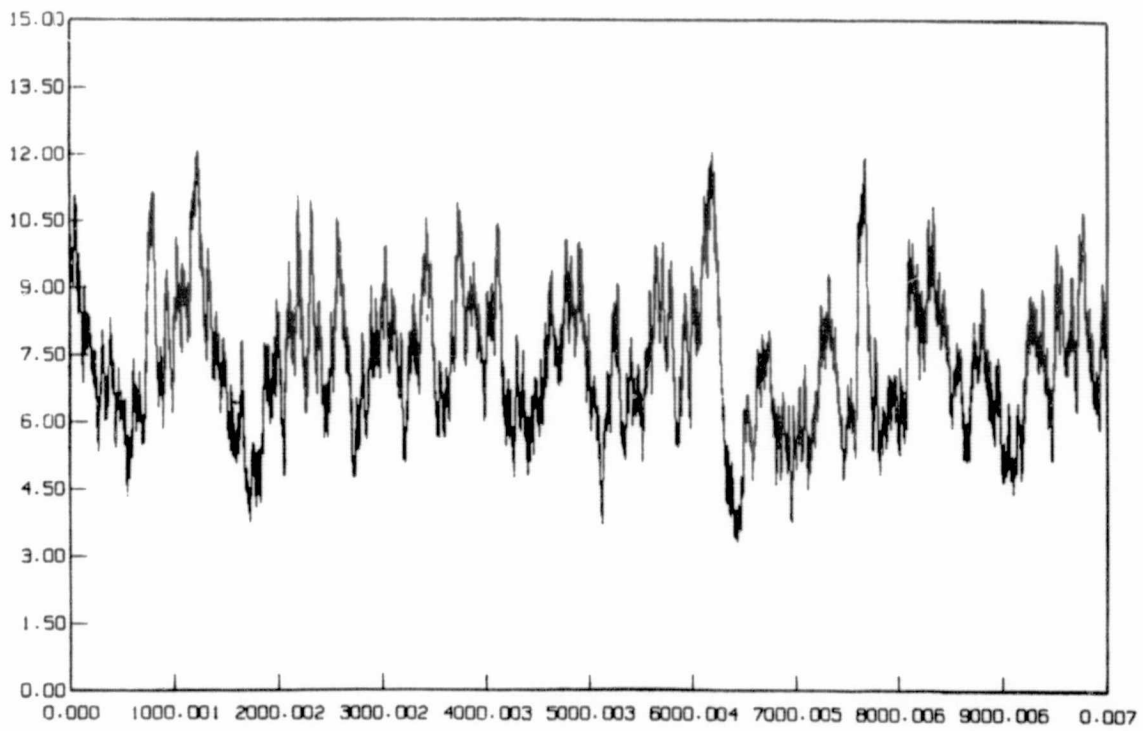
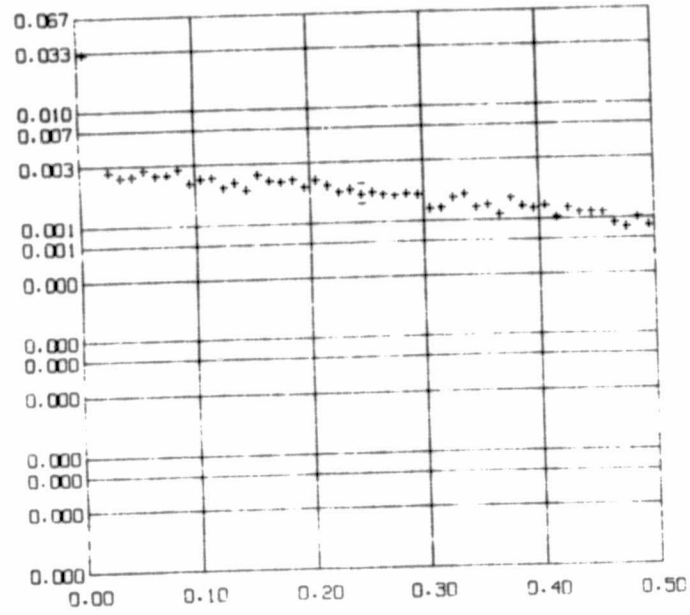


Figure 6

ORIGINAL PAGE IS
OF POOR QUALITY

EVAPORATION



GROUND WETNESS

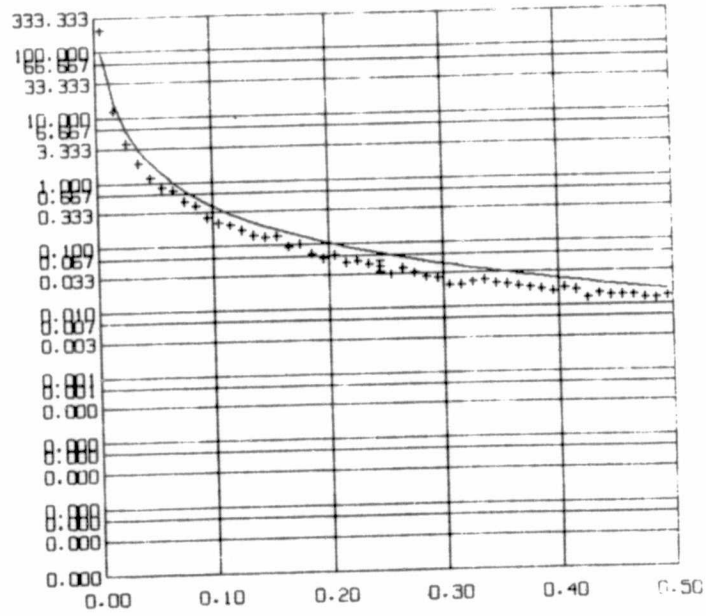


Figure 7

ORIGINAL PAGE IS
OF POOR QUALITY

BETA

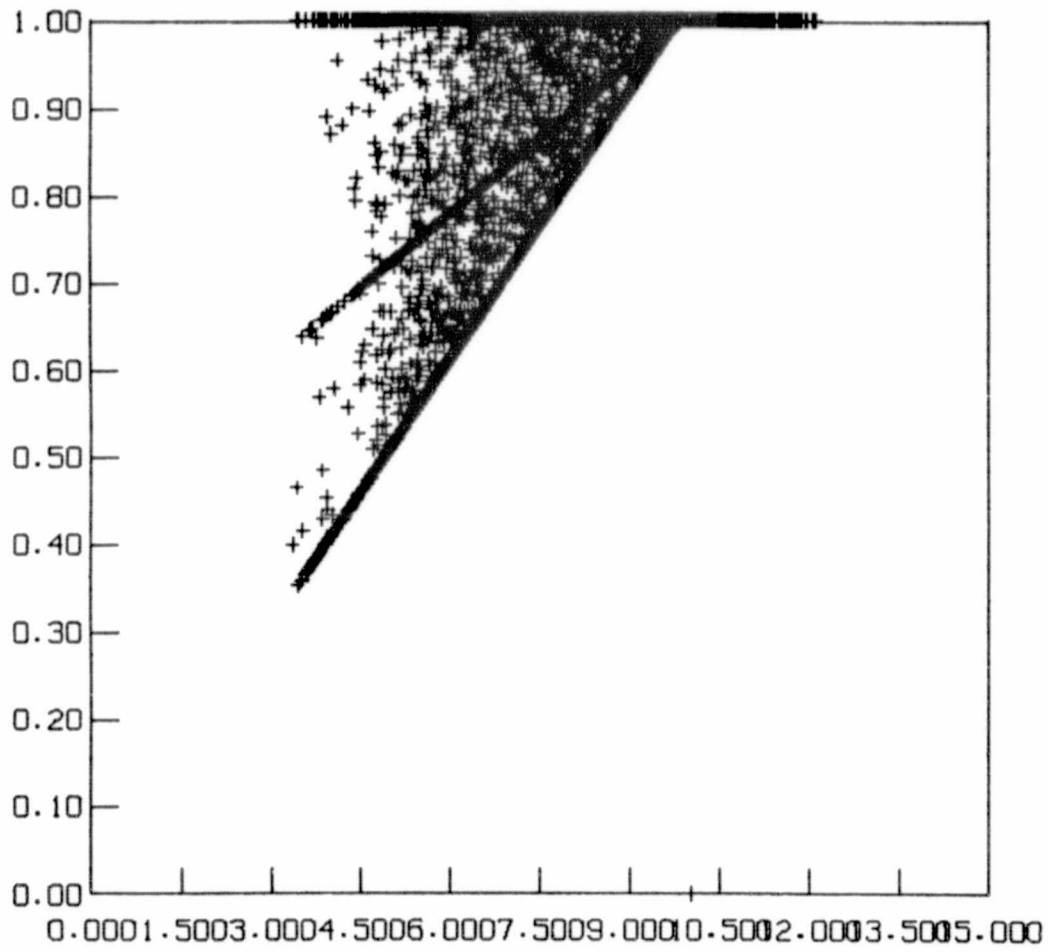


Figure 8

D65

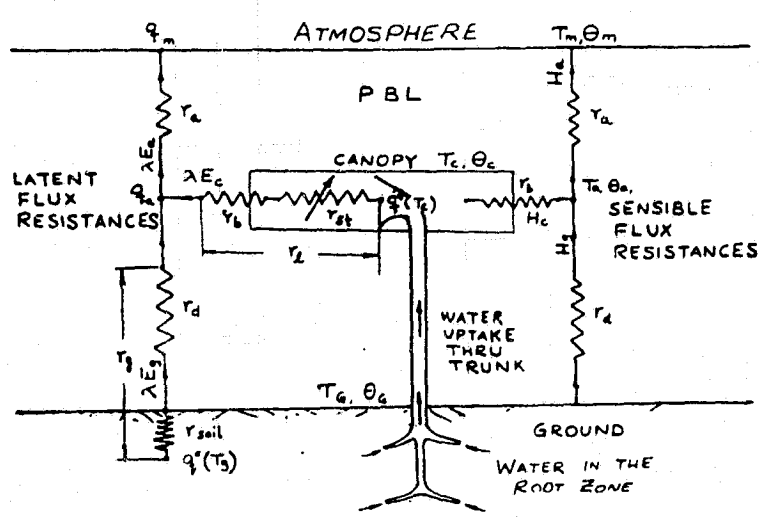
N84 22104

ORIGINAL PAGE IS
OF POOR QUALITY

TIME DEPENDENT LAND AND VEGETATION CANOPY TEMPERATURES

Y. C. Sud

A simple interactive biosphere (SIB) is under development for use in the GLAS GCM. It is based on an electrical analogue of turbulent transport processes that produce heat and moisture fluxes between land and the atmosphere. A schematic sketch of the land surface configuration with canopies of vegetation interacting with the ambient air and the planetary boundary layer atop is shown below:



SCHEMATIC SKETCH OF SIB-FLUXES

The driving potential (temperature or vapor pressure) produces fluxes (heat or moisture) across the intervening medium. These flux transports are affected by a resistance network. For example, the resistance across the mixed layer is r_a which equals the inverse of the product of wind velocity and bulk friction and heat flux transport coefficients in the Deardorff (1972) formulation. We also introduce the atmospheric resistances r_d and r_b to represent corresponding resistance between ground and ambient air and vegetation canopy and ambient air. For calculating moisture fluxes, through evapotranspiration, additional resistances r_{soil} and r_{st} are introduced to allow for the drop in vapor pressure across the pores of the soil or stomatal cavities of leaves of vegetation. Assuming that PBL adjustment time scale is small compared to the period of a diurnal cycle, a quasi-steady state calculation of fluxes and the ground and canopy temperatures is satisfactory. The basic equations are:

I Ground and Canopy Temperature Tendency Equations

$$1) \quad C_c \frac{\partial T_c}{\partial t} = R_{nc} - H_c - \lambda E_c$$

ORIGINAL PAGE IS
OF POOR QUALITY

$$2) C_g \frac{\partial T_g}{\partial t} = R_{ng} - H_g - \lambda E_g$$

II Heat fluxes between the various nodes of the network are given by

$$3a) H_c = (T_c - T_a) \frac{\rho q}{r_b}$$

$$3b) H_g = (T_g - T_a) \frac{\rho q}{r_d}$$

$$3c) H_a = (T_a - T_m) \frac{\rho q}{r_a}$$

III Similarly, the moisture fluxes are given by

$$4a) \lambda E_c = \frac{(e^*(T_c) - e_a)}{r_e} \frac{\rho q}{r}$$

$$4b) \lambda E_g = \frac{(e^*(T_g) - e_a)}{r_g} \frac{\rho q}{r}$$

$$4c) \lambda E_a = \frac{e_a - e_m}{r_a} \frac{\rho q}{\gamma}$$

where $r_c = r_{st} + r_b$ and

$$r_g = r_{soil} + r_d$$

An implicit backward calculation of the canopy temperature modifies (1) to:

$$C_c \frac{\partial T_c}{\partial t} = R_{nc} + \frac{\partial R_{nc}}{\partial T_g} \Delta T_g + \frac{\partial R_n}{\partial T_c} \Delta T_c - H_g - \frac{\partial H_g}{\partial T_a} \Delta T_g - \frac{\partial H_g}{\partial T_c} \Delta T_c - \lambda E_g - \frac{\partial \lambda E_g}{\partial T_g} \Delta T_g - \frac{\partial \lambda E_c}{\partial T_c} \Delta T_c$$

On re-arranging it gives

$$5) \left\{ \frac{C_c}{\Delta t} - \frac{\partial R_{nc}}{\partial T_c} + \frac{\partial H_c}{\partial T_c} + \frac{\partial \lambda E_c}{\partial T_c} \right\} \Delta T_c + \left\{ - \frac{\partial R_{nc}}{\partial T_g} + \frac{\partial H_c}{\partial T_g} + \frac{\partial \lambda E_c}{\partial T_g} \right\} \Delta T_g = R_{nc} - H_c - \lambda E_c$$

Which on taking the partial derivatives of various heat and moisture flux terms gives

ORIGINAL PAGE IS
OF POOR QUALITY

$$\begin{aligned}
 6) \quad & \Delta T_c \left[\frac{C_c}{\Delta t} + C_{cc} 4\sigma T_c^3 + \left(\frac{r_a^{-1} + r_d^{-1}}{1 + r_b/r_a + r_b/r_d} \right) \rho C_p \right. \\
 & \left. + \left(\frac{e^*(T_c) b (r_a^{-1} + r_g^{-1})}{T_c^2 (1 + r_c/r_a + r_c/r_g)} \right) \frac{\rho C_p}{\gamma} \right] \\
 & + \Delta T_g \left[-C_{cg} 4\sigma T_g^3 - \left(\frac{r_d^{-1}}{1 + r_b/r_a + r_b/r_d} \right) \rho C_p \right. \\
 & \left. - \left(\frac{e^*(T_g) b r_g^{-1}}{T_g^2 (1 + r_c/r_a + r_c/r_g)} \right) \frac{\rho C_p}{\gamma} \right] = R_{nc} - H_c - \lambda E_c
 \end{aligned}$$

Similarly, an implicit backward difference form of the ground temperature tendency equation yields.

$$\begin{aligned}
 7) \quad & \Delta T_g \left[\frac{C_g}{\Delta t} + C_{gg} 4\sigma T_g^3 + \left(\frac{r_a^{-1} + r_b^{-1}}{1 + r_d/r_a + r_d/r_b} \right) \rho C_p \right. \\
 & \left. + \left(\frac{e^*(T_g) b (r_a^{-1} + r_c^{-1})}{T_g^2 (1 + r_s/r_a + r_s/r_c)} \right) \frac{\rho C_p}{\gamma} \right] \\
 & + \Delta T_c \left[-C_{gc} 4\sigma T_c^3 - \left(\frac{r_b^{-1}}{1 + r_d/r_a + r_d/r_b} \right) \rho C_p \right. \\
 & \left. - \left(\frac{e^*(T_c) b r_c^{-1}}{T_c^2 (1 + r_s/r_a + r_s/r_c)} \right) \frac{\rho C_p}{\gamma} \right] = R_{ng} - H_g - \lambda E_g
 \end{aligned}$$

In the above equation all the resistances are assumed to be constant within the timestep. However, to account for their dependence on stability and windspeed etc. explicit functions of their dependence on these variables is required. Once that is done, the functional form in terms of ΔT_g and ΔT_c (eliminating the intermediate temperature ΔT_a) can be written and those derivatives can be included in (6) and (7).

A set of solutions for the prescribed values of various resistances (see Table 1) and other constants for steady state input as well as for a simple sinusoidal input of R_{nc} and R_{ng} are shown in Figs. 1a and 1b. Apparently the solutions are stable and depict a realistic diurnal cycle.

Table 1. Prescribed Resistances

#	Type of Resistance	Symbol	Value in sec/m
1	PBL Turbulent Transport	r_a	10.0
2	Aerodynamic Bulk in the Canopy	r_b	5.0
3	Ground to Canopy	r_d	50.0
4	Stomatal (leaves)	r_l	25.0 + 2500/Net Radiation with a maximum of 525
5	Capillary Diffusion of Soil Moisture for Evaporation	r_{soil}	100.00

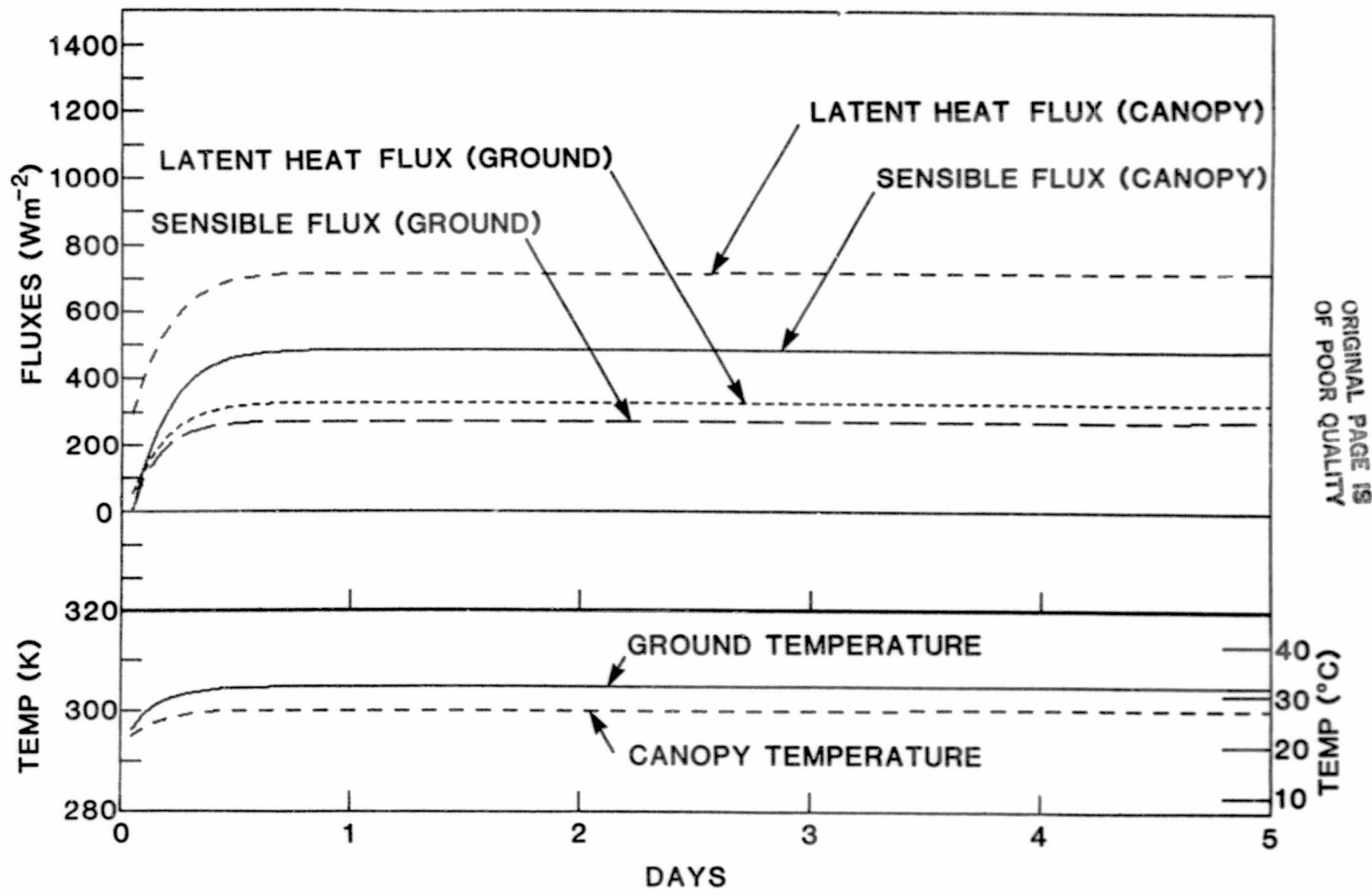
Other Prescribed Constants

- 1) Heat Capacity of the Canopy = 0.25 ly K⁻¹
- 2) Heat Capacity of the Ground = 2.5 ly K⁻¹
- 3) Initial Canopy Temperature = 293 K
- 4) Initial Ground Temperature = 293 K

- 5) Initial Air Temperature = 293 K
- 6) Radiation Flux into the Canopy S_N in ly/day
 $S_N = 500. + 1000. \sin(\omega t)$ or 1000.
- 7) Radiation Flux into the Ground S_G in ly/day
 $S_G = 250. + 500. \sin(\omega t)$ or 500.

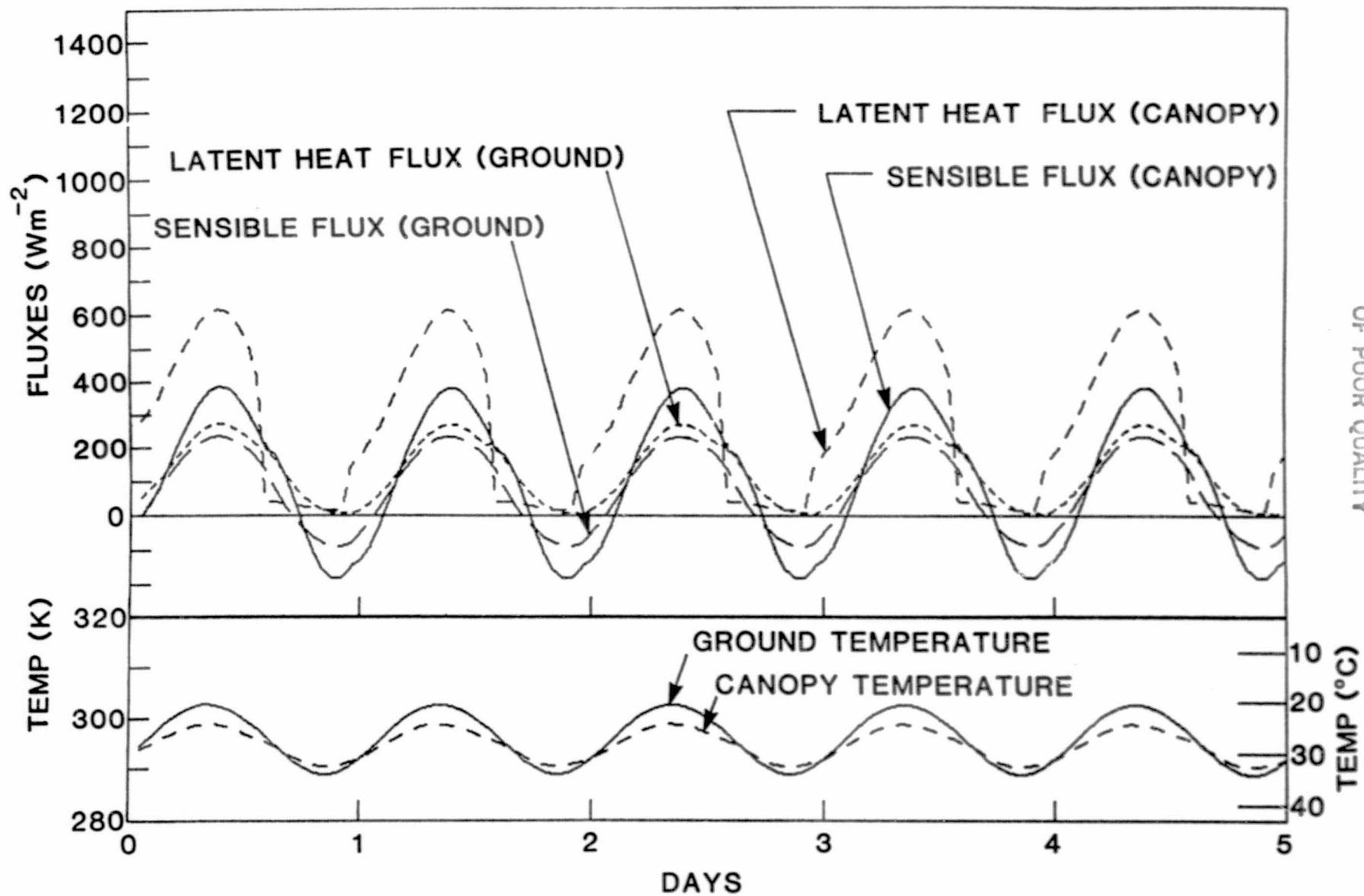
REFERENCES

- Sellers, P. 1983: A simple biosphere (SIB) model for the general circulation models. Hydrological Science Branch NASA/Goddard Space Flight Center Greenbelt, MD 20771.
- Deardorff, J. W. 1972: Parameterization of the planetary boundary layer for use in general circulation models. Mon. Wea. Rev., 100, 93-106.



ORIGINAL PAGE IS
OF POOR QUALITY

Fig. 1a. Sensible and latent heat fluxes ($W m^{-2}$) from the land and vegetation canopy for a steady state input of net radiation.



ORIGINAL PAGE IS
OF POOR QUALITY

Fig. 1b. Sensible and latent heat fluxes ($W m^{-2}$) from the land and vegetation canopy for a sinusoidal input of net radiation.

D-36
N84 22105

A NEW PARAMETERIZATION OF 15 MICRON RADIATIVE TRANSFER FOR A GCM

R. L. Wobus, J. Susskind, and M.-L. C. Wu

In order to make the Wu-Kaplan longwave radiative transfer parameterization (Krishnamurthy, 1982) presently used in the 9-layer GLAS GCM more suitable for use at higher horizontal and vertical resolutions, we are replacing the fixed CO₂ transmittance tables and climatological O₃ transmittances with appropriate models. In this report, we show results of off-line tests of simple models of CO₂ transmittance as a function of atmospheric temperature profile and surface pressure, based on the technique used by Susskind et al. (1983) in the GLAS physical retrieval scheme. The models are evaluated in terms of transmittance error, flux divergence error, and equilibrium temperature error.

The transmittances of CO₂ averaged over each of the spectral bands 500-660 cm⁻¹ and 660-800 cm⁻¹ are modeled, following Susskind et al., 1983, as products of effective layer transmittances as

$$\tilde{\tau}_{i,j} = \prod_{k=i}^{j-1} \tilde{\tau}_{k,k+1}^i$$

where $\tilde{\tau}_{i,j}$ is the model of the band averaged transmittance $\tau_{i,j}$ between levels i and j (see Fig. 1). The first factor, $\tilde{\tau}_{i,i+1}^i$, is a model of the single layer transmittance $\tau_{i,i+1}$; the remaining factors $\tilde{\tau}_{k,k+1}^i$ ($k \neq i$), which represent the effective layer transmittance between levels k and $k+1$ for radiation from level i , are layer models of transmittance ratios $\tau_{i,k+1} / \tau_{i,k}$.

The temperature dependence of CO₂ transmittance in each layer is modeled as a two-term linear expansion in layer temperature $T_{k,k+1}$ as in Susskind et al. (1983):

$$\tilde{\tau}_{k,k+1}^i = a_{k,k+1}^i + b_{k,k+1}^i T_{k,k+1}$$

To include the effect of elevated terrain, we study two additional forms of layer model, a three-term model linearly dependent on temperature and surface pressure P_S (which determines layer height and thickness in the σ -coordinate GCM)

$$\tilde{\tau}_{k,k+1}^i = a_{k,k+1}^i + b_{k,k+1}^i T_{k,k+1} + c_{k,k+1}^i P_S$$

and a four-term bilinear model:

$$\tilde{\tau}_{k,k+1}^i = a_{k,k+1}^i + b_{k,k+1}^i T_{k,k+1} + c_{k,k+1}^i P_S + d_{k,k+1}^i P_S T_{k,k+1}$$

The model coefficients (a, b, c, and d) are computed by regression using line-by-line transmittances computed for four 64-level climatological temperature profiles (standard, January equator, January 70°N, July 70°N) with four surface pressures (1000 mb, 910 mb, 730 mb, 550 mb). For each level and layer, we find the coefficients which minimize

$$\sum_{\alpha} \{ \tau_{k,k+1}^i - \tau_{k,k+1\alpha} \}^2 \quad k = i$$

or

$$\sum_{\alpha} \{ \tau_{ik\alpha} - \tau_{k,k+1\alpha} \}^2 \quad k \neq i$$

where α identified each of the four (2-term model) or sixteen (3- or 4-term model) profiles.

The residual errors in transmittance associated with these models are shown in Table 1. The errors due to ignoring temperature variation are reduced by a factor of 5 or more and those due to ignoring elevated terrain are reduced by a factor of 15 or more. The largest errors occur in the stratosphere because significant climatological thermal structure is averaged out in the 9-layer model's upper layers.

We test in the Wu-Kaplan scheme three transmittance models retaining 2, 3, or 4 terms in each layer model. Since the pressure coefficients c and d are an order of magnitude smaller for the transmittance ratios ($k \neq i$) than for the single layer transmittances ($k=i$), we also evaluate two computationally efficient mixed models in which 3- or 4-term layer models are used for the single layer transmittances and 2-term models are used for transmittance ratios. These models are compared with a fixed transmittance table based on the standard profile (current method) and with the line-by-line transmittances.

Flux divergence errors due to approximate treatment of CO₂ are obtained by comparing LW flux divergences calculated using each transmittance model and using the standard profile with those obtained using line-by-line transmittances. Climatological water vapor profiles are used. We obtain equilibrium temperature errors, representing an upper bound on the temperature changes expected in the GCM, by calculating the temperature changes necessary in each layer and at the earth's surface to offset the error in flux divergence--that is, the change of equilibrium temperature assuming all other terms in the thermodynamic equation are fixed.

The RMS errors (averaged over layers and temperature profiles) are shown in Figure 2. The errors are generally largest in the upper layer, especially over elevated terrain (low P_S). More of the error in the present method is due to variation of surface pressure than to temperature variation, as shown by the relatively large errors for the 2-term model. The mixed models perform nearly as well as the complete 3 and 4 term models, especially at near-standard surface pressures. The smaller errors at low P_S for the 3 and 4 term models show the effect of improved resolution in the stratosphere.

We plan to refine the models by including additional temperature profiles and to test one model in the GLAS GCM. A similar model for ozone transmittance will be developed and tested.

REFERENCES

- Krishnamurthy, V., 1982: Documentation of the Wu-Kaplan longwave radiative routine. NASA Tech. Memo. 83926, 93 pp.
- Susskind, J., J. Rosenfield, D. Reuter, 1983: An accurate radiative transfer model for use in the direct physical inversion of HIRS2 and MSU temperature sounding data. J. Geophys. Res., 88, 8550-8568.

Table 1 - Transmittance Model Errors
500-600 cm^{-1} /660-800 cm^{-1}

4 Profiles ($P_s = 1000 \text{ mb}$)

<u>Model</u>	<u>Max. Error</u>	<u>RMS Error</u>
Standard Profile	.0264/.0358	.0116/.0157
2-Term	.0034/.0045	.0011/.0013
3-Term	.0054/.0070	.0016/.0021
4-Term	.0039/.0050	.0015/.0019

16 Profiles ($P_s = 1000, 910, 730, 550 \text{ mb}$)

<u>Model</u>	<u>Max. Error</u>	<u>RMS Error</u>
Standard Profile	.1115/.1474	.0475/.0639
3-Term	.0068/.0090	.0020/.0027
4-Term	.0067/.0082	.0019/.0026

Table 1 - Transmittance Model Errors
 500-600 cm^{-1} /660-800 cm^{-1}

4 Profiles ($P_S = 1000 \text{ mb}$)

<u>Model</u>	<u>Max. Error</u>	<u>RMS Error</u>
Standard Profile	.0264/.0358	.0116/.0157
2-Term	.0034/.0045	.0011/.0013
3-Term	.0054/.0070	.0016/.0021
4-Term	.0039/.0050	.0015/.0019

16 Profiles ($P_S = 1000, 910, 730, 550 \text{ mb}$)

<u>Model</u>	<u>Max. Error</u>	<u>RMS Error</u>
Standard Profile	.1115/.1474	.0475/.0639
3-Term	.0068/.0090	.0020/.0027
4-Term	.0067/.0082	.0019/.0026

ORIGINAL PAGE IS
OF POOR QUALITY

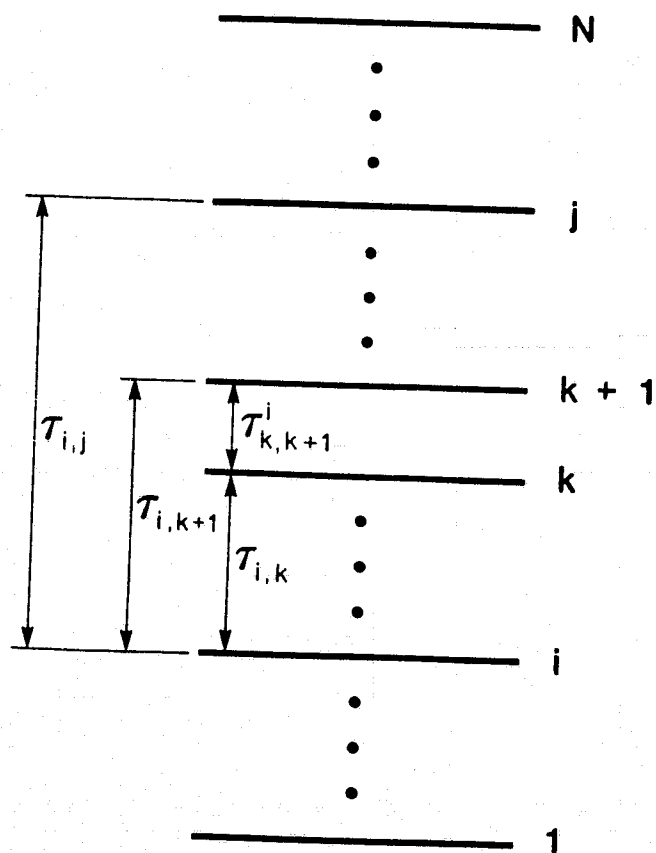


Fig. 1. Indexing scheme for σ -levels and for transmittance model terms.

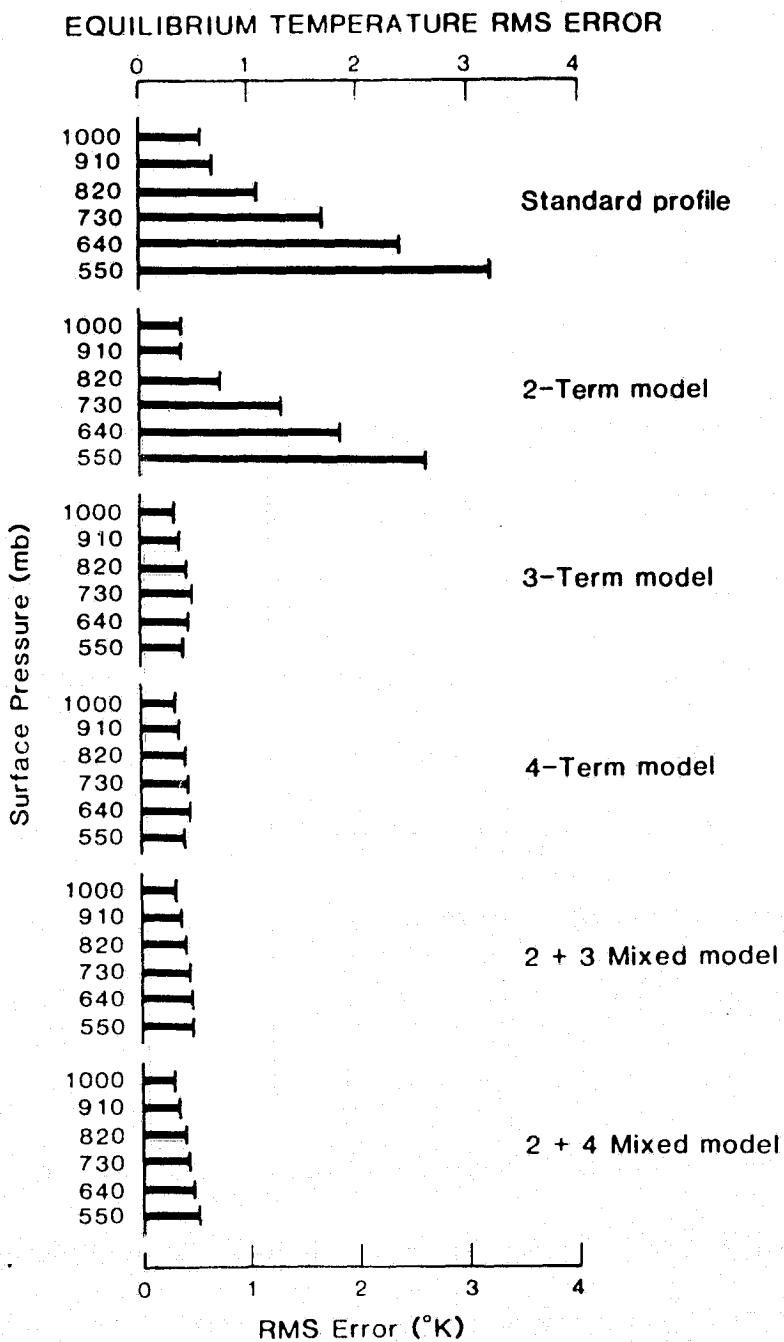


Fig. 2. Cooling rate RMS errors (averaging over all layers and over four surface pressures) for the standard profile (present method) and for the five models. In the 2+3 and 2+4 mixed models 3- or 4-term layer models are used for single layer transmittance and 2-term layer models for transmittance ratios.

D. SENSITIVITY EXPERIMENTS

PRECEDING PAGE BLANK NOT FILMED

GCM SENSITIVITY TO 1982-83 EQUATORIAL PACIFIC SEA SURFACE
TEMPERATURE ANOMALIES

M. J. Fennessy, L. Marx, and J. Shukla

As documented by the Climate Analysis Center (CAC) the El Nino warm equatorial Pacific sea surface temperature (SST) event of 1982-83 is outstanding in comparison to earlier events. The mature phase SST anomalies were of record magnitude and extent, with greater than 3°C anomalies extending from the South American coast to 150W in January (Fig. 1). The January outgoing longwave radiation (OLR) anomaly field depicted a large region of increased convective activity from 160E to 100W along the equator. The Southern Oscillation Index (SOI, Tahiti minus Darwin sea level pressure (SLP)) reached a record low, and a Northern Hemisphere record negative 700 mb height anomaly was observed in the northeast Pacific. For a complete documentation of the evolution of these and other observed climatic anomalies see the CAC special Climate Diagnostics bulletins (1982-83) and Quiroz (1983).

Several general circulation model (GCM) studies (Rowntree, 1972; Julian and Chervin, 1978; Keshavamurty, 1982; Shukla and Wallace, 1983) simulated many of the basic features of the observed atmospheric response to SST anomalies representative of the mature stage of previous El Nino events. The tropical features included an eastward shift of the region of maximum convective activity, increased low level equatorial Pacific westerlies, and anomalous anticyclonic couplets straddling the equator aloft. The most pronounced extra-tropical anomaly observed was also simulated, that being the Pacific-North American (PNA) like pattern (Wallace and Gutzler, 1981) in the upper level geopotential height field over the northeast Pacific and North America. Although the general features of the "composite El Nino event" were correctly simulated in most of these experiments, significant variations between experiments utilizing different initial conditions were noted (Shukla and Wallace, 1983).

The current study examines the response of the GLAS climate model to the much larger 1982-83 SST anomalies as obtained from CAC. Two separate 75 day experiments (control and anomaly simulation pairs) were started from observed initial conditions on 16 Dec. 1982 and initial conditions on 16 Dec. 1979 taken from a 2 year model control run after one year of simulation, respectively. The January control and anomaly SST fields used in both experiments are shown in Figs. 1b and 1c, respectively. Notable is the greatly extended region of very warm ($\geq 29^\circ\text{C}$) SST water in the anomaly simulation. The January SST anomaly field is representative of the other months of the experiments, all of which had a much larger region of very warm SST in the anomaly simulation than in the previously noted GCM studies.

The model used is an improved version of the GLAS B-grid GCM used by Shukla and Wallace (1983). The most important physical change in the model is the inclusion of the surface flux parameterization of Deardorff (1972) as modified by Randall (1976). An important improvement in the model simulations is the removal of the climate drift towards unrealistically high temperatures in the tropics, which was noted by Shukla and Wallace (1983). The model's climatology is described by Randall (1982).

PRECEDING PAGE BLANK NOT FILMED

Most of the differences (anomaly minus control) were quite similar in the two experiments, thus we will concentrate on the 1982-83 experiment and note appreciable differences in the 1979-80 experiment when they occur.

Precipitation and Heating

The January 1983 precipitation difference field (hereafter differences referenced are anomaly minus control) shown in Fig. 2 exhibits a wide region of enhanced precipitation from 160E to 80W in the anomaly simulation, as well as a region of decreased precipitation to the west. These differences, as well as the positive differences over SW Brazil and the Gulf of Mexico agree well with the CAC January 1983 OLR anomalies (not shown). There is an obvious direct relation between the positive precipitation differences and the extent of the very warm ($\sim 29^{\circ}\text{C}$) SST in the anomaly simulation (Fig. 1c). This is qualitatively in agreement with the results of Shukla and Wallace (1983), however the anomalous regions are of much greater extent in the current study. These precipitation differences developed quickly (within 2 weeks) and persisted throughout the course of the experiment. The precipitation differences are reflected in the 11-60 day average control (Fig. 3a) and anomaly (Fig. 3b) total atmospheric diabatic heating fields. The strength of the widespread anomalous heating was reflected in the zonally averaged 30°S - 30°N 200-1000 mb thickness time series (not shown), which had a positive difference steadily growing up to a magnitude of 75 geopotential meters by the end of the experiments.

Evaporation and Moisture Convergence

The largest evaporation differences (not shown) were around 4 mm/day and occurred over the regions of warmest SST in the anomaly simulation. The main contributor to the greatly enhanced precipitation was the highly anomalous moisture convergence (also not shown). This agrees with the results of Shukla and Wallace (1983), as does the enhanced low level equatorial westerlies to the west of the SST anomaly (Fig. 4). The large evaporation differences were due to the combined effects of warmer SST and stronger surface winds.

Sea Level Pressure

The sea level pressure (SLP) differences showed a strong (~ 2 mb) Southern Oscillation signal, as seen in the 11-60 day average differences for the 1982-83 experiment (Fig. 5a) and the 1979-80 experiment (Fig. 5b). This suggests that the SST anomalies are capable of producing the sea level pressure pattern of the Southern Oscillation as observed in the mature stage of an El Niño event.

Geopotential Height and Wind Fields at Upper Levels

From such a strong and widespread tropical heating anomaly one might, in the light of linear theory and past observations, naturally expect to see extra-tropical responses. Both experiments had anomalous anticyclonic circulations aloft straddling the equator in the eastern Pacific, although they were much weaker than those observed. The ~ 10 degree eastward shift of the anticyclonic couplet observed from January to February was roughly simulated in the 1982-83 experiment. A PNA-like pattern is evident in the CAC observed January 1983 200 mb northern hemisphere height anomaly field, although by February, the anomalous pattern, though still very strong, undergoes large changes.

The 1982-83 11-25 day average 300 mb geopotential height difference field (Fig. 6) shows a PNA pattern looking quite like the observed January anomalies. However, the 31-60 day average of this same field (not shown) shows quite a different pattern, which resembles more the observed February anomaly pattern, rather than the PNA or January pattern. The 1979-80 geopotential difference fields (not shown) were again hard to interpret, although they resembled the observed February anomaly pattern more than the PNA-like pattern throughout the course of the experiment.

The CAC winter 1983 200 mb zonal wind field (not shown) had a large ($\sim -20\text{m/s}$) negative anomaly over the central and eastern equatorial Pacific, flanked by large ($\sim 20\text{m/s}$) positive anomalies at roughly 30°S and 30°N . The 1982-83 11-60 day average 300 mb zonal wind difference field (Fig. 7) shows that the negative anomaly was correctly simulated, although the positive anomalies flanking it are both too weak and shifted eastward as compared to the observed anomalies. However, it does seem that the model, at least qualitatively, correctly simulated the local strengthening of the subtropical jet of either hemisphere.

In conclusion, the results in the tropics seem clear. The SST anomalies force anomalous precipitation and heating over the areas of very warm ($\geq 29^\circ\text{C}$) SST. In addition, they result in anomalous low level westerlies and upper level easterlies in the equatorial Pacific. The upper level easterlies are related to a forced anomalous upper level anticyclone couplet straddling the equator. The SST anomalies produce the SO signal of sea level pressure correctly.

The extra-tropical results are not nearly so clear. There is a strong extra-tropical response, although it varies greatly with both time and initial conditions. The first couple of weeks of the 1982-83 experiment did show a PNA like pattern in the 300 mb geopotential height difference field. The lack of recognition of much of the difference patterns is perhaps not to be unexpected, as the 1982-83 tropical heating anomaly is of unprecedented magnitude and extent.

REFERENCES

- Deardorff, J. W., 1972: Parameterization of the planetary boundary layer for use in general circulation models. Mon. Wea. Rev., 100, 93-106.
- Julian, P. R., and R. M. Chervin, 1978: A study of the Southern Oscillation and Walker circulation phenomenon. Mon. Wea. Rev., 106, 1433-1451.
- Keshavamurty, R. N., 1982: Response of the atmosphere to sea surface temperature anomalies over the equatorial Pacific and the teleconnections of the Southern Oscillation. J. Atmos. Sci., 39, 1241-1259.
- National Meteorological Center Climate Analysis Center, 1982-83: Special Climate Diagnostics Bulletins, #1-6.
- Quiroz, R. S., 1983: The Climate of the "El Nino" Winter of 1982-83, A Season of Extraordinary Climatic Anomalies. Mon. Wea. Rev., 111, 1685-1706.
- Randall, D. A., 1976: The interaction of the planetary boundary layer with large-scale circulations. PhD thesis, UCLA, 247pp.

Randall, D. A., 1982: Monthly and seasonal simulations with the GLAS Climate Model. Proceedings of the Workshop on Intercomparison of Large-Scale Models Used for Extended Range Forecasts of the European Centre for Medium-Range Weather Forecasts, Reading, England (to appear).

Rowntree, P. R., 1972: The influence of tropical east Pacific Ocean temperatures on the Atmosphere. Quart. J. Roy. Meteor. Soc., 98, 290-321.

Shukla, J. and J. M. Wallace, 1983: Numerical simulation of the Atmospheric Response to Equatorial Pacific Sea Surface Temperature Anomalies. J. Atmos. Sci., 40, 1613-1630.

Wallace, J. M. and D. S. Gutzler, 1981: Teleconnections in the geopotential height field during the Northern Hemisphere Winter. Mon. Wea. Rev., 109, 784-812.

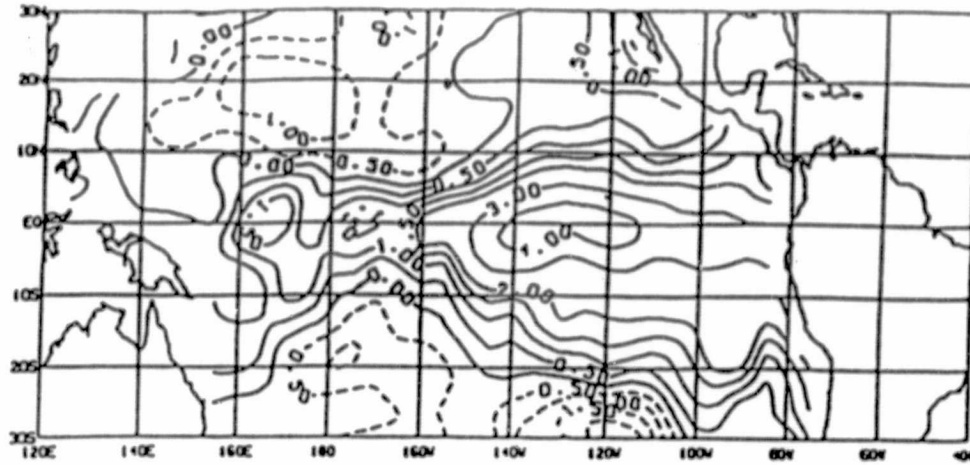


Fig. 1a

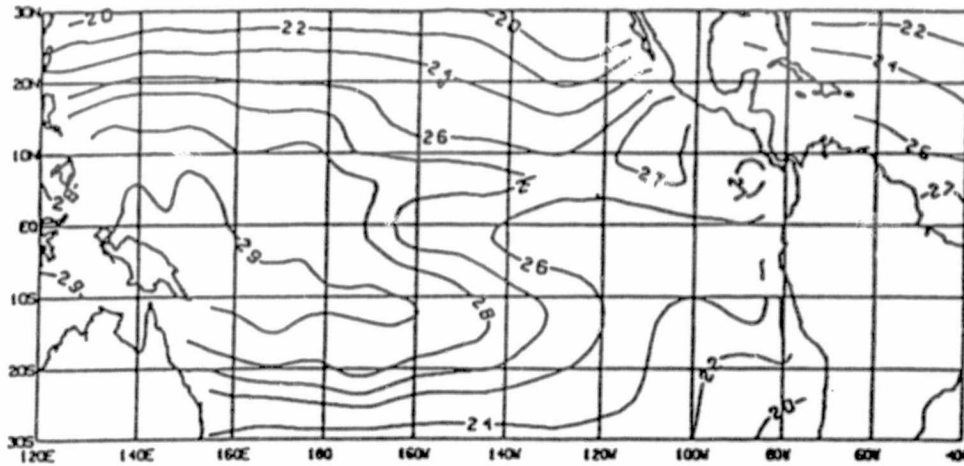


Fig. 1b

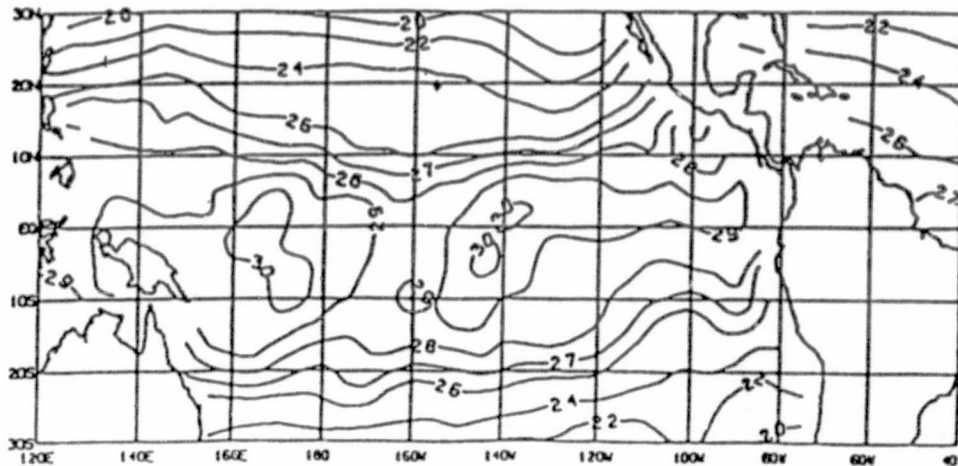


Fig. 1c

Fig. 1 January 1983 sea surface temperature fields for a) anomaly minus control difference, b) control simulation and c) anomaly simulation. (anomaly obtained from CAC) Units are $^{\circ}\text{C}$. Dashed contours are negative.

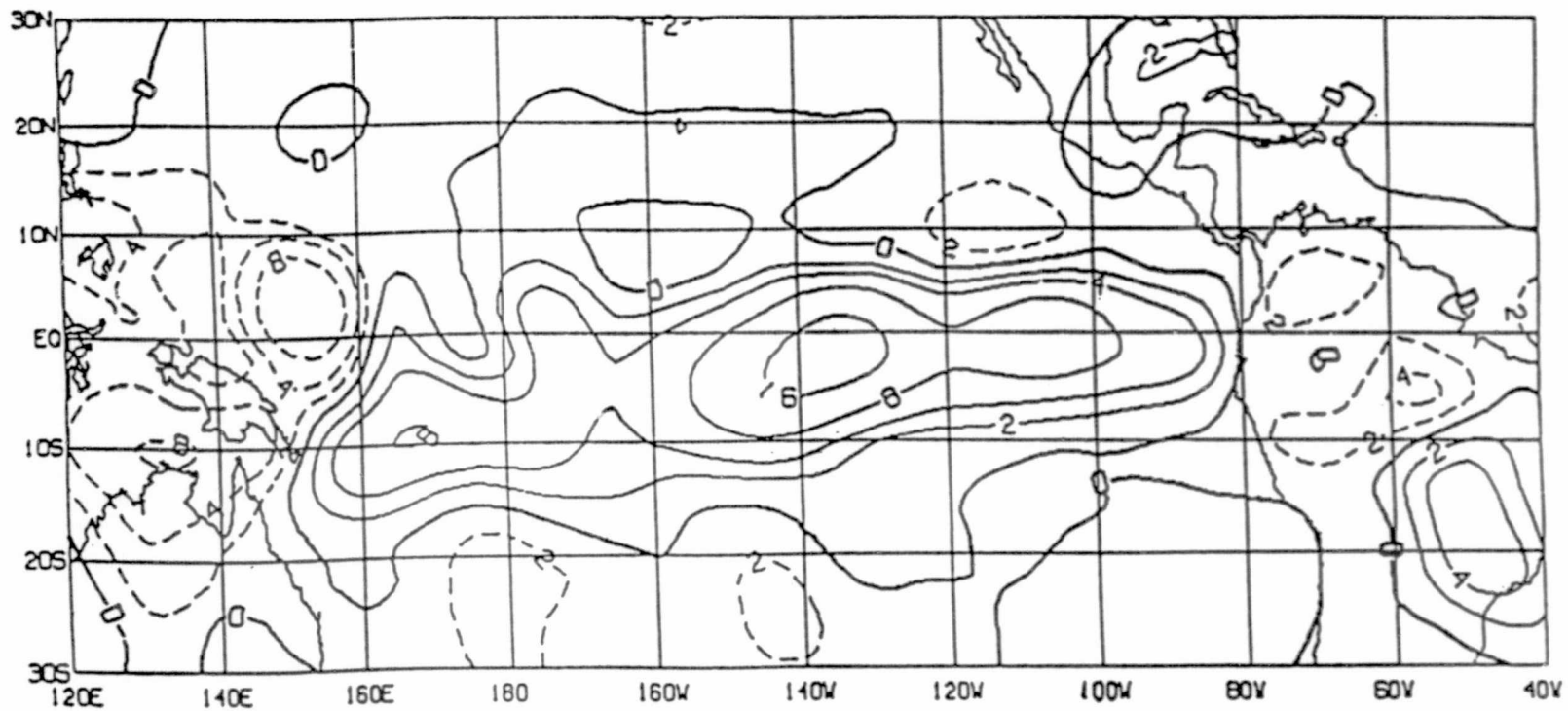
ORIGINAL PAGE IS
OF POOR QUALITY

Fig. 2. January 1983 anomaly minus control precipitation difference. Units are mm/day. Dashed contours are negative.

ORIGINAL PAGE IS
OF POOR QUALITY

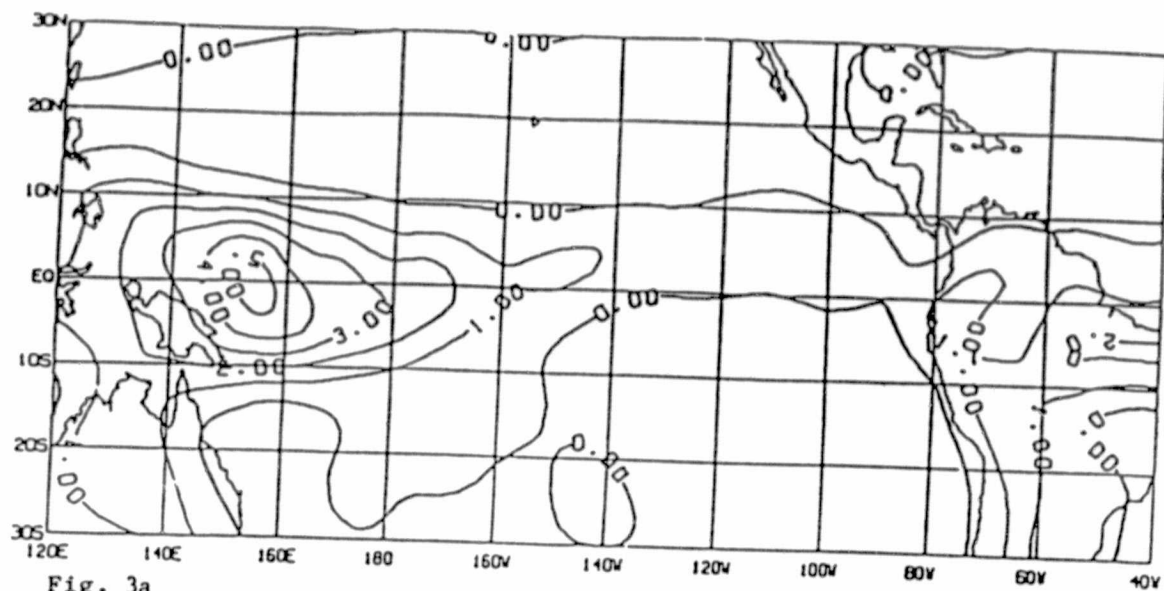


Fig. 3a

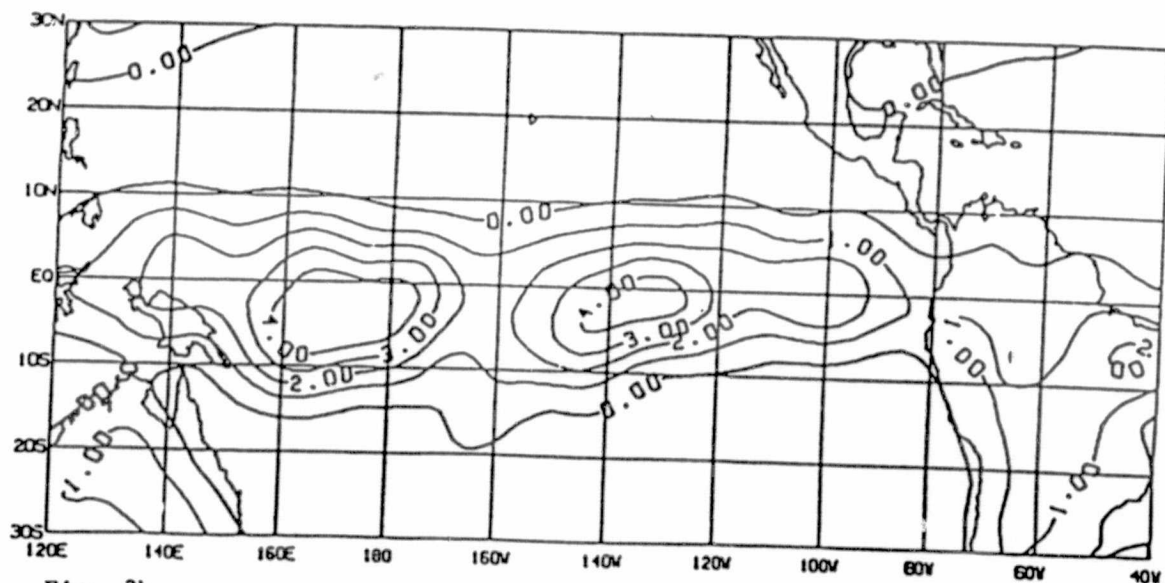


Fig. 3b

Fig. 3 11-60 day average 1982-83 modeled total atmospheric diabatic heating field for a) control and b) anomaly. Units are $^{\circ}\text{C}/\text{day}$.

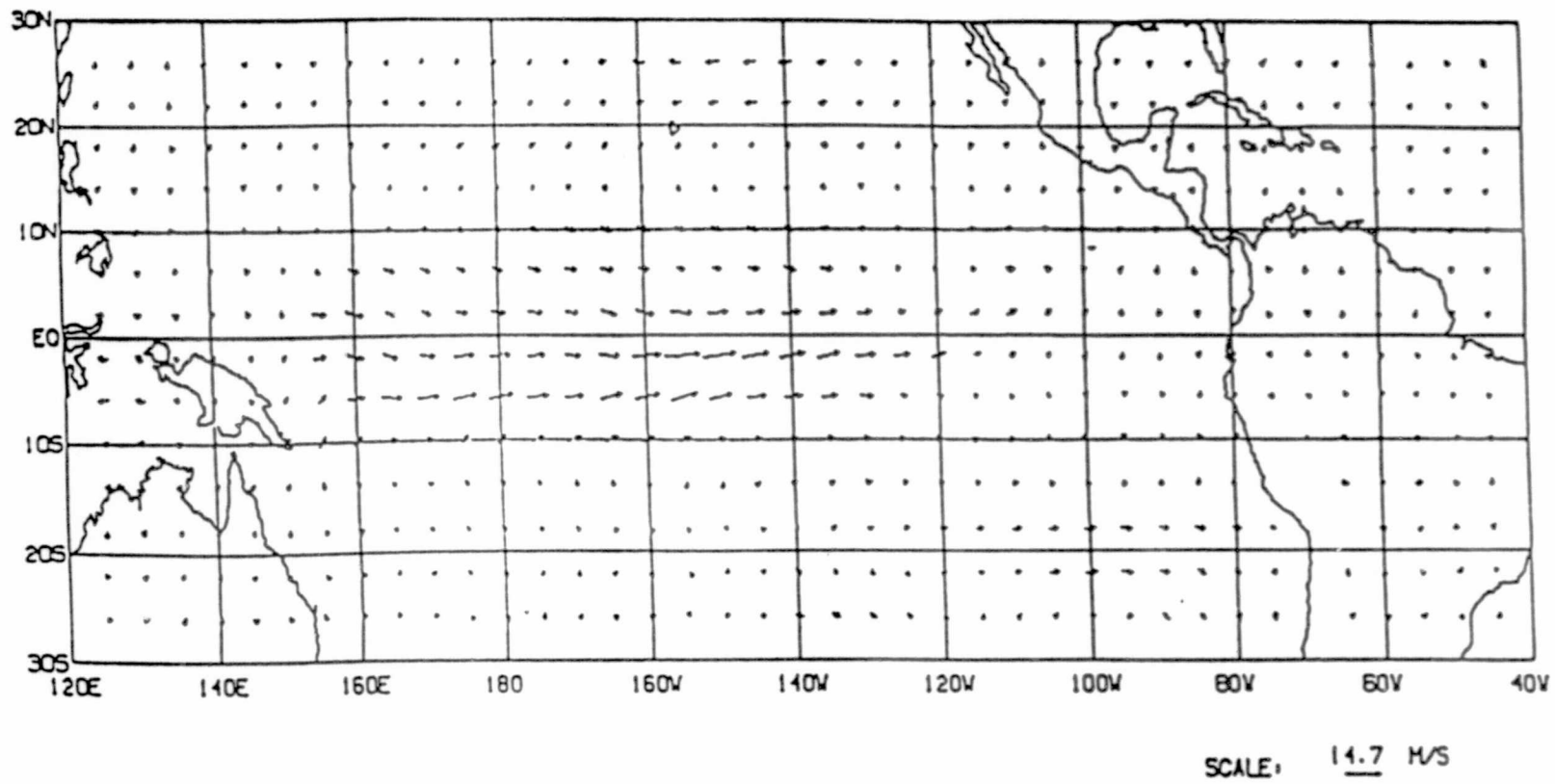
ORIGINAL PAGE IS
OF POOR QUALITY

Fig. 4. 11-60 day average 1982-83 anomaly minus control 850 mb vector wind difference. Maximum = 14.7 m/s.

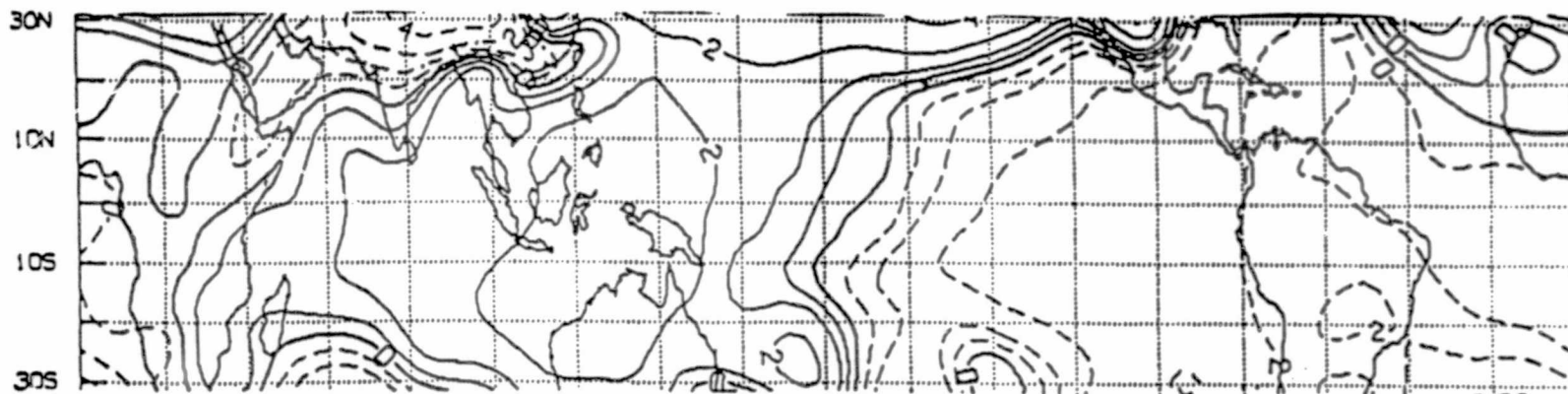


Fig. 5a

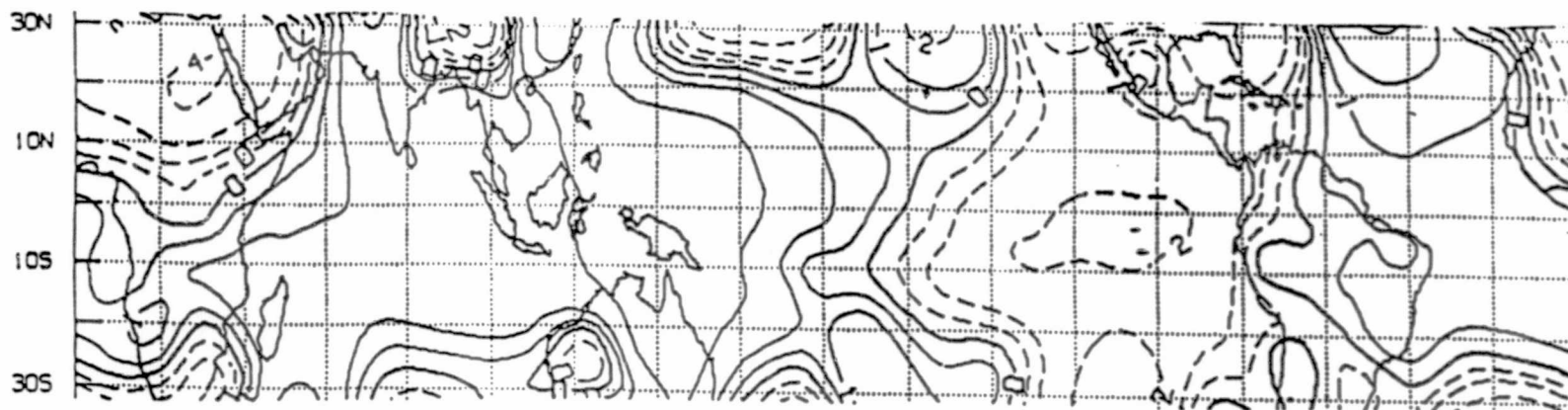


Fig. 5b

Fig. 5 11-60 day average 1982-83 anomaly minus control sea level pressure difference for a) 1982-83 and b) 1979-80. Contours are $\pm 0.5, 1, 2, 4$ mb. Dashed contours are negative.

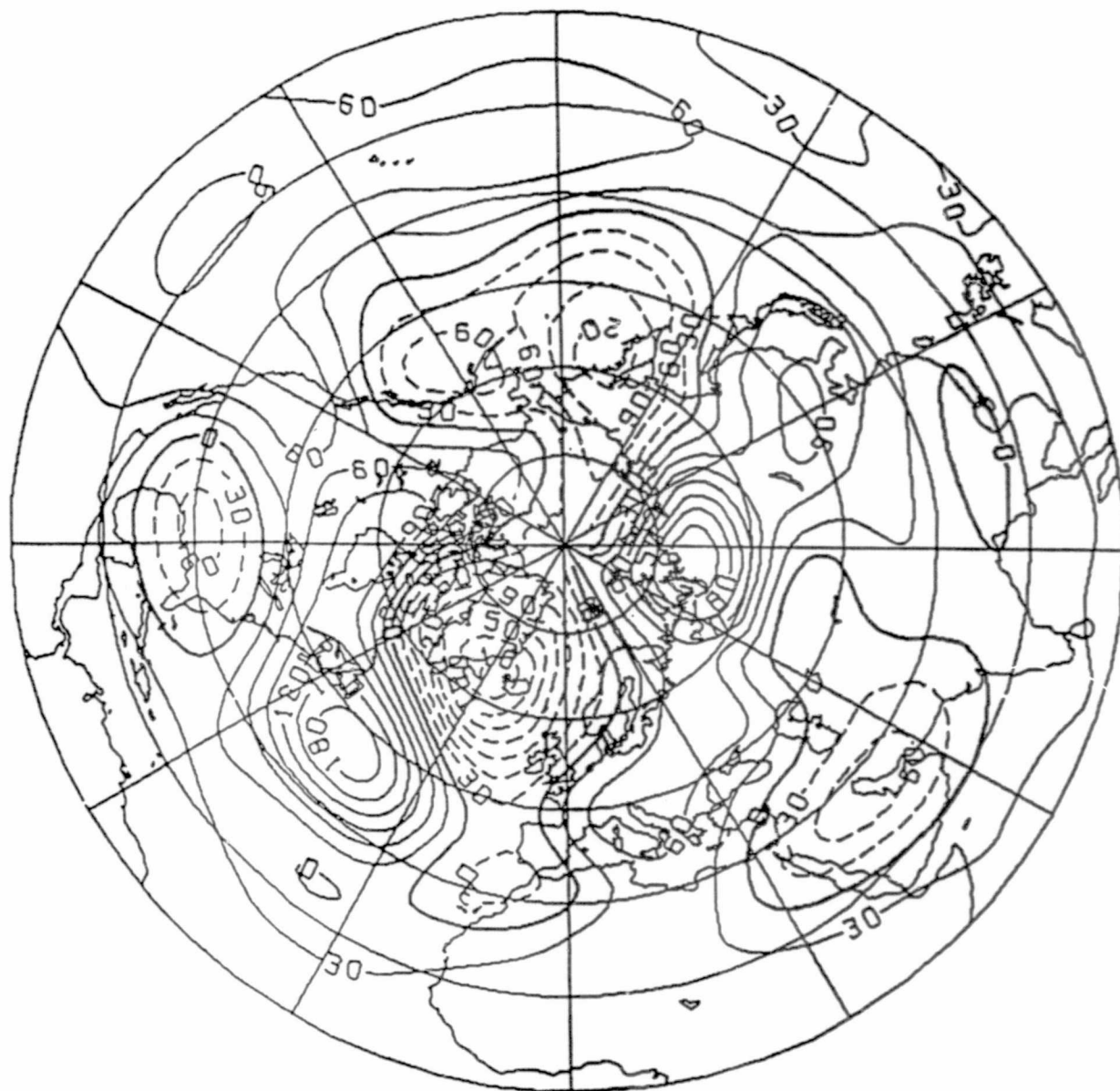


Fig. 6 11-25 day average 1982-83 anomaly minus control 300 mb geopotential height difference. Units are geopotential meters. Dashed contours are negative.

ORIGINAL PAGE IS
OF POOR QUALITY

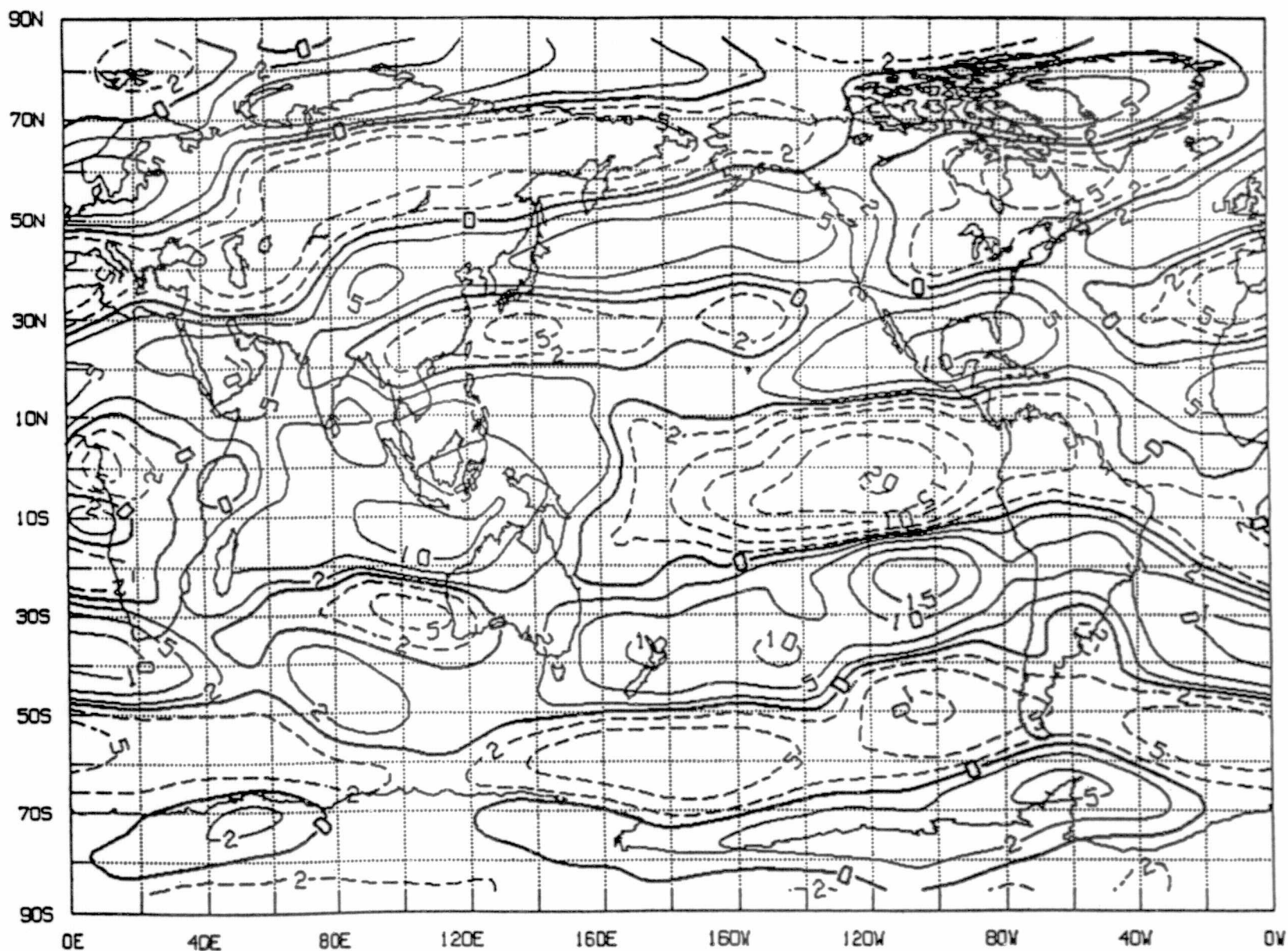


Fig. 7 11-60 day average 1982-83 anomaly minus control 300 mb zonal wind difference. Contours are $\pm 2, 5, 10, 15, 20$ m/s. Dashed contours are negative.

1
58
N84 22107

IMPACT OF PRESCRIBED DIABATIC HEATING ON SHORT RANGE WEATHER FORECASTS

L. Marx and J. Shukla

1. INTRODUCTION

Using the 9 layer general circulation model developed at the Goddard Laboratory for Atmospheric Sciences (GLAS), several 4 to 5 day integrations were made to assess the impact that latent heating processes (supersaturation and moist convective) have on the model forecasts. In an earlier study by Shukla (1981) it was hypothesized that because of strong interaction between dynamics and moist convection, small initial errors grow very fast and make short range forecasting difficult. The purpose of this study was to examine if prescribed heating rates can improve the forecasts for a few days.

To undertake this study, several runs were made. First a control run was made using the model in its standard form. This run was made for 5 days beginning on 17 January 1979. The observations during this period have been analyzed by both the National Meteorological Center (NMC) as well as at GLAS. The latter analysis includes asynoptic aircraft and satellite observations assimilated into the analysis by a model as described by Baker (1983). This control run used initial conditions based on GLAS analysis. Two control runs were made with the clouds removed from both the shortwave and longwave calculations using initial conditions from GLAS analysis for one and NMC analysis for the other. In all other respects they are the same as the first control run. A fourth control run was made running as the second control run, but simulating 4 days beginning one day later on 18 January 1979. Two reduced heating runs were made: one without latent and diffusive heatings (except for surface evaporation) but including dry convective adjustment and radiative heating, the second without any heating except for dry convective adjustment to maintain model stability. Several constant heating runs were made which can be divided into two classes: those with heating prescribed by the temperature error after 24 hours into the future and those with heating prescribed by the temperature error from the past 24 hours. A detailed comparison and discussion will follow in Sections 3 and 4.

2. MODEL

The GLAS general circulation model used in this study is a 9 sigma layer, 4 by 5 degree 2nd order B-grid model. The vertical extent is limited to 10 mb. with equal sigma layer spacing.

The hydrodynamical portion of the model employs potential temperature as the basic prognostic thermodynamic variable. Moisture (specific humidity) is carried in the flow as a tracer. A single pass matsuno scheme is used for time integration. Fourier filtering of the u wind flux terms and the pressure gradient terms near the poles as well as dry convective adjustment are performed at each time step.

The physical processes include: a simple single layer planetary boundary parameterization, surface and interlayer friction, cumulus convection, super-saturation cloudiness, solar (shortwave) and terrestrial (longwave) heatings, ground hydrological processes, diffusive heating and dry convective adjustment. All processes except longwave heating are determined at each model simulated half hour. Longwave heating tendencies are determined at 5 hour intervals and applied at each half hour. A Shapiro filter is applied at each model half hour to the pressure and winds. At each 24 hour period the global pressure is re-adjusted to compensate for time/space truncation loss.

The following are imposed as boundary conditions on the model and are only time interpolated to their climatological values:

- 1) Surface albedo
- 2) Sea surface temperature
- 3) Soil moisture
- 4) Ozone distribution in the lower stratosphere

These boundary conditions remove the time dependency of these fields from the model allowing a more direct view of the atmospheric response. The model is described by Randall (1982).

3. EXPERIMENTS

Several model runs were made which can be divided into four classes:

- 1) Control runs
- 2) Reduced heating runs
- 3) Constant heating runs based on future temperature error
- 4) Constant heating runs based on past temperature error

Most runs used initial conditions based on GLAS analysis from either 17 January 1979 or 18 January 1979. One control run used NMC analysis initial conditions for 17 January. Each run was verified against GLAS analysis, NMC analysis or sometimes both for each 24 hour period the experiment spanned. Runs starting on 17 January ran 5 days and those starting on 18 January ran 4 days. Table 3.1 gives a summary of the control runs.

TABLE 3.1

RUN	IC*	STARTING DATE	DESCRIPTION
C1	G	17 January	Standard model run.
C2	G	17 January	Standard model run except clouds suppressed when radiation calculations are performed.
C3	N	17 January	Same model as C2.
C4	G	18 January	Same model as C2.

*Initial conditions: G = GLAS ANALYSIS N = NMC ANALYSIS

The design of the experiment runs is to perform a run without heating due to supersaturation, moist convection, or vertical diffusion. The radiation heatings (both solar and terrestrial) are retained along with surface latent and sensible heatings. Such a run will have a forecast error when compared with observations or a control run defined as:

$$\text{Error} = \text{Forecast} - \text{Observation (or control)}$$

If after a fixed period of time (24 hours in these experiments) the temperature error is determined, this error can be used to replace the heating field for the suppressed heatings by changing its sign and applying this correction at each half hour (each physics calculation) after dividing the correction by 48. Thus:

$$\text{Correction} = -\text{Error}/48$$

For comparison a run has also been made with no heatings except surface sensible and latent heatings. Table 3.2 summarized the two reduced heating runs.

TABLE 3.2

RUN	STARTING DATE	DESCRIPTION
R1	17 January	Same model as C2 except supersaturation, convective, and diffusive heatings suppressed.
R2	17 January	Same as R1 except all radiation heatings suppressed.

With R1 and the two sets of observations (GLAS, denoted by G, and NMC, denoted by N) and the control run C2, two classes of experimental runs have been performed: In one set of runs the heating rate is such as to make no error in a 24 hour forecast. These runs will be called future error runs. In the other set of runs the heating rate is based on the error of the last 24 hours. The heating would be expected to give good forecast skill up to 24 hours since the errors generated by the lack of heating should be compensated by the constant heating field. Errors after 24 hours would indicate if skill can be obtained by retaining this heating field. This assumes that the forecast error in ordinary models is caused by diurnal phenomena which largely cancel during the 24 hour period viz. the heatings in question. Table 3.3 summarizes the future error correction heating experiments.

TABLE 3.3

RUN	STARTING DATE	DESCRIPTION
F1	17 January	Same model as R1 with heatings replaced by constant field $Q = G - R1$ at 24 hours (18 Jan.).
F2	17 January	Same model as F1 with $Q = N - R1$ at 24 hours.
F3	17 January	Same model as F1 with $Q = C2 - R1$ at 24 hours.

The past error class will indicate the forecasts skill of a constant heating which can easily be determined in a running model and will show if it meets or improves the skill obtained by more complex parameterizations currently used in most models. This will again show the importance of diurnal variations in the removed heatings. Table 3.4 summarizes the past error correction heating experiments.

TABLE 3.4

RUN	STARTING DATE	DESCRIPTION
P1	18 January	Same model as F1.
P2	18 January	Same model as F2.
P3	18 January	Same model as F3.

All control runs were verified against both GLAS and NMC observations except for C3 which was compared against NMC only. All other runs were compared against their appropriate observations or control runs. These verifications consisted of zonal r.m.s. wind vector errors and zonal r.m.s. temperature errors for both the entire zone and only those points where land occurs, since better observations over land should aid in the forecast skill. Table 3.5 shows the verification fields used for the various runs that were performed.

TABLE 3.5

RUN	VERIFICATIONS	RUN	VERIFICATIONS	RUN	VERIFICATIONS
C1	GLAS, NMC	C2	GLAS, NMC	C3	NMC
C4	GLAS, NMC	R1	GLAS, NMC	R2	R1
F1	GLAS	F2	NMC	F3	C2
P1	GLAS	P2	NMC	P3	C2

4. RESULTS

The results presented here are reduced to two areas by vertical and horizontal averaging: northern hemisphere tropics from 2-22 N. and northern hemisphere mid latitudes from 26-70 N. The southern hemisphere is not presented since the data are too sparse to have any significant meaning.

Let X be an arbitrary run, then $EG(X)$ is defined as the r.m.s. errors determined by $X-G$, the GLAS analysis. Similarly, $EN(X)$ is the r.m.s. error field $X-N$, the NMC analysis. A measure of skill, S , between two arbitrary runs X and

Y, would be $E0(X)-E0(Y)$ with 0 being either G or N in both cases. X therefore would have better skill than Y if S is negative.

4.1 Impact of no cloud radiation interaction

The two control runs C1 and C2 when compared as shown in Table 4.1 indicate that removing cloud radiation interaction improves forecasting skill in mid latitudes. This is likely due to the excessive cloudiness generated by the model in this area. The skill increases with time since the model starts with few clouds and requires 1-2 days to fully develop their distribution. Note that the r.m.s. error in the temperature in mid latitudes is significantly high even after one day of simulation. In the tropics the r.m.s. temperature error does not grow much after one day where as it continues to increase in the mid latitudes. This is what would generally be expected since the tropics are largely diurnally driven and the mid latitudes, especially in winter, are baroclinically driven with synoptic time scales being dominant. The smaller differences and values of the temperature r.m.s. errors over land indicate that the sea surface temperature contrast with the atmosphere and the highly developed low pressure centers in the oceans give a much higher variance in temperature contrast with the atmosphere and the highly developed low pressure centers in the oceans give a much higher variance in temperature and wind than over land. The wind errors show a similar distribution to the temperature errors. Figure 1 shows the growth of the mid latitude r.m.s. errors for C1 and C2.

TABLE 4.1

TROPICAL R.M.S. ERRORS FOR C2 Vs C1
(Initial conditions starting 17 January 1979)

MODEL TIME	OVER ALL POINTS				OVER LAND POINTS			
	EG(C2)-EG(C1)		EG(C1)		EG(C2)-EG(C1)		EG(C1)	
	WIND	TEMP	WIND	TEMP	WIND	TEMP	WIND	TEMP
24 hours	0.0	-0.0	7.9	2.2	0.0	-0.0	4.6	1.4
48 hours	0.1	-0.0	9.4	2.5	0.1	-0.0	5.6	1.4
72 hours	0.0	-0.1	10.5	2.7	0.2	-0.1	5.8	1.6
96 hours	0.1	-0.1	11.1	2.9	0.2	-0.1	6.1	1.7
120 hours	0.5	-0.1	11.6	2.9	0.2	-0.1	6.2	1.7

TABLE 4.1 (CONT.)

MID LATITUDE R.M.S. ERRORS FOR C2 Vs C1
(Initial conditions starting 17 January 1979)

MODEL TIME	OVER ALL POINTS				OVER LAND POINTS			
	EG(C2)-EG(C1)		EG(C1)		EG(C2)-EG(C1)		EG(C1)	
	WIND	TEMP	WIND	TEMP	WIND	TEMP	WIND	TEMP
24 hours	0.0	-0.1	8.4	3.4	0.0	-0.0	4.5	2.0
48 hours	-0.0	-0.1	11.0	4.4	0.0	-0.1	5.9	2.6
72 hours	-0.2	-0.3	13.6	5.4	-0.1	-0.1	6.7	3.1
96 hours	-0.5	-0.4	15.7	6.2	-0.3	-0.2	8.4	3.5
120 hours	-0.7	-0.5	17.2	6.8	-0.4	-0.3	9.4	4.1

4.2 Impact of the removal of latent heating

Comparing the reduced heating run R1 with C2 seen in Table 4.2 shows that the lack of latent heat processes in the model atmosphere gives a noticeable increase in forecast error, particularly in the tropics where such processes are a major factor in forcing the atmosphere. Since clouds are normally more heavily distributed over oceans than over land, a smaller variance can be expected over the land points as the expected latent heating will be less. Note the errors are larger than the full model control run (C1) as would be expected.

TABLE 4.2

TROPICAL R.M.S. ERRORS FOR R1 Vs C2
(Initial conditions starting 17 January 1979)

MODEL TIME	OVER ALL POINTS				OVER LAND POINTS			
	EG(R1)-EG(C2)		EG(C2)		EG(R1)-EG(C2)		EG(C2)	
	WIND	TEMP	WIND	TEMP	WIND	TEMP	WIND	TEMP
24 hours	-0.2	0.4	7.9	2.2	-0.0	0.2	4.6	1.3
48 hours	-0.8	1.1	9.5	2.4	-0.5	0.5	5.7	1.4
72 hours	-1.1	1.7	10.6	2.6	-1.0	0.7	6.0	1.5
96 hours	-1.2	2.4	11.2	2.8	-1.1	1.0	6.4	1.6
120 hours	-1.2	2.9	12.1	2.8	-0.7	1.2	6.4	1.6

TABLE 4.2 (CONT.)

MID LATITUDE R.M.S. ERRORS FOR R1 Vs C2
(Initial conditions starting 17 January 1979)

MODEL TIME	OVER ALL POINTS				OVER LAND POINTS			
	EG(R1)-EG(C2)		EG(C2)		EG(R1)-EG(C2)		EG(C2)	
	WIND	TEMP	WIND	TEMP	WIND	TEMP	WIND	TEMP
24 hours	-0.0	0.2	8.4	3.4	0.0	0.1	4.5	2.0
48 hours	0.0	0.4	11.0	4.3	-0.0	0.2	5.9	2.5
72 hours	-0.2	0.8	13.4	5.2	-0.2	0.4	6.6	3.0
96 hours	-0.1	1.2	15.2	5.8	-0.2	0.5	8.1	3.3
120 hours	0.5	1.5	16.5	6.3	-0.1	0.6	9.0	3.9

4.3 Impact of constant heating using future error correction

Examining Table 4.3 the future error correction experiments show some forecast skill improvement in the mid latitudes. When using the GLAS analysis for verification some skill persists in the temperature field over land for all 5 days of simulation. Higher initial skill but less persistence can be seen over all points. Negligible skill and persistence can be seen in the wind field. NMC analysis verification shows similar initial skill but much less persistence than the GLAS analysis. Note that the actual wind error is higher and the temperature error is somewhat lower than the GLAS analysis verification.

TABLE 4.3

TROPICAL R.M.S. ERRORS FOR F1 Vs C2
(Initial conditions starting 17 January 1979)

MODEL TIME	OVER ALL POINTS				OVER LAND POINTS			
	EG(F1)-EG(C2)		EG(C2)		EG(F1)-EG(C2)		EG(C2)	
	WIND	TEMP	WIND	TEMP	WIND	TEMP	WIND	TEMP
24 hours	0.1	-0.5	7.9	2.2	0.1	-0.2	4.6	1.3
48 hours	-0.6	-0.1	9.5	2.4	-0.5	0.0	5.7	1.4
72 hours	-0.2	0.1	10.6	2.6	-0.3	-0.0	6.0	1.5
96 hours	1.1	0.4	11.2	2.8	0.3	0.2	6.4	1.6
120 hours	2.6	0.8	12.1	2.8	1.4	0.6	6.4	1.6

TABLE 4.4

MID LATITUDE R.M.S. ERRORS FOR P1 Vs C4
(Initial conditions starting 18 January 1979)

MODEL TIME	OVER ALL POINTS				OVER LAND POINTS			
	EG(P1)-EG(C4)		EG(C4)		EG(P1)-EG(C4)		EG(C4)	
	WIND	TEMP	WIND	TEMP	WIND	TEMP	WIND	TEMP
24 hours	0.6	0.1	7.8	2.2	0.3	0.1	4.5	1.4
48 hours	0.4	0.2	9.3	2.4	-0.2	0.1	5.6	1.3
72 hours	1.4	0.4	10.4	2.6	0.2	0.1	6.3	1.6
96 hours	2.5	0.8	11.2	2.6	0.8	0.4	6.3	1.6

MID LATITUDE R.M.S. ERRORS FOR P1 Vs C4
(Initial conditions starting 18 January 1979)

MODEL TIME	OVER ALL POINTS				OVER LAND POINTS			
	EG(P1)-EG(C4)		EG(C4)		EG(P1)-EG(C4)		EG(C4)	
	WIND	TEMP	WIND	TEMP	WIND	TEMP	WIND	TEMP
24 hours	0.5	0.1	8.3	3.2	0.3	-0.1	4.1	1.8
48 hours	1.2	0.2	12.3	4.4	0.9	-0.1	5.7	2.5
72 hours	2.0	0.6	14.7	5.2	1.5	0.2	7.4	3.0
96 hours	2.8	1.3	15.9	5.6	1.5	0.5	8.1	3.4

MID LATITUDE R.M.S. ERRORS FOR P2 Vs C4
(Initial conditions starting 18 January 1979)

MODEL TIME	OVER ALL POINTS				OVER LAND POINTS			
	EN(P2)-EN(C4)		EN(C4)		EN(P2)-EN(C4)		EN(C4)	
	WIND	TEMP	WIND	TEMP	WIND	TEMP	WIND	TEMP
24 hours	0.0	-0.2	9.6	2.4	-0.0	-0.2	5.9	1.4
48 hours	0.3	0.1	11.0	2.7	0.3	-0.1	6.7	1.6
72 hours	1.6	0.4	11.5	2.7	0.2	0.1	7.3	1.6
96 hours	3.2	0.9	12.3	2.8	1.3	0.4	7.1	1.6

MID LATITUDE R.M.S. ERRORS FOR P2 Vs C4
(Initial conditions starting 18 January 1979)

MODEL TIME	OVER ALL POINTS				OVER LAND POINTS			
	EN(P2)-EN(C4)		EN(C4)		EN(P2)-EN(C4)		EN(C4)	
	WIND	TEMP	WIND	TEMP	WIND	TEMP	WIND	TEMP
24 hours	0.0	0.0	9.3	3.0	0.0	-0.1	4.8	1.7
48 hours	1.0	0.6	13.0	4.0	0.6	0.2	6.3	2.1
72 hours	2.0	1.3	15.5	4.9	1.3	0.8	8.0	2.6
96 hours	2.4	1.9	16.6	5.3	1.4	1.0	8.7	2.9

4.5 One day observation errors

After only 24 hours of integration substantial errors at higher altitudes (the top sigma levels) were seen in the model forecast error. The cloudless radiation control run (C2) when verified against GLAS analysis showed temperature errors as high as 18.7 C north of the eastern Siberian Arctic coast in the top sigma level. Similar values could be found elsewhere in this region. At the same level errors as high as 19.3 C in southern Greenland, 18.0 C in northern Scandinavia, and 16.6 C over Bangladesh were also found. Errors over oceanic areas well away from land never exceeded 6 C at this level. In the next lower sigma level, errors as high as 20.4 C were found over the eastern Siberian Arctic coast. The other mentioned regions showed quite different errors. Maximum errors at this level were also found over northern Canada (16.8 C), Antarctica (29.6 C), and near Hawaii (13.8). Here several oceanic areas had large temperature errors.

When compared against NMC analysis larger areas with larger errors can be found throughout the globe in the top levels. The largest error is 22.3 again off the eastern Siberian Arctic coast in the top level. Similarly large errors are found over the previously mentioned areas with much larger errors over the oceans and added large errors over Antarctica. The next lower sigma level shows smaller errors than the GLAS analysis, but still substantial (as high as 17.9 C). The errors decrease as one nears the surface, but the impact that these errors have in detecting any skill in the constant heating experiments is overwhelmingly large. The constant heating amplitudes are nearer 2 C/day making their impact quite negligible.

4.6 Other experiment results

The two runs made using the model temperature error (F3 and P3) showed less error with respect to the original control run (C2). As seen in Table 4.6 the future error correction run (F3) had much smaller temperature errors in both the tropics and mid latitudes. The wind errors are also somewhat smaller than seen in the other future error correction runs. This shows that other uncertainties in the model: dynamics, initial conditions, filtering, etc. give much greater errors than the supersaturation and convective heatings. The past error correction run (P3) shows similar error growth in the tropics as the future error correction run. The mid latitudes shows much greater error growth (but less than other past error correction runs). This suggests that the original purpose of these experiments may have had some validity in the tropics were it not for the uncertainties in the model and the initial conditions.

TABLE 4.6

EC2(F3): ERRORS FOR FUTURE ERROR CORRECTION USING C2
(Initial conditions starting 17 January 1979)

MODEL TIME	TROPICAL R.M.S. ERRORS				MID LATITUDE R.M.S. ERRORS			
	Over All Pts		Over Land Pts		Over All Pts		Over Land Pts	
	WIND	TEMP	WIND	TEMP	WIND	TEMP	WIND	TEMP
24 hours	3.5	0.6	1.4	0.3	0.8	0.3	0.4	0.1
48 hours	5.2	1.1	2.4	0.5	1.8	0.6	0.8	0.3
72 hours	6.9	1.5	3.7	0.7	3.2	1.1	1.4	0.4
96 hours	8.8	1.8	3.7	0.7	3.2	1.1	1.4	0.4
120 hours	10.8	2.1	5.8	1.1	7.1	2.3	3.2	0.9

EC2(P3): ERRORS FOR FUTURE ERROR CORRECTION USING C2
(Initial conditions starting 18 January 1979)

MODEL TIME	TROPICAL R.M.S. ERRORS				MID LATITUDE R.M.S. ERRORS			
	Over All Pts		Over Land Pts		Over All Pts		Over Land Pts	
	WIND	TEMP	WIND	TEMP	WIND	TEMP	WIND	TEMP
24 hours	7.9	2.2	4.6	1.3	8.4	3.4	4.5	2.0
48 hours	9.4	2.0	5.2	1.1	8.9	3.1	4.9	1.8
72 hours	9.8	2.2	5.7	1.2	9.8	3.5	5.4	1.9
96 hours	10.6	2.3	6.1	1.1	11.3	3.8	6.3	2.1

5. CONCLUSIONS

The suppressing of the cloud radiation interaction (both shortwave and longwave) improves the forecast skill of the model. This advantage comes from the excessive cloudiness (with respect to observations) that the model tends to generate. Forecast errors within 24 hours in the temperature field are too large so that correcting them as errors in the diabatic heating does not improve the forecast skill of the model.

REFERENCES

- Baker, W. E., 1983: Objective analysis and assimilation of observational data from FGGE. Mon. Wea. Rev., 111, 328-342.
- Randall, D., 1982: Monthly and seasonal simulations with the GLAS climate model. ECMWF workshop report.
- Shukla, J., 1981: Predictability of the tropical atmosphere, NASA Tech. Memo. No. 83829.

ORIGINAL PAGE IS
OF POOR QUALITY

CLOUD RADIATION vs NO CLOUD RADIATION
MID-LATITUDE RMS TEMPERATURE
ERRORS OVER ALL POINTS

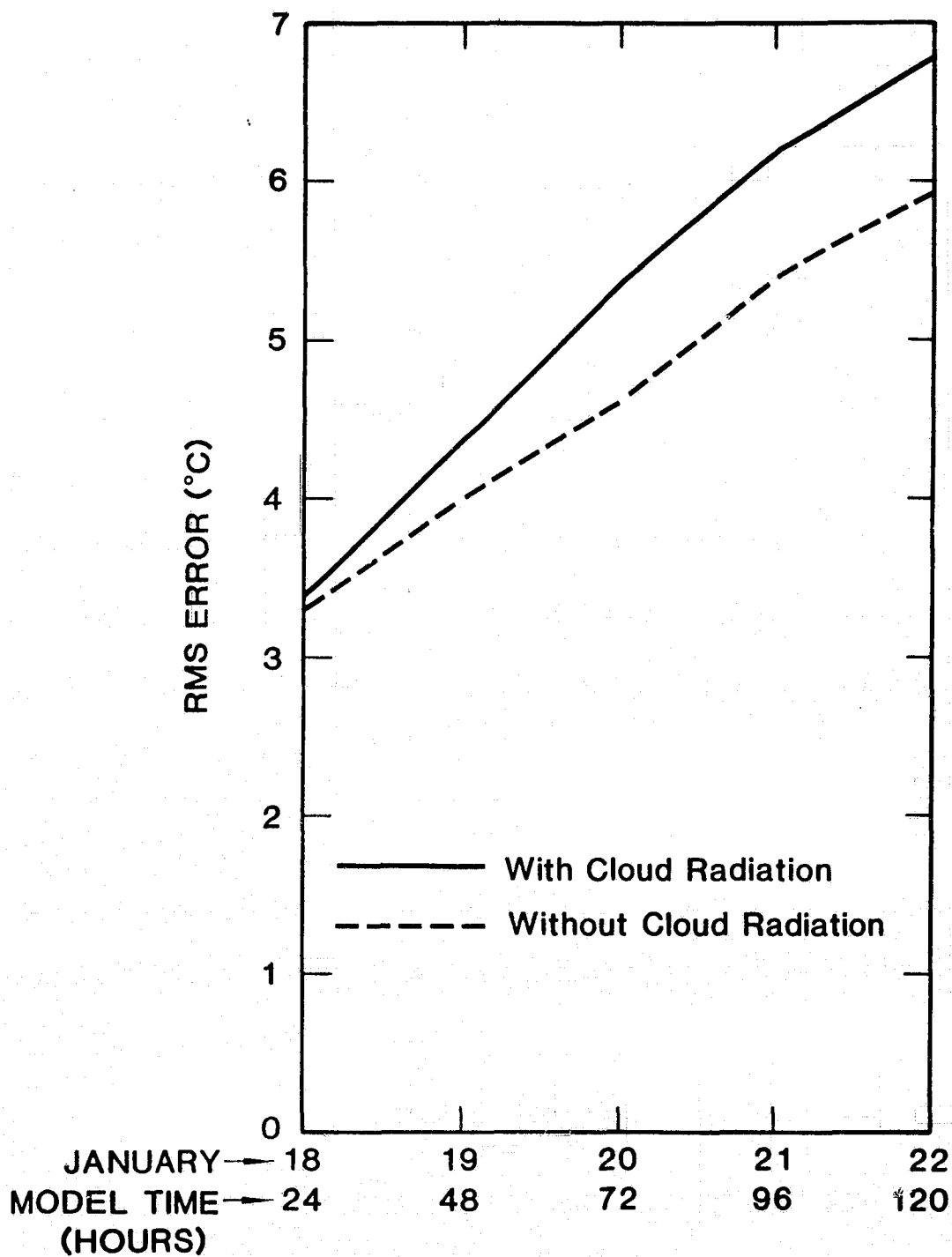


Figure 1

THE SENSITIVITY OF A GENERAL CIRCULATION MODEL TO SAHARAN DUST HEATING

D. A. Randall, T. Carlson, and Y. Mintz

During the Northern summer, sporadic outbreaks of wind-borne Saharan dust are carried out over the Atlantic by the tropical easterlies. Optical depths due to the dust can reach 3 near the African coast, and the dust cloud can be detected as far west as the Caribbean Sea (Carlson, 1979).

In order to obtain insight into the possible effects of Saharan dust on the weather and climate of North Africa and the tropical Atlantic Ocean, we have performed simulation experiments with the Climate Model of the Goddard Laboratory for Atmospheric Sciences. The most recent version of the model is described by Randall (1982). The model produces realistic simulations of many aspects of the observed climate and its seasonal variation.

We prescribed the dust heating rates directly as an additional term in the thermodynamic energy equation of the model. The horizontal distribution of the prescribed heating was based on the observed summer mean optical depth distribution for 1974, as described by Carlson (1979). Fig. 1 shows the distribution used, normalized so that the maximum value (near the African coast) is 1.0. We decided not to include any dust over land, first because as discussed below, our method for relating heating rates to optical depth is only applicable over the ocean; second, because the distribution of optical depths over land is unknown in any case; and third, because the effects of the dust may be small over land where direct dust heating of the atmosphere is partly compensated for by reduced sensible heat transfer at the earth's surface.

We made one model run in which the maximum optical depth was 1.0, and a second in which the maximum optical depth was 2.0. In a third run (the "control"), the atmosphere was assumed to be dust-free. All three runs were initialized from the observed state of the atmosphere for June 15, 1979, and run to 00Z, July 1, without any dust heating. In the two runs with dust, the optical depths were assumed to increase linearly with time, from zero to their maximum values, over the two-day period 00 July 1 to 00 July 3, then to remain constant with time for ten days, and finally to decrease linearly with time to zero over two days. The idea was to crudely simulate the episodic nature of real dust outbreaks.

The three-dimensional distribution of dust heating was determined as follows. The vertical profiles of daily-mean clear-sky dust heating rates due to solar and terrestrial radiation were tabulated separately, as functions of optical depth and with 50 mb vertical resolution, using the results of Carlson and Benjamin (1980). These tables, as well as the geographical distribution of optical depth, were provided as input to the model. On each time-step, and for each grid-point, the model interpolated within the tables to find the daily-mean solar and terrestrial dust heating rates as functions of height, using the appropriate optical depth. Finally, the daily-mean solar heating rates due to dust were converted into instantaneous values by taking into account the instantaneous solar zenith angle.

We present here some results representing averages over the five-day period July 8-12, by which time the effects of the dust should be maximal. Longitudinal

means of various quantities were computed, as functions of latitude, for the regions labeled "West," "Center," and "East" in Fig. 2.

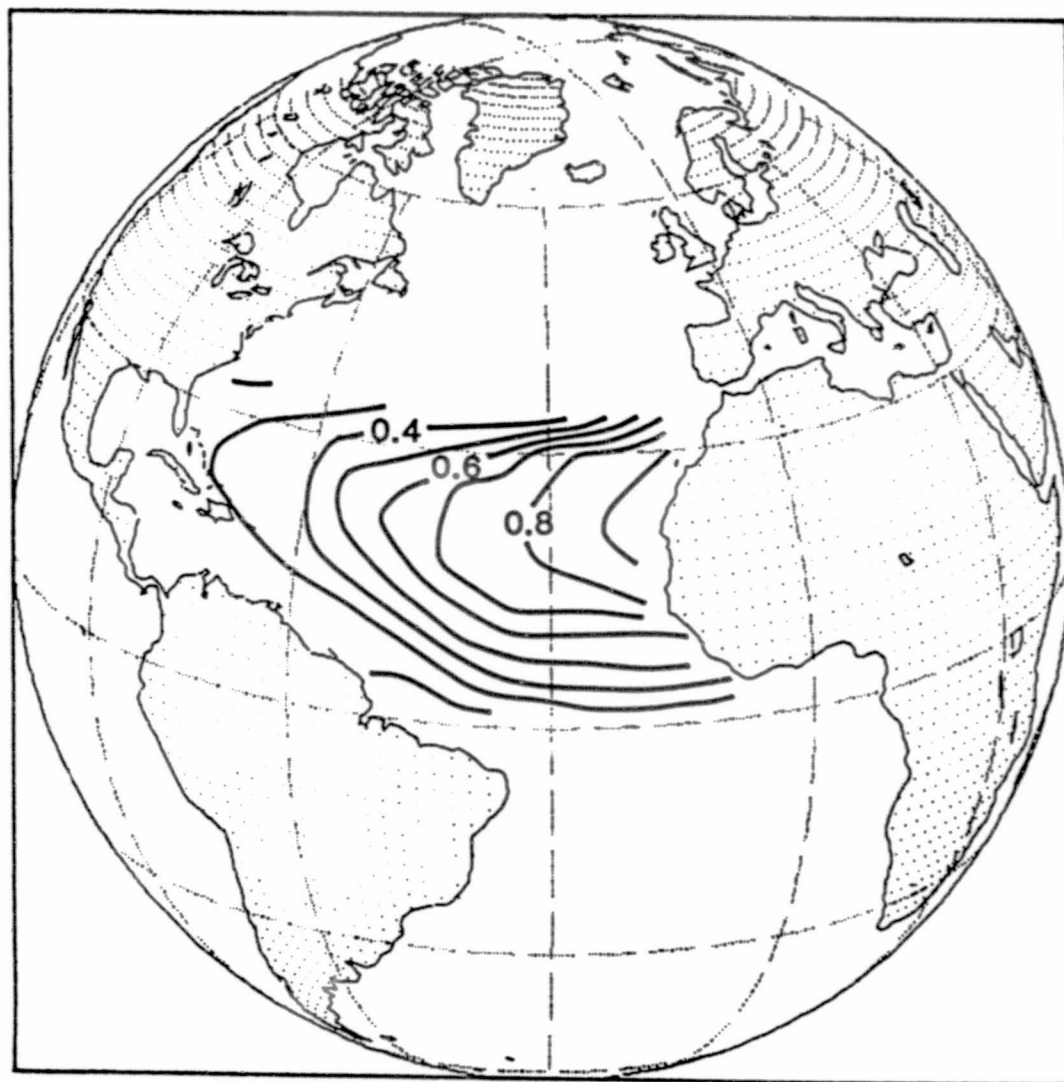
Fig. 3 shows the precipitation results. For the central and western regions, the dust seems to produce a narrowing and intensification of the tropical rain belt. This effect is systematic and progressive, i.e., it is stronger for optically thick dust than for optically thin dust. Fig. 4 shows the results for the 950 mb wind components. The easterlies are markedly reduced by the dust, particularly for the western region. This is interesting, since in nature it is the easterlies that transport the dust.

The results of our experiments indicate that the effects of Saharan dust outbreaks on the weather and climate of the tropical Atlantic may be significant.

REFERENCES

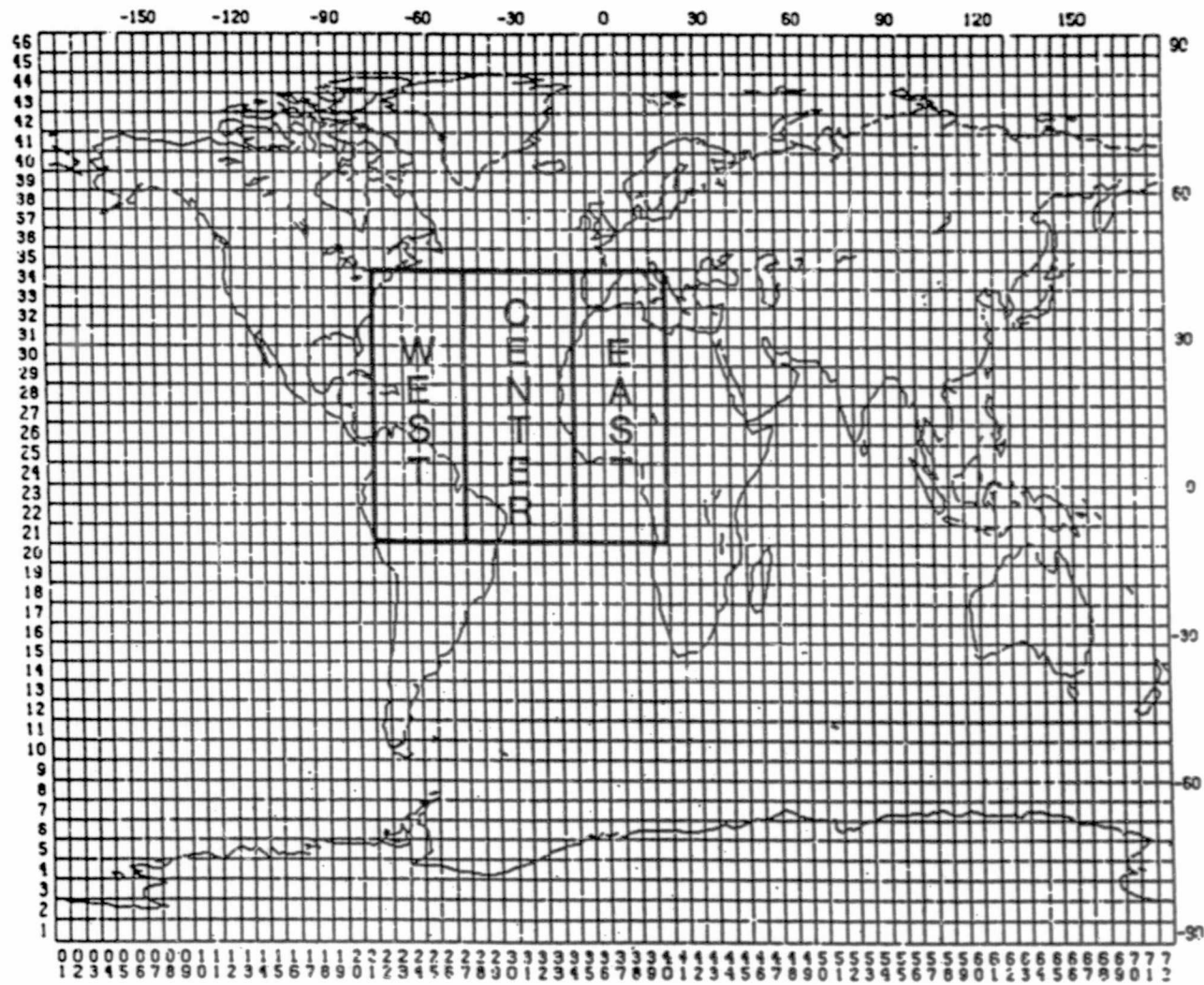
- Carlson, T. N., 1979: Atmospheric turbidity in Saharan dust outbreaks as determined by analyses of satellite brightness data. Mon. Wea. Rev., 107, 322-335.
- Carlson, T. N., and S. G. Benjamin, 1980: Radiative heating rates for Saharan dust. J. Atmos. Sci., 37, 193-213.
- JSC, 1981: Experts Meeting on Aerosols and Climate, Geneva, 27-31 October 1980. WMO-IUGG WCP-12.
- Randall, D. A., 1982: Monthly and seasonal simulations with the GLAS Climate Model. Proceedings of the Workshop on Intercomparison of Large-Scale Models Used for Extended Range Forecasts of the European Centre for Medium-Range Weather Forecasts, Reading, England (to appear).

NORMALIZED OPTICAL DEPTH



ORIGINAL PAGE IS
OF POOR QUALITY

Figure 1: Prescribed distributions of the optical depth for Saharan dust, normalized so that the maximum value (near the Africa coast) is 1.0.



ORIGINAL PAGE IS
OF POOR QUALITY

Figure 2: Locations of the three regions for which longitudinally averaged results are given in Figs. 6-8.

TOTAL PRECIPITATION (mm day⁻¹)

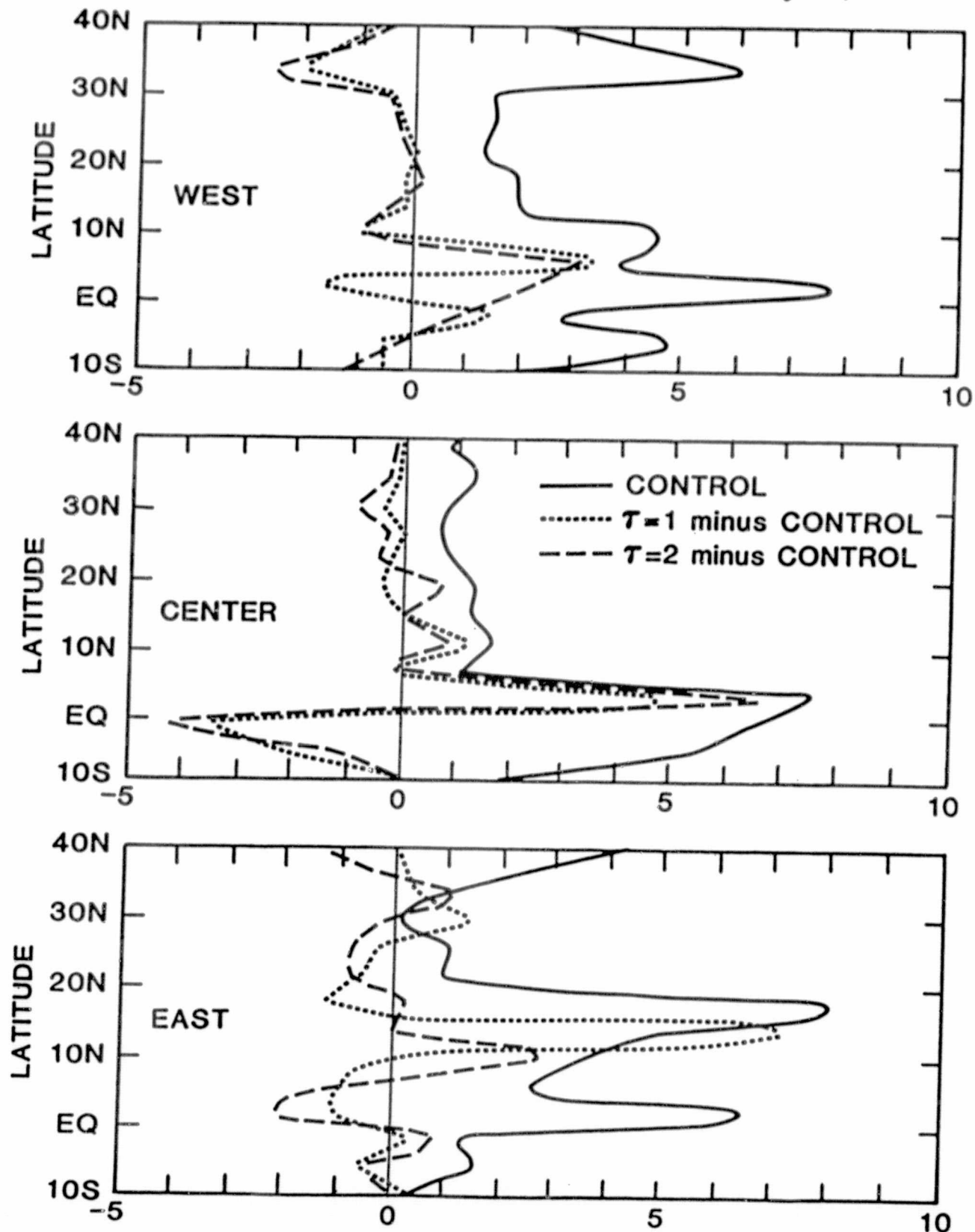


Figure 3: Longitudinally averaged simulated precipitation.

ORIGINAL PAGE IS
OF POOR QUALITY

950 mb ZONAL WIND (ms^{-1})

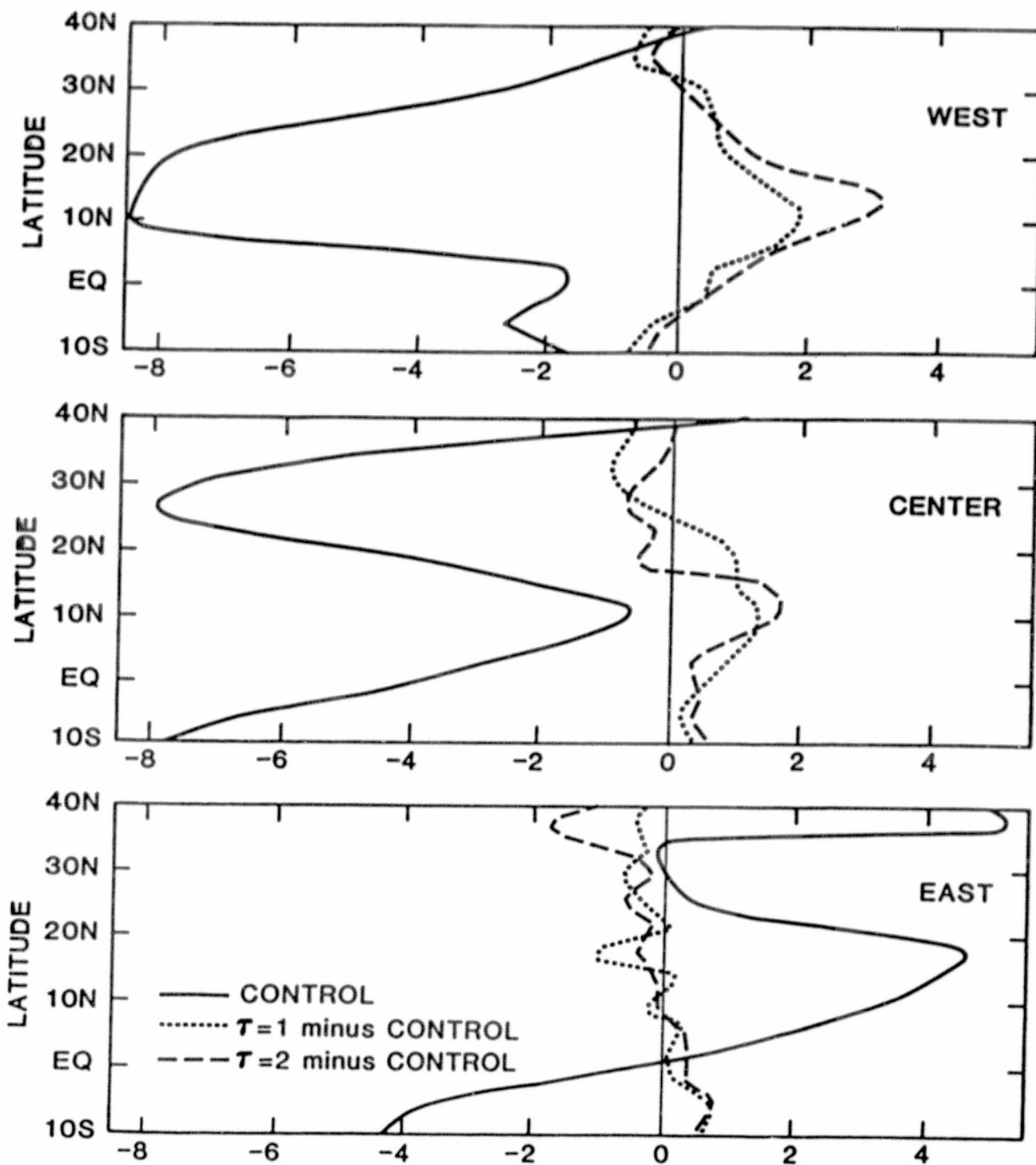


Figure 4: Longitudinally averaged simulated 950 mb zonal wind.

INFLUENCE OF SURFACE ROUGHNESS OF A DESERT

Y. C. Sud and W. E. Smith

A numerical simulation study, using the current GLAS climate GCM, was carried out to examine the influence of low bulk aerodynamic drag parameter in the deserts. To the best of our knowledge, this is perhaps the only influence that has not been investigated so far, as opposed to surface albedo and soil moisture. Subsequent to Charney (1975), and his series of July simulation studies at GISS (Charney et al., 1977), showing the importance of albedo feedback in tropical desert border regions, many studies have been made by modelers to understand the role of albedo and soil moisture on the summertime circulation (see for example Sud and Fennessy, (1982, 1983), Shukla and Mintz (1982), Yeh et al. (1983), Walker and Rowntree (1977), and Rind (1982)). However, the bulk drag and heat transfer parameters in the GCMs are crudely specified. It turns out that the bulk parameters also experience a drastic reduction as forested land changes to a desert.

The GLAS GCM has Deardorff (1972) parameterization of the planetary boundary layer wherein the surface roughness effect is explicitly introduced by surface roughness height. It is currently 0.45 m for all land surfaces. Slade (1968) gives a value of 3.0×10^{-4} m for smooth deserts. We decided to adopt a value of 2.0×10^{-4} m for all deserts (also used for oceans) in our study. Fig. 1 shows all the desert regions. We ran two simulations from the observed NMC analysis for June 15, 1979. The control run had a surface roughness height of 0.45 m everywhere on land, whereas the anomaly run had a surface roughness height 2.0×10^{-4} m for deserts and 0.45 m elsewhere on land. The first sixteen days were ignored as an initial adjustment period. The two simulations were compared for the last 31 days representing the mean July circulation.

We notice that the precipitation in the Sahara Desert was significantly reduced, pushing the ITCZ further south, (Fig. 2). Thus far, the too far northward location of the ITCZ in the Sahara has been recognized as a weakness of the GLAS climate model. Use of a realistic roughness height has effectively improved this situation. In the continental U.S., the simulated midwest is colder and the precipitation in the eastern region is 4 mm/day, as opposed to a maximum of 8 mm/day (observations 3-4 mm/day). This may also be seen in Fig. 2. Fig. 3 shows the corresponding changes in diabatic heating. Again, this aspect of the new simulation is more realistic. Detailed diagnostics showed that the improvements were realized, in part, due to increased longwave cooling of deserts resulting from much larger excursions of diurnal ground temperature. Longwave cooling is highly nonlinear due to the fourth power of temperature effect on radiation. It therefore has to yield more cooling for a larger diurnal temperature oscillation. Fig. 4 shows this vividly for a set of sample points in the Sahara Desert. There is a considerable amplification of diabatic heating change vis-a-vis sensible heating change.

This study reveals the importance of yet another feedback effect of a desert on itself, that is produced by the reduction in surface roughness height of land once the vegetation dies and desert forms. Apart from affecting the moisture convergence, low bulk transport coefficients of a desert lead to enhanced longwave cooling and sinking which together reduce precipitation by Charney's (1975) mechanism. Thus, this effect, together with albedo and soil

moisture influence, try to perpetuate a desert condition through its geophysical feedback effect. Thereby, the study further suggests that man-made deserts is a viable hypothesis.

REFERENCES

- Charney, J. G., 1975: Dynamics of deserts and drought in the Sahel. Quart. J. Roy. Met. Soc., 101, 193.
- Charney, J. G., W. J. Quirk, S. H. Chow, and J. Kornfield, 1977: A comparative study of the effects of albedo change on drought in semi-arid regions. J. Atmos. Sci., 34, 1366.
- Shukla, J., and Y. Mintz, 1982: The influence of land surface evapotranspiration on the earth's climate. Science, 215, 1498.
- Sud, Y. C., and M. J. Fennessy, 1983: Influence of evaporation anomaly in semi-arid regions in the July circulation: A numerical study. J. Climatology. (in press)
- Sud, Y. C., and M. J. Fennessy, 1982: A study of the influence of surface albedo on July circulation in semi-arid regions using the GLAS GCM. J. Climatology, 2, 105-125.
- Walker, J., and P. R. Rowntree, 1977: The effect of soil moisture and rainfall in a tropical model. Quart. J. Roy. Met. Soc., 103, 29.
- Yeh, T. C., R. T. Wetherald, and S. Manabe, 1983: The effect of soil moisture on the short term climate and hydrology--a numerical experiment. (To be published)

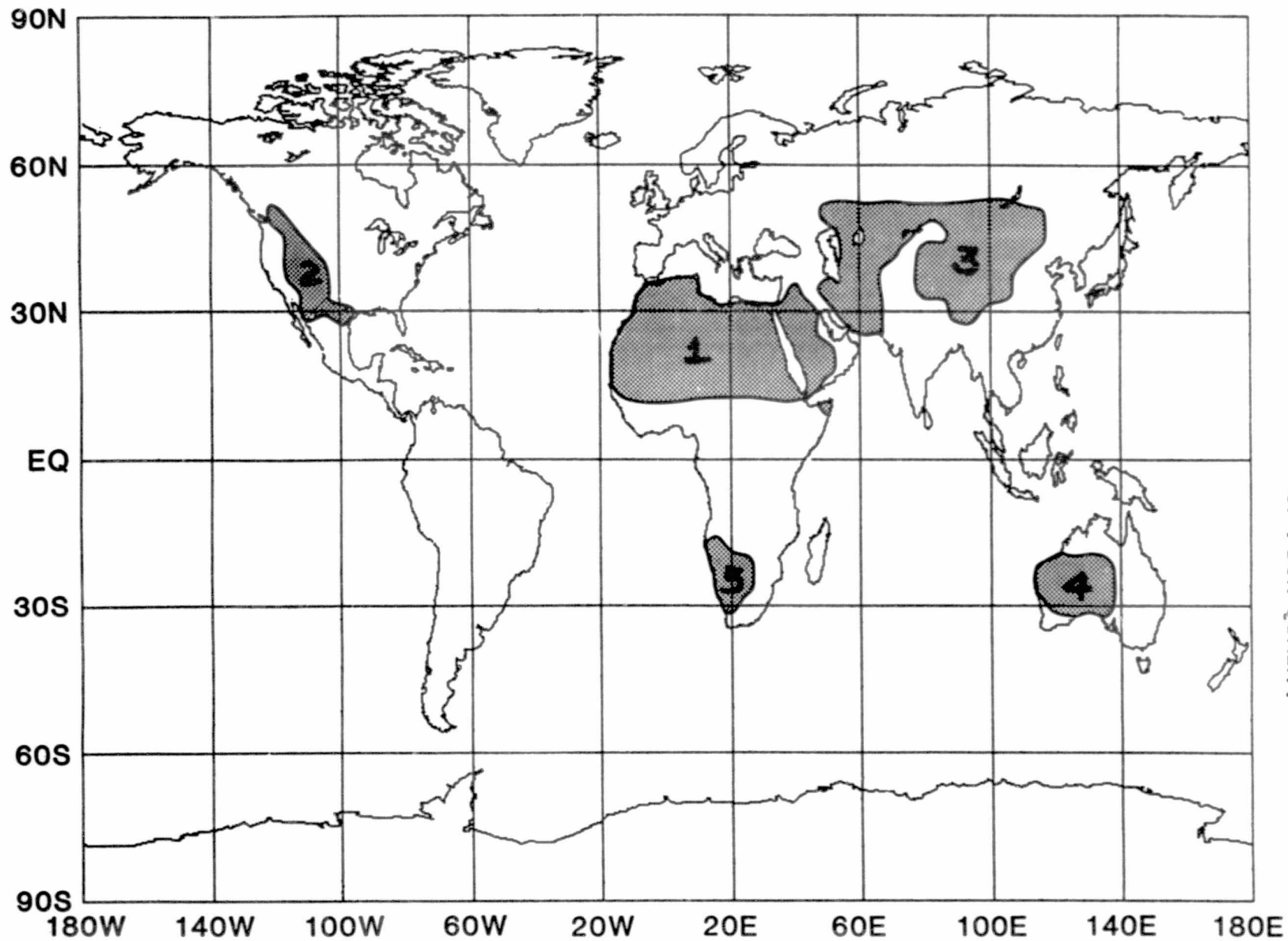


Fig. 1. Five desert regions in which the surface roughness was reduced to 2.0×10^{-4} m from the normal prescribed value of 0.45 m on land.

PRECIPITATION DIFFERENCES (mm/day)

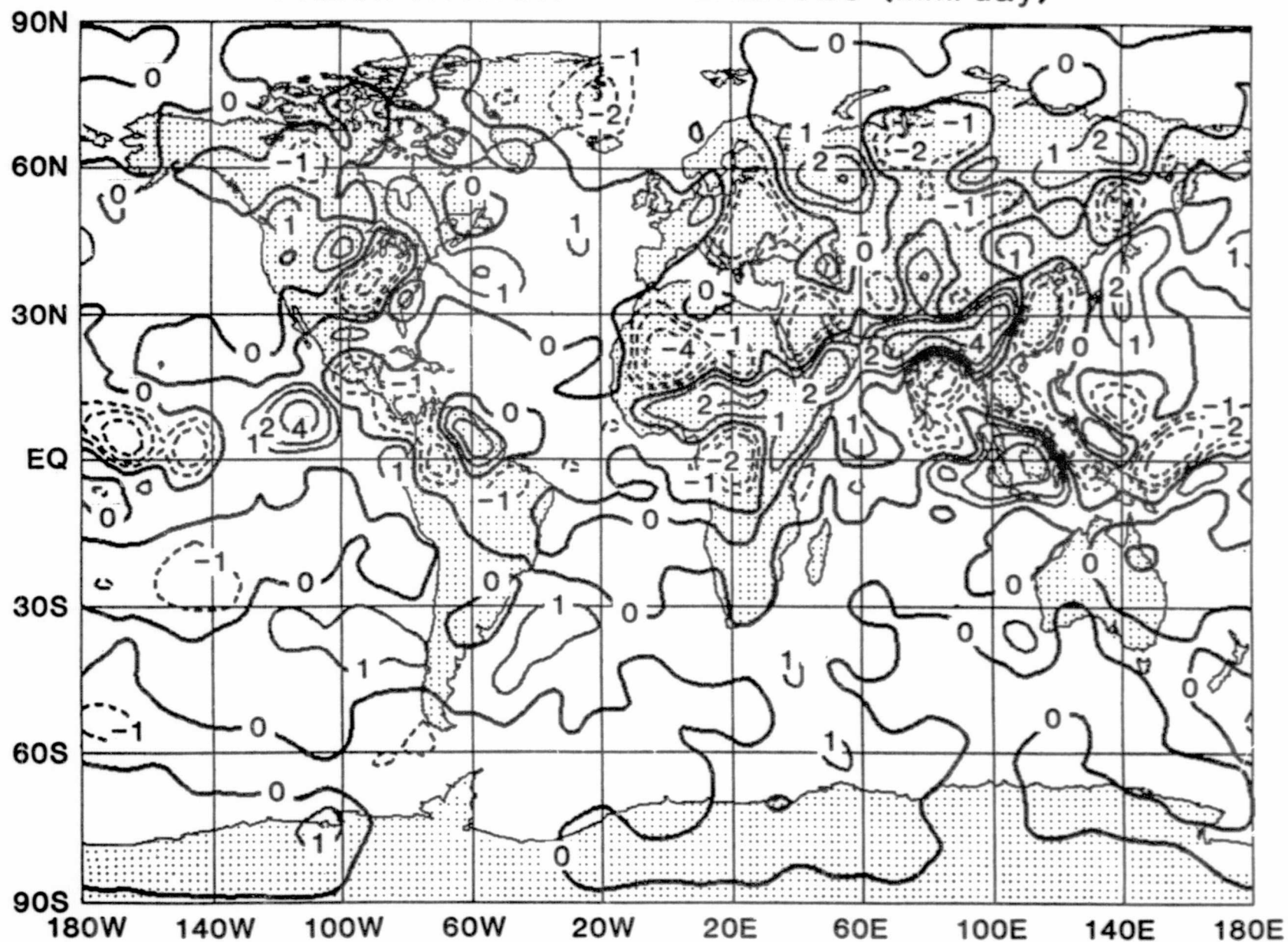
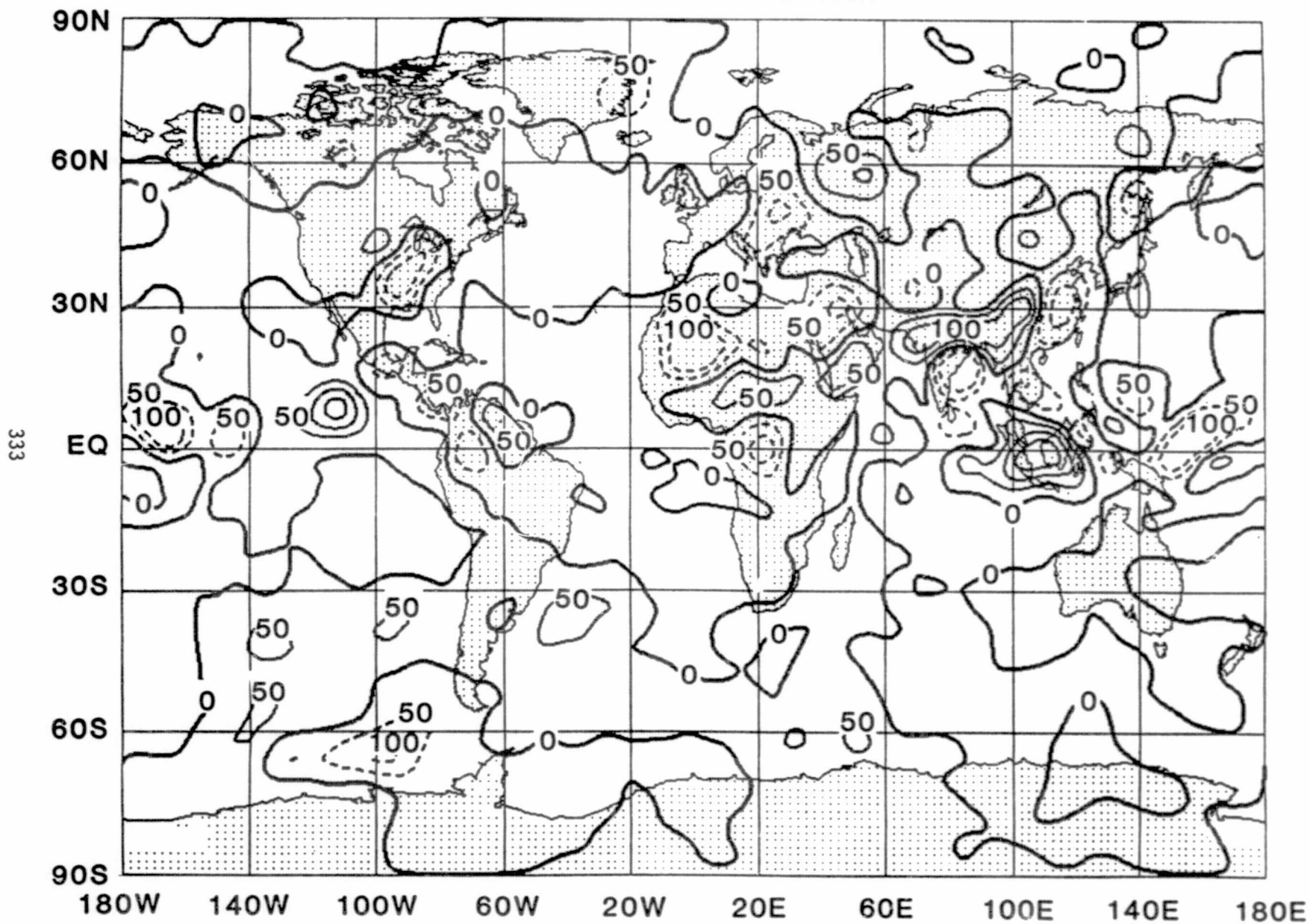


Fig. 2. Differences in precipitation between the two runs in mm/day (Anomaly-Control).

332

ORIGINAL PAGE IS
OF POOR QUALITY

DIABATIC HEATING Wm^{-2}



ORIGINAL PAGE IS
OF POOR QUALITY

Fig. 3. Differences in diabatic heating between the two runs in $W m^{-2}$ (Anomaly-Control).

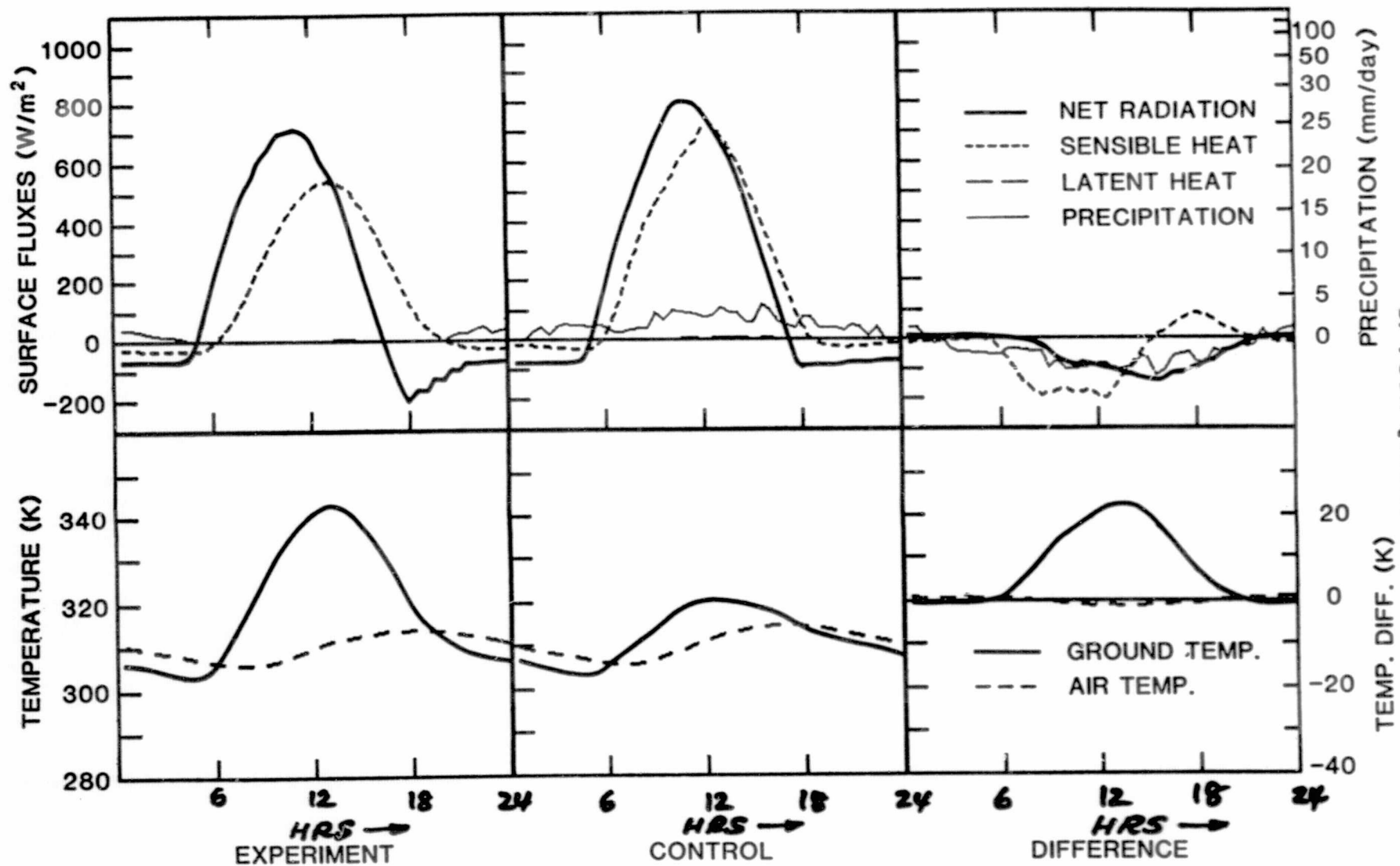


Fig. 4. 30 day average diurnal profile of various fluxes.

ROLE OF SOIL MOISTURE IN MAINTAINING DROUGHTS

Y. C. Sud and W. E. Smith

In this study, a set of simulations made with the GLAS climate GCM were used to investigate the influence of soil moisture on the persistence of an ongoing drought. For this purpose, the case study of drought of the summer of 1980 was selected. The difference in the simulation of two identical twin runs: one with the climatological normal soil moisture and the other with anomalous soil moisture for drought conditions, were examined on the mean monthly circulation. It was found that a reduction in soil moisture did indeed produce a corresponding reduction in precipitation. However, the pattern of the rainfall anomaly was not identical to the soil moisture (evapotranspiration) anomaly but had a good resemblance with observations.

The importance of the feedback effect of evapotranspiration (which has a direct dependence on soil moisture) on rainfall has been intuitively recognized for a long time. However, attempts to verify it by measurements led to confusing and somewhat misleading evidences. Based on these studies, the subject became controversial (see Stidd (1968) for a discussion of this controversy). Recently, many GCM simulation studies have been performed to investigate the role of soil moisture on ensuing circulation and precipitation. Accordingly, it is now generally recognized that the soil moisture has a strong influence on evapotranspiration, cumulus convection, rainfall, climate and mean monthly circulation. This feedback can be complex, depending upon the season and structure of the anomalous forcing.

With this background, we were motivated to examine the role of reduced soil moisture in the drought stricken regions on maintaining the ongoing drought. We selected the drought of the summer of 1980 in the United States. Whereas it was easy to obtain the observed analysis of the global atmosphere for this period (months of June and July), however, the corresponding soil moisture data had to be constructed. For this purpose, we utilized forty years of station rainfall data to obtain the normal soil moisture by the method given in Fennessy and Sud (1983). Then, using the observed monthly rainfall at various stations for the year 1980, the mean monthly soil moistures for that year were calculated. From these two calculations, the soil moisture anomaly values at various stations were obtained. Finally, these anomalies were averaged to obtain the soil moisture anomalies at the GCM grid which were used to produce the anomalous soil moisture dataset for 1980. However, the calculation of anomalies was confined to the continental U.S., because a global dataset of rainfall was unavailable.

Two simulations were run with the GLAS climate model as modified by Randall (1982) and subsequently further updated by Sud and Smith¹ (1984). In these runs, the initial conditions were based on the mean monthly observations for the month (June 7 through July 6, 1980). We designate the mean conditions to correspond to June 21, 1980. Starting from that day, both simulations were run until the end of August. While the simulations are still being analyzed, we present the

¹ See the article by Sud and Smith, "An ensemble formulation of PBL fluxes in a GCM," in this review.

following preliminary results to show the strong influence of soil moisture on the future rainfall that is consistent with the maintenance of an ongoing drought.

In the model, we use a β -function to allow for the availability of water for evapotranspiration. The β -function depends upon the soil moisture and is a multiplying factor which obtains actual evapotranspiration from potential evapotranspiration calculated by bulk aerodynamic formulas in the model.

Figs. 1a and 1b show the β -function anomaly as a difference between the β -function values in the two runs. In these simulations, the soil moisture was prescribed, which implies that the β -function was prescribed. The simulated differences in the latent and sensible fluxes, between the two runs, are shown in Figs. 2 and 3. These anomaly fields show a very strong correspondence with the β -function anomaly fields. That was to be naturally expected for the following reason: In these simulations, the convective clouds (which dominate in the summer hemisphere) do not interact with the radiation, hence the net radiation balance at any grid point is approximately constant. This implies that the sum of sensible and latent fluxes in the two runs is approximately the same. However, β -function governs the partition between the two fluxes which is indeed seen in their structure.

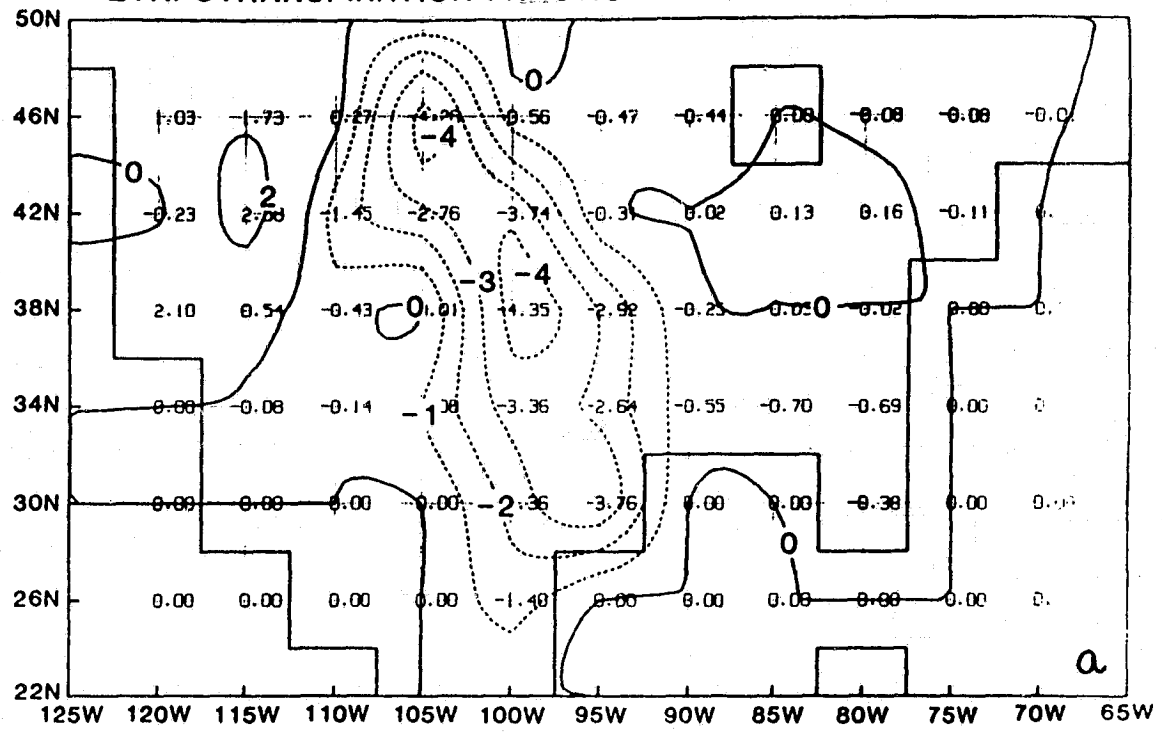
The corresponding precipitation anomalies are shown in Fig. 4. These have a complex structure because they are affected by circulation as well as surface fluxes. A good correlation between precipitation and evapotranspiration anomalies is evident in the results but it is not as strong as that between evapotranspiration and β -function. Nevertheless and more importantly, the rainfall anomaly patterns somewhat resemble the observations. Thus, these results not only show a strong dependence of rainfall on soil moisture but the agreement of simulations with the observations suggest a possible skill in climate forecasting based on this input. Besides, the dynamic structure of the precipitation anomalies allude to the dynamic character of a drought in the normal course of its duration. However, it must be pointed out that these findings are preliminary and are based on the analysis of one simulation with the GLAS climate GCM. More experiments are necessary to provide further support for these findings.

REFERENCES

- Fennessy, M. J., and Y. C. Sud, 1983: A study of the influence of soil moisture on future precipitation. NASA Tech. Memo. 85042.
- Randall, D. A., 1982: Monthly and seasonal simulations with the GLAS climate model. Proceedings of the workshop on Intercomparison of Large-Scale Models Used for Extended Range Forecasts of the European Centre for Medium Range Weather Forecasts, Reading, England, pp. 107-166.
- Stidd, C. K., 1968: Local moisture and precipitation. Reprint No. 45A, Center for Water Resources Research, Desert Research Institute, University of Nevada.
- Sud, Y. C., and W. E. Smith, 1984: An ensemble formulation of surface fluxes in a GCM. Accepted for publication in Boundary Layer Meteorology.

ORIGINAL PAGE IS
OF POOR QUALITY

EVAPOTRANSPIRATION FRACTION x 10. JULY DIFFERENCE



EVAPOTRANSPIRATION FRACTION x 10. AUGUST DIFFERENCE

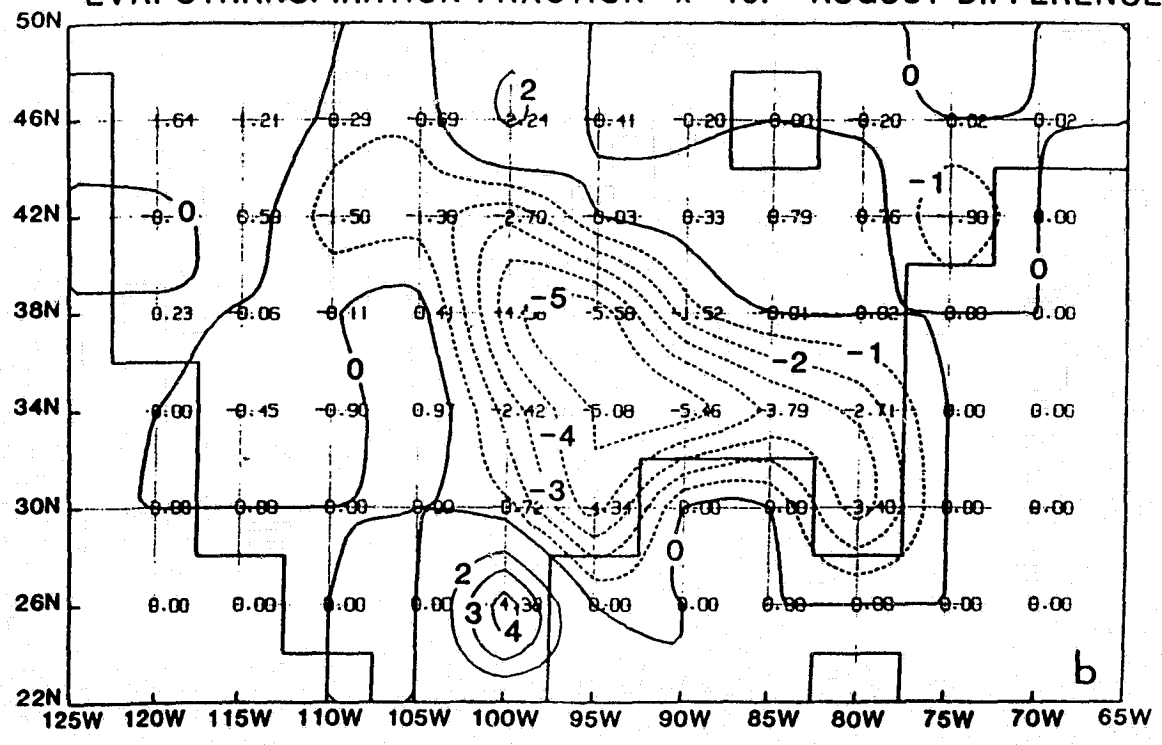


Figure 1

ORIGINAL PAGE IS
OF POOR QUALITY

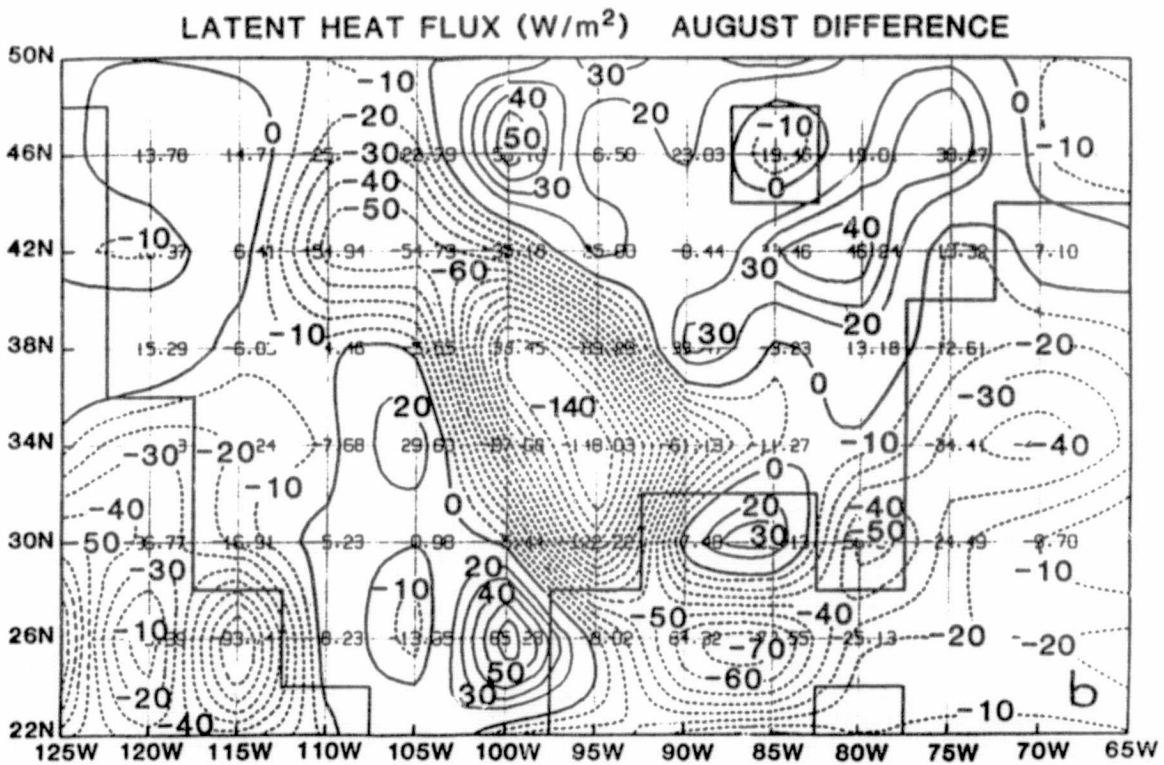
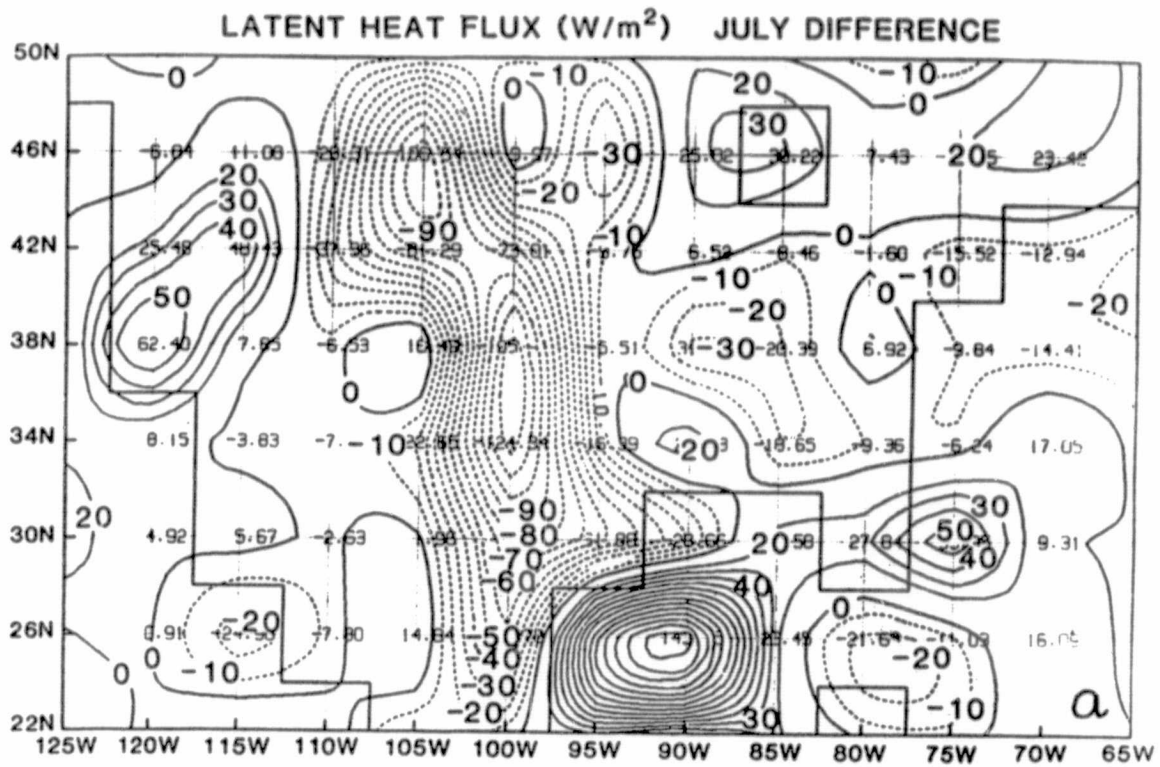


Figure 2

ORIGINAL PAGE IS
OF POOR QUALITY

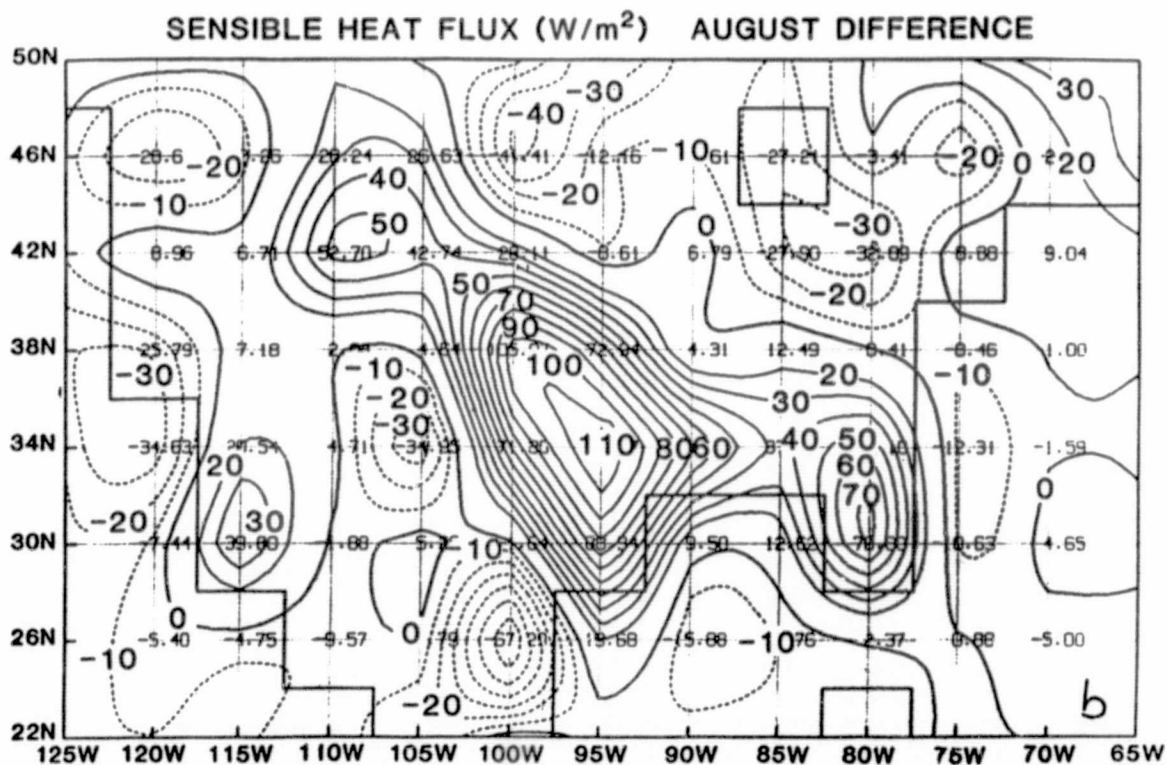
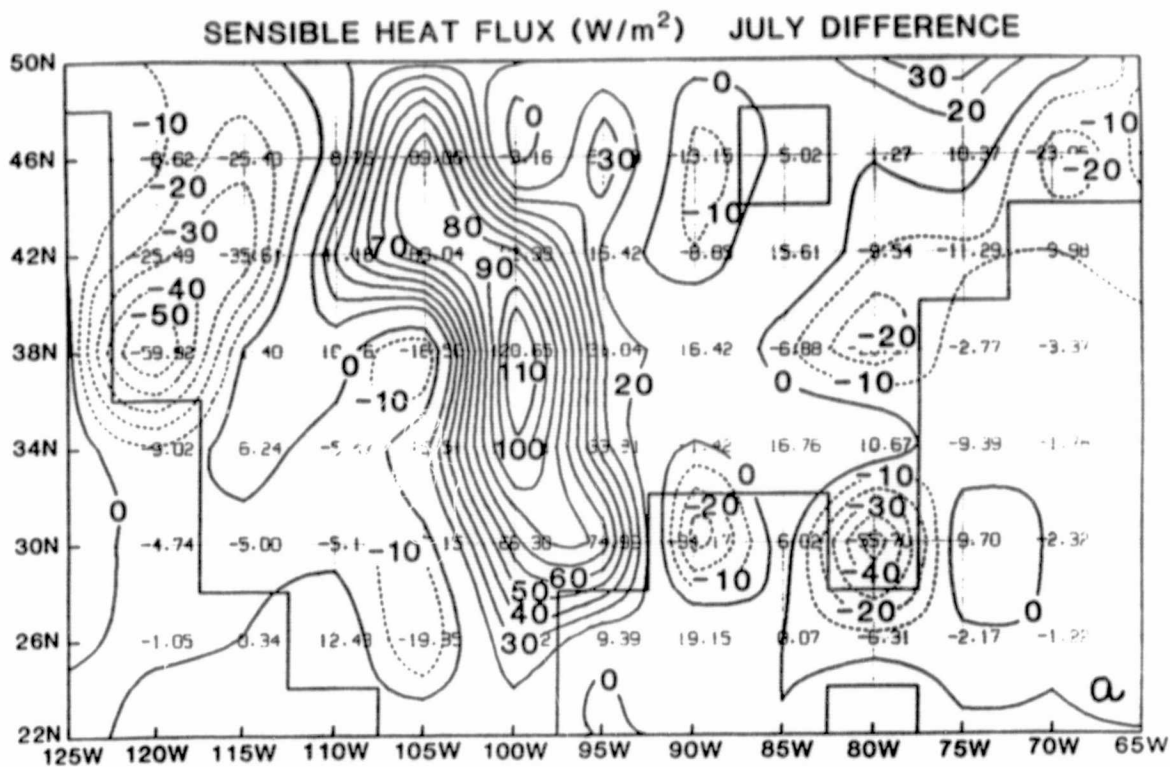


Figure 3

ORIGINAL PAGE IS
OF POOR QUALITY

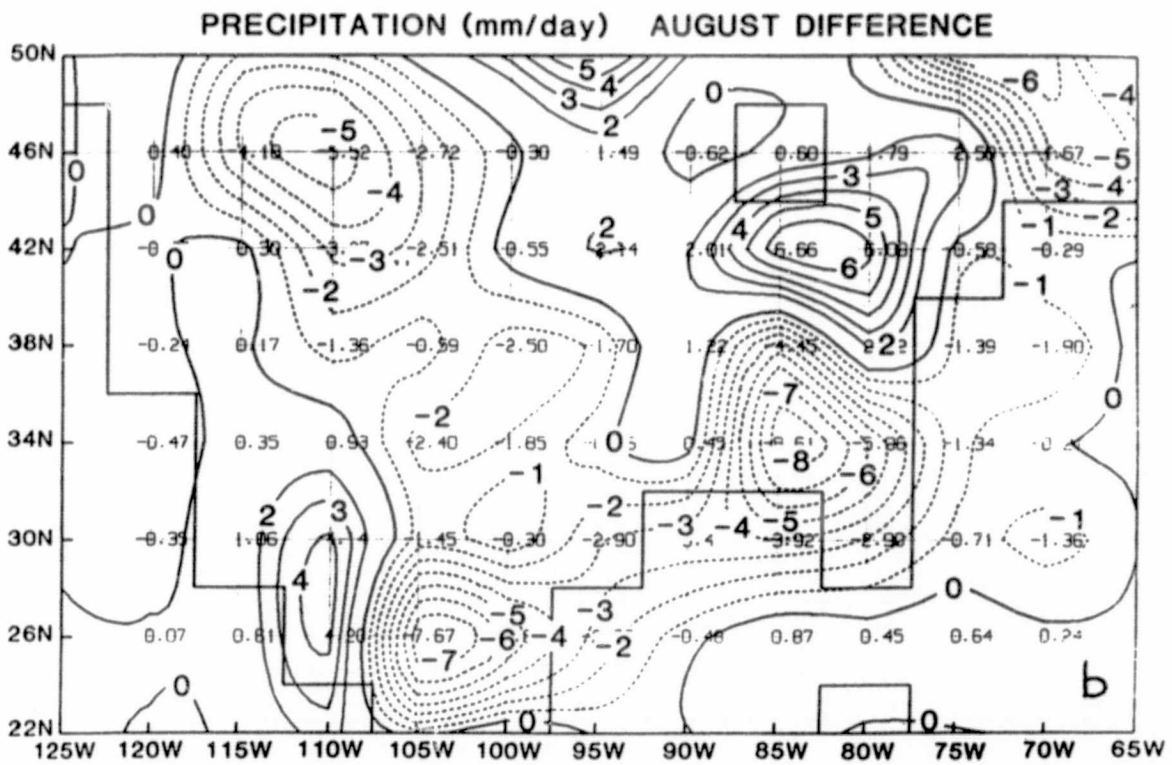
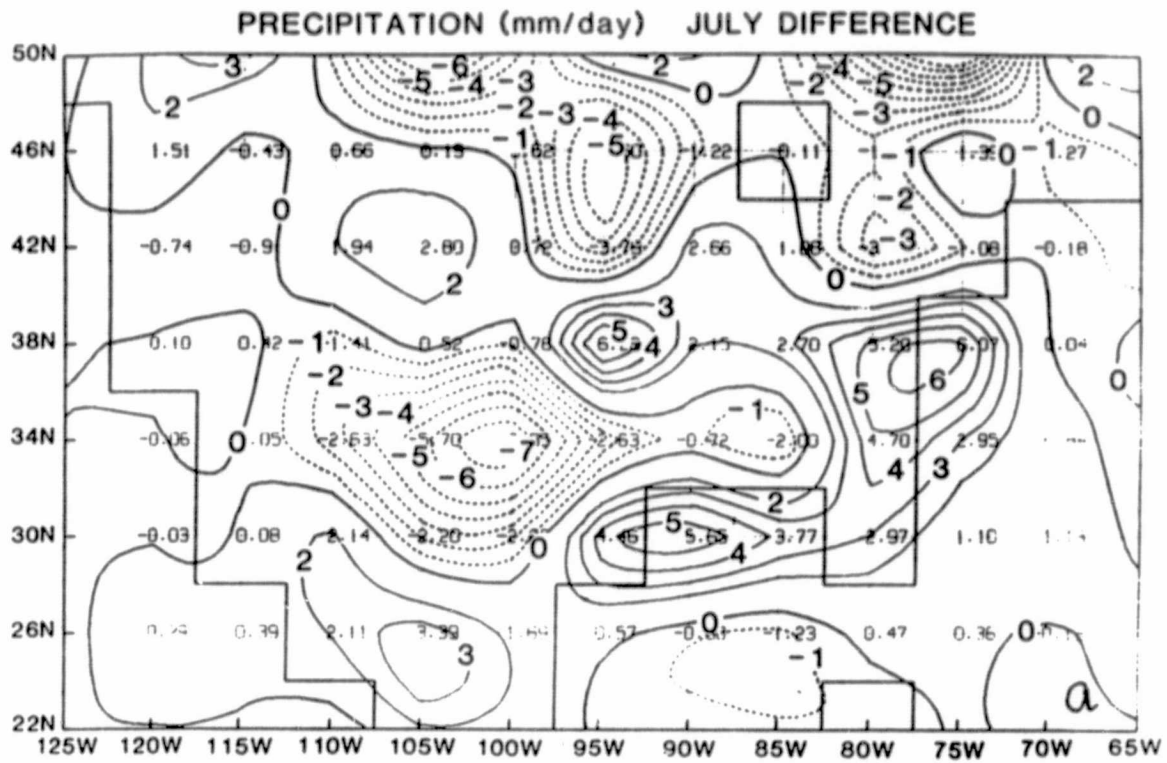


Figure 4

E. SOFTWARE DEVELOPMENT

0117
10
1247

AN ASYNCHRONOUS MFLINK FOR USE WITH THE UCLA CLIMATE MODEL

J. Abeles and M. Suarez

An "asynchronous MFLINK" has been developed to allow the model to continue processing while the data is staged to tape. Currently, integration of the model is stopped while the output history is MFLINKed to the front end. The time spent in MFLINK varies considerably between jobs, depending on the size of the output, operator response, and occurrence of I/O errors that require retries. On the average, the UCLA model is spending about 20% of its wall-clock time on MFLINKs. The asynchronous MFLINK capability presented here will allow us to cover this I/O wall-clock time with computations. The procedure is as follows.

When the model begins, a secondary job on a different account also begins. This secondary job is the staging job. It communicates with the model through a common "talkfile" located in a pool. The variables read from this file tell it when it should wake up and begin the MFLINK of the data. It also contains the strings for the MFLINK as well as several communication parameters. The model writes the file and lets the program know what time to begin the MFLINK. It also will tell it when the model has finished so that the staging program can also end. In return, the staging program writes to the file that it is up and running and it has or has not successfully staged the data to tape. When the staging program "wakes up" to begin staging the data, it attempts to attach the files to be staged. The model will give these files to the account when they are ready to be staged. After they have been successfully staged, they are given back to the model account for reuse.

PRECEDING PAGE BLANK NOT FILMED

IV. SUMMER LECTURE SERIES

PRECEDING PAGE BLANK NOT FILMED

June 27, 1983

A DYNAMICAL BASIS FOR THE PARAMETERIZATION OF ORGANIZED
DEEP CONVECTION IN LARGE-SCALE NUMERICAL MODELS

M. W. Moncrieff/Imperial College, England

Cloud models used in present convective parameterization schemes are extremely simple and most schemes do not incorporate cloud models. As a result, quantities such as horizontal momentum are either crudely represented (or more usually ignored) and downdraught transports are generally not represented explicitly. More significantly, the transport of thermodynamical and dynamical quantities are never consistently formulated because dynamical cloud models are not currently used in convective parameterization schemes.

Observational case studies and numerical simulations over recent years have shown that deep convection can assume a number of distinct regimes. These vary from clouds with transient updraughts and downdraughts to highly organized quasi-steady severe storms and squall lines. It has been shown that synoptic scale control by the vertical shear and localized convergence are crucially important, particularly when related to the convective available potential energy. It is therefore unlikely that a single type of cloud model can be expected to adequately represent convective transports.

It is not known at present if dynamical models are essential in convective parameterization, but obviously the hypothesis should be tested. It is generally accepted that organized convection can directly affect the structure of certain mesoscale and subsynoptic systems such as hurricanes, cloud clusters, convective complexes, squall lines, etc. However, present large scale simulation models cannot resolve these features and parameterized clouds can only influence the large-scale fields through differential heating/drying, boundary layer and radiative interactions. Future high resolution models and mesoscale models in particular may be more sensitive to dynamical parameterization than current models and sophisticated cloud models should be of interest in this context.

A hierarchy of steady, nonlinear, semi-analytic models of different types of convection have been produced by the author and colleagues (Moncrieff and Green, 1972; Moncrieff and Miller, 1976; Moncrieff, 1978, 1981; Thorpe, Miller and Moncrieff, 1980, 1982). These provide a theoretical framework for determining the cloud outflow fluxes of both dynamic and thermodynamic quantities, which can be used to formulate dynamical transports in parameterization schemes. This has been achieved by exploiting certain Lagrangian conservation properties of steady flow, from which an equation for the vertical displacement of particles can be obtained and the outflow entropy, energy and momentum fluxes and the inflow/outflow mass fluxes can be determined from solution to the equation. These fluxes are determined in terms of grid-scale parameters such as convective available potential energy (CAPE), cloud layer shear, and horizontal pressure gradients. One of the significant features is that a number of dynamically distinct regimes of convection can be shown to exist. Five main types of system (called Classical, Steering-level, Jump, Propagating and Cellular) models are identified, respectively representing arche-types of convection in zero shear, large shear, mid-latitude squall lines, tropical squall lines and cellular convection. The downdraught is an important aspect in the first four of these and the cloud scale transport of momentum is very distinctive, in some cases counter-gradient.

Two main processes need to be represented in parameterization. First, and most important, the subsidence drying and warming which exists as a response to the convective transports and second, the outflow fluxes (detrainment) into the environment. The models referred to above express the outflow fluxes in analytic form in terms of grid-scale variables and parameters. Moreover, the subsidence can be determined analytically by making the simple assumption (necessary in present formulation of convective parameterization) that convective mass balance is achieved on the gridscale, together with the assumption that the cloud updraught area is much smaller than the grid area. Hence, both the horizontal and vertical fluxes can be calculated directly for the cloud models and a closed scheme obtained. In reality the gridscale response to cloud mass transports is more complicated, but this requires further investigation and analysis for instance to establish dynamical adjustment theory.

At the present time, the convective amplitudes are obtained by specifying the cloud induced inflow shear, which effectively means specifying an inflow Richardson number in the case of the Classical and Steering-level models. It would be interesting to explore alternative closure assumptions, and to investigate the possibility of using the dynamical cloud models in association with other parameterization techniques.

REFERENCES

- Moncrieff, M. W., and J. S. A. Green, 1972: The propagation and transfer properties of steady convective overturning in shear. Quart. J. Roy. Met. Soc., 98, 336-352.
- Moncrieff, M. W., and M. J. Miller, 1976: The dynamics and simulation of tropical cumulonimbus and squall lines. Quart. J. Roy. Met. Soc., 102, 373-394.
- Moncrieff, M. W., 1978: The dynamical structure of two-dimensional steady convection in constant vertical shear. Quart. J. Roy. Met. Soc., 104, 543-567.
- Moncrieff, M. W., 1980: A theory of organised steady convection and its transport properties. Quart. J. Roy. Met. Soc., 107, 29-50.
- Thorpe, A. J., M. J. Miller, and M. W. Moncrieff, 1980: Dynamical models of two dimensional updraughts. Quart. J. Roy. Met. Soc., 107, 463-485.
- Thorpe, A. J., M. J. Miller, and M. W. Moncrieff, 1982: Two dimensional convection in non-constant shear: A model of mid-latitude squall lines. Quart. J. Roy. Met. Soc., 108, 757-760.

July 12, 1983

SOME PROPERTIES OF TRANSIENT PHENOMENA IN THE EXTRA-TROPICAL REGION
AND THEIR IMPORTANCE IN THE SEASONAL MEAN FLOW

B. J. Hoskins/University of Reading, England

In recent years, numerical simulations of the growth and decay of baroclinic waves have provided a lot of information on the zonally averaged fluxes of heat and westerly momentum by such waves. However, observational studies have increasingly focused on the time averaging operator and the latitude-longitude distribution of transient eddy behavior, and much more understanding of this is required.

It is convenient, when studying data for one season, to divide the transient eddies into those on the synoptic time-scale and those of lower frequency. Where the dividing line is placed is not crucial, but a ten-day period is used in the study described here for the Northern Hemisphere 1979-1980 winter. The synoptic time-scale eddies exhibit maximum kinetic energy in storm-tracks slightly downstream and poleward of the Atlantic and Pacific jet maxima. Their vector heat flux convergence is largest at lower tropospheric levels and takes the form of a mean heating poleward of the storm-track and cooling on the equatorial flank. In the three-dimensional domain it is not sufficient to discuss the westerly momentum flux by the eddies; the effect on the mean vertical component of vorticity must be considered. However, the eddy vorticity flux convergence is dominated by the smallest scales, and is not easily related to qualitative features of the eddies.

An alternative approach is via the anisotropic part of the horizontal velocity correlation tensor which has components $M = 1/2 \overline{u'^2 - v'^2}$ and $N = \overline{u'v'}$. The axis of this tensor gives the local orientation of the eddies and the magnitude a measure of the extension of the eddies. When the velocity field is almost that of plane waves, the horizontal group velocity relative to the mean flow is also related to this tensor. Finally, the eddy vorticity flux convergence may be written in terms of second derivatives of M and N . An approximation which is generally valid for the eddies under consideration allows all these features to be simply related to the "vector" $\underline{E} = (-2M, -N) = (\overline{v'^2 - u'^2}, -\overline{u'v'})$.

For the synoptic time-scale eddies, \underline{E} points predominantly downstream in the storm-tracks, associated with the meridional extension of these eddies. The divergence of \underline{E} at the start of the storm-track implies a tendency to accelerate the mean flow in that region. Thus the synoptic time-scale eddies force the mean flow in the sense of reducing the baroclinic component but increasing the barotropic component in the upstream region of the storm-track.

The lower frequency eddies have a very different signature. Their kinetic energy is predominantly in the jet exit regions, in particular in the Pacific. As shown by their \underline{E} , their structure corresponds to an oscillation in the position of the exit of the jet. The sense of the mean vorticity forcing is such as to decrease the mean flow where it is strong and increase it where it is weak, acting in the sense of converting mean to eddy kinetic energy. The heat flux by these eddies appears to be less important.

A consistent picture of the feedback of different time-scales onto the seasonal mean flow is beginning to emerge from data studies, and modeling studies are being planned which will test the hypothesized linkages.

LOW FREQUENCY VARIABILITY AND TROPICAL-EXTRATROPICAL INTERACTIONS

Dennis L. Hartmann/University of Washington-Seattle

Currently there is intense interest in interactions between the tropics and mid-latitudes because of the association between seasonal anomalies in the two regions. In this investigation the relationships between mid-latitude 500 mb anomalies and tropical heating anomalies on time scales of weeks to seasons are studied using outgoing IR to characterize the tropical convective heating. The data are first used to form 5-day means and the mean seasonal cycle and the interannual variability of seasonal means are then removed. The time scales considered are then between about 10 days and 90 days.

By correlating the mid-latitude height anomalies with the tropical precipitation anomalies it can be shown that, on the time scales considered here, the predominant correlation patterns are those associated with Rossby waves propagating from mid-latitudes into the tropics and influencing the tropical convection. The mid-latitude Rossby waves can significantly influence convection to within 5 degrees of the equator.

During Northern Hemisphere winter the convection anomalies over the northwestern tropical Pacific Ocean (~10N, 140E) are significantly correlated with 500 mb height anomalies over the entire Western Hemisphere, including the Atlantic Ocean sector. The pattern of this correlation is very suggestive of the patterns produced by forcing a model with a zonally varying basic state which is barotropically unstable.

In summary, most of the coupling between mid-latitudes and tropics during Northern Hemisphere winter seems to result from Rossby waves originating in middle latitudes, propagating into the tropics and influencing the circulation and convection there. One important source of low frequency variability in mid-latitudes is the barotropic instability produced by the east-west variations in the time-mean state. These facts are likely to prove important in extended range forecasting.

UNIT
75
2113

V. RECENT PUBLICATIONS

RECENT PUBLICATIONS

- Atlas, R., W. E. Baker, E. Kalnay, and M. Halem, 1983: Application of scatterometer data to global weather prediction. Research Activities in Atmospheric and Oceanic Modeling.
- Baker, 1983: Objective analysis and assimilation of observational data from FGGE. Mon. Wea. Rev., 111, 328-342.
- Baker, W., and J. Paegle, 1983: The influence of the tropics on the prediction of ultralong waves. Part I: Tropical wind field. Mon. Wea. Rev., 111, 1341-1355.
- Balgovind, R., A. Dalcher, M. Ghil, and E. Kalnay, 1983: A stochastic-dynamic model for the spatial structure of forecast error statistics. Mon. Wea. Rev., 111, 701-722.
- Bloom, S. C., 1983: The use of dynamical constraints in the analysis of mesoscale rawinsonde data. Tellus, 35A, 363-378.
- Chen, T.-C., and J. Shukla, 1983: Diagnostic analysis and spectral energetics of a blocking event in the GLAS climate model simulation. Mon. Wea. Rev., 111, 3-22.
- Daunt, S. J. A., T. Atakan, W. E. Blass, G. W. Halsey, D. E. Jennings, D. C. Reuter, J. Susskind, and J. W. Brault, 1983: The 12 μm band of ethane: A high resolution laboratory analysis. Astrophysical J., in press.
- Duffy, D., and R. Atlas, 1983: Significant wave height predictions utilizing Seasat scatterometer data. EOS, 64, 1062.
- Ghil, M., and J. Tavantzis, 1983: Global Hopf bifurcation in a simple climate model. SIAM J. Appl. Math., 1019-1041.
- Ghil, M., and M. Buys, 1983: Mathematical methods of celestial mechanics illustrated by simple examples of planetary motion. Milankovitch and Climate: Understanding the Response to Orbital Forcing, A. Berger, J. Hays, J. Imbrie, G. Kukla and B. Saltzman (eds.), Reidel, Dordrecht/Boston, in press.
- Ghil, M., R. Benzi, and G. Parisi, 1983: Turbulence and Predictability in Geophysical Fluid Dynamics and Climate Dynamics. North-Holland Publ. Co., in press.
- Goswami, B. N., 1983: Theoretical study of multiple equilibria in simple axisymmetric tropical circulations. Tellus, 35A, 119-135.
- Harrison, D. E., and Stephen Stalos, 1983: On the wind-driven ocean circulation. J. Mar. Res., 40, 773-791.
- Helfand, H. M., and E. Kalnay, 1983: A mechanism for open or closed cellular convection. J. Atmos. Sci., 40, 631-650.

- Helfand, H. M., and J. Labraga, 1983: A level 2.4 second-order closure model for the prediction of turbulence. Research Activities in Atmospheric and Oceanic Modelling. I. D. Rutherford, ed., GARP Working Group on Numerical Experimentation.
- Hoffman, R., and E. Kalnay, 1983: Lagged average forecasting, an alternative to Monte Carlo forecasting. Tellus, 35A, 100-118.
- Kalnay, E., and R. Atlas, 1983: Global analyses of ocean surface fluxes using Seasat scatterometer winds. EOS, 64, 1069.
- Kalnay, E., and R. Livezey, 1983: Weather predictability beyond a week: An introductory review. Turbulence and Predictability in Geophysical Fluid Dynamics and Climate Dynamics. (M. Ghil, R. Benzi and G. Parisi, eds.), North-Holland, in press.
- Labraga, J., and H. M. Helfand, 1983: Selection of a best candidate higher-order closure scheme for turbulence in the GLAS Fourth Order GCM. Research Activities in Atmospheric and Oceanic Modelling. I. D. Rutherford, ed., GARP Working Group on Numerical Experimentation.
- Le Treut, H., and M. Ghil, 1983: Orbital forcing, climatic interactions, and glaciatic cycles. J. Geophys. Res., 88C, 5167-5190.
- Merkine, L., and R. Balgovind, 1983: Barotropic instability of weakly non-parallel zonal flows. Geophys. Astrophys. Fluid Dynamics, 25 157-190.
- Navon, I. M., and R. deVilliers, 1983: Combined penalty multiplier optimization methods to enforce integral invariants conservation. Mon. Wea. Rev., 111, 1228-1243.
- Navon, I. M., 1983: Conservation laws in fluid dynamics and the enforcement of their preservation in numerical discretizations. Seminar on the Numerical Solution of Partial Differential Equations, February 1983, Pretoria, pp. 1-57.
- Navon, I. M., 1983: A Numerov-Galerkin technique applied to a finite-element shallow water equations model with enforced conservation of integral invariants and selective lumping. J. Comp. Physics, 52, 313-339.
- Paegle, J., and W. E. Baker, 1983: The influence of the tropics on the prediction of ultralong waves. Part II: Latent heating. Mon. Wea. Rev., 111, 1356-1371.
- Randall, D. A., 1983: On the joint bimodality of temperature and moisture near stratocumulus tops. NASA Tech. Memo. 84962, 19 pp.
- Shukla, J., and K. C. Mo, 1983: Seasonal and geographical variation of blocking. Mon. Wea. Rev., 111, 388-402.
- Shukla, J., and D. S. Gutzler, 1983: Interannual variability and predictability of 500 mb geopotential heights over the Northern Hemisphere. Mon. Wea. Rev., 111, 1273-1279.

- Shukla, J., and J. M. Wallace, 1983: Numerical simulation of the atmospheric response to equatorial Pacific sea surface temperature anomalies. J. Atmos. Sci., 40, 1613-1647.
- Shukla, J., 1983: Comments on natural variability and predictability. Mon. Wea. Rev., 111, 581-585.
- Shukla, J., and Daniel A. Paolino, 1983: The Southern oscillation and long range forecasting of the summer monsoon rainfall over India. Mon. Wea. Rev., 111, 1830-1837.
- Straus, David M., 1983: On the role of the seasonal cycle. J. Atmos. Sci., 40, 303-313.
- Suarez, M., A. Arakawa, and D. Randall, 1983: The parameterization of the planetary boundary layer in the UCLA general circulation model: Formulation and results. Mon. Wea. Rev., 111, 2224-2243.
- Suarez, M., and A. Arakawa, 1983: Vertical differencing of the primitive equations in sigma-coordinates. Mon. Wea. Rev., 111, 34-45.
- Susskind, J., J. Rosenfield, and D. Reuter, 1983: An accurate radiative transfer model for use in the direct physical inversion of HIRS2 and MSU temperature sounding data. J. Geophys. Res., 88C, 8550-8568.
- Susskind, J., 1983: Vertical temperature sounding of the atmosphere. Satellite Sensing of the Third Planet. A. Henderson Sellers, eds., Taylor and Francis Ltd. London., in press.
- Takacs, L. L., and R. C. Balgovind, 1983: High-latitude filtering in global grid-point models. Mon. Wea. Rev., 111, 2005-2015.

VI. GMSB STAFF

PRECEDING PAGE BLANK NOT FILMED

GMSB STAFF

Civil Service

Robert Atlas
Wayman Baker
Dean Duffy
Mark Helfand
Eugenia Kalnay
David Randall
Debora Sabatino
Jagadish Shukla
David Straus
Max Suarez
Yogesh Sud
Joel Susskind

USRA

Steve Bloom
I. M. Navon
Dennis Reuter
Richard Wobus
Noah Wolfson

RRAs

Jeff Augenbaum
Reinout Boers
Jim Kinter
Siegfried Schubert
Fredrick Semazzi
Glenn White
Carl Youngblut

M/A-COM Sigma Data

Jim Abeles
Manina Almeida
Greg Avesian
Ramesh Balgovind
Bill Battle
Yevgenia Brin
Sol Broder
Herb Carus
Tom Corsetti
Amnon Dalcher
Cheryl Derrington
John Dlouhy
Ron Dlouhy
Greg Dozier
Jim Edelmann
Mike Fennessy
Jim Firestone
Lena Fornito
Jane Hamelink
Kyle Henderson
Dan Iredell
Sarah Jackson
Bert Katz
Dave Lamich
Min-Nan Lee
Sung-Yung Lee
Mike Mandelberg
Larry Marx
Kingtse Mo

FRAs

Mark Cane
Michael Ghil
Ed Harrison
M.-J. Munteanu
Y. Mintz

Mark Nestler
Minh Nguyen
Dan Paolino
Jim Pfaendtner
Bill Phillips
Ernie Pittarelli
Sandy Postman
Andy Pursch
Bob Rosenberg
Joan Rosenfield
Laura Rumburg
Kathy Schmidt
Richard Sciafford
Stan Scott
Butch Sheppard
Brian Sherbs
Bill Smith
Marie Smoes
Steve Stalos
Farhad Tahmasebi
Lawrence Takacs
Joseph Terry
Lora Thompson
Dave Wallace
Mary Ann Wells
Jack Woollen
Barbara Worley
Peter Wu

PRECEDING PAGE BLANK NOT FILMED

VII. AUTHOR INDEX

PRECEDING PAGE BLANK NOT FILMED

Abeles, J.	171, 222, 231, 343	Moncrieff, M. W.	347
Atlas, R.	1, 2, 7, 14, 53	Munteanu, M.-J.	23, 45, 65, 68
Augenbaum, J.	87, 90	Navon, I. M.	106, 150
Baker, W.	1, 7, 14	Paolino, D.	180
Balgovind, R. C.	131	Pfaendtner, J.	113
Bloom, S.	95, 101, 106	Piraino, P.	23, 45, 60, 65, 68
Carlson, T.	323	Pittarelli, E.	171
Cohn, S.	87	Pursch, A.	53
Corsetti, T.	215, 247, 251	Rambaldi, S.	219
Dlouhy, R.	5, 6	Randall, D.	171, 215, 247, 251, 254, 257, 261, 266, 323
Duffy, D.	14	Reuter, D.	28, 33, 41, 60
Fennessy, M. J.	301	Schopf, P.	233
Firestone, J.	2	Schubert, S.	157
Halem, M.	1, 5, 6, 7, 14,	Semazzi, F.	164
Harshvardhan	251	Shukla, J.	180, 185, 196, 219 301, 312
Hartmann, D. L.	350	Smith, W. E.	270, 335, 329
Helfand, H. M.	14	Straus, D. M.	175, 185
Hoffman, R.	79, 141	Suarez, M.	171, 215, 222, 227, 231, 233, 251, 275, 343
Hoskins, B. J.	205, 349	Sud, Y.	196, 270, 285, 329, 335
Jacobowicz, O.	65, 68	Susskind, J.	1, 28, 33, 41, 45, 49, 53, 60, 292
Kalnay, E.	1, 7, 14, 23, 49, 68, 79, 141, 149	Takacs, L. L.	79, 106, 119, 131
Katz, B.	175	White, G.	193, 205, 209
Lindzen, R. S.	175	Wobus, R. L.	239, 292
Livezey, R.	149	Wu, M.-L.	292
Marchesin, D.	87	Youngblut, C.	243, 245
Marx, L.	301, 312		
Mintz, Y.	323		
Mo, K.	190, 193, 219		
Moeng, C.-H.	254		